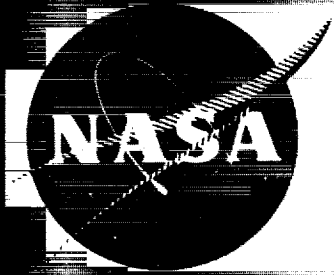


N 70 14384

NASA CR-72498

UURL H910254-50



SYSTEMATIC TWO-DIMENSIONAL CASCADE TESTS

VOL. 1 - DOUBLE CIRCULAR-ARC HYDROFOILS

by

W. L. Taylor, T. A. Murrin, R. M. Colombo

UNITED AIRCRAFT RESEARCH LABORATORIES

Prepared for

NATIONAL AERONAUTICS AND SPACE ADMINISTRATION

NASA Lewis Research Center

Contract NAS3-4184

Werner R. Britsch, Project Manager

CASE FILE
COPY

NOTICE

This report was prepared as an account of Government-sponsored work. Neither the United States, nor the National Aeronautics and Space Administration (NASA), nor any person acting on behalf of NASA:

- A.) ~~Makes any warranty or representation, expressed or implied, with respect to the accuracy, completeness, or usefulness of the information contained in this report, or that the use of any information, apparatus, method, or process disclosed in this report may not infringe privately-owned rights; or~~
- B.) ~~Assumes any liabilities with respect to the use of, or for damages resulting from the use of, any information, apparatus, method or process disclosed in this report.~~

As used above, "person acting on behalf of NASA" includes any employee or contractor of NASA, or employee of such contractor, to the extent that such employee or contractor of NASA or employee of such contractor prepares, disseminates, or provides access to any information pursuant to his employment or contract with NASA, or his employment with such contractor.

Requests for copies of this report should be referred to

National Aeronautics and Space Administration
Scientific and Technical Information Facility
P. O. Box 33
College Park, Md. 20740

NASA CR-72498
UARL H910254-50

CONTRACTOR REPORT

SYSTEMATIC TWO-DIMENSIONAL CASCADE TESTS

VOL. 1 - DOUBLE CIRCULAR-ARC HYDROFOILS

by

W. E. Taylor, T. A. Murrin, R. M. Colombo

UNITED AIRCRAFT RESEARCH LABORATORIES
East Hartford, Connecticut 06108

Prepared for

NATIONAL AERONAUTICS AND SPACE ADMINISTRATION

December 19, 1969

CONTRACT NAS3-4184

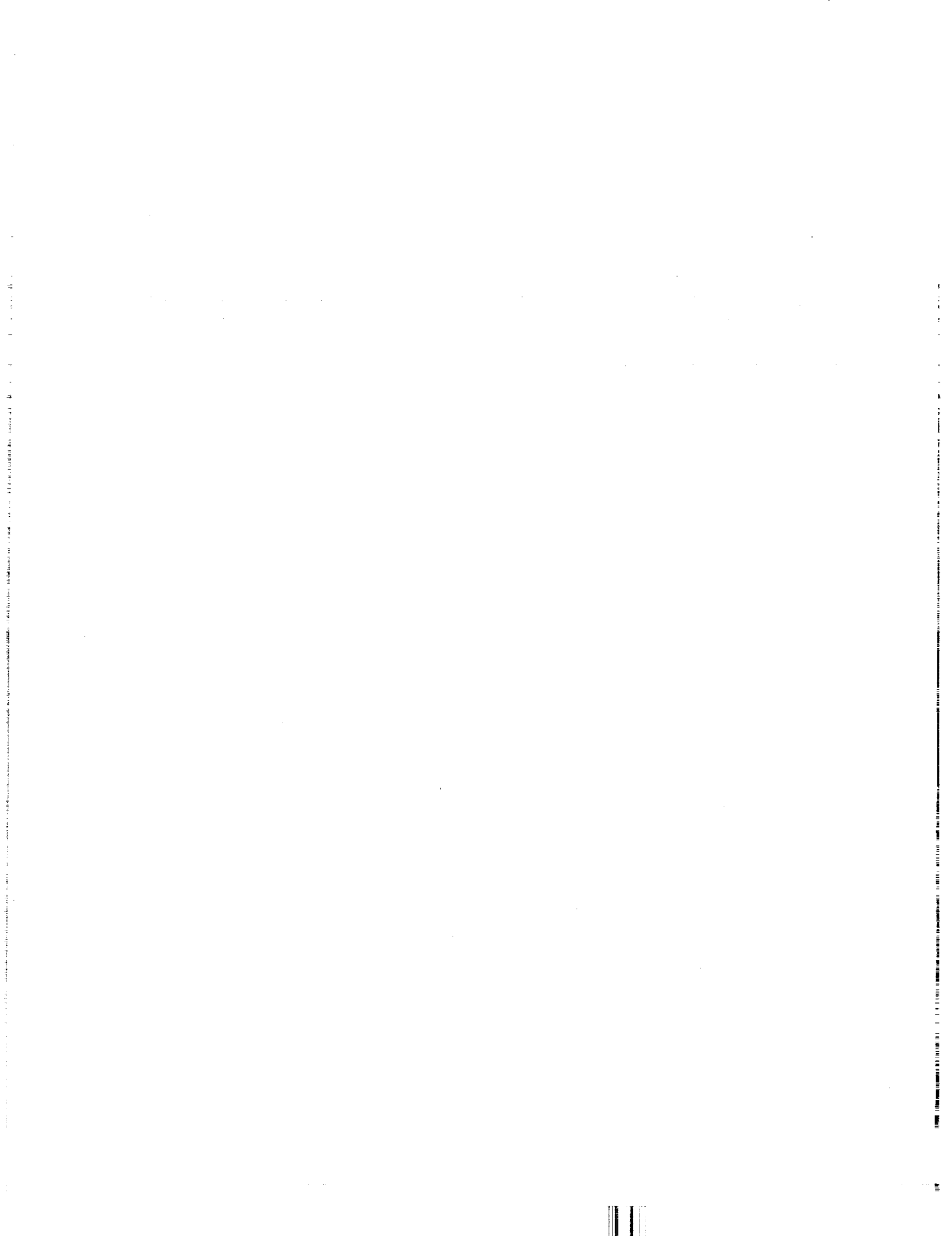
NASA Lewis Research Center
Cleveland, Ohio

Werner R. Britsch, Project Manager
Liquid Rocket Technology Branch



FOREWORD

The experimental investigation described herein, which was conducted by the Research Laboratories of the United Aircraft Corporation, was performed under NASA Contract NAS3-4184. The work was done under the management of the NASA Project Manager, Mr. Werner R. Britsch, Liquid Rocket Technology Branch, NASA Lewis Research Center. Technical direction was provided by L. J. Herrig, Special Projects Division, NASA Lewis Research Center.



Report CR-72498

Systematic Two-Dimensional Cascade Tests

Vol. 1 - Double Circular-Arc Hydrofoils

TABLE OF CONTENTS

	<u>Page</u>
FOREWORD	iii
LIST OF ILLUSTRATIONS	ix
ABSTRACT	xi
SUMMARY	1
INTRODUCTION	2
ACKNOWLEDGMENTS	3
TEST APPARATUS	
UARL Cascade Water Tunnel	
<u>Basic Considerations</u>	4
<u>Facility Configuration</u>	4
<u>Cascade Test Section</u>	6
Hydrofoil Profiles	
<u>Basic Profile</u>	8
<u>Static Pressure Instrumentation</u>	8
<u>Slotted Hydrofoils</u>	8

TABLE OF CONTENTS
(Contd.)

	<u>Page</u>
Instrumentation	9
PROCEDURES	
Test Program	10
Test Procedure	11
Data Reduction Procedure	13
PRESENTATION OF RESULTS	14
DISCUSSION	
Flow Distributions	16
Cascade Performance	16
<u>Total Pressure Loss Coefficient</u>	16
<u>Turning Angle</u>	17
<u>Diffusion Factor</u>	17
<u>Wake Momentum Thickness Ratio</u>	18
<u>Static Pressure Rise Coefficient</u>	18
Hydrofoil Pressure Distributions	18
Cavitation Index	19
DATA CORRELATION AND COMPARISON	
Minimum Loss	20
Carpet Plot	20
Pressure Distributions	21

TABLE OF CONTENTS
(Concluded)

	<u>Page</u>
CONCLUDING REMARKS	22
APPENDIX I - Equations for Data Reduction	25
APPENDIX II - List of Symbols	28
REFERENCES	31
TABLE I - Coordinates for Double Circular-Arc Profiles	32
TABLE II - Index to Cascade Test Configurations	34



LIST OF ILLUSTRATIONS

Figure

- 1 Cascade Water Tunnel
- 2 Water Tunnel Inlet Installation
- 3 Cascade Test Section
- 4 Porous Side Wall Assembly
- 5 Double Circular-Arc Profiles
- 6 Location of Static Pressure Instrumentation: Suction and Pressure Surfaces
- 7 Static Pressure Instrumentation in 40-Deg Camber Double Circular-Arc Hydrofoils
- 8 Slot Configuration for Double Circular-Arc Hydrofoils
- 9 Slotted Double Circular-Arc Hydrofoil
- 10 Directional Probes
- 11 Data Acquisition System
- 12 Cascade Nomenclature
- 13 Cascade Flow Distributions: $i = -4$ deg
- 14 Cascade Flow Distributions, Spanwise: $i = 1$ deg
- 15-110 Cascade Characteristics as Functions of Incidence
- 111 Pressure Distribution for Double Circular-Arc Hydrofoils
- 112 Pressure Distribution for Slotted Double Circular-Arc Hydrofoils
- 113 Cavitation on a Cascade of Double Circular-Arc Hydrofoils
- 114 Propagating Cavitation on a Cascade of Double Circular-Arc Hydrofoils

LIST OF ILLUSTRATIONS
(Concluded)

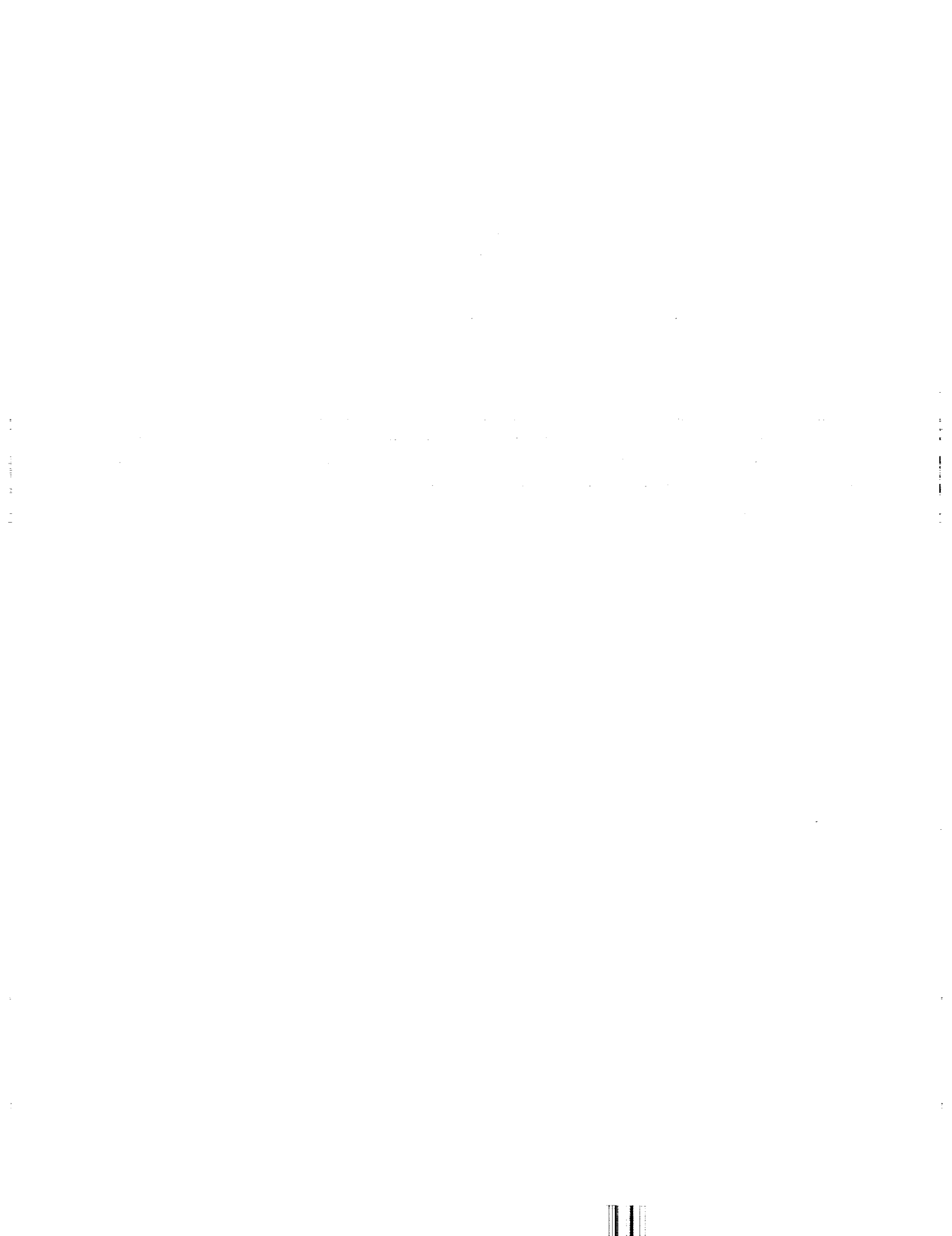
Figure

- 115 Reference Minimum-Loss Incidence Angle for Zero-Degree Camber Double Circular-Arc Hydrofoils
- 116 Slope Factor for Reference Minimum-Loss Incidence Angle - Double Circular-Arc Hydrofoils
- 117 Reference Minimum-Loss Deviation Angle for Zero-Degree Camber Double Circular-Arc Hydrofoils
- 118 Slope Factor for Reference Minimum-Loss Deviation Angle - Double Circular-Arc Hydrofoils
- 119 Incidence and Deviation Angles for Minimum Total Pressure Loss Coefficient
- 120 Turning Angle Carpet Plots for Double Circular-Arc Hydrofoils

ABSTRACT

Performance parameters and incipient cavitation indices are presented for double (Vol. 1) and multiple (Vol. 2) circular-arc hydrofoils tested over a range of systematically introduced variables in a rectilinear cascade tunnel which uses water as the test medium. Cascade configurations included various combinations of an inlet flow angle ($\beta_{IN} = 50, 60, 70$ and 75 deg), a cascade solidity ($\sigma = 0.75, 1.00$ and 1.50) and angles of incidence between positive and negative stall.

For a range of corresponding cascade variables, test results with the double circular-arc hydrofoils indicate the probability of correlating water tunnel cascade data with results from cascade tests wherein air was used as the test medium, since similar trends for the test parameters are evident. Correlations of incidence angle at the minimum loss point are in excellent agreement; correlations of deviation angle at the minimum loss point indicate maximum differences of less than three degrees.



SUMMARY

Performance parameters and incipient cavitation indices were measured for cascades of two families of different circular-arc type profiles: one profile family was developed by superimposing a symmetrical double circular-arc base profile on various circular-arc mean camber lines; the second was developed by superimposing a symmetrical multiple circular-arc base profile on various NASA four-digit series (M606) mean camber lines. Cascade configurations included various combinations of an inlet flow angle ($\beta_{1N} = 50, 60, 70$ and 75 deg), a cascade solidity ($\sigma = 0.75, 1.00$ and 1.50) and an incidence angle between positive and negative stall. For each configuration, measurements were obtained for presenting the following performance parameters as functions of incidence angle: total pressure loss coefficient (\bar{w}), turning angle (θ), deviation angle (δ°), diffusion factor (D), wake momentum thickness ratio (θ^*/s), cascade static pressure rise coefficient ($\Delta p/q_1$) and cavitation index (K). Results from cascade tests with a family of double circular-arc hydrofoils are reported in Vol. 1, and results from cascade tests with a family of multiple circular-arc hydrofoils are reported in Vol. 2.

In addition to presenting the performance of eleven different double circular-arc hydrofoils tested in systematically varied cascade geometries, Vol. 1 contains performance data for cascades of slotted 40 and 45-deg camber, double circular-arc hydrofoils and surface pressure distributions for cascades of slotted and unslotted 40-deg camber double circular-arc hydrofoils. These cascades were tested at an inlet flow angle of 60 deg, solidities of 0.75, 1.00 and 1.50 and a range of incidence angles between positive and negative stall.

The incidence and deviation angles corresponding to the point of minimum total pressure loss coefficient were correlated and are presented as functions of the inlet angle. Summary plots in the form of carpet plots are also presented which illustrate the variation in turning angle as a function of angle-of-attack with the variables, inlet flow angle, cascade solidity and hydrofoil camber angle. For each cascade configuration, the value of incidence angle for minimum total pressure loss coefficient and the deviation angle at this incidence are compared with the values determined from an empirical correlation which was based upon experimental data obtained with cascades which used air as the test medium.

The test results indicate systematic changes in the performance parameters with changes in the test geometries and also that these water cascade data may be readily correlated with two-dimensional cascade data obtained using air as the test medium.

INTRODUCTION

In order to meet future demands for high efficiency, low weight and improved cavitation characteristics in pumping equipment, continued refinement is required in the accuracy and range of applicability of both the experimental data and the analytical procedures which form the basis for modern pump design techniques. For many applications involving high flow rates, such as in large liquid fuel rocket engines, the above performance requirements are best satisfied by multi-stage axial-flow pumps. At the present time, one of the more successful techniques for the selection of blade geometries for the various radial stations in axial-flow machinery is based upon the use of data obtained from experiments in two-dimensional, rectilinear cascades.

A substantial amount of the cascade data, compiled by a number of investigators to support axial-flow compressor development, can be applied to pump design. However, these data are deficient in two important respects: 1) the inlet flow angle range to which the data apply does not include all conditions of interest in pump design, for example, large inlet angles relative to the axial direction, and 2) information relative to cavitation performance of the blade elements is not available.

A water tunnel was designed and erected at the United Aircraft Research Laboratories (UARL) in which cascade tests may be performed under cavitating and noncavitating conditions throughout a range of cascade variables. Under Contract NAS3-4184, with the National Aeronautics and Space Administration, certain modifications were made to the facility to increase the degree of control over the test section flow, and an experimental program was initiated to determine the two-dimensional turning and loss performance and the cavitation index of a series of double circular-arc hydrofoils which were tested with various combinations of flow angles relative to the cascade inlet plane, flow angles relative to the blade mean line (incidence angle) and spacings between adjacent hydrofoils. The broad range of these test variables enabled the correlation of a design reference point and the presentation of the test data in the form of carpet plots which are useful for design evaluations. In addition, these data extend the available compilation of two-dimensional cascade data to include both other fluids and higher inlet flow angles. The data therefore provide the means for correlating liquid and air cascade data and extending the range of fundamental empirical data as required for blade element design of axial-flow turbomachinery.

ACKNOWLEDGMENTS

Recognition is extended to W. F. Perkins¹ for his many contributions to the design and operation of the water tunnel facility and to the analytical procedures required for machine computation of the test data; to K. L. Dauphinais² for writing and checking the machine program required for data reduction; to F. S. Owen³ for his technical and administrative guidance during the major period of the contract.

1 Lockheed Aircraft Corporation

2 Project Analyst, United Aircraft Research Laboratories

3 Manager, Propulsion Laboratory, United Aircraft Research Laboratories

TEST APPARATUS

UARL Cascade Water Tunnel

Basic Considerations

In a rectilinear cascade, a linear two-dimensional array of blades is used to simulate the blade geometry at a discrete radial location in a three-dimensional axial-flow machine. Measurements can then be obtained for determining the static pressure rise, total pressure loss coefficient and flow turning angle for this blade profile and blade spacing at various angles of incidence. By testing cascades which simulate different radial stations, the flow characteristics through the blade rows in an axial-flow stage may be approximated by stacking the two-dimensional performance measurements of the blade elements.

A basic goal in the design of a cascade test section is that the flow in the cascade test apparatus approximates the two-dimensional flow that would exist in an infinite array of blades having infinite span. This requires that means be provided in the test equipment to control wall boundary layer development and to contour the walls confining the flow so that the interference produced by the walls is minimized. Additional design specifications related to cascade performance testing are that the test apparatus have the flexibility to accommodate various cascade geometries and that the blade Reynolds number be greater than 2.5×10^5 to minimize the possibility of laminar separation from the blade surfaces.

In order to conduct cavitation tests under controlled conditions, the design of the flow circuit must be such that: 1) cavitation will occur on the test blades before it occurs on the circuit components; 2) the system will permit operation with test section pressures which are above and below atmospheric pressures; 3) contamination of the test medium by solid particles, dissolved ions and dissolved gases will be minimized, since these contaminants may become nuclei for premature formation of cavitation.

Facility Configuration

Overall design of the water tunnel was largely dictated by the requirements for determining cascade cavitation coefficients and avoiding cavitation elsewhere in the test loop. The facility was therefore designed as a vertical, variable-pressure, closed loop arranged such that the main components of the test section are accessible from ground level. The test section is oriented such that the inlet plane of the cascade is horizontal to eliminate hydrostatic pressure gradients along the length of the cascade, which would otherwise affect blade cavitation inception. In order to provide sufficient net positive suction head at the pump

inlets to prevent pump cavitation, the water circulating pumps are located at the lowest point in the test loop.

A drawing of the water tunnel is shown in Fig. 1. In this vertical flow circuit, the flow is discharged from the pumps, diffused and turned in a system of ducts and settled in a rectangular chamber containing both a honeycomb flow straightener and graded-porosity screens for reducing large scale turbulence. Subsequent guide vane sections provide the required flow alignment and a means for attachment between the settling chamber and interchangeable cascade inlet nozzles. The flow is first accelerated by the inlet nozzle, then passed through the cascade test section and finally discharged into a large plenum tank from which the flow completes the circuit to the circulating pumps.

The flow is accelerated to the prescribed velocity relative to the test section by means of one of the four interchangeable nozzles which were designed for inlet flow angles of 50, 60, 70 and 75 deg as measured relative to the axial direction (which is normal to the cascade inlet plane). The design of the nozzles was greatly influenced by factors related to cavitation testing. The horizontal orientation of the cascade inlet plane required the nozzle to accelerate the flow downward to the cascade plane from the region of low static head which is present at the top of the inlet ducting. Therefore, the maximum vertical distance between the blade leading edge plane and the top of the inlet ducting was limited to the dynamic head at the test section. This insured lower static pressures at the cascade than at the top of the ducting, thereby minimizing the possibility of cavitation in this ducting. This dimension placed design restrictions on not only the maximum length available for the inlet nozzle but also the maximum height of the inlet cross section. This height, and a width which was restricted by the diameter of the plenum tank, limited the area contraction ratios of the relatively short inlets to 9.08, 11.4, 11.1 and 14.2 for the 50, 60, 70 and 75-deg nozzles, respectively. The contours for the nozzle walls were selected from an analysis of minimum length, two-dimensional contractions for accelerating flow (Ref. 1). Installations of the 50 and 75-deg inlets with the test section assembly are shown in Fig. 2.

The cascade test section assembly is supported from the fixed head of a 10-ft diameter plenum tank. The plenum tank has an operating pressure range between one and 100 psia, as required for establishing the desired cavitating or non-cavitating test conditions, and contains windows at the sides and top for observation. Enclosing the test section assembly within a removable pressure shell (plenum tank) affords the advantages of: 1) allowing complete accessibility of the test section when the plenum is open; 2) permitting relatively light-weight construction of the test section assembly, since immersion of the test section in the test fluid insures that the differential pressures acting on the test

section walls are low throughout the operating pressure range of the tunnel; 3) minimizing the problem of air and water leakage in a test section which incorporates both interchangeable parts and variable geometry end walls and yet operates over a wide range of test pressures.

The three main flow pumps were fabricated from zinc-free bronzes and stainless steel. Each pump is driven by a 10 hp motor and is capable of delivering water flows at a rate of 1700 gpm with a head rise of 16 ft.

Contamination of the water used in the facility is minimized by special water processing equipment. In addition, the facility is constructed primarily of stainless steel to avoid solid particle shedding. Solid particles contained in the test medium are removed by various filters, one of which provides continuous three-micron filtration at a flow rate of 100 gpm. Dissolved minerals are removed from the test water by a commercial ion-exchange type demineralizer which provides water comparable to distilled water in conductivity, a measure of dissolved mineral content. The resistivity of the water from this unit was 10^6 ohms per centimeter. Dissolved gases may be removed by a cold-water deaerator which can reduce the gas content to three parts per million.

Cascade Test Section

The test section (Fig. 3) was designed to establish both a uniform flow along the cascade inlet plane and a periodic (blade-to-blade) flow downstream of the cascade. These are necessary conditions to insure that the flow about each blade is identical; accomplishment of these goals provides a flow which is representative of the flow through an infinite cascade. Approximations of flow uniformity and periodicity are achieved by removal of the wall boundary layers and by contouring the end walls to minimize undesirable perturbation of the mainstream flow.

The boundary layer which develops along the walls of the inlet nozzle is removed upstream of the test section by means of step-type slots located on all four walls of the nozzle (Fig. 3). The boundary layer flow intercepted by each of the four step slots is ducted through individual throttling valves to a common pump. Within the test section, porous side walls are used for removal of boundary layer flow in the immediate vicinity of the cascade as required for the simulation of two-dimensional flow through the cascade (Ref. 2). A porous wall assembly consists essentially of a rectangular plenum with an interchangeable porous metal wall which is fabricated from sintered woven wire mesh. A photograph of a porous side-wall assembly with the blades installed is presented in Fig. 4.

Perturbations of flow streamlines (to obtain uniformity) are accomplished by means of variable geometry end walls located at each end of the cascade as shown in Fig. 3. These end walls are comprised of three sections; a flexible wall which connects the rigid inlet nozzle end wall to an adjustable end wall, an adjustable end wall which is analogous to one surface of a cascade blade, and a tailboard which extends downstream from the adjustable end wall. Actuation of these endwall sections enables independent adjustment of the gap between the end blades of the cascade and the adjustable end wall, the angle of the adjustable end wall and the angle of the tailboard. The convex, flexible end wall is porous (Fig. 3) to permit removal of the endwall boundary layer, thereby decreasing any tendency toward flow separation from this surface. Flow through the flexible porous wall and each porous side wall is independently controlled.

Blade aspect ratio and the number of blades to incorporate into a cascade assembly are selected somewhat arbitrarily. An aspect ratio of two was chosen as a compromise between the structural problem of blade bowing or bending, that would be associated with high aspect ratio blades, and the undesirable three-dimensional flow effects, that would occur with low aspect ratio blades. A compromise was also made between the large number of blades desired for simulation of the infinite cascade and the practical considerations of cost and test section size. Based upon general information obtained from previous experimental testing at UARL with a cascade tunnel which used air as the test medium and from the experimental evidence from NASA cascade tests (Ref. 3), it was decided to establish five blades as the minimum number to be included at the greatest blade spacing (4 in.) considered in the current test program. These considerations, together with a specified minimum blade-chord Reynolds number of 5×10^5 and the selection of a 3-in. blade chord, established a minimum test section velocity of 22 ft per second. With a 5100 gpm facility pump capability, the maximum cascade inlet flow area for each of the inlet flow angles was known. In order to remain within these limits, a rectangular cross-section having a 6-in. span with a 24-in. length was selected for the 50 and 60-deg inlet nozzles and a 6-in. span with a 36-in. length was used for the 70 and 75-deg inlet nozzles.

The remaining considerations involved in selecting the test section configuration were primarily associated with the desire that the facility accommodate configuration changes with relative ease. For this purpose, the design included interchangeable sidewall components, to simplify changes in the blade spacing, and remote actuators to permit adjustment of blade incidence, flexible endwall contour and tailboard angle without the need for opening the large plenum tank.

Hydrofoil Profiles

Basic Profile

The double circular-arc profile, for which both upper and lower surfaces are defined by circular arcs, was selected as the basic test profile, and its performance therefore is being established to provide the basis against which the performance of alternate profiles may be judged.

The choice of the circular-arc profile was based upon its successful use at low supersonic velocities by virtue of a capability for delaying the onset of separation resulting from shock wave-boundary layer interaction. It was presumed that a profile which delays shock wave formations and their adverse effects should also delay the incidence of cavitation because both local supersonic regions and cavitation areas are introduced similarly by the blade profile pressure distributions.

The profiles are described by the camber angle (ϕ), which is the acute angle formed by the intersection of tangents to the profile meanline at the leading and trailing edges, and by the ratio of the maximum profile thickness to the chord length. The profiles of the hydrofoils for this test program (Fig. 5) include camber angles of 0, 10, 20, 25, 30, 40 and 45 deg, with a maximum thickness ratio of 6 percent, and camber angles of 0, 20, 30 and 40 deg, with a thickness ratio of 10 percent. Coordinates of the profiles are presented in Table I. The 3-in. chord, 6-in. span hydrofoil blades were fabricated from stainless steel and were polished to a surface finish of 8 microinches (rms). The leading and trailing edge radii were 0.10 percent of the blade chord. The blades were supported in the test section by stub shafts welded to the blade ends at the leading edge (Fig. 4) to simplify remote adjustment of incidence.

Static Pressure Instrumentation

Static pressure instrumentation was installed in two of the 6-percent thickness ratio, 40-deg camber angle hydrofoils for obtaining surface pressure distributions for a range of cascade test variables. Twelve 0.022-in. diameter orifices were drilled in the suction surface of one hydrofoil and 12 also in the pressure surface of the other hydrofoil at the locations shown in Fig. 6. Pressure was led out by means of stainless steel tubing laid in grooves milled into both the blade surface opposite the instrumented surface and along one of the stub shafts. The grooves were filled with an epoxy cement, and the surface was refinished to the original contour. Instrumented hydrofoils are shown in Fig. 7.

Slotted Hydrofoils

Both 40 and 45-deg camber hydrofoils were slotted to the configuration shown in Fig. 8; a slotted hydrofoil is shown in Fig. 9. The slot meanline penetrated

the suction surface at the 35-percent chord station and had an inclination of 31 deg relative to the blade chord line. The slot was tapered 8 deg and had a discharge height, normal to the slot meanline, of 0.0625 in. Webs, 0.140-in. wide at the 0 and 100 percent span stations and 0.063-in. wide at the 33.3 and 66.7 percent span stations, were retained to provide structural rigidity in the slotted hydrofoils. Static pressure taps were also installed in two of the 40-deg camber slotted hydrofoils at the locations shown in Fig. 6. Due to the location of the slot, static tap Number 4 on the suction surface and static tap Number 5 on the pressure surface were necessarily omitted. Locations of the pressure taps relative to the slot may be determined from Figs. 6 and 8. It may be noted from Fig. 8 that two static pressure taps are located within the slot.

Instrumentation

The performance of a cascade of hydrofoils was determined from static and total pressures and flow directions measured both upstream and downstream of the cascade. Static pressures were measured by means of sidewall orifices which were spaced at one inch intervals along the length of the cascade. This arrangement of orifices provided an indication of the degree of uniformity of both the inlet and exit flows and therefore was useful for adjusting test section flow conditions as well as for indicating the cascade static pressure rise. Total pressures and flow angles were measured by means of the two-dimensional, directional probes shown in Fig. 10; these probes were capable of measuring flow angle to an accuracy of $\pm 1/4$ deg. The designation "wedge" refers to the probe cross section at the hole location. The probes were remotely positioned in the spanwise direction. The upstream probe and the upstream static pressure orifices were located in a plane which was 0.6 chord length (axially) upstream of the plane of leading edges. The axial position of the downstream probe traversing plane was varied so that the streamwise distance between the blade trailing edge plane and the probe was between one and two chord lengths for all cascade configurations.

An automatic data acquisition system (Fig. 11), which was used to record cascade performance data, stored the data on paper tape. The tape-stored data were processed by a high-speed digital computer. The data recorded from the upstream and downstream measurement stations included total pressures and flow angles, which were continuously acquired during traverses of the probes, and the local wall static pressures along the length of the cascade. The pressures and flow angles were also visually displayed during testing, using strip chart recorders for readout of probe traverse data and both a multi-tube mercury manometer and an x-y plotter for indication of the individual wall static pressures.

Each of the inlet flow nozzles was provided with a window in the upper wall, aligned with the window at the top of the plenum tank, through which the central portion of the cascade could be observed and photographed during cavitation tests.

For visual detection of cavitation, the test section was illuminated from strobe lights which also provided the short duration, high intensity illumination required for cavitation photographs.

PROCEDURES

Test Program

This program was established to determine, experimentally, the performance, over a range of incidence angles, of a family of double circular-arc profiles with various inlet flow angles and cascade solidities. Incidence angle is defined as the difference between the inlet flow angle and the tangent to the meanline at the leading edge of a hydrofoil. For the double circular-arc profile, the incidence angle (i) is related to angle-of-attack (α), which is a reference angle used by many investigators (e.g., Refs. 2 and 3), through the expression

$$i = \alpha - \phi/2$$

The broad range of test variables included in this investigation enables the correlation of this experimental data throughout regions of interest to both axial-flow pump and compressor designers. The test configurations, which consisted of various combinations of inlet flow angles ($\beta_{LN} = 50, 60, 70$ and 75 deg) and cascade solidities ($\sigma = 0.75, 1.00$ and 1.50) with the double circular-arc hydrofoils shown in Fig. 5, are presented in Table II. The 50 and 60-deg inlet flow angles are in the range of cascade tests which were conducted for the development of axial-flow compressors and therefore provide a means for comparing and correlating these water cascade data with cascade data obtained from other test programs where air was used as the test medium. The 70 and 75-deg inlet flow angles are in the range of interest for pump design and are also of importance for extrapolating the correlations of compressor cascade data to these higher inlet flow angles.

Each of the cascade configurations, represented by a particular profile shape, inlet flow angle and cascade solidity, was tested over an incidence range which included the points of positive and negative stall, where stall is defined as the point at which the total pressure loss coefficient is double the minimum value.

Test Procedure

The test procedure for each set of cascade hydrofoils involved extensive iterative adjustments of the various flow control devices to achieve the best approximation to the desired two-dimensional flow in the cascade. At the start of this procedure, the hydrofoils were set at an angle estimated to be close to the incidence angle corresponding to the point of blade minimum total pressure loss coefficient. The flow velocity was then adjusted to provide a Reynolds number (Re_c) based upon the chord length of approximately 5×10^5 . The results from various cascade tests (e.g., Refs. 2 and 3) indicated that this value of Re_c was well above the critical Reynolds number range. Therefore, extensive laminar separation from the hydrofoil surfaces was unlikely and the effects of Reynolds number on the cascade performance parameters was expected to be minor. The endwall geometries and boundary layer control flow rates were then progressively adjusted to produce uniform distributions of inlet and exit wall static pressures and inlet flow angles along the full length of the cascade.

After a relatively uniform inlet distribution was obtained (inlet flow angle constant to within ± 0.8 deg of the value at the center of the cascade), the distributions of exit flow angle and total pressure were examined in the same manner; the porous endwall flow rate and tailboard settings were adjusted accordingly to improve periodicity of the exit flow. A calculation was then made to determine if the dynamic pressure ratio across the cascade was within ± 0.05 of the value computed from an approximation of the two-dimensional continuity equation which is defined by:

$$\left(\frac{q_2}{q_1}\right)_{2D} = \left[\frac{1}{2} \left(\frac{\cos\beta_1}{\cos\beta_2} + \sqrt{\left(\frac{\cos\beta_1}{\cos\beta_2}\right)^2 + 2\bar{w}} \right) \right]^2 \quad (1)$$

where:

$$\bar{w} = \frac{1}{s} \int_0^s \frac{\Delta P}{q_1} dy \quad (2)$$

These terms are defined in Appendix I.

Equation (1) was used to estimate the adjustments required to control the sidewall boundary layer thickness, thereby eliminating spanwise divergence or convergence of the streamlines and producing effective two-dimensional flow. If required, an appropriate change in sidewall flow rate was made, and the inlet flow was resurveyed since changes in blade loading affect the inlet flow field. An iterative procedure for evaluating and modifying upstream and downstream flow fields was thus established. A minimum of three complete iteration cycles was required for the first test of a cascade configuration before both upstream and downstream flow fields were acceptably uniform or before it had become obvious that significant improvement in flow uniformity could not be obtained. The time required for the iteration procedure varied from a minimum of approximately three hours to a maximum of about eight hours.

After obtaining the data for an initial test point of a configuration, subsequent test points were established by changing the blade-chord angle in approximately 2-deg increments until an incidence range was covered which included minimum loss incidence and values of incidence corresponding to twice the minimum loss. Each additional test point required an iterative procedure of flow adjustment identical to that described for the initial test point except that only one iteration was generally required. Approximately two hours were required to establish the flow uniformity and obtain the data for each additional test point.

A great variation in flow removal was required for cascade boundary layer control throughout the extremes of incidence angle between positive and negative stall. During tests of high cambered hydrofoils at incidence angles approaching positive stall, the porous wall boundary layer control system was required to remove a substantial portion of the mainstream flow to achieve two-dimensional flow conditions. Under conditions of severe separation or in the range of the highest static pressure ratios, the two-dimensional condition could not always be achieved even though maximum flow was being removed by the porous wall boundary layer control system.

During tests of low cambered hydrofoils at incidence angles approaching negative stall, the boundary layer control system was required to remove only a small portion of the mainstream flow to achieve two-dimensionality. For some low static pressure ratio conditions, two-dimensionality was often achieved without use of the porous wall boundary layer control system. Extreme low static pressure ratio conditions were encountered when it was impossible to achieve two-dimensional flow even though this boundary layer control system was not utilized.

Although some of the test conditions near positive and negative stall incidence were not two-dimensional, test points were obtained in this region in order to provide data which are useful for achieving a reasonably meaningful extrapolation of the two-dimensional data. Some of the data in the low loss

regions are reported as being non two-dimensional. These test points were however determined to be two-dimensional within the required limits through a comparison of a hand computation of the experimental q_2/q_1 ratio with the theoretical value at the time the tests were conducted. Subsequent computer computation using the tape-stored data resulted in a difference between the experimental and theoretical values of q_2/q_1 which exceeded the allowable value of ± 0.05 , but only slightly. Nonetheless, these values are reported as non two-dimensional data. It should be noted that even the data points near stall were generally within a few percentage points of being classified "two-dimensional" as defined in this report.

Before conducting cavitation tests, the water was deaerated for a minimum of six hours either by using the deaerator system or by reducing the pressure in the plenum tank. The cavitation index was determined from the point of cavitation desinence by first reducing the test section pressure until fully developed cavitation was established along the cascade and then gradually increasing the pressure until the cavitation disappeared (cavitation desinence). At this point the absolute pressure, dynamic pressure and temperature in the free stream were recorded for calculation of the cavitation index. A minimum of two hours was required for the cavitation measurements.

Data Reduction Procedure

The measurements of cascade static pressures, total pressures and flow angles were stored on paper tape by the data acquisition system (Fig. 11) and were later converted to cascade performance parameters by a computer program. This program computed and tabulated the flow angle and wall static pressure distributions along the entire cascade and also the hydrofoil wake parameters for each wake traversed. The equations and methods used in calculating the cascade performance parameters are outlined in Appendix I; the significance of the various terms in these expressions may be determined by reference to Fig. 12 which is a schematic presentation of cascade nomenclature. The computed distributions of pressure and flow angle were then examined to determine the uniformity and periodicity of the flow for the particular test configuration. In addition, the pressure and flow angle distributions over the two central gaps of the cascade were averaged to give representative values for inlet and exit flow angles, total pressure loss, momentum thickness ratio and inlet and exit static pressures. The diffusion factors and deviation angles for each cascade configuration were determined from the averaged inlet and exit flow angles.

The nondimensional cavitation index, K , was calculated from the inlet static pressure (p_1) at which cavitation had just disappeared from the hydrofoil surfaces and the vapor pressure of the water (p_v) at the test temperature using the expression:

$$K = \frac{p_i - p_v}{q_1} \quad (3)$$

PRESENTATION OF RESULTS

Prior to conducting the systematic cascade tests, a comprehensive evaluation of the flow uniformity and periodicity in the tunnel was made with a cascade configuration consisting of 10-deg camber angle, 6-percent thickness ratio, double circular-arc hydrofoils arranged for a solidity of 1.0. The 75-deg inlet nozzle was used in these tests to evaluate the tunnel performance under one of the more difficult of the test conditions, since nonuniformities of the flow in the cascade tunnel were anticipated to be more severe at the highest inlet angle (Ref. 3). Typical cascade test results obtained during these experiments are shown in Figs. 13 and 14 for incidence angles of -4 and one deg, respectively. These figures present wall static pressure coefficient and midspan flow angle distributions, which were measured upstream and downstream of the cascade, and total pressure loss coefficients, which were calculated for the individual hydrofoils by integrating the midspan wake total pressure deficit for each hydrofoil over one gap. The exit flow angles were calculated by averaging the incremental values of flow angle measured in the wake-free regions of the exit flow. A measure of the degree to which the two-dimensional pressure rise was achieved in the actual cascade is indicated for each test condition by the relative values of the "two-dimensional" $[(q_2/q_1)_{2D}]$ and experimental $[(q_2/q_1)_E]$ dynamic pressure ratios. The "two-dimensional" dynamic pressure ratio was calculated from the two-dimensional continuity equation (Eq. 1) using values of inlet and exit angle and total pressure loss coefficient measured for the two hydrofoils nearest to the center of the cascade. Figure 14 also includes the pressure and flow angle distributions measured at two alternate stations which were 1 and 2 in. from the side wall.

For each of the test configurations, the characteristics of the performance parameters are presented as functions of the incidence in Figs. 15 through 110; the order of presentation is shown in Table II. Inlet flow angles for the cascade tests were determined from flow surveys along the length of the cascade at the upstream measuring station. The average angles from the flow surveys were slightly different from the nozzle angles and are therefore presented for each test point together with the presentations of cascade performance parameters in Figs. 15 through 110. Results from tests with the slotted hydrofoils are presented with the results from the corresponding unslotted hydrofoil tests in Figs. 60 through 62 ($\phi = 40$ deg) and 66 through 68 ($\phi = 45$ deg).

Pressure distributions for the unslotted and slotted 40-deg camber, 6-percent thickness ratio hydrofoils at various incidence angles are presented in Figs. 111 and 112, respectively, for solidities of 0.75, 1.00 and 1.50; the inlet nozzle angle for these data was 60 deg.

Cavitation in the cascade water tunnel was photographed for a cascade of 20-deg camber angle, 10-percent thickness ratio, double circular-arc hydrofoils installed with a solidity of 1.50. Photographs of cavitation for incidence angles of 5.1 and 2 deg are shown in Figs. 113 and 114 (one-half of the center hydrofoil had been blackened to compare surface contrasts as an aid to cavitation visualization). Figure 114 ($i = 2$ deg) shows a time varying cavitation pattern caused by nonuniform inlet conditions. The cavitation shown propagated to the right (downstream) at approximately 10 ft/sec. When the inlet flow nonuniformity was less severe as in Fig. 113, the cavitation did not propagate and the bubble size changed simultaneously on all hydrofoils.

A convenient reference point which may be used as the basis for developing empirical cascade performance prediction systems is the incidence angle at which minimum loss occurs. Using the minimum total pressure loss coefficient as a reference, these test data were correlated in a manner similar to that which was used for determining the correlation presented in Ref. 4. For the correlation of the double circular-arc hydrofoil data, the variable, minimum loss incidence angle or deviation angle, for a given cascade configuration is assumed to be a linear function of the minimum loss incidence (or deviation) for the zero degree camber hydrofoil and a correction term related to the camber angle. In equation form, these reference angles may be expressed as

$$i = i_{\bullet} + n\phi$$

and

$$\delta^{\circ} = \delta_{\bullet}^{\circ} + m\phi$$

where i_{\bullet} and δ_{\bullet}° are the values for the zero degree camber hydrofoil and n and m are the respective rates of change of incidence and deviation with camber angle.

The minimum loss incidence angles for zero degree camber hydrofoils (i_{\bullet}) and slope factors (n) are presented as functions of inlet angle in Figs. 115 and 116; the minimum loss deviation angles for zero degree camber hydrofoils (δ°) and slope factors (m) are presented as functions of inlet angle in Figs. 117 and 118. Figure 119 presents the reference incidence and deviation obtained from the water cascade data correlation and the reference incidence and deviation developed from an empirically derived correlation of data from cascade tests wherein air was used as the test medium (Ref. 4). Typical values of minimum loss incidence and deviation obtained from the cascade water tunnel tests are also presented in Fig. 119.

Correlation of the turning angle data is presented in the form of carpet plots (Ref. 5) in Fig. 120. This manner of presentation facilitates interpolation of turning angle data for arbitrary cascades of the double circular-arc profiles.

DISCUSSION

Flow Distributions

The flow distribution data (Figs. 13 and 14) show that the inlet flow was uniform along the cascade, with respect to the measured sidewall static pressure distribution, to within one blade gap of the end walls and that the inlet flow angles for the five central hydrofoils varied by less than ± 0.5 deg from the value at the center of the cascade. Exit angles were generally within ± 0.8 deg of the exit flow angle from the centermost hydrofoil (blade No. 6). Blade-to-blade variations of total pressure loss coefficient generally occurred in a nonsystematic manner; that is, these variations could not be simply correlated with differences in the individual hydrofoil loadings resulting from variations in either blade angle setting ($\pm 1/4$ deg) or inlet flow angle.

Cascade Performance

Examination and comparison of the cascade performance data (Figs. 15 through 110) reveal behavior characteristics or limiting values of the various cascade performance parameters which are noted in the following discussions.

Total Pressure Loss Coefficient

Evaluation of the curves of total pressure loss coefficient versus incidence angle indicated a general trend for the minimum value of total pressure loss

coefficient to increase with increasing camber, solidity and inlet flow angle. The hydrofoil operating range, as defined by the incidence angles where the total pressure loss coefficient is double the minimum value, generally decreased with increasing camber, solidity and inlet flow angle. The hydrofoil thickness ratio (6 and 10 percent) did not affect the total pressure loss coefficients to a significant degree with respect to either the minimum loss value or the operating range. Minimum total pressure loss coefficients for the slotted hydrofoils were significantly greater than those for the unslotted hydrofoils and, except for $\phi = 45$ with $\sigma = 1.50$ (Fig. 68), occurred at higher incidence angles.

Turning Angle

The turning angles for the low cambered hydrofoils ($\phi = 0$ and 10 deg) increased linearly with incidence angle for all solidities and inlet flow angles; for a given hydrofoil profile, the slope of the turning angle versus incidence angle curve increased with increasing solidity but was relatively unchanged with increasing inlet flow angle. The slopes of the turning angle versus incidence angle curves for the higher cambered hydrofoils decreased with incidence angle as either solidity or inlet flow angle was increased. With the exception of the slotted hydrofoils, a point of maximum turning angle was realized for at least one hydrofoil profile with each inlet nozzle; beyond this point the turning angle was either constant or else decreased within the test range. Except for the solidity of 0.75, turning angles for the 40 and 45-deg camber slotted hydrofoils did not exhibit a region where a pronounced decrease in slope occurred with increasing incidence angle, a characteristic of the unslotted hydrofoils; turning increased throughout the incidence angle range at solidities of both 1.00 and 1.50 (Figs. 61 and 62, $\phi = 40$ deg and Figs. 67 and 68, $\phi = 45$ deg).

Diffusion Factor

For the unslotted hydrofoils, the range of test variables resulted in diffusion factors as high as 0.60, as shown in Figs. 67, 68, 104, 109 and 110. This value of the diffusion factor is indicated in Ref. 6 to be the point beyond which momentum thickness, and therefore total pressure losses, will increase rapidly because of flow separation. Unfortunately, the test range of this program was not adequate to substantiate this trend with diffusion factor. At the minimum loss point, the diffusion factors for the 40 and 45-deg camber unslotted hydrofoils were generally between 0.45 and 0.60 and the minimum total pressure loss coefficients were between 0.016 and 0.025, indicating a gradual loss increase with diffusion factor. Diffusion factors for the highly cambered hydrofoils, when operated at incidence angles greater than that for minimum loss coefficient, attained maximum values in a manner similar to that shown by the characteristics of the pressure rise coefficients. This does not detract from the usefulness of the diffusion factor as a loading parameter since the diffusion factor was developed specifically

for evaluation of conditions relative to the region of minimum loss. At the incidence angle for minimum total pressure loss coefficient, the diffusion factors for the slotted hydrofoils were between 0.45 and 0.55; at higher incidence angles the diffusion factors were greater than 0.60.

Wake Momentum Thickness Ratio

For cascades of both slotted and unslotted hydrofoils, the variations of wake momentum thickness ratio with the cascade geometry were similar to the variations of total pressure loss coefficient. For cascades of low camber hydrofoils, the rate of increase of wake momentum thickness ratio was not as great as the rate of increase in loss coefficient at incidence angles approaching negative stall.

Static Pressure Rise Coefficient

The wide range of test variables resulted in static pressure rise coefficients greater than 0.60 for some of the configurations as shown for example in Figs. 68, 107 and 110. For the unslotted hydrofoils, values of $\Delta p/q_1$ above 0.50 were generally associated with the initiation of a decrease in the slope of the turning angle curve; the value of $\Delta p/q_1$, at which the slope started to decrease, increased with increasing cascade solidity. The maximum values of $\Delta p/q_1$ obtained from the slotted hydrofoils were not substantially different from the values obtained for the unslotted hydrofoils.

Hydrofoil Pressure Distributions

The pressure distributions along the surfaces of unslotted and slotted hydrofoils are presented for a range of incidence angle for the 40-deg camber, 6-percent thickness ratio hydrofoils installed at solidities of 0.75, 1.00 and 1.50 with the 60-deg inlet nozzle (Figs. 111 and 112, respectively). With increasing incidence angle, the unslotted hydrofoil pressure distributions show forward shifts of the minimum pressure point on the suction surface: the most rearward position was the 50-percent chord station, occurring at a solidity of 0.75 (Fig. 111a); the most forward position was the 18-percent chord station, occurring at a solidity of 1.50 (Fig. 111c). A change in the boundary layer characteristics on the suction surface, as indicated by a sharp increase in local pressure near the trailing edge, appears at incidence angles of -12 deg ($\sigma = 0.75$), -8 deg ($\sigma = 1.00$) and -8 deg ($\sigma = 1.50$); separation along the suction surface, as indicated by a region of relatively constant pressure near the trailing edge and increasing minimum pressure peak, appears at the higher incidence angles.

The slotted hydrofoil pressure distributions show minimum pressure points at about the 30-percent chord location for incidence angles greater than -8 deg and at about the 40-percent chord location for incidence angles of -8 deg and less, at all solidities. Separation along the suction surfaces apparently occurred at incidence angles greater than 0 deg, as evidenced by the increasing local static pressures starting at the minimum pressure point.

Cavitation Index

The cavitation indices presented represent the highest pressures at which cavitation could be observed on the hydrofoils. Because of the required low operating pressures, cavitation, when occurring on the hydrofoils, also occurred within the boundary layer control systems reducing their effectiveness in maintaining two-dimensional flows. As a result, the inlet flow distributions were often nonuniform, and cavitation was most prevalent from both the surface of the porous, flexible, convex end wall and the adjacent hydrofoil. However, cavitation did appear uniformly on the hydrofoils further from the porous, flexible, convex end wall, and the cavitation indices were obtained from observations on the surfaces of these hydrofoils.

Because of the use of the porous sidewall boundary layer control system, viewing of cavitation was possible only from above or below the cascade and this created some special problems. Adequate illumination and viewing could not always be achieved for the cavitation studies, especially when testing the highly cambered hydrofoils at a solidity of 1.50. The more difficult problem was that of attempting to determine cavitation desinence on the pressure surfaces of a hydrofoil while observing through the cavitation bubbles swept from the porous end wall and the leading adjacent blade. This uncertainty of the presence of cavitation made impractical the measurement of cavitation from the pressure surfaces of the hydrofoils, and the results presented therefore generally represent suction surface cavitation.

When testing the low camber hydrofoils, cavitation in the nozzle or from the suction slots of the boundary layer control system was often detected before cavitation was observed along the hydrofoil surfaces. When these conditions occurred, the test data were invalid and additional tests were conducted at higher incidence angles where cavitation occurred at higher pressures in an attempt to generate curves of cavitation test data for the hydrofoils.

DATA CORRELATION AND COMPARISON

Minimum Loss

The comparison of minimum loss incidence angles as determined from the double circular-arc (DCA) hydrofoils and the Ref. 4 correlations, which are presented in Fig. 119, shows that the incidence variations with camber and solidity are quite similar for the two correlation systems. For the two correlations, the values of minimum loss incidence for each solidity differ by less than one degree at $\phi = 0$. At β_{1N} of 50 and 60 deg, the slopes of the incidence curves are more negative for the DCA correlation; at $\beta_{1N} = 70$ deg, the slopes are nearly identical; at $\beta_{1N} = 75$ deg, the slopes of the curves are less negative for the DCA correlation.

The values of minimum loss incidence indicated on Fig. 119 by the open symbols were obtained from the performance curves (Figs. 15 through 110) to show the fit of the experimental data with the correlations. It is evident that these results agree very closely with the DCA correlation.

The comparison of minimum loss deviation angles (Fig. 119) shows that similar trends of the deviation angle variation with camber and solidity are obtained from the two correlations. The DCA correlation results in generally higher deviation angles from low camber hydrofoils for all four inlet flow angles. Comparing these results from the two correlation systems shows that the greatest difference in the values of minimum loss deviation throughout the range presented by the correlations is on the order of 2 1/2 deg. The values of minimum loss deviation obtained from the performance curves also indicate a reasonable fit with the DCA correlation.

Carpet Plot

The cascade data are summarized using a carpet plotting technique (Ref. 5). This technique presents a function of several independent variables on a single two-dimensional graph. This graphic presentation facilitates the selection of a blade camber angle and angle-of-attack which will provide the turning angle specified by a design velocity vector diagram. Within the range of the test parameters, the carpet plots which are presented in Fig. 120 may be used to predict the turning angle and angle-of-attack for arbitrary cascade geometries which incorporate various combinations of camber angle, inlet flow angle and solidity. The carpet plotted data comprise a range of camber angles from 0 to 45 deg, inlet angles of 50, 60, 70 and 75 deg and solidities of 0.75, 1.00 and 1.50.

This plotting technique features an abscissa scale with a shifting origin. The origin was shifted in the x direction by an amount proportional to the increment of the variable represented. In this case, each carpet plot is separated from the next by a number of units proportional to the difference in camber. In order to avoid overlapping of the carpets, the ordinate scale was shifted vertically a number of units proportional to the solidity. For solidities above 0.75, turning (θ) is given by the following expression:

$$\theta = R - 32 (\sigma - 0.75) \quad (4)$$

where R is the actual ordinate scale on the carpet plot.

Each of the individual plots on Fig. 120 presents turning angle, angle-of-attack and inlet flow angle for a prescribed solidity and camber angle. For a given solidity, similar carpet plots, or a portion of a carpet plot, may be constructed for intermediate camber angles by linear interpolation between corresponding values of α and β_1 on the given carpet plots for higher and lower camber angles. The individual carpet plots representing increasing camber angle were separated such that four units in the horizontal direction represent one degree of camber.

In a similar manner, carpet plots, or a portion of a carpet plot, may be constructed for an intermediate solidity by linear interpolation between corresponding values of α and β_1 on carpet plots which differ in solidity but have the same camber angle. For this interpolation, 16 units represent a change in solidity of 0.25. A double interpolation is required for plots involving both intermediate camber angles and solidities.

Pressure Distributions

At incidence angles of -12 and -10 deg and a solidity of 0.75, the pressure distributions for slotted (Fig. 112) and unslotted (Fig. 111) hydrofoils indicate that the minimum pressure coefficients on the suction surface of the slotted hydrofoils were slightly more negative but occurred at the same chordal station as those for the unslotted hydrofoil configurations.

At a solidity of 1.00, the pressure distributions for slotted and unslotted hydrofoils for incidence angles of -6, -4 and -2 deg indicate no appreciable difference in either the magnitude or the location of the suction surface pressure peaks which occur between the 35 and 40-percent chord stations. For incidence angles of -12, -10 and -8 deg, the pressure distributions for slotted and unslotted

hydrofoils indicate lower pressures at the 35-percent chord station on the suction surface of the slotted blades and also appreciable differences in the pressure distributions along the entire pressure surfaces.

For a solidity of 1.50, the pressure distributions indicate lower pressures on the pressure surface of the slotted hydrofoils to about the 25-percent chord station at all incidence angles. For incidence angles of -5, -3 and -2 deg, the minimum pressures on the suction surface of the slotted hydrofoils were lower than those along the unslotted hydrofoils. The minimum pressure peaks on the slotted hydrofoils occurred downstream of the 30-percent chord station for all incidence angles; the minimum pressure peaks on the unslotted hydrofoils occurred upstream of the 30-percent chord station for incidence angles greater than -7 deg.

CONCLUDING REMARKS

A program was completed in a cascade water tunnel for which a family of double circular-arc hydrofoils was tested over a range of incidence angles with a systematic variation in the inlet flow angle and cascade solidity. The test range included inlet flow angles which are of interest for the design of both axial-flow pumps and compressors, and the test measurements included the determination of cavitation points in addition to those required for calculating the cascade performance parameters.

The turning angle data were correlated by the carpet plotting technique which permits the determination of turning angle for arbitrary cascades of double circular-arc hydrofoils by means of interpolations within the limits of the test variables. The carpet plots indicate an orderly progression of the turning angle as has been previously reported for cascade tests in which air was used as the test medium. The test data were further summarized and evaluated by correlating the incidence angles and deviation angles for the points of minimum total pressure loss coefficient and comparing the results with a set of curves developed from an empirical correlation of cascade data using air as the test medium. The differences between the two correlations are primarily in the slopes of the curves and suggest changes in the assumptions or terms of the expressions which were used to adapt the air-data correlation to the double circular-arc profile. The reasonable agreement between these correlations of air and water cascade data suggest confidence in employing air cascade data and correlations for the design of axial-flow pumps for noncavitating flows.

Results from the slotted hydrofoil tests were well below expectations with respect to the cascade operating range, minimum total pressure loss coefficient and turning angle. With the exception of the results for $\sigma = 0.75$, the data

indicate that slots did not increase the positive-stall incidence angle range; the negative-stall incidence angle range was decreased for all test configurations. Although the incidence angles for minimum total pressure loss coefficient were greater for the slotted hydrofoils (except for $\phi = 45$, $\sigma = 1.50$), this did not result in improved performance at $\sigma = 1.00$ and 1.50 because the corresponding loss coefficients were so high. Reasons for the poor performance are most likely related to slot geometry rather than slot location along the chord. From profile pressure distribution measurements of unslotted hydrofoils, the chordwise position of the slot on the suction surface was established to lie within a region downstream of the minimum pressure point but upstream of the indicated separation region. This region provided both the pressure difference necessary to induce flow through the slot and a slot position where the momentum of the fluid ejected from the slot could be used to reinforce an attached boundary layer rather than attempt to re-establish an already separated boundary layer. The slot performance could possibly be improved by making the following changes to the slot profile along the downstream surface of the slot: (1) increase the radius of the $0.020 r$ corner at the pressure surface, (2) increase the radius of the $0.200 r$ corner at the suction surface. These modifications would reduce the probability of flow separation from the slot lip on the pressure surface (as indicated by the reduced operating range toward negative stall) and improve the probability of a Coanda-type flow of the fluid ejected from the slot along the suction surface.

The data presented are adequate for the determination of systems for predicting the performance of double circular-arc profiles in cascades or for determining terms for correcting current prediction systems (for other profiles) to include the double circular-arc profile. In addition, an operating range correlation may also be established within the limits of positive and negative stall, which are defined herein as the angles at which the total pressure loss coefficient is double the minimum value. Although this definition for the operating range is a useful criteria for judging the relative merits of arbitrary profiles in cascades, it is too restrictive and another criteria such as 0.04 plus the minimum total pressure loss coefficient would be useful for defining the maximum operating range of various profiles, especially for those which have a very low minimum total pressure loss coefficient or a shallow total pressure loss coefficient characteristic. This extended range was not included in this experimental program because of the two-dimensionality specification for the test data which would be difficult to achieve in the high-loss test regions. Whether or not this two-dimensionality can be achieved, a test program with a limited number of cascades is recommended to measure cascade performance at incidence angles both higher and lower than those reported and therefore to define the maximum operating limits of the cascades. In spite of the fact that the test conditions may not be two-dimensional, the data points will provide some optimism in extrapolating current test data for empirical correlations of operating range.

A need is indicated to test, in a systematic manner, cascades with diffusion factors and static pressure rise coefficients greater than 0.6 to further qualify the cascade loading limit definitions. These tests should explore: (1) the effects of Reynolds number, tunnel turbulence level and blade surface finish on laminar separation and therefore the consequent effects on cascade performance, (2) the use of boundary layer trips or surface roughness for overcoming laminar separation, and (3) the use of slots at the tip regions of hydrofoils for the purpose of reducing stall at the cascade side walls and therefore increasing the cascade operating range. Static pressure measurements at various spanwise stations across the blades should be obtained for a discrete number of these tests for evaluating the effects of the test variables on the pressure profiles.

The cavitation tests revealed a necessity for further effort in defining the cavitation index throughout the cascade operating range. The tests require observations from both above the suction surface and through the side walls, along the span of the hydrofoils, in order to determine the cavitation indices for both suction and pressure surfaces. Although cavitation is most prevalent at stations along the suction surface, it may also occur on the pressure surface under conditions approaching negative stall. Observation of cavitation through the side walls will prevent the use of a porous wall boundary layer control system, with consequent effects of the boundary layer on the cavitation index. Therefore, a series of tests in which cavitation may be observed from above the suction surface should be conducted with and without boundary layer control thereby establishing a correction term for the cavitation indices measured in non two-dimensional flow.

APPENDIX I

Equations for Data Reduction

For the acquisition of data, the test procedures were established to: (1) exclude turning angle measurements within the wake regions, (2) measure flow angles and total pressures only at the midspan position, and (3) adjust the flow conditions to provide effective two-dimensional flow through the cascade. An expression based upon the continuity equation was derived for determining the two-dimensional dynamic pressure ratio to provide a reference for estimating the two-dimensionality of the test data. This expression,

$$\left(\frac{q_2}{q_1}\right)_{2D} = \left[\frac{1}{2} \left(\frac{\cos \beta_1}{\cos \beta_2} + \sqrt{\left(\frac{\cos \beta_1}{\cos \beta_2}\right)^2 + 2\bar{\omega}} \right) \right]^2 \quad (1)$$

is an approximation to the two-dimensional continuity equation in which the integrations are performed for a sine-squared variation of total pressure and a sine variation of angle across a blade wake. This approximation, which includes wake blockage effects on the exit flow area, is valid within experimental error if (1) the total pressure loss coefficient, $\bar{\omega}$, is less than 0.10, (2) the flow angle variations from the mean exit flow angle are less than 15 deg, and (3) the width of the wakes at the measuring station are less than the blade spacing. This expression was derived using the methods prescribed in Ref. 2. Effective two-dimensional flow was assumed when the average experimental dynamic pressure ratio was within ± 0.05 of the value computed by the above expression using the average measured exit flow angle.

The total pressure loss coefficient, $\bar{\omega}$, is the nondimensionalized total pressure loss across a blade wake averaged across the blade spacing and is expressed by the formula

$$\bar{\omega} = \frac{1}{s} \int_0^s \frac{P_1 - P_2}{q_1} dy \quad (2)$$

The experimental dynamic pressure ratio is expressed as

$$\left(\frac{q_2}{q_1}\right)_E = \frac{P_1 - P_2}{P_1 - P_1} \quad (3)$$

APPENDIX I
(Contd.)

An expression developed in Ref. 7 to relate the total pressure loss coefficient to the wake momentum thickness (θ^*) and wake shape factor (H) at the downstream measuring station is given by

$$\bar{\omega} = 2 \left(\frac{\theta^*}{c} \right)_2 \frac{\sigma}{\cos \beta_2} \left(\frac{\cos \beta_1}{\cos \beta_2} \right)^2 \left\{ \frac{\frac{2H_2}{3H_2-1}}{\left[1 - \left(\frac{\theta^*}{c} \right)_2 \frac{\sigma H_2}{\cos \beta_2} \right]^3} \right\} \quad (4)$$

which indicates the contributions by the cascade geometry terms: σ , β_1 , β_2 , and the aerodynamic terms: θ^* , H (the contribution of the expression within the braces was stated in Ref. 7 to be very small). For the presentation of cascade characteristics, the momentum thickness is ratioed to the blade spacing and the total pressure loss coefficient expression is given by

$$\bar{\omega} = \frac{2}{\cos \beta_2} \left(\frac{\theta^*}{s} \right)_2 \left(\frac{\cos \beta_1}{\cos \beta_2} \right)^2 \left\{ \frac{\frac{2H_2}{3H_2-1}}{\left[1 - \left(\frac{\theta^*}{s} \right)_2 \frac{H_2}{\cos \beta_2} \right]^3} \right\} \quad (5)$$

The momentum thickness ratio was calculated from the expression

$$\frac{\theta^*}{s} = \frac{1}{s} \int_{\delta_{\ell y}}^{\delta_{uy}} \left(1 - \frac{v}{v_0} \right) \frac{v}{v_0} dy \quad (6)$$

where the limits of integration are the wake boundaries. This expression, by inclusion of the Bernoulli equation, becomes

$$\frac{\theta^*}{s} = \frac{1}{s} \int_{\delta_{\ell y}}^{\delta_{uy}} \left[\sqrt{1 - \frac{\Delta P}{q_2}} - \left(1 - \frac{\Delta P}{q_2} \right) \right] dy \quad (7)$$

APPENDIX I
(Concluded)

In Ref. 6, it was stated that a factor to be used for wake thickness correlations is the diffusion of blade surface velocities because of the contribution of this diffusion to the wake shape. A diffusion factor (D) developed in Ref. 6 is expressed for incompressible flow as

$$D = \left(1 - \frac{\cos \beta_1}{\cos \beta_2} \right) + \frac{\cos \beta_1}{2\sigma} (\tan \beta_1 - \tan \beta_2) \quad (8)$$

The significance of this diffusion factor is restricted to the region of minimum loss.

APPENDIX II

List of Symbols

A	Flow area, sq in.
c	Hydrofoil chord length, in.
C_P	Pressure coefficient, $\frac{P_{local} - P_1}{P_1 - P_1}$
D	Diffusion factor, $\left(1 - \frac{\cos \beta_1}{\cos \beta_2}\right) + \frac{\cos \beta_1}{2\sigma} (\tan \beta_1 - \tan \beta_2)$
H	Boundary layer form factor, δ^*/θ^*
i	Incidence angle, angle between inlet-flow direction and tangent to meanline at leading edge, deg, $i = \beta_1 - \left(\gamma^\circ + \frac{\phi}{2}\right)$, $\therefore i = \alpha - \frac{\phi}{2}$
K	Cavitation index, $\frac{P_1 - P_v}{P_1 - P_1}$
m	Slope factor in deviation angle relation, $m = (\delta^\circ - \delta_0^\circ)/\phi$
n	Slope factor in incidence angle relation, $n = (i - i_0)/\phi$
P	Total pressure, lb/sq in.
p	Static pressure, lb/sq in.
P_v	Vapor pressure, lb/sq in.
ΔP	Static pressure difference, $p_2 - p_1$, lb/sq in.
q	Dynamic pressure, lb/sq in.
Re_c	Reynolds number based on chord length, $\frac{Vc}{\nu}$
r	Radius, in.
s	Blade spacing, in.

APPENDIX II
(Contd.)

t	Maximum profile thickness, in.
V	Velocity, ft/sec
X	Chordal station
y	Coordinate normal to axis, in.
α	Angle-of-attack, angle between inlet-flow direction and blade-chord angle, deg
β	Flow angle, angle between flow direction and axial direction, deg
γ°	Blade chord angle, angle between blade chord and axial direction, deg
δ	Wake full thickness
δ°	Deviation angle, angle between exit-flow direction and tangent to blade mean camber line at trailing edge, deg
δ^*	Boundary layer displacement thickness, $\int_{\delta_{fy}}^{\delta_{uy}} \left(1 - \frac{V}{V_0}\right) dy$
θ	Turning angle, $\beta_1 - \beta_2$, deg
θ^*	Wake momentum-defect thickness, $\int_{\delta_{fy}}^{\delta_{uy}} \left(1 - \frac{V}{V_0}\right) \frac{V}{V_0} dy$
ν	Kinematic viscosity, sq ft/sec
ρ	Density, slugs/cu ft
σ	Solidity, ratio of chord to spacing
ϕ	Camber angle, difference between tangent angles at leading and trailing edges, deg
$\bar{\omega}$	Total pressure loss coefficient

APPENDIX II
(Concluded)

Subscripts

E	Experimental
l_y	Wake boundary from lower surface
N	Nominal
o	Free stream
u_y	Wake boundary from upper surface
1	Station at cascade inlet
2	Station at cascade exit
2D	Two-dimensional
•	Value for zero degree camber hydrofoil

REFERENCES

1. Lin, T. C.: Ducts for Accelerated Flow. ASME Proceedings of the Second U. S. National Congress on Mechanics, June 1954.
2. Emery, J. C., L. J. Herrig, J. R. Erwin and A. R. Felix: Systematic Two-Dimensional Cascade Tests of NACA 65-Series Compressor Blades at Low Speeds. NACA Report 1368, 1958.
3. Erwin, J. R. and J. C. Emery: Effect of Tunnel Configuration and Testing Technique on Cascade Performance. NACA Report 1016, 1951.
4. Johnsen, I. A. and R. O. Bullock (Editors): Aerodynamic Design of Axial-Flow Compressors. NASA Report SP-36, 1965.
5. Felix, A. R.: Summary of 65-Series Compressor-Blade Low-Speed Cascade Data by Use of the Carpet-Plotting Technique. NACA Technical Note 3913, February 1957.
6. Lieblein, S., F. C. Schwenk and R. L. Broderick: Diffusion Factor for Estimating Losses and Limiting Blade Loadings in Axial-Flow Compressor Blade Elements. NACA RM E53D01, 1953.
7. Lieblein, S. and W. H. Roudebush: Theoretical Loss Relations for Low-Speed Two-Dimensional-Cascade Flow. NACA Report TN3662, March 1956.

TABLE I

Coordinates for Double Circular-Arc Profiles

Camber Angle (Deg)	0°		10°	20°		
	6%	10%	6%	6%	10%	
Thickness Ratio (%)						
Chordal Station (% Chord)	<u>y/c upper surface (%)</u>					
0.0	0.10	0.10	0.10	0.10	0.10	
8.33	0.93	1.53	1.62	2.29	2.94	
16.67	1.67	2.80	2.92	4.14	5.29	
25.00	2.23	3.77	3.94	5.56	7.09	
33.33	2.67	4.43	4.65	6.57	8.37	
41.67	2.90	4.87	5.09	7.18	9.12	
50.00	3.00	5.00	5.23	7.38	9.38	
58.33	2.90	4.87	5.09	7.18	9.12	
66.67	2.67	4.43	4.65	6.57	8.37	
75.00	2.23	3.77	3.94	5.56	7.09	
83.33	1.67	2.80	2.92	4.14	5.29	
91.67	0.93	1.53	1.62	2.29	2.94	
100.00	0.10	0.10	0.10	0.10	0.10	
	<u>y/c lower surface (%)</u>					
0.0	-0.10	-0.10	-0.10	-0.10	-0.10	
8.33	-0.93	-1.53	-0.23	0.42	-0.19	
16.67	-1.67	-2.80	-0.42	0.76	-0.35	
25.00	-2.23	-3.77	-0.58	1.03	-0.47	
33.33	-2.67	-4.43	-0.68	1.22	-0.55	
41.67	-2.90	-4.87	-0.76	1.33	-0.61	
50.00	-3.00	-5.00	-0.77	1.38	-0.62	
58.33	-2.90	-4.87	-0.76	1.33	-0.61	
66.67	-2.67	-4.43	-0.68	1.22	-0.55	
75.00	-2.23	-3.77	-0.58	1.03	-0.47	
83.33	-1.67	-2.80	-0.42	0.76	-0.35	
91.67	-0.93	-1.53	-0.23	0.42	-0.19	
100.00	-0.10	-0.10	-0.10	-0.10	-0.10	

TABLE I
(Concluded)

Camber Angle (Deg)	25°		30°		40°		45°
	6%	6%	6%	10%	6%	10%	6%
Thickness Ratio (%)							
Chordal Station (% Chord)	y/c upper surface (%)						
0.0	0.10	0.10	0.10	0.10	0.10	0.10	0.10
8.33	2.64	3.00	3.67	3.77	4.48	4.15	4.15
16.67	4.76	5.41	6.58	6.74	7.95	7.41	7.41
25.00	6.40	7.25	8.80	9.01	10.58	9.87	9.87
33.33	7.55	8.55	10.35	10.58	12.40	11.59	11.59
41.67	8.24	9.33	11.27	11.54	13.49	12.61	12.61
50.00	8.47	9.58	11.58	11.84	13.84	12.95	12.95
58.33	8.24	9.33	11.27	11.54	13.49	12.61	12.61
66.67	7.55	8.55	10.35	10.58	12.40	11.59	11.59
75.00	6.40	7.25	8.80	9.01	10.58	9.87	9.87
83.33	4.76	5.41	6.58	6.74	7.95	7.41	7.41
91.67	2.64	3.00	3.67	3.77	4.48	4.15	4.15
100.00	0.10	0.10	0.10	0.10	0.10	0.10	0.10
	y/c lower surface (%)						
0.0	-0.10	-0.10	-0.10	-0.10	-0.10	-0.10	-0.10
8.33	0.79	1.10	0.48	1.80	1.17	2.15	2.15
16.67	1.41	2.00	0.88	3.26	2.12	3.89	3.89
25.00	1.89	2.69	1.18	4.40	2.87	5.23	5.23
33.33	2.20	3.19	1.40	5.19	3.40	6.19	6.19
41.67	2.40	3.48	1.54	5.68	3.72	6.76	6.76
50.00	2.47	3.58	1.58	5.84	3.82	6.95	6.95
58.33	2.40	3.48	1.54	5.68	3.72	6.76	6.76
66.67	2.20	3.19	1.40	5.19	3.40	6.19	6.19
75.00	1.89	2.69	1.18	4.40	2.87	5.23	5.23
83.33	1.41	2.00	0.88	3.26	2.12	3.89	3.89
91.67	0.79	1.10	0.48	1.80	1.17	2.15	2.15
100.00	-0.10	-0.10	-0.10	-0.10	-0.10	-0.10	-0.10

TABLE II

Index to Cascade Test Configurations

<u>Inlet Flow Angle (Deg)</u>	<u>Camber Angle (Deg)</u>	<u>Thickness Ratio (%)</u>	<u>Solidity</u>	<u>Fig. No.</u>
50	0	6	0.75	15
			1.00	16
			1.50	17
50	0	10	0.75	18
			1.00	19
			1.50	20
50	10	6	0.75	21
			1.00	22
			1.50	23
50	20	6	0.75	24
			1.00	25
			1.50	26
50	20	10	0.75	27
			1.00	28
			1.50	29
50	30	6	0.75	30
			1.00	31
			1.50	32
50	40	6	0.75	33
			1.00	34
			1.50	35
50	40	10	0.75	36
			1.00	37
			1.50	38
50	45	6	0.75	39
			1.00	40
			1.50	41
60	0	6	0.75	42
			1.00	43
			1.50	44
60	0	10	0.75	45
			1.00	46
			1.50	47
60	10	6	0.75	48
			1.00	49
			1.50	50

TABLE II
(Contd.)

<u>Inlet Flow Angle (Deg)</u>	<u>Camber Angle (Deg)</u>	<u>Thickness Ratio (%)</u>	<u>Solidity</u>	<u>Fig. No.</u>
60	20	6	0.75	51
			1.00	52
			1.50	53
60	20	10	0.75	54
			1.00	55
			1.50	56
60	30	6	0.75	57
			1.00	58
			1.50	59
60	40	6	0.75	60*
			1.00	61*
			1.50	62*
60	40	10	0.75	63
			1.00	64
			1.50	65
60	45	6	0.75	66*
			1.00	67*
			1.50	68*
70	0	6	0.75	69
			1.00	70
			1.50	71
70	0	10	0.75	72
			1.00	73
			1.50	74
70	10	6	0.75	75
			1.00	76
			1.50	77
70	20	6	0.75	78
			1.00	79
			1.50	80
70	20	10	0.75	81
			1.00	82
			1.50	83
70	25	6	0.75	84
			1.00	85
			1.50	86
70	30	6	0.75	87
			1.00	88
			1.50	89

TABLE II
(Concluded)

<u>Inlet Flow Angle (Deg)</u>	<u>Camber Angle (Deg)</u>	<u>Thickness Ratio (%)</u>	<u>Solidity</u>	<u>Fig. No.</u>
70	30	10	0.75	90
			1.00	91
			1.50	92
75	0	6	0.75	93
			1.00	94
			1.50	95
75	0	10	0.75	96
			1.00	97
			1.50	98
75	10	6	0.75	99
			1.00	100
			1.50	101
75	20	6	0.75	102
			1.00	103
			1.50	104
75	20	10	0.75	105
			1.00	106
			1.50	107
75	25	6	0.75	108
			1.00	109
			1.50	110

* Includes cascade characteristics of slotted hydrofoils

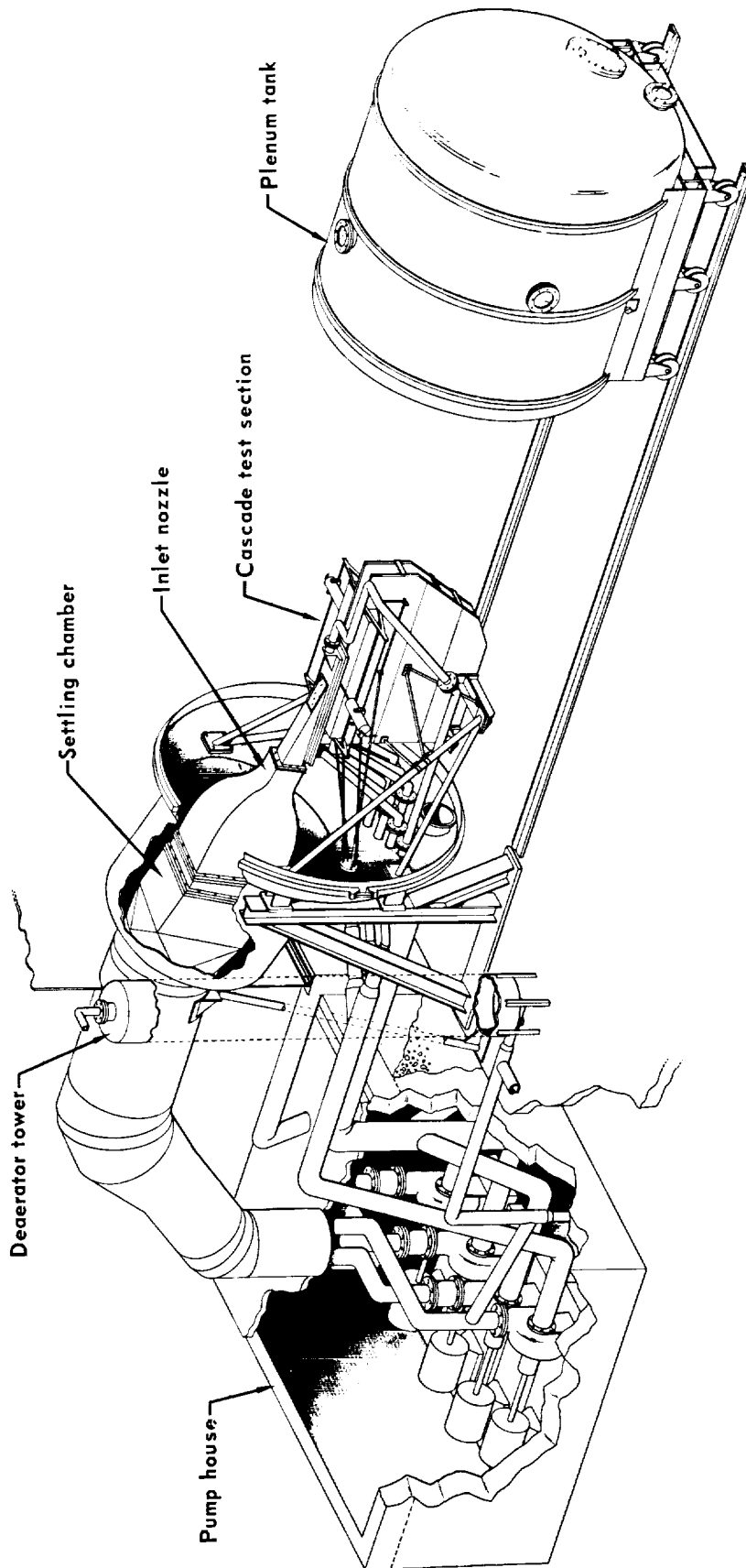
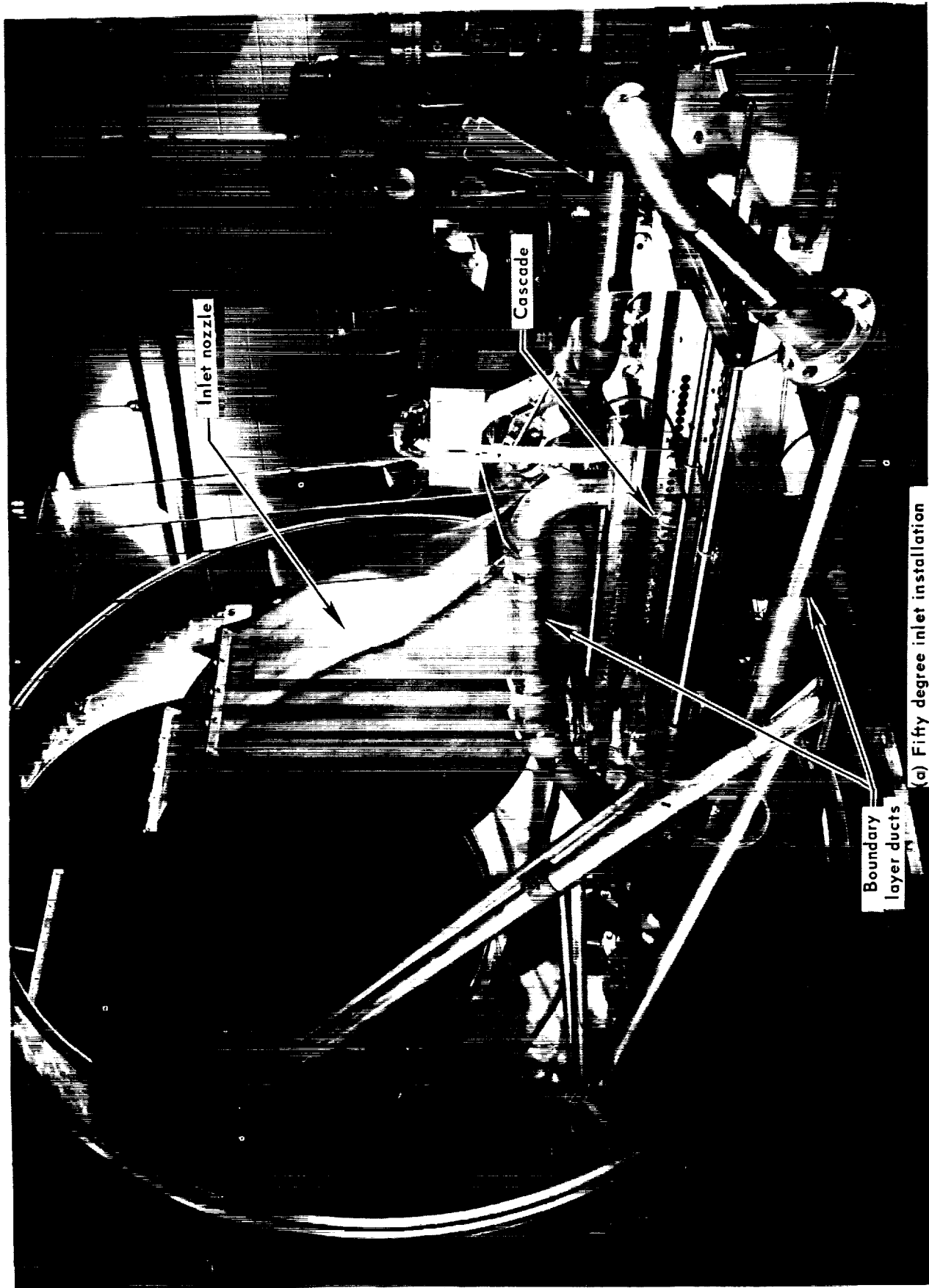


Figure 1.— Cascade water tunnel



(a) Fifty degree inlet installation

Figure 2. Water tunnel inlet installation.

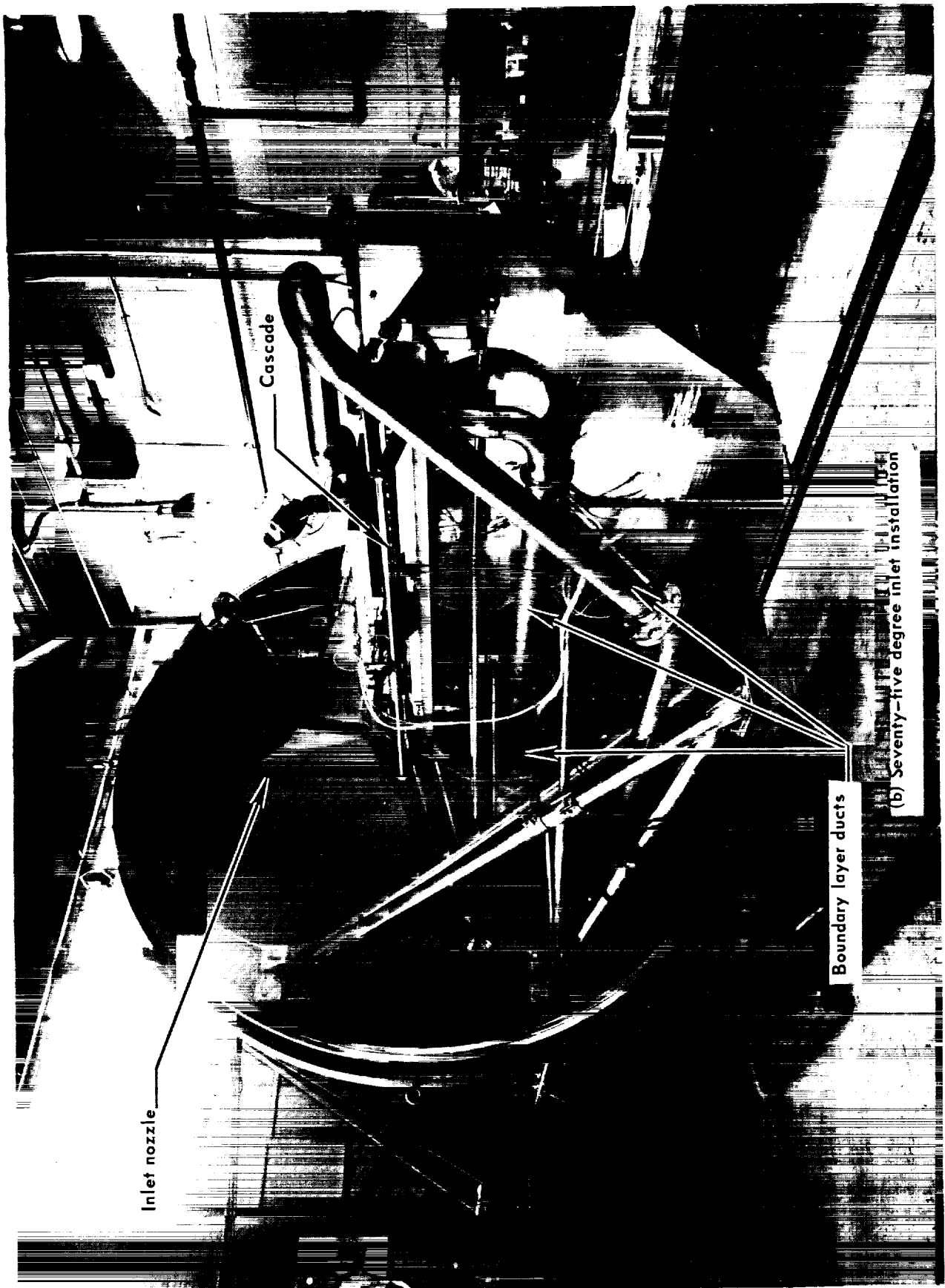


Figure 2. - Concluded.

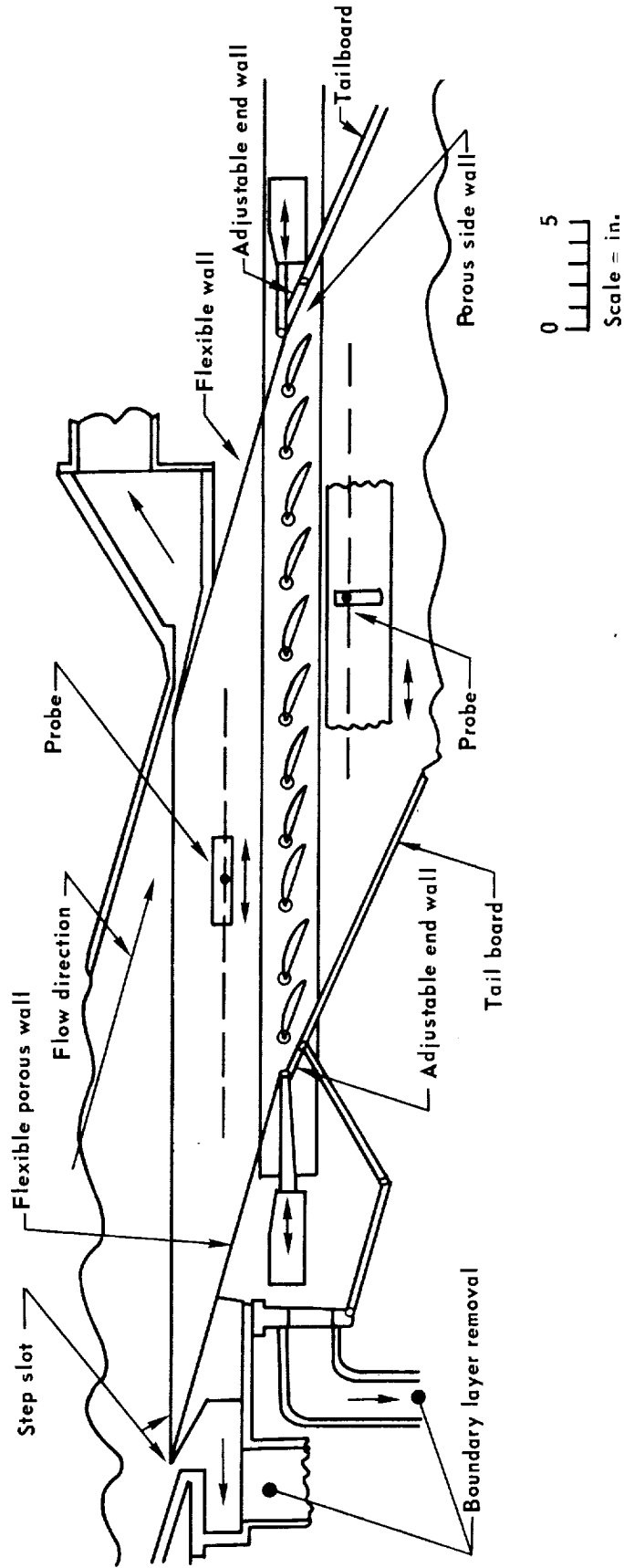


Figure 3. - Cascade test section.

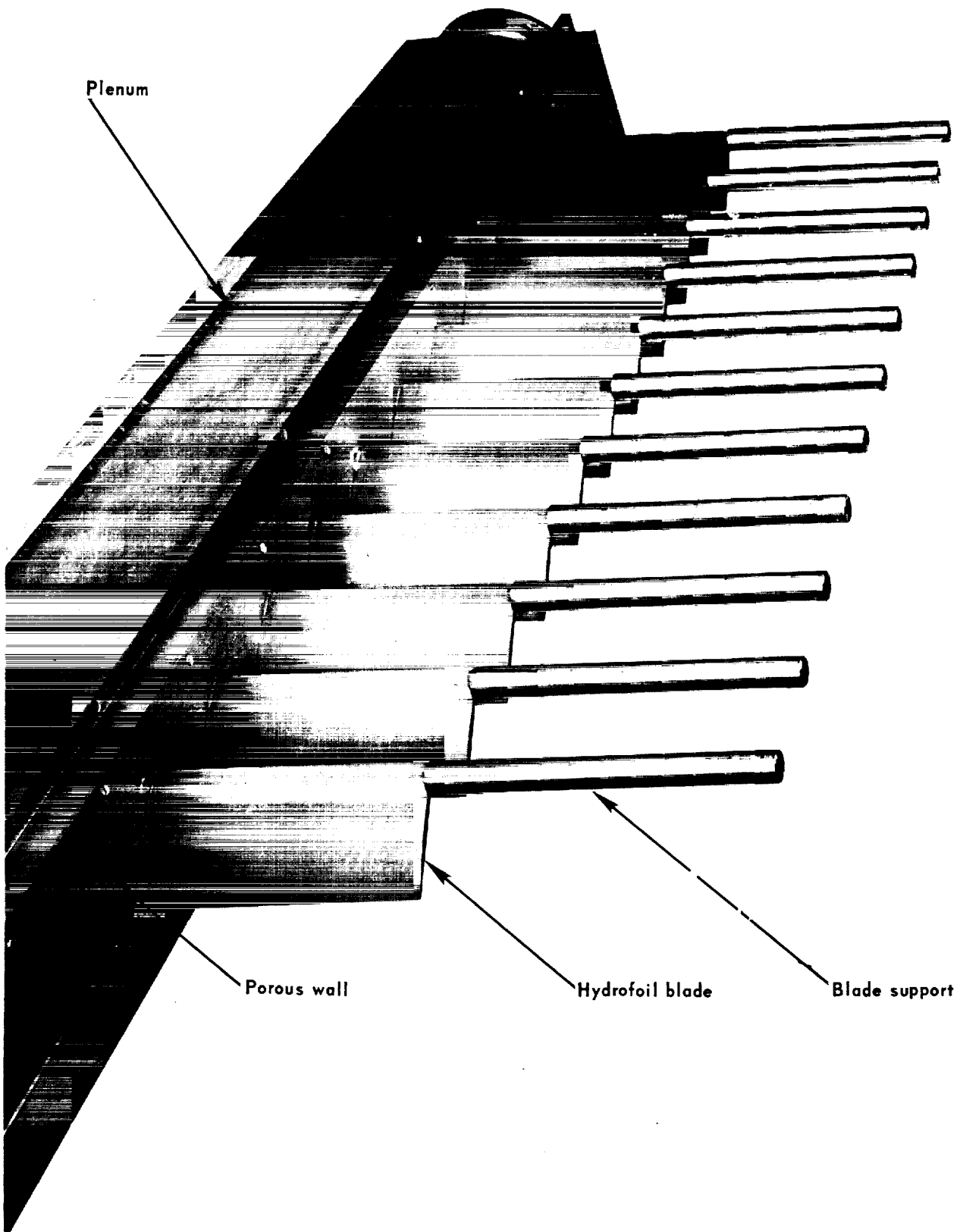
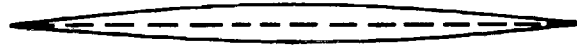
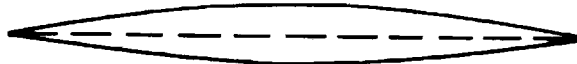


Figure 4. - Porous sidewall assembly.



(a) $\Phi = 0$, $t/c = 0.06$



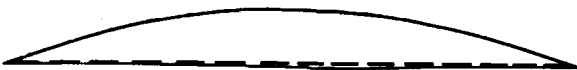
(b) $\Phi = 0$, $t/c = 0.10$



(c) $\Phi = 10$, $t/c = 0.06$



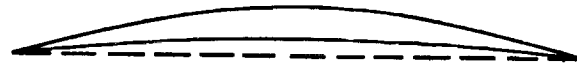
(d) $\Phi = 20$, $t/c = 0.06$



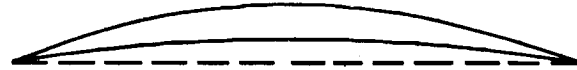
(e) $\Phi = 20$, $t/c = 0.10$

Figure 5. - Double circular-arc profiles.





(f) $\Phi = 25$, $t/c = 0.06$



(g) $\Phi = 30$, $t/c = 0.06$



(h) $\Phi = 30$, $t/c = 0.10$



(i) $\Phi = 40$, $t/c = 0.06$

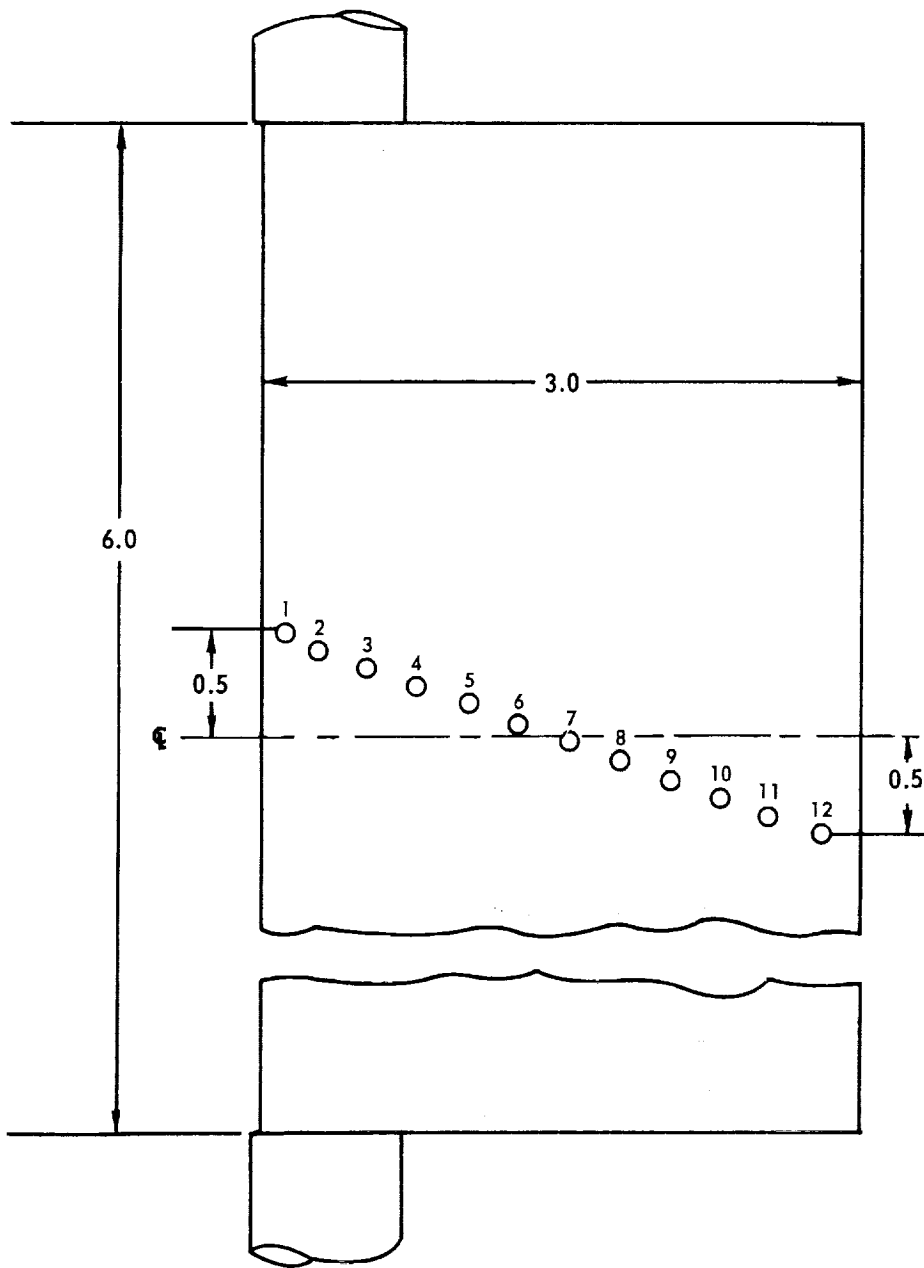


(j) $\Phi = 40$, $t/c = 0.10$

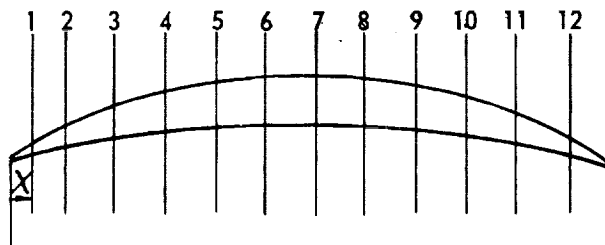


(k) $\Phi = 45$, $t/c = 0.06$

Figure 5. - Concluded.



NO.	X	% CHORD
1	0.125	4.16
2	0.250	8.33
3	0.500	16.67
4	0.750	25.00
5	1.000	33.33
6	1.250	41.60
7	1.500	50.00
8	1.750	58.33
9	2.000	66.67
10	2.250	75.00
11	2.500	83.33
12	2.750	91.67



Note: All dimensions are in inches

Figure 6. - Location of static pressure instrumentation - suction and pressure surfaces.

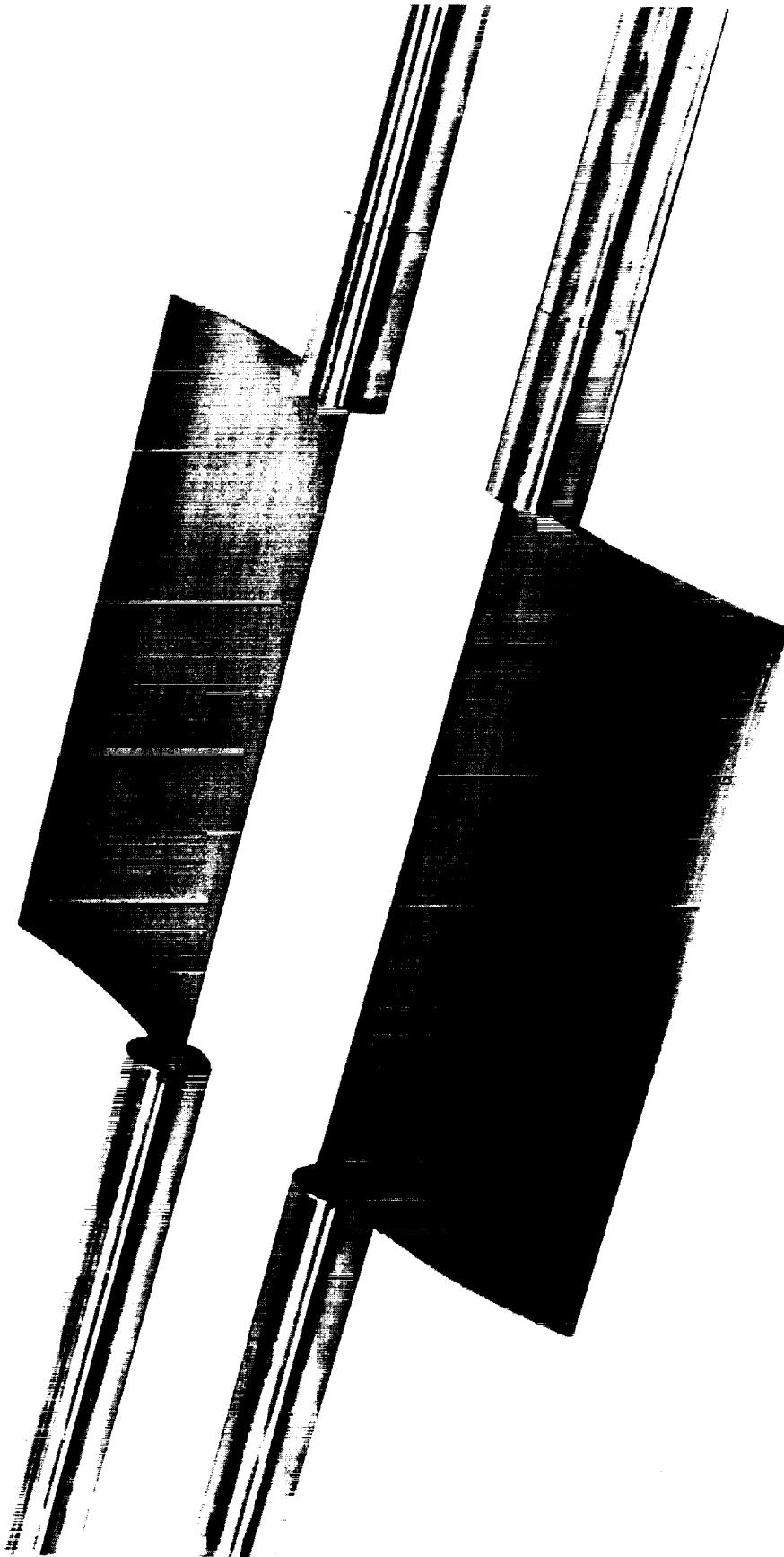


Figure 7. — Static pressure instrumentation in 40-deg camber double circular-arc hydrofoils.

() NUMBERS CORRESPOND TO STATIC PRESSURE TAP LOCATIONS

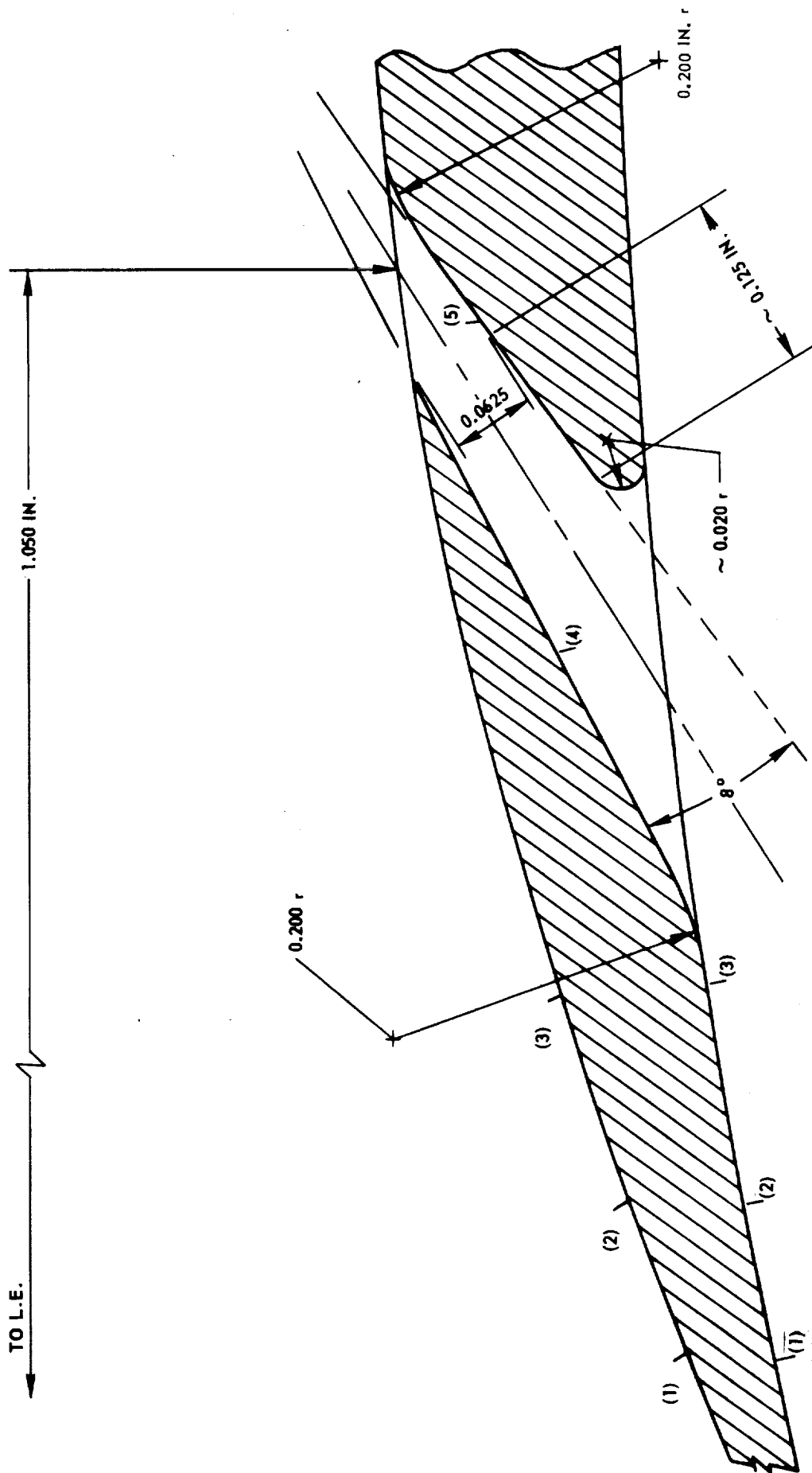
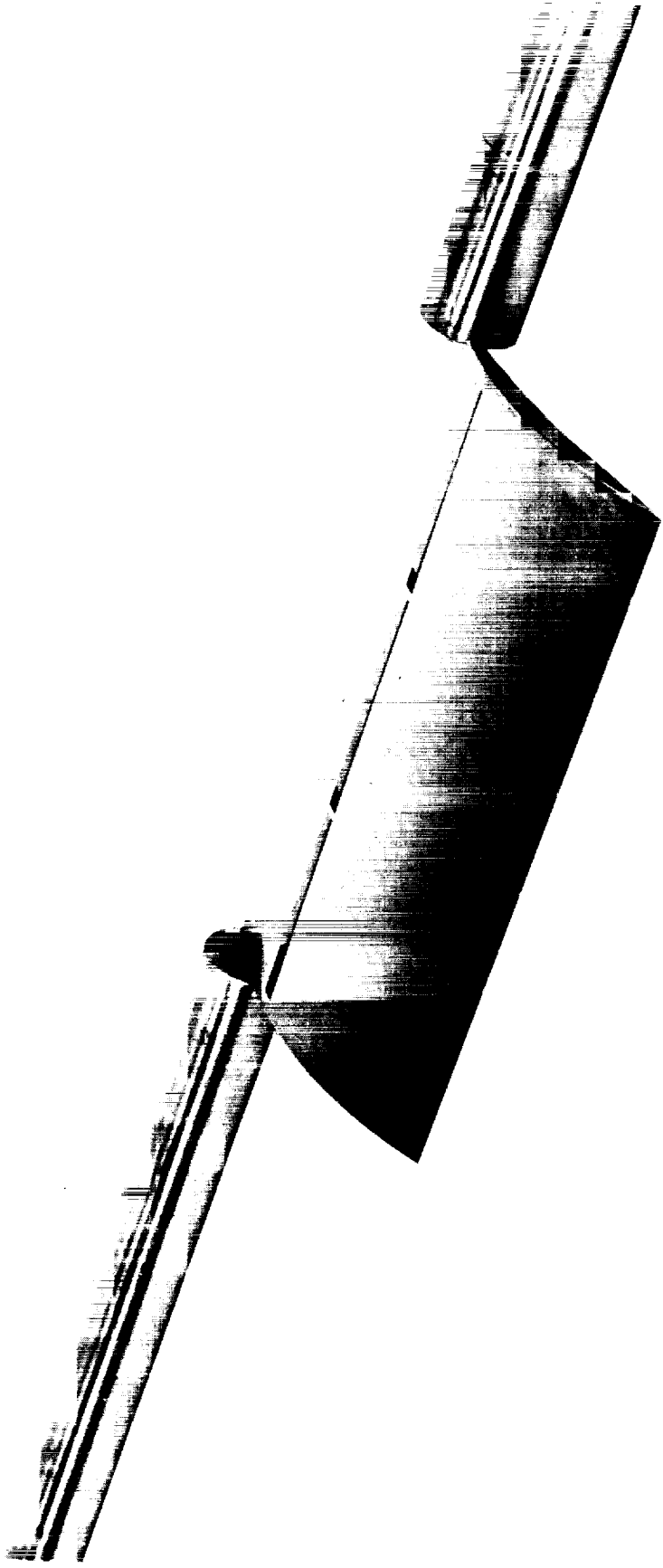
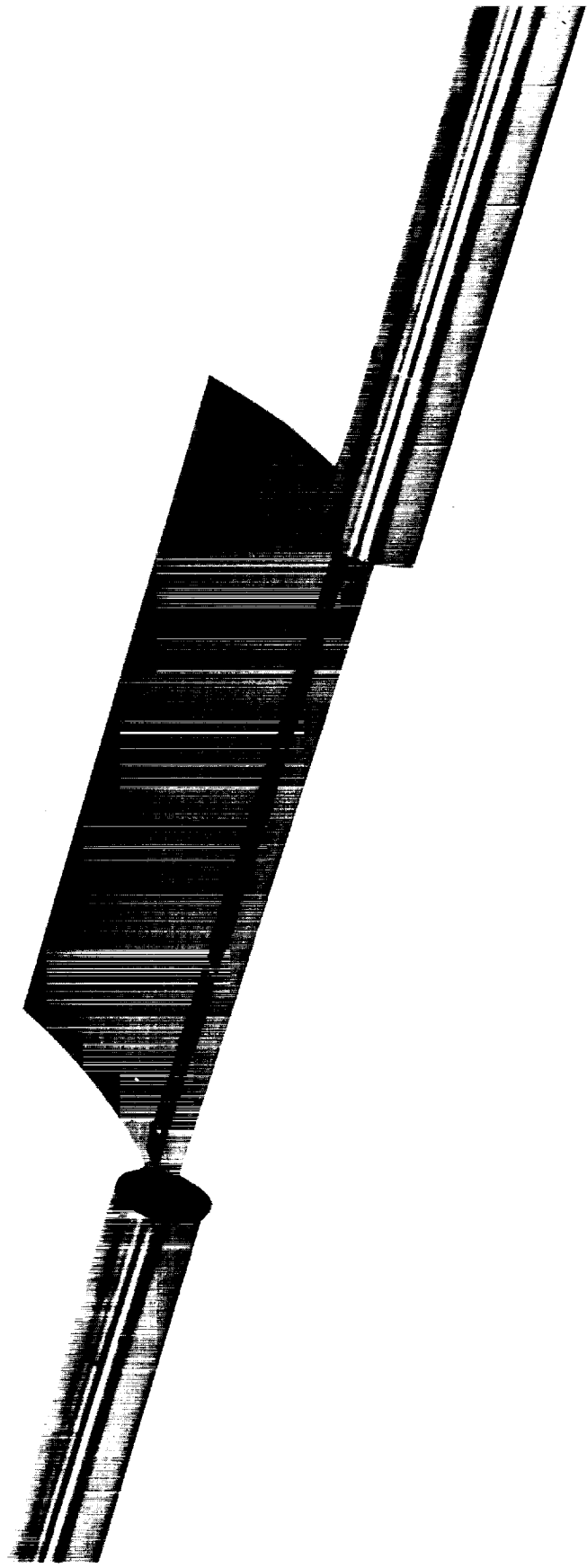


Figure 8.— Slot configuration for double circular-arc hydrofoils.



(a) Suction surface.

Figure 9. — Slotted double circular-arc hydrofoil.



(b) Pressure surface .

Figure 9. - Concluded



a. Wedge (upstream)



b. Kiel-wedge combination
(downstream)

Figure 10. -Directional probes

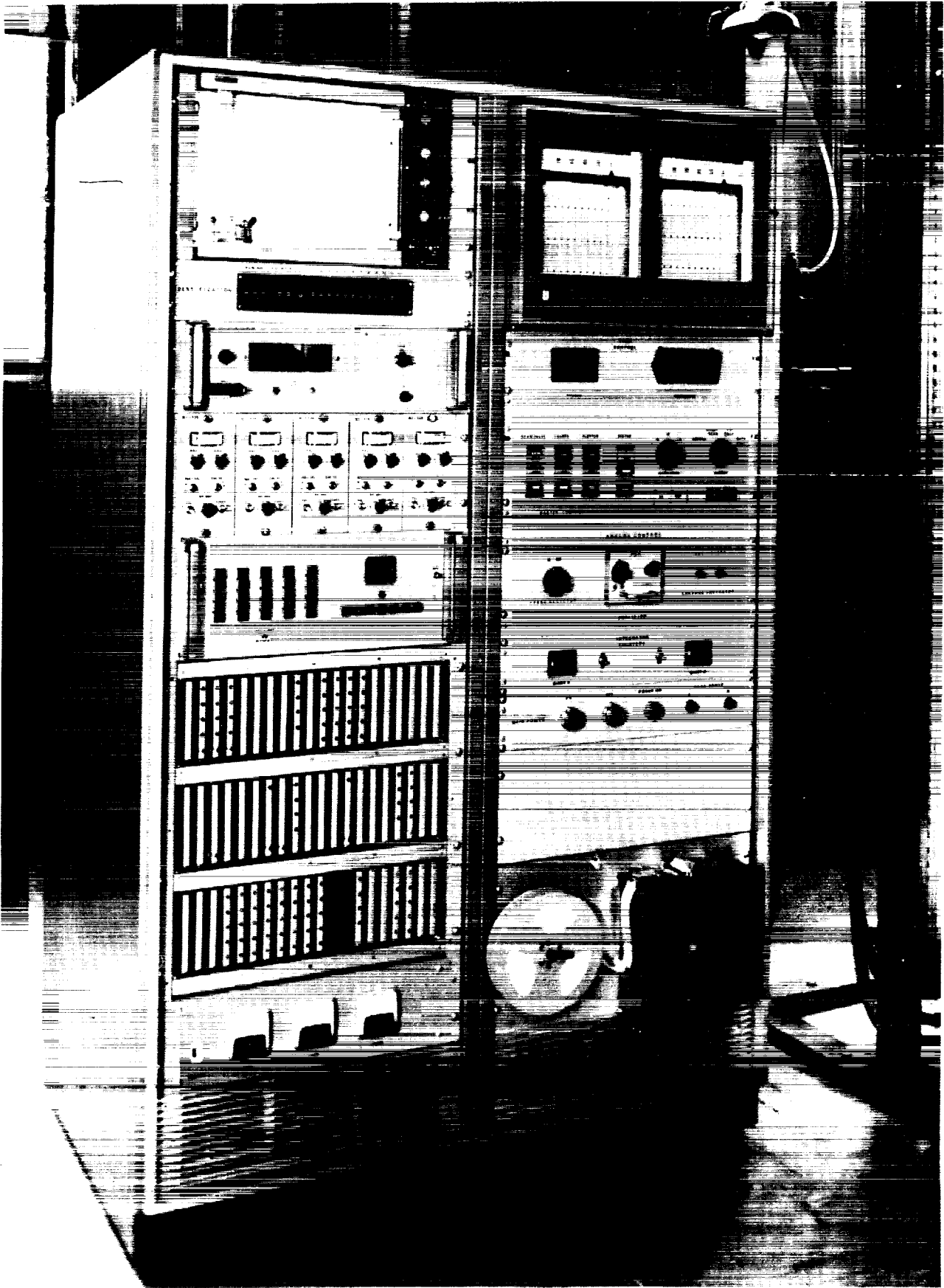


Figure 11. - Data acquisition system.

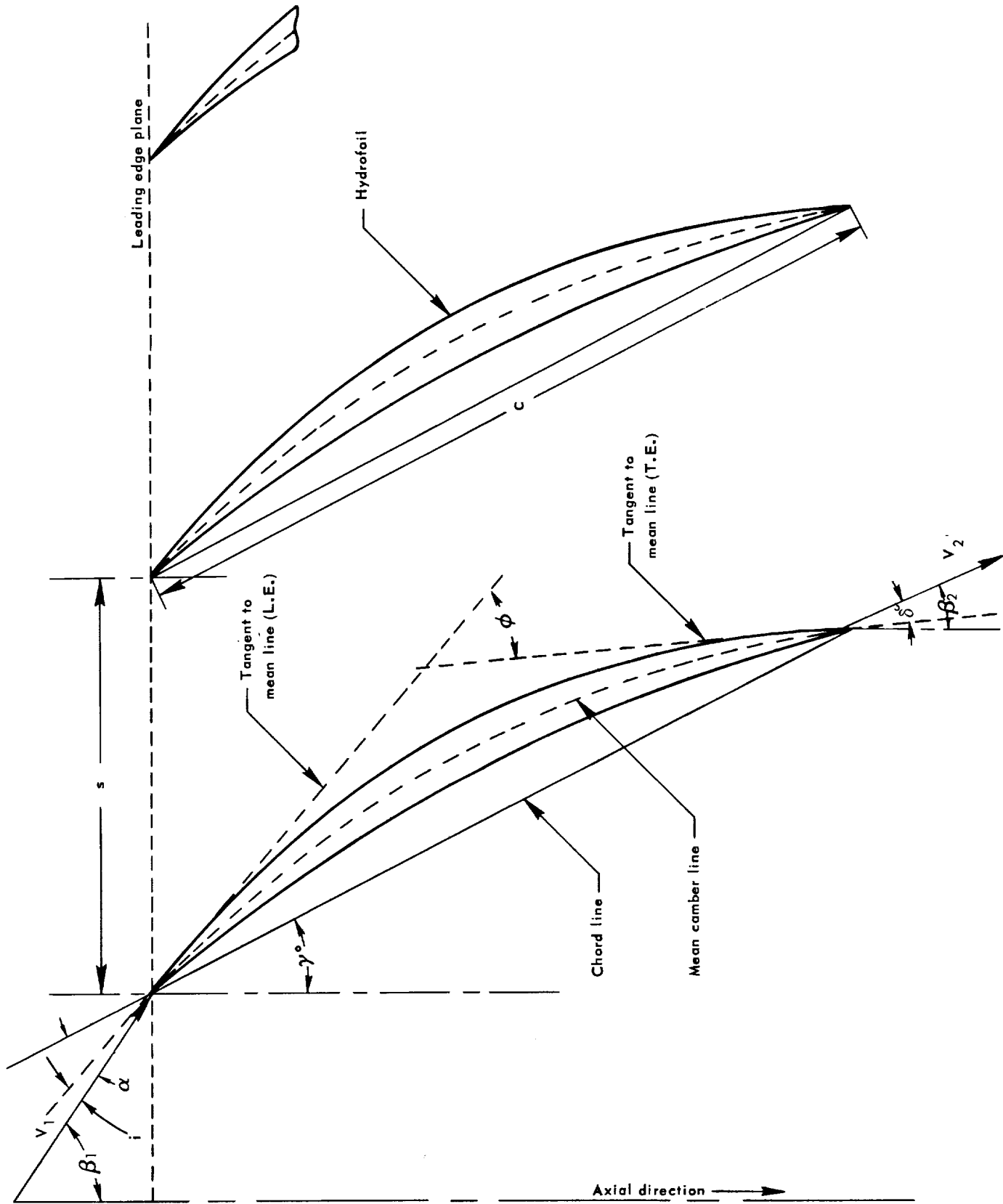
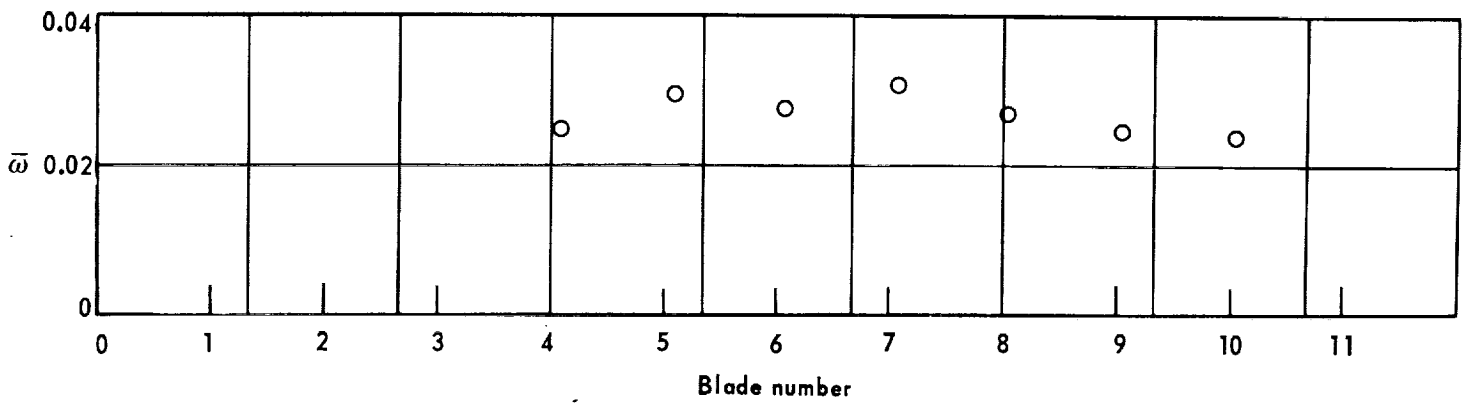
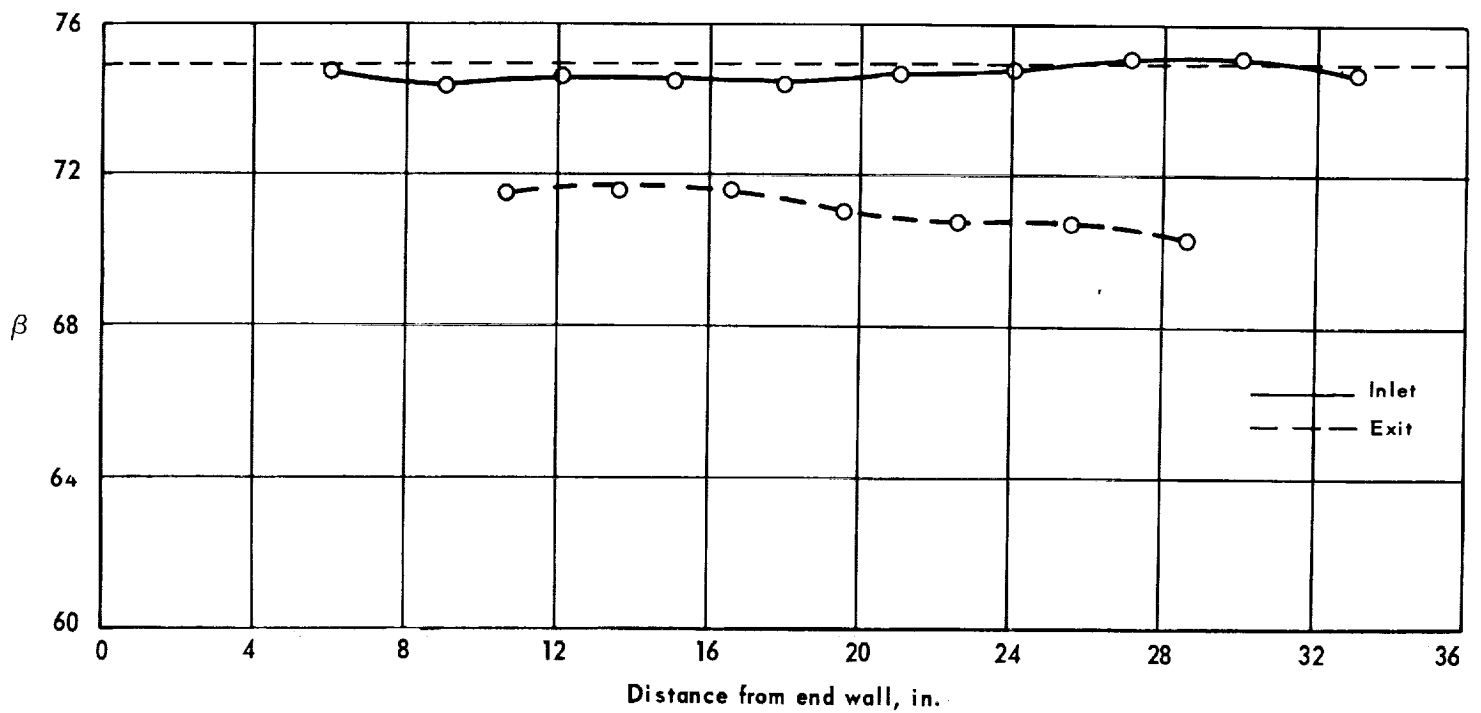
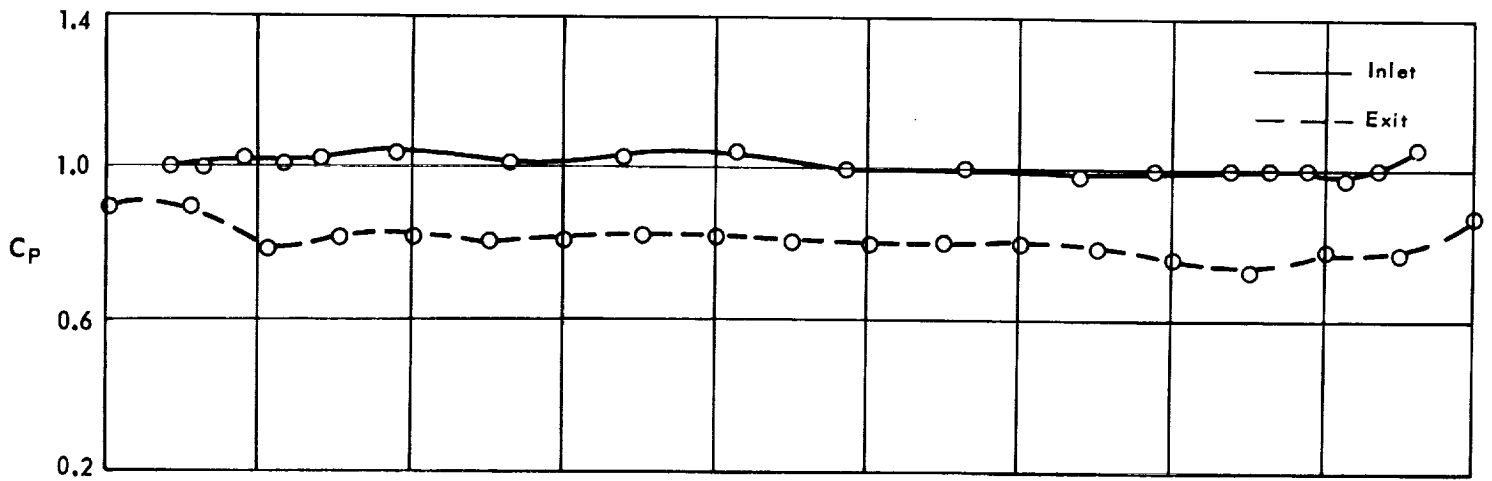
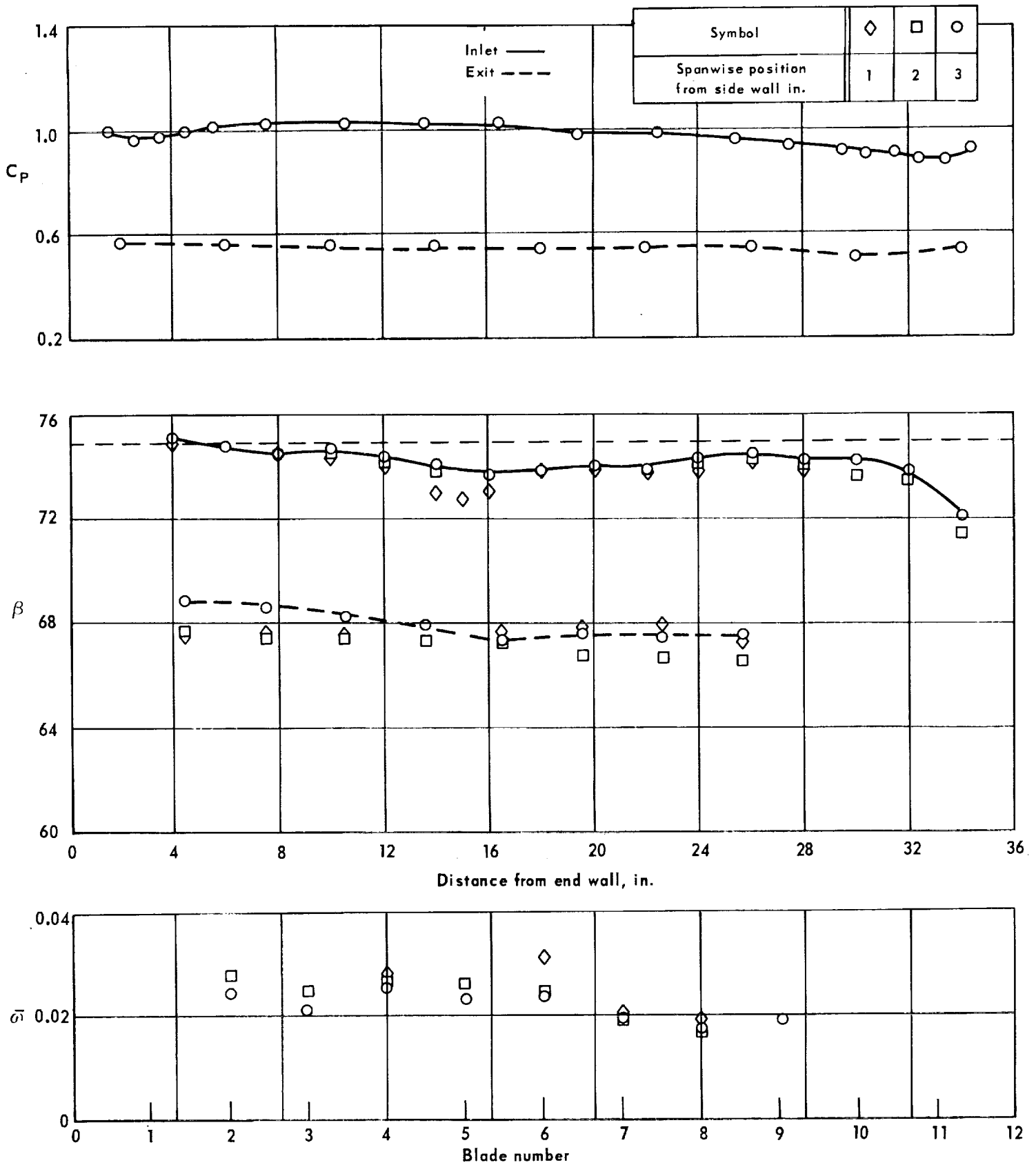


Figure 12: - Cascade nomenclature.



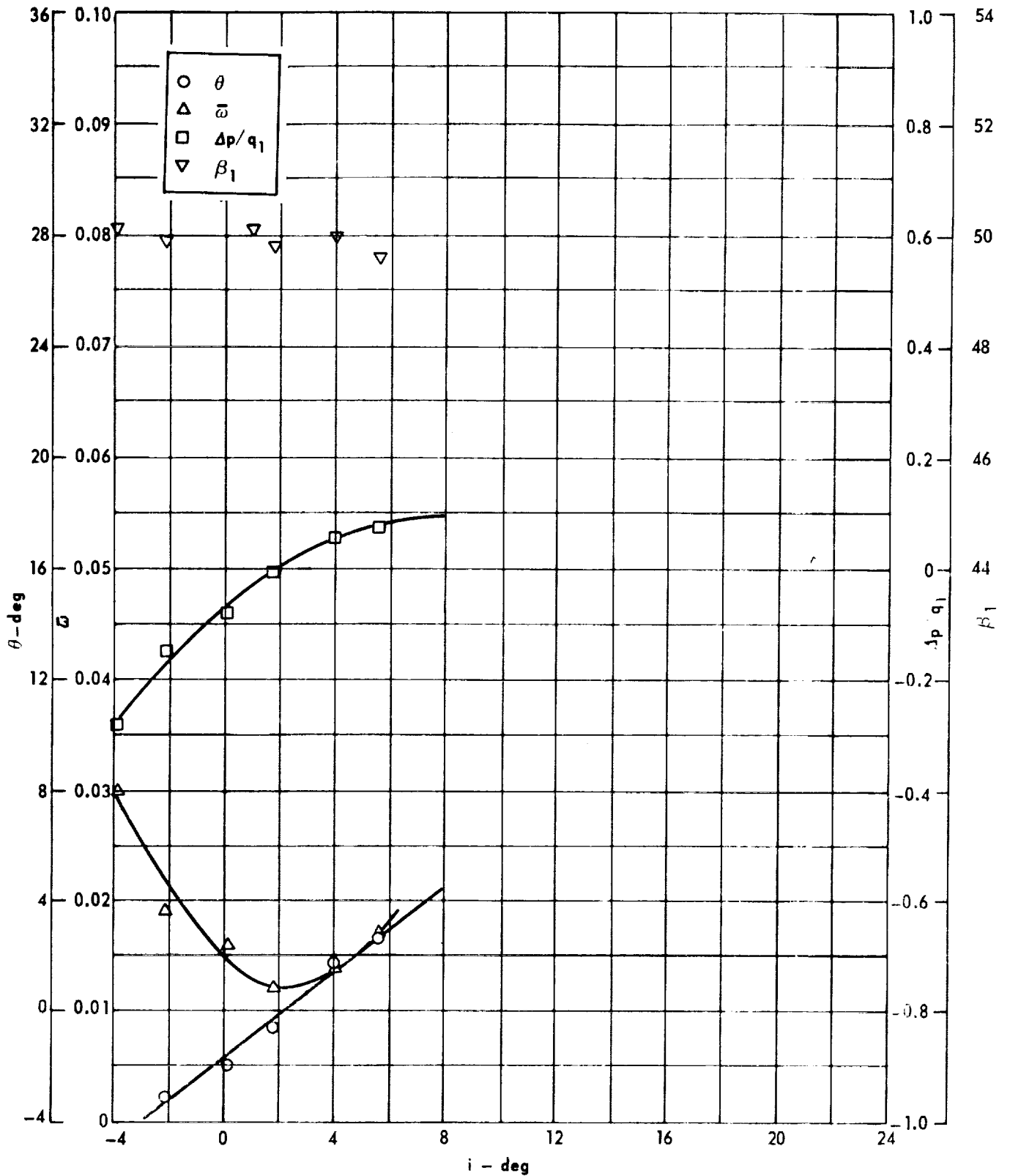
$(q_2/q_1)_{2D} = 0.76 ; (q_2/q_1)_E = 0.79$
 $\beta_{1N} = 75, \phi = 10, \sigma = 1.0$

Figure 13. - Cascade flow distributions. $i = 4$ deg



$(q_2/q_1)_{2D} = 0.59 ; (q_2/q_1)_E = 0.54$
 $\beta_{1N} = 75, \phi = 0, \sigma = 1.0$

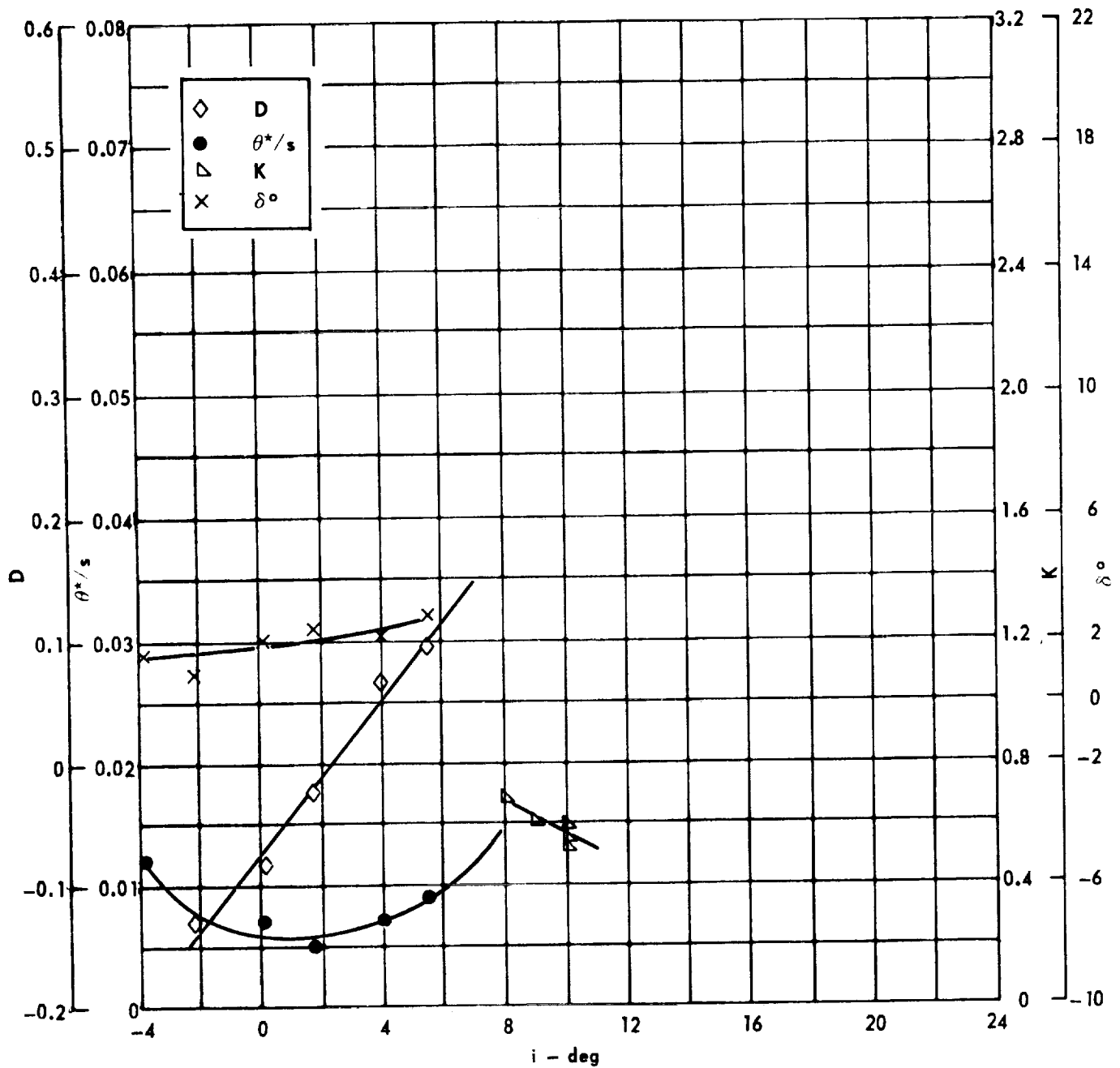
Figure 14. - Cascade flow distributions - spanwise; $i = 1$ deg



Cascade configuration : $\beta_{1N} = 50$, $\sigma = 0.75$
 Double circular-arc profile : $\phi = 0$, $t/c = 0.06$

(a) $\theta, \bar{\omega}, \Delta p / q_1, \beta_1$

Figure 15 . - Cascade characteristics as functions of incidence.

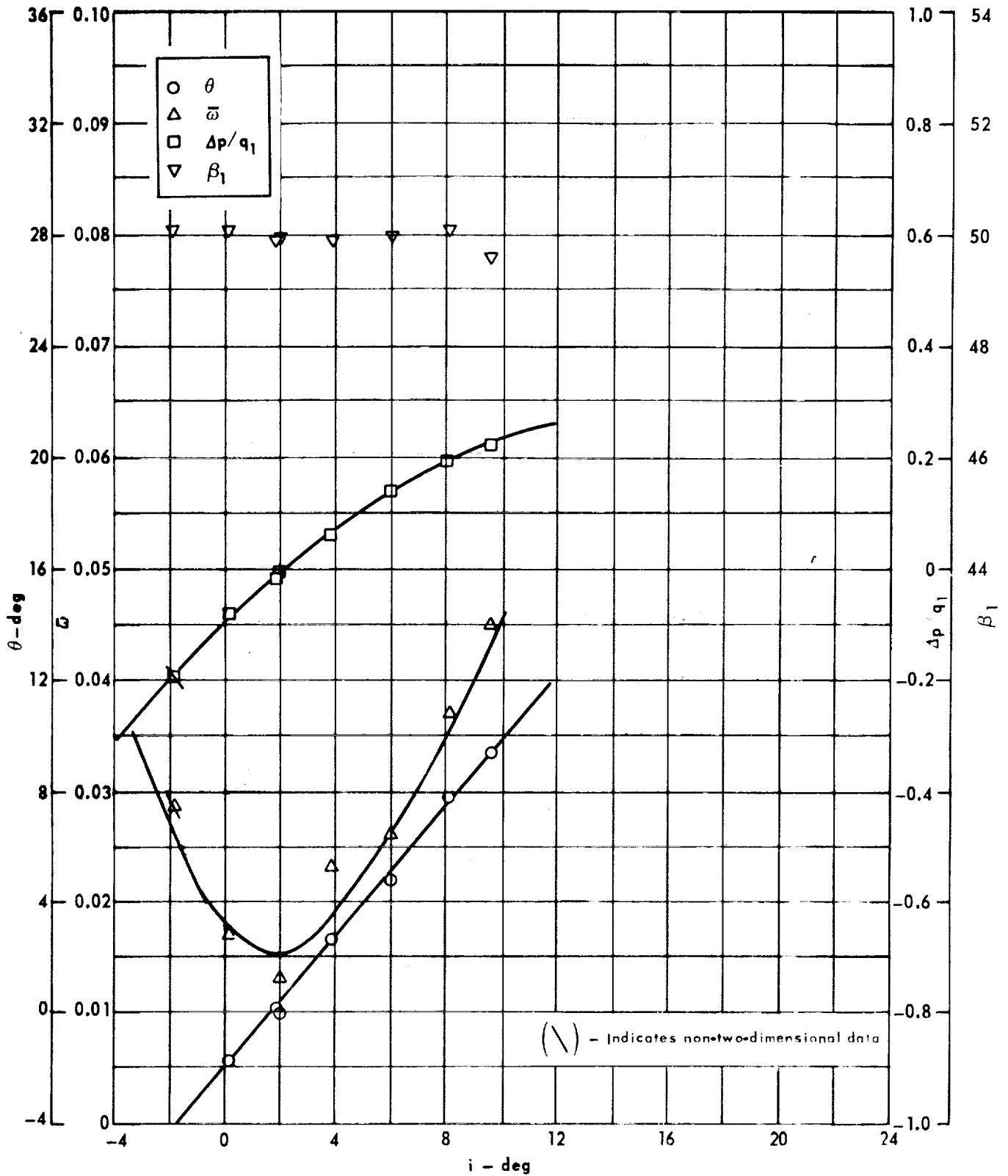


Cascade configuration : $\beta_{1N} = 50, \sigma = 0.75$

Double circular-arc profile : $\phi = 0, t/c = 0.06$

(b) D, θ^*/s , K, δ°

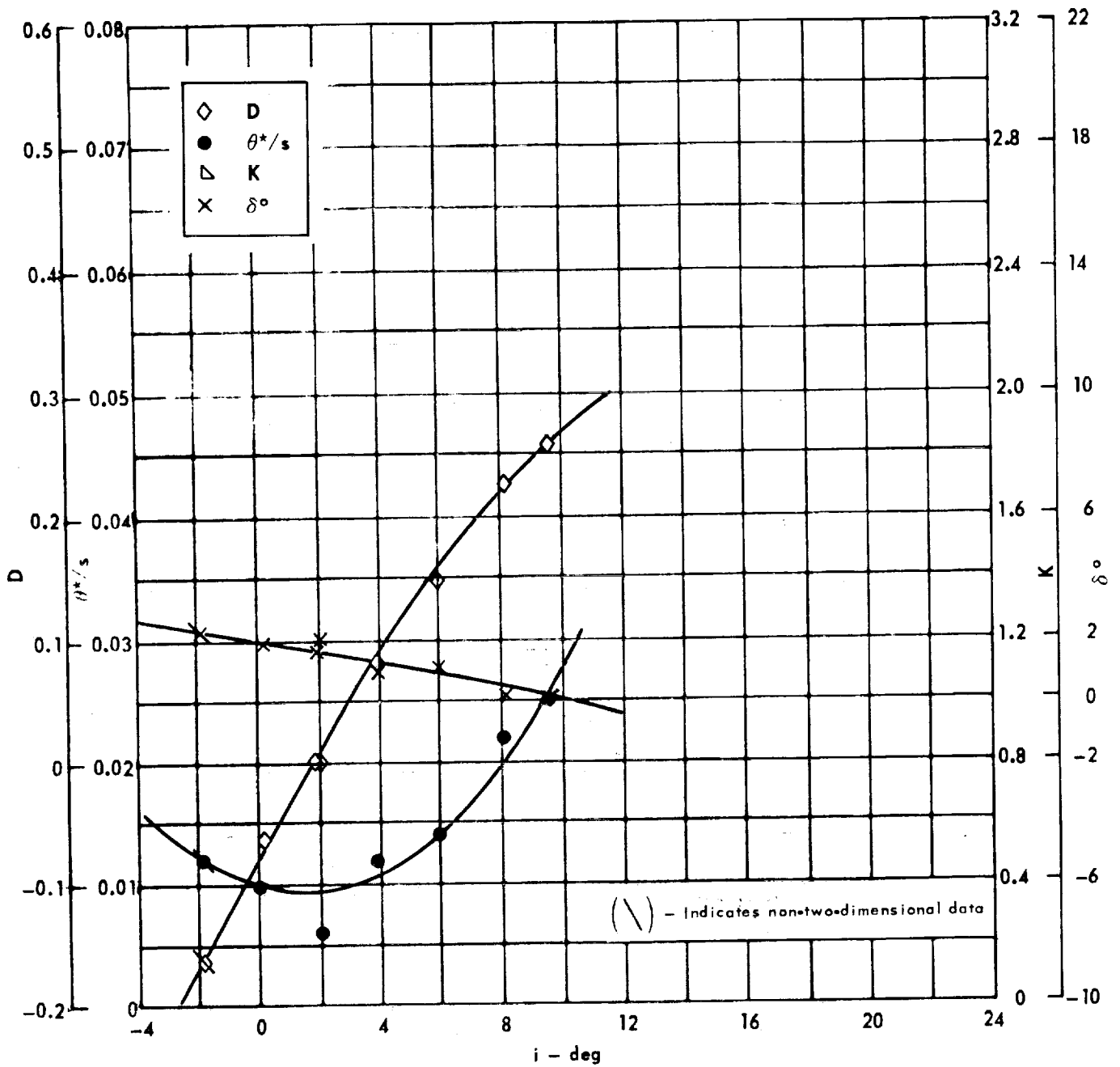
Figure 15. - Concluded.



Cascade configuration: $\beta_{1N} = 50$, $\sigma = 1.00$
 Double circular-arc profile: $\phi = 0$, $t/c = 0.06$

(a) $\theta, \bar{w}, \Delta p / q_1, \beta_1$

Figure 16 . - Cascade characteristics as functions of incidence.

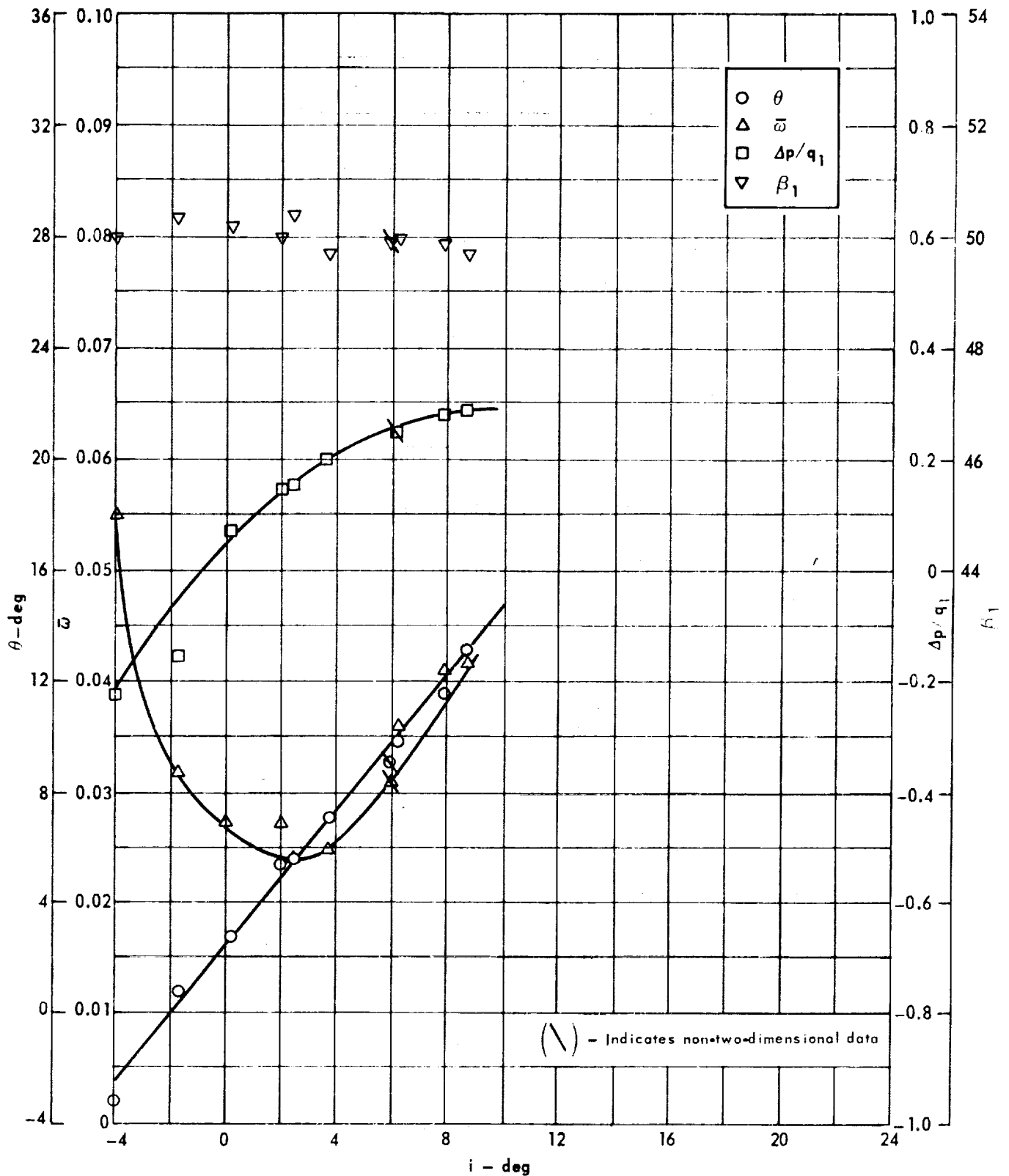


Cascade configuration: $\beta_{1N} = 50$, $\sigma = 1.00$

Double circular-arc profile: $\phi = 0$, $t/c = 0.06$

(b) $D, \theta^*/s, K, \delta^\circ$

Figure 16 . - Concluded.

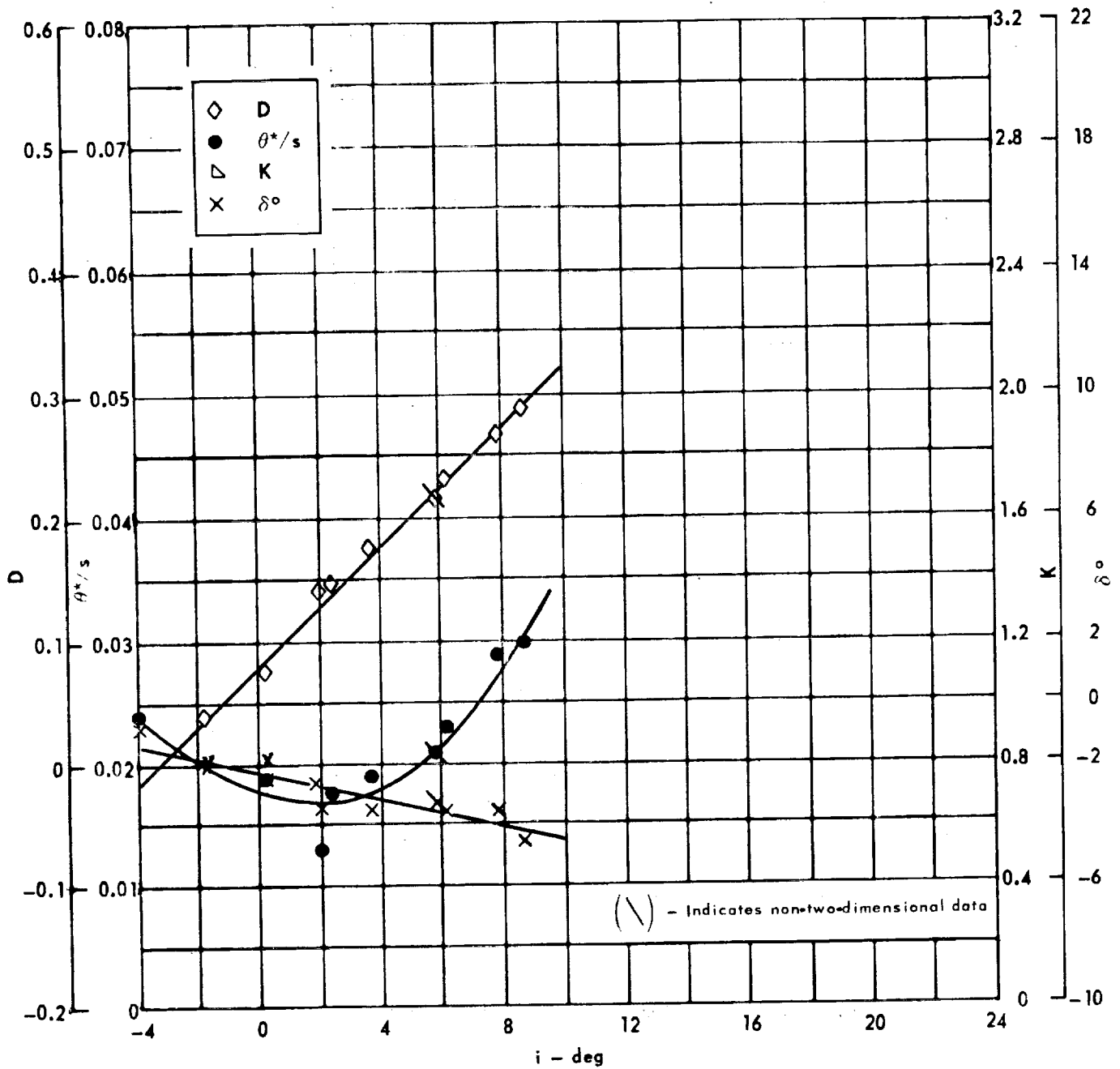


Cascade configuration: $\beta_{1N} = 50, \sigma = 1.50$

Double circular-arc profile: $\phi = 0, t/c = 0.06$

(a) $\theta, \bar{\omega}, \Delta p/q_1, \beta_1$

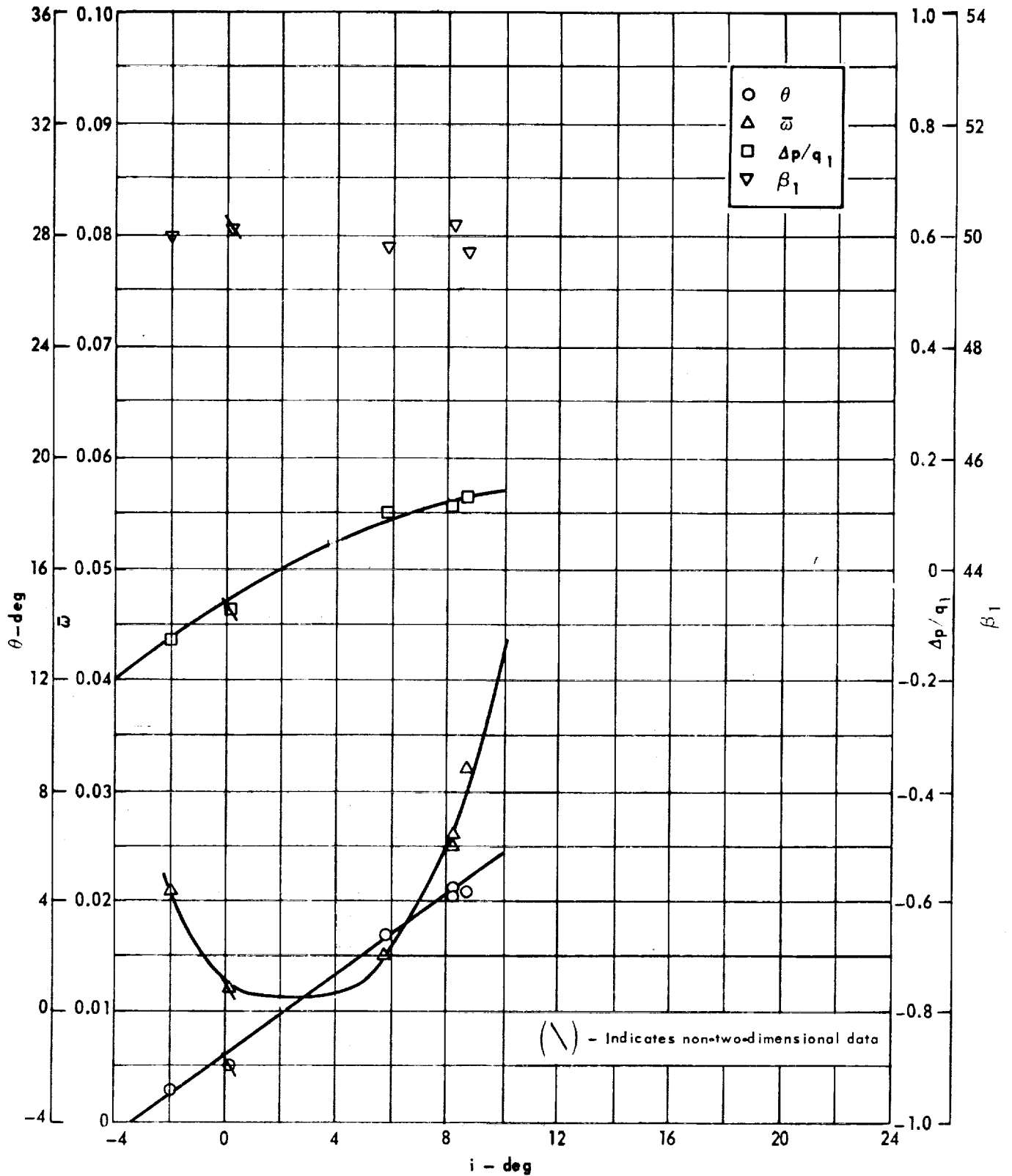
Figure 17. - Cascade characteristics as functions of incidence.



Cascade configuration: $\beta_{1N} = 50$, $\sigma = 1.50$
 Double circular-arc profile: $\phi = 0$, $t/c = 0.06$

(b) D, θ^*/s , K, δ°

Figure 17 . - Concluded.

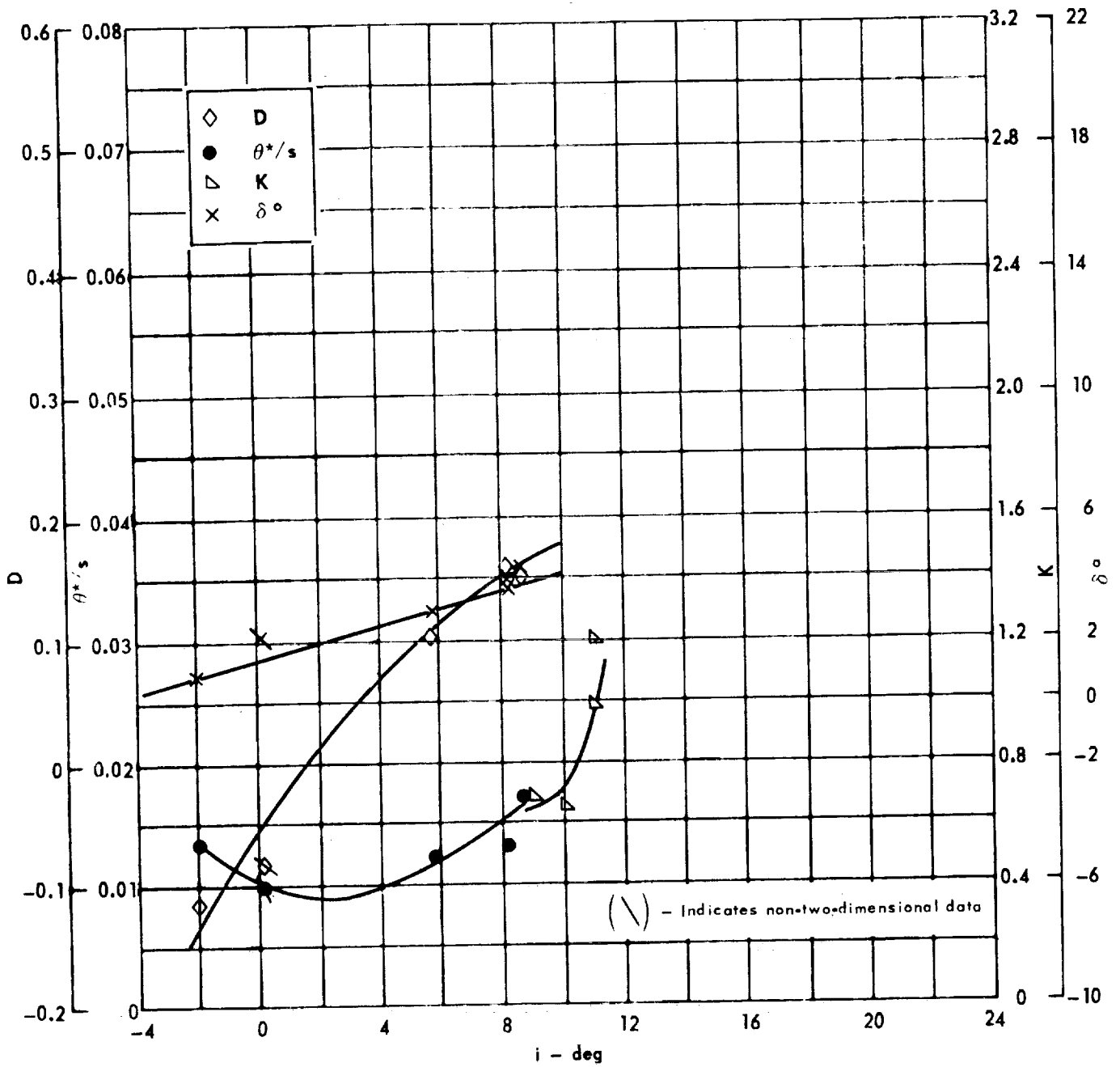


Cascade configuration: $\beta_{1N} = 50$, $\sigma = 0.75$

Double circular-arc profile: $\phi = 0$, $r/c = 0.10$

(a) $\theta, \bar{\omega}, \Delta p/q_1, \beta_1$

Figure 18 . - Cascade characteristics as functions of incidence.

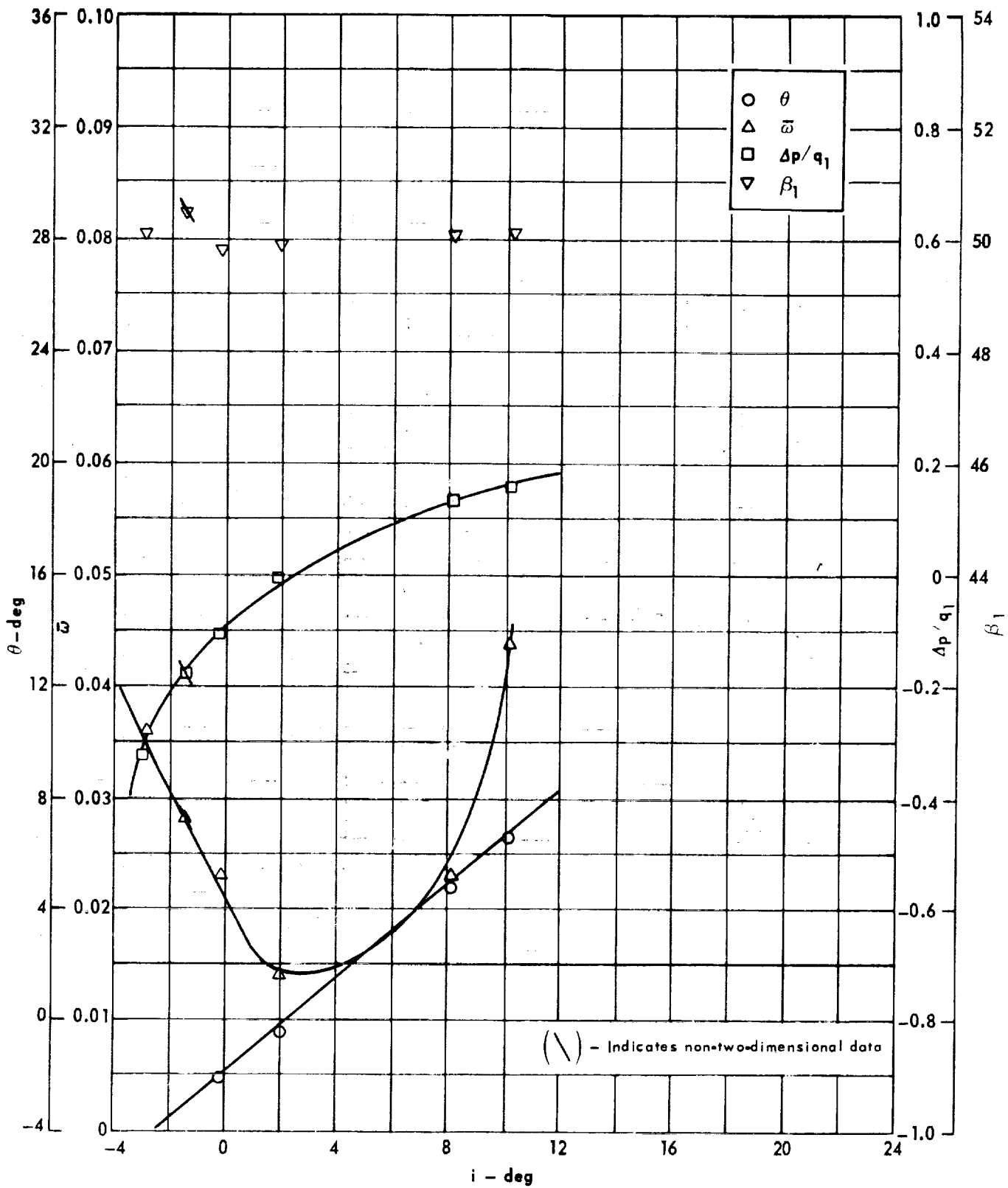


Cascade configuration: $\beta_{1N} = 50, \sigma = 0.75$

Double circular-arc profile: $\phi = 0, t/c = 0.10$

(b) D, θ^*/s , K, δ°

Figure 18 . - Concluded.

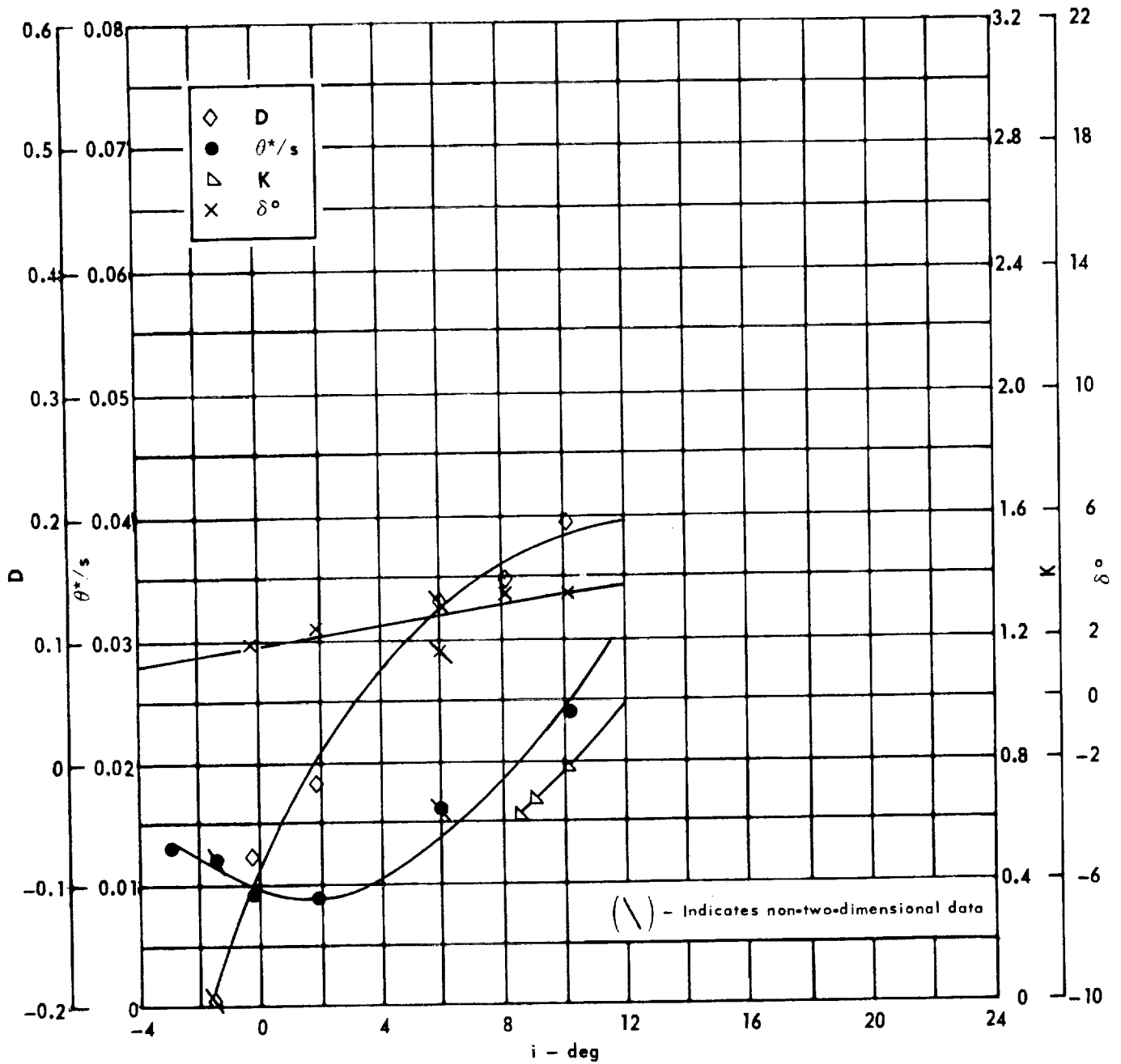


Cascade configuration : $\beta_{1N} = 50, \sigma = 1.00$

Double circular-arc profile : $\phi = 0, t/c = 0.10$

(a) $\theta, \bar{w}, \Delta p/q_1, \beta_1$

Figure 19 . - Cascade characteristics as functions of incidence.

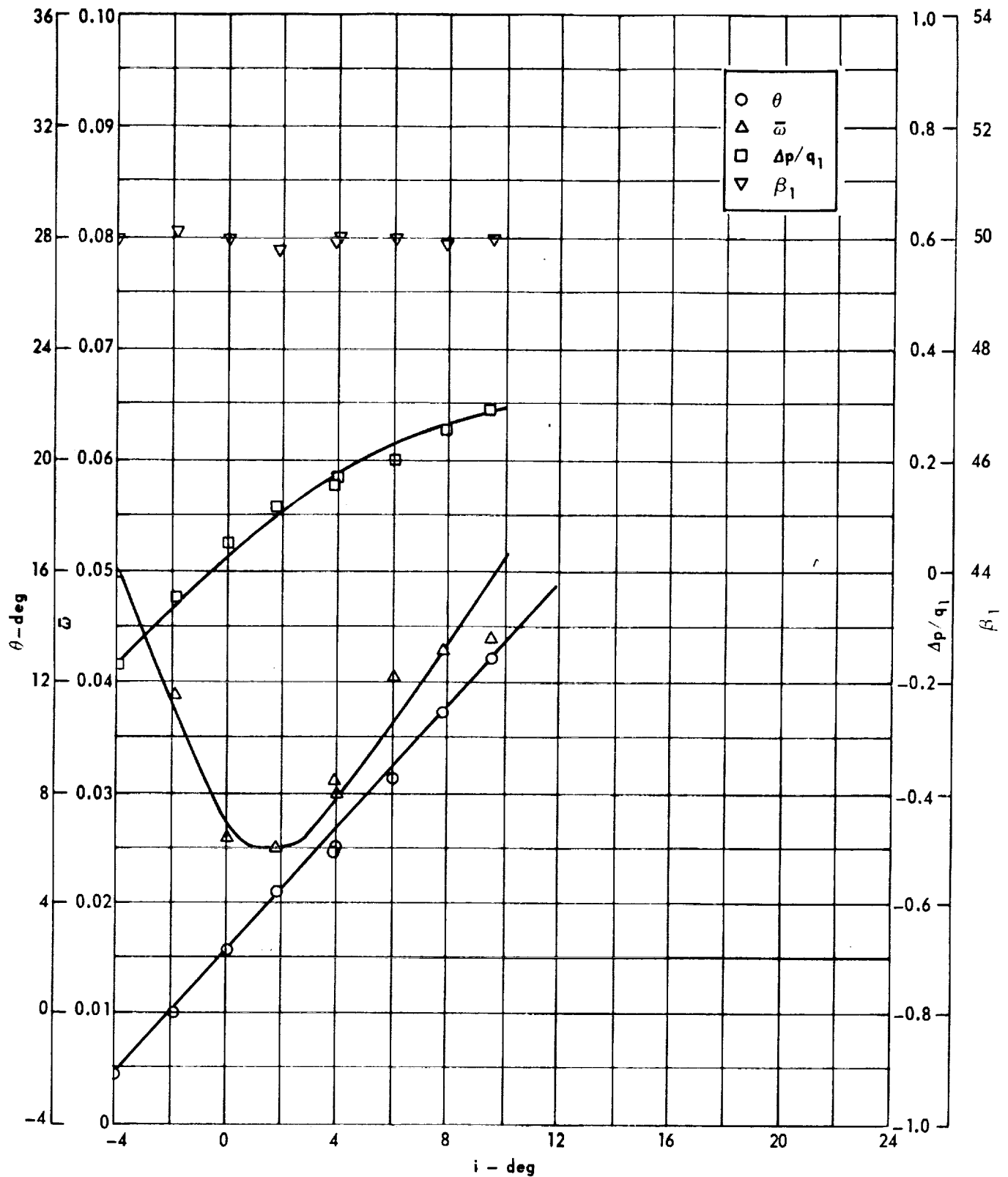


Cascade configuration: $\beta_{1N} = 50, \sigma = 1.00$

Double circular-arc profile: $\phi = 0, t/c = 0.10$

(b) $D, \theta^*/s, K, \delta^\circ$

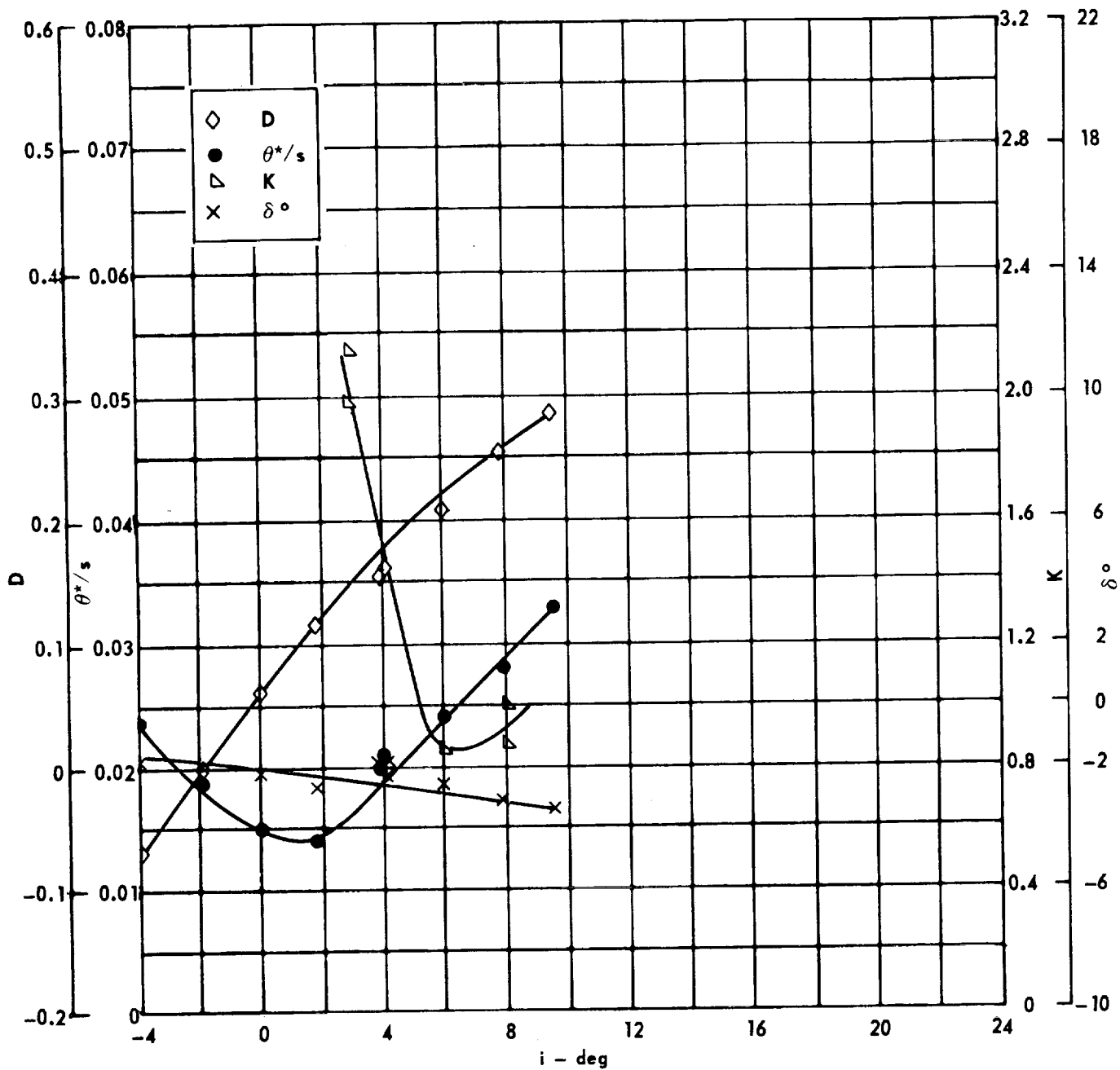
Figure 19 . - Concluded.



Cascade configuration : $\beta_{1N} = 50$, $\sigma = 1.50$
 Double circular-arc profile : $\phi = 0$, $t/c = 0.10$

(a) $\theta, \bar{\omega}, \Delta p/q_1, \beta_1$

Figure 20 . - Cascade characteristics as functions of incidence.

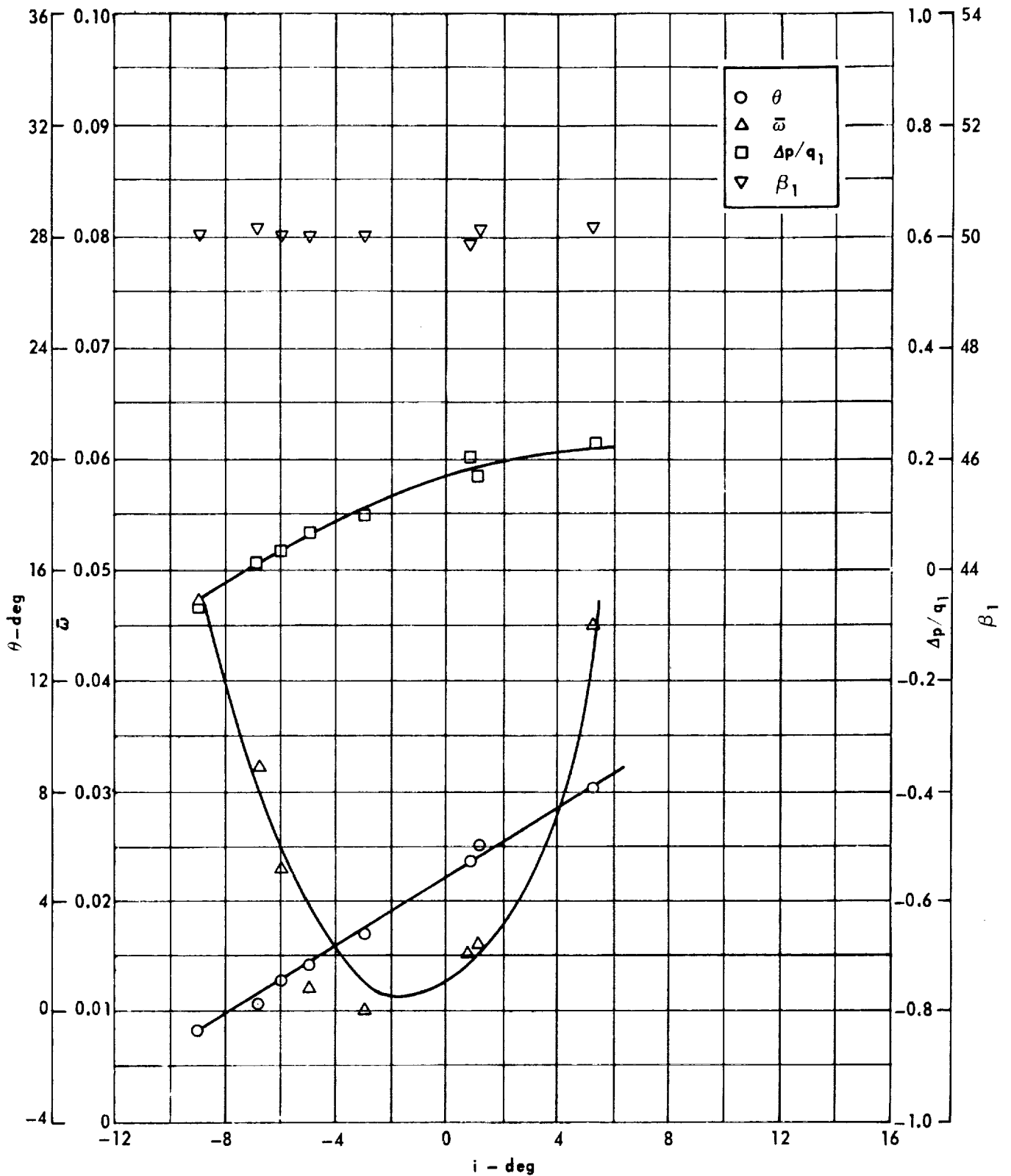


Cascade configuration: $\beta_{1N} = 50$, $\sigma = 1.50$

Double circular-arc profile: $\phi = 0$, $t/c = 0.10$

(b) $D, \theta^*/s, K, \delta^\circ$

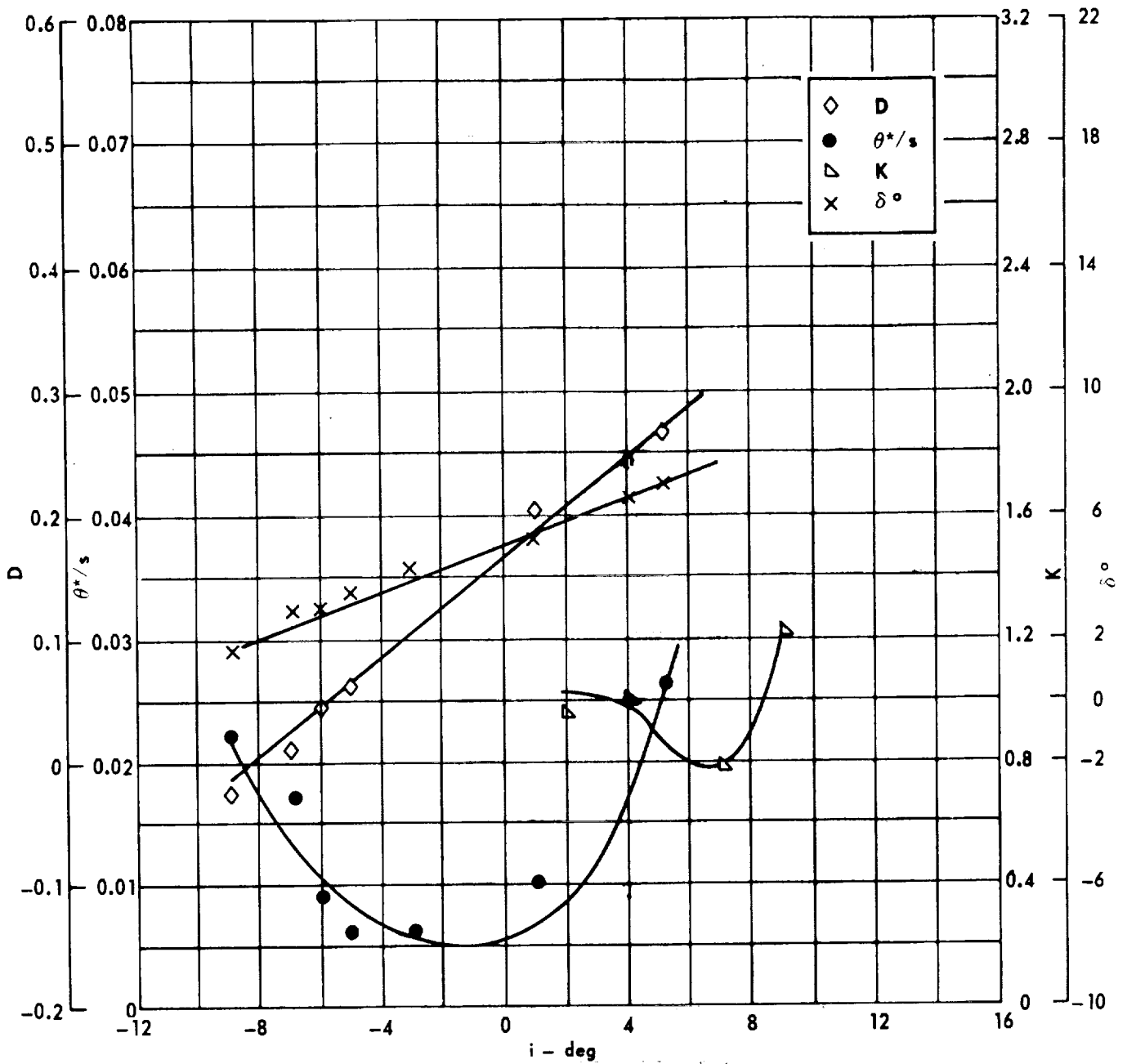
Figure 20 . - Concluded.



Cascade configuration : $\beta_{1N} = 50$, $\sigma = 0.75$
 Double circular-arc profile : $\phi = 10$, $t/c = 0.06$

(a) $\theta, \bar{\omega}, \Delta p / q_1, \beta_1$

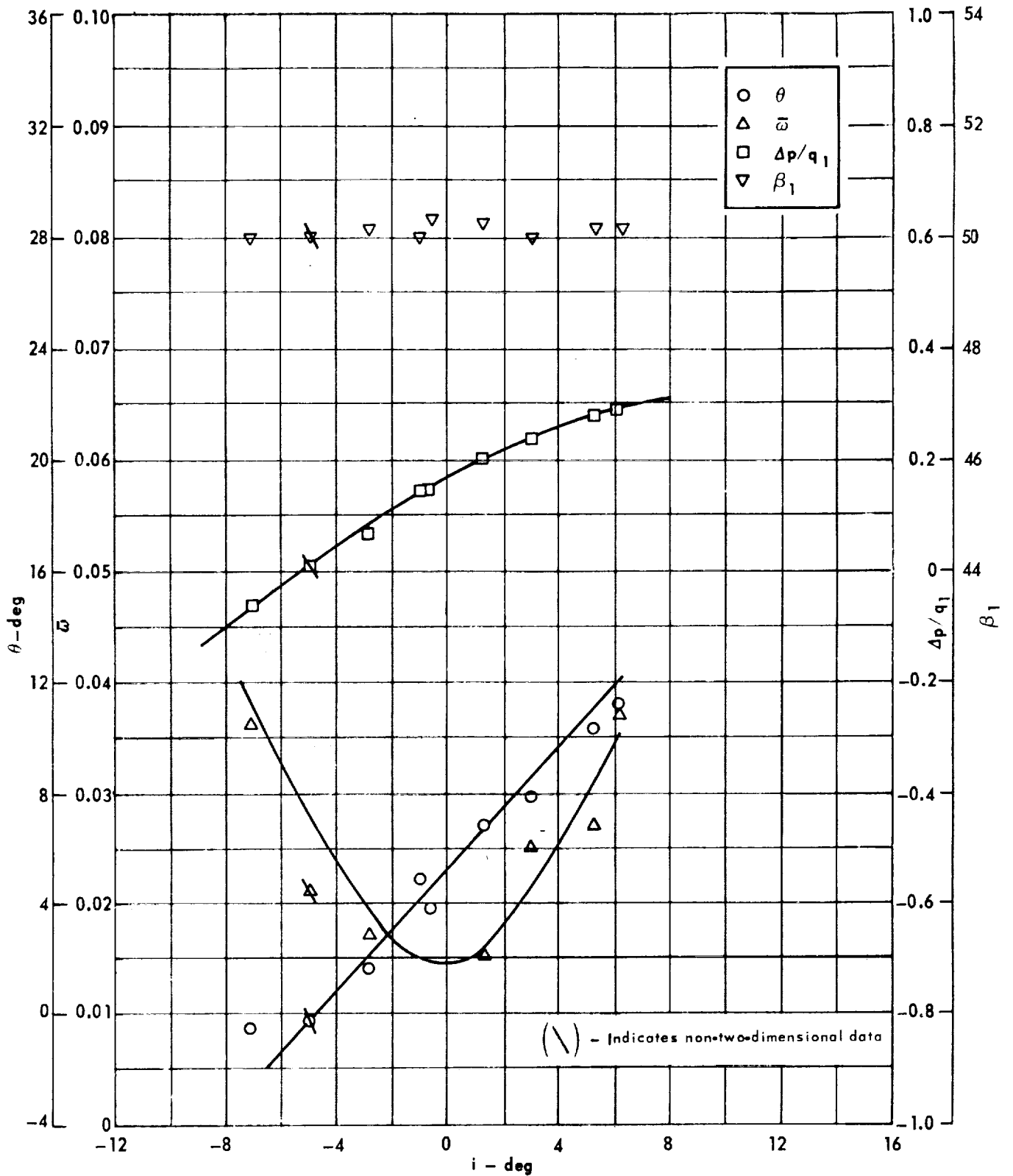
Figure 21 . - Cascade characteristics as functions of incidence.



Cascade configuration: $\beta_{1N} = 50, \sigma = 0.75$
 Double circular-arc profile: $\phi = 10, t/c = 0.06$

(b) D, θ^*/s , K, δ°

Figure 21. - Concluded.

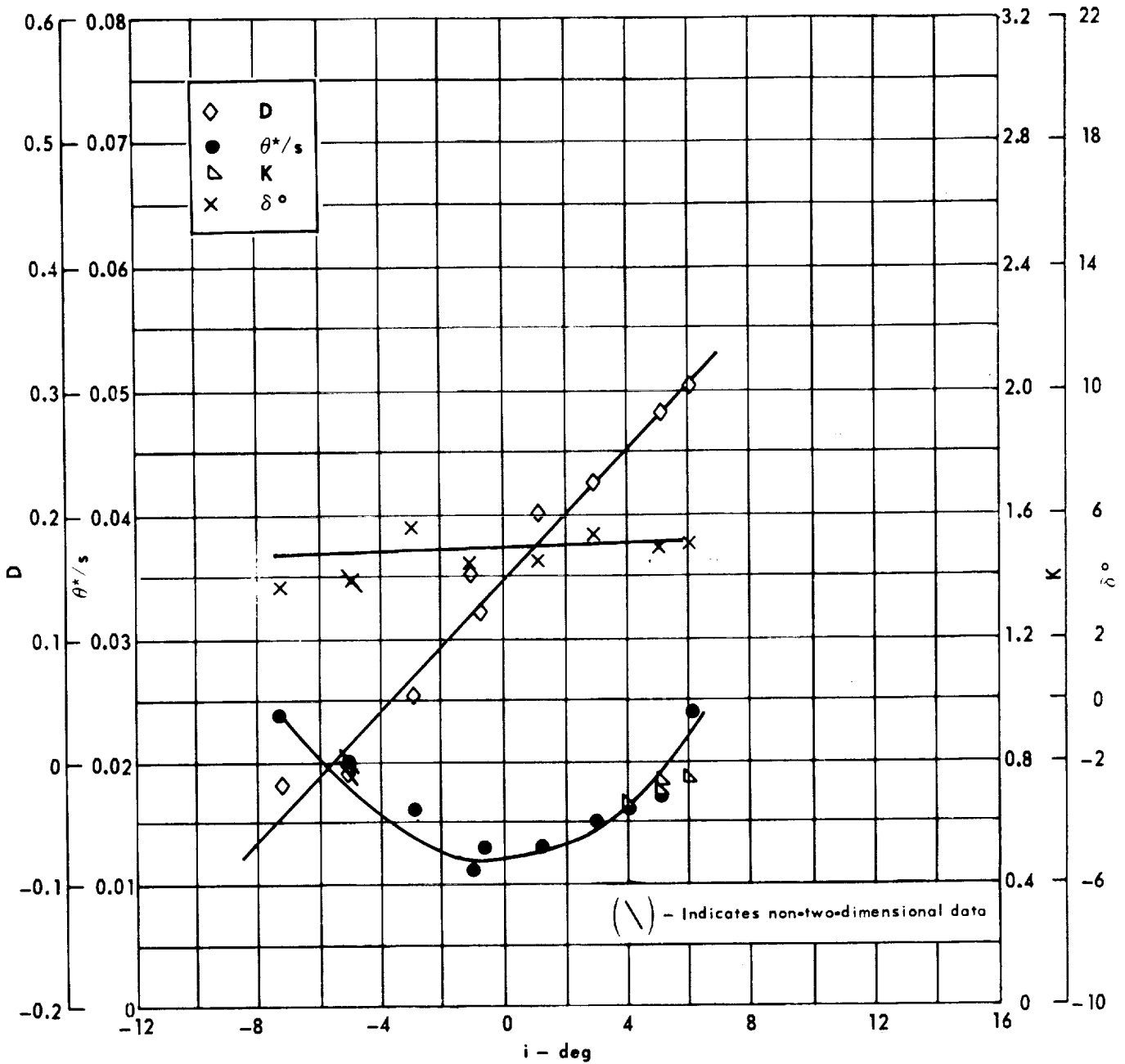


Cascade configuration : $\beta_{1N} = 50, \sigma = 1.00$

Double circular-arc profile : $\phi = 10, t/c = 0.06$

(a) $\theta, \bar{\omega}, \Delta p/q_1, \beta_1$

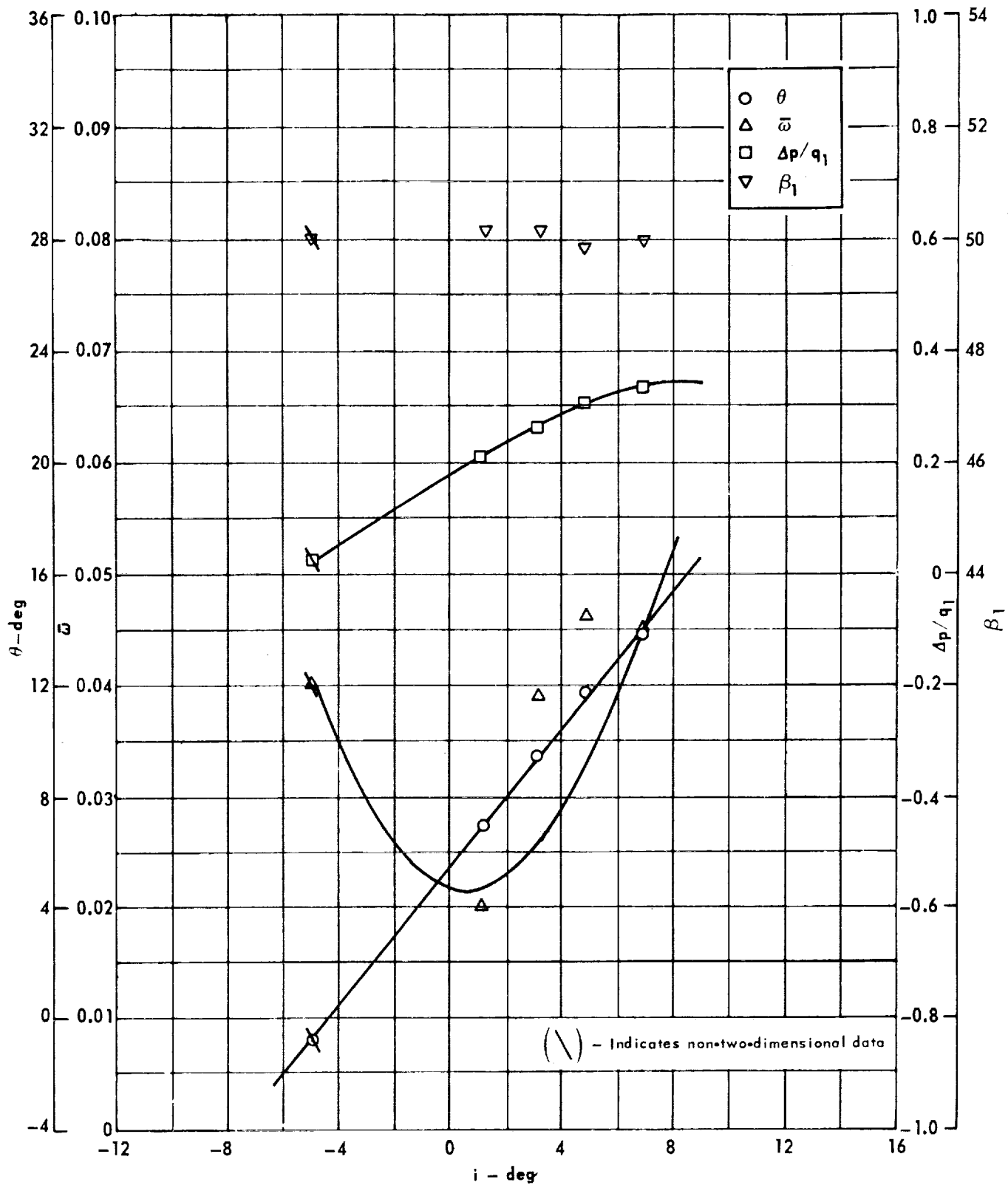
Figure 22. - Cascade characteristics as functions of incidence.



Cascade configuration : $\beta_{1N} = 50, \sigma = 1.00$
 Double circular-arc profile : $\phi = 10, t/c = 0.06$

(b) D, θ^*/s , K, δ°

Figure 22. - Concluded.



Cascade configuration: $\beta_{1N} = 50, \sigma = 1.50$

Double circular-arc profile: $\phi = 10, t/c = 0.06$

(a) $\theta, \bar{\omega}, \Delta p/q_1, \beta_1$

Figure 23 . - Cascade characteristics as functions of incidence.

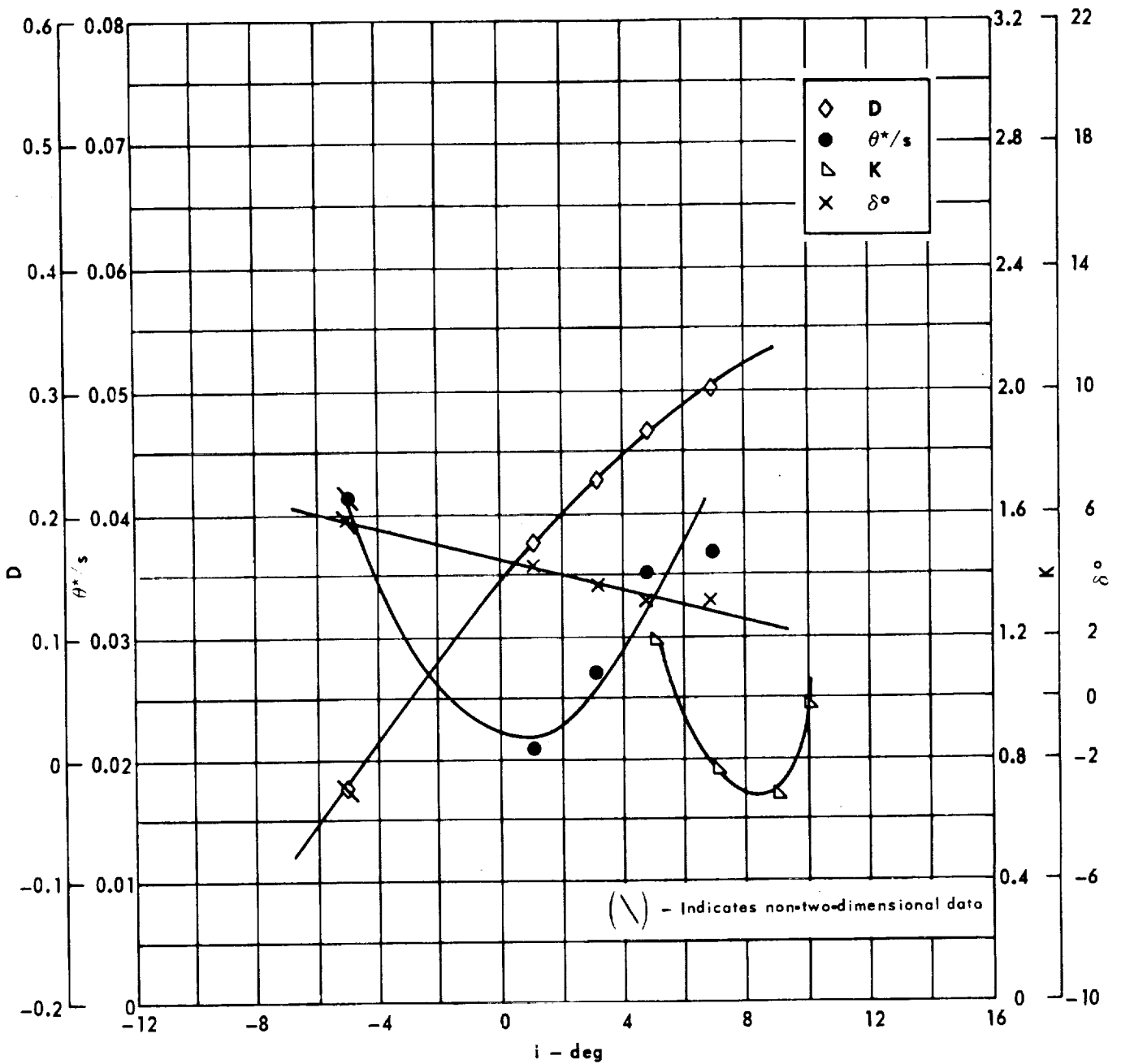
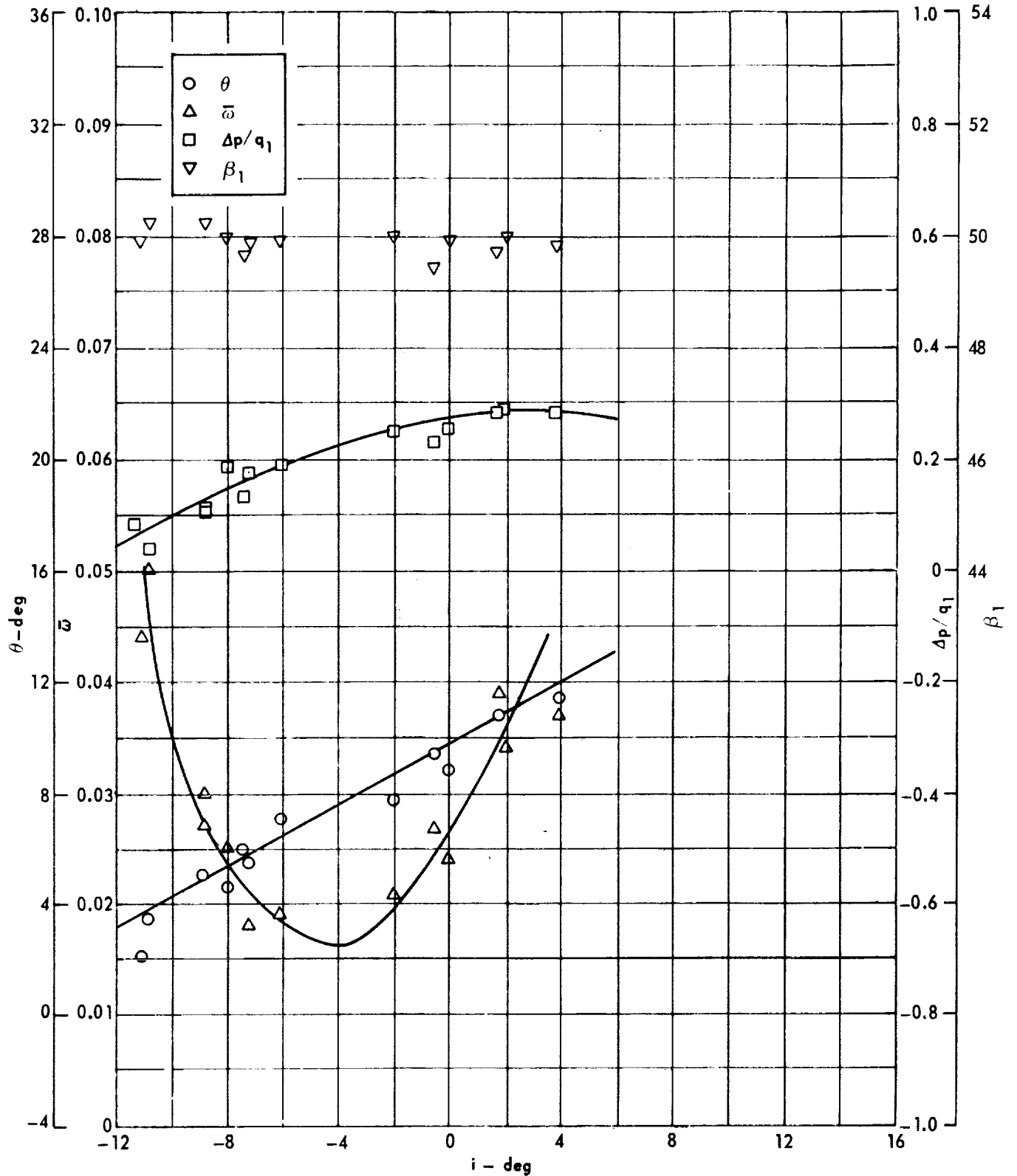


Figure 23. - Concluded.

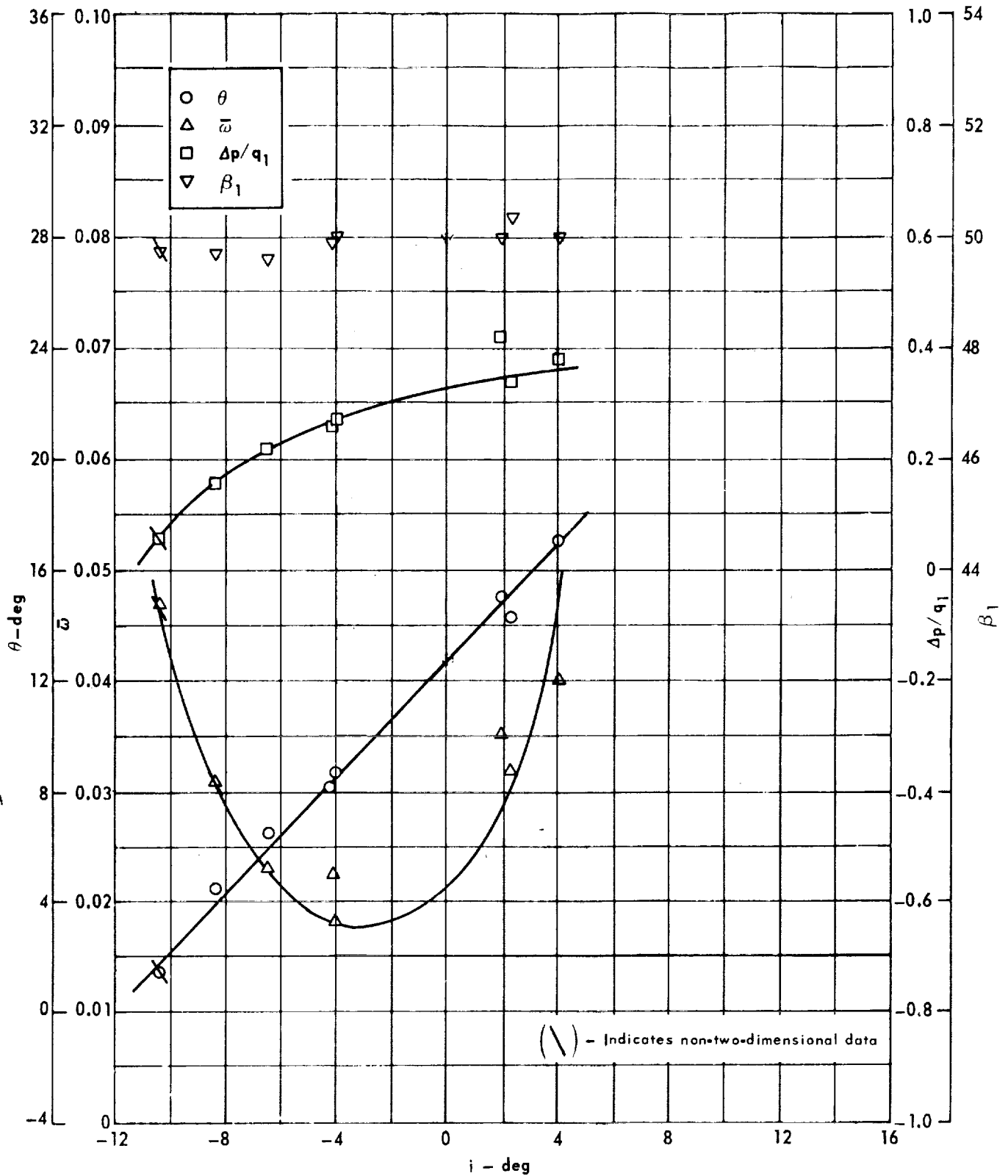


Cascade configuration : $\beta_{1N} = 50, \sigma = 0.75$

Double circular-arc profile : $\phi = 20, r/c = 0.06$

(a) $\theta, \bar{\omega}, \Delta p/q_1, \beta_1$

Figure 24. - Cascade characteristics as functions of incidence.

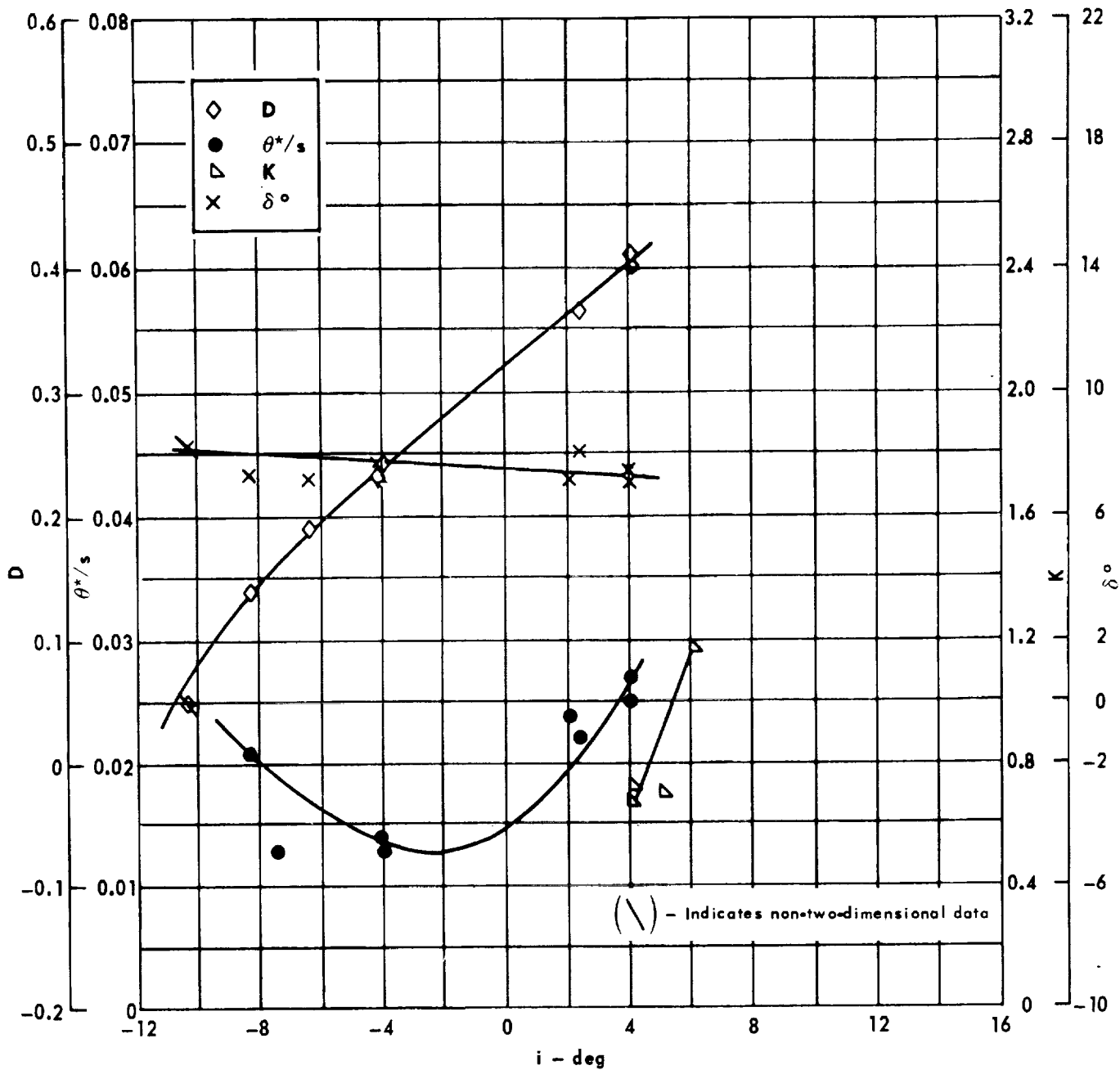


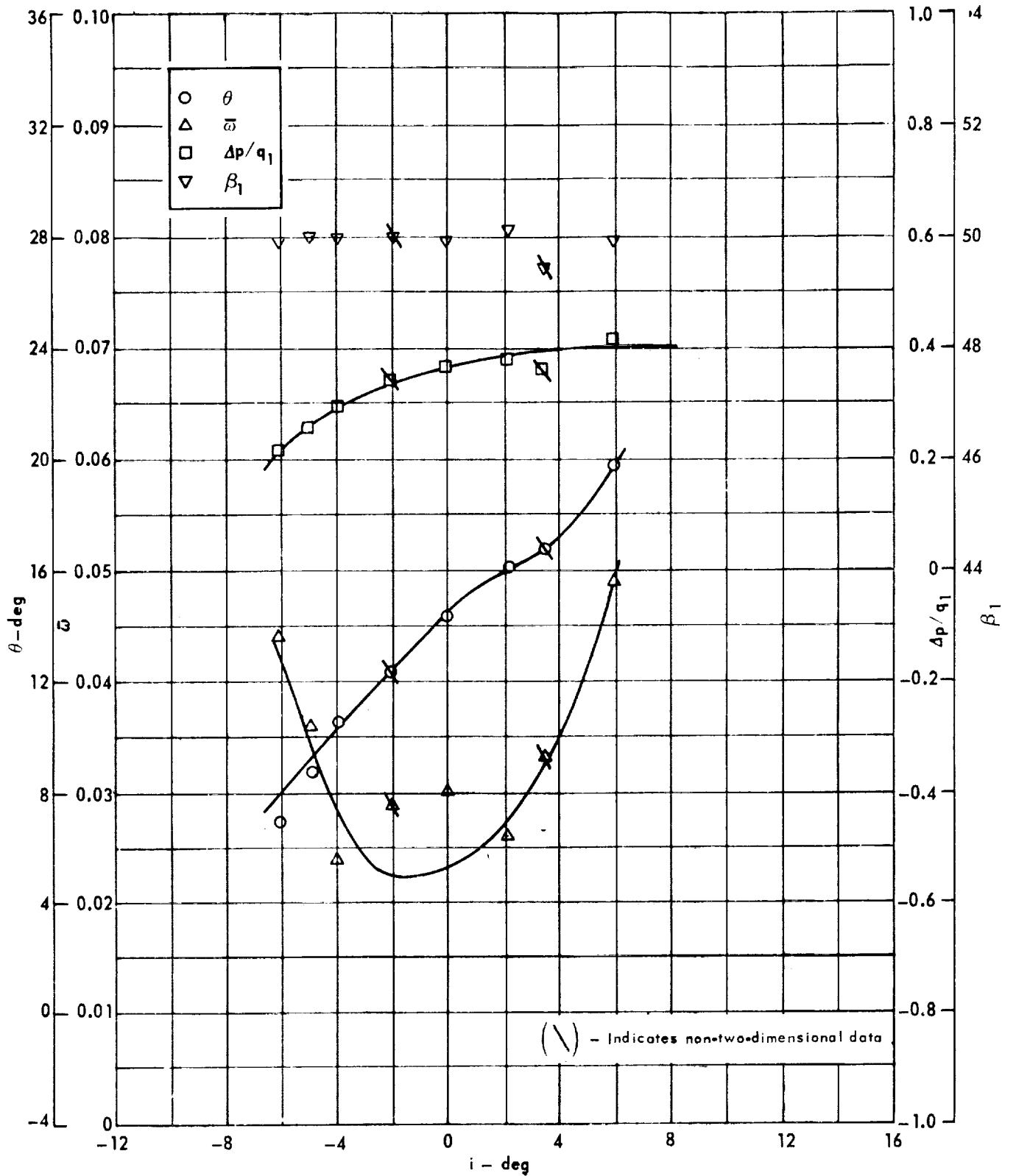
Cascade configuration : $\beta_{1N} = 50, \sigma = 1.00$

Double circular-arc profile : $\phi = 20, r/c = 0.06$

(a) $\theta, \bar{\omega}, \Delta p/q_1, \beta_1$

Figure 25. - Cascade characteristics as functions of incidence.





Cascade configuration : $\beta_{1N} = 50$, $\sigma = 1.50$

Double circular-arc profile : $\phi = 20$, $t/c = 0.06$

(a) $\theta, \bar{w}, \Delta p/q_1, \beta_1$

Figure 26. - Cascade characteristics as functions of incidence.

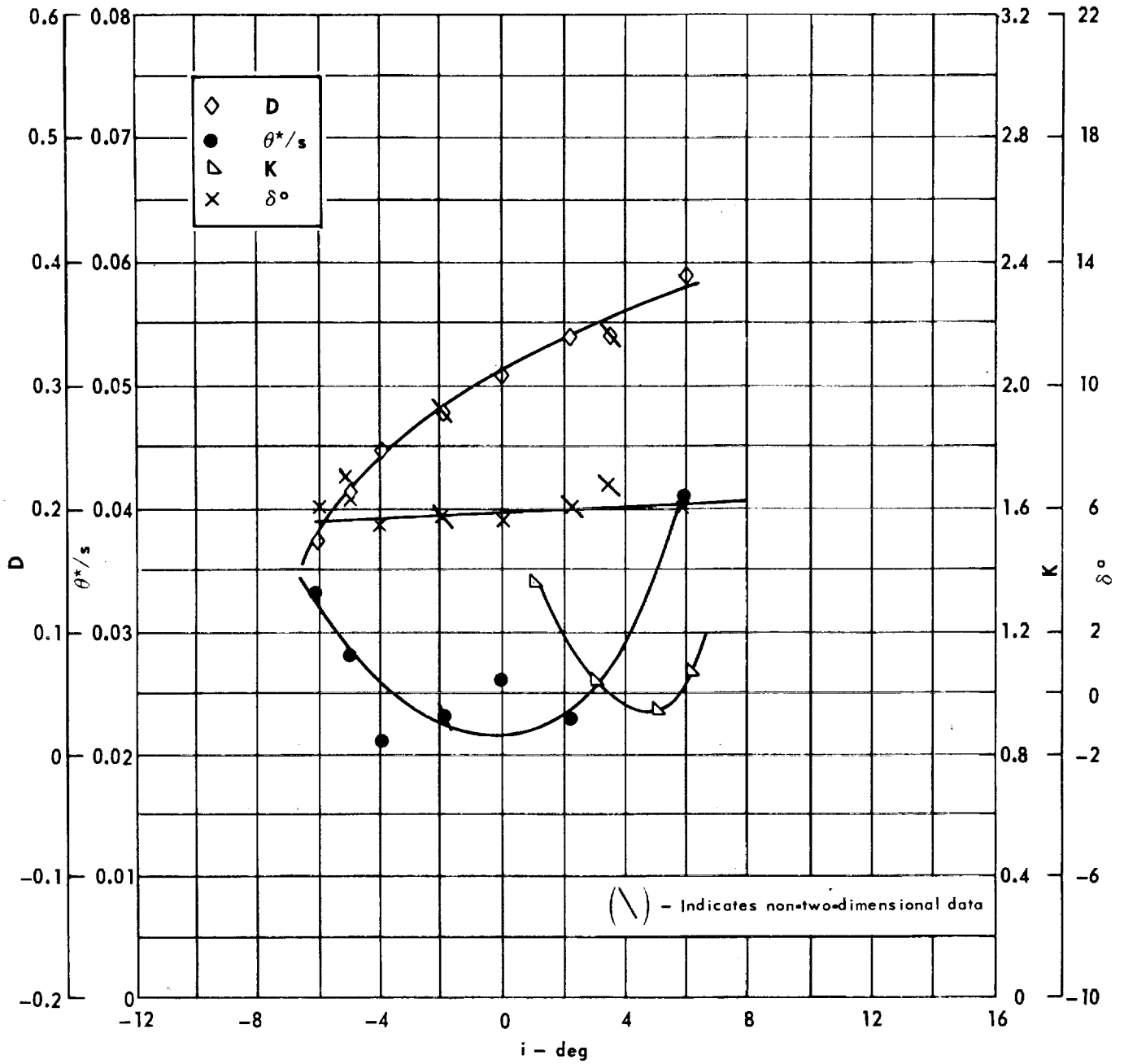
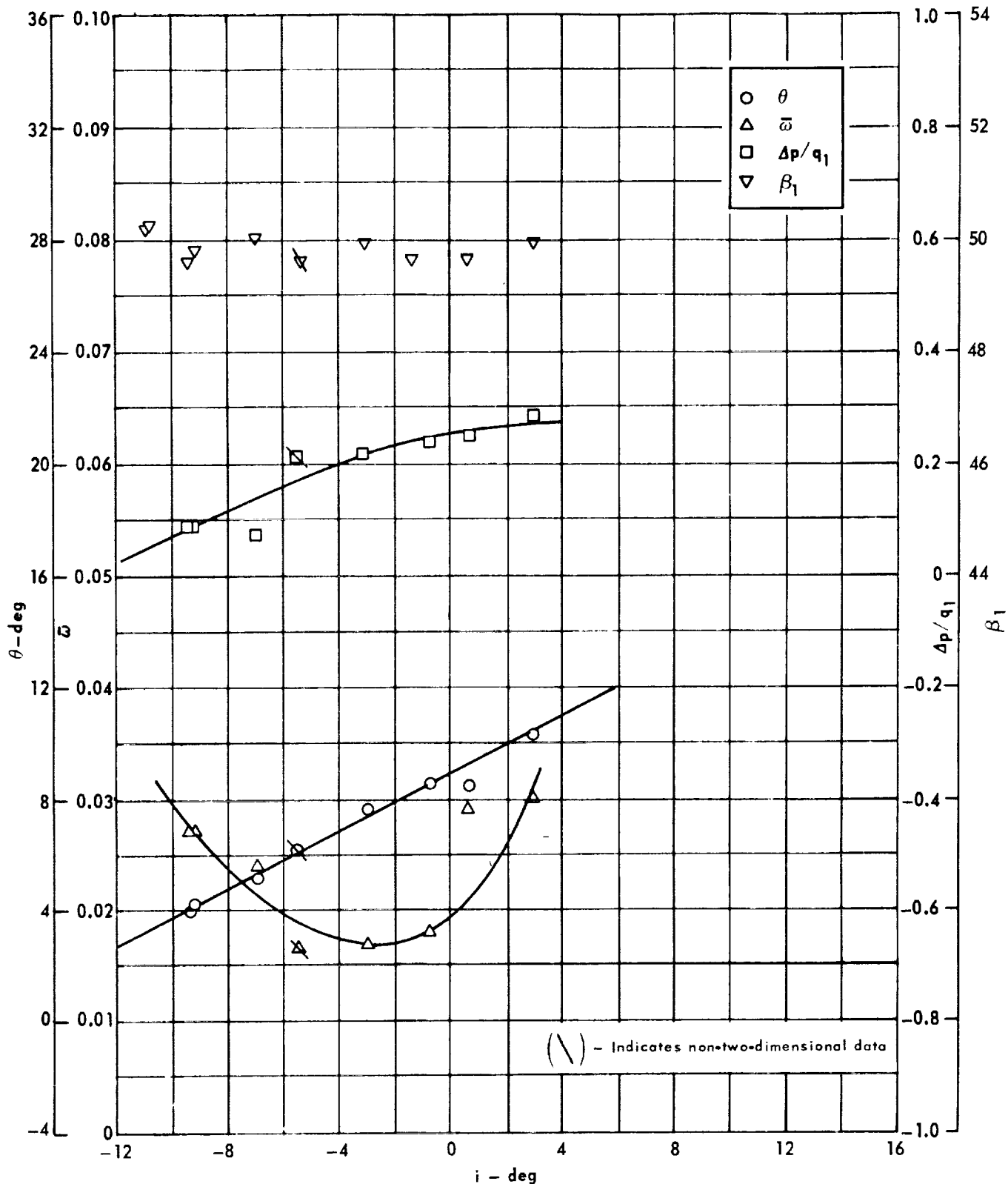


Figure 26. - Concluded.

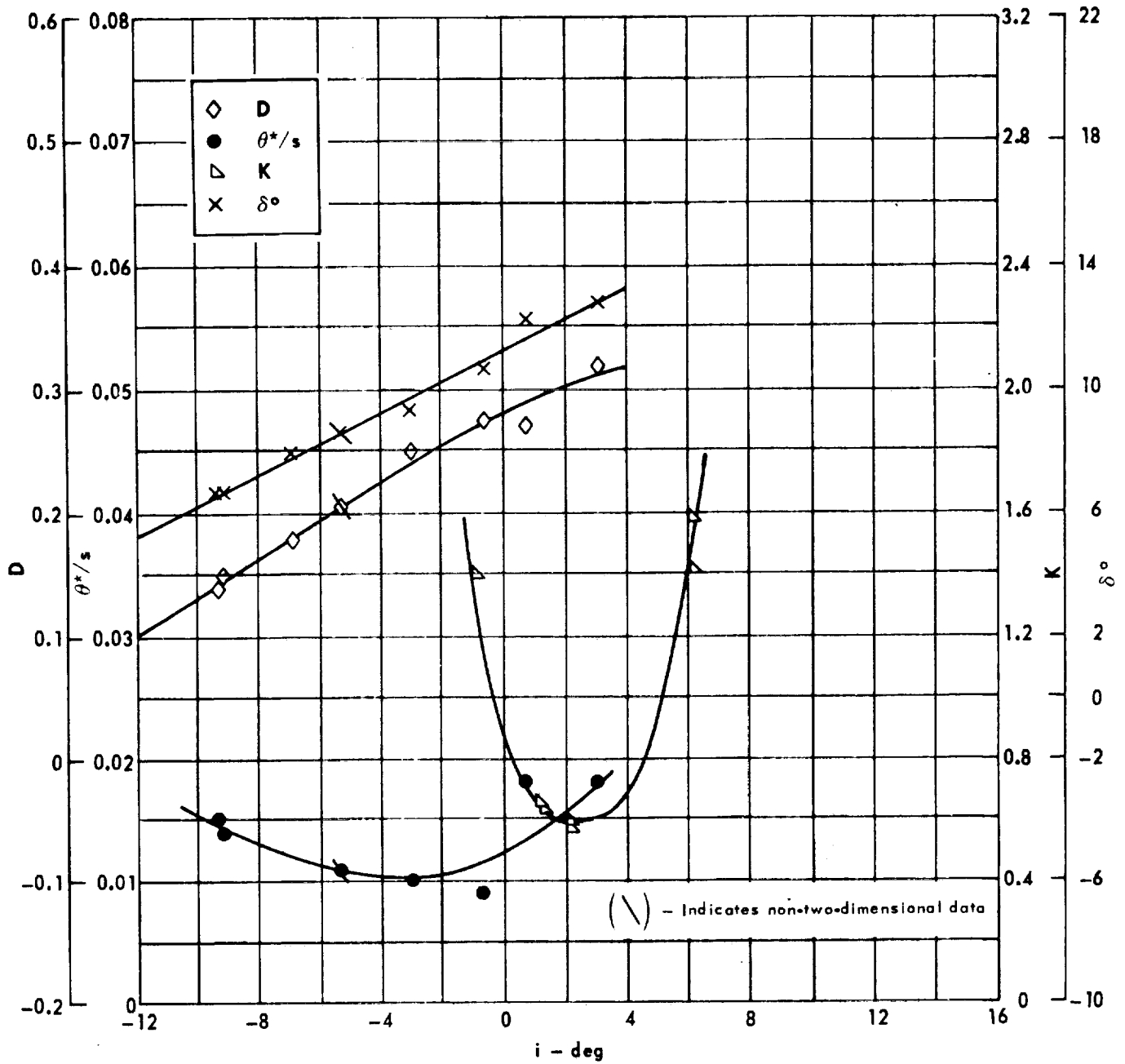


Cascade configuration : $\beta_{1N} = 50, \sigma = 0.75$

Double circular-arc profile : $\phi = 20, t/c = 0.10$

(a) $\theta, \bar{\omega}, \Delta p/q_1, \beta_1$

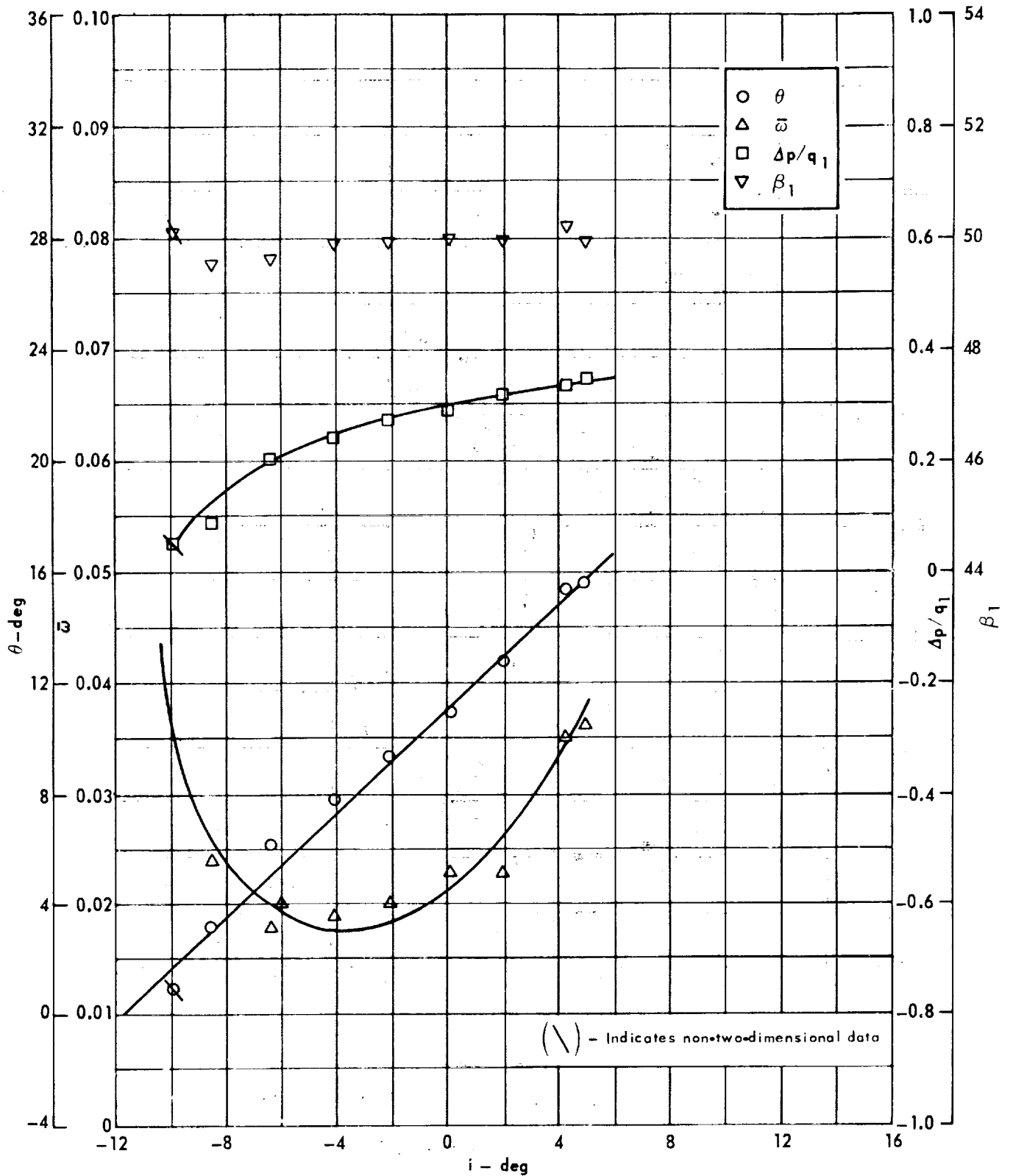
Figure 27 . - Cascade characteristics as functions of incidence.



Cascade configuration: $\beta_{IN} = 50, \sigma = 0.75$
 Double circular-arc profile: $\phi = 20, t/c = 0.10$

(b) D, θ^*/s , K, δ°

Figure 27. - Concluded.

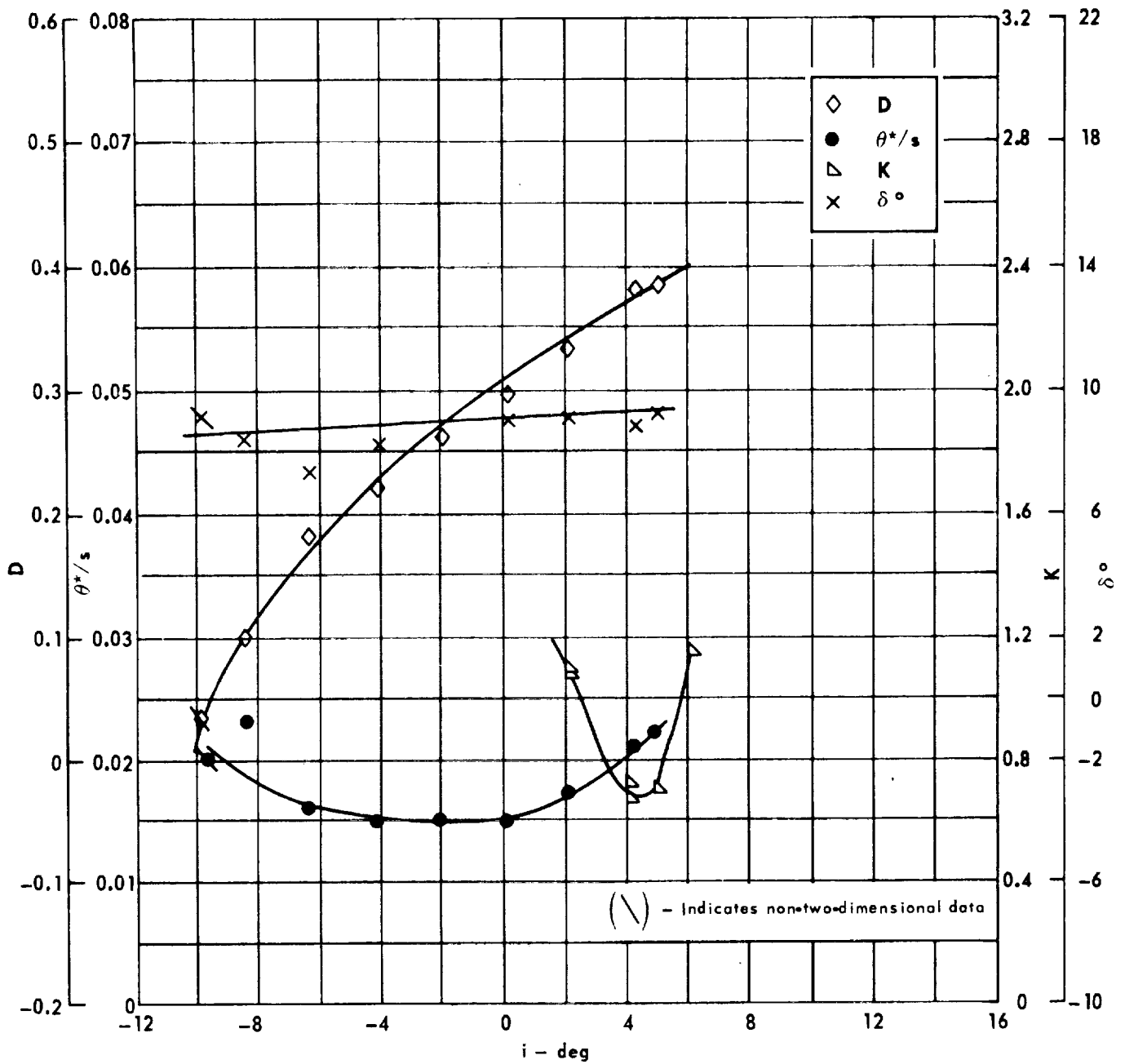


Cascade configuration : $\beta_{1N} = 50, \sigma = 1.00$

Double circular-arc profile : $\phi = 20, t/c = 0.10$

(a) $\theta, \bar{\omega}, \Delta p/q_1, \beta_1$

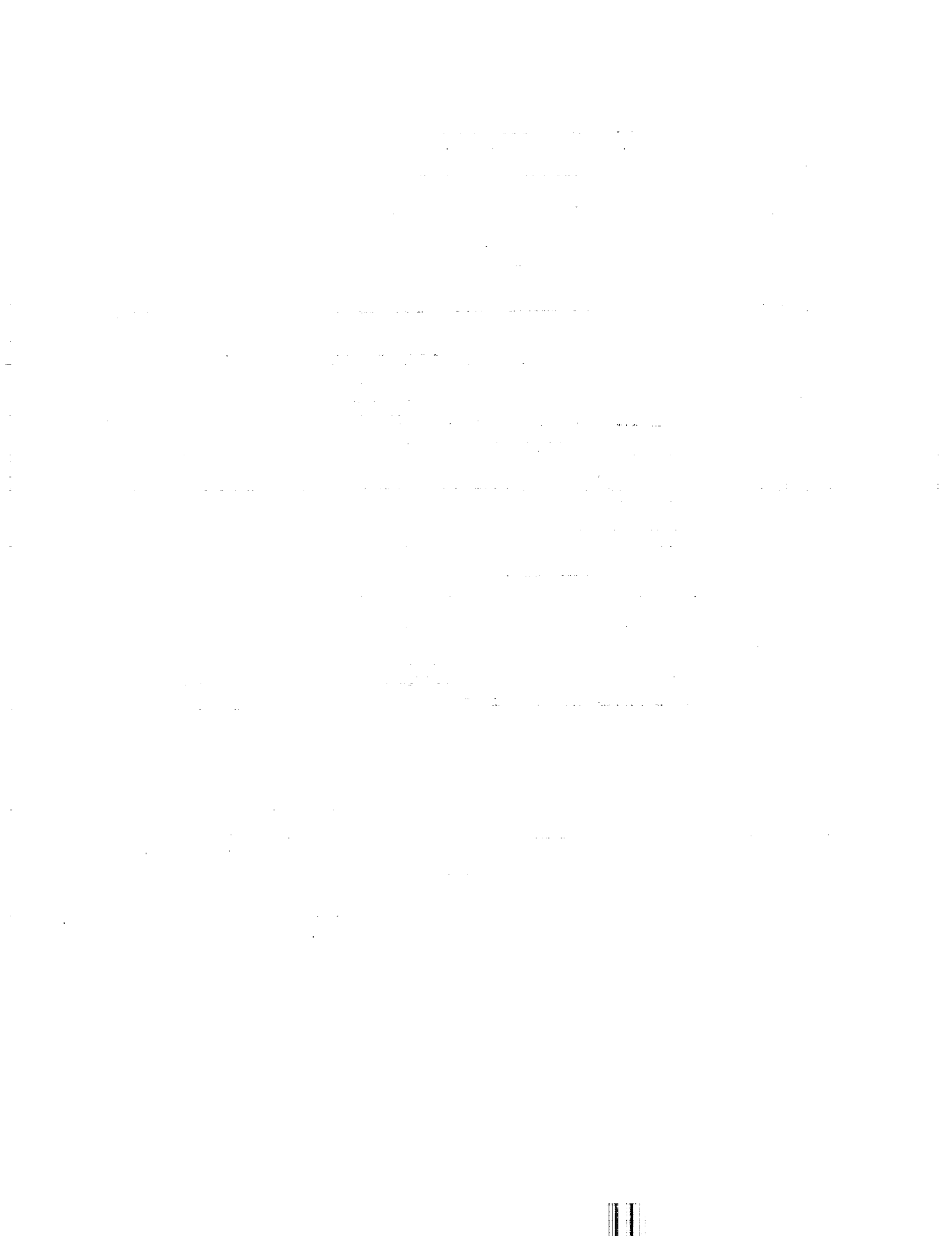
Figure 28 . - Cascade characteristics as functions of incidence.

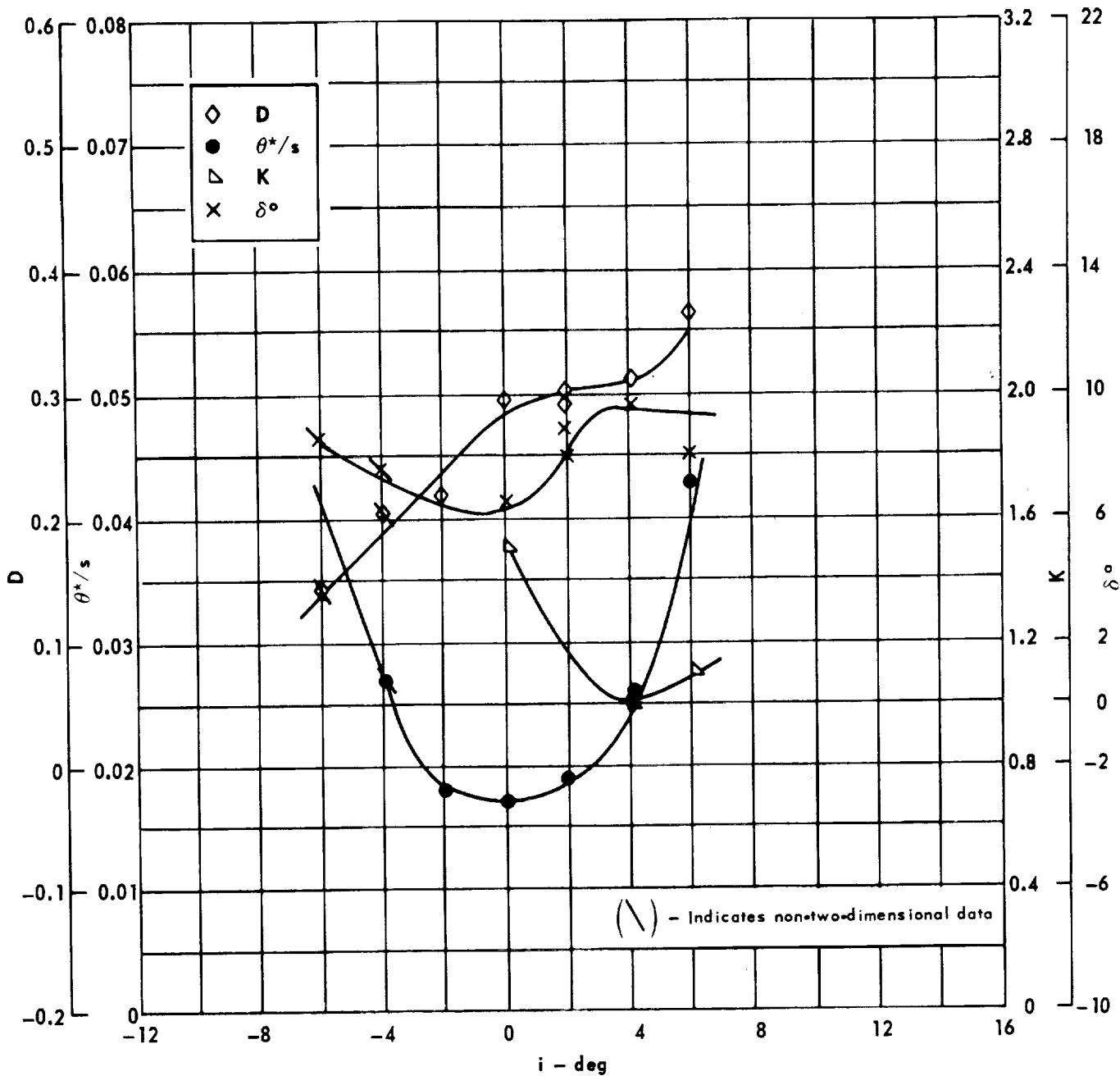


Cascade configuration : $\beta_{1N} = 50, \sigma = 1.00$
 Double circular-arc profile : $\phi = 20, t/c = 0.10$

(b) D, θ^*/s , K, δ°

Figure 28. - Concluded.

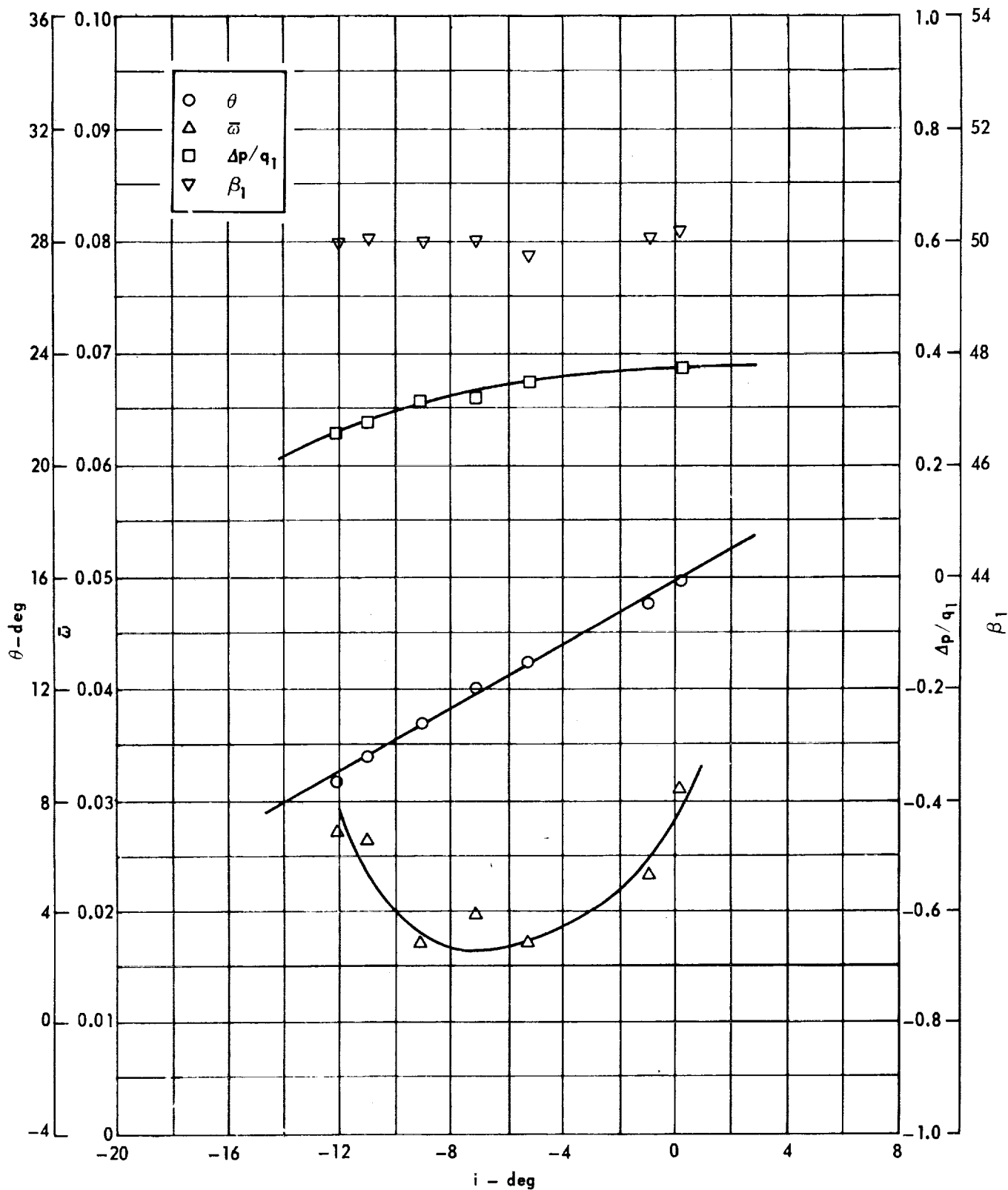




Cascade configuration: $\beta_{1N} = 50, \sigma = 1.50$
 Double circular-arc profile: $\phi = 20, t/c = 0.10$

(b) D, θ^*/s , K, δ°

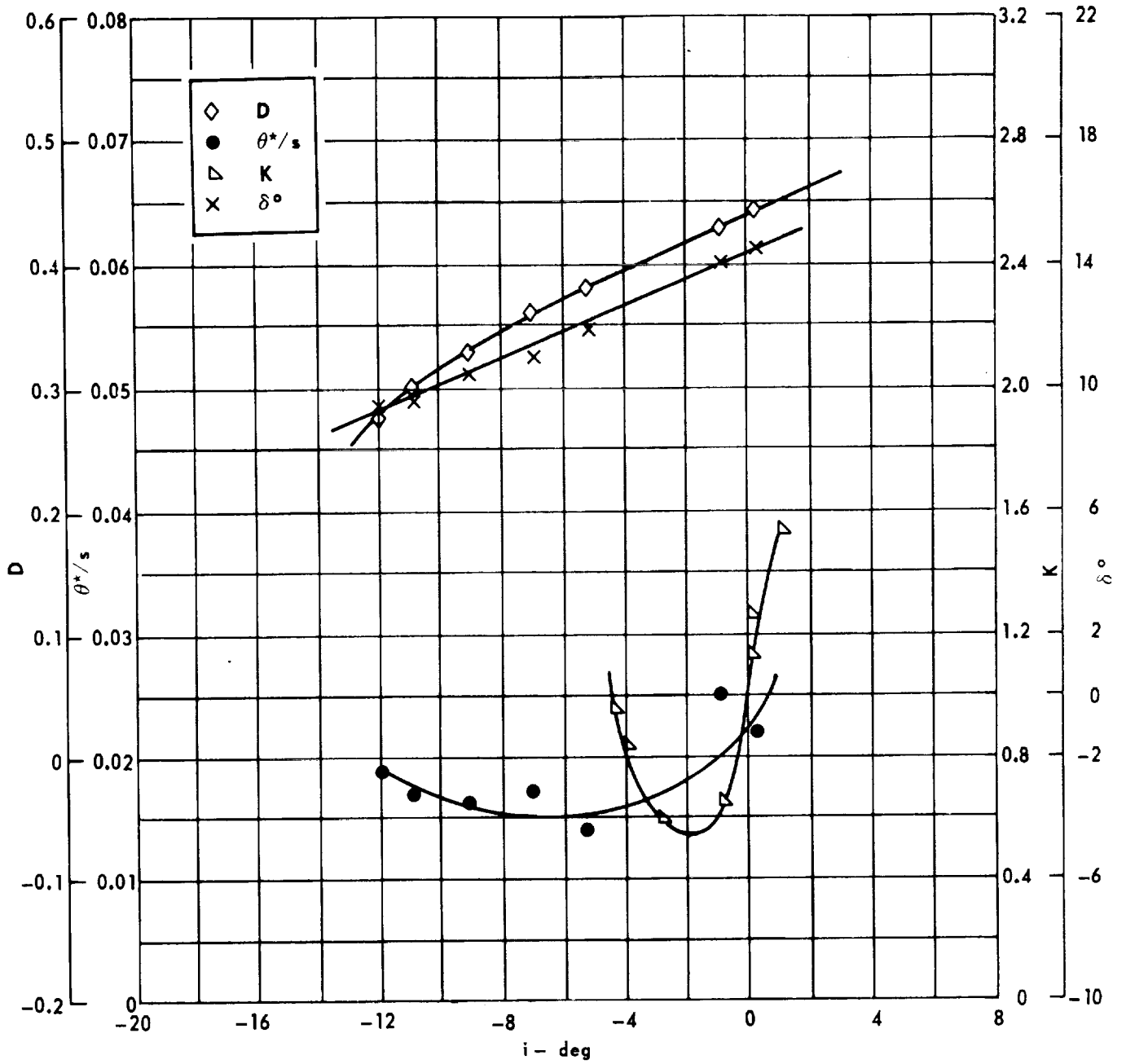
Figure 29. - Concluded.



Cascade configuration : $\beta_{1N} = 50, \sigma = 0.75$
 Double circular-arc profile : $\phi = 30, t/c = 0.06$

(a) $\theta, \bar{\omega}, \Delta p/q_1, \beta_1$

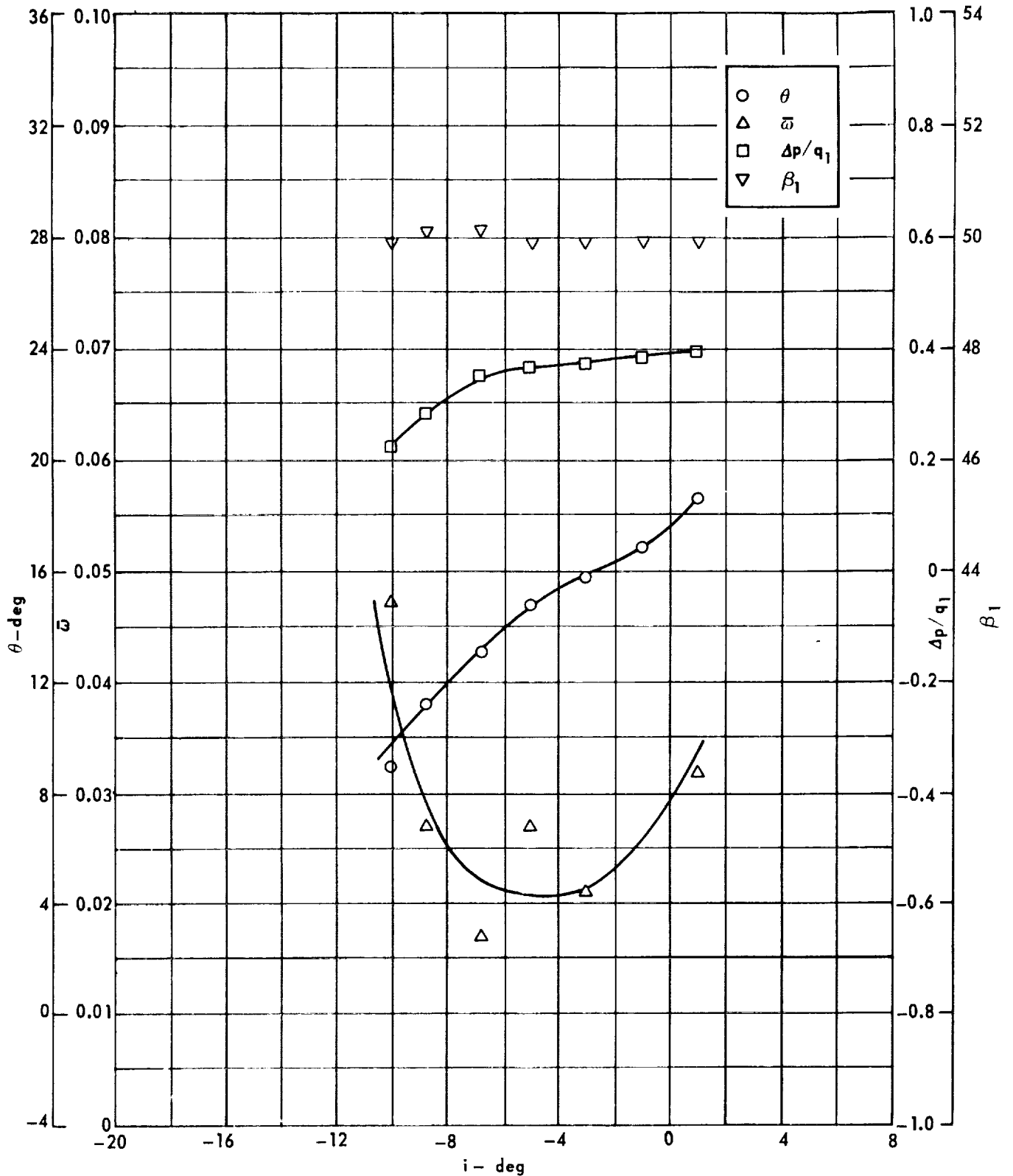
Figure 30 . - Cascade characteristics as functions of incidence.



Cascade configuration: $\beta_{1N} = 50, \sigma = 0.75$
 Double circular-arc profile: $\phi = 30, t/c = 0.06$

(b) D, θ^*/s , K, δ°

Figure 30. - Concluded.

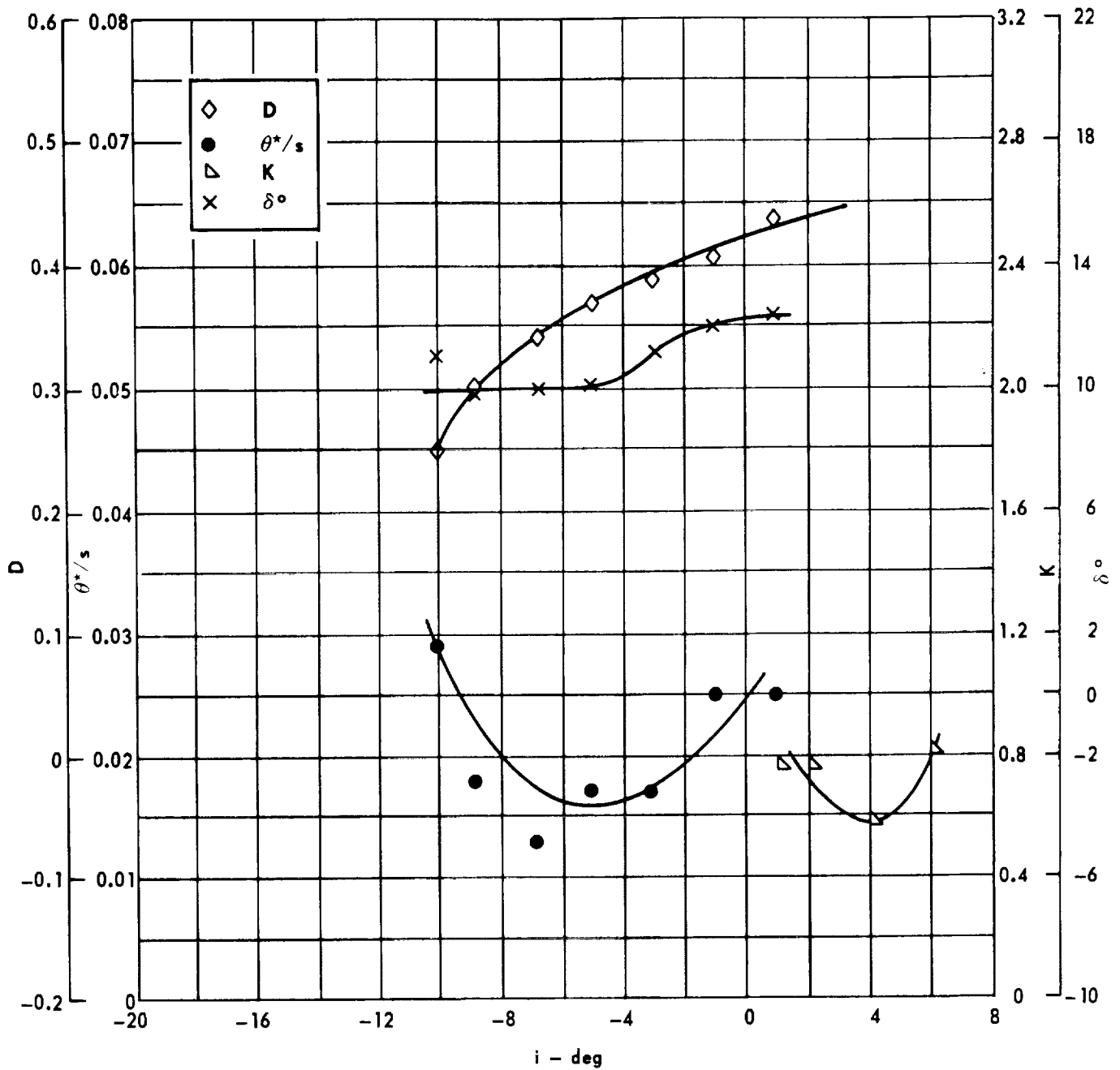


Cascade configuration : $\beta_{1N} = 50, \sigma = 1.00$

Double circular-arc profile : $\phi = 30, t/c = 0.06$

(a) $\theta, \bar{\omega}, \Delta p/q_1, \beta_1$

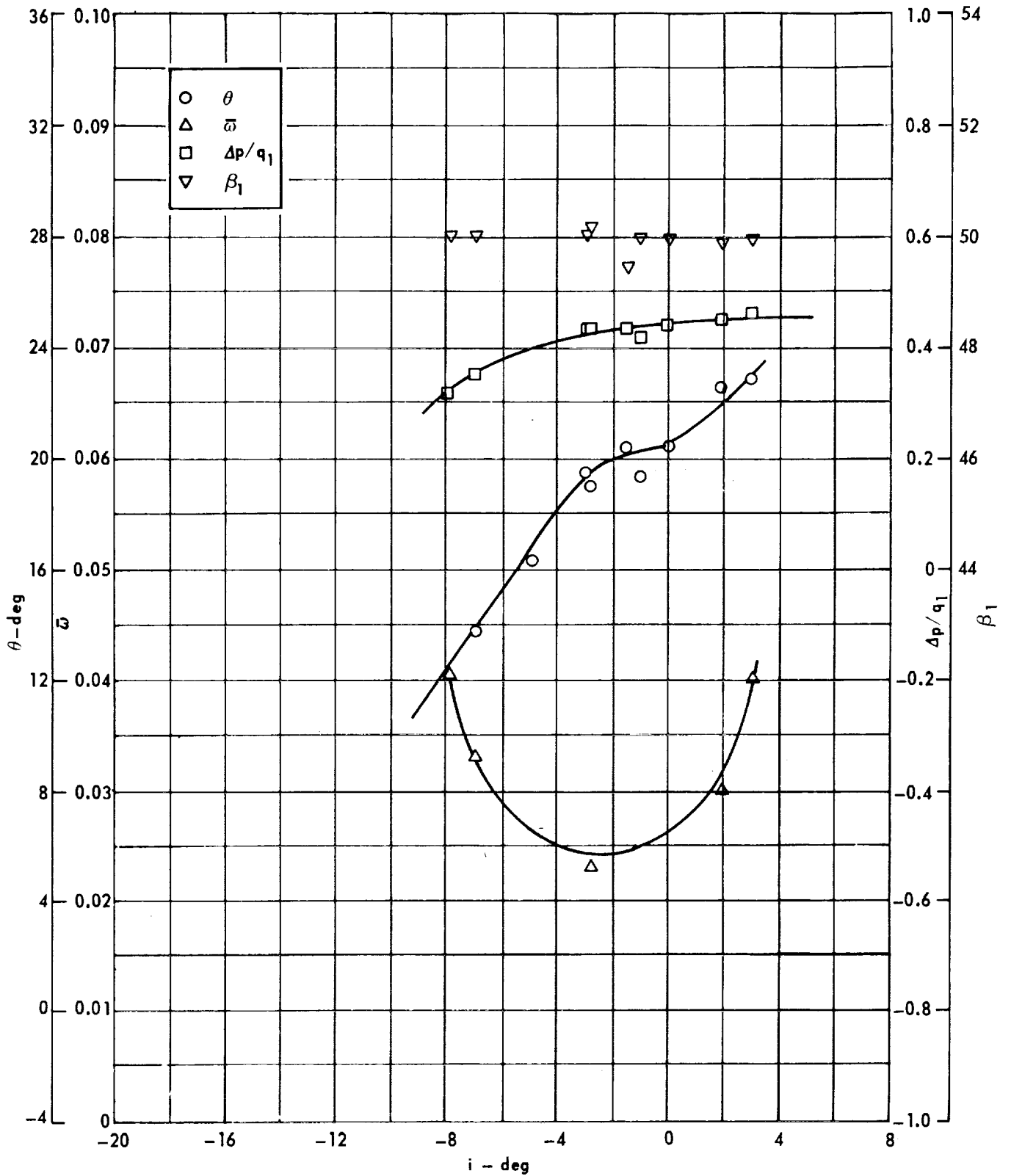
Figure 31. - Cascade characteristics as functions of incidence.



Cascade configuration: $\beta_{1N} = 50, \sigma = 1.00$
 Double circular-arc profile: $\phi = 30, t/c = 0.06$

(b) D, θ^*/s , K, δ°

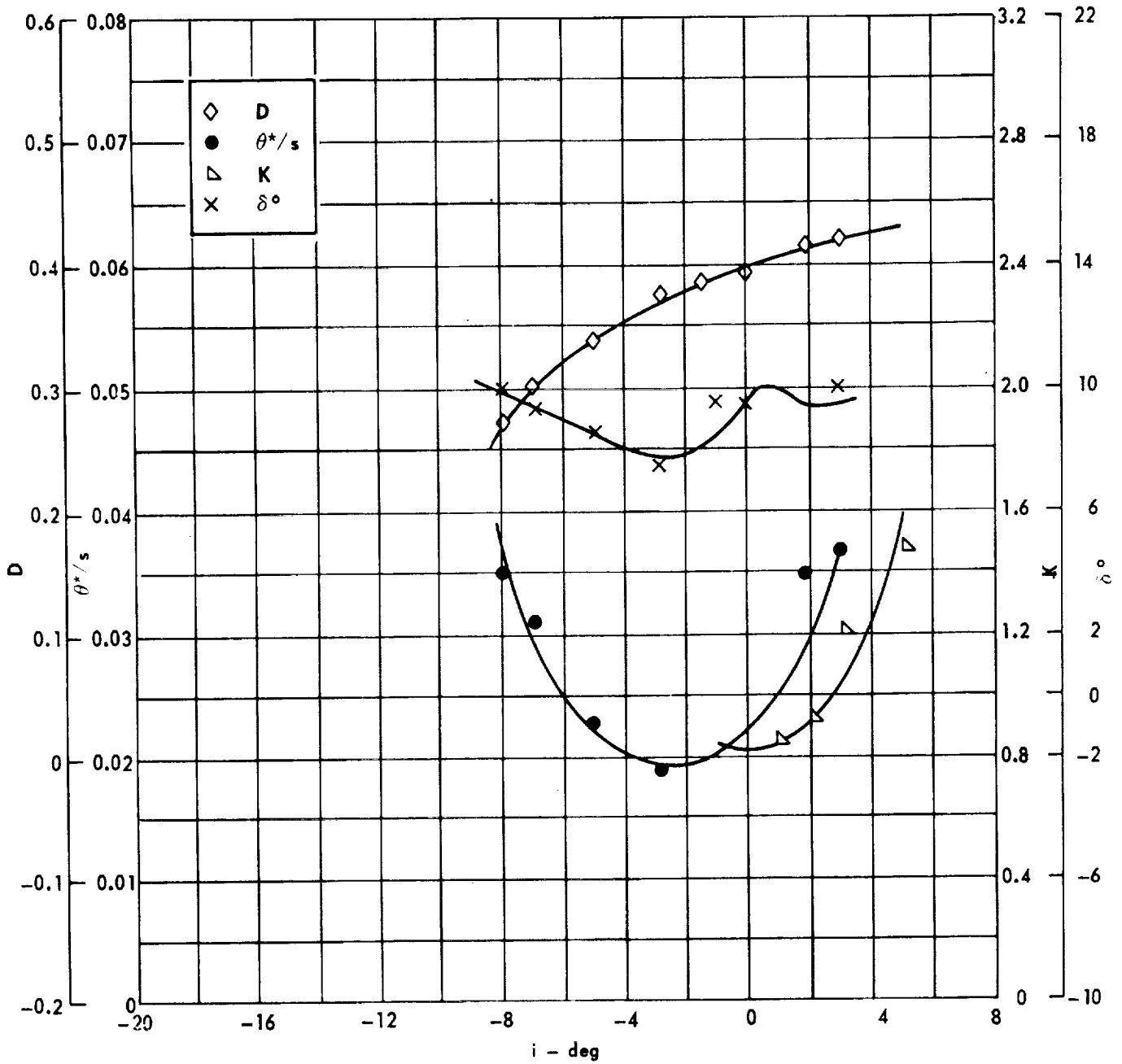
Figure 31. - Concluded.



Cascade configuration : $\beta_{1N} = 50, \sigma = 1.50$
 Double circular-arc profile : $\phi = 30, t/c = 0.06$

(a) $\theta, \bar{\omega}, \Delta p/q_1, \beta_1$

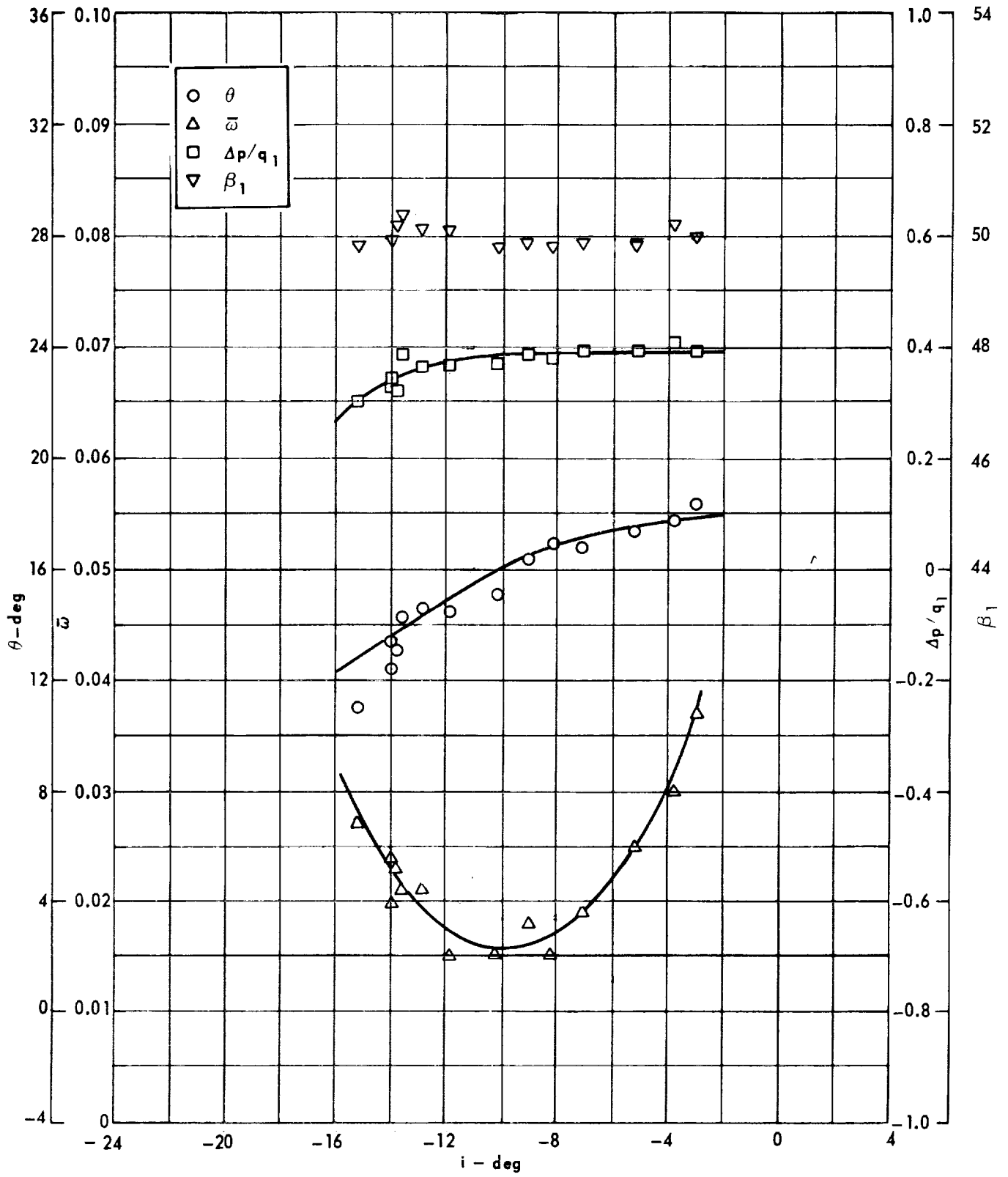
Figure 32. - Cascade characteristics as functions of incidence



Cascade configuration : $\beta_{1N} = 50, \sigma = 1.50$
 Double circular-arc profile : $\phi = 30, t/c = 0.06$

(b) D, θ^*/s , K, δ°

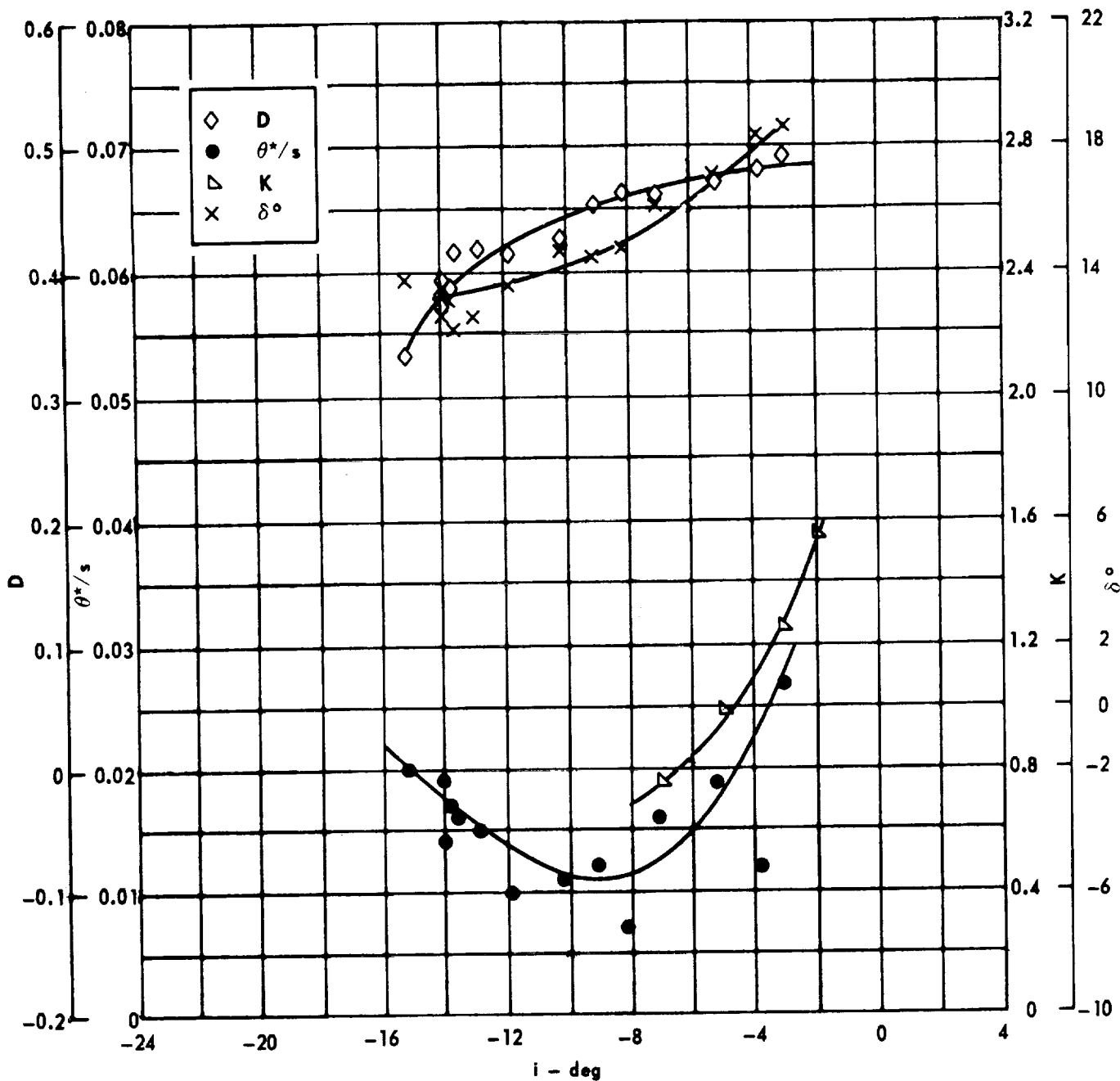
Figure 32. - Concluded.



Cascade configuration : $\beta_{1N} = 50$, $\sigma = 0.75$
 Double circular-arc profile : $\phi = 40$, $t/c = 0.06$

(a) $\theta, \bar{\omega}, \Delta p/q_1, \beta_1$

Figure 33 . - Cascade characteristics as functions of incidence.

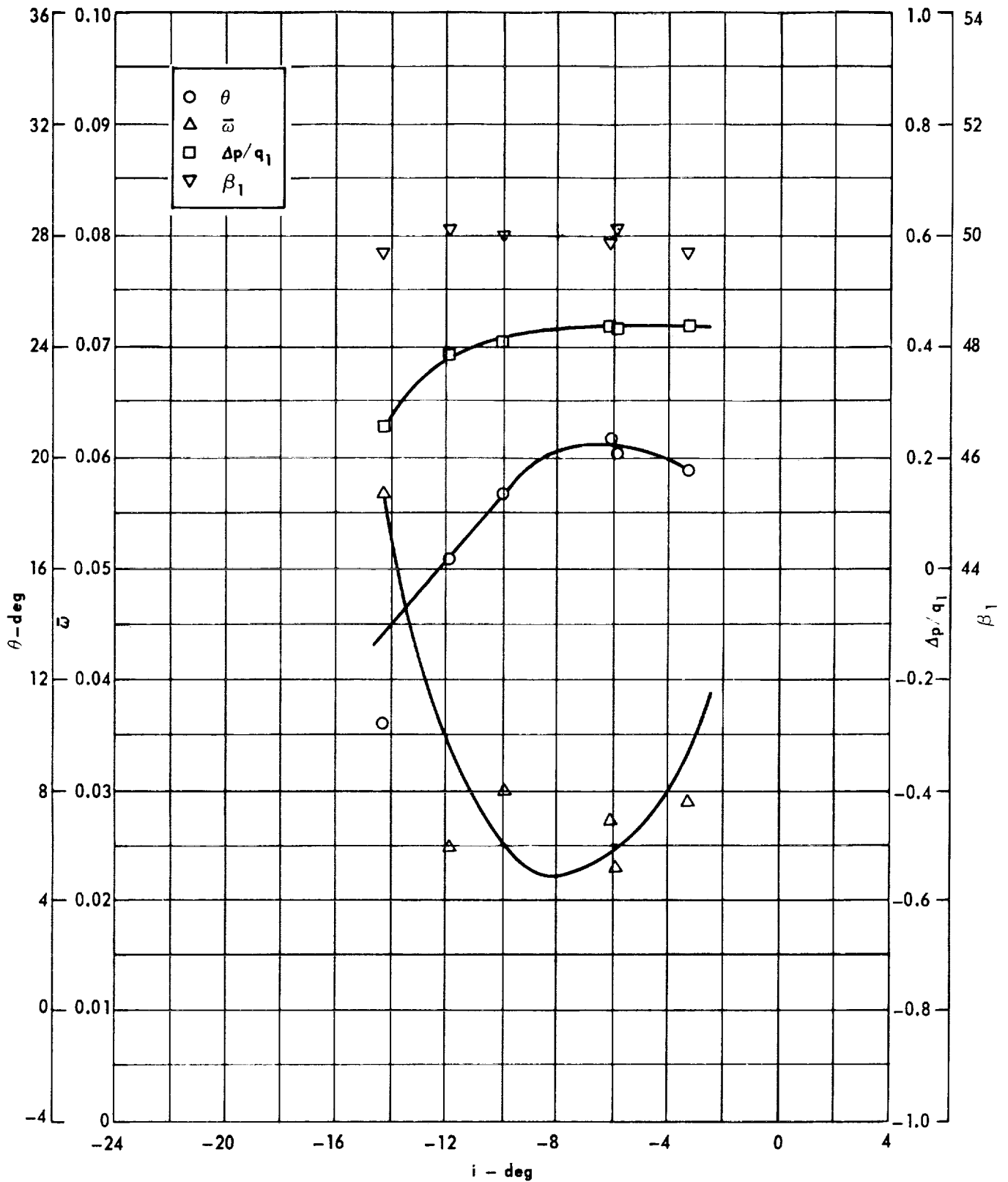


Cascade configuration : $\beta_{1N} = 50$, $\sigma = 0.75$

Double circular-arc profile : $\phi = 40$, $t/c = 0.06$

(b) D, θ^*/s , K, δ°

Figure 33 . - Concluded.

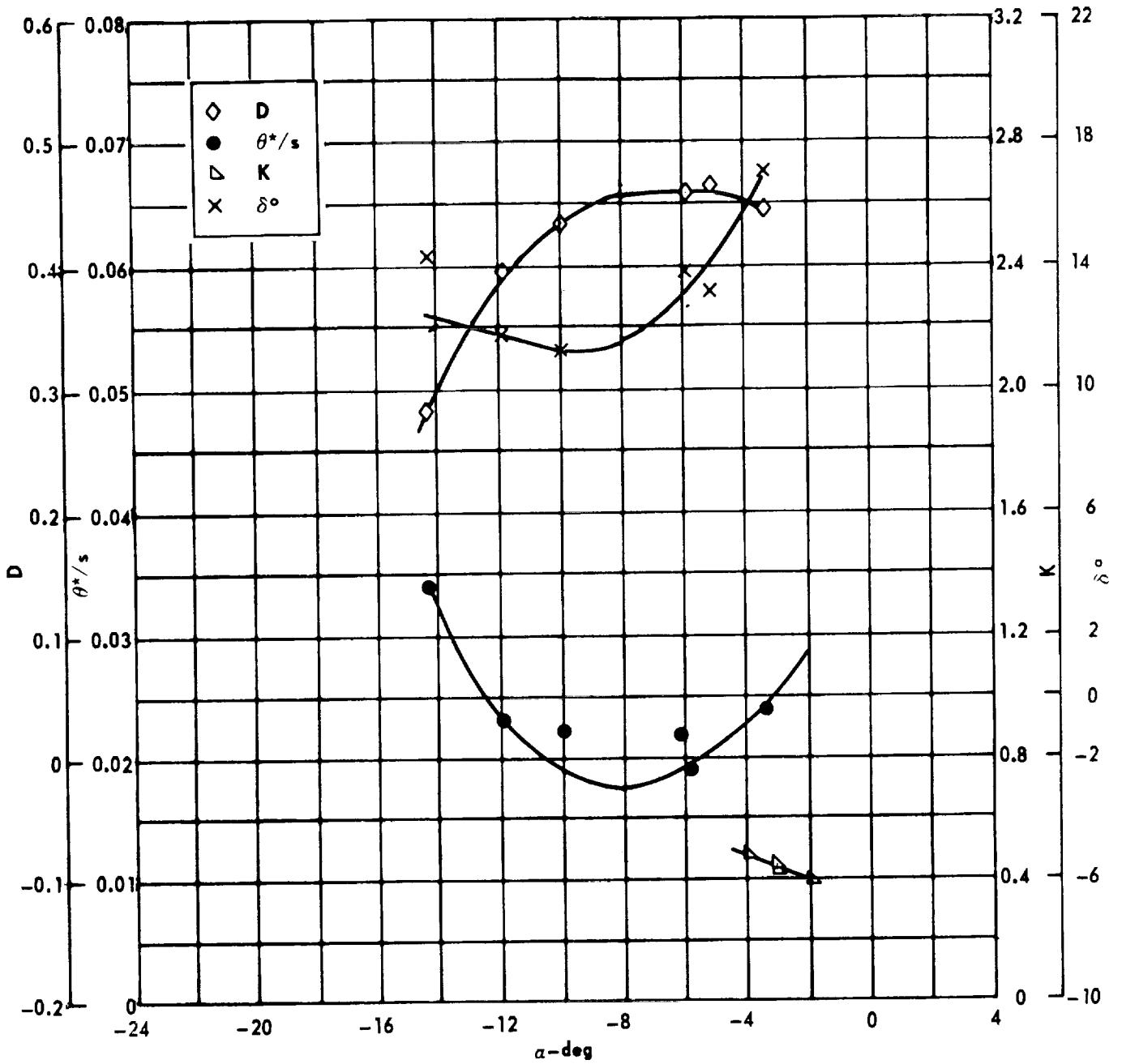


Cascade configuration: $\beta_{1N} = 50$, $\sigma = 1.00$

Double circular-arc profile: $\phi = 40$, $r/c = 0.06$

(a) $\theta, \bar{\omega}, \Delta p/q_1, \beta_1$

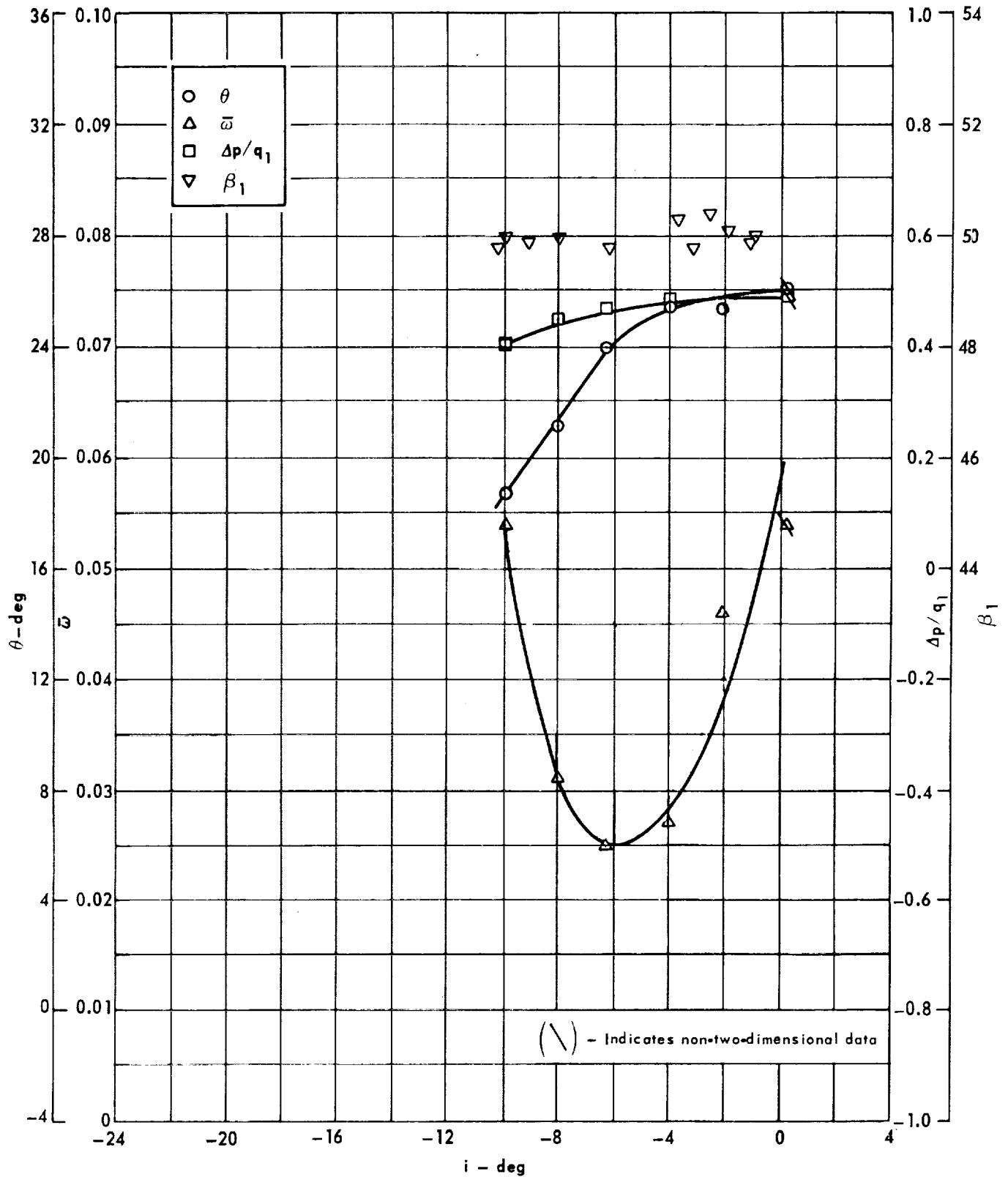
Figure 34 . - Cascade characteristics as functions of incidence.



Cascade configuration: $\beta_{1N} = 50$, $\sigma = 1.00$
 Double circular-arc profile: $\phi = 40$, $t/c = 0.06$

(b) D, θ^*/s , K, δ°

Figure 34 . - Concluded.

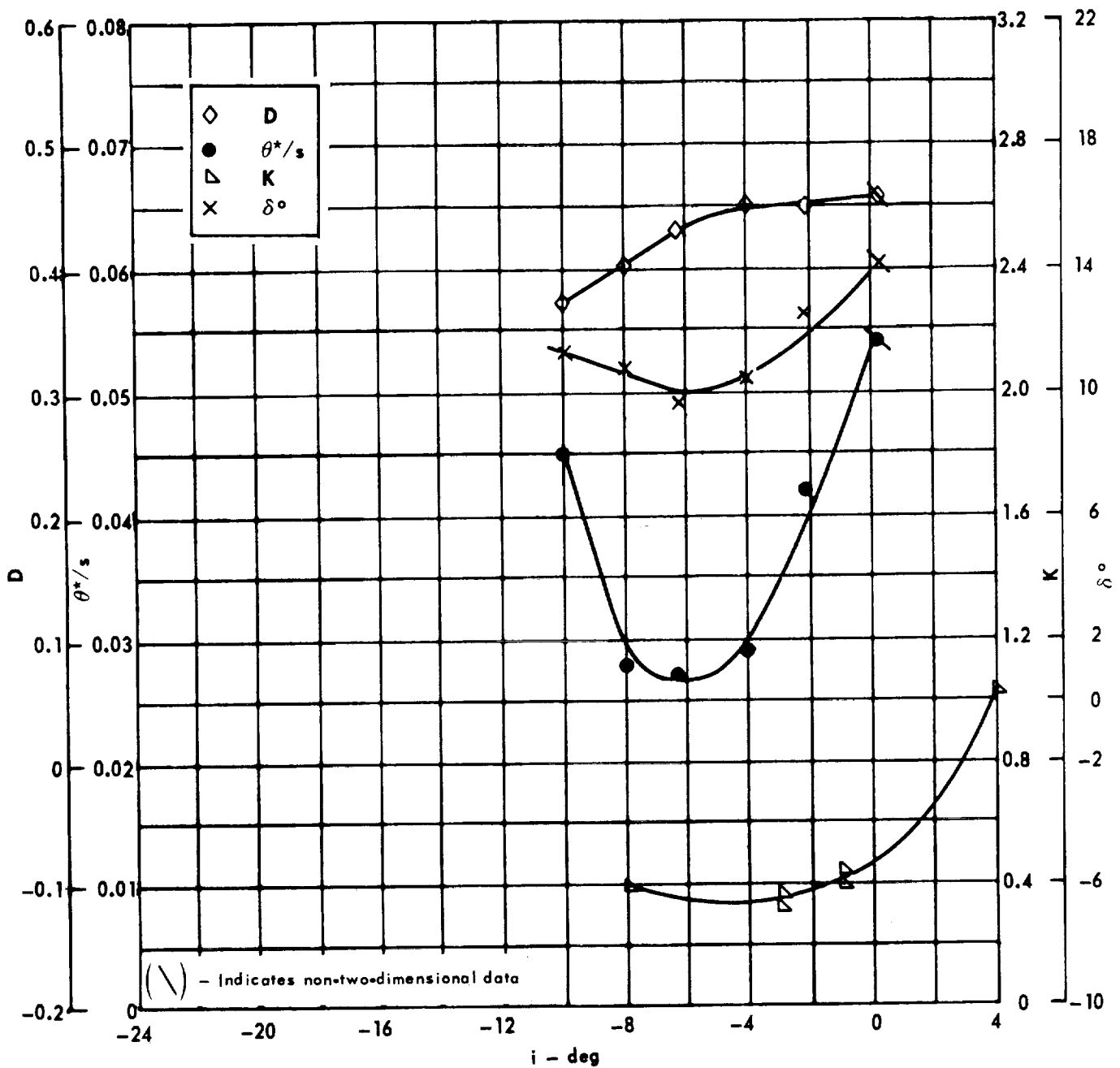


Cascade configuration : $\beta_{1N} = 50$, $\sigma = 1.50$

Double circular-arc profile : $\phi = 40$, $t/c = 0.06$

(a) $\theta, \bar{\omega}, \Delta p/q_1, \beta_1$

Figure 35. - Cascade characteristics as functions of incidence.

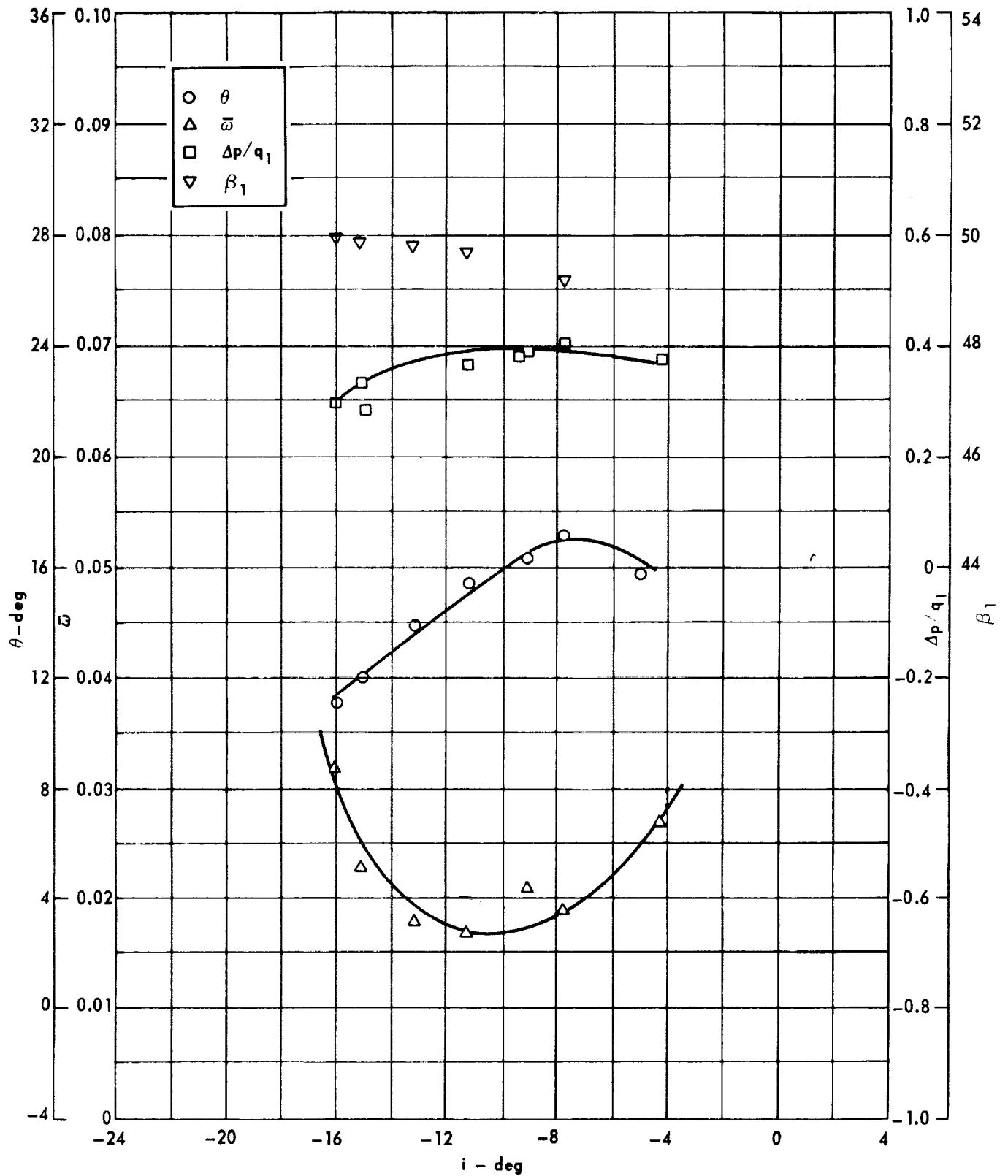


Cascade configuration: $\beta_{1N} = 50$, $\sigma = 1.50$

Double circular-arc profile: $\phi = 40$, $t/c = 0.06$

(b) D, θ^*/s , K, δ°

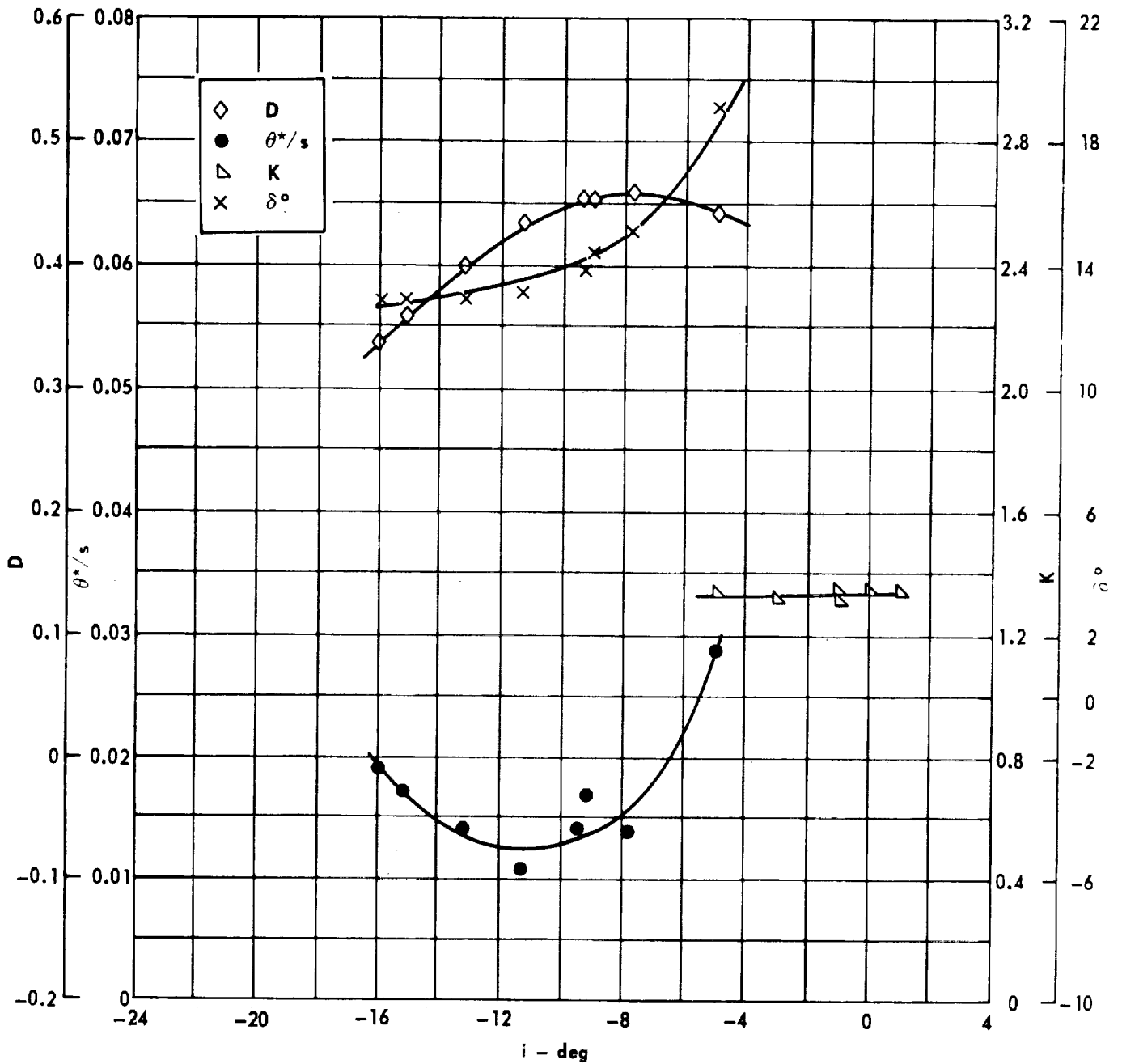
Figure 35! . - Concluded.



Cascade configuration: $\beta_{1N} = 50$, $\sigma = .75$
 Double circular-arc profile: $\phi = 40$, $t/c = 0.10$

(a) $\theta, \bar{\omega}, \Delta p/q_1, \beta_1$

Figure 36 . - Cascade characteristics as functions of incidence.

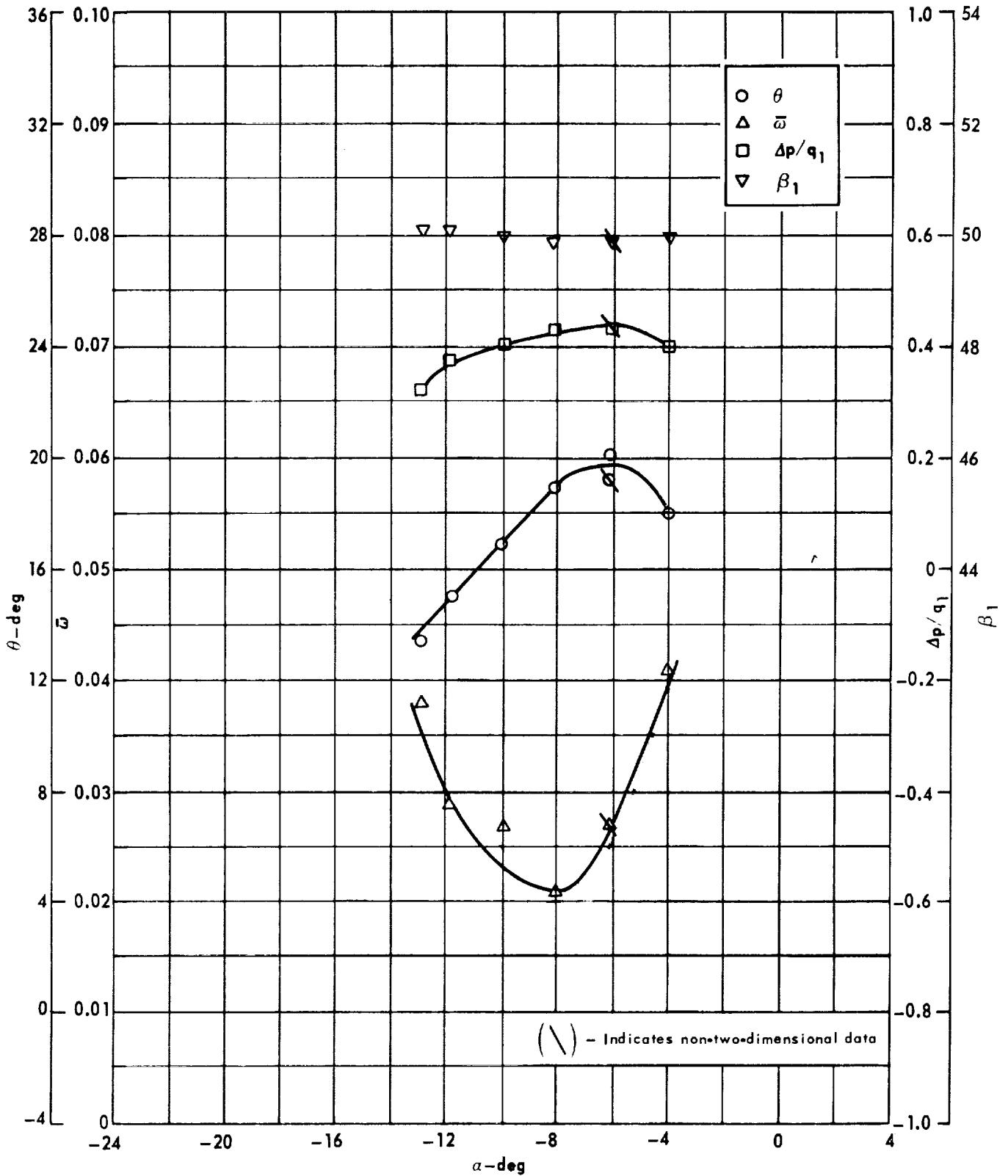


Cascade configuration: $\beta_{1N} = 50$, $\sigma = 0.75$

Double circular-arc profile: $\phi = 40$, $r/c = 0.10$

(b) D, θ^*/s , K, δ°

Figure 36 . - Concluded.

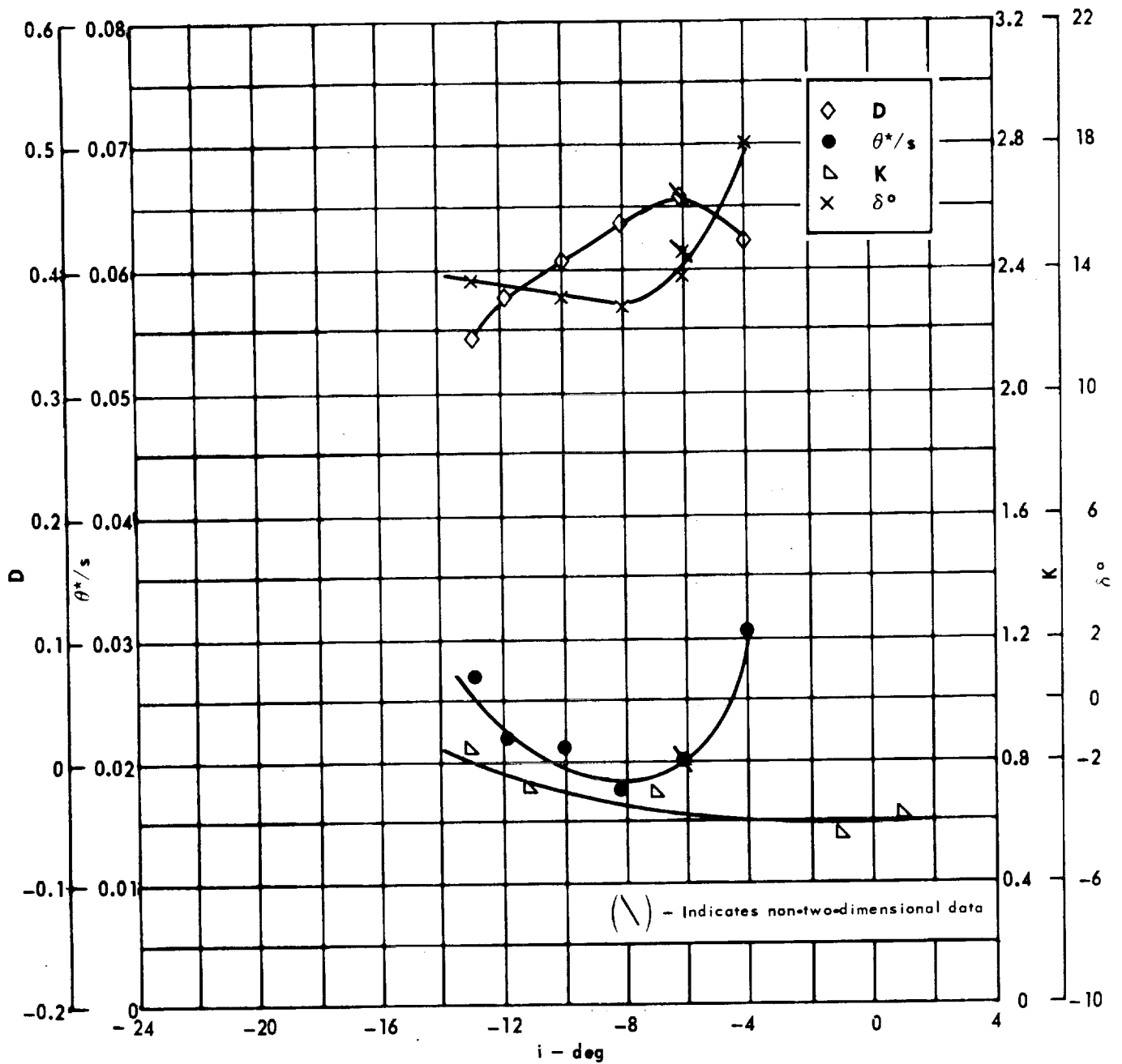


Cascade configuration : $\beta_{1N} = 50$, $\sigma = 1.00$

Double circular-arc profile : $\phi = 40$, $t/c = 0.10$

(a) $\theta, \bar{\omega}, \Delta p/q_1, \beta_1$

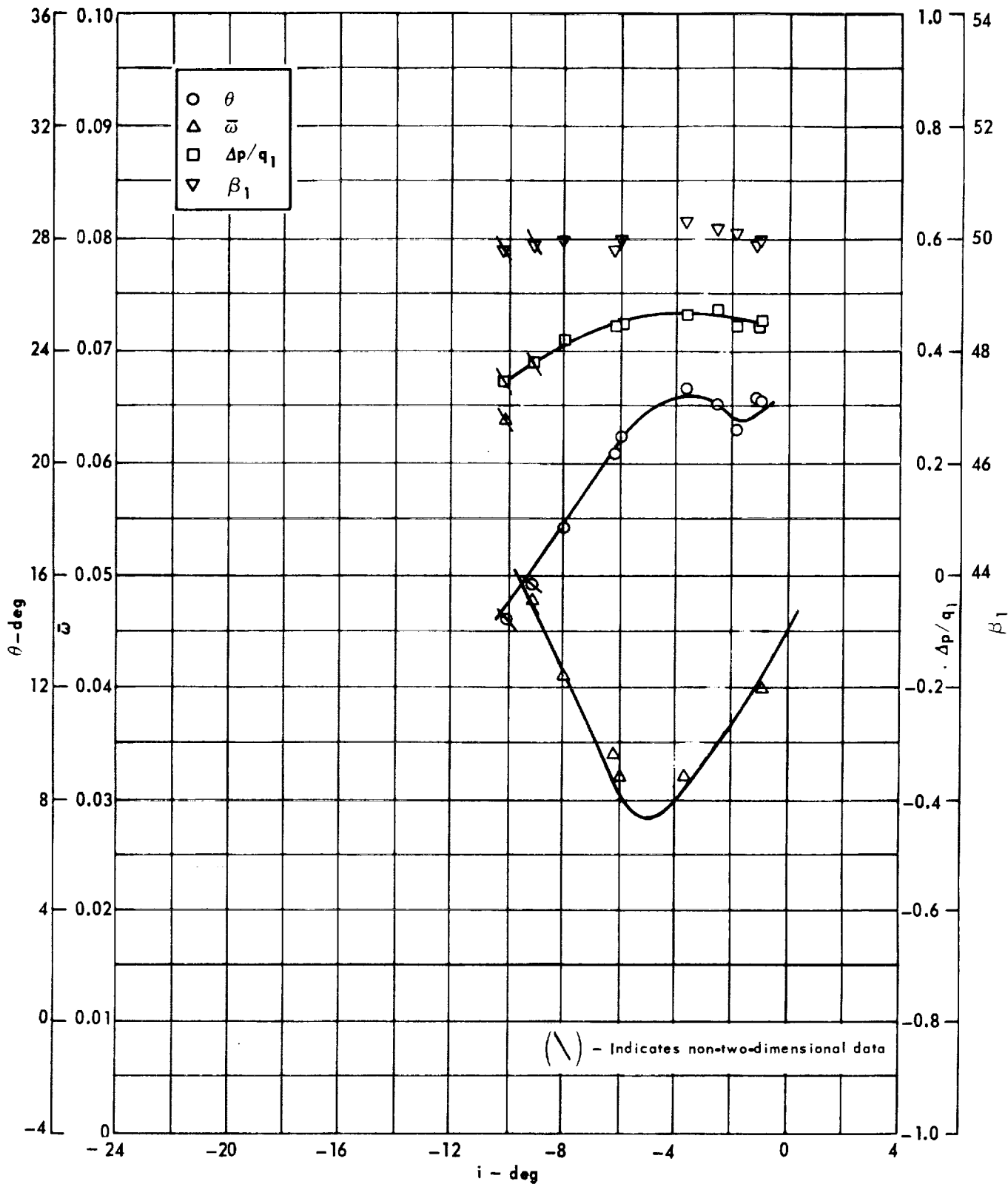
Figure 37 . - Cascade characteristics as functions of incidence.



Cascade configuration : $\beta_{1N} = 50$, $\sigma = 1.00$
 Double circular-arc profile : $\phi = 40$, $t/c = 0.10$

(b) D, θ^*/s , K, δ°

Figure 37 . - Concluded.

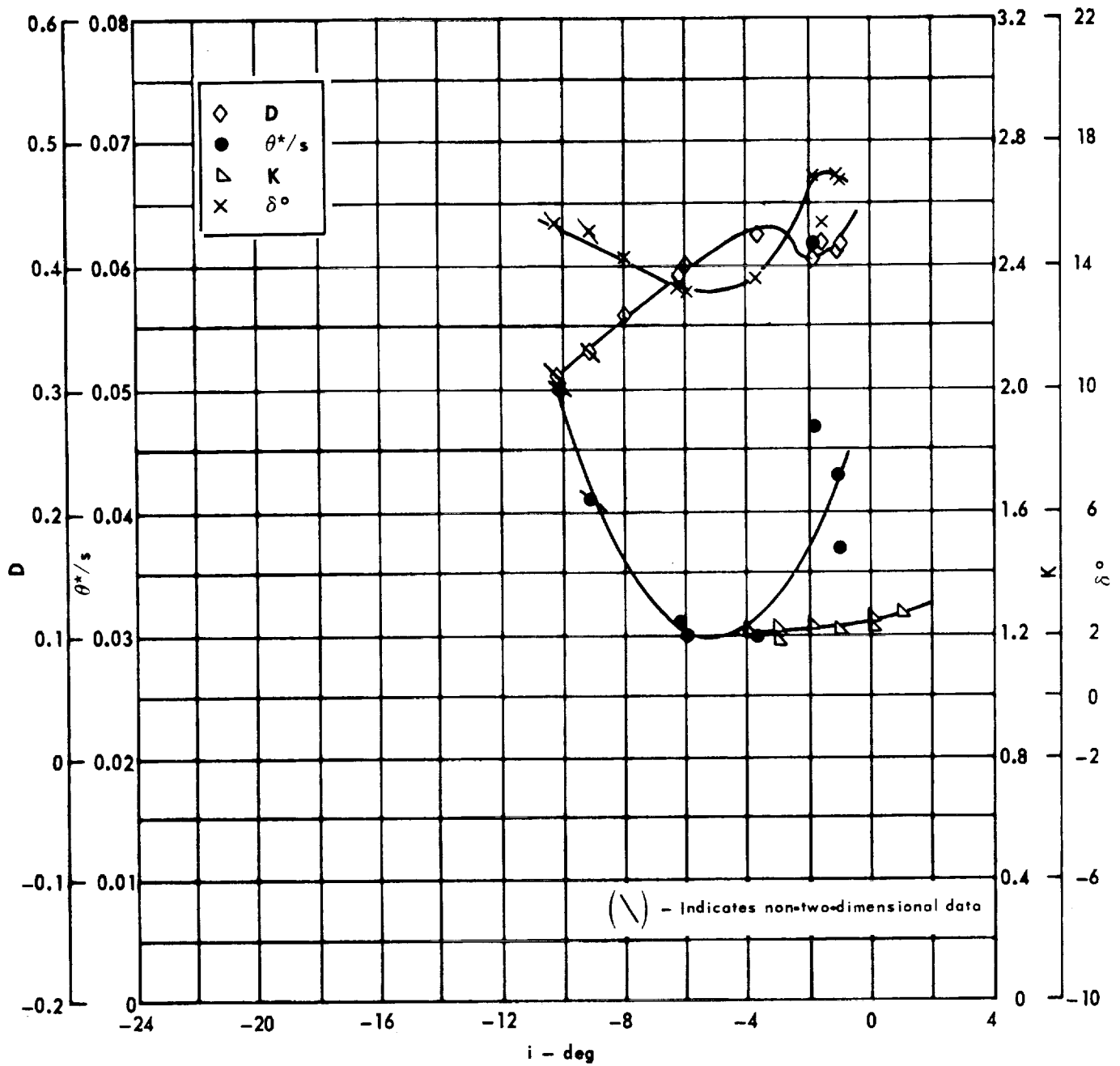


Cascade configuration: $\beta_{1N} = 50$, $\sigma = 1.50$

Double circular-arc profile: $\phi = 40$, $t/c = 0.10$

(a) $\theta, \bar{\omega}, \Delta p/q_1, \beta_1$

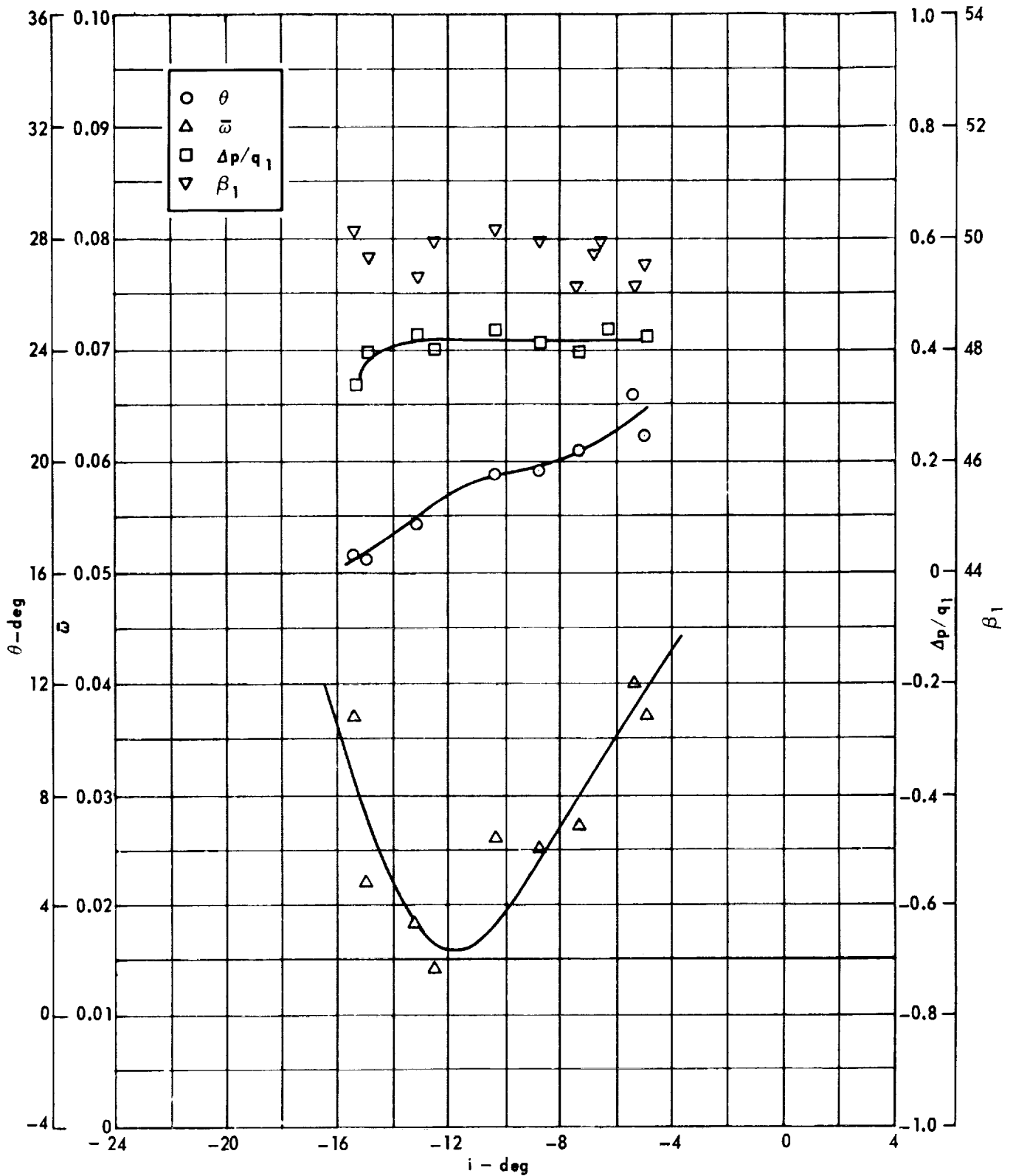
Figure 38 . - Cascade characteristics as functions of incidence.



Cascade configuration: $\beta_{1N} = 50, \sigma = 1.50$
 Double circular-arc profile: $\phi = 40, t/c = 0.10$

(b) $D, \theta^*/s, K, \delta^\circ$

Figure 38 . - Concluded.

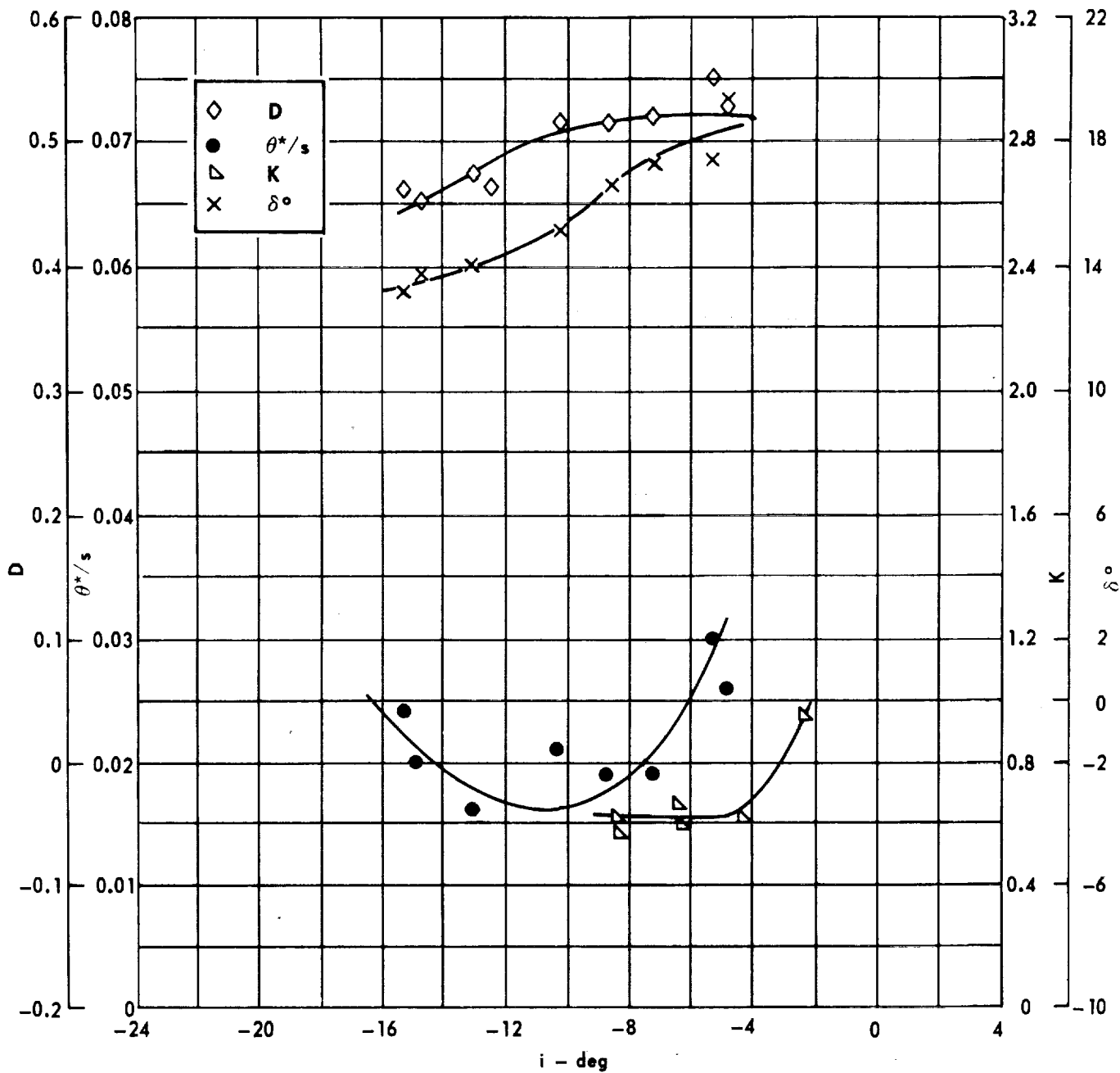


Cascade configuration : $\beta_{1N} = 50, \sigma = 0.75$

Double circular-arc profile : $\phi = 45, t/c = 0.06$

(a) $\theta, \bar{\omega}, \Delta p/q_1, \beta_1$

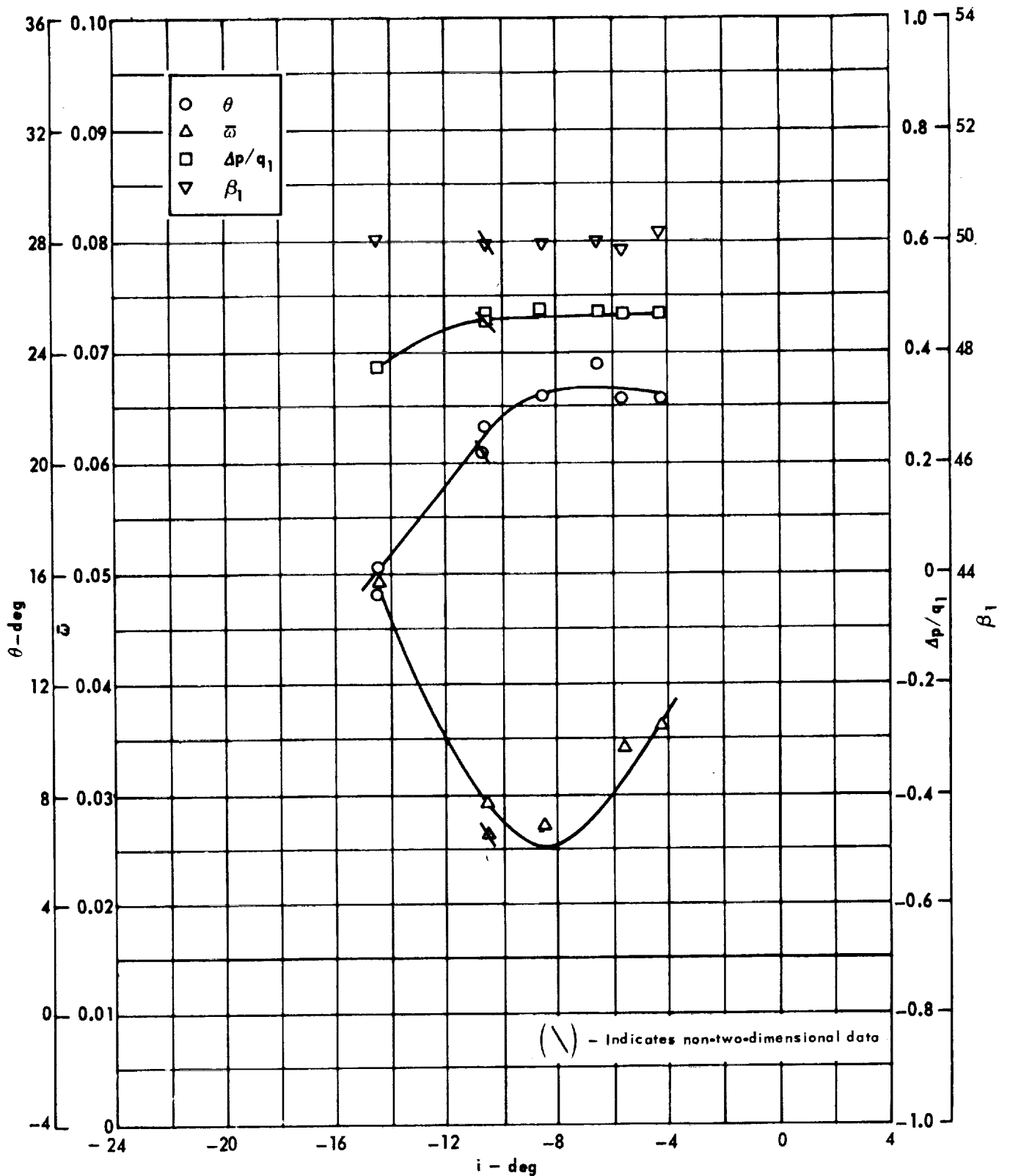
Figure 39 . - Cascade characteristics as functions of incidence.



Cascade configuration : $\beta_{1N} = 50, \sigma = 0.75$
 Double circular-arc profile : $\phi = 45, t/c = 0.06$

(b) D, θ^*/s , K, δ°

Figure 39 . - Concluded.

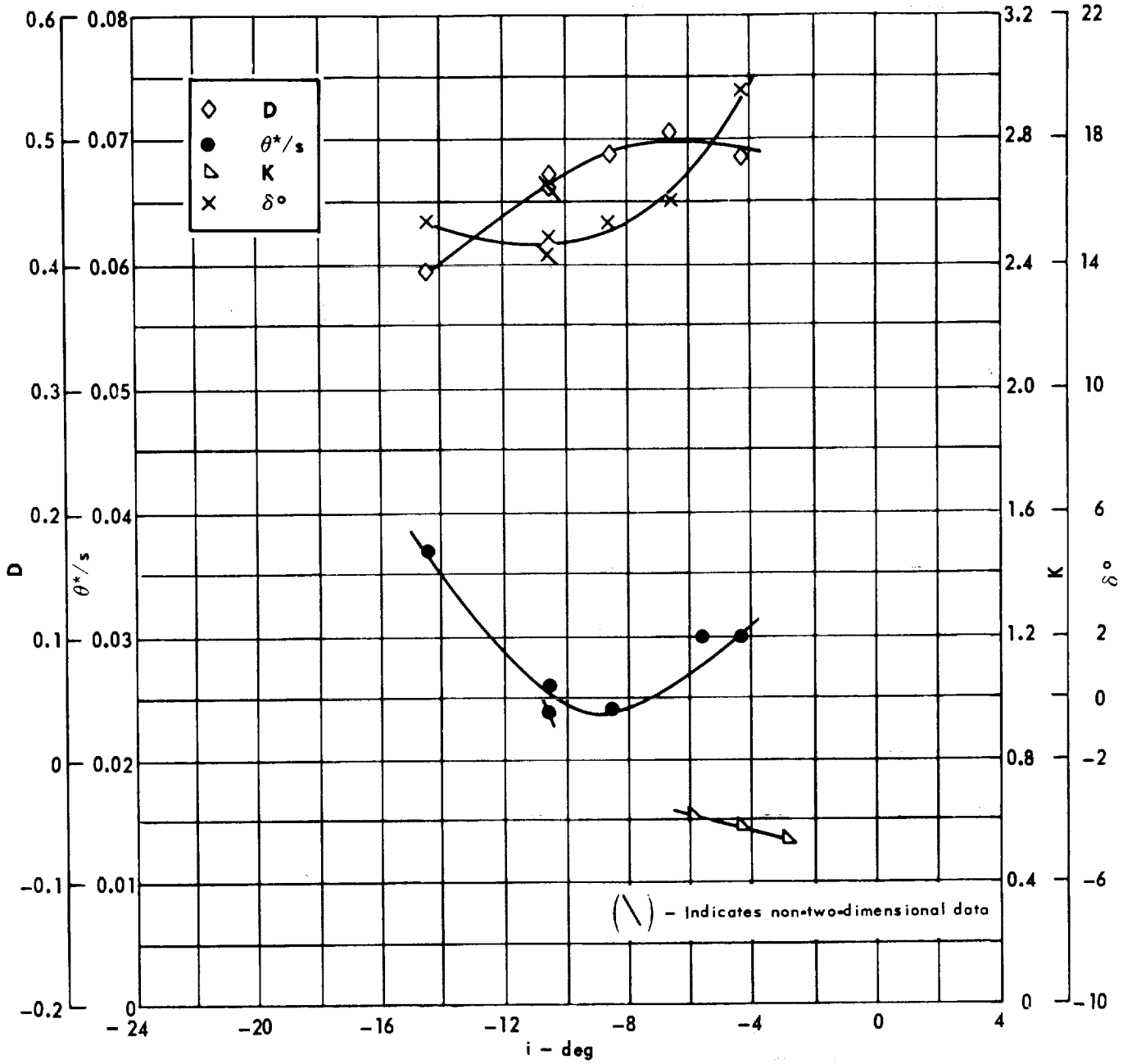


Cascade configuration: $\beta_{1N} = 50$, $\sigma = 1.00$

Double circular-arc profile: $\phi = 45$, $t/c = 0.06$

(a) $\theta, \bar{w}, \Delta p/q_1, \beta_1$

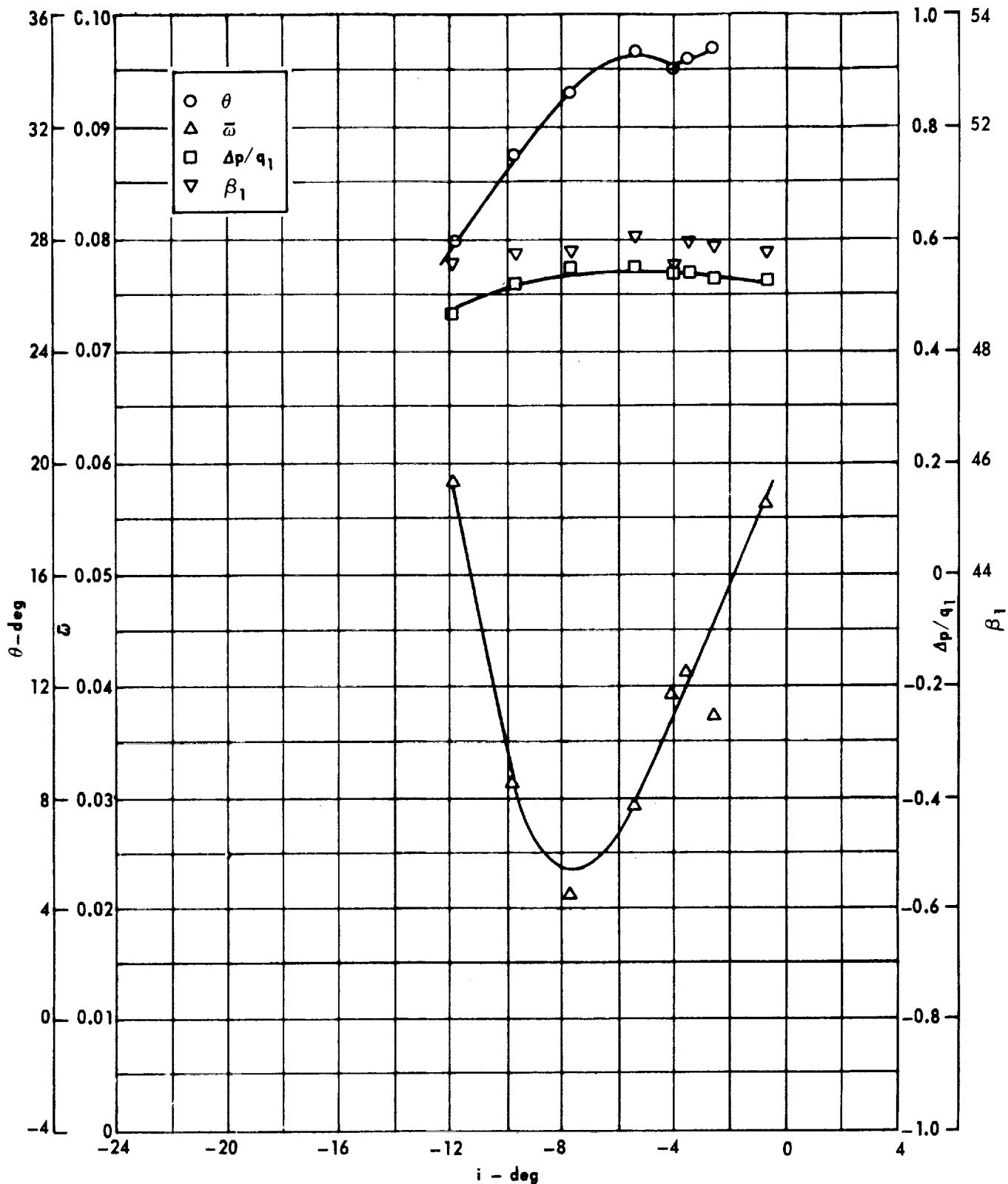
Figure 40 . - Cascade characteristics as functions of incidence.



Cascade configuration: $\beta_{1N} = 50$, $\sigma = 1.00$
 Double circular-arc profile: $\phi = 45$, $r/c = 0.06$

(b) D, θ^*/s , K, δ°

Figure 40. - Concluded.

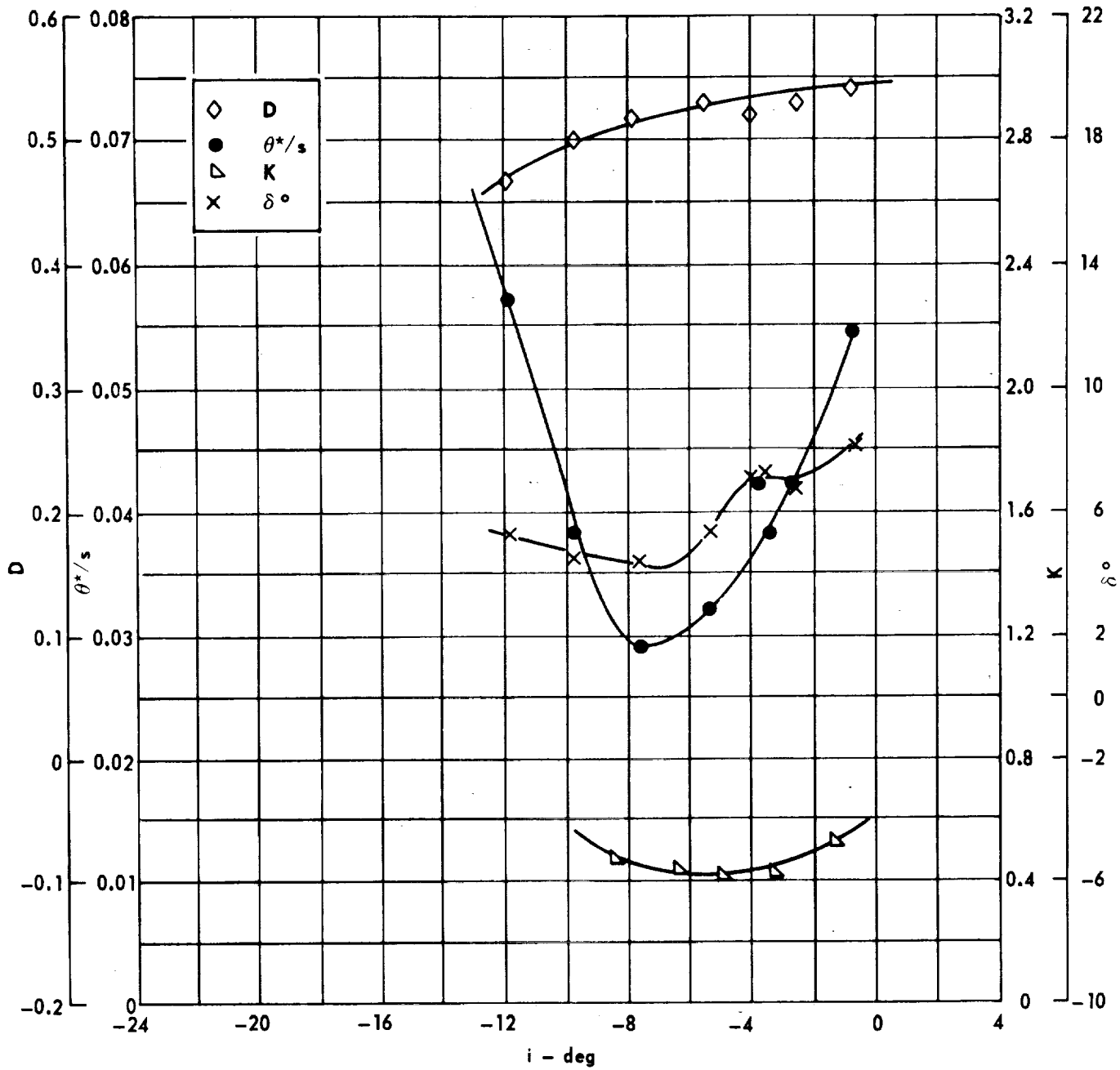


Cascade configuration : $\beta_{1N} = 50$, $\sigma = 1.50$

Double circular-arc profile : $\phi = 45$; $t/c = 0.06$

(a) $\theta, \bar{\omega}, \Delta p / q_1, \beta_1$

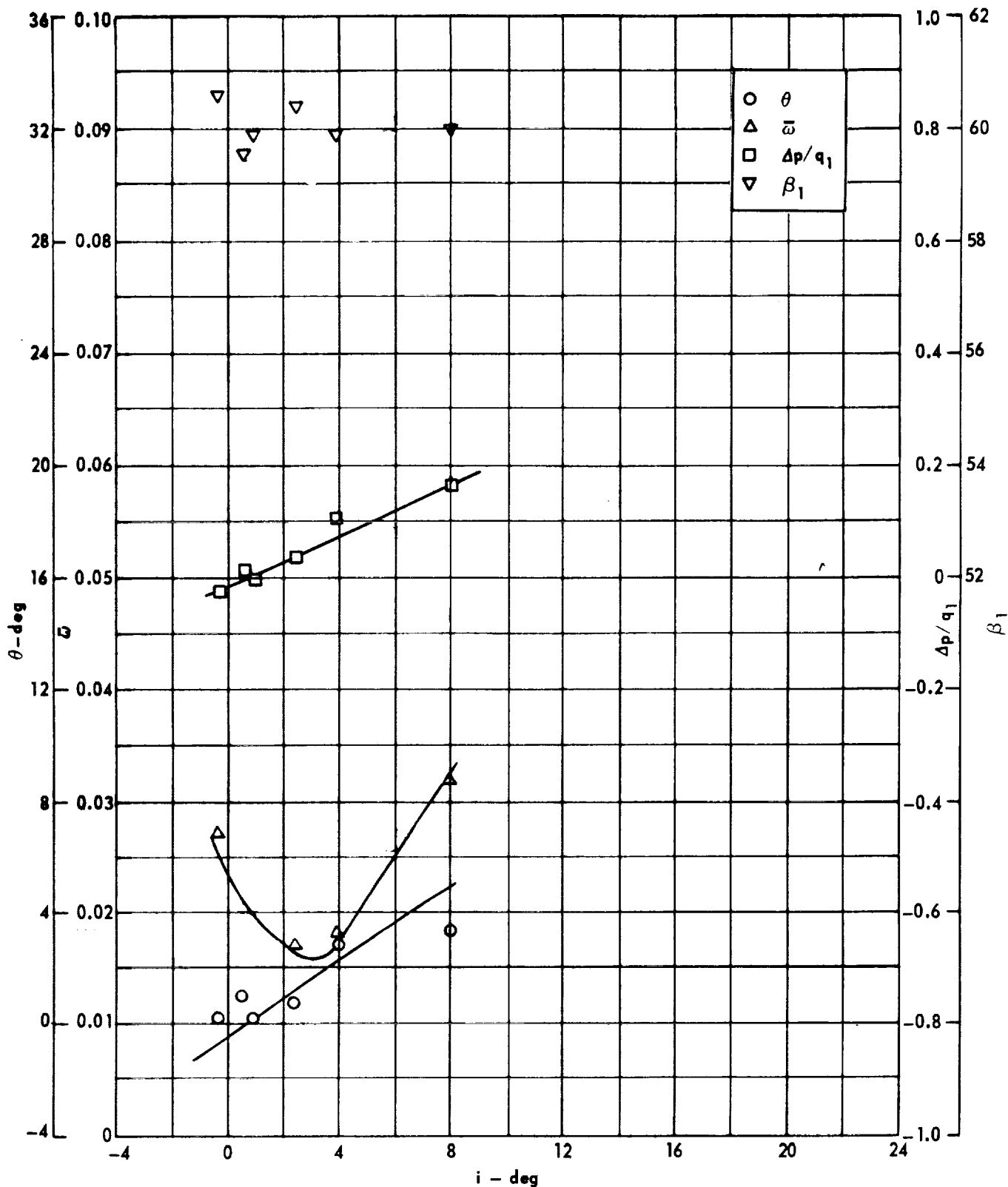
Figure 41 . - Cascade characteristics as functions of incidence.



Cascade configuration : $\beta_{1N} = 50$, $\sigma = 1.50$
 Double circular-arc profile : $\phi = 45$, $t/c = 0.06$

(b) D, θ^*/s , K, δ°

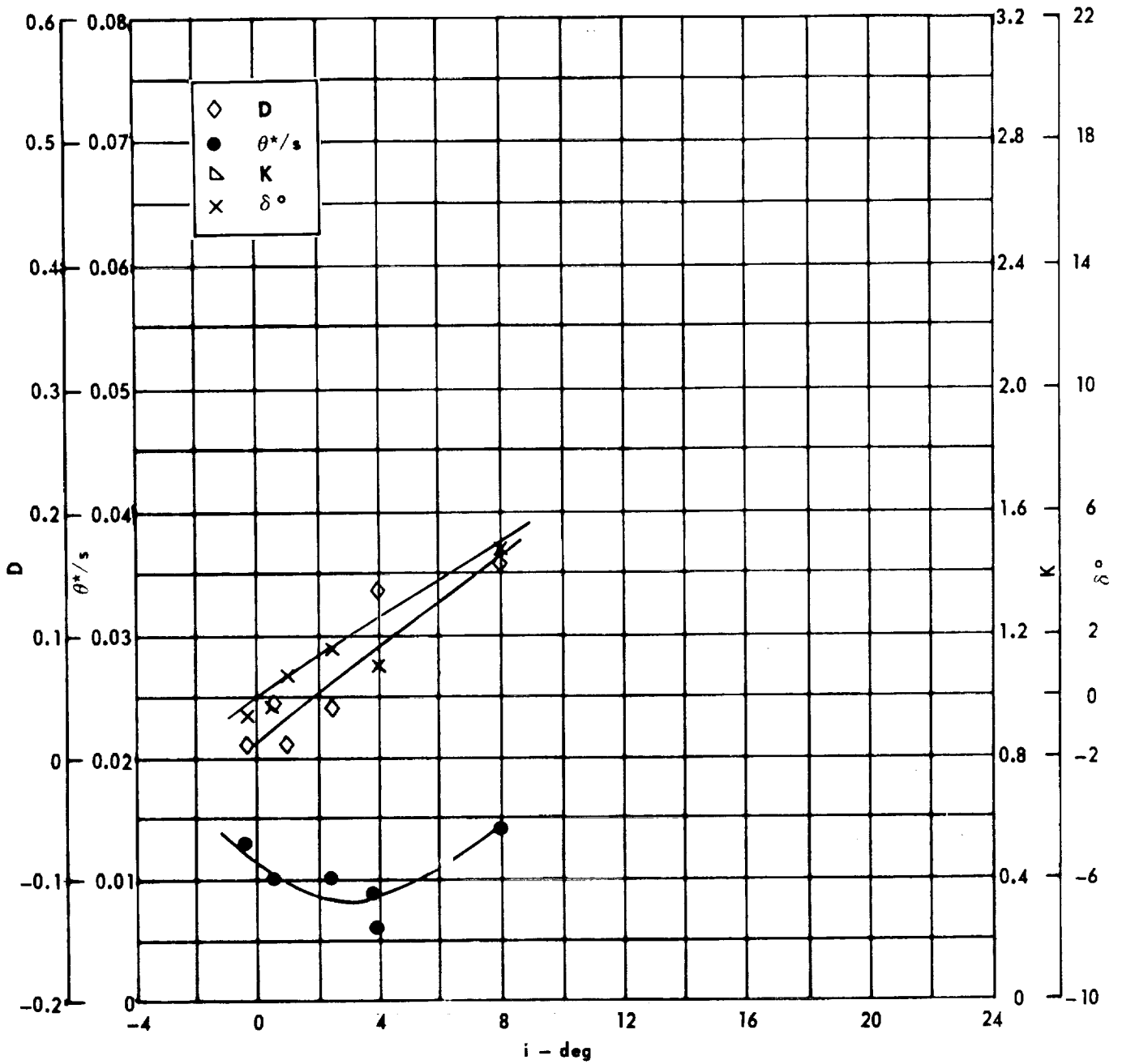
Figure 41 . - Concluded.



Cascade configuration : $\beta_{1N} = 60, \sigma = 0.75$
 Double circular-arc profile : $\phi = 0, t/c = 0.06$

(a) $\theta, \bar{\omega}, \Delta p/q_1, \beta_1$

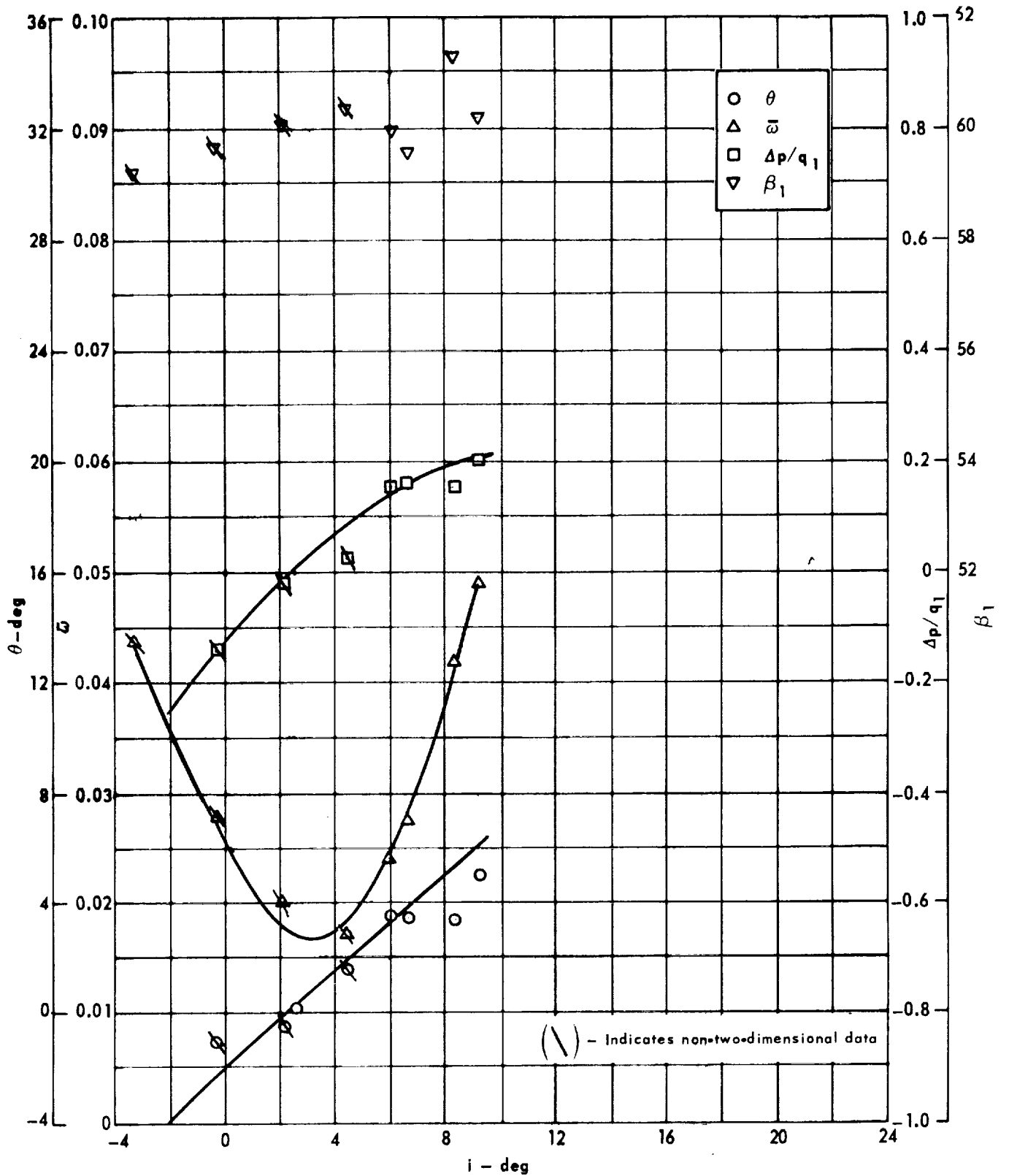
Figure 42 . - Cascade characteristics as functions of incidence.



Cascade configuration : $\beta_{1N} = 60, \sigma = 0.75$
 Double circular-arc profile : $\phi = 0, t/c = 0.06$

(b) D, θ^*/s , K, δ°

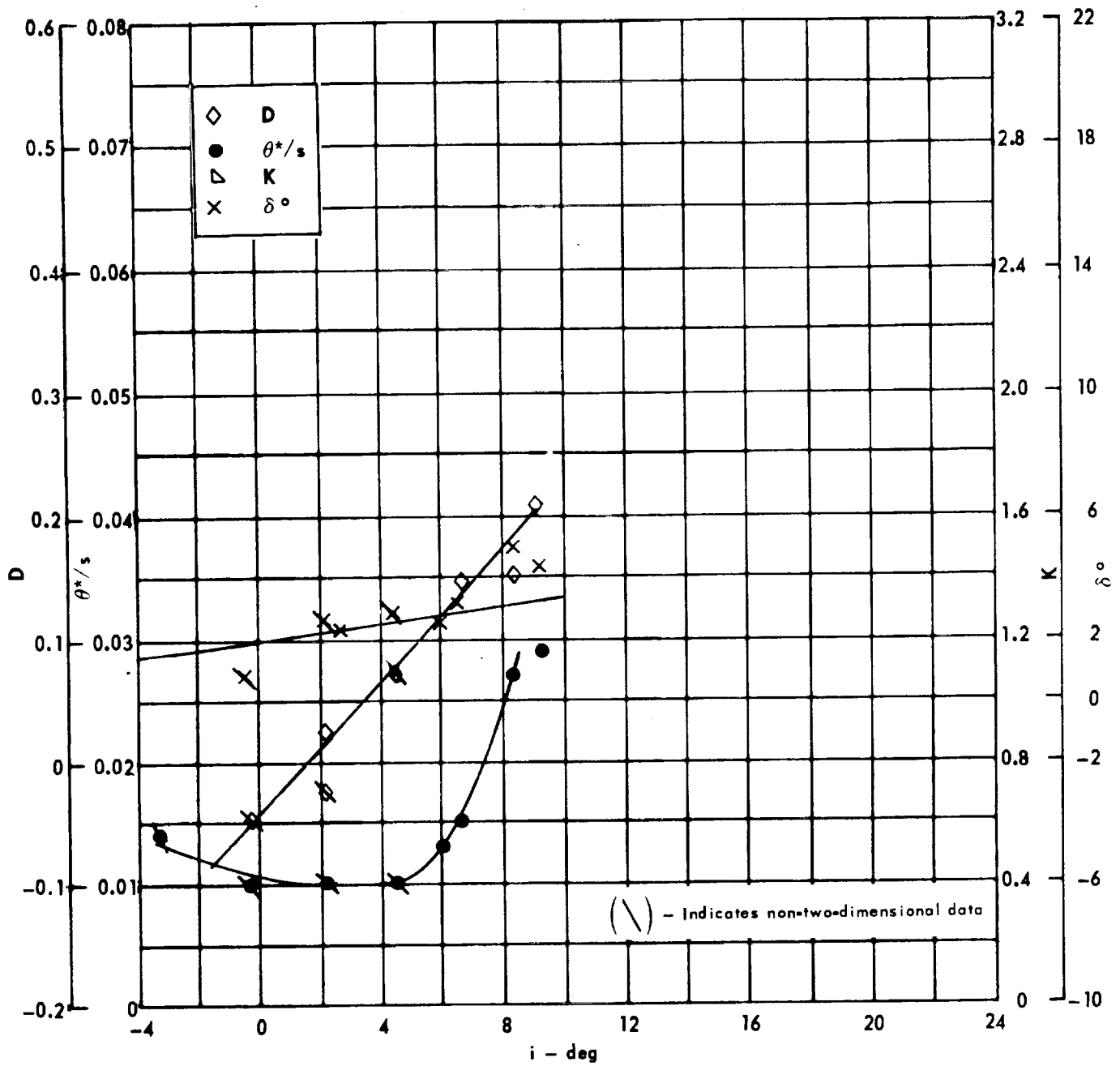
Figure 42 . - Concluded.



Cascade configuration : $\beta_{1N} = 60, \sigma = 1.00$
 Double circular-arc profile : $\phi = 0, t/c = 0.06$

(a) $\theta, \bar{\omega}, \Delta p/q_1, \beta_1$

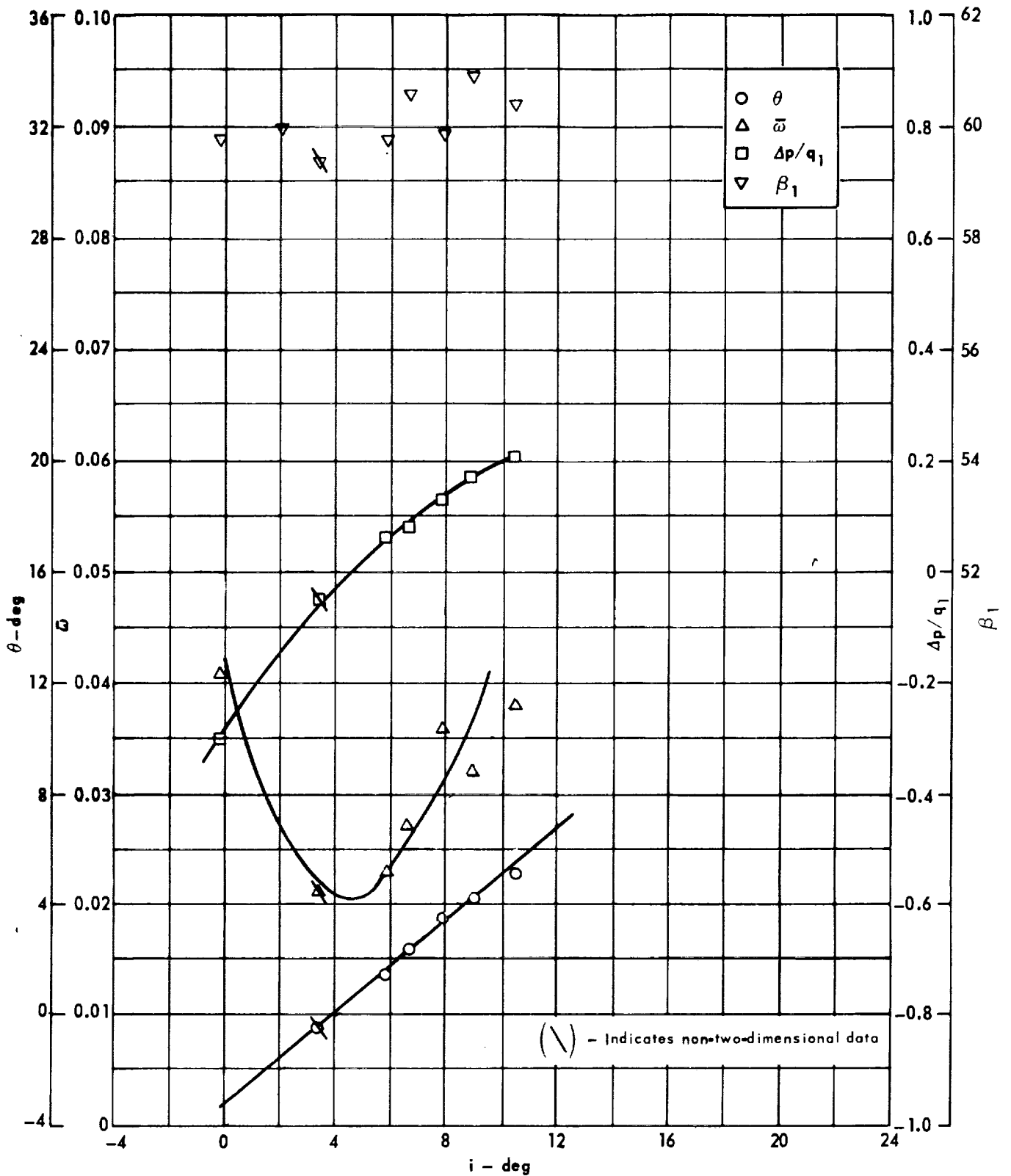
Figure 43. - Cascade characteristics as functions of incidence.



Cascade configuration: $\beta_{1N} = 60$, $\sigma = 1.00$
 Double circular-arc profile: $\phi = 0$, $t/c = 0.06$

(b) D, θ^*/s , K, δ°

Figure 43. - Concluded.



Cascade configuration : $\beta_{1N} = 60, \sigma = 1.50$

Double circular-arc profile : $\phi = 0, t/c = 0.06$

(a) $\theta, \bar{\omega}, \Delta p/q_1, \beta_1$

Figure 44. - Cascade characteristics as functions of incidence.

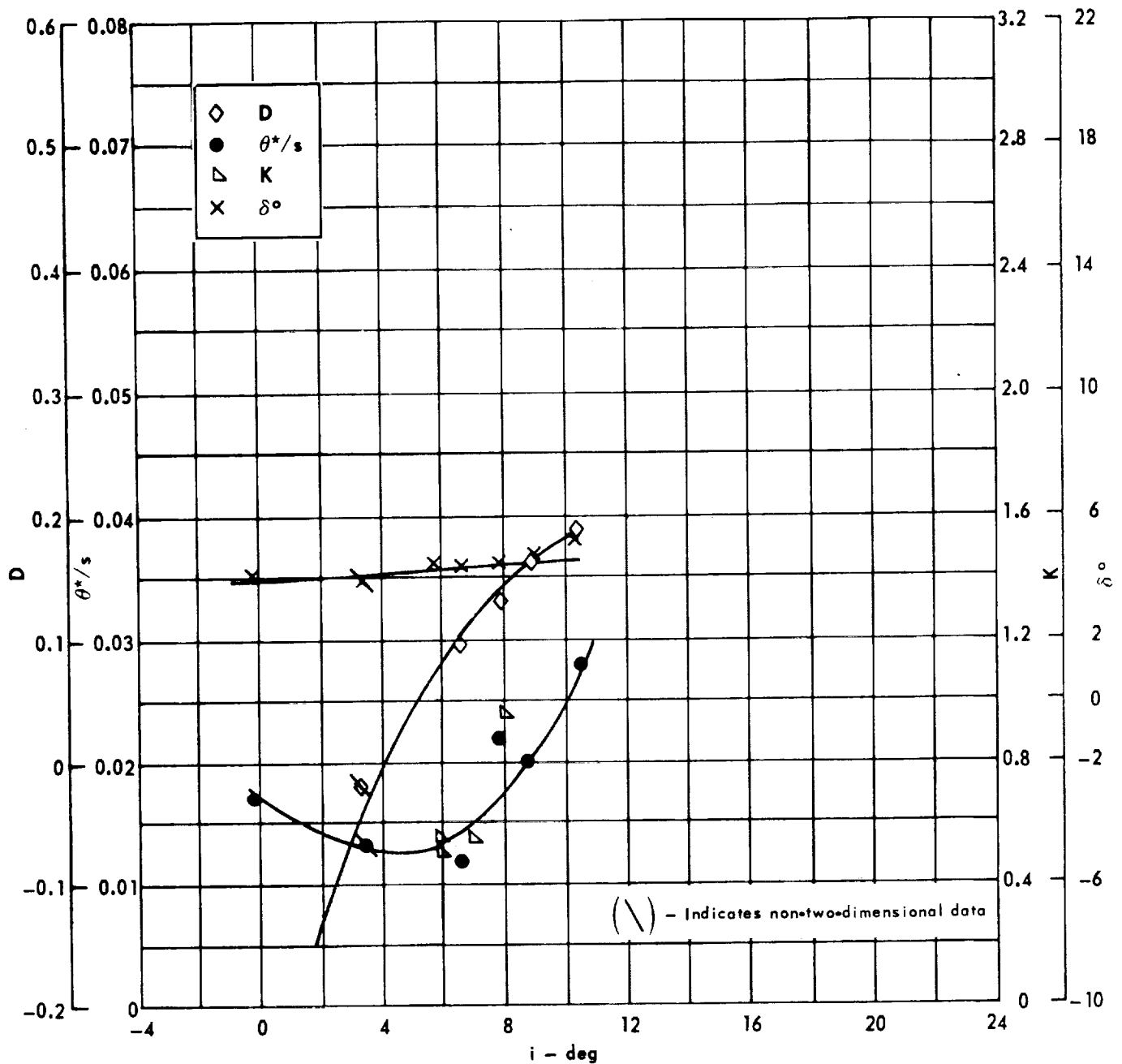
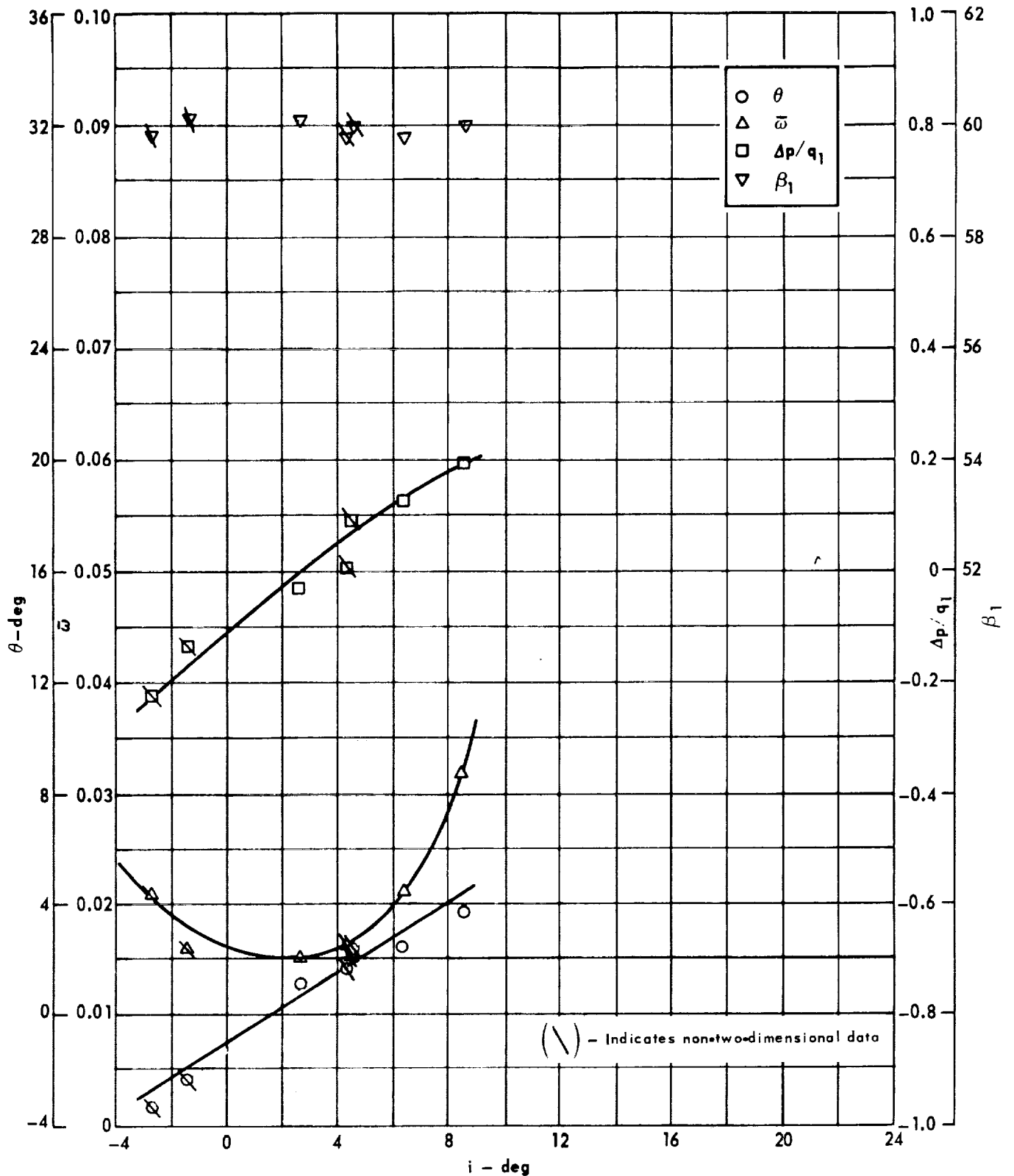


Figure 44. - Concluded.

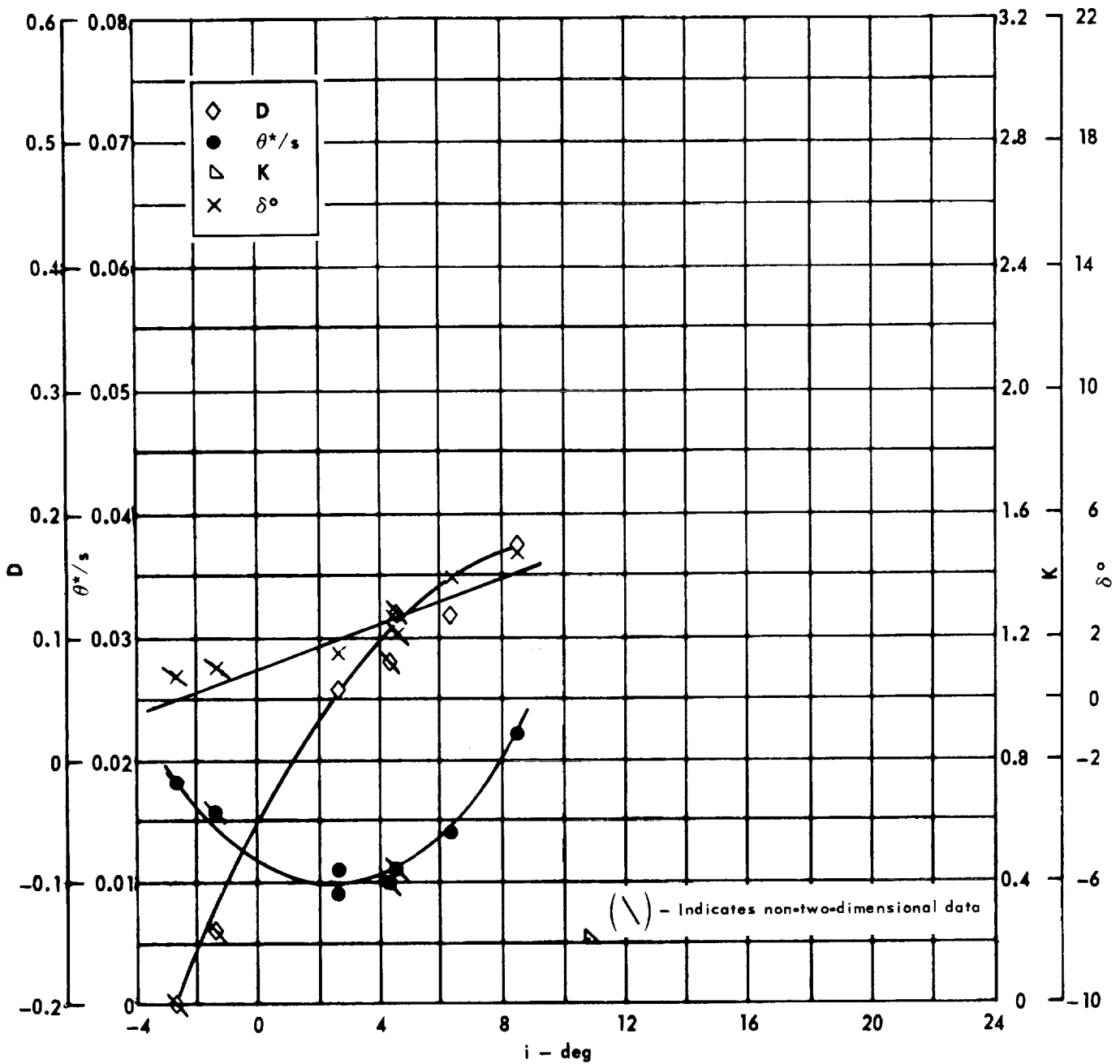


Cascade configuration : $\beta_{1N} = 60, \sigma = 0.75$

Double circular-arc profile : $\phi = 0, t/c = 0.10$

(a) $\theta, \bar{\omega}, \Delta p/q_1, \beta_1$

Figure 45. - Cascade characteristics as functions of incidence.

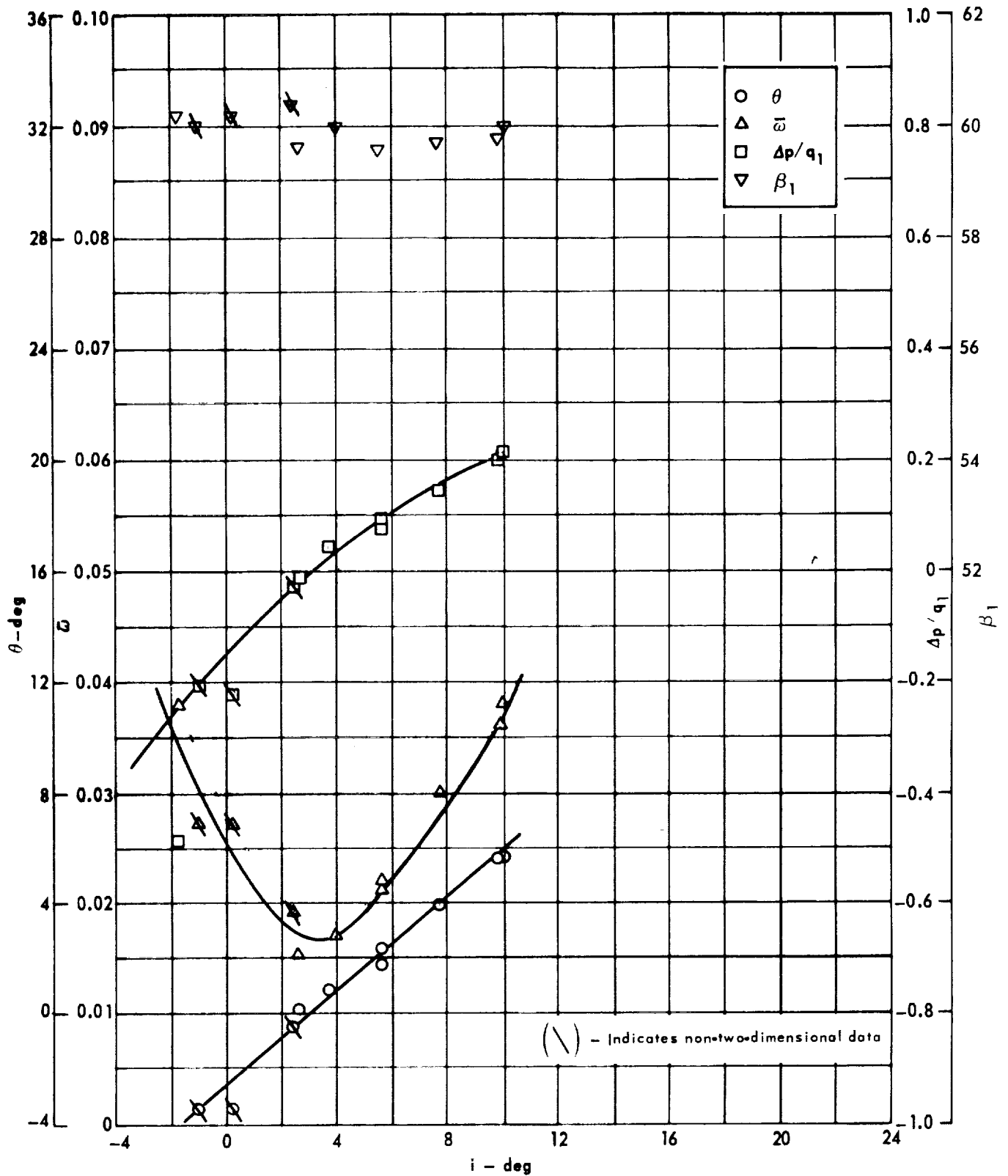


Cascade configuration: $\beta_{1N} = 60$, $\sigma = 0.75$

Double circular-arc profile: $\phi = 0$, $t/c = 0.10$

(b) D, θ^*/s , K, δ°

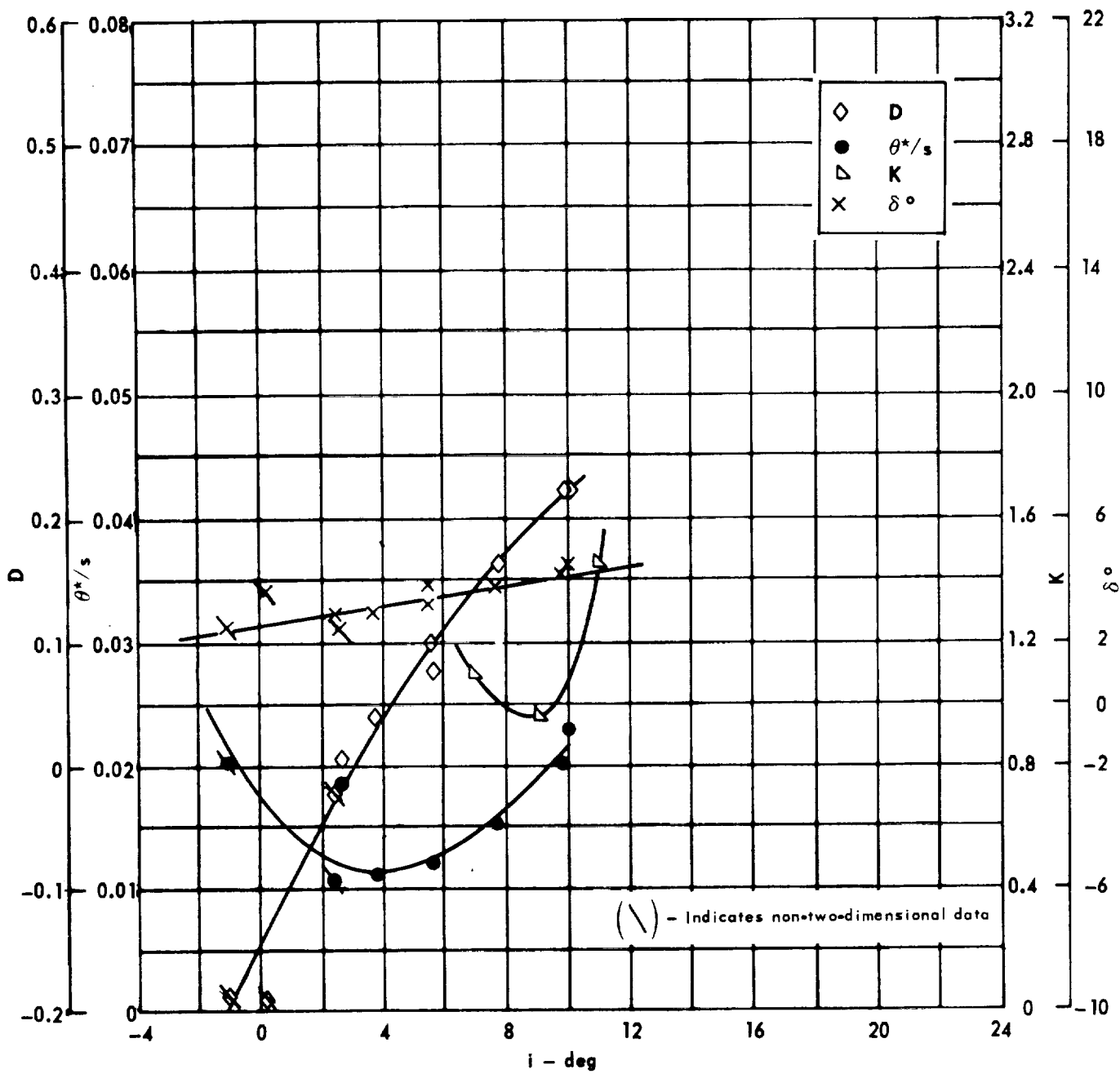
Figure 45 . - Concluded.



Cascade configuration: $\beta_{1N} = 60, \sigma = 1.00$
 Double circular-arc profile: $\phi = 0, t/c = 0.10$

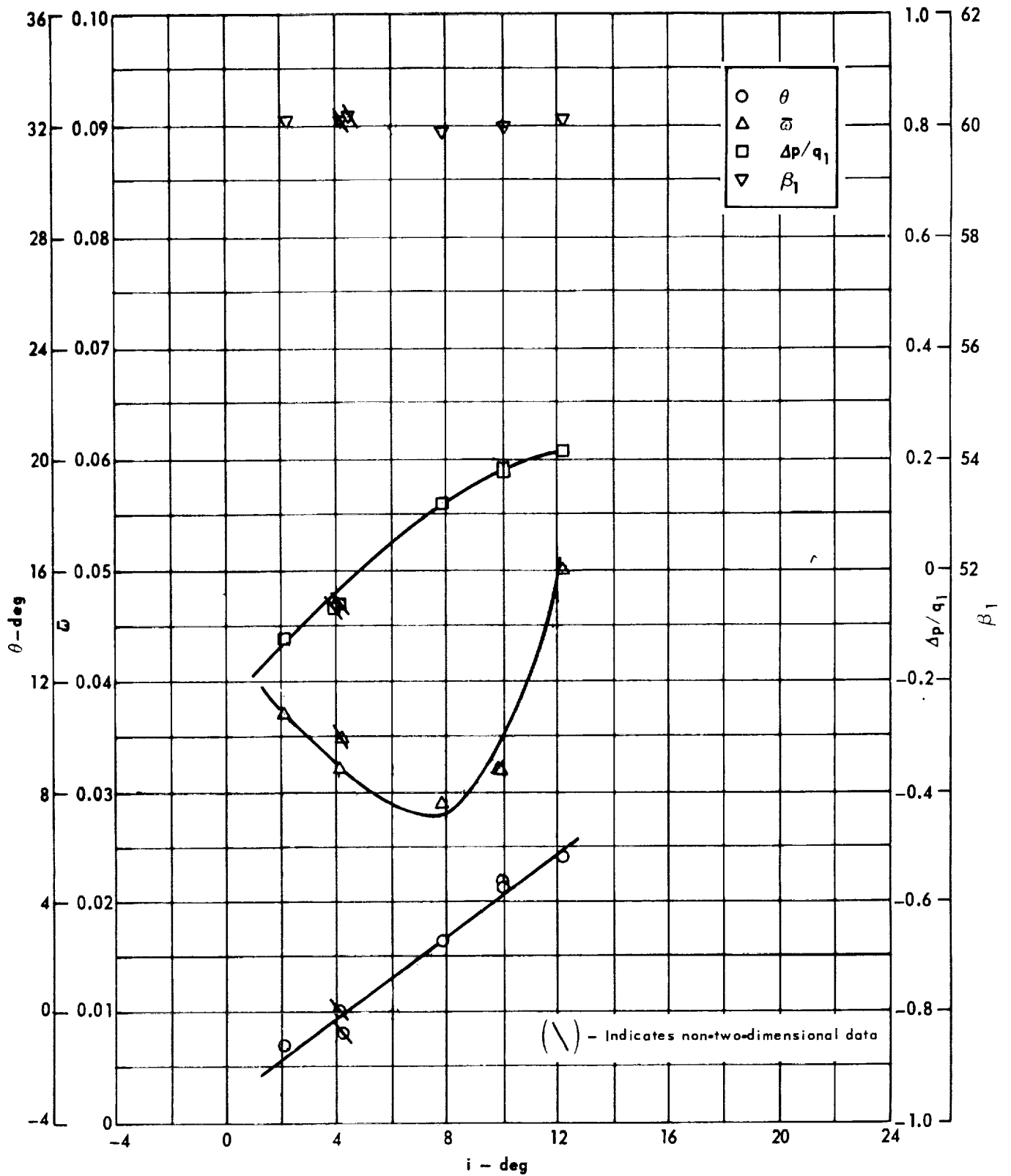
(a) $\theta, \bar{\omega}, \Delta p/q_1, \beta_1$

Figure 46. - Cascade characteristics as functions of incidence.



Cascade configuration: $\beta_{1N} = 60, \sigma = 1.00$
 Double circular-arc profile: $\phi = 0, t/c = 0.10$
 (b) $D, \theta^*/s, K, \delta^\circ$

Figure 46 . - Concluded.

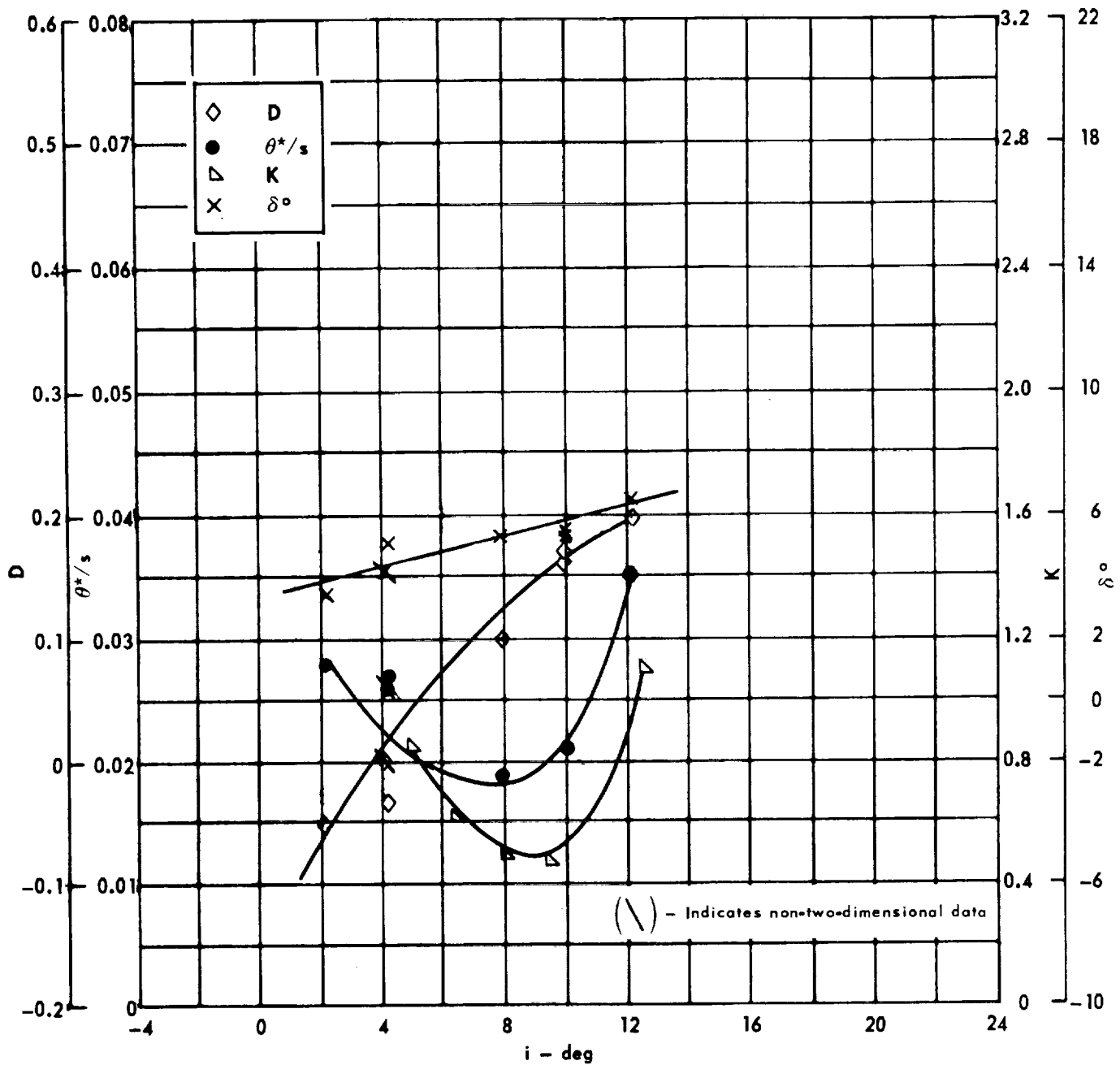


Cascade configuration : $\beta_{1N} = 60$, $\sigma = 1.50$

Double circular-arc profile : $\phi = 0$, $t/c = 0.10$

(a) $\theta, \bar{\omega}, \Delta p/q_1, \beta_1$

Figure 47 . - Cascade characteristics as functions of incidence.

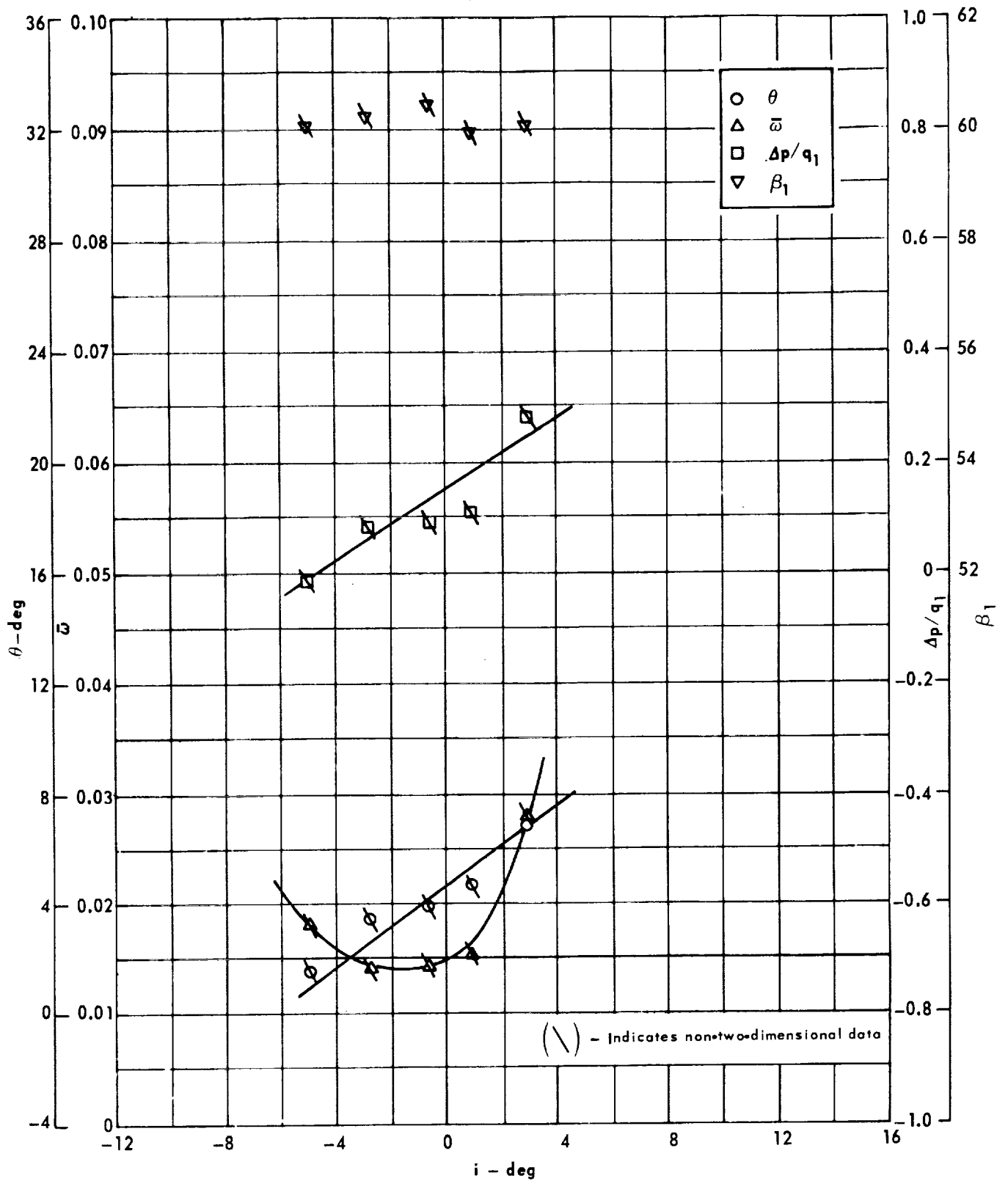


Cascade configuration: $\beta_{1N} = 60, \sigma = 1.50$

Double circular-arc profile: $\phi = 0, t/c = 0.10$

(b) D, θ^*/s , K, δ°

Figure 47 . - Concluded.

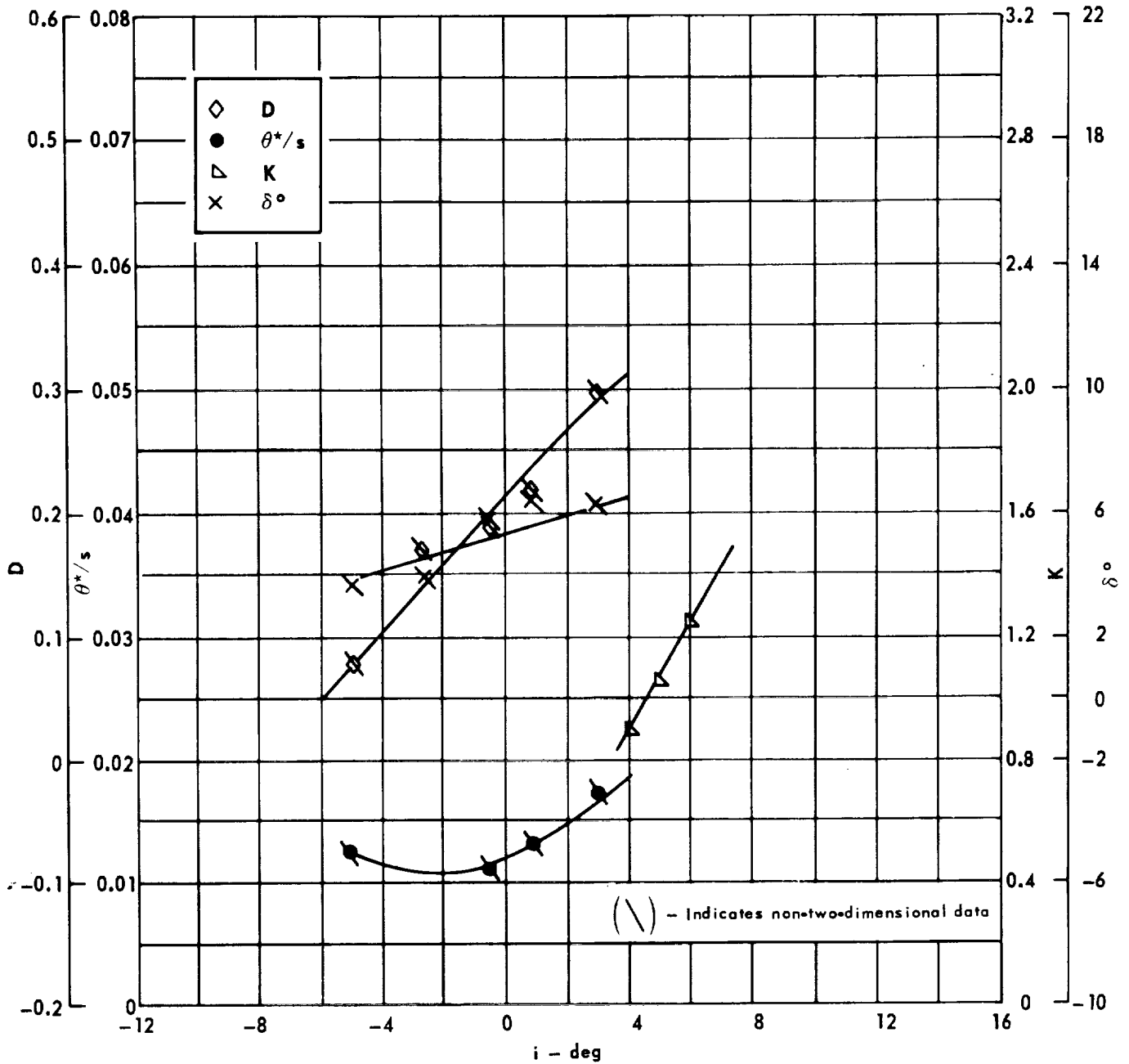


Cascade configuration: $\beta_{1N} = 60$, $\sigma = 0.75$

Double circular-arc profile: $\phi = 10$, $t/c = 0.06$

(a) $\theta, \bar{\omega}, \Delta p/q_1, \beta_1$

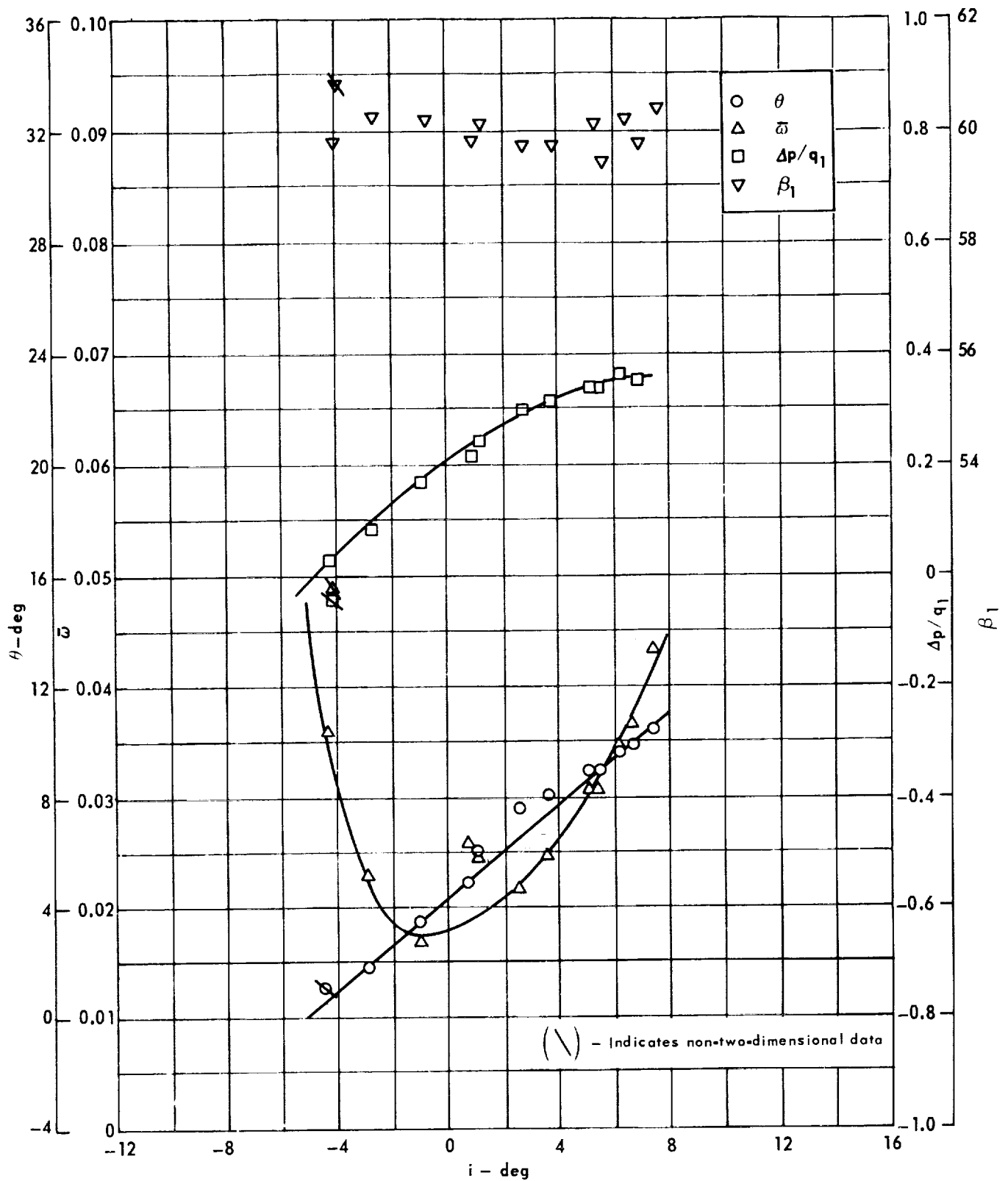
Figure 48. - Cascade characteristics as functions of incidence.



Cascade configuration: $\beta_{1N} = 60, \sigma = 0.75$
 Double circular-arc profile: $\phi = 10, t/c = 0.06$

(b) D, θ^*/s , K, δ°

Figure 48. - Concluded.



Cascade configuration : $\beta_{1N} = 60, \sigma = 1.00$

Double circular-arc profile : $\phi = 10, t/c = 0.06$

(a) $\theta, \bar{\omega}, \Delta p/q_1, \beta_1$

Figure 49. - Cascade characteristics as functions of incidence.

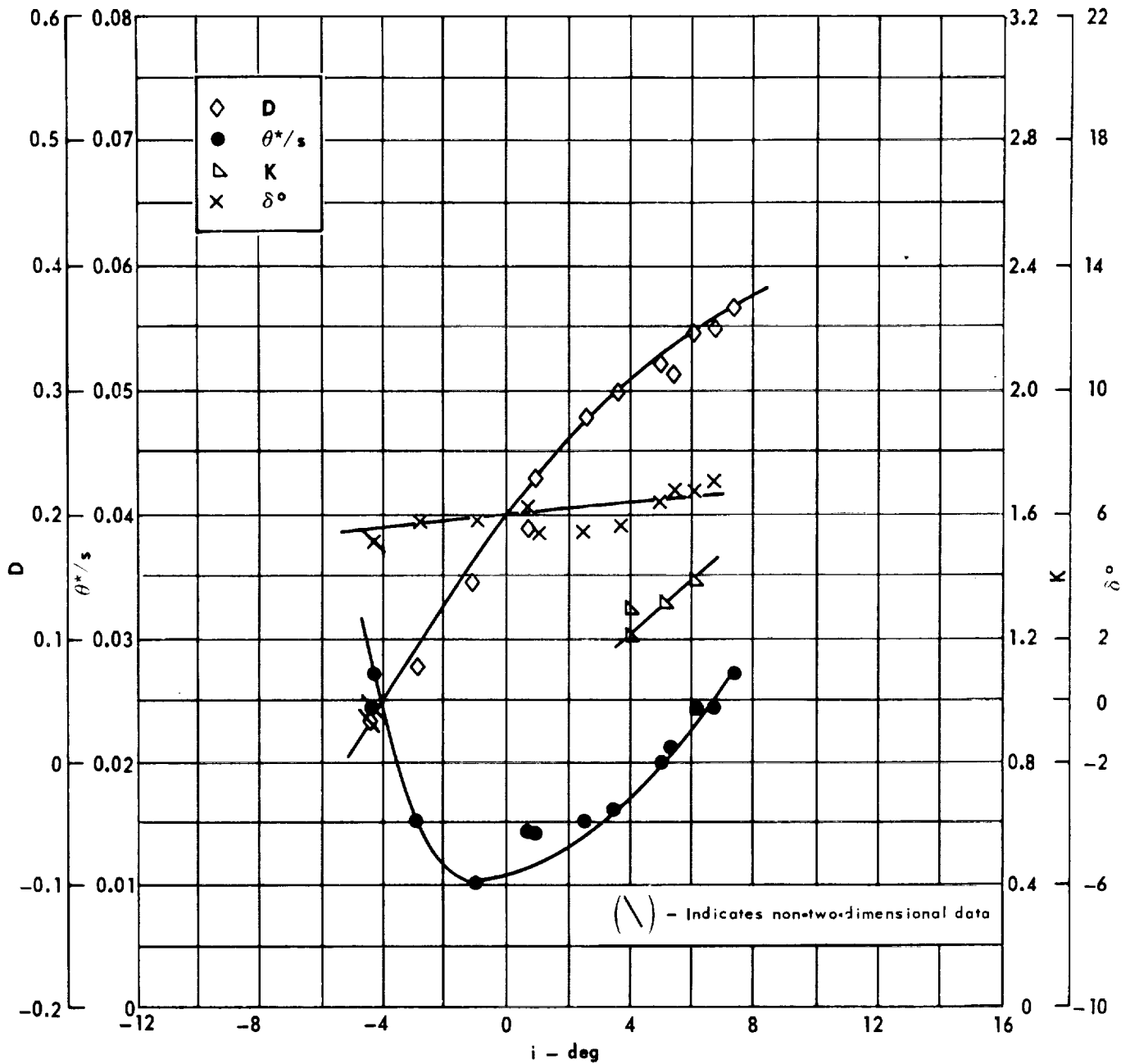
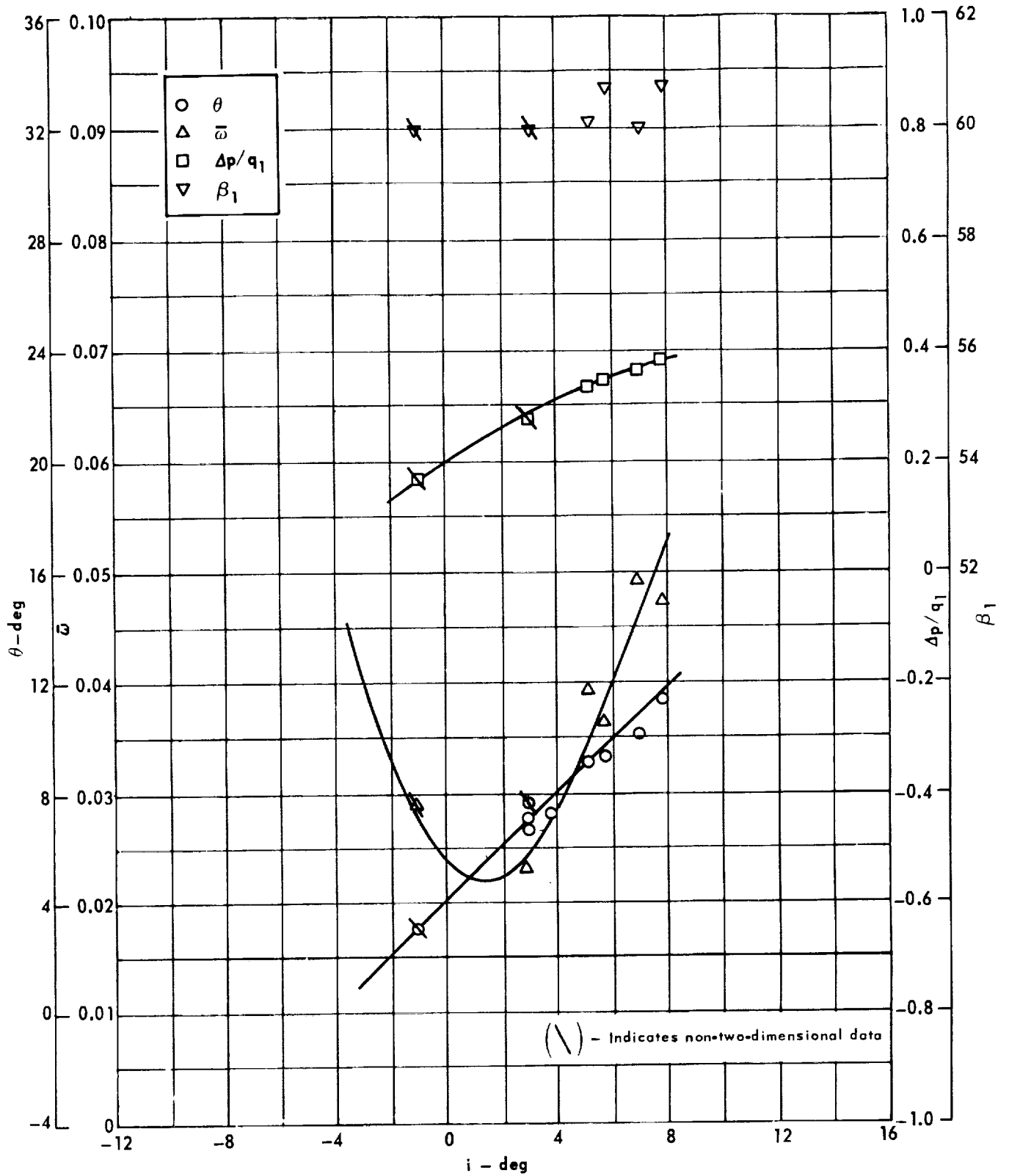


Figure 49. - Concluded.

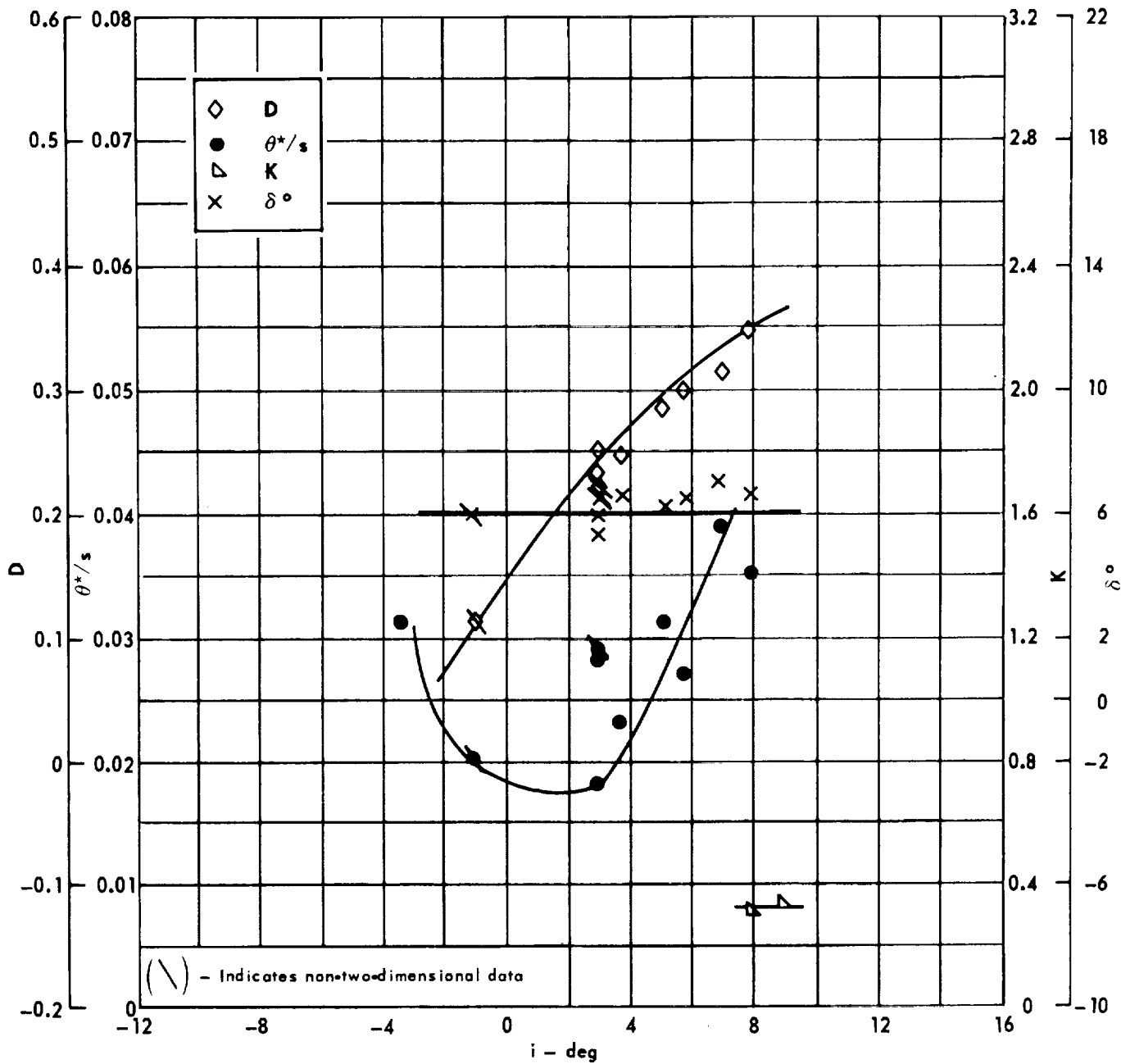


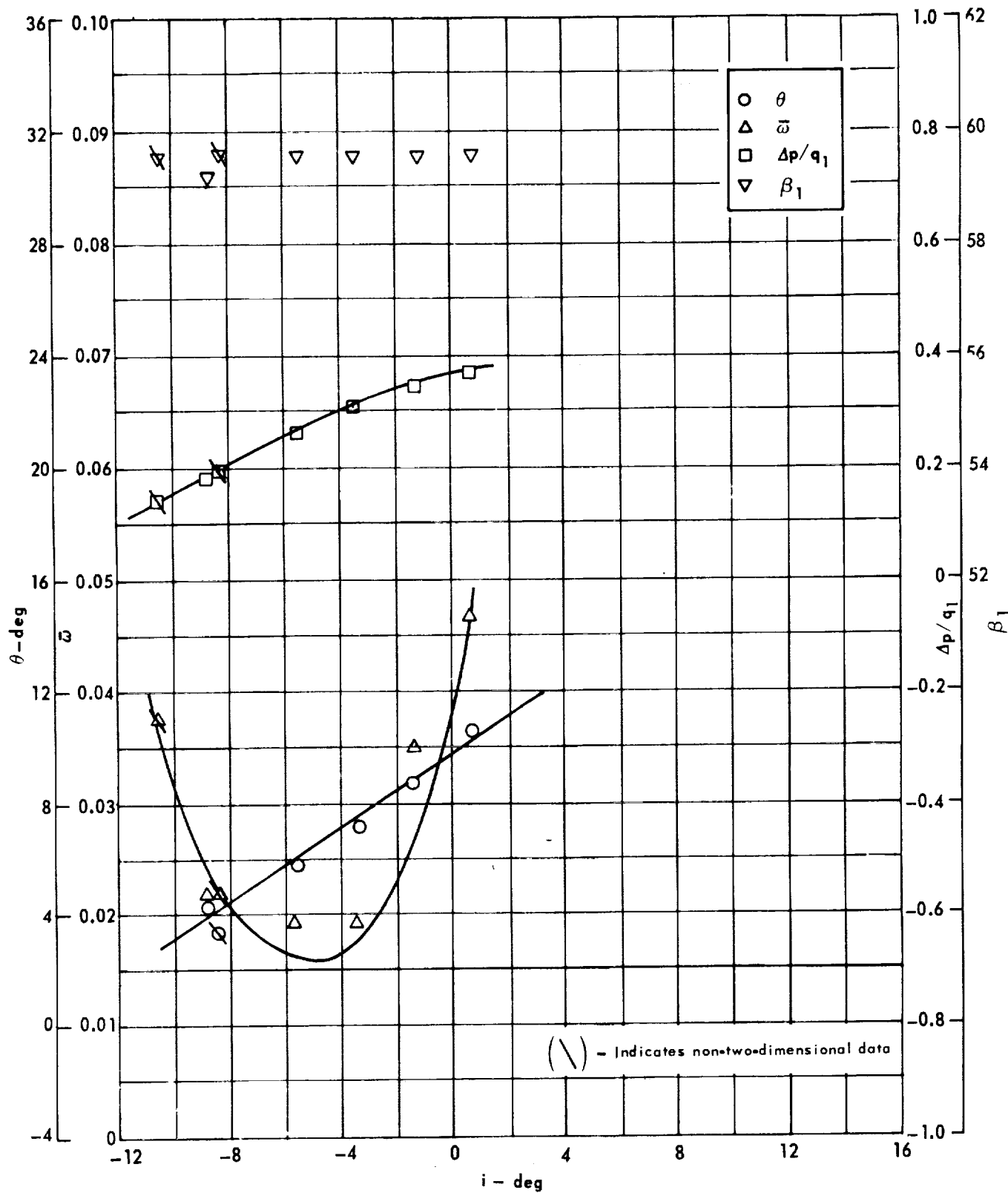
Cascade configuration: $\beta_{1N} = 60$, $\sigma = 1.50$

Double circular-arc profile: $\phi = 10$, $t/c = 0.06$

(a) $\theta, \bar{\omega}, \Delta p/q_1, \beta_1$

Figure 50. - Cascade characteristics as functions of incidence.

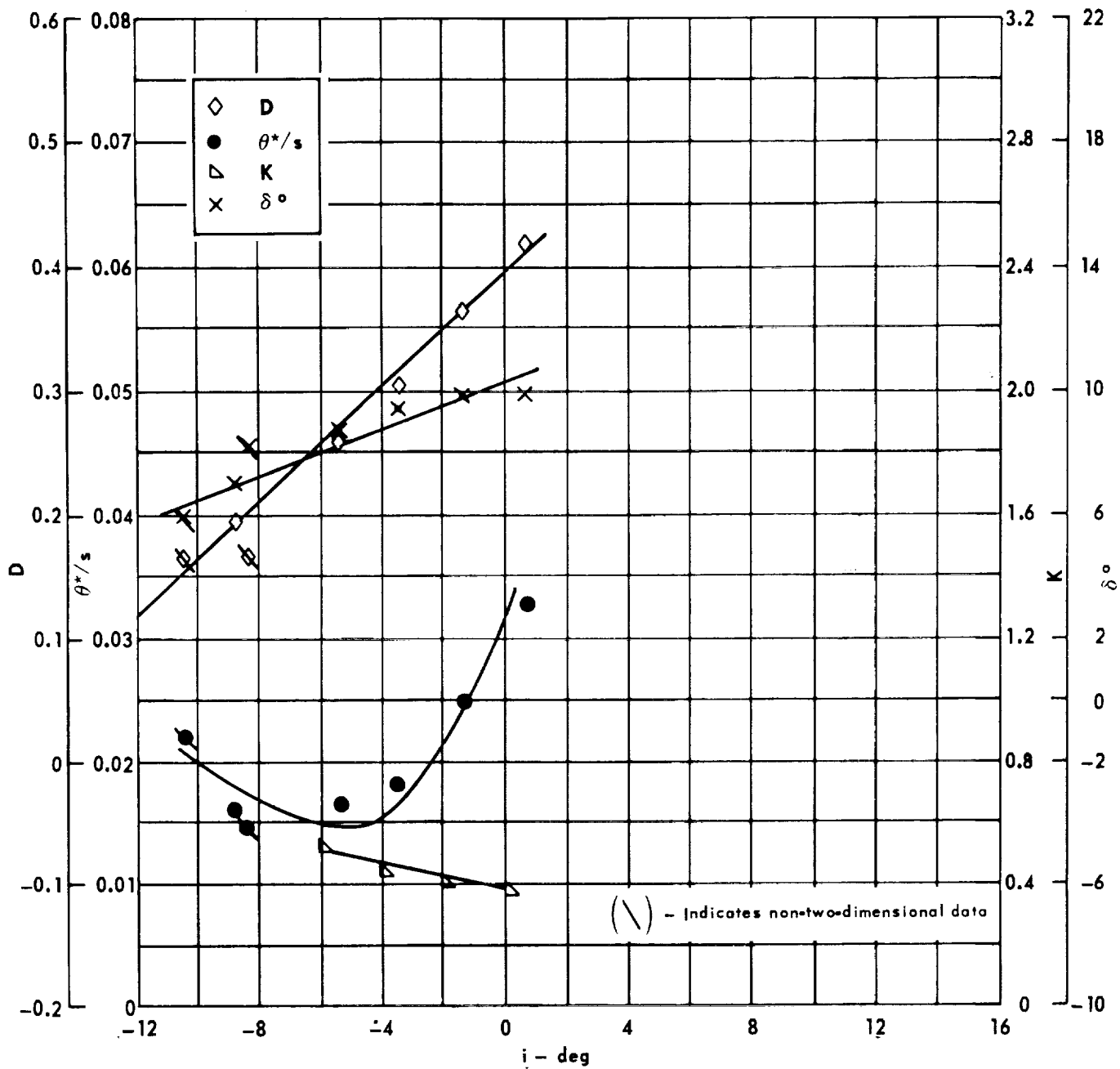




Cascade configuration : $\beta_{1N} = 60$, $\sigma = 0.75$
 Double circular-arc profile : $\phi = 20$, $t/c = 0.06$

(a) $\theta, \bar{\omega}, \Delta p/q_1, \beta_1$

Figure 51 . - Cascade characteristics as functions of incidence.

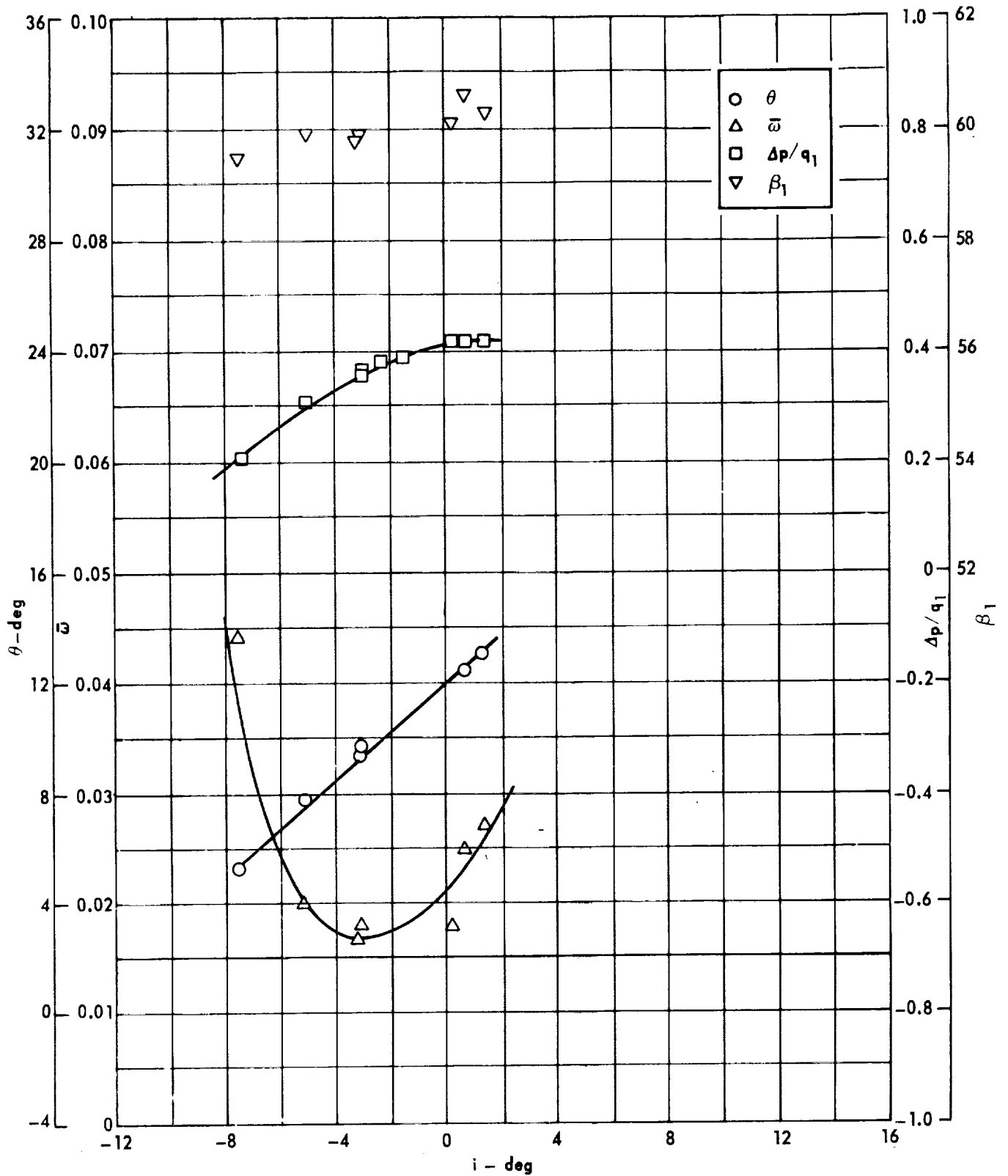


Cascade configuration: $\beta_{1N} = 60$, $\sigma = 0.75$

Double circular-arc profile: $\phi = 20$, $t/c = 0.06$

(b) D, θ^*/s , K, δ°

Figure 51 . - Concluded.

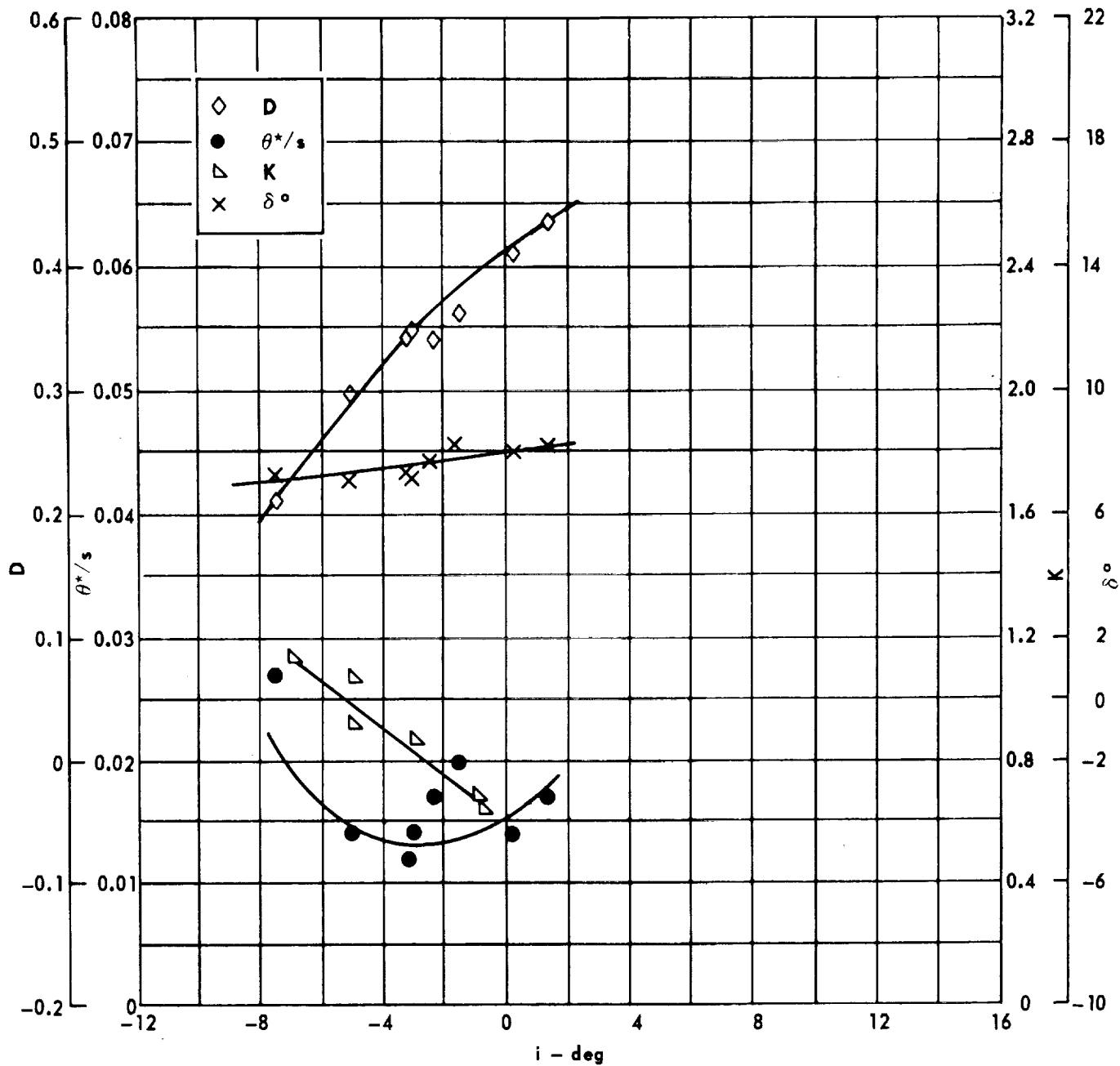


Cascade configuration : $\beta_{1N} = 60, \sigma = 1.00$

Double circular-arc profile : $\phi = 20, t/c = 0.06$

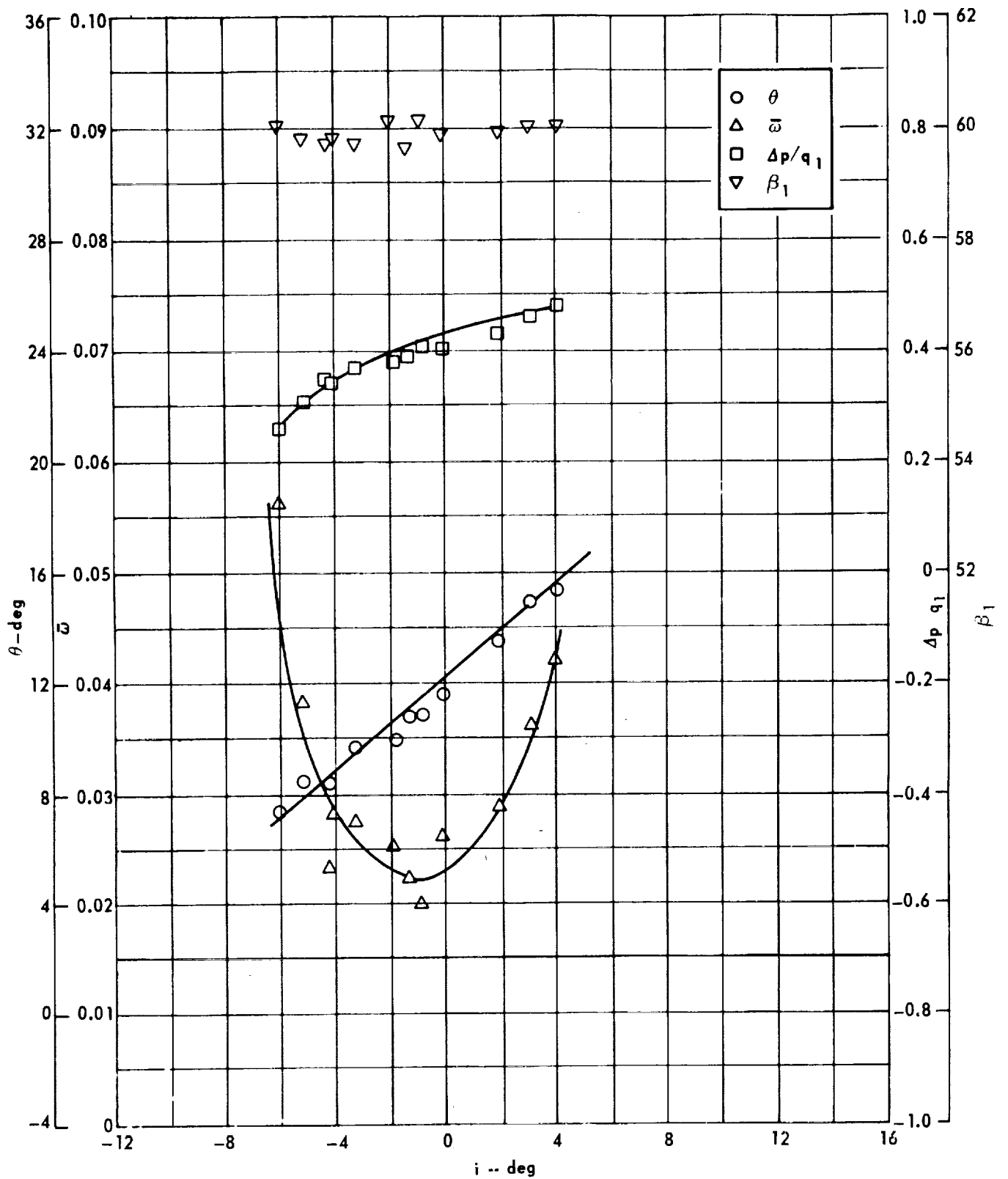
(a) $\theta, \bar{\omega}, \Delta p/q_1, \beta_1$

Figure 52 . - Cascade characteristics as functions of incidence.



Cascade configuration : $\beta_{1N} = 60, \sigma = 1.00$
 Double circular-arc profile : $\phi = 20, t/c = 0.06$
 (b) D, θ^*/s , K, δ°

Figure 52 . - Concluded.

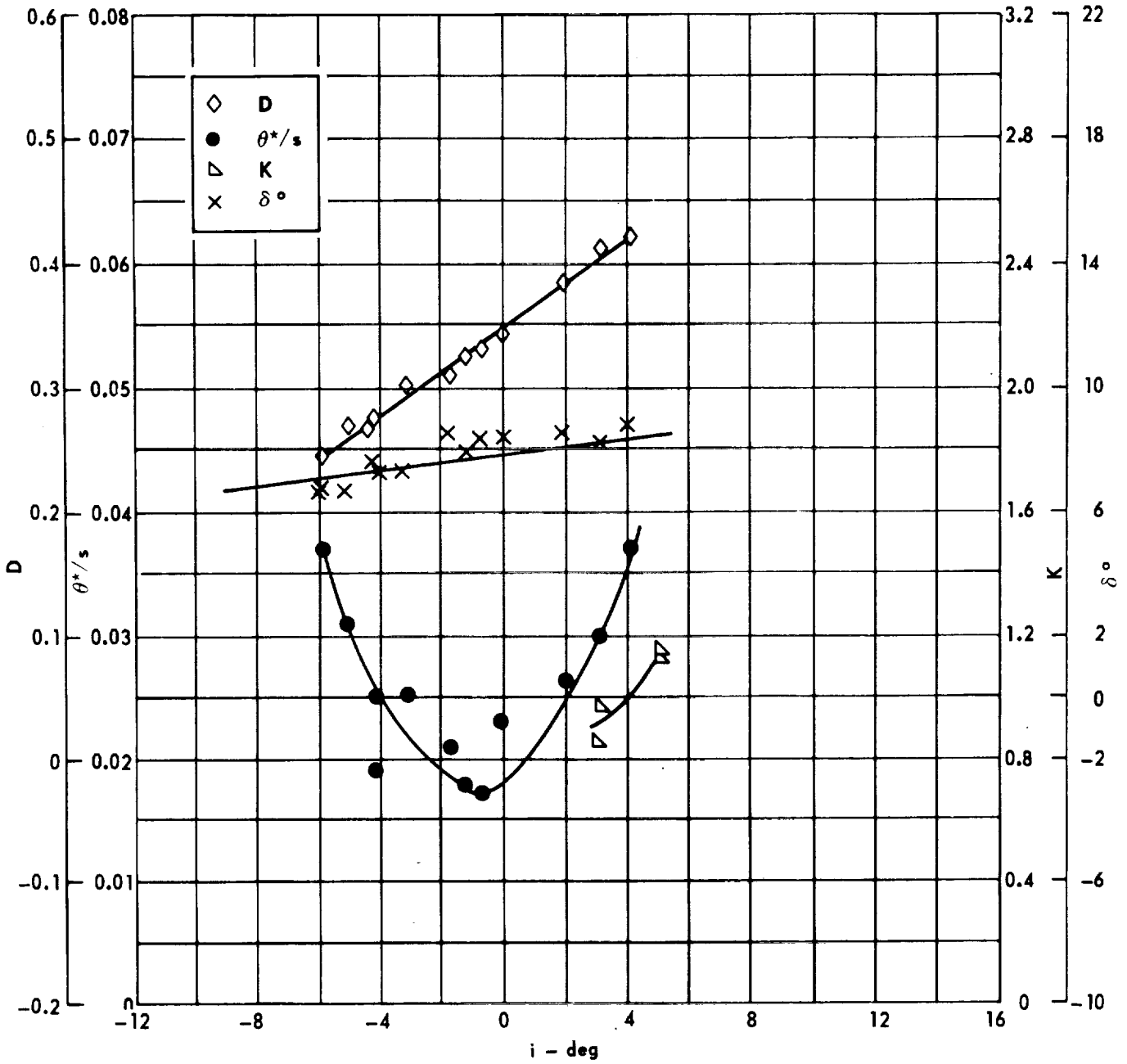


Cascade configuration : $\beta_{1N} = 60, \sigma = 1.50$

Double circular-arc profile : $\phi = 20, t/c = 0.06$

(a) $\theta, \bar{\omega}, \Delta p/q_1, \beta_1$

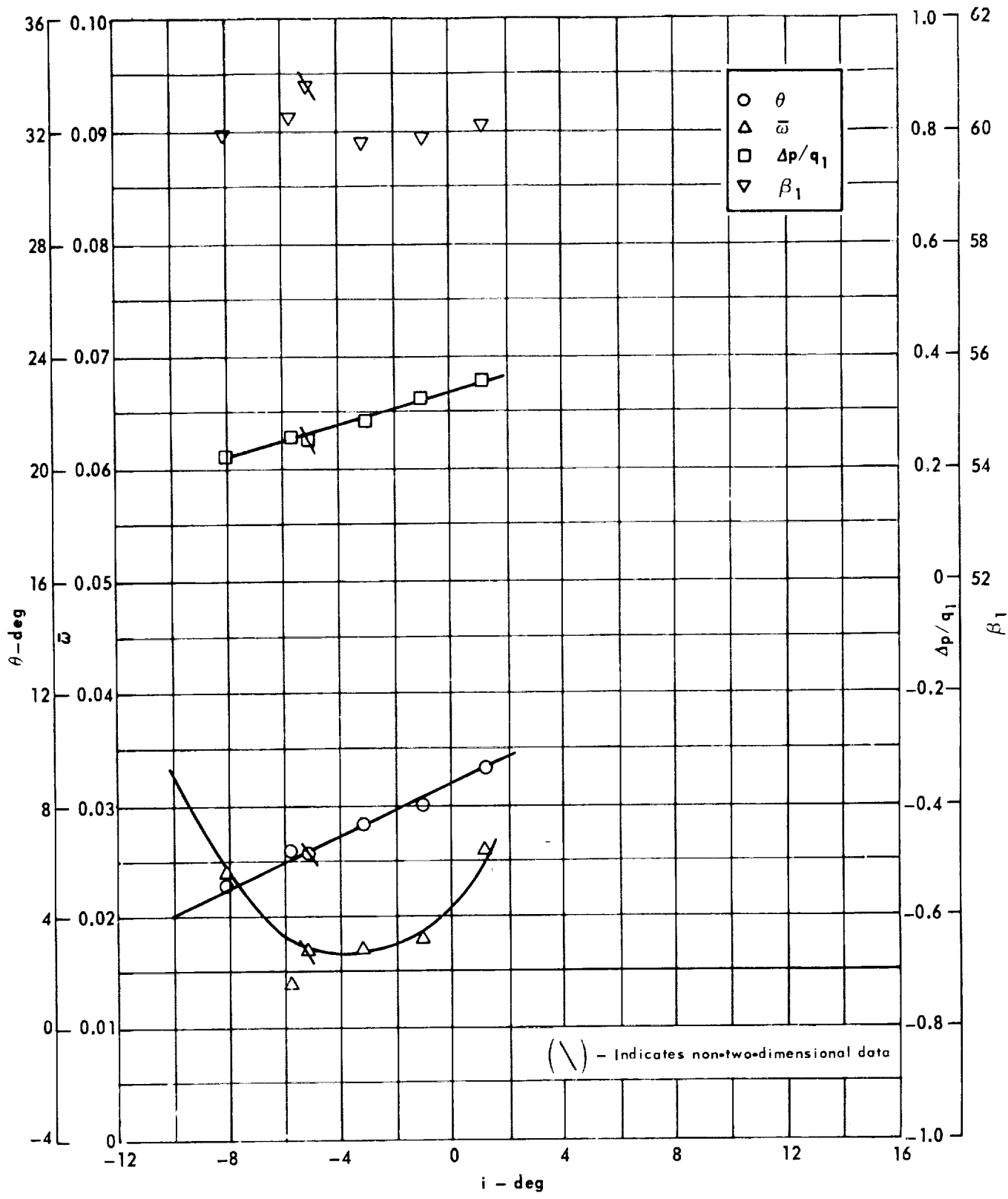
Figure 53 . - Cascade characteristics as functions of incidence.



Cascade configuration : $\beta_{1N} = 60$, $\sigma = 1.50$
 Double circular-arc profile : $\phi = 20$, $t/c = 0.06$

(b) D, θ^*/s , K, δ°

Figure 53 . - Concluded.

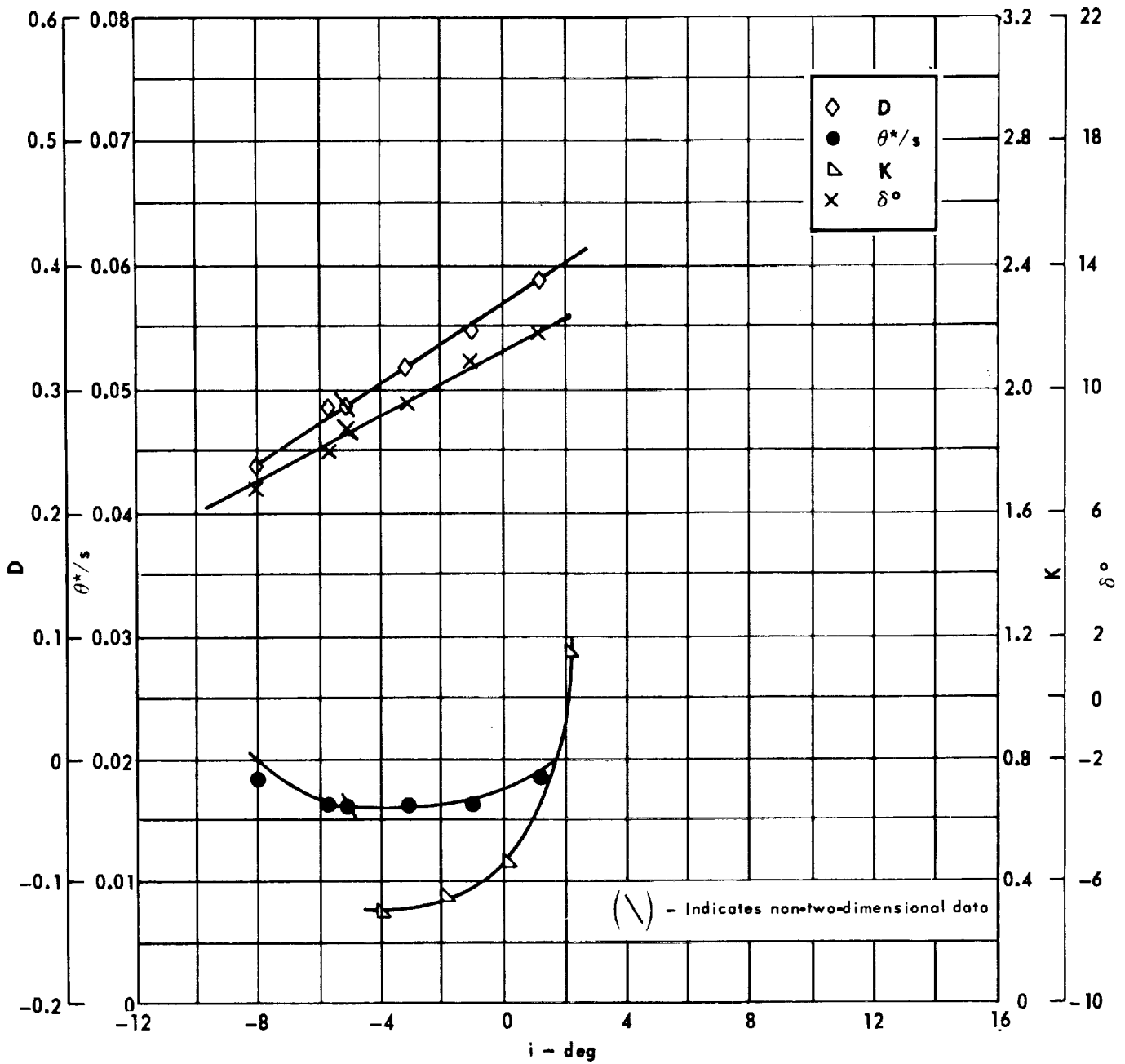


Cascade configuration: $\beta_{1N} = 60^\circ, \sigma = 0.75$

Double circular-arc profile: $\phi = 20^\circ, t/c = 0.10$

(a) $\theta, \bar{\omega}, \Delta p/q_1, \beta_1$

Figure 54 . - Cascade characteristics as functions of incidence.

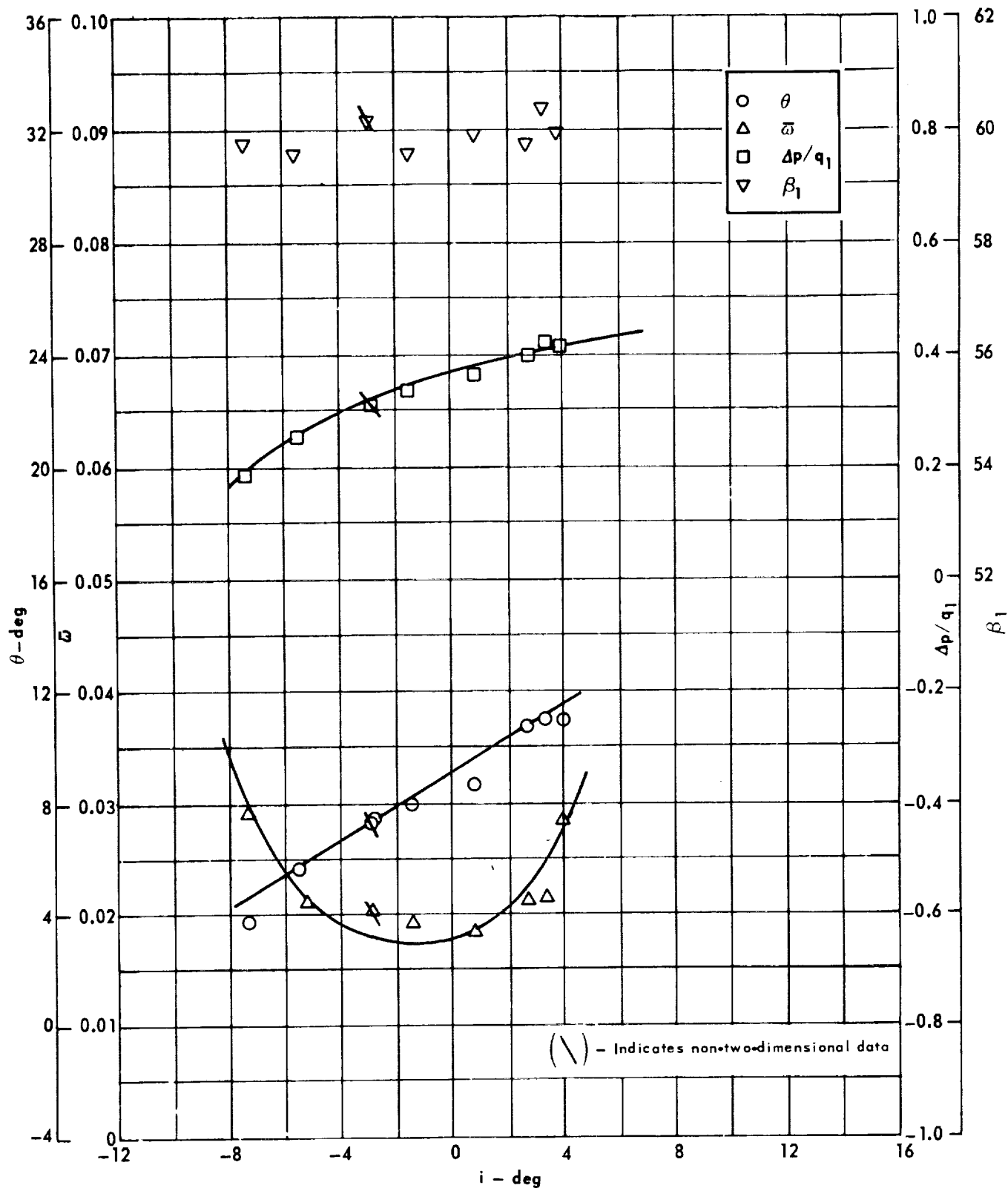


Cascade configuration: $\beta_{1N} = 60$, $\sigma = 0.75$

Double circular-arc profile: $\phi = 20$, $t/c = 0.10$

(b) D, θ^*/s , K, δ°

Figure 54 . - Concluded.

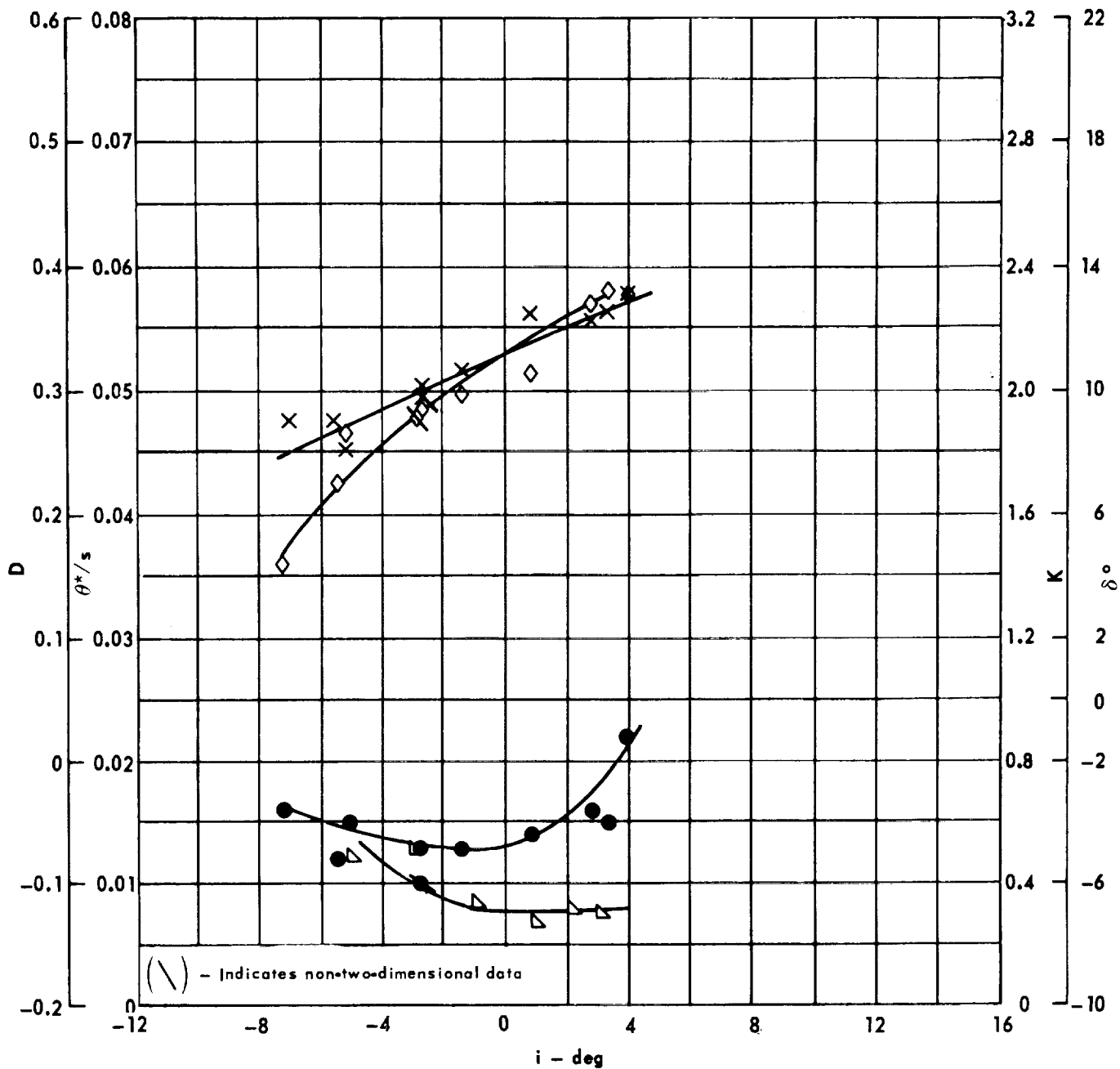


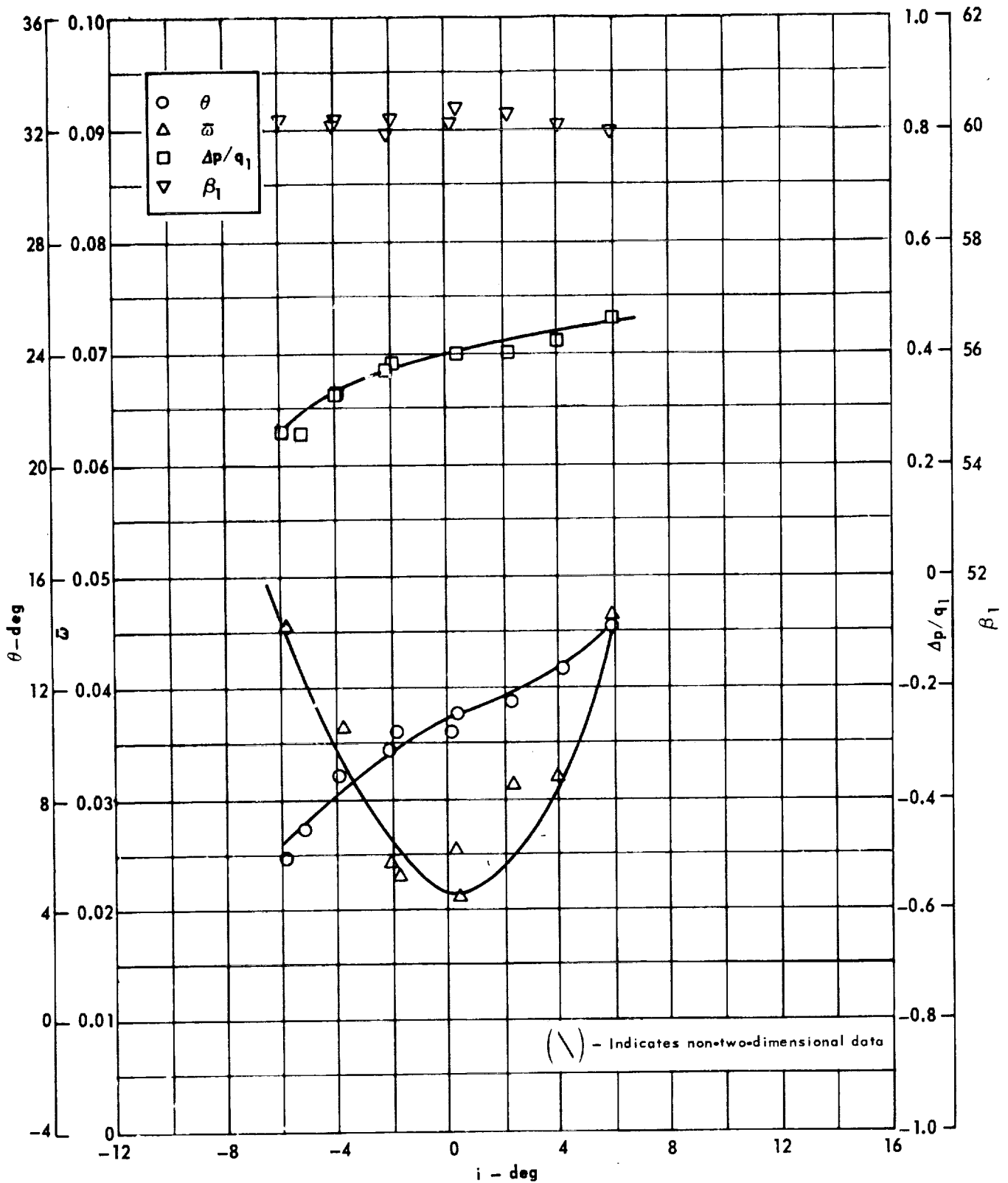
Cascade configuration: $\beta_{1N} = 60$, $\sigma = 1.00$

Double circular-arc profile: $\phi = 20$, $t/c = 0.10$

(a) $\theta, \bar{\omega}, \Delta p/q_1, \beta_1$

Figure 55 . - Cascade characteristics as functions of incidence.



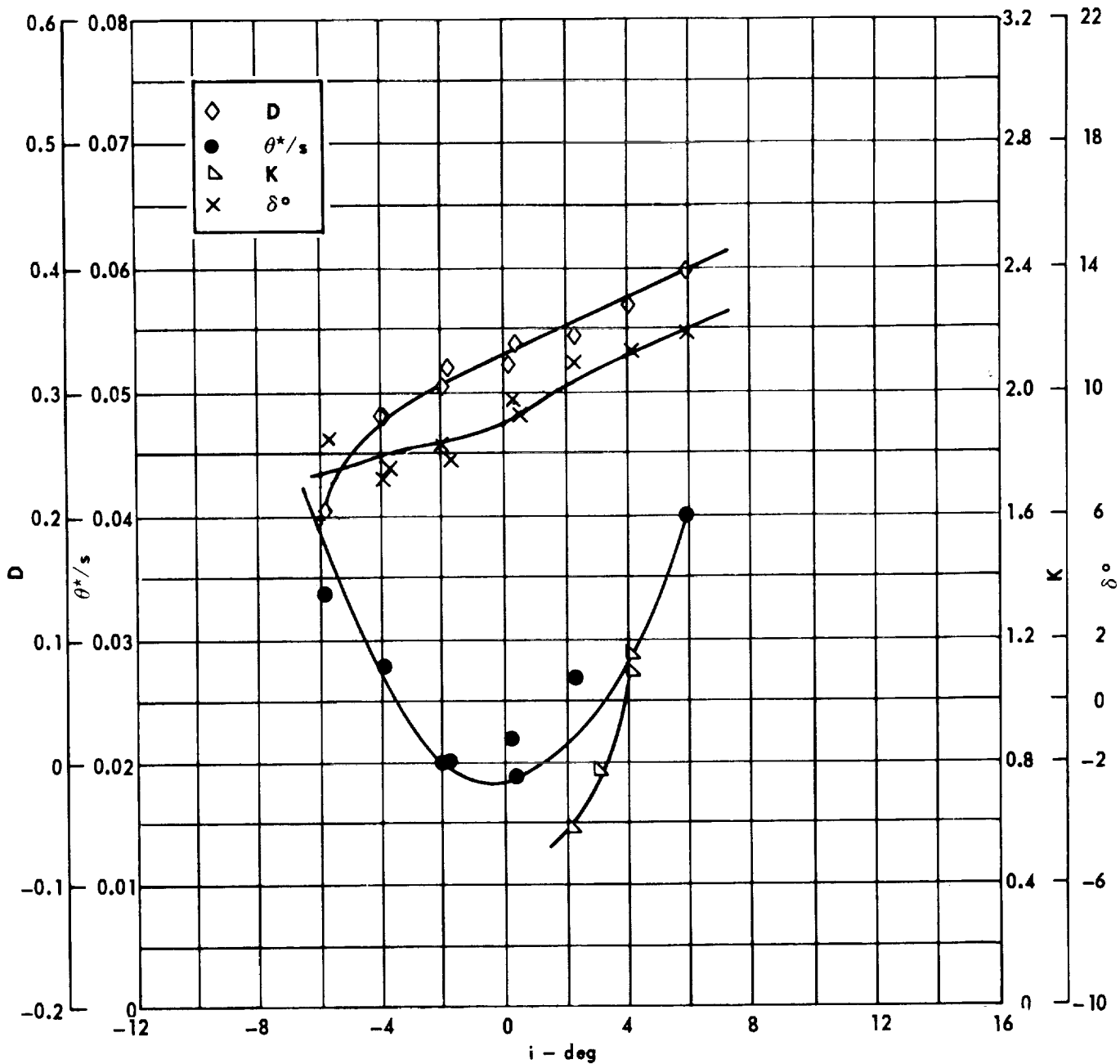


Cascade configuration : $\beta_{1N} = 60$, $\sigma = 1.50$

Double circular-arc profile : $\phi = 20$, $t/c = 0.10$

(a) $\theta, \omega, \Delta p/q_1, \beta_1$

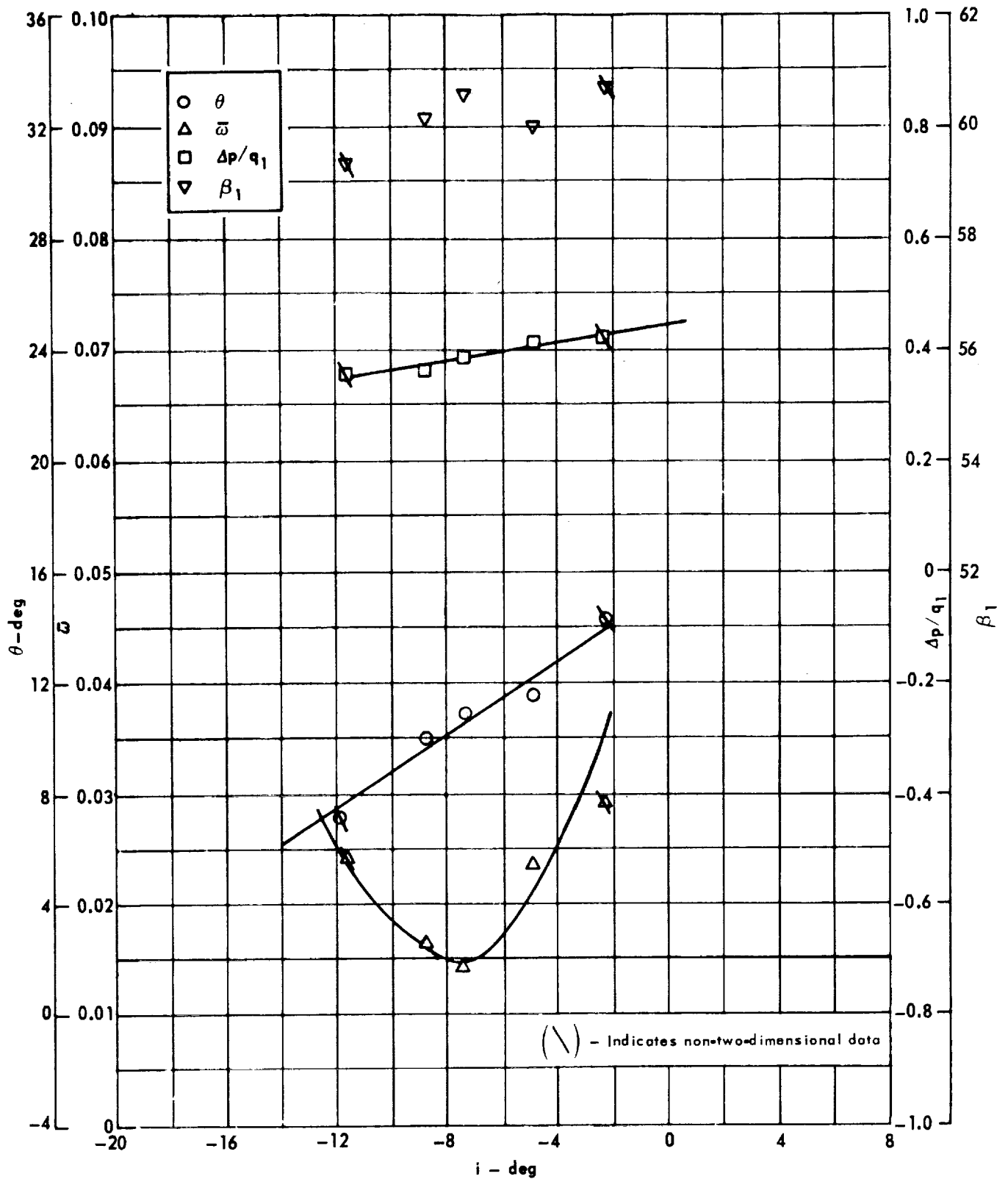
Figure 56 . - Cascade characteristics as functions of incidence.



Cascade configuration : $\beta_N = 60$, $\sigma = 1.50$
 Double circular-arc profile : $\phi = 20$, $t/c = 0.10$

(b) D, θ^*/s , K, δ°

Figure 56. - Concluded.

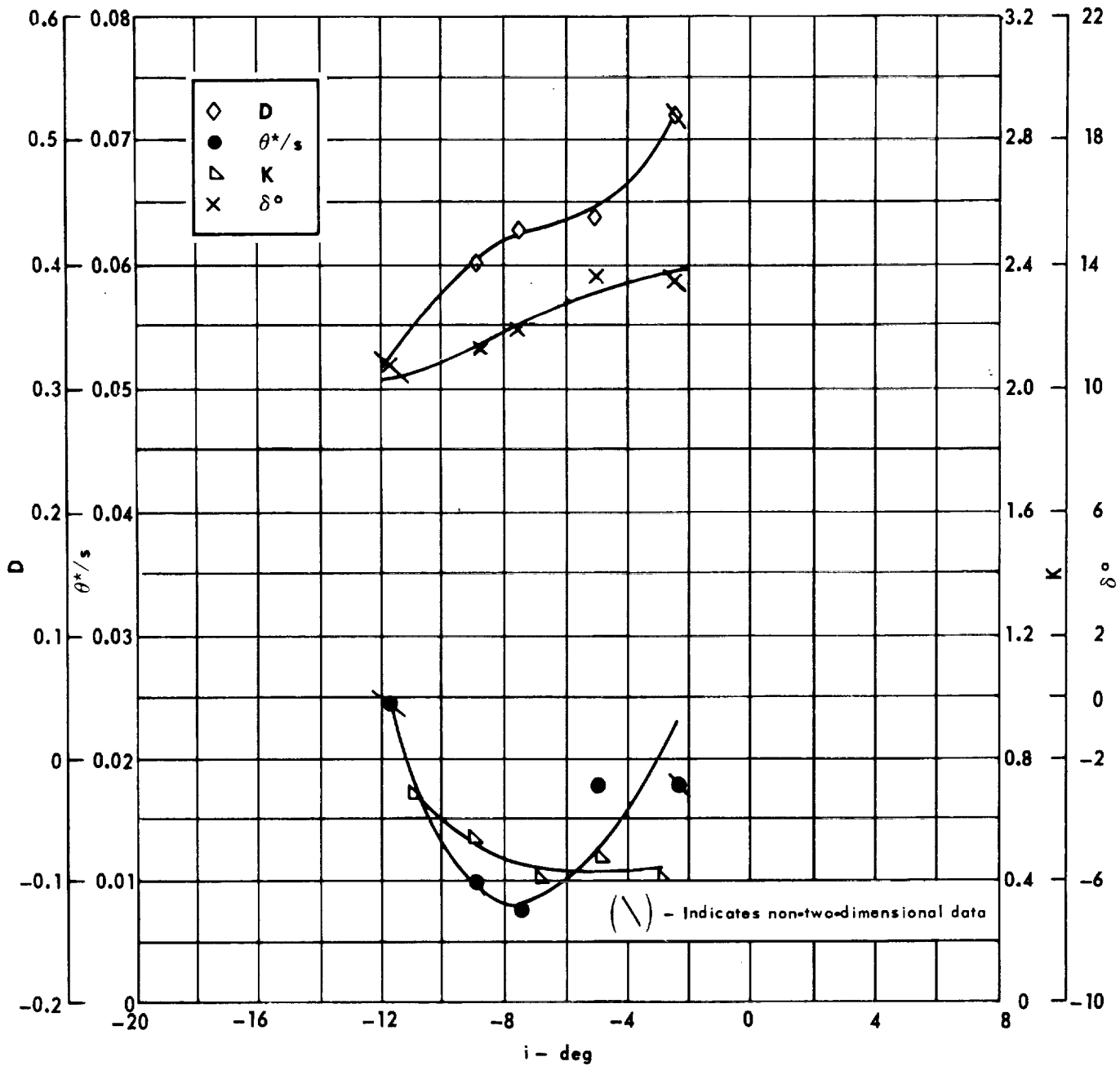


Cascade configuration: $\beta_{1N} = 60$, $\sigma = 0.75$

Double circular-arc profile: $\phi = 30$, $t/c = 0.06$

(a) $\theta, \bar{\omega}, \Delta p/q_1, \beta_1$

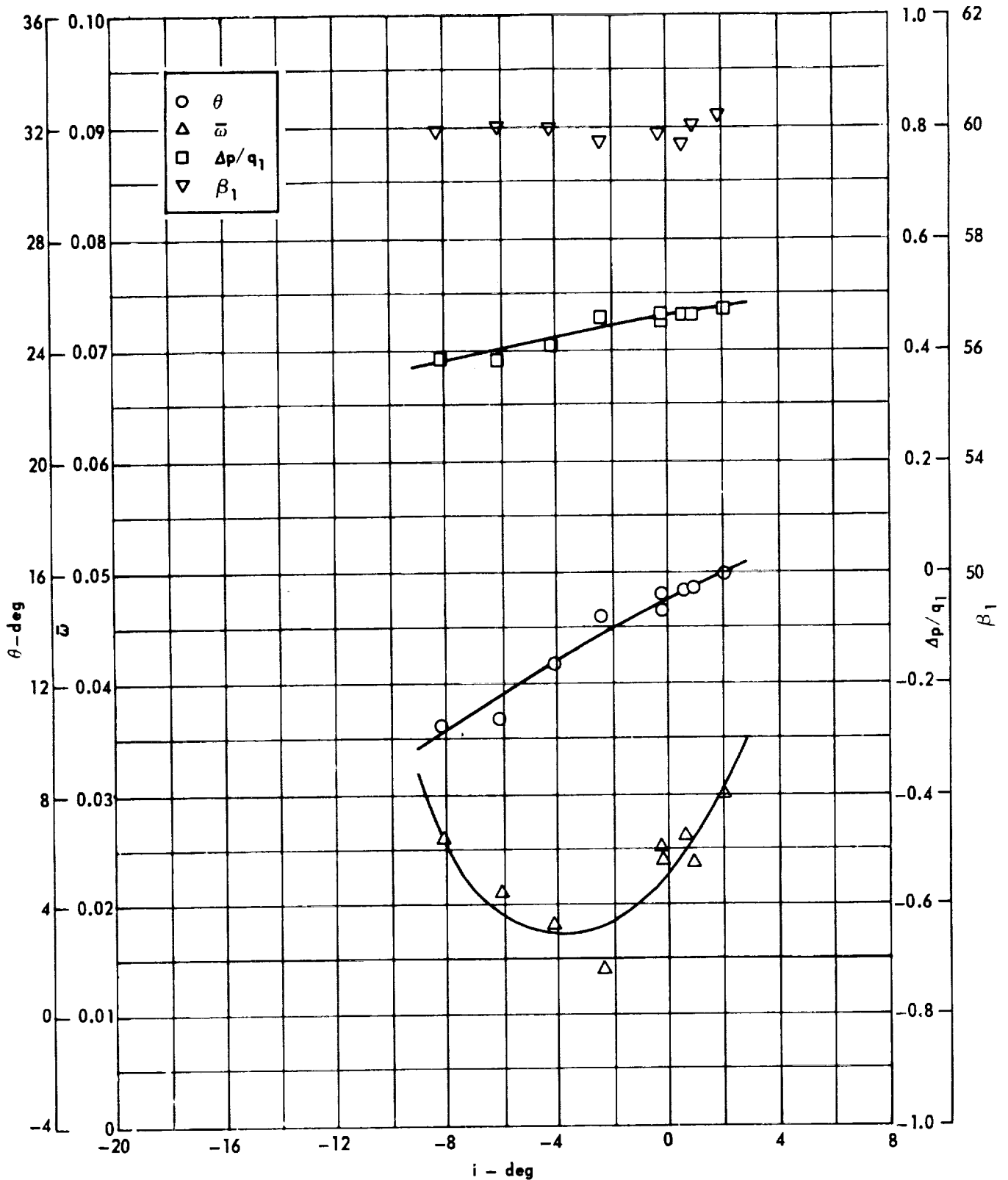
Figure 57 . - Cascade characteristics as functions of incidence.



Cascade configuration: $\beta_{1N} = 60, \sigma = 0.75$
 Double circular-arc profile: $\phi = 30, t/c = 0.06$

(b) D, θ^*/s , K, δ°

Figure 57 . - Concluded.

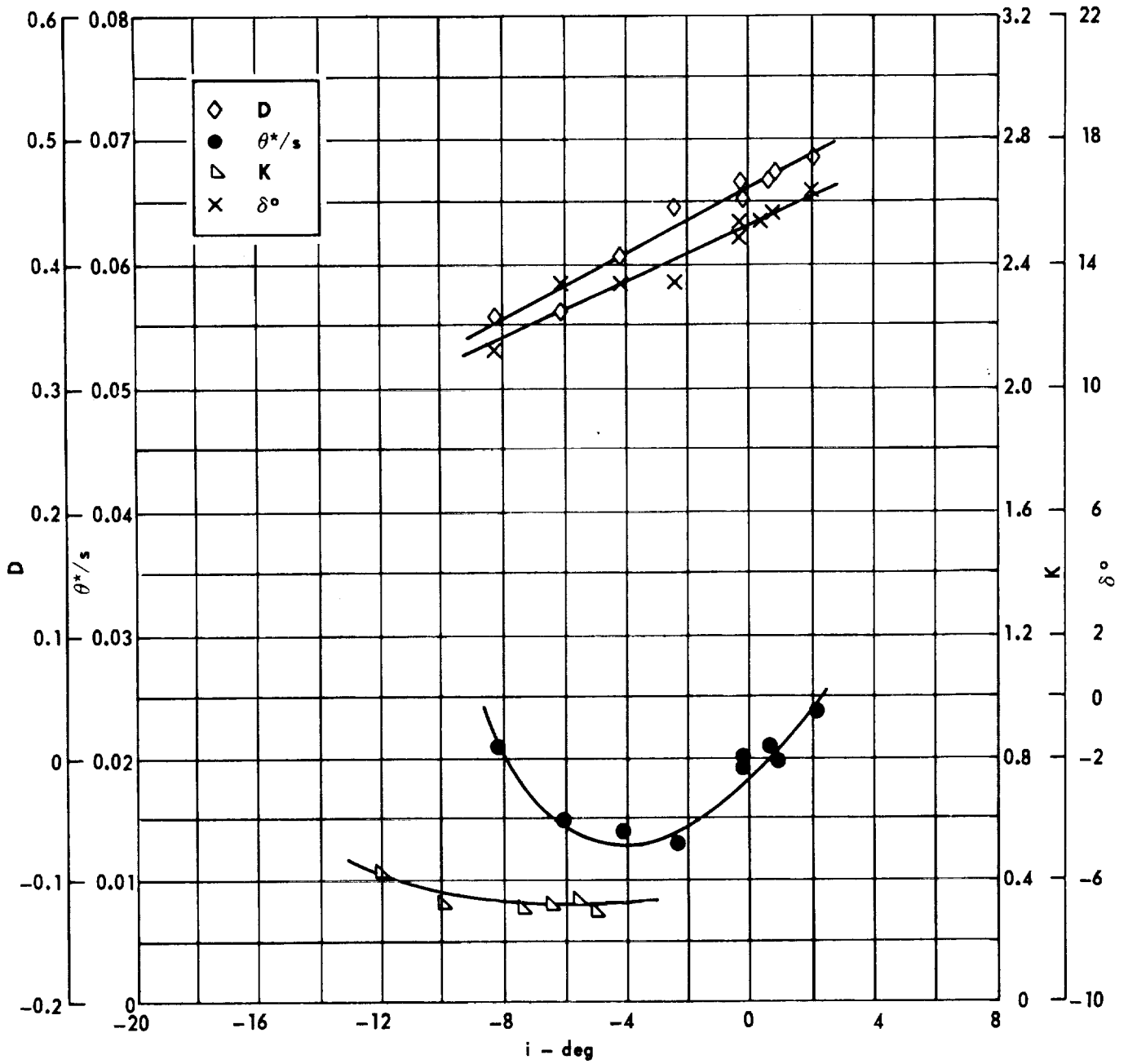


Cascade configuration : $\beta_{1N} = 60$, $\sigma = 1.00$

Double circular-arc profile : $\phi = 30$, $t/c = 0.06$

(a) $\theta, \bar{\omega}, \Delta p/q_1, \beta_1$

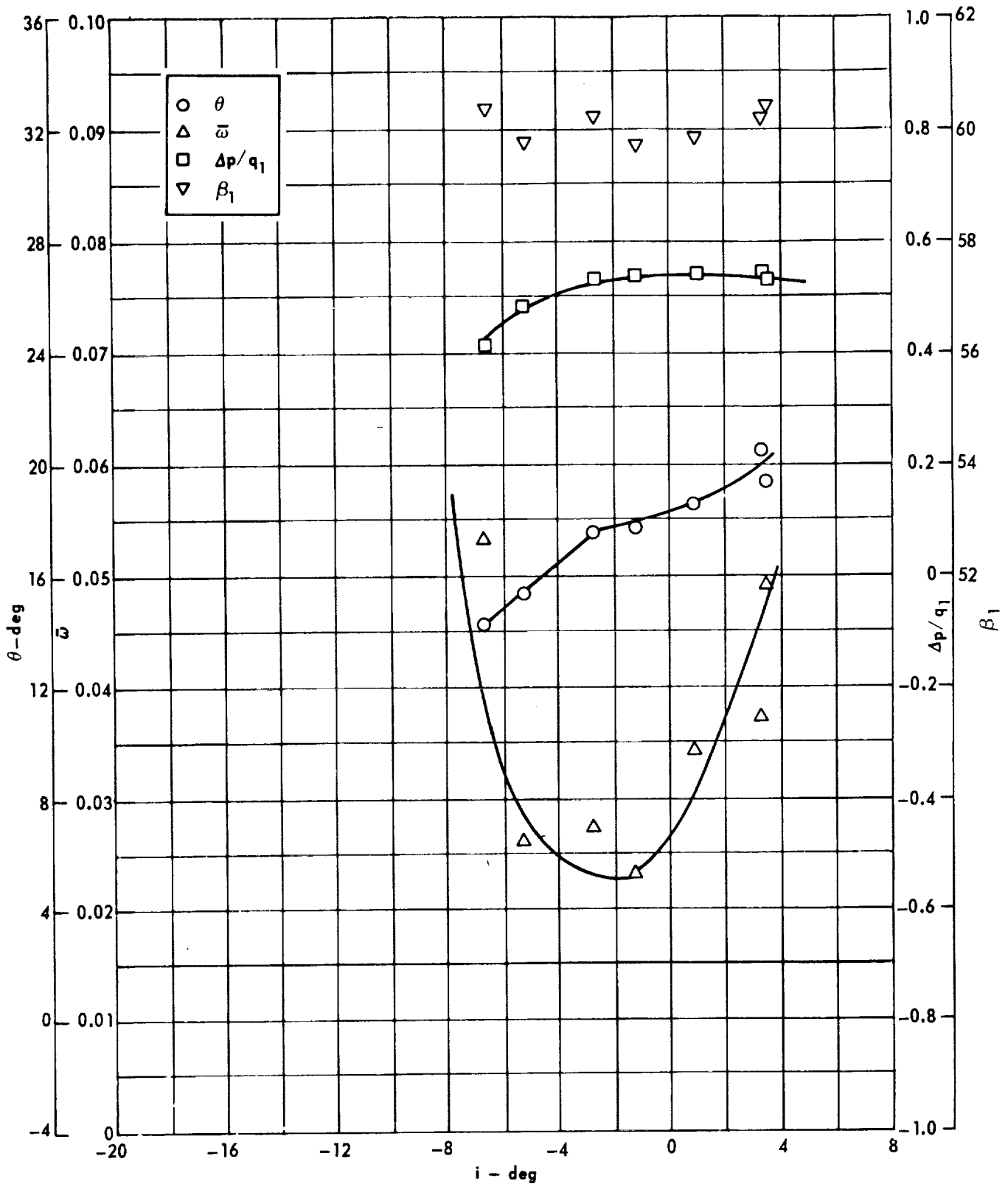
Figure 58 . - Cascade characteristics as functions of incidence.



Cascade configuration : $\beta_{1N} = 60, \sigma = 1.00$
 Double circular-arc profile : $\phi = 30, t/c = 0.06$

(b) D, θ^*/s , K, δ°

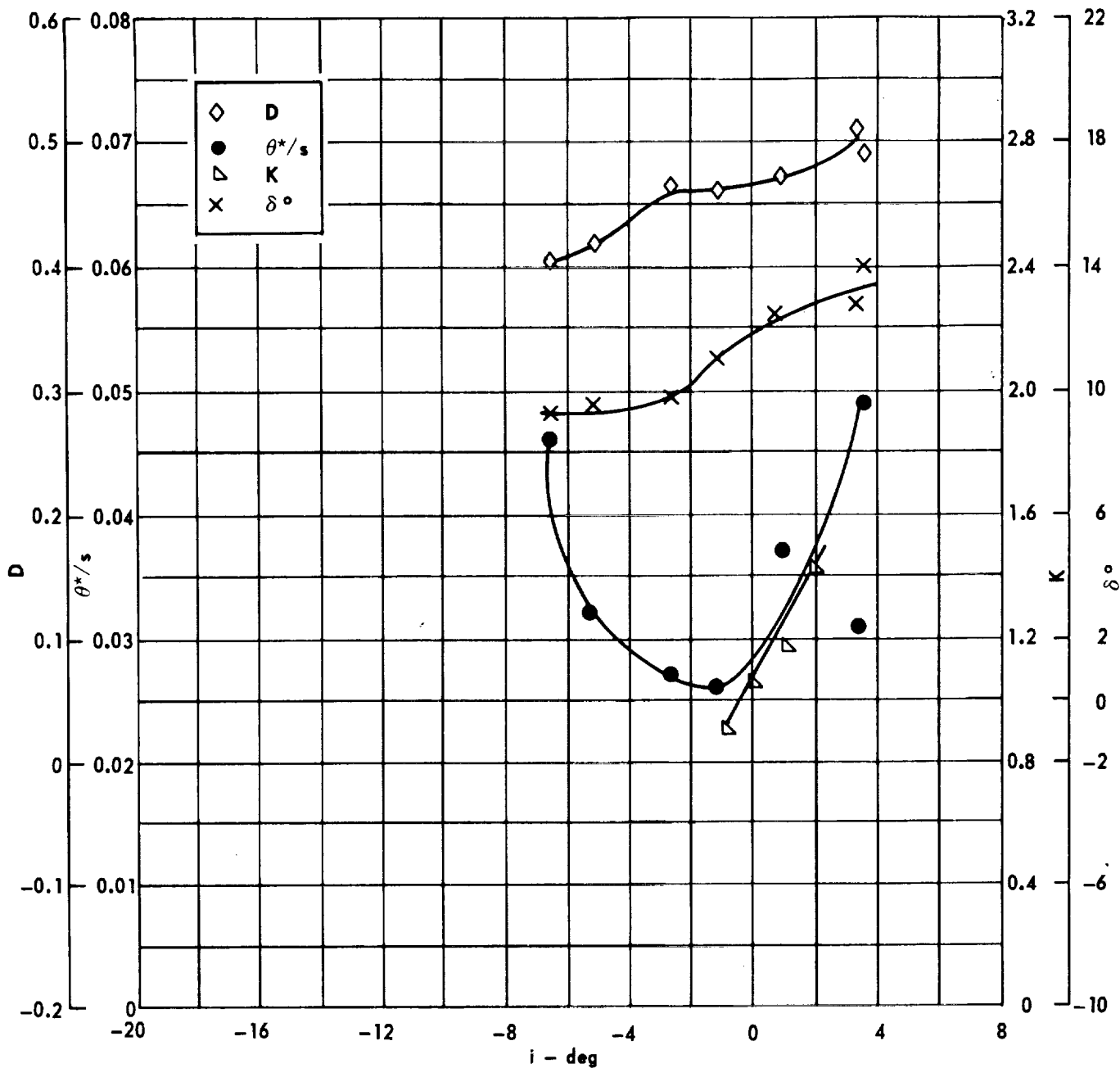
Figure 58 . - Concluded.



Cascade configuration : $\beta_{1N} = 60, \sigma = 1.50$
 Double circular-arc profile : $\phi = 30, t/c = 0.06$

(a) $\theta, \bar{\omega}, \Delta p/q_1, \beta_1$

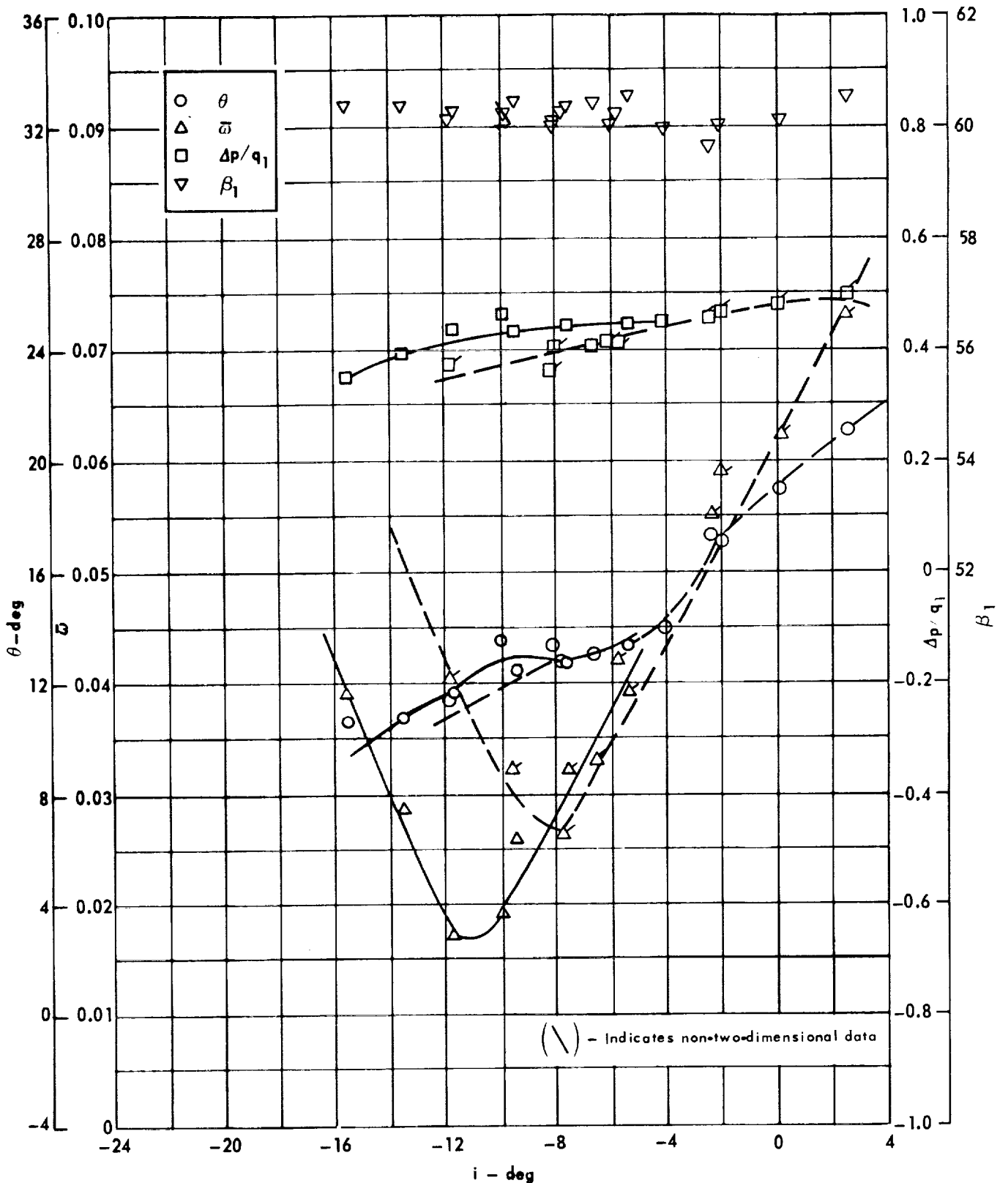
Figure 59. - Cascade characteristics as functions of incidence.



Cascade configuration : $\beta_{1N} = 60, \sigma = 1.50$
 Double circular-arc profile : $\phi = 30, r/c = 0.06$

(b) $D, \theta^*/s, K, \delta^\circ$

Figure 59 . - Concluded.



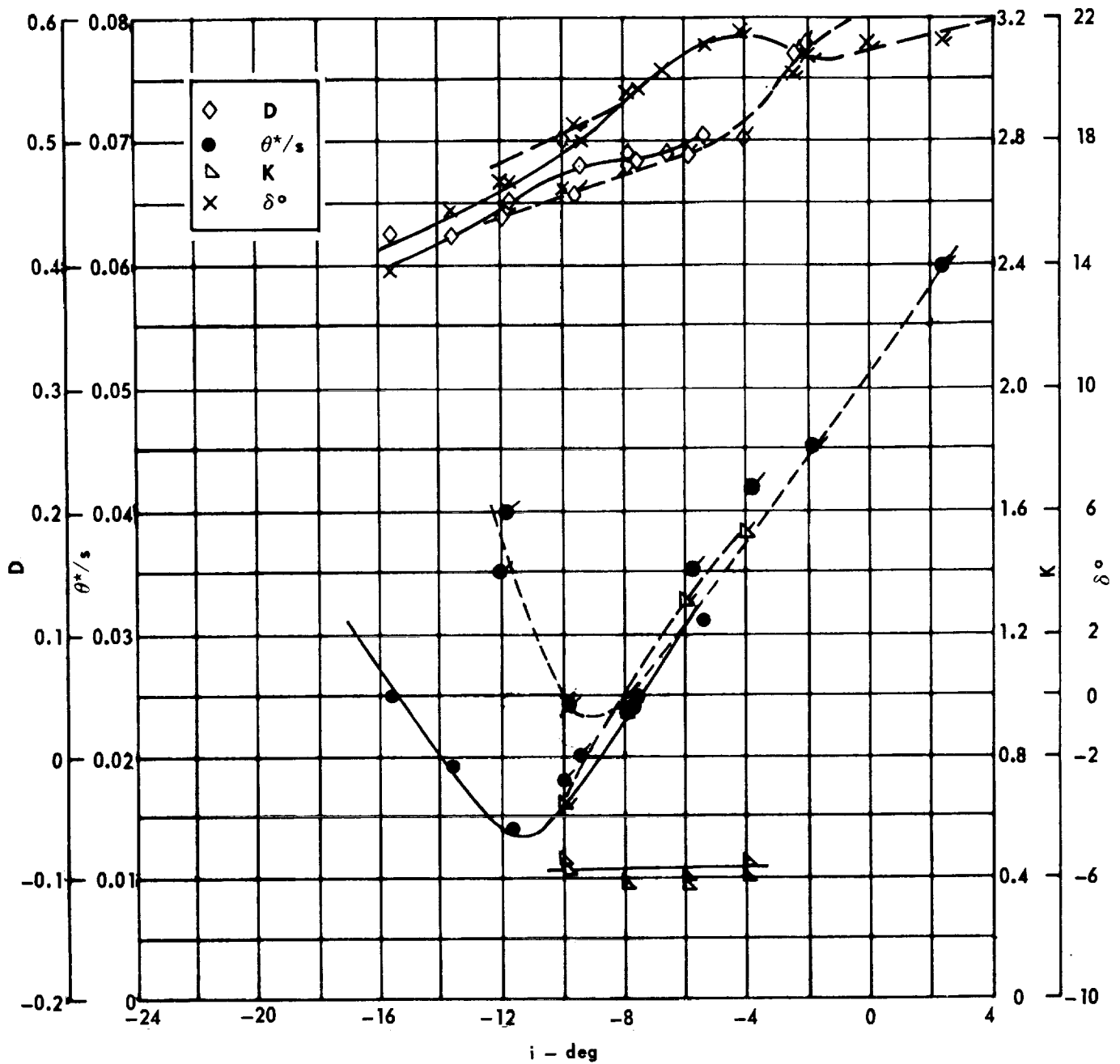
Cascade configuration: $\beta_{1N} = 60$, $\sigma = 0.75$

Double circular-arc profile: $\phi = 40$, $t/c = 0.06$

--- Slotted hydrofoils (flagged)

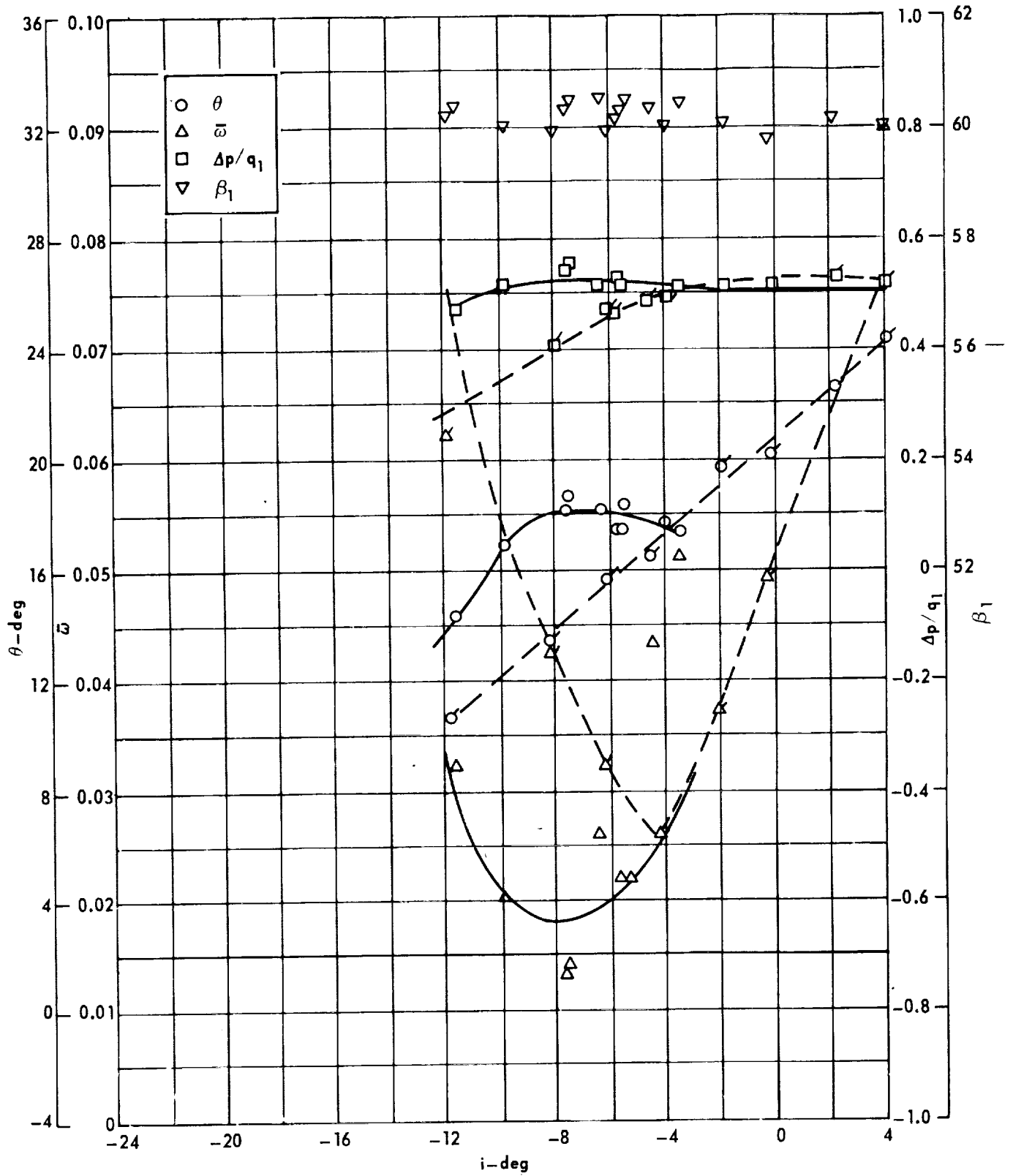
(a) $\theta, \bar{w}, \Delta p/q_1, \beta_1$

Figure 60 . - Cascade characteristics as functions of incidence.



Cascade configuration: $\beta_{1N} = 60$, $\sigma = 0.75$
 Double circular-arc profile: $\phi = 40$, $t/c = 0.06$
 - - - Slotted hydrofoils (flagged)
 (b) D, θ^*/s , K, δ°

Figure 60 . - Concluded.



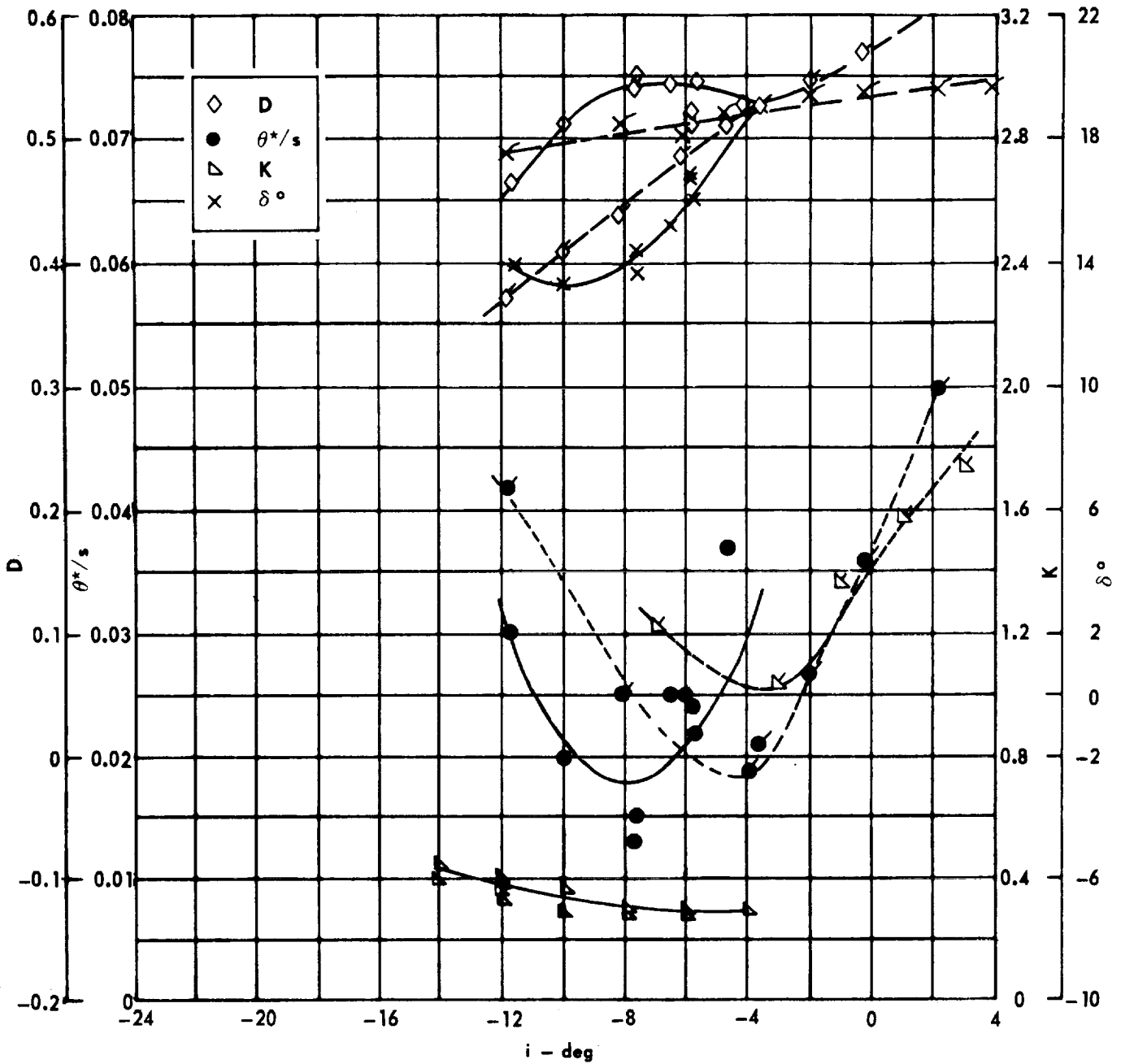
Cascade configuration: $\beta_{1N} = 60, \sigma = 1.00$

Double circular-arc profile: $\phi = 40, t/c = 0.06$

--- Slotted hydrofoils (flagged)

(a) $\theta, \bar{\omega}, \Delta p/q_1, \beta_1$

Figure 61. - Cascade characteristics as functions of incidence.



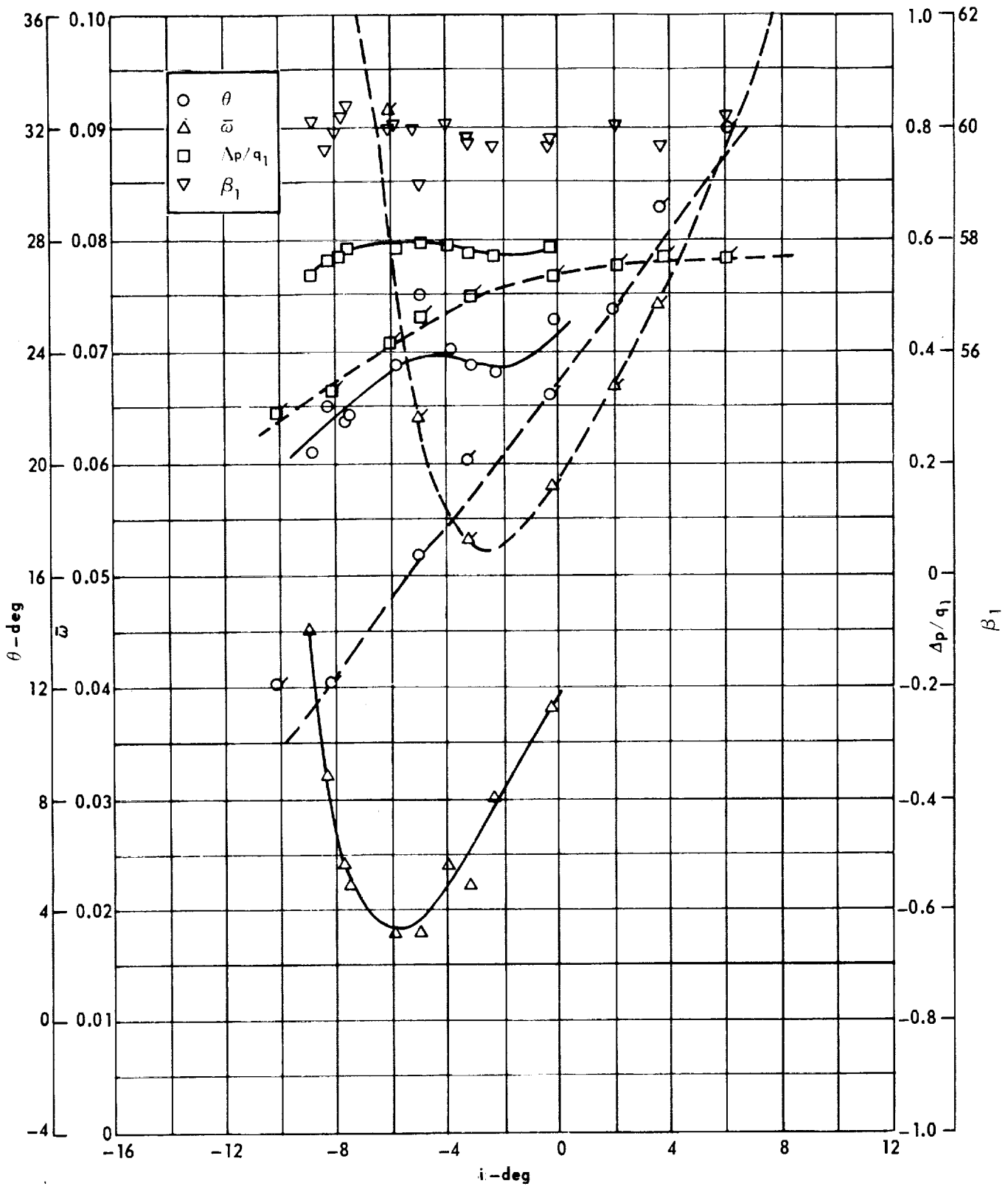
Cascade configuration : $\beta_{1N} = 60$, $\sigma = 1.00$

Double circular-arc profile : $\phi = 40$, $t/c = 0.06$

- - - Slotted hydrofoils (flagged)

(b) D, θ^*/s , K, δ°

Figure 61 . - Concluded.



Cascade configuration: $\beta_{1N} = 60$, $\sigma = 1.50$
 Double circular-arc profile: $\phi = 40$, $t/c = 0.06$
 --- Slotted hydrofoils (flagged)
 (a) $\theta, \bar{\omega}, \Delta p/q_1, \beta_1$

Figure 62. - Cascade characteristics as functions of incidence.

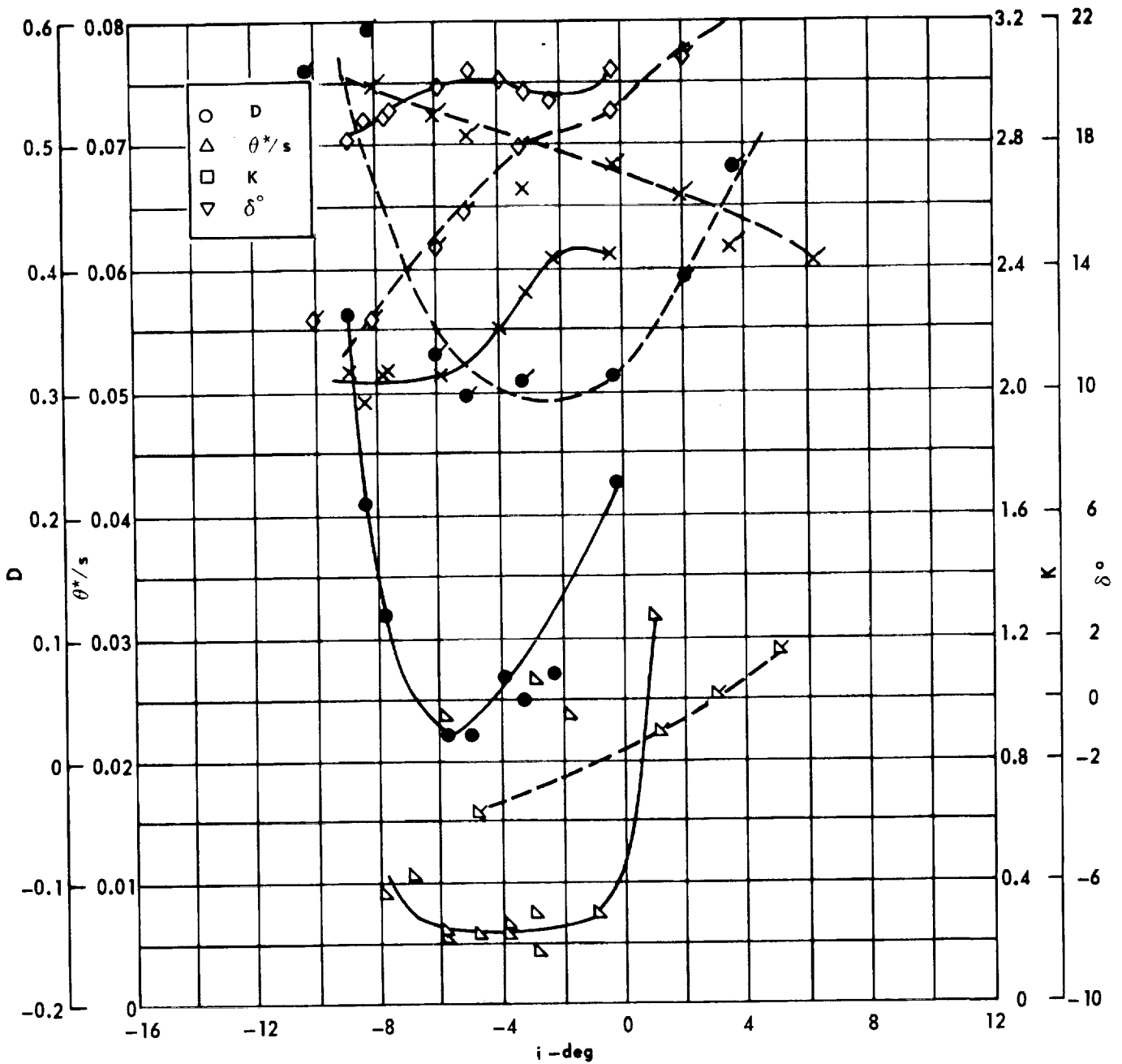
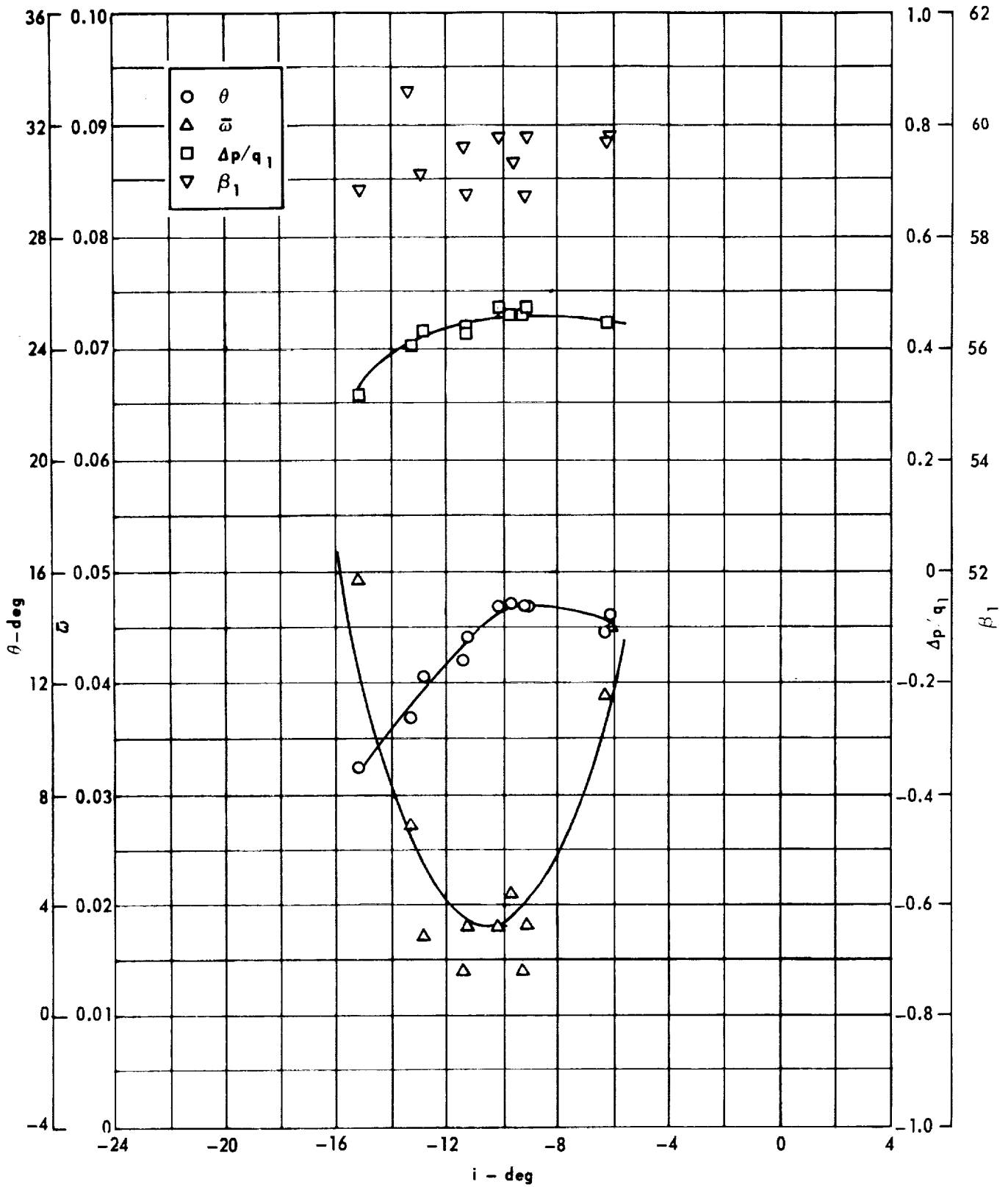


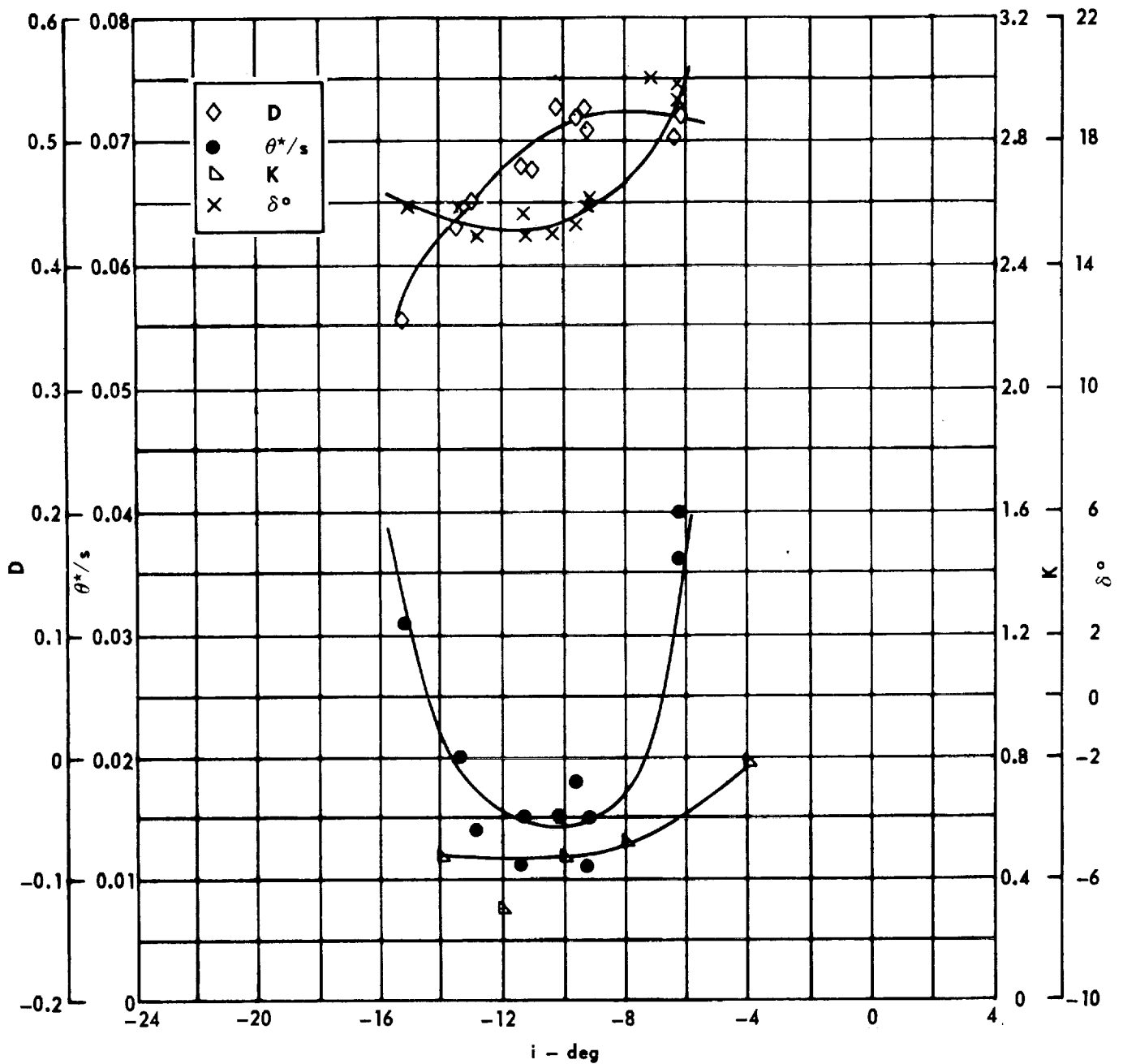
Figure 62. - Concluded.



Cascade configuration: $\beta_{1N} = 60$, $\sigma = 0.75$
 Double circular-arc profile: $\phi = 40$, $t/c = 0.10$

(a) $\theta, \bar{\omega}, \Delta p/q_1, \beta_1$

Figure 63 . - Cascade characteristics as functions of incidence.

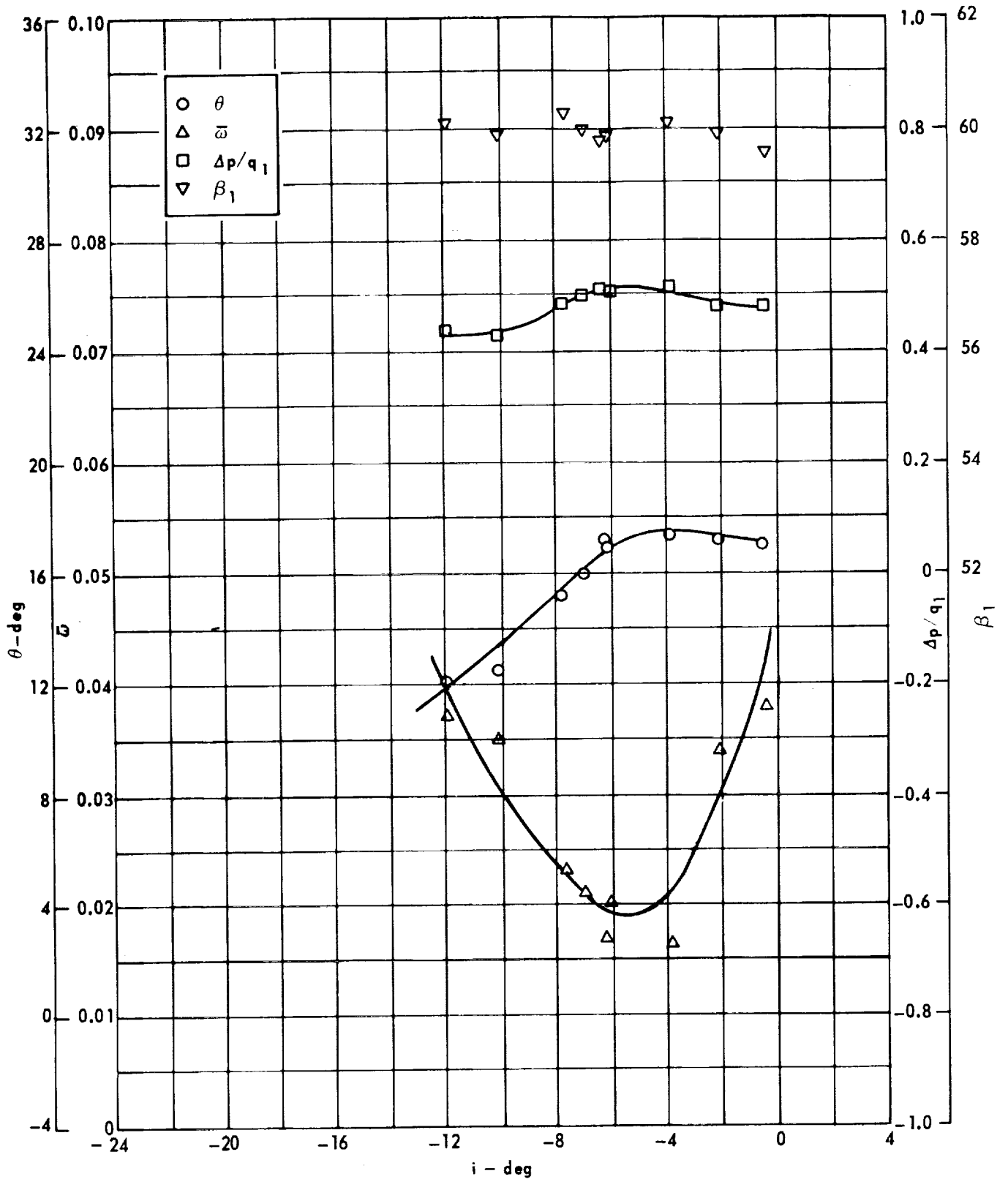


Cascade configuration: $\beta_{1N} = 60$, $\sigma = 0.75$

Double circular-arc profile: $\phi = 40$, $t/c = 0.10$

(b) D, θ^*/s , K, δ°

Figure 63 . - Concluded.

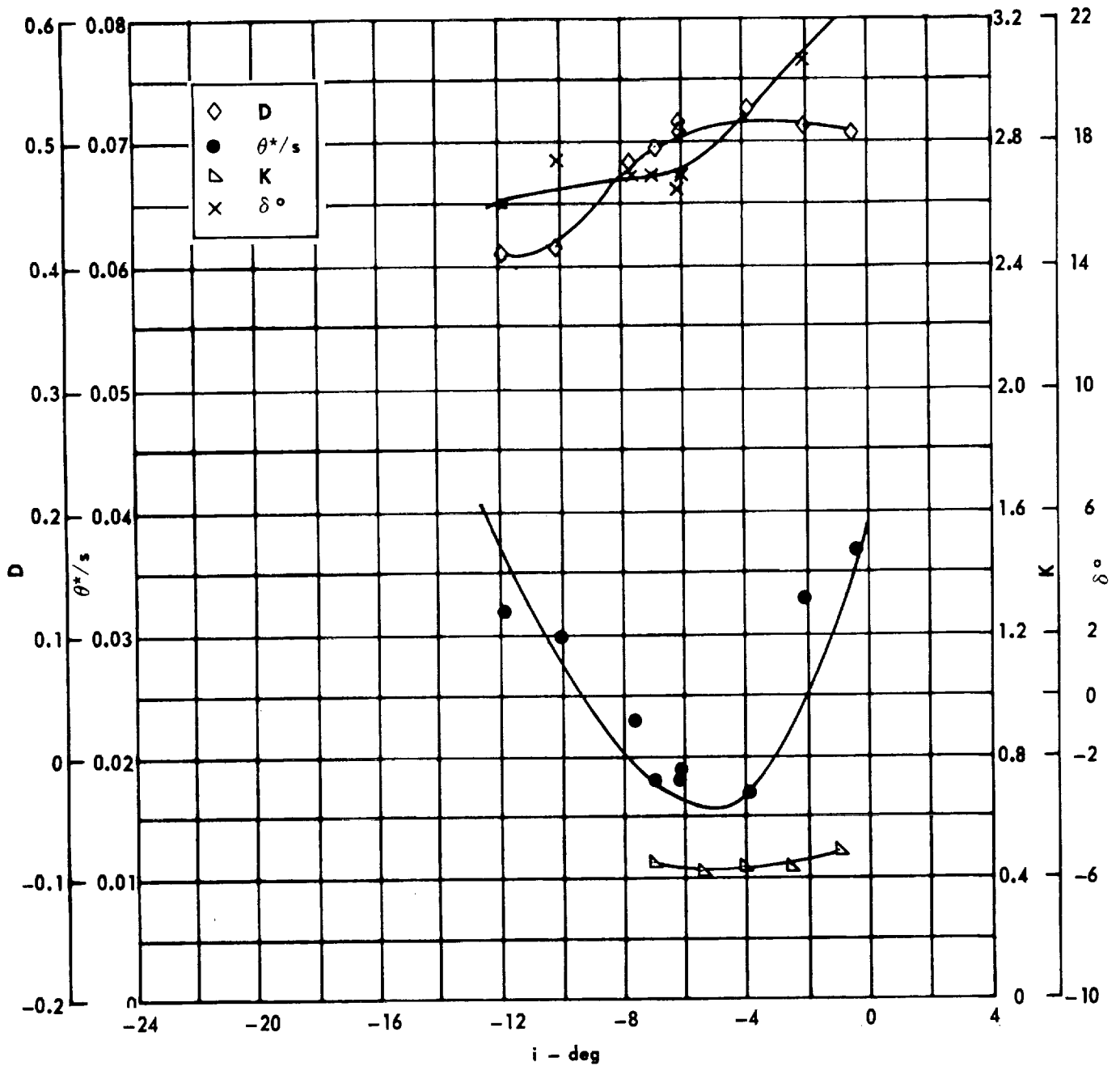


Cascade configuration : $\beta_{1N} = 60$, $\sigma = 1.00$

Double circular-arc profile : $\phi = 40$, $t/c = 0.10$

(a) $\theta, \bar{\omega}, \Delta p/q_1, \beta_1$

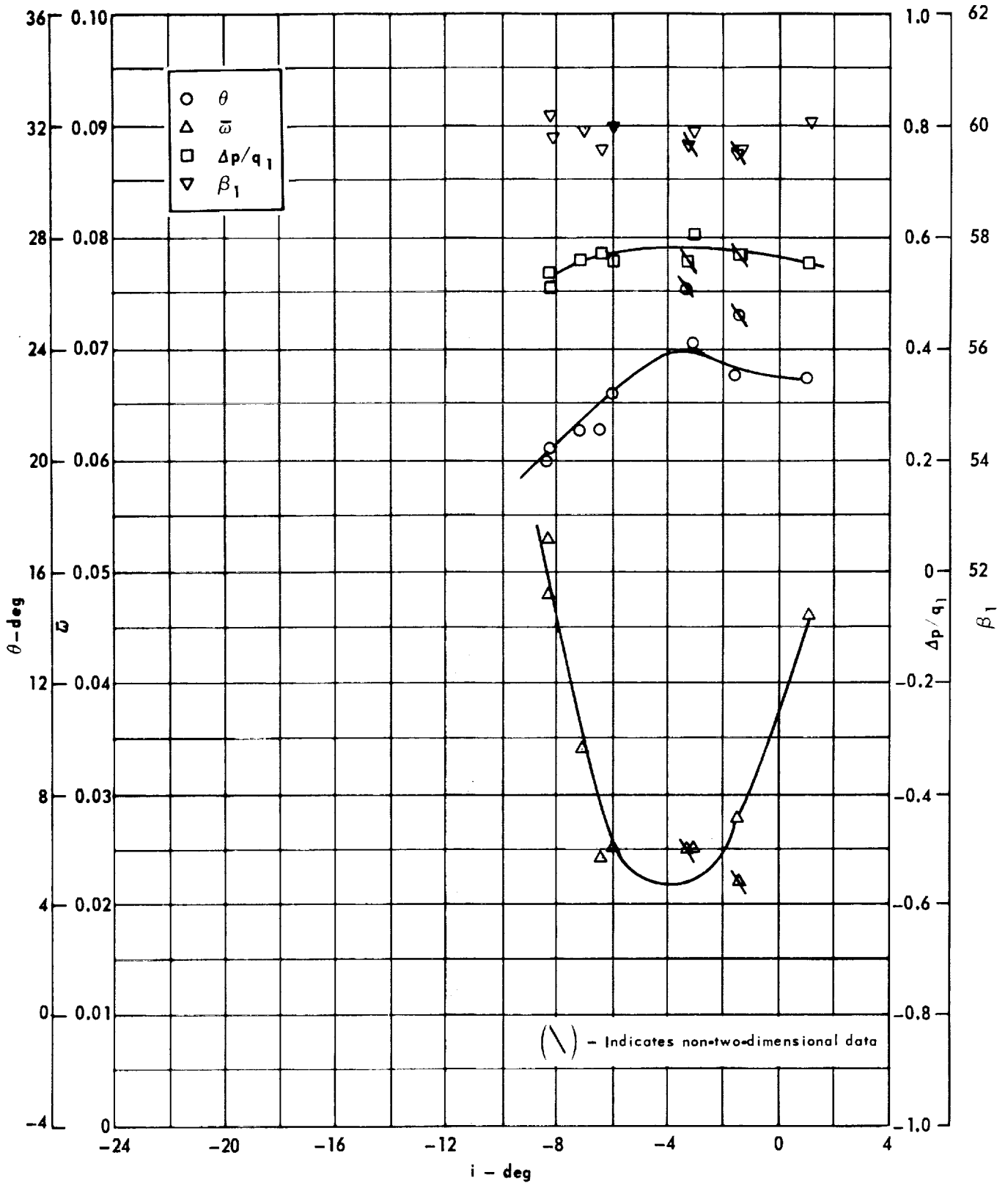
Figure 64 . - Cascade characteristics as functions of incidence.



Cascade configuration: $\beta_{1N} = 60$, $\sigma = 1.00$
 Double circular-arc profile: $\phi = 40$, $t/c = 0.10$

(b) D, θ^*/s , K, δ°

Figure 64 . - Concluded.

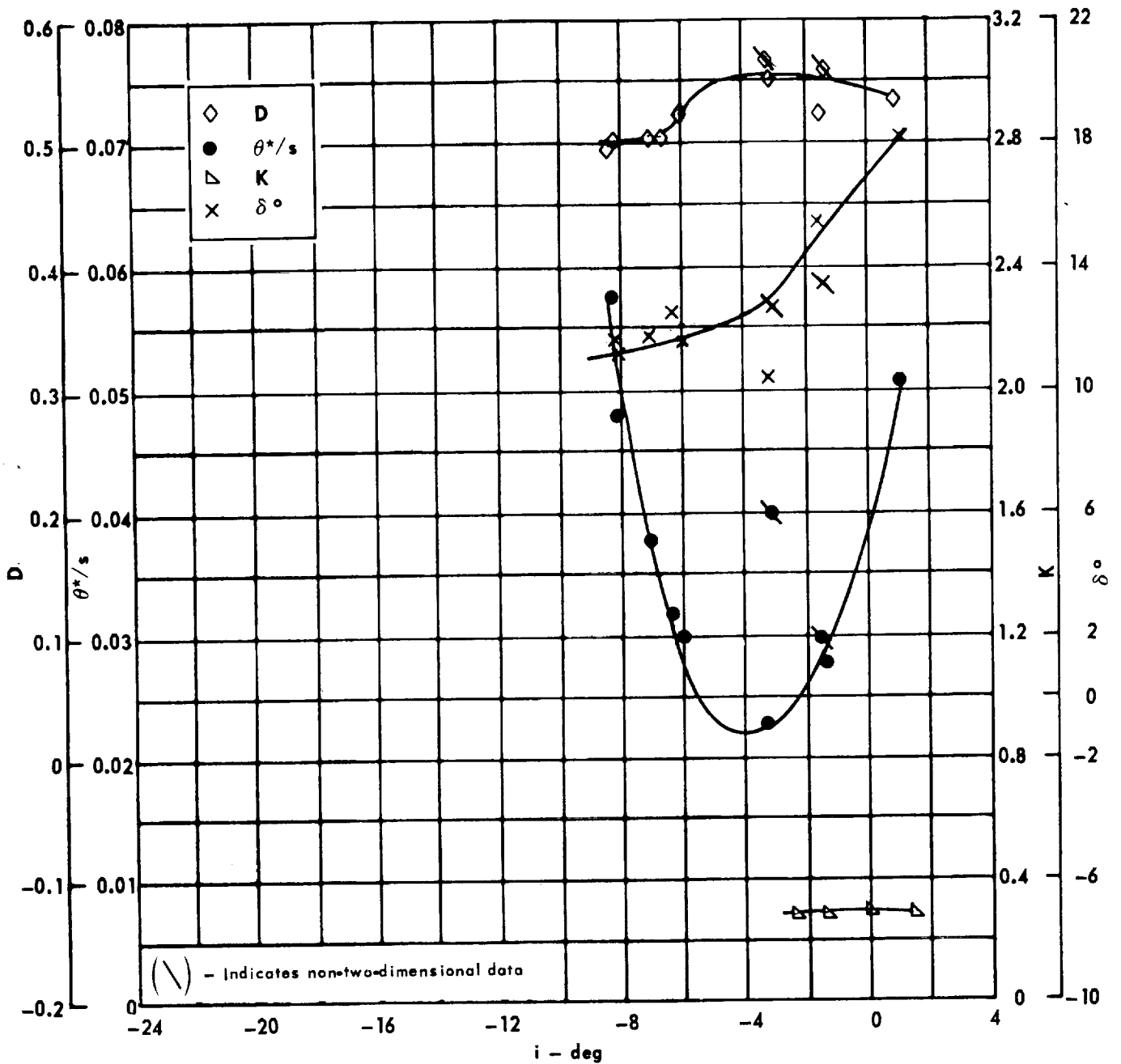


Cascade configuration: $\beta_{1N} = 60, \sigma = 1.50$

Double circular-arc profile: $\phi = 40, t/c = 0.10$

(a) $\theta, \bar{\omega}, \Delta p/q_1, \beta_1$

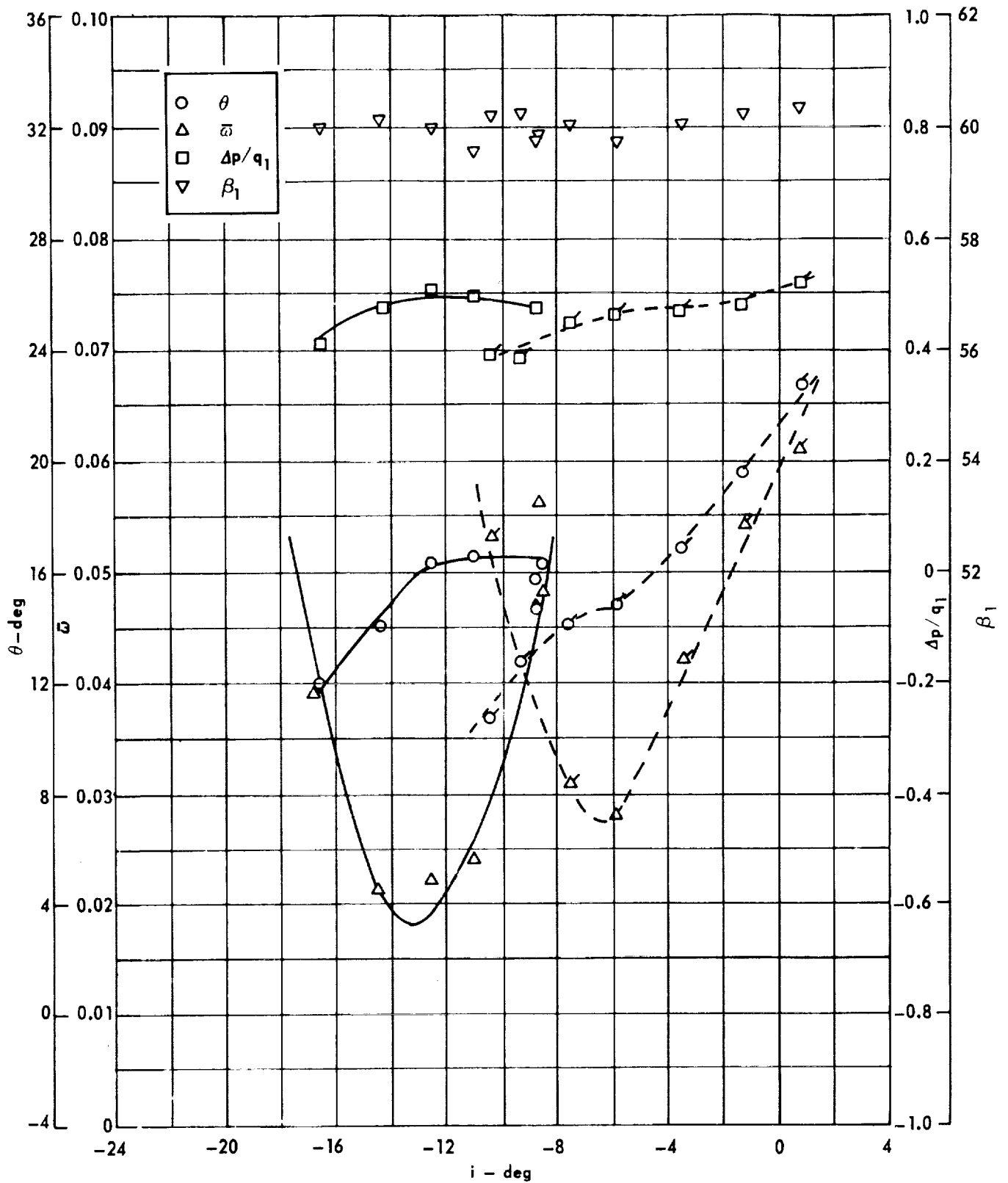
Figure 65. - Cascade characteristics as functions of incidence.



Cascade configuration: $\beta_{1N} = 60^\circ$, $\sigma = 1.50$
 Double circular-arc profile: $\phi = 40^\circ$, $t/c = 0.10$

(b) D, θ^*/s , K, δ°

Figure 65 . - Concluded.



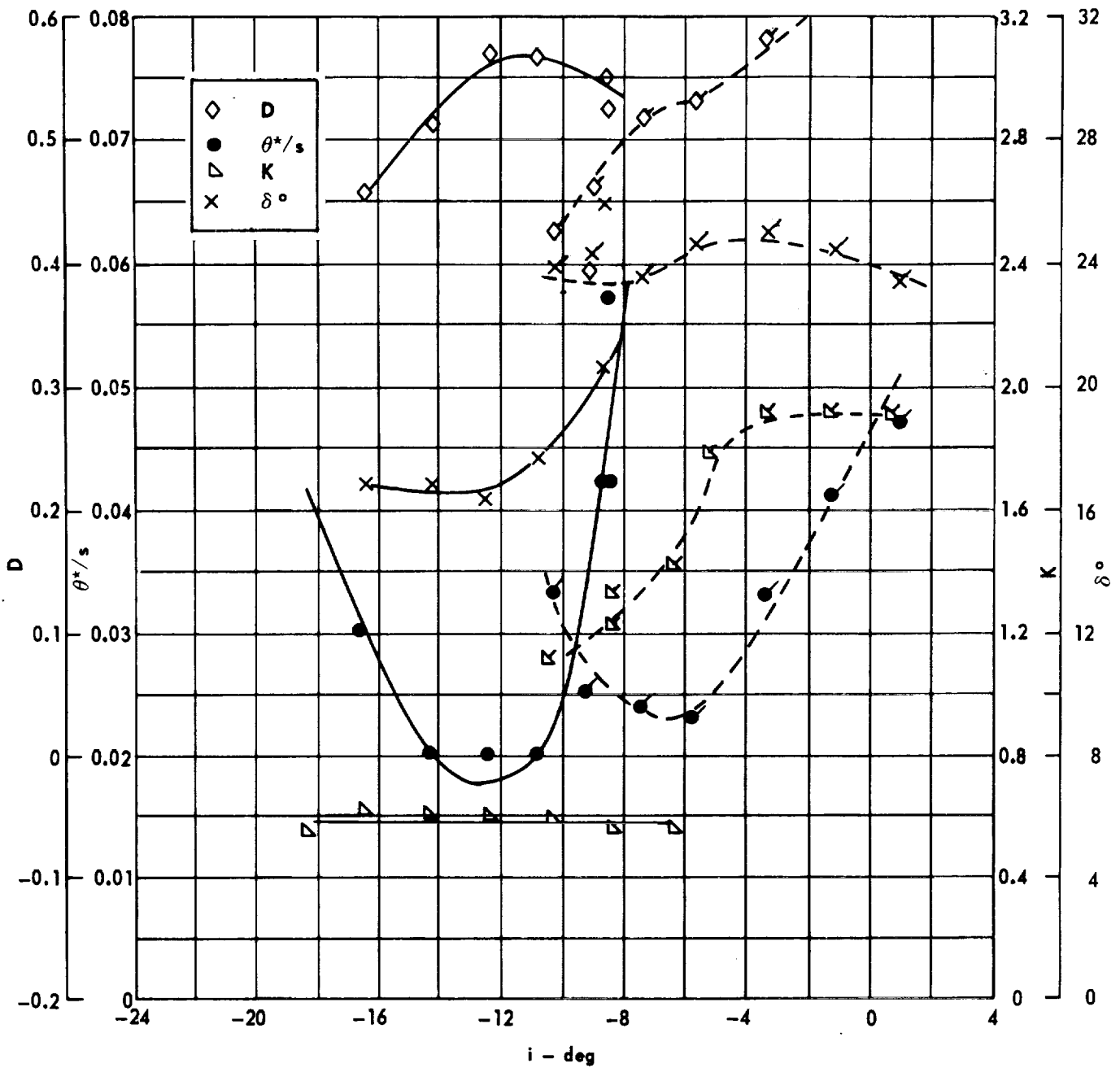
Cascade configuration : $\beta_{1N} = 60, \sigma = 0.75$

Double circular-arc profile : $\phi = 45, t/c = 0.06$

- - - Slotted hydrofoils (flagged)

(a) $\theta, \bar{w}, \Delta p/q_1, \beta_1$

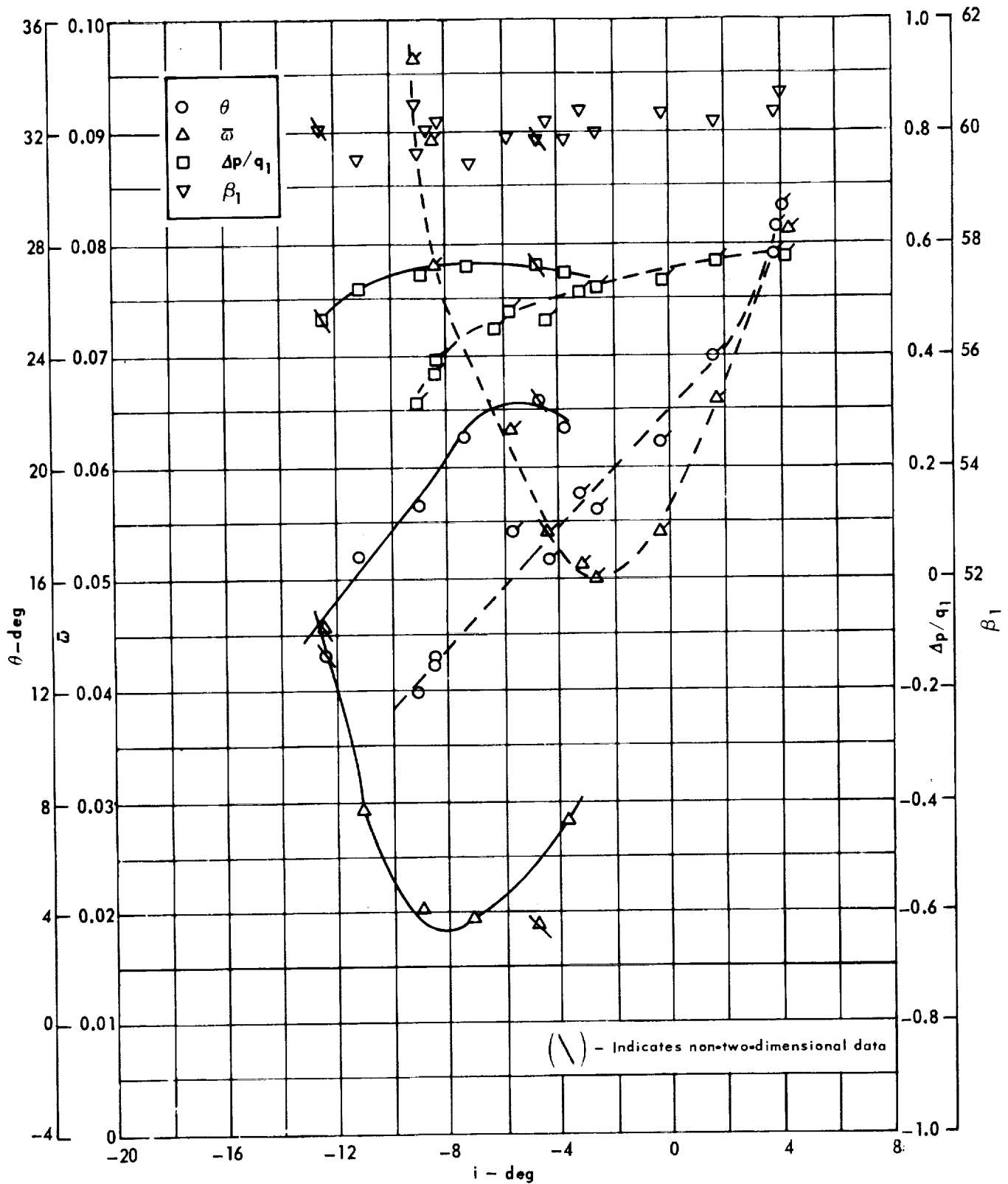
Figure 66 . - Cascade characteristics as functions of incidence.



Cascade configuration : $\beta_{1N} = 60, \sigma = 0.75$
 Double circular-arc profile : $\phi = 45, t/c = 0.06$
 - - - Slotted hydrofoils (flagged)

(b) D, θ^*/s , K, δ°

Figure 66 . - Concluded.



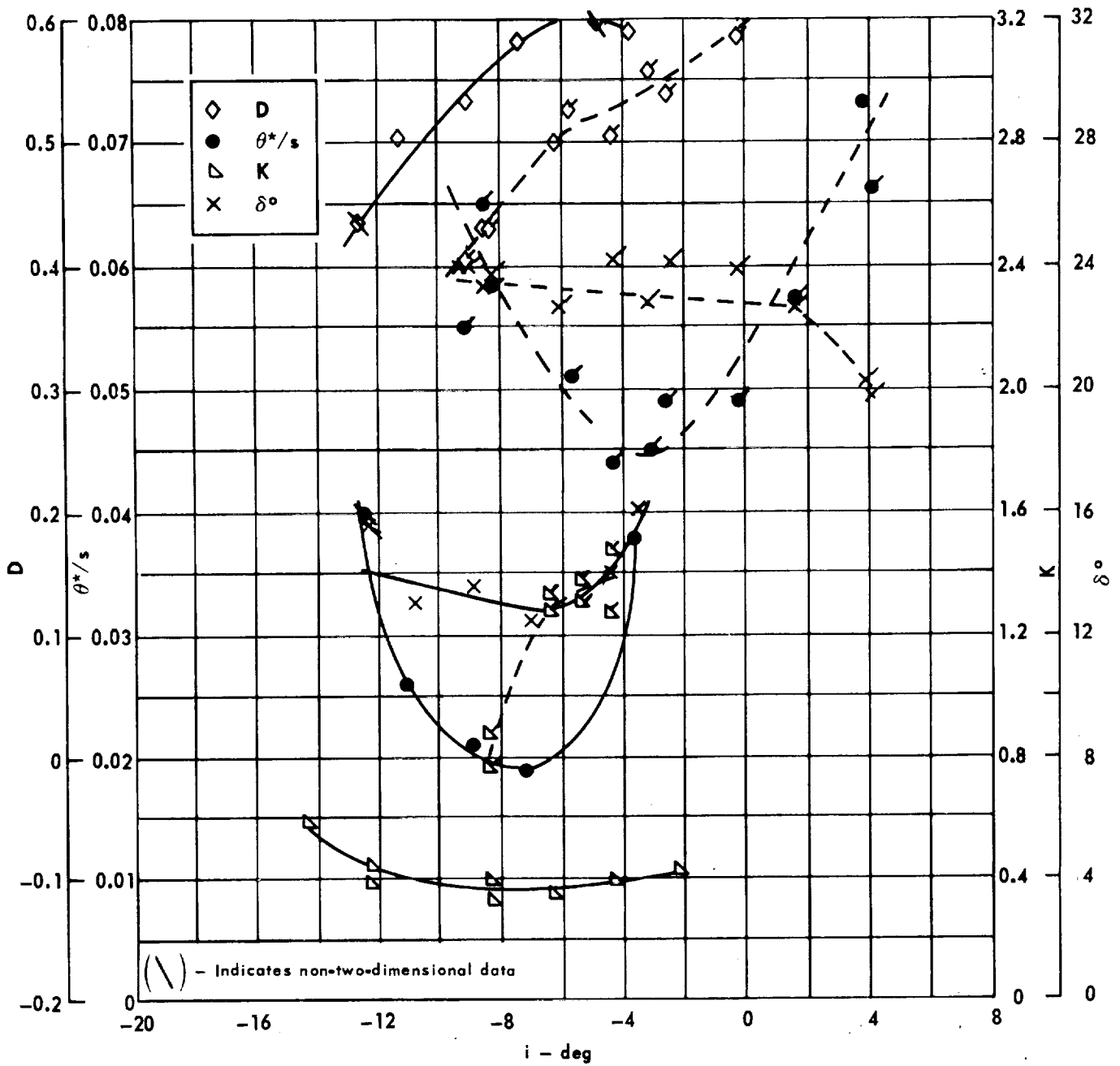
Cascade configuration : $\beta_{1N} = 60, \sigma = 1.00$

Double circular-arc profile : $\phi = 45^\circ, t/c = 0.06$

--- Slotted hydrofoils (flagged)

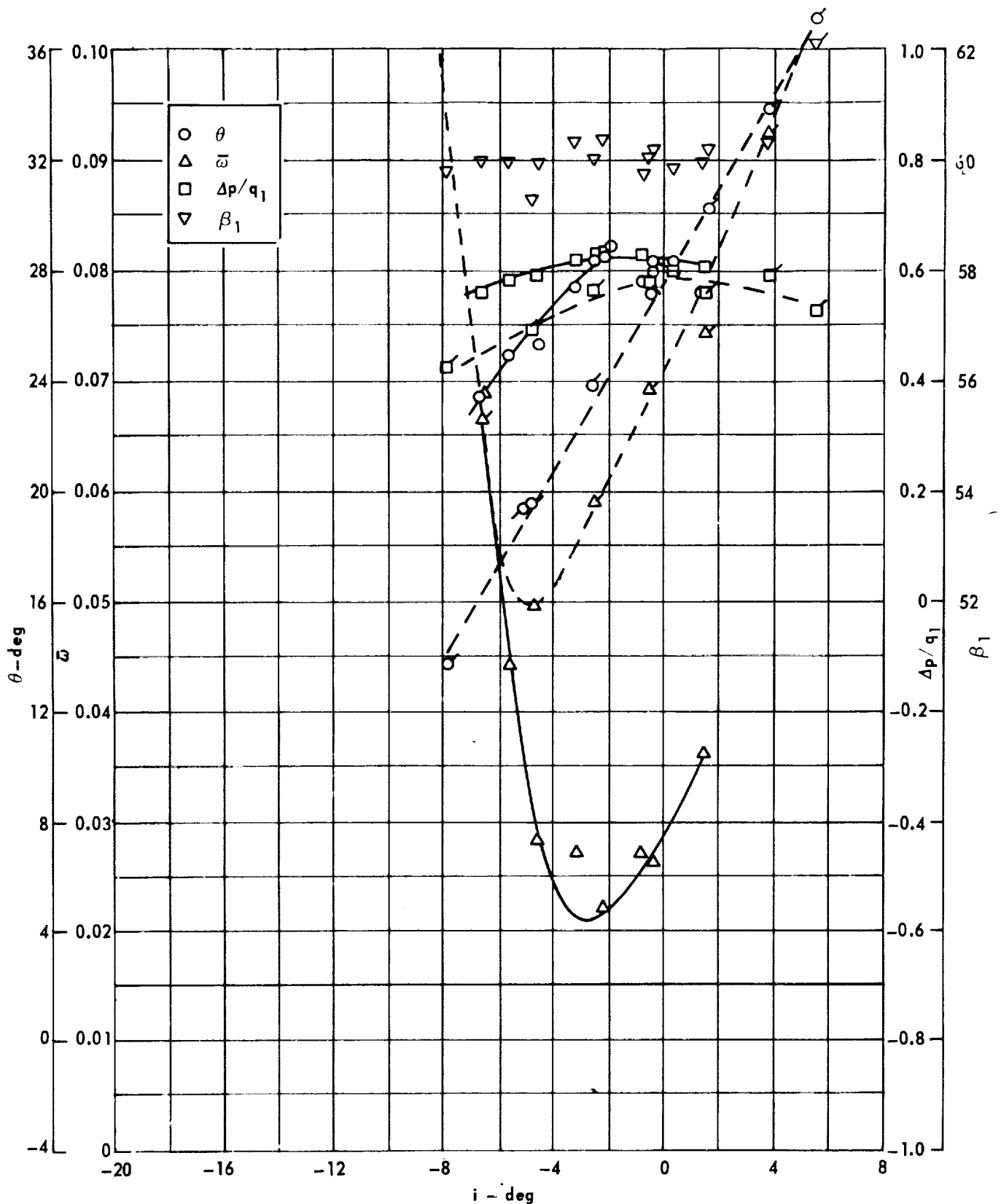
(a) $\theta, \bar{\omega}, \Delta p/q_1, \beta_1$

Figure 67. - Cascade characteristics as functions of incidence.



Cascade configuration: $\beta_{1N} = 60, \sigma = 1.00$
 Double circular-arc profile: $\phi = 45, t/c = 0.06$
 - - - Slotted hydrofoils (flagged)
 (b) D, θ^*/s , K, δ°

Figure 67. - Concluded.



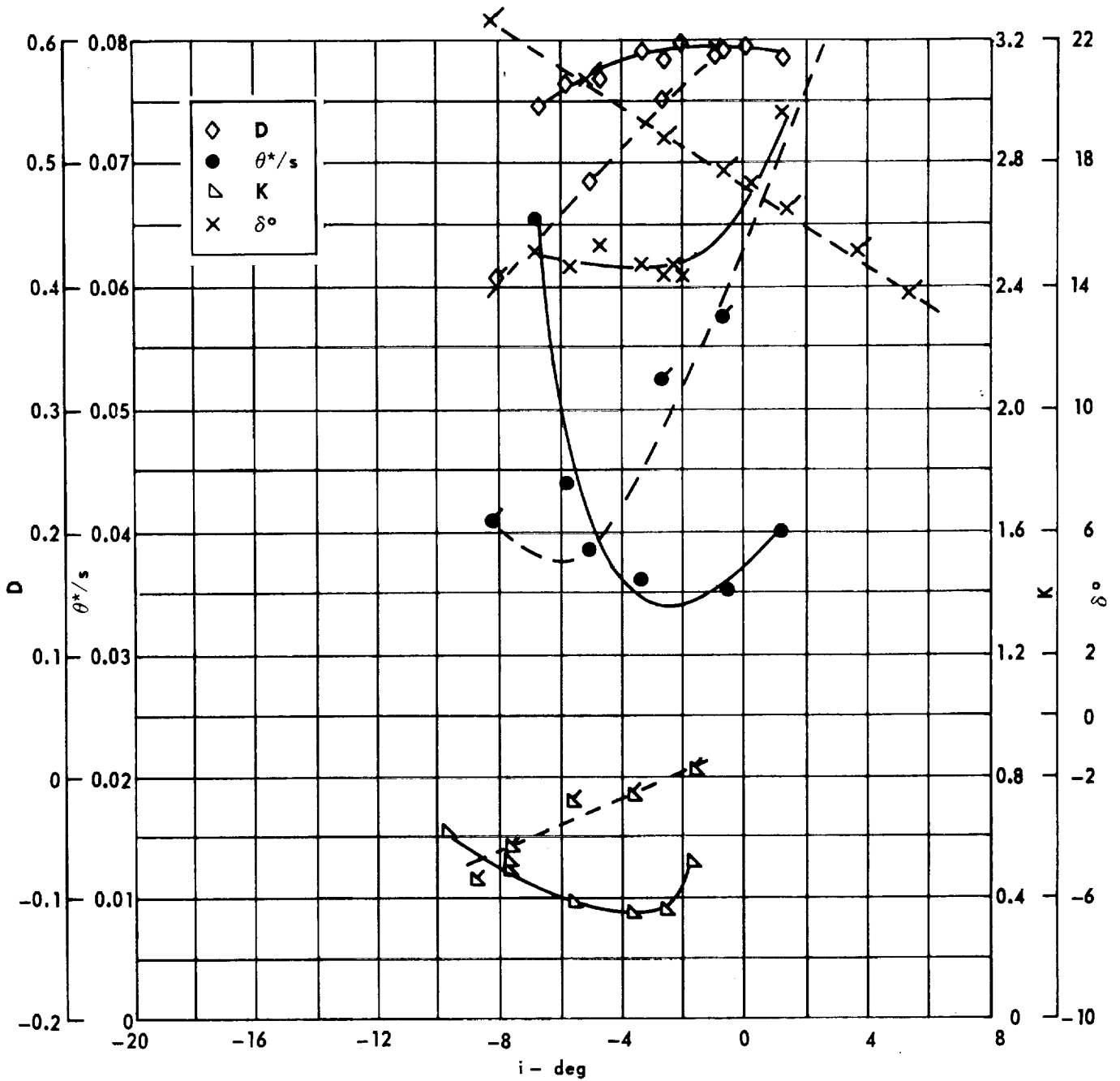
Cascade configuration : $\beta_{1N} = 60$, $\sigma = 1.50$

Double circular-arc profile : $\phi = 45$, $t/c = 0.06$

--- Slotted hydrofoils (flagged)

(a) $\theta, \bar{w}, \Delta p/q_1, \beta_1$

Figure 68 . - Cascade characteristics as functions of incidence.



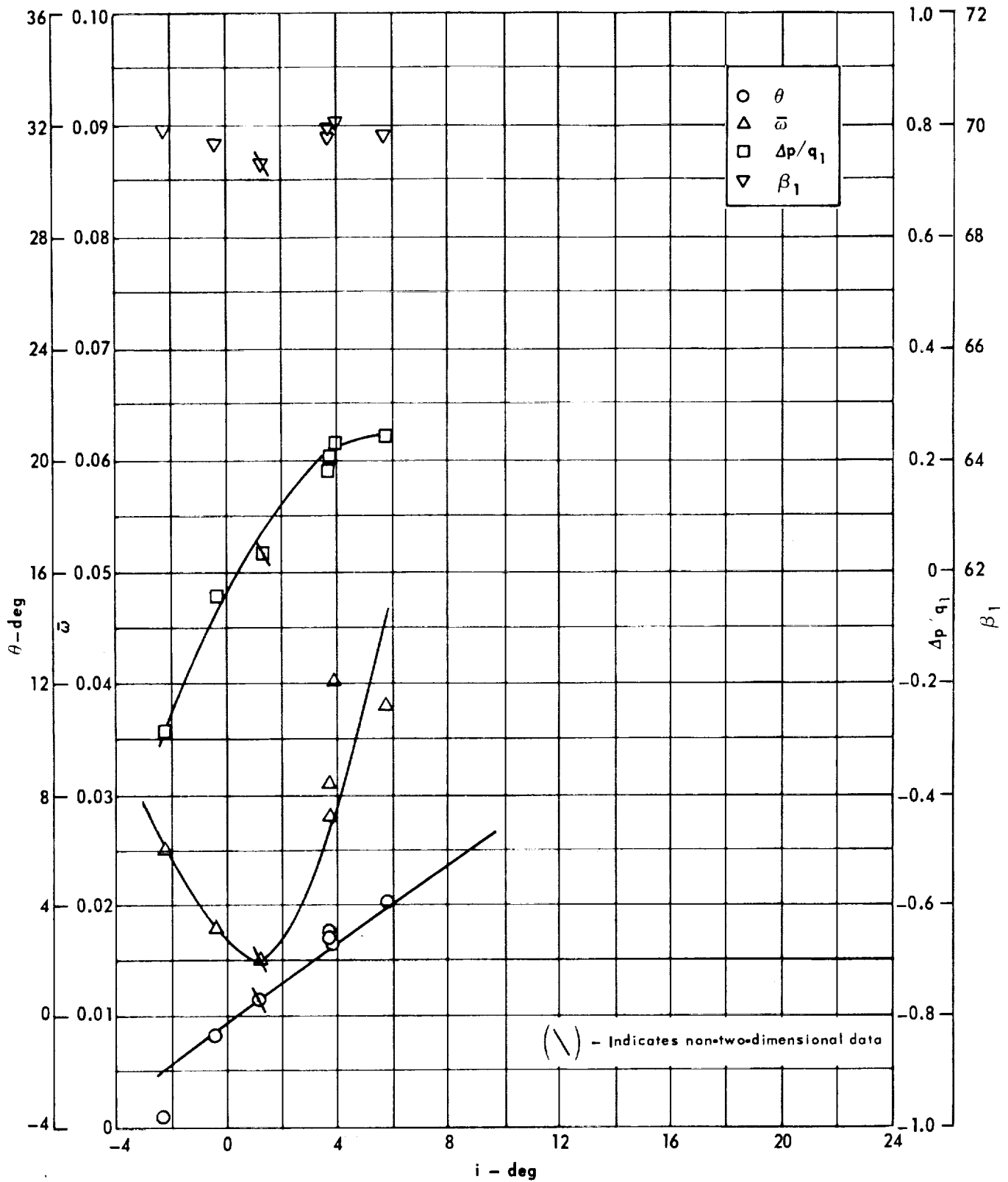
Cascade configuration: $\beta_{1N} = 60, \sigma = 1.50$

Double circular-arc profile: $\phi = 45, t/c = 0.06$

- - - Slotted hydrofoils (flagged)

(b) D, $\theta^*/s, K, \delta^\circ$

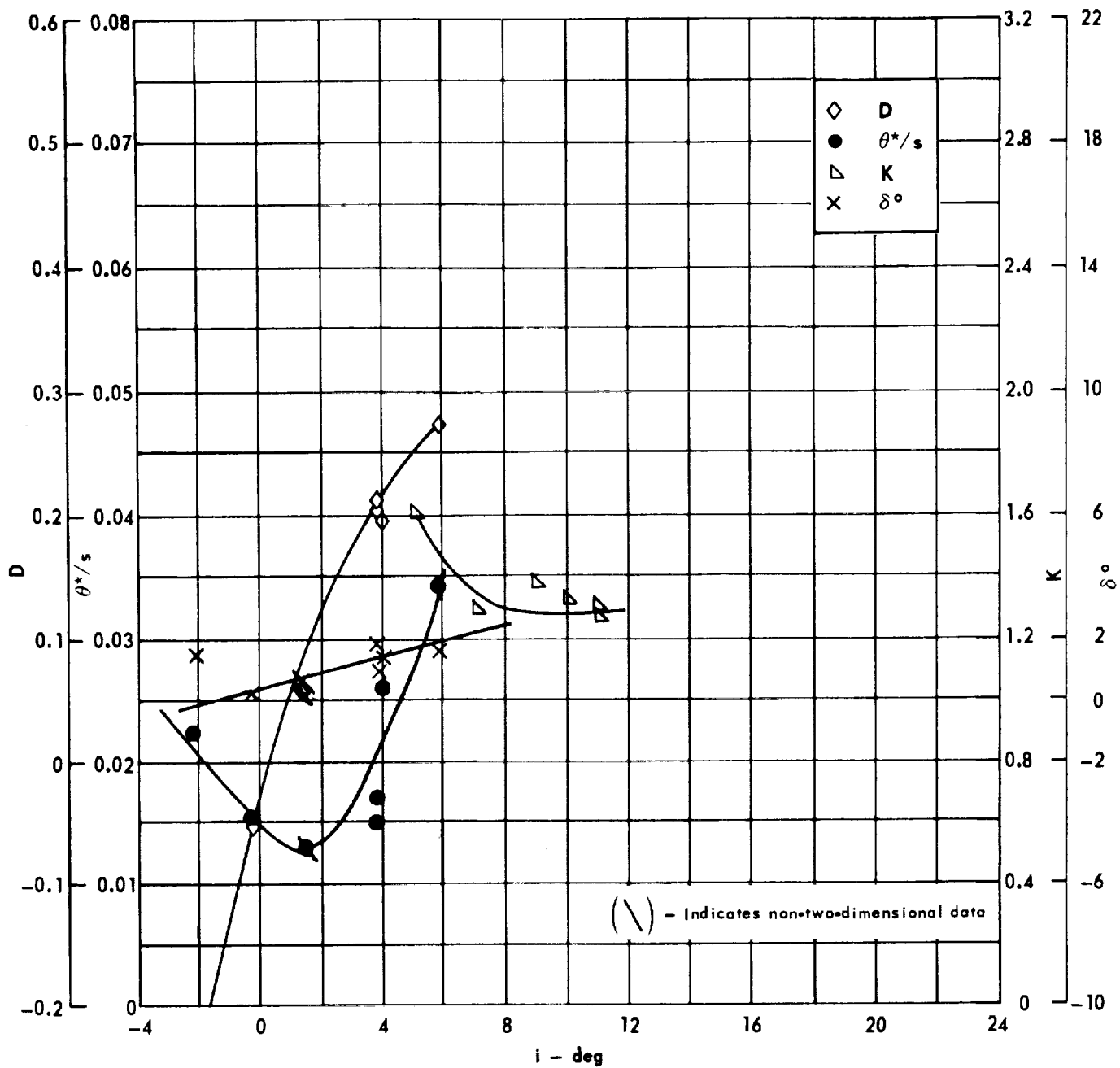
Figure 68. - Concluded.



Cascade configuration: $\beta_{1N} = 70, \sigma = 0.75$
 Double circular-arc profile: $\phi = 0, t/c = 0.06$

(a) $\theta, \bar{\omega}, \Delta p/q_1, \beta_1$

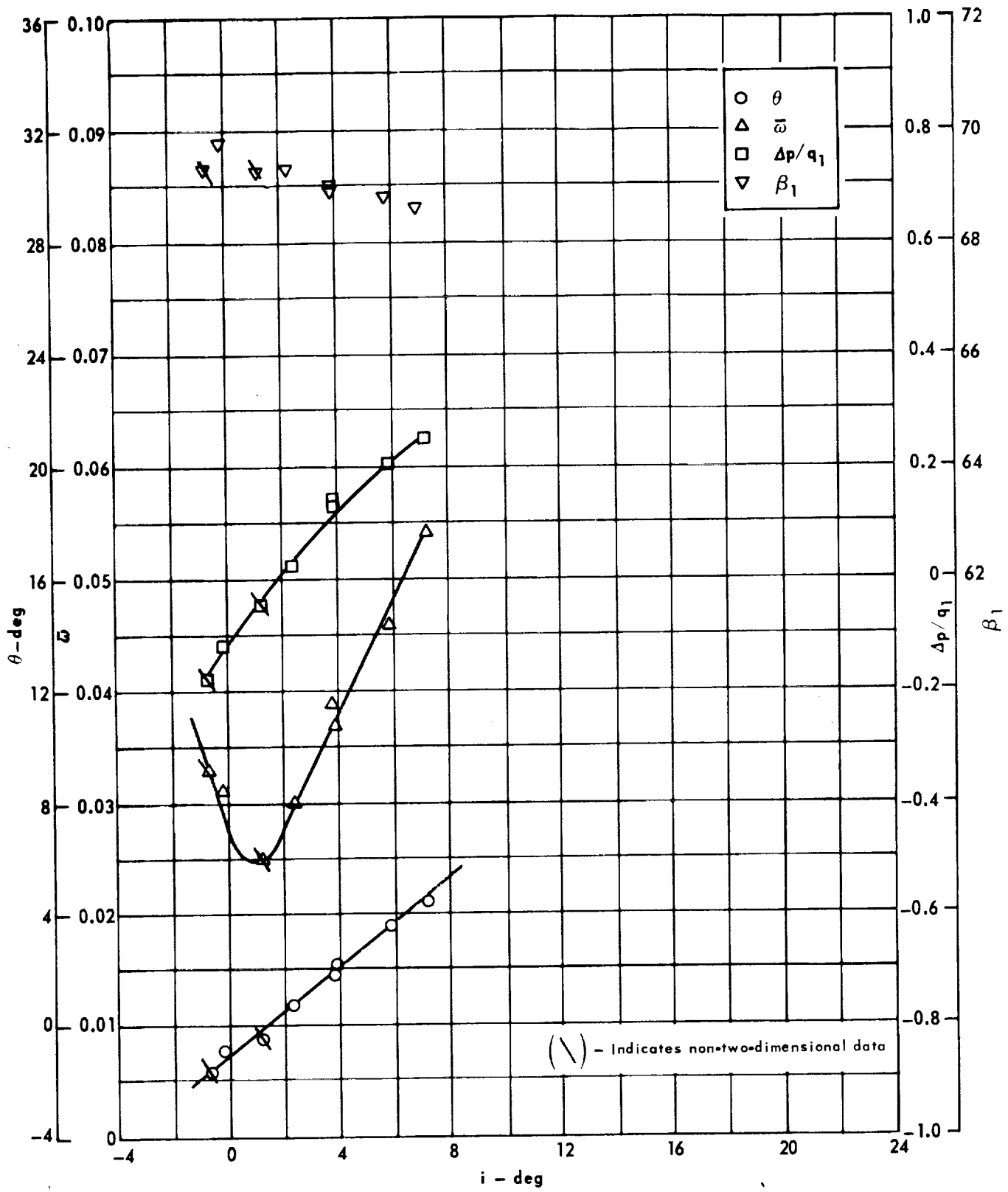
Figure 69. - Cascade characteristics as functions of incidence.



Cascade configuration: $\beta_{1N} = 70, \sigma = 0.75$
 Double circular-arc profile: $\phi = 0, t/c = 0.06$

(b) D, θ^*/s , K, δ°

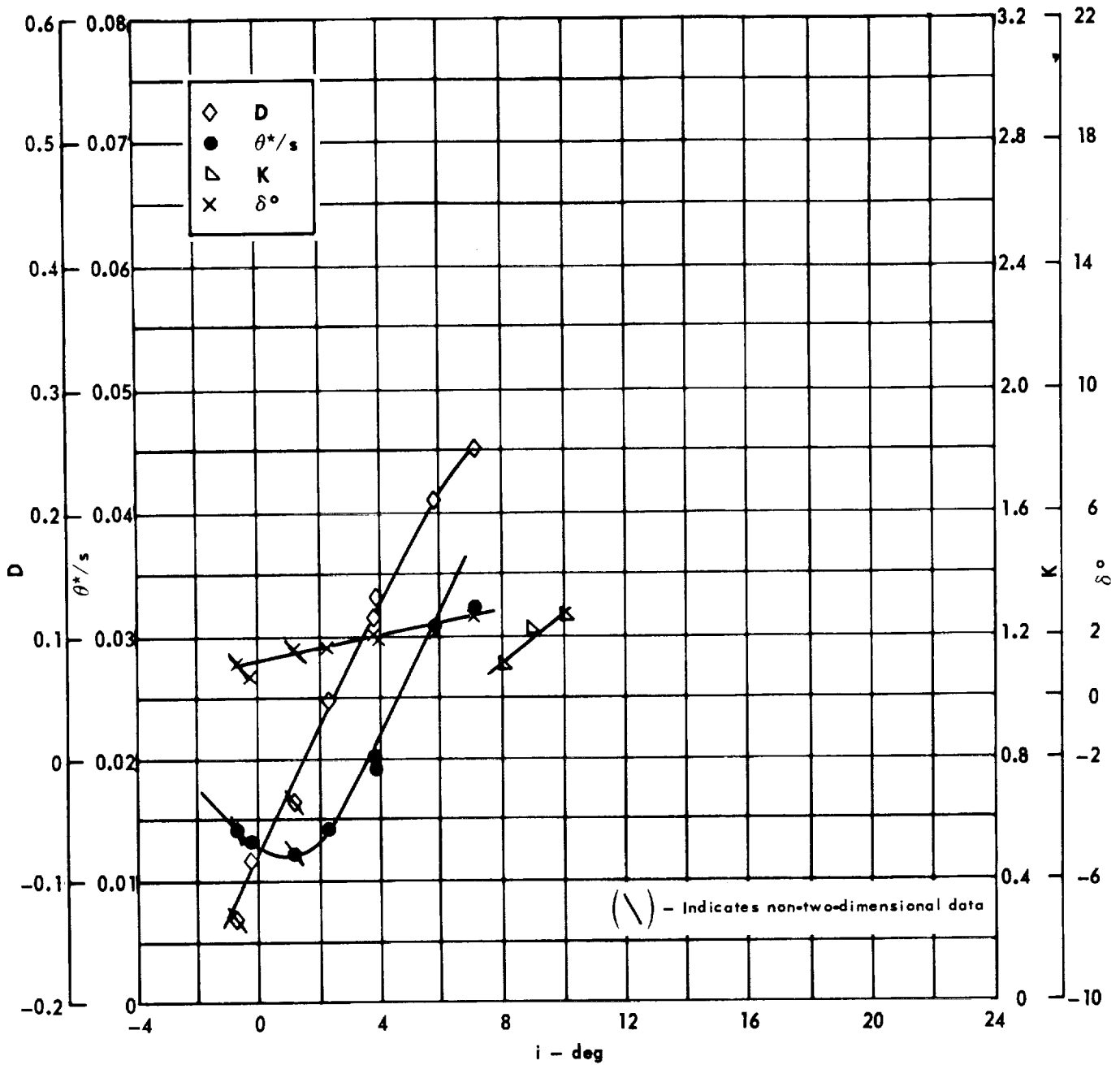
Figure 69. - Concluded.



Cascade configuration: $\beta_{1N} = 70$, $\sigma = 1.00$
 Double circular-arc profile: $\phi = 0^\circ$, $t/c = 0.06$

(a) $\theta, \bar{\omega}, \Delta p/q_1, \beta_1$

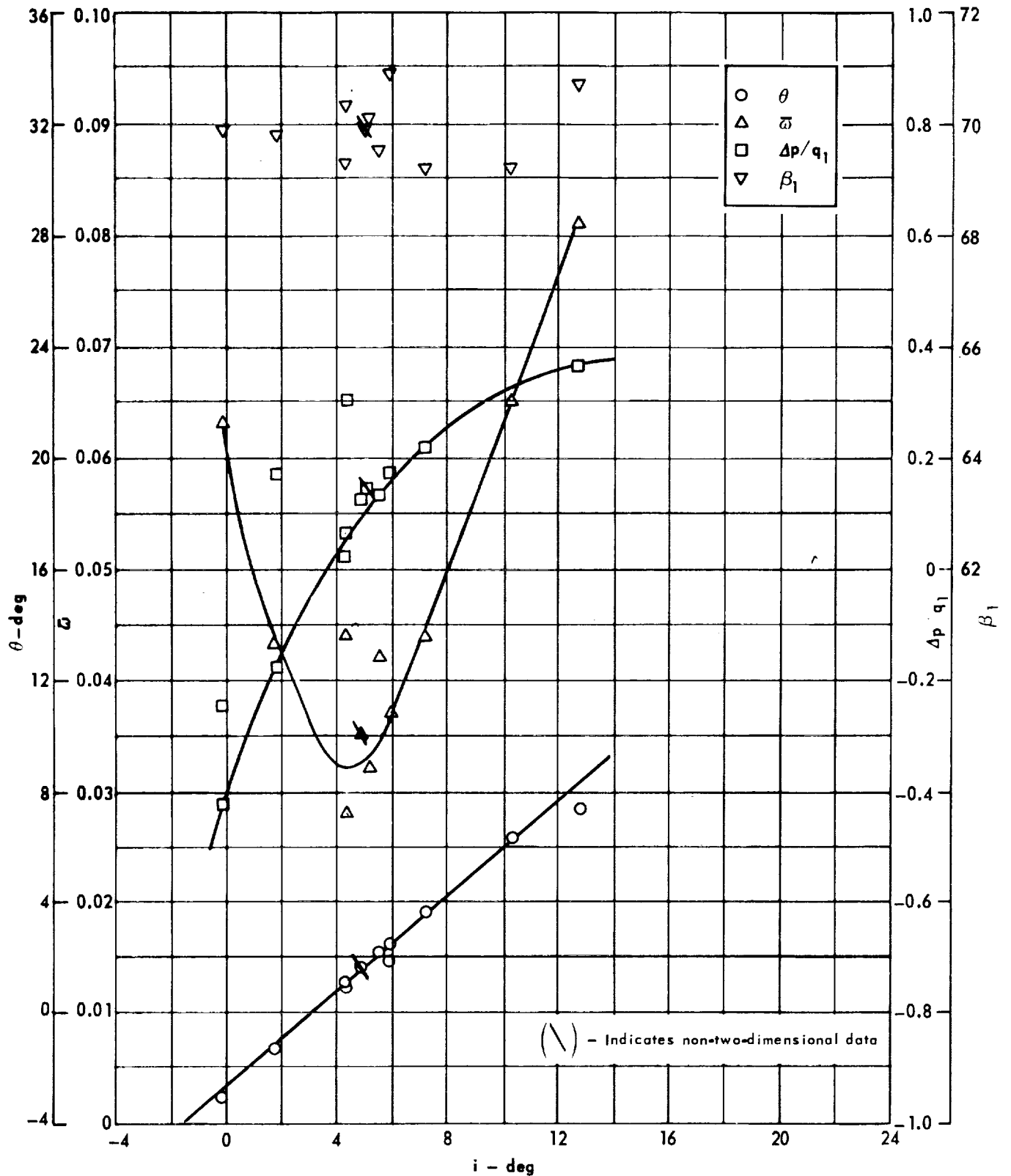
Figure 70. - Cascade characteristics as functions of incidence,



Cascade configuration: $\beta_{1N} = 70$, $\sigma = 1.00$
 Double circular-arc profile: $\phi = 0$, $t/c = 0.06$

(b) D, θ^*/s , K, δ°

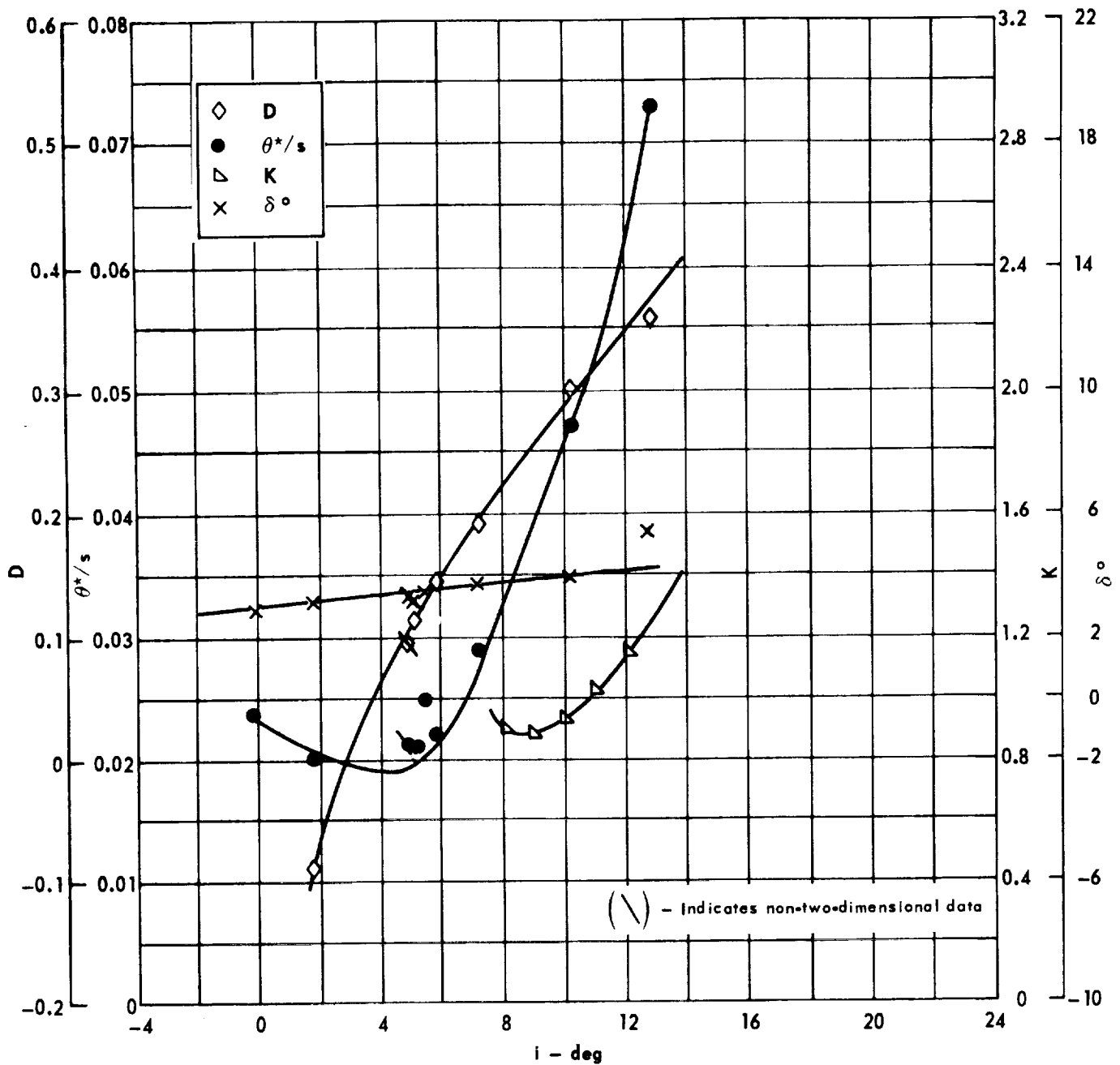
Figure 70 . - Concluded.



Cascade configuration: $\beta_{1N} = 70, \sigma = 1.50$
 Double circular-arc profile: $\phi = 0, t/c = 0.06$

(a) $\theta, \bar{w}, \Delta p/q_1, \beta_1$

Figure 71 . - Cascade characteristics as functions of incidence.

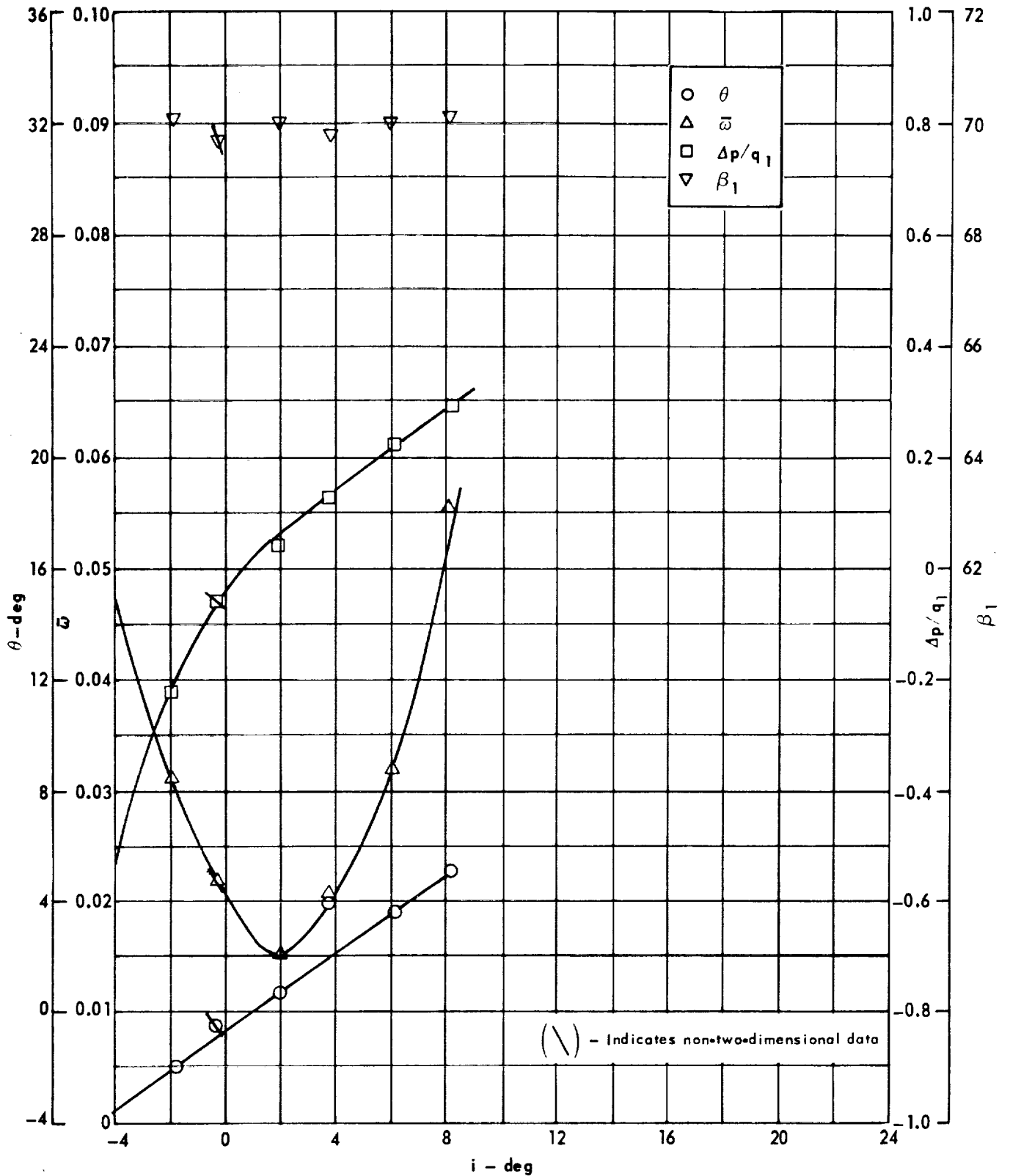


Cascade configuration: $\beta_{1N} = 70$, $\sigma = 1.50$

Double circular-arc profile: $\phi = 0$, $t/c = 0.06$

(b) D, θ^*/s , K, δ°

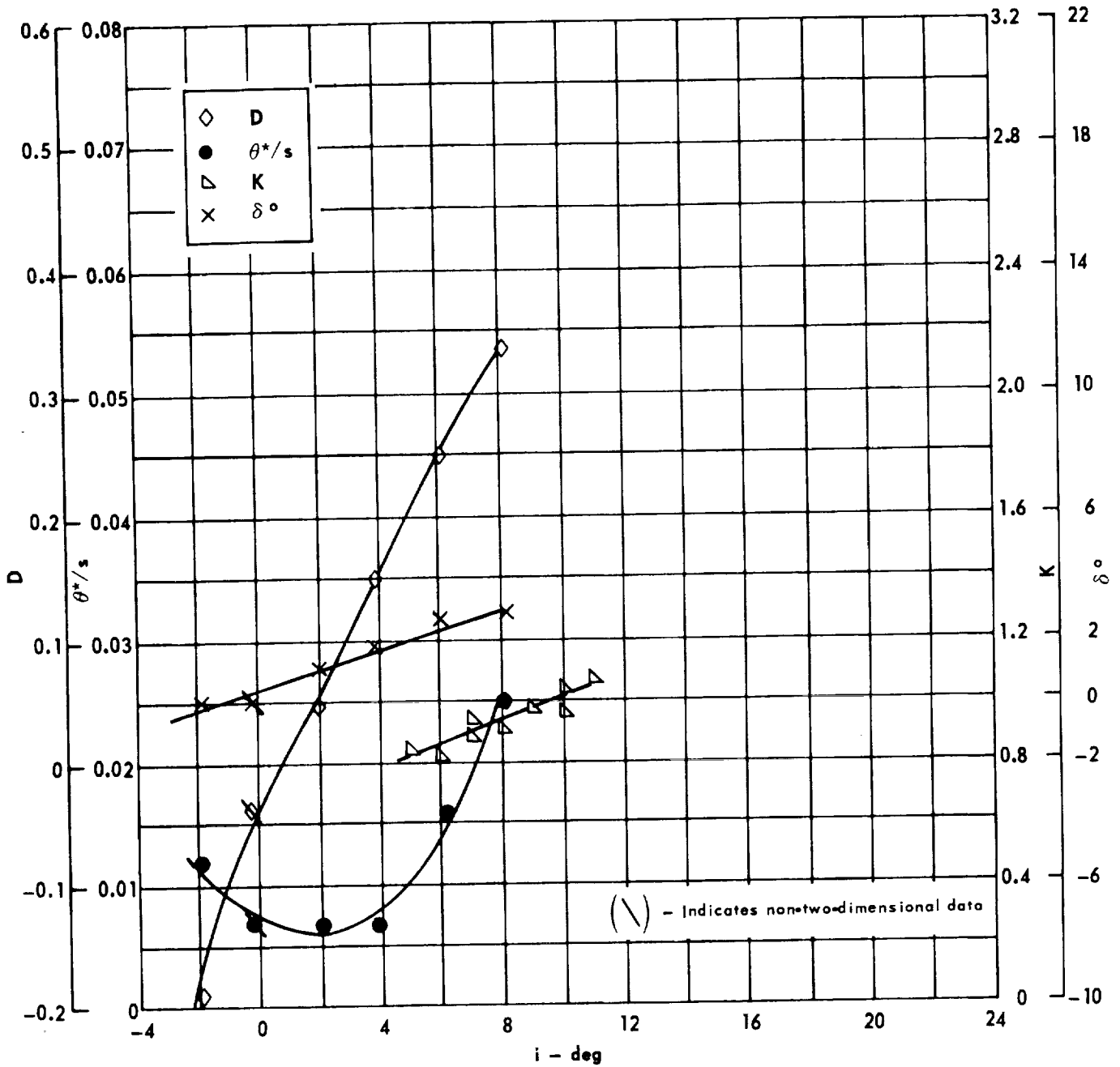
Figure 71 . - Concluded.



Cascade configuration : $\beta_{1N} = 70, \sigma = 0.75$
 Double circular-arc profile : $\phi = 0, t/c = 0.10$

(a) $\theta, \bar{\omega}, \Delta p/q_1, \beta_1$

Figure 72. - Cascade characteristics as functions of incidence.

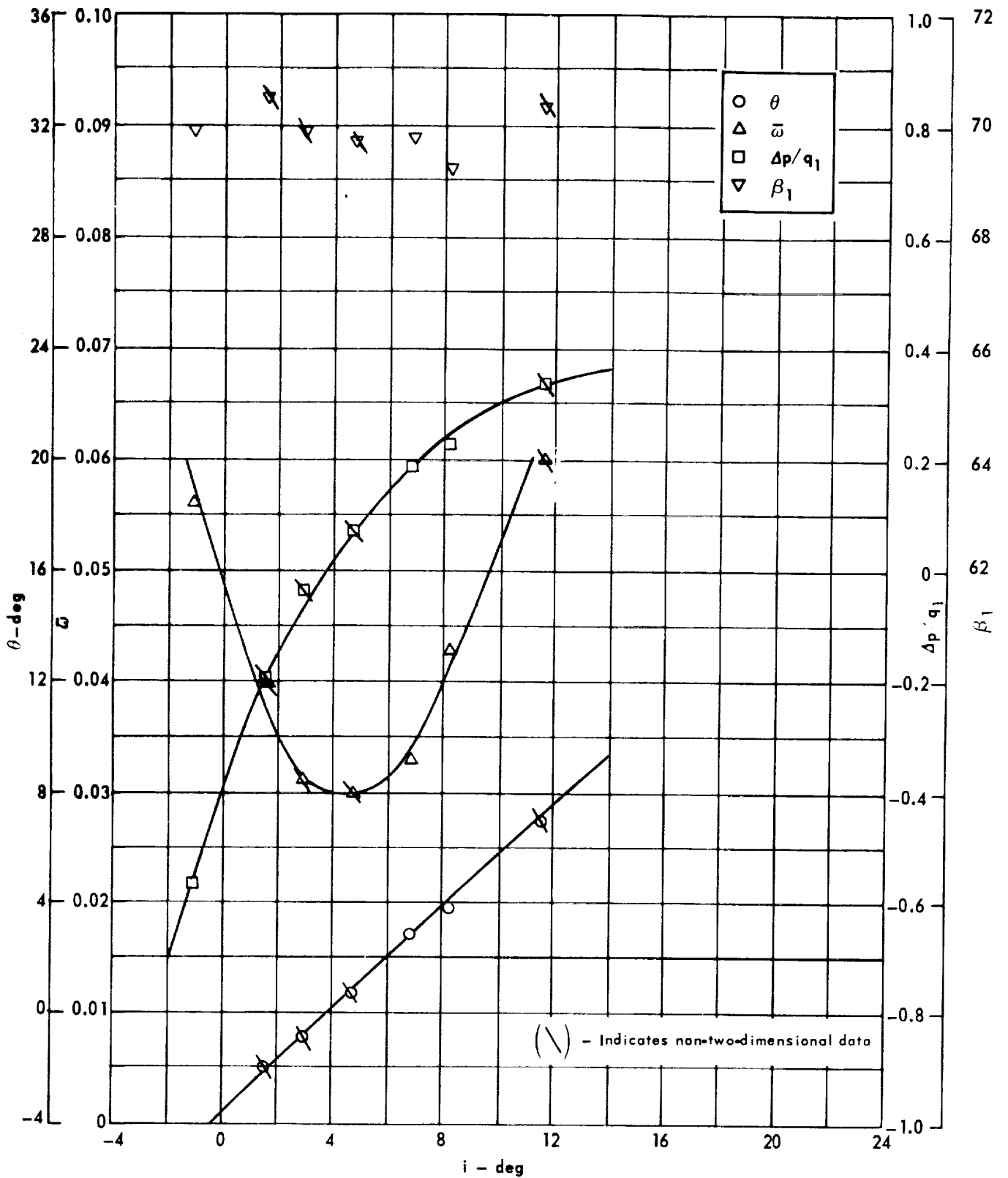


Cascade configuration: $\beta_{1N} = 70, \sigma = 0.75$

Double circular-arc profile: $\phi = 0, t/c = 0.10$

(b) D, θ^*/s , K, δ°

Figure 72 . - Concluded.

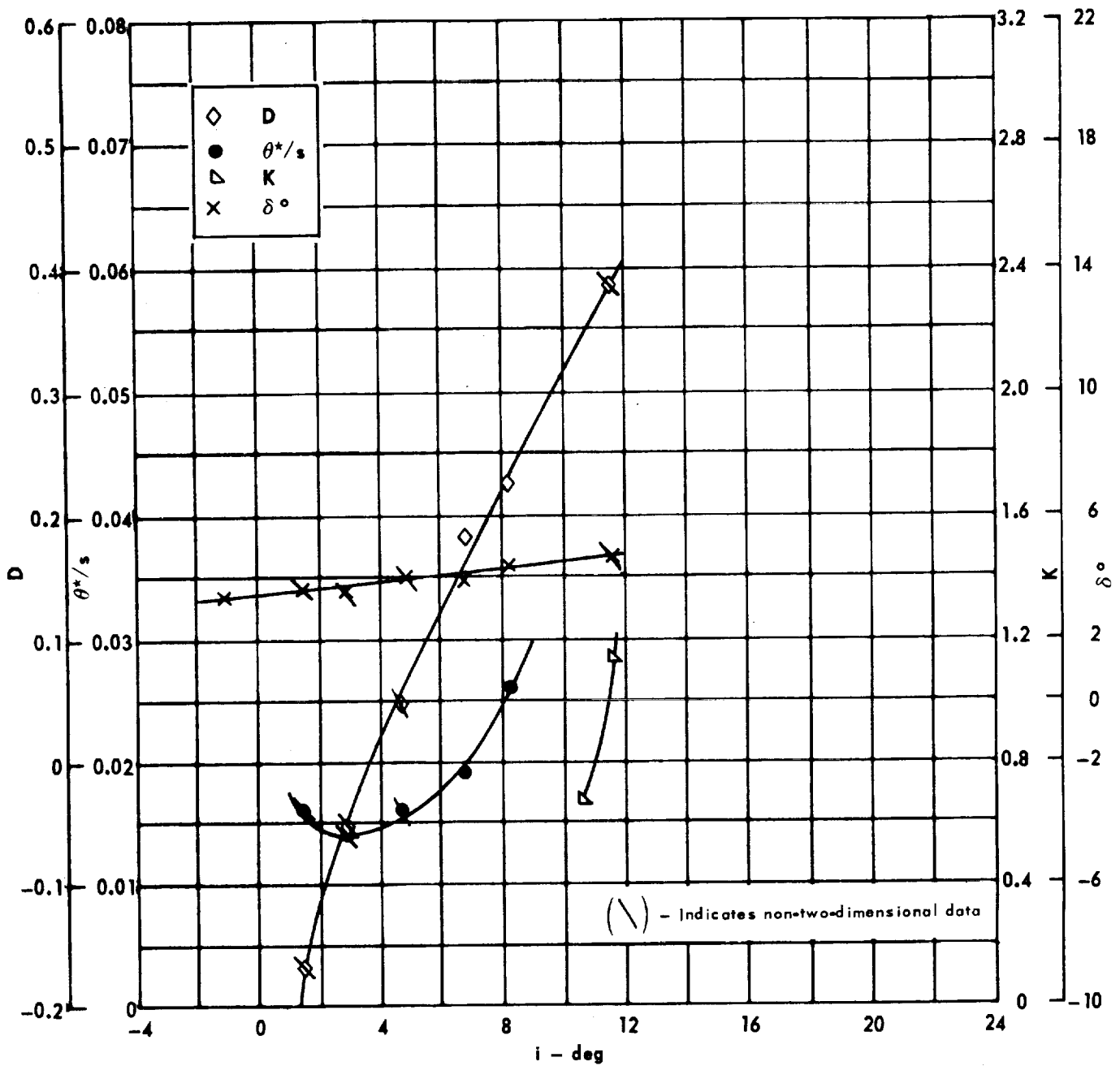


Cascade configuration: $\beta_{1N} = 70$, $\sigma = 1.00$

Double circular-arc profile: $\phi = 0$, $t/c = 0.10$

(a) $\theta, \bar{\omega}, \Delta p/q_1, \beta_1$

Figure 73. - Cascade characteristics as functions of incidence.

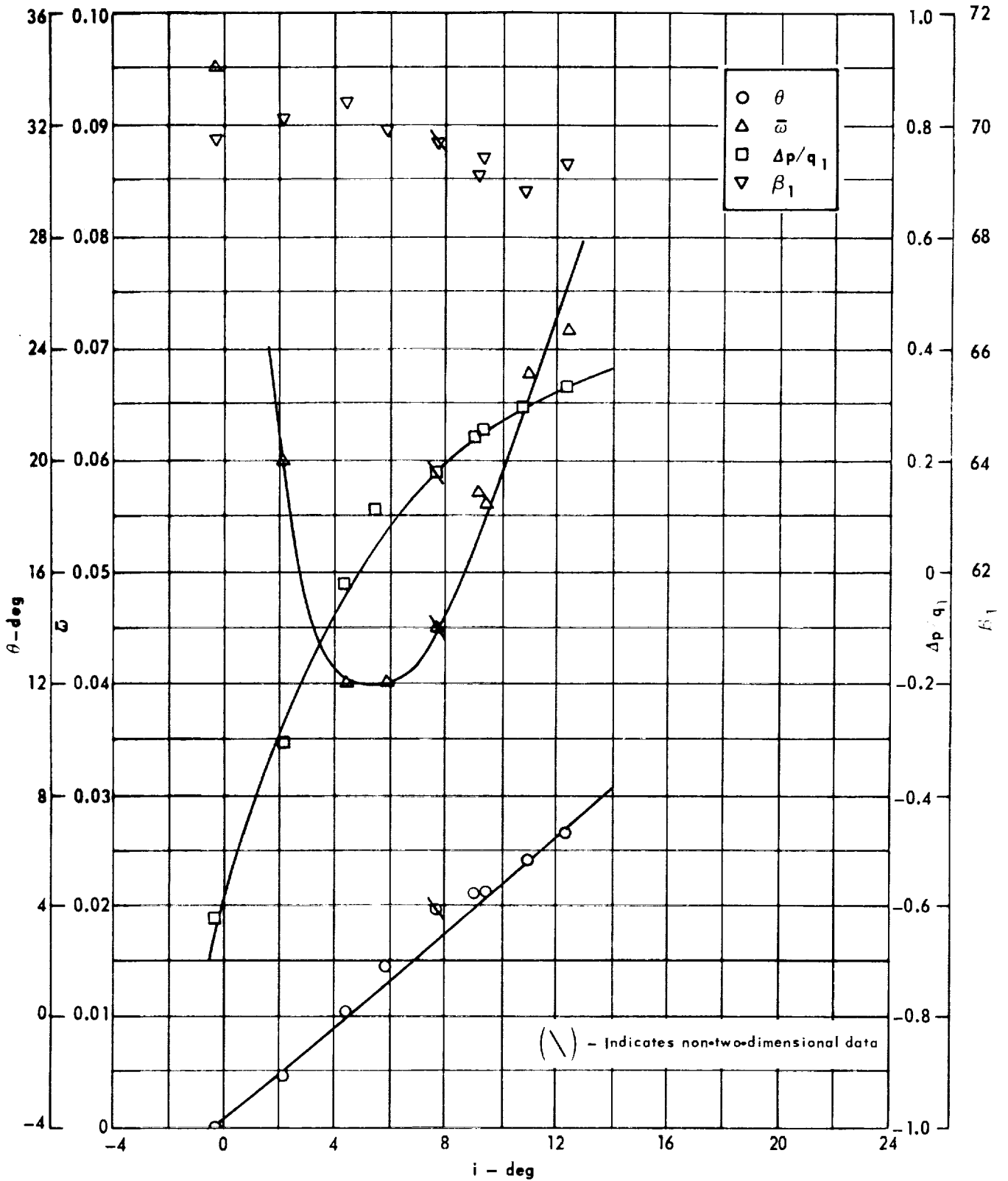


Cascade configuration: $\beta_{1N} = 70, \sigma = 1.00$

Double circular-arc profile: $\phi = 0, t/c = 0.10$

(b) D, θ^*/s , K, δ°

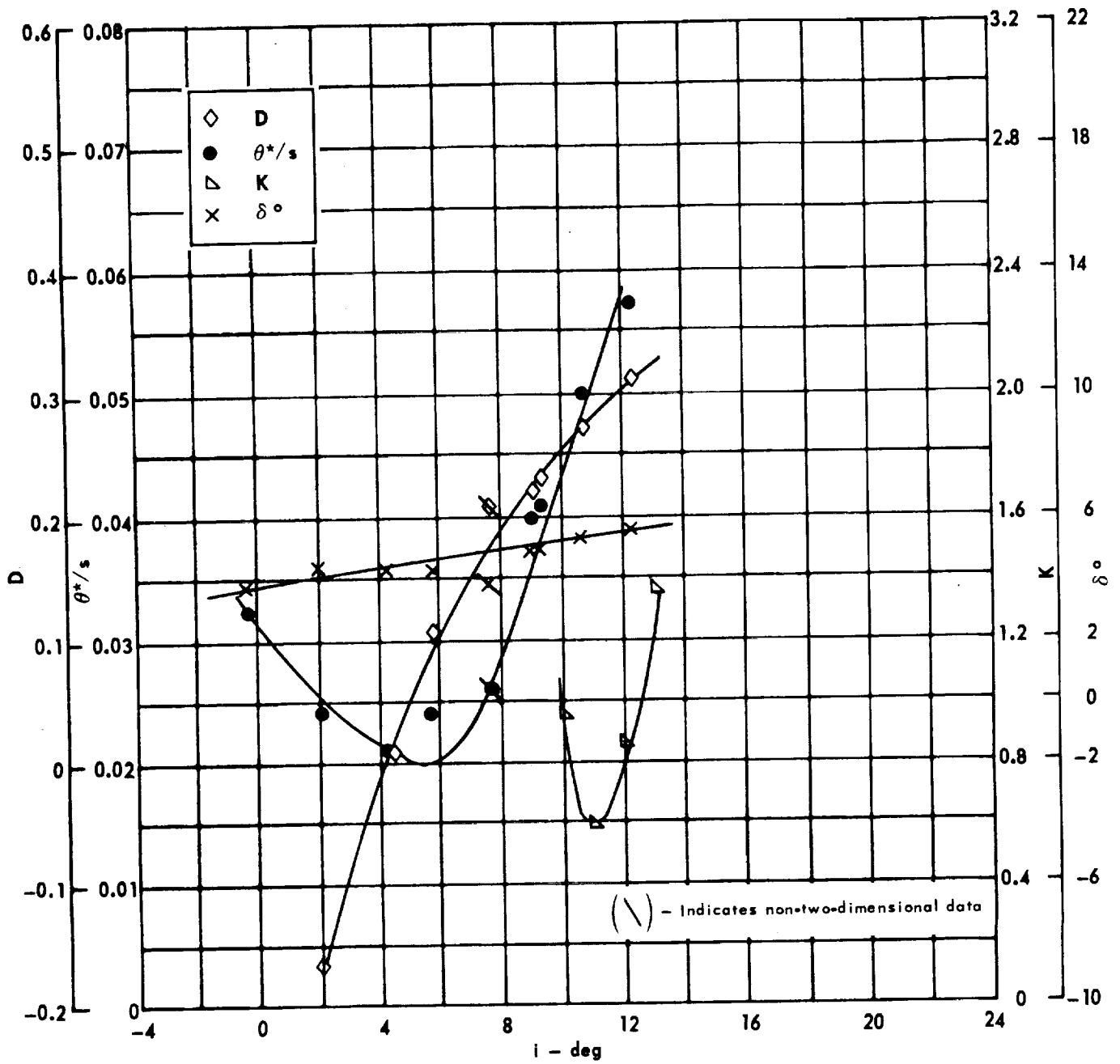
Figure 73. - Concluded.



Cascade configuration: $\beta_{1N} = 70, \sigma = 1.50$
 Double circular-arc profile: $\phi = 0, \tau = c = 0.10$

(a) $\theta, \bar{\omega}, \Delta p/q_1, \beta_1$

Figure 74. - Cascade characteristics as functions of incidence.

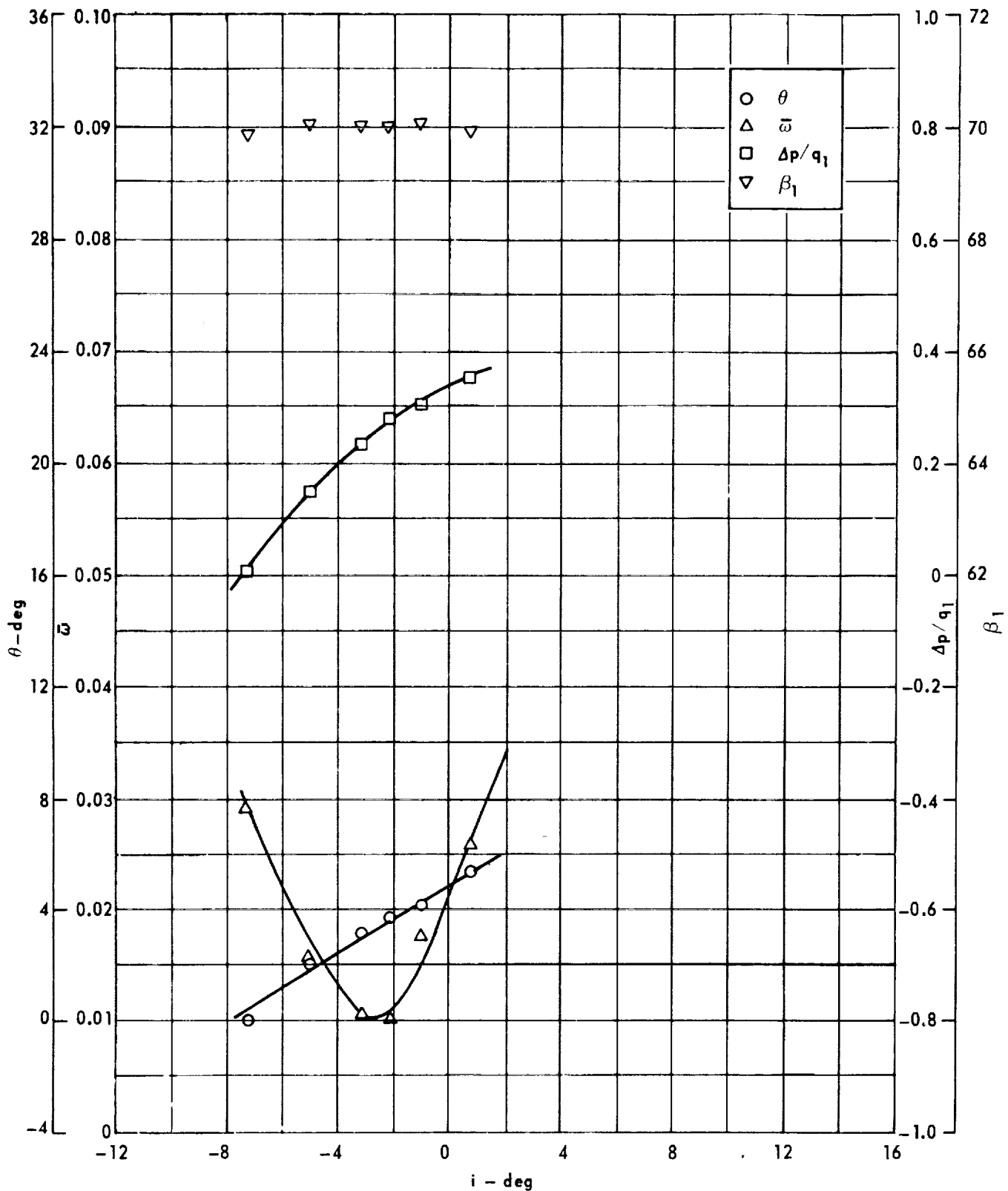


Cascade configuration: $\beta_{1N} = 70$, $\sigma = 1.50$

Double circular-arc profile: $\phi = 0$, $t/c = 0.10$

(b) D, θ^*/s , K, δ°

Figure 74. - Concluded.

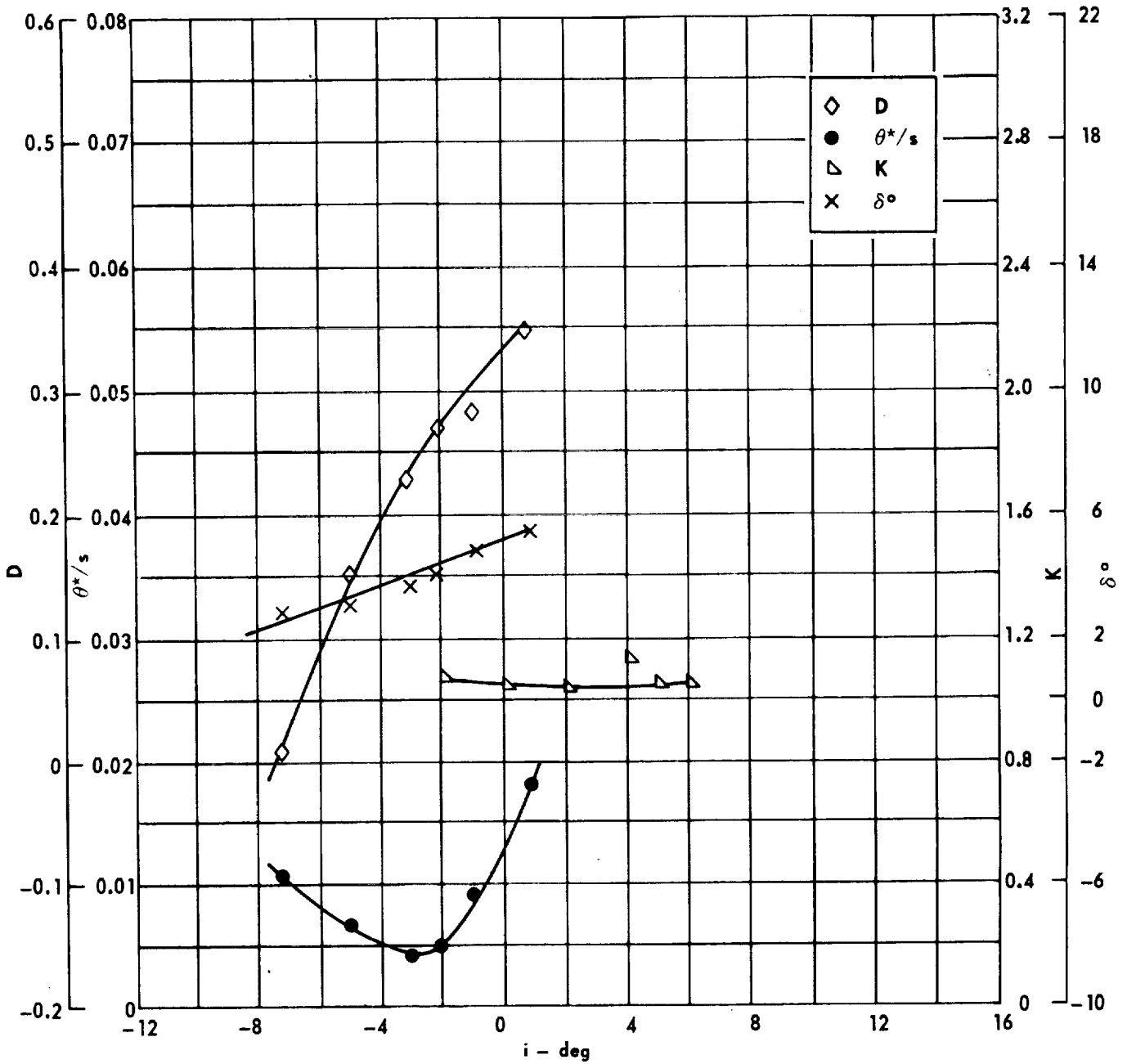


Cascade configuration: $\beta_{1N} = 70, \sigma = 0.75$

Double circular-arc profile: $\phi = 10, t/c = 0.06$

(a) $\theta, \bar{\omega}, \Delta p/q_1, \beta_1$

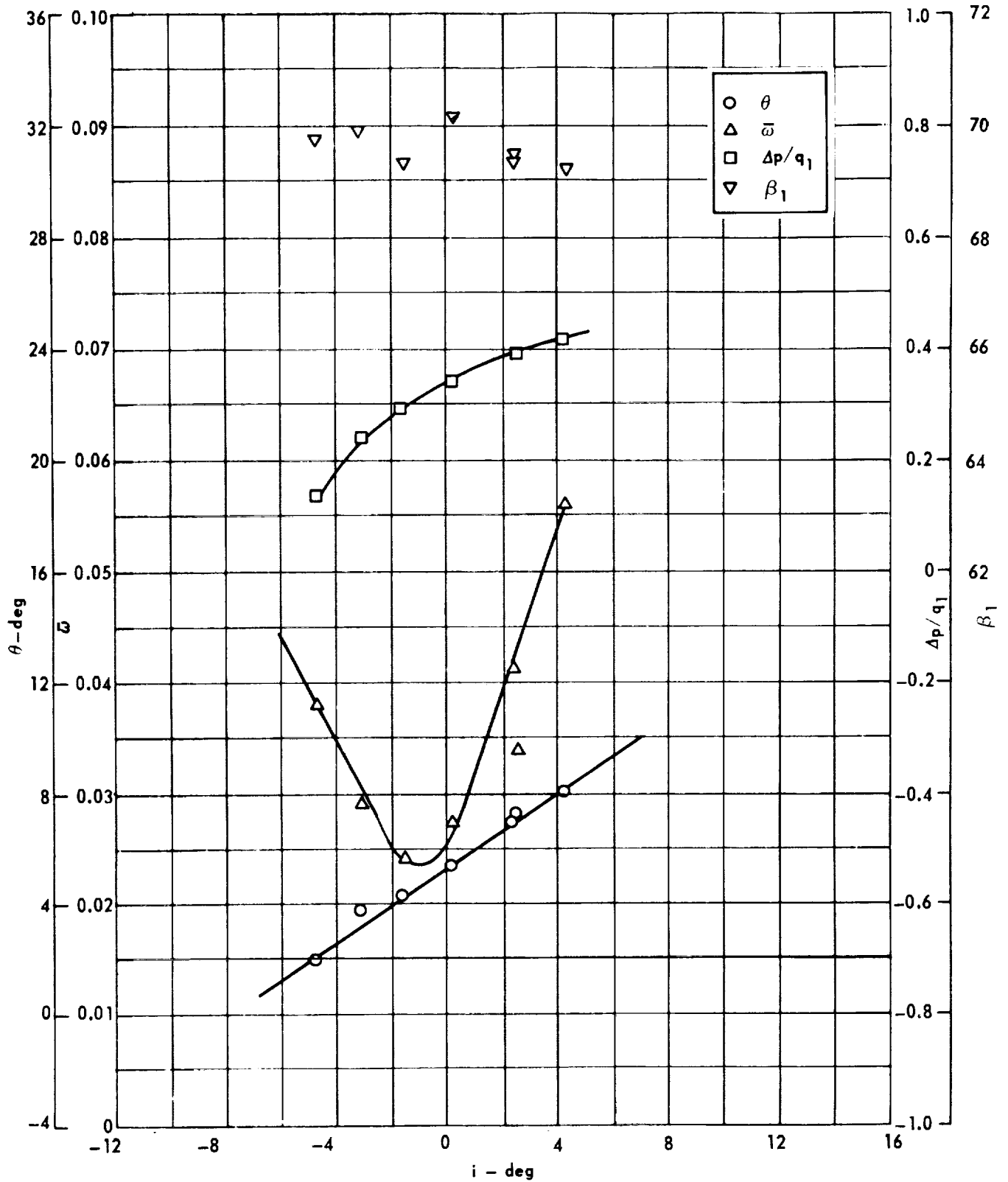
Figure 75. - Cascade characteristics as functions of incidence.



Cascade configuration: $\beta_{1N} = 70, \sigma = 0.75$
 Double circular-arc profile: $\phi = 10, r/c = 0.06$

(b) D, θ^*/s , K, δ°

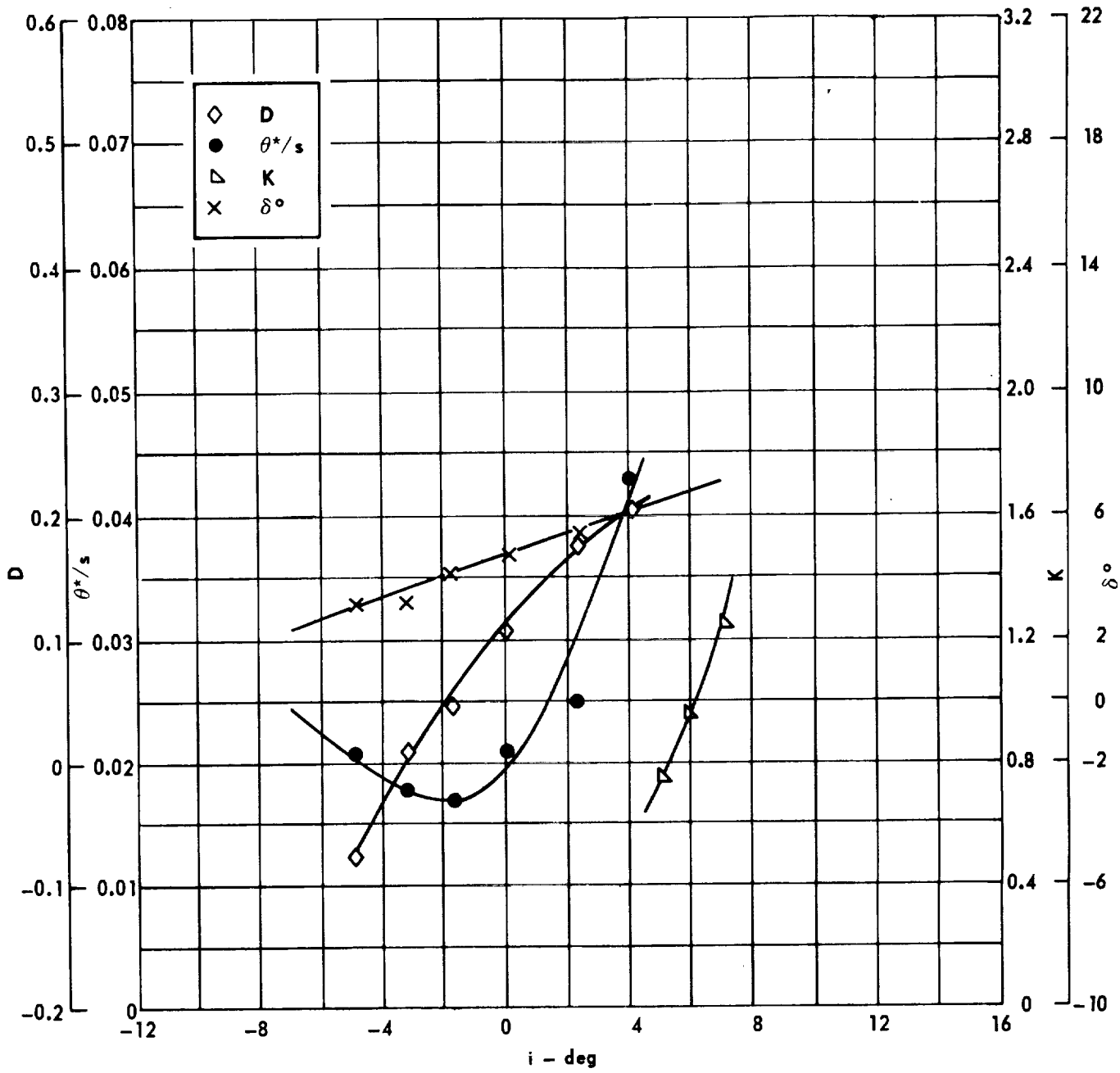
Figure 75. - Concluded.



Cascade configuration: $\beta_{1N} = 70$, $\sigma = 1.00$
 Double circular-arc profile: $\phi = 10$, $t/c = 0.06$

(a) $\theta, \bar{\omega}, \Delta p/q_1, \beta_1$

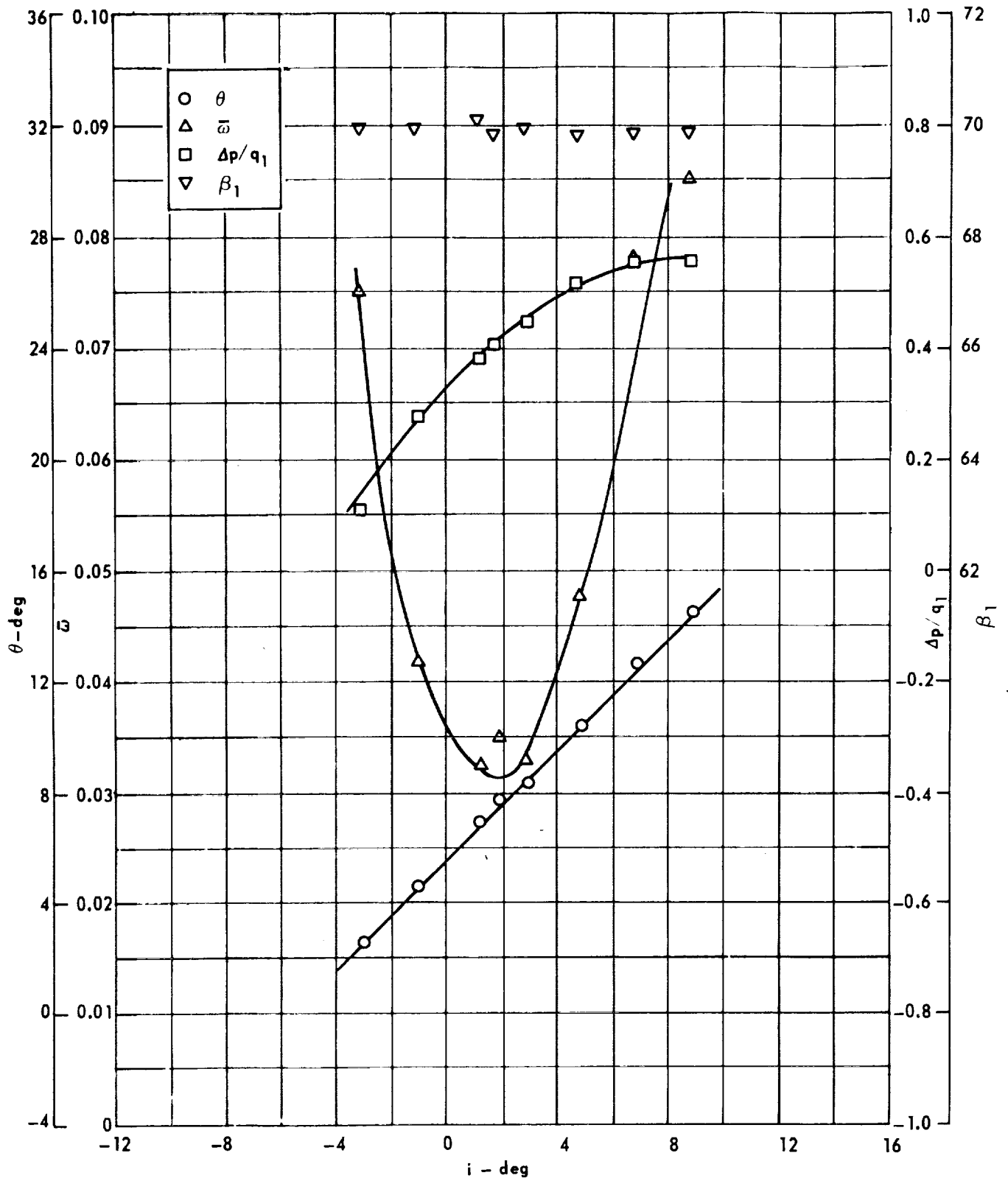
Figure 76 . - Cascade characteristics as functions of incidence.



Cascade configuration : $\beta_{1N} = 70$, $\sigma = 1.00$
 Double circular-arc profile : $\phi = 10$, $t/c = 0.06$

(b) D, θ^*/s , K, δ°

Figure 76. - Concluded.

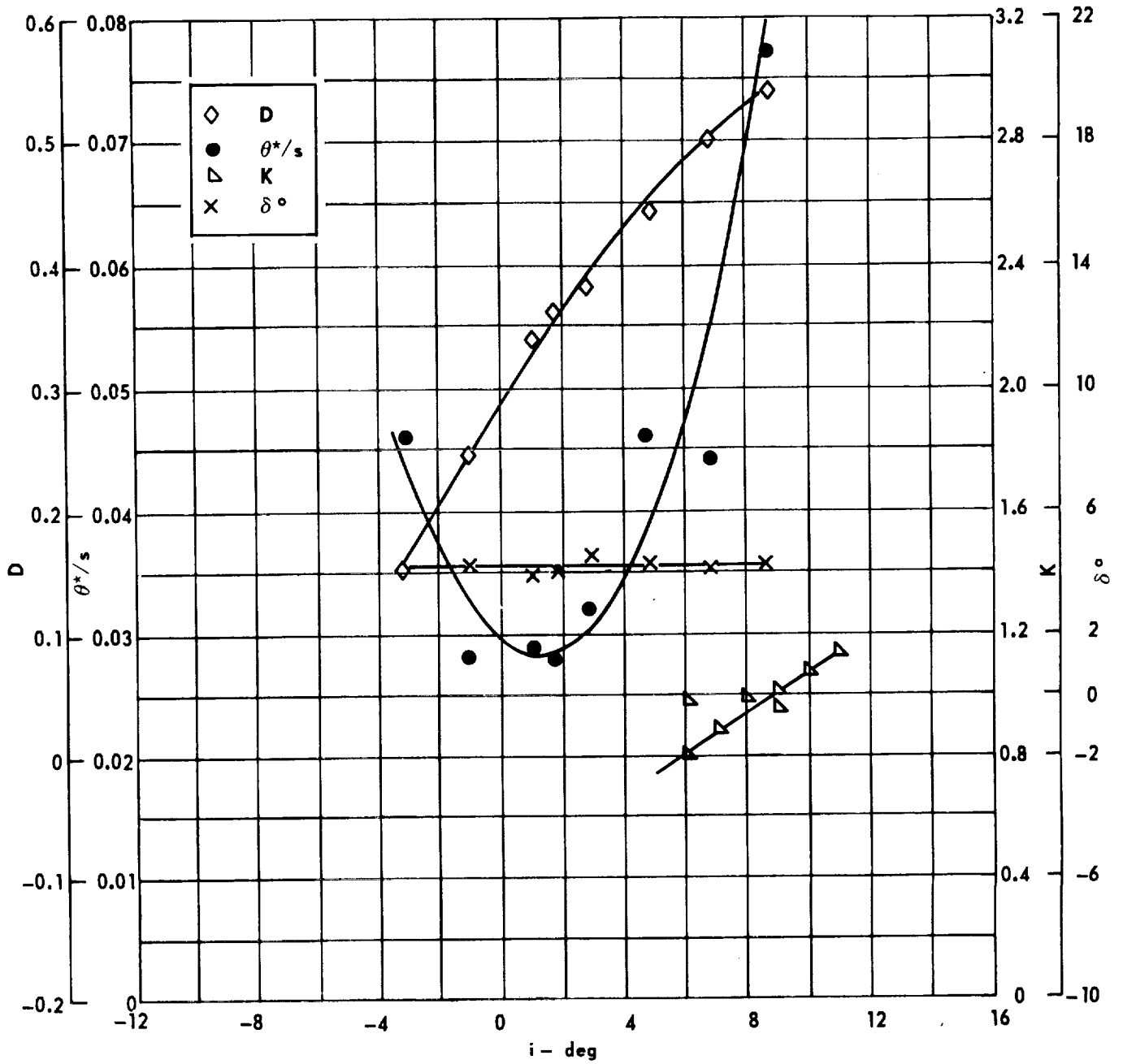


Cascade configuration : $\beta_{1N} = 70$, $\sigma = 1.50$

Double circular-arc profile : $\phi = 10$, $r/c = 0.06$

(a) $\theta, \bar{\omega}, \Delta p/q_1, \beta_1$

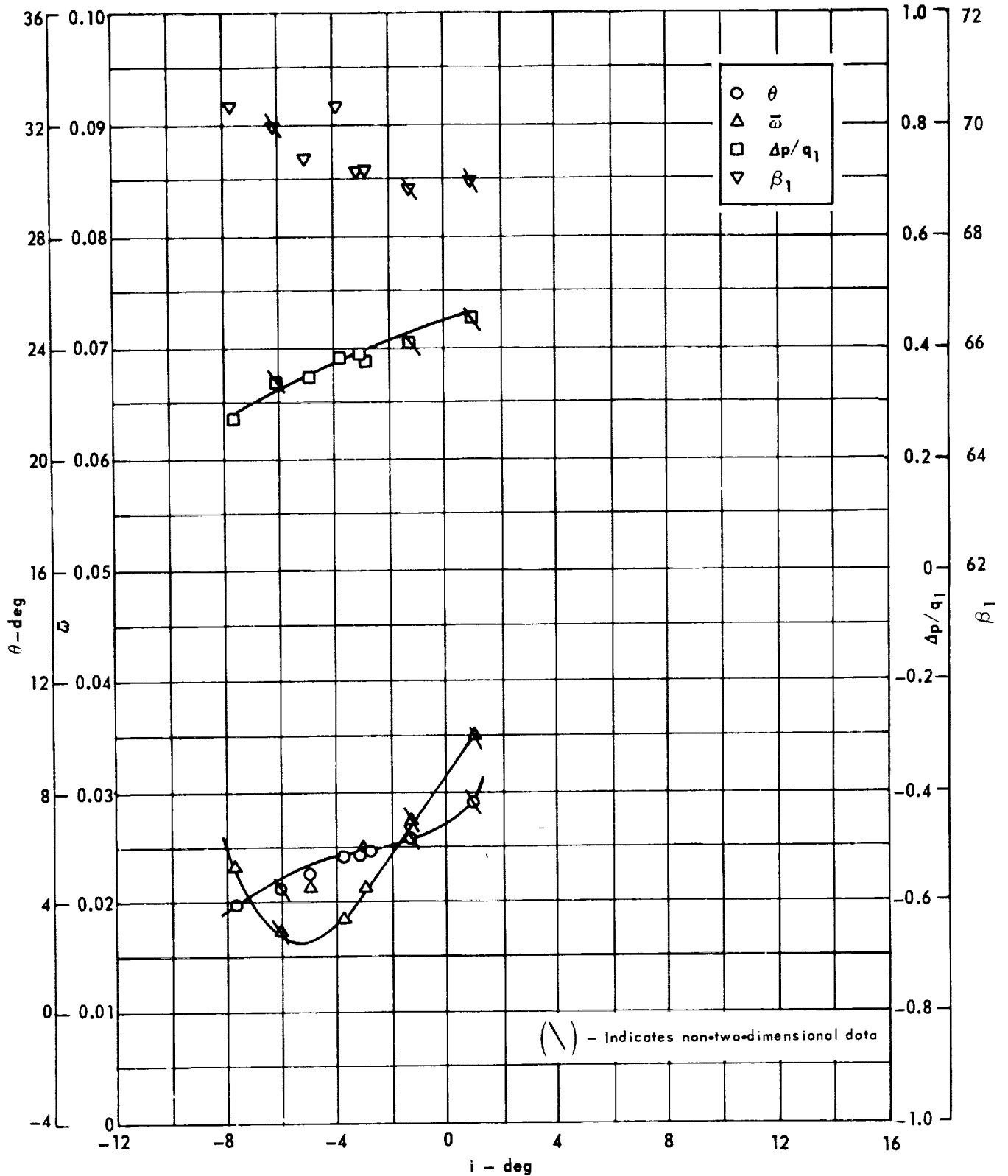
Figure 77 - Cascade characteristics as functions of incidence.



Cascade configuration: $\beta_{1N} = 70, \sigma = 1.50$
 Double circular-arc profile: $\phi = 10, t/c = 0.06$

(b) $D, \theta^*/s, K, \delta^\circ$

Figure 77 - Concluded.

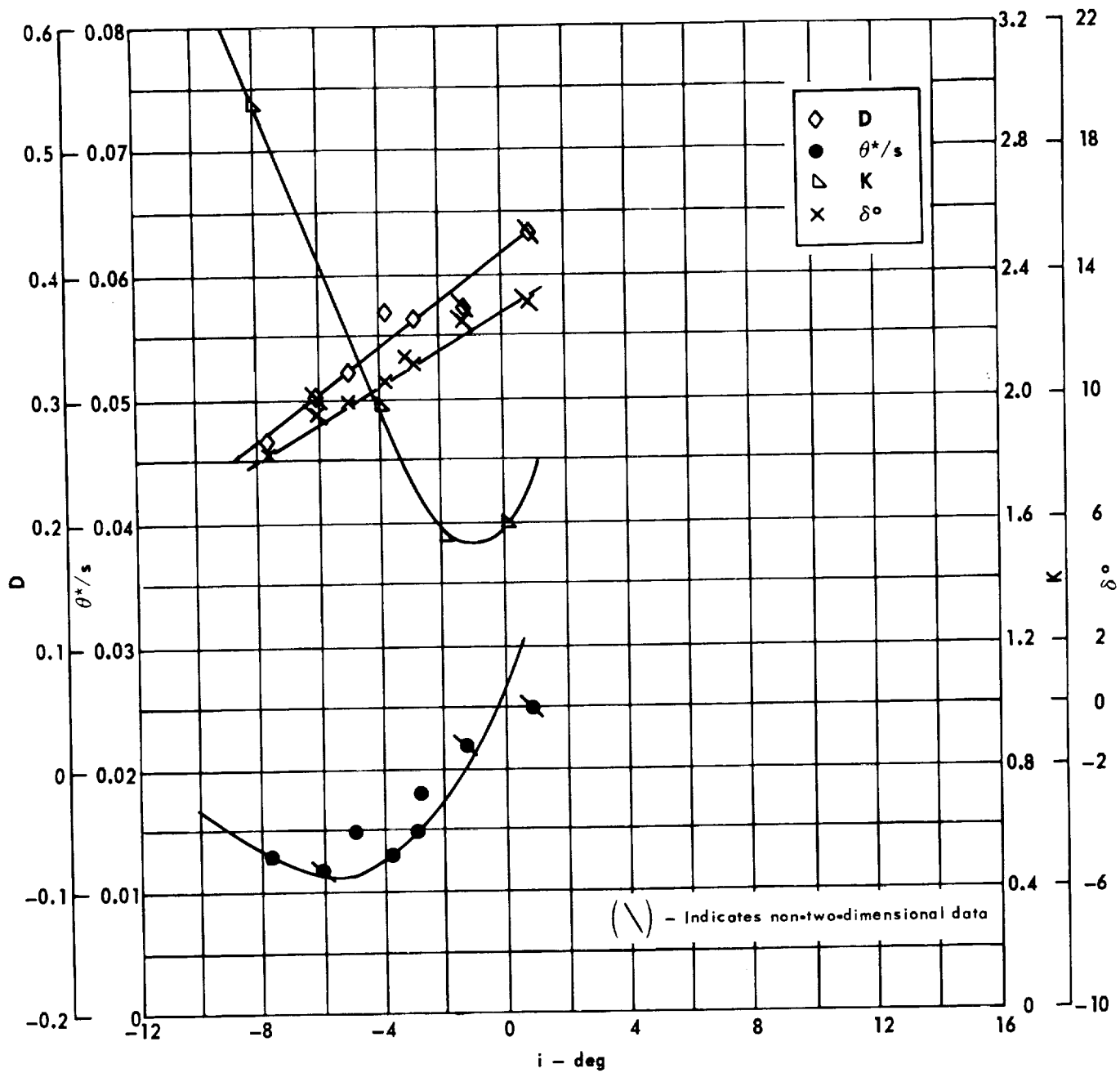


Cascade configuration : $\beta_{1N} = 70$, $\sigma = 0.75$

Double circular-arc profile : $\phi = 20$, $t/c = 0.06$

(a) $\theta, \bar{\omega}, \Delta p/q_1, \beta_1$

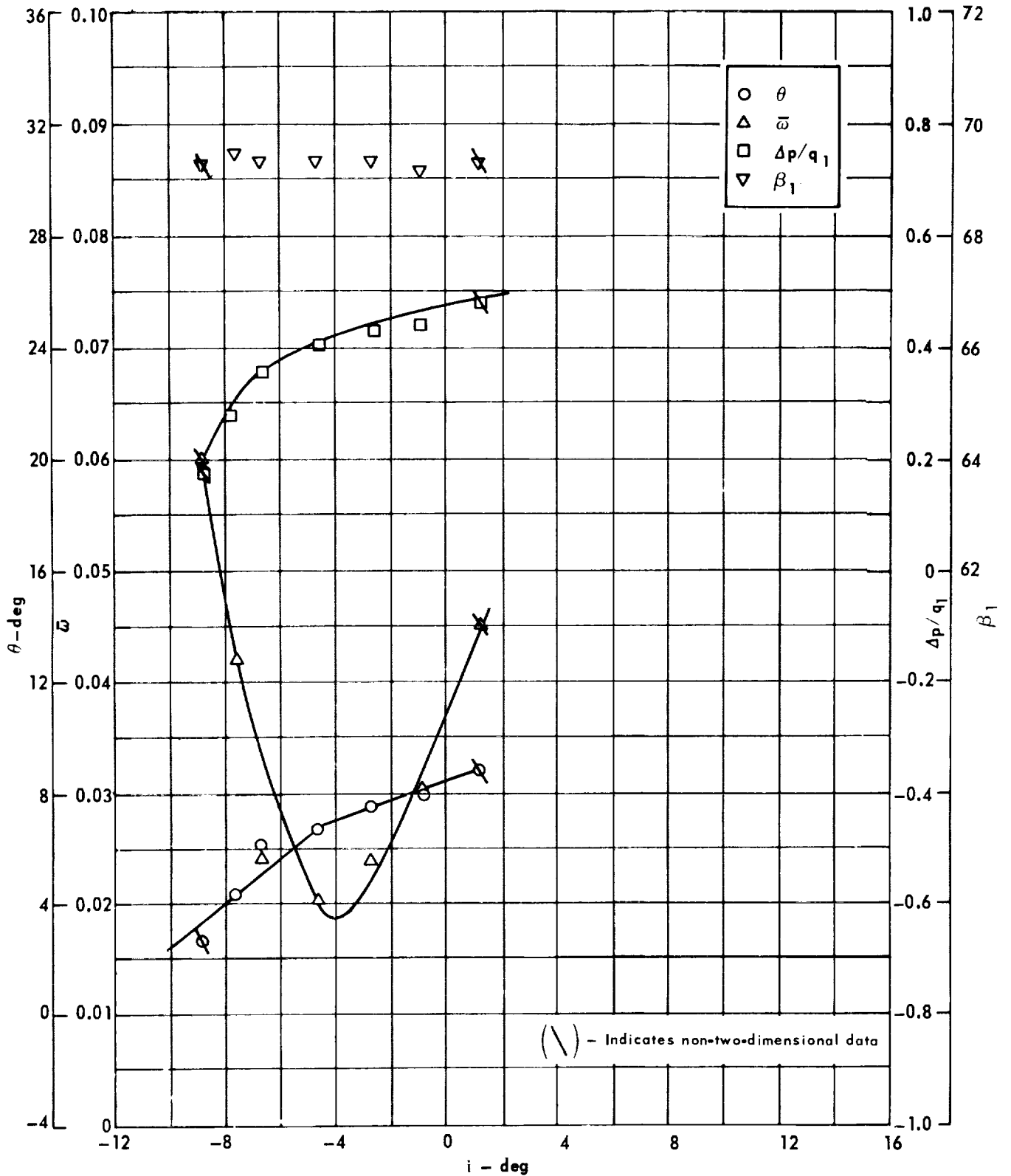
Figure 78. - Cascade characteristics as functions of incidence.



Cascade configuration : $\beta_{1N} = 70$, $\sigma = 0.75$
 Double circular-arc profile : $\phi = 20$, $t/c = 0.06$

(b) D, θ^*/s , K, δ°

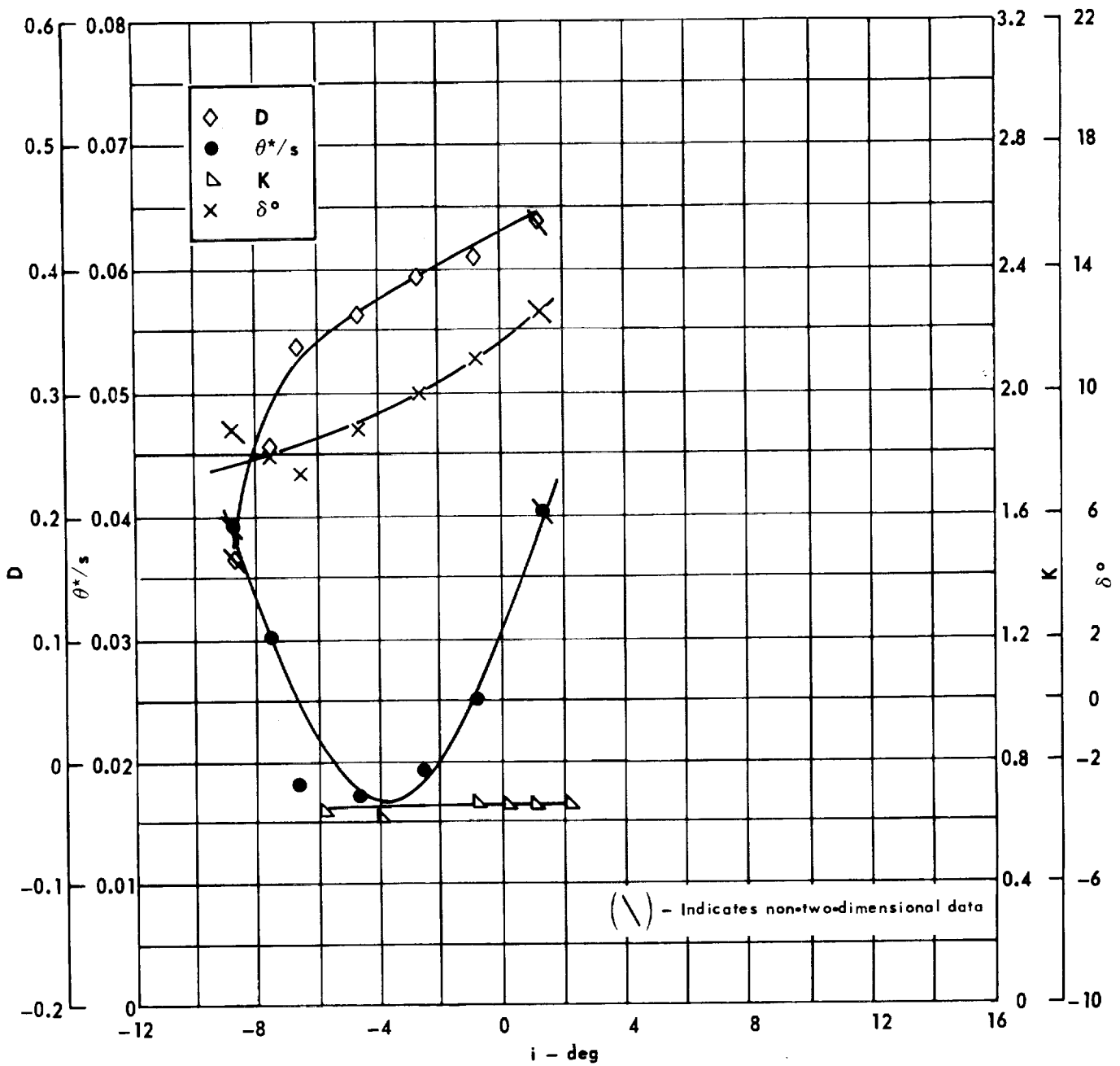
Figure 78 . - Concluded.



Cascade configuration : $\beta_{1N} = 70, \sigma = 1.00$
 Double circular-arc profile : $\phi = 20, t/c = 0.06$

(a) $\theta, \bar{\omega}, \Delta p/q_1, \beta_1$

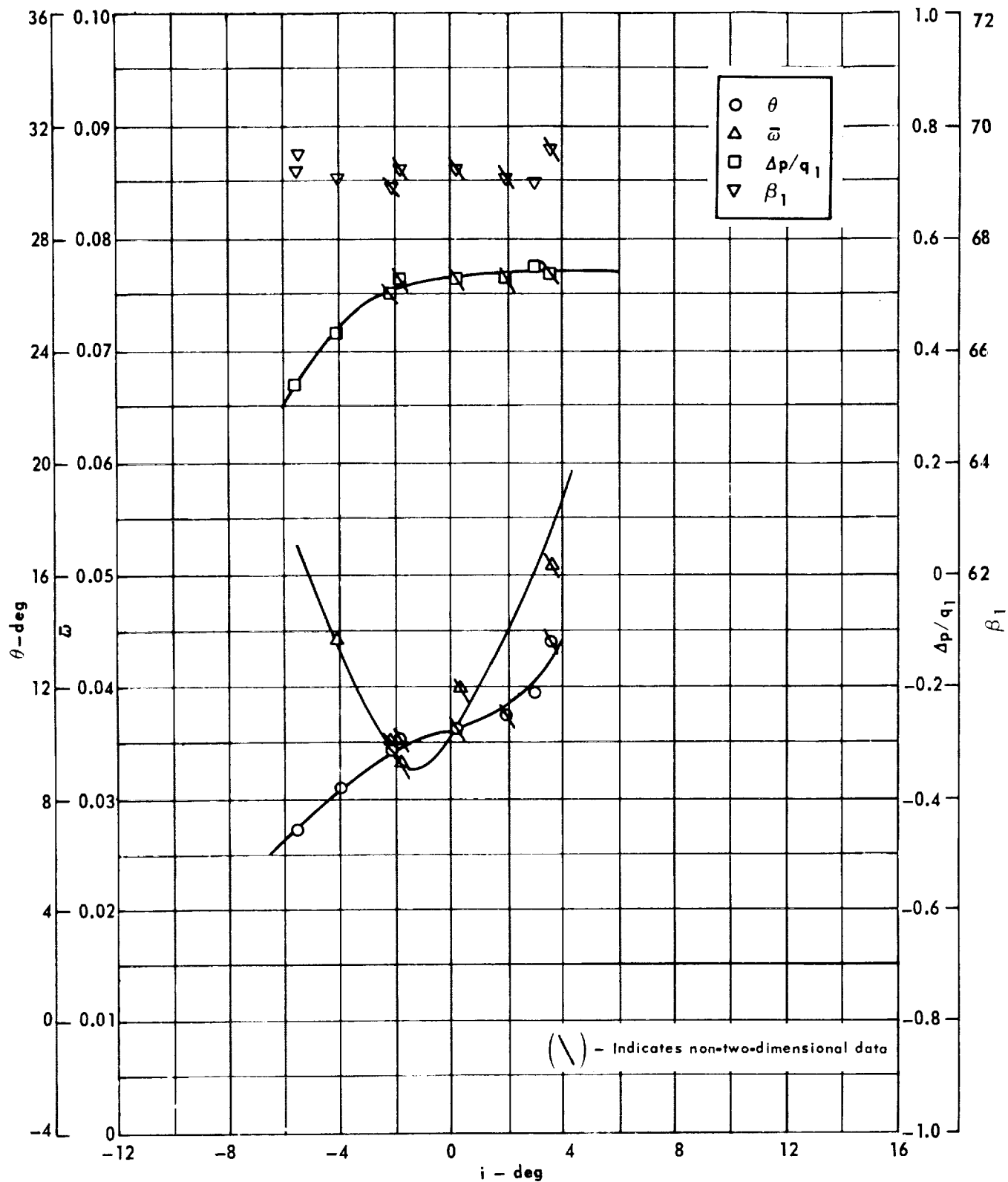
Figure 79. - Cascade characteristics as functions of incidence.



Cascade configuration: $\beta_{1N} = 70$, $\sigma = 1.00$
 Double circular-arc profile: $\phi = 20$, $r/c = 0.06$

(b) D, θ^*/s , K, δ°

Figure 79. - Concluded.

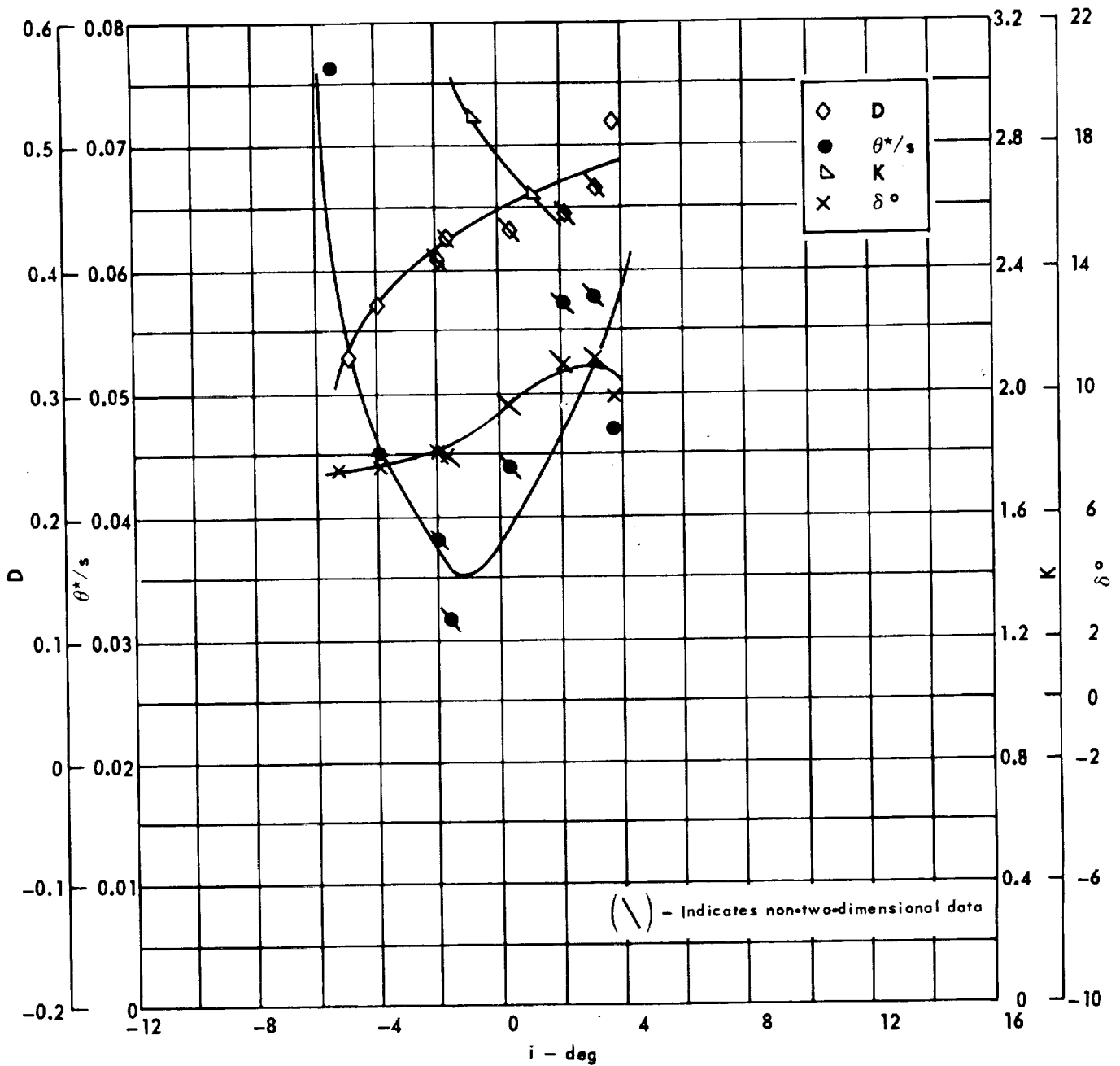


Cascade configuration: $\beta_{1N} = 70$, $\sigma = 1.50$

Double circular-arc profile: $\phi = 20$, $t/c = 0.06$

(a) $\theta, \bar{\omega}, \Delta p/q_1, \beta_1$

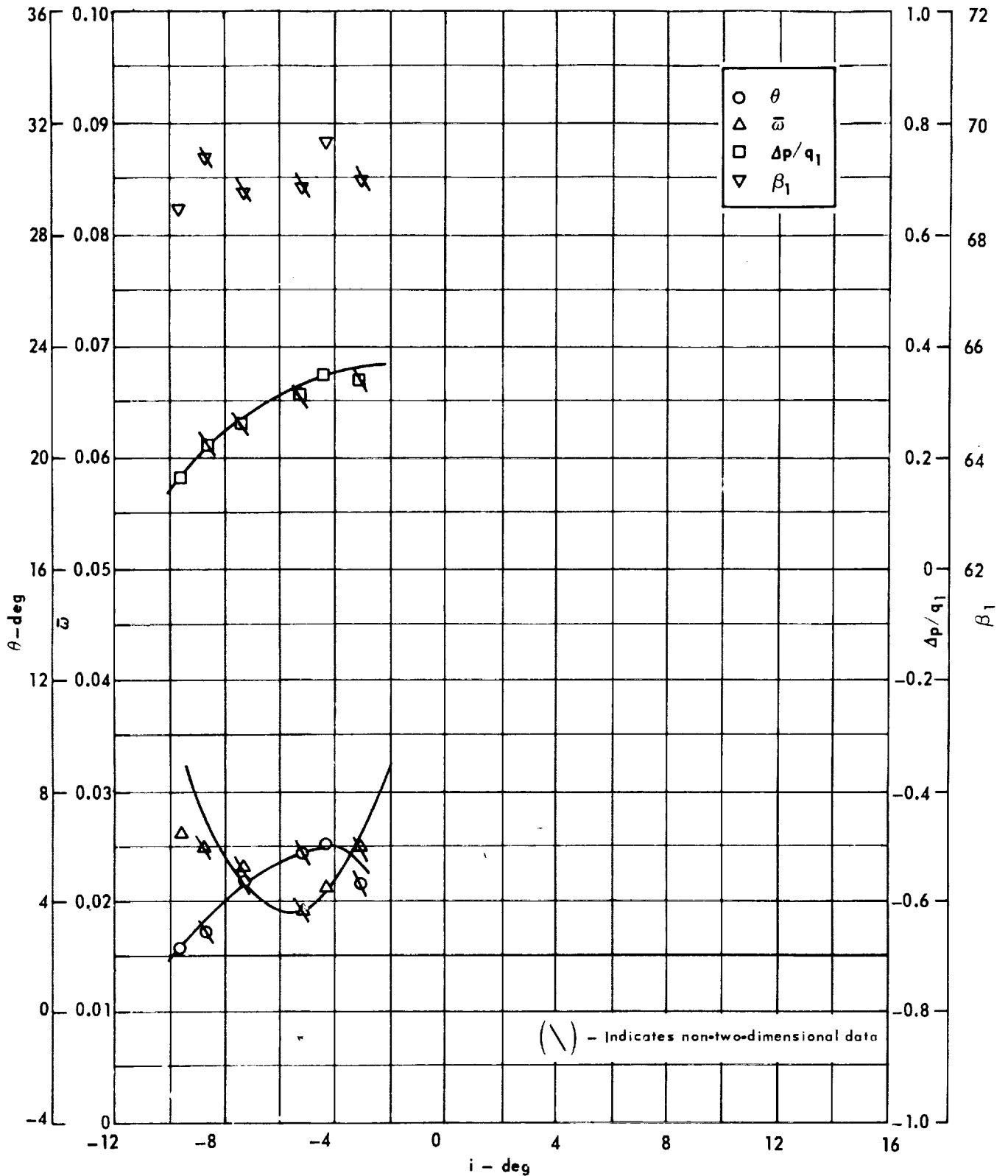
Figure 80. - Cascade characteristics as functions of incidence.



Cascade configuration: $\beta_{1N} = 70, \sigma = 1.50$
 Double circular-arc profile: $\phi = 20, t/c = 0.06$

(b) D, θ^*/s , K, δ°

Figure 80 . - Concluded.

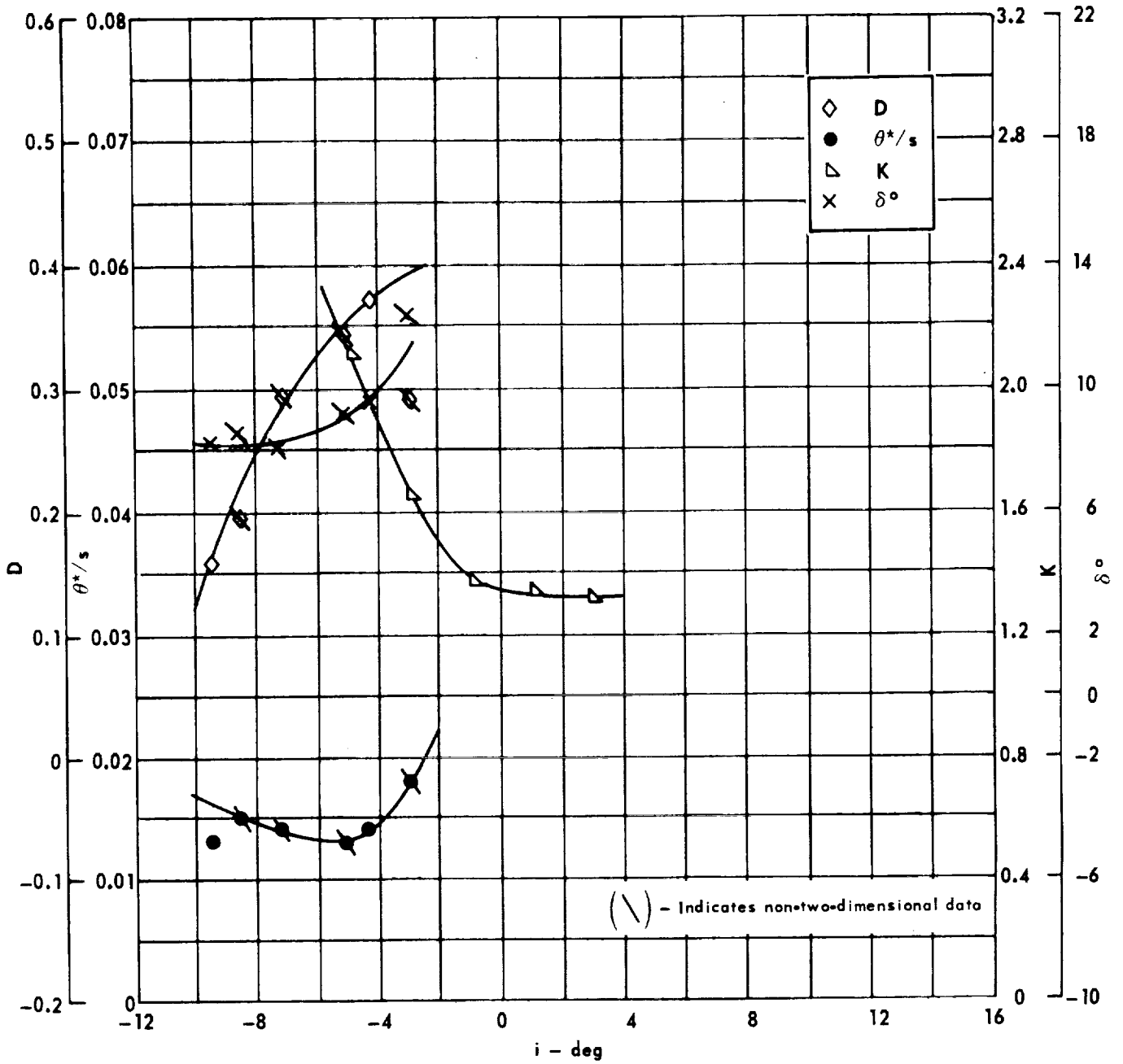


Cascade configuration: $\beta_{1N} = 70, \sigma = 0.75$

Double circular-arc profile: $\phi = 20, t/c = 0.10$

(a) $\theta, \bar{\omega}, \Delta p/q_1, \beta_1$

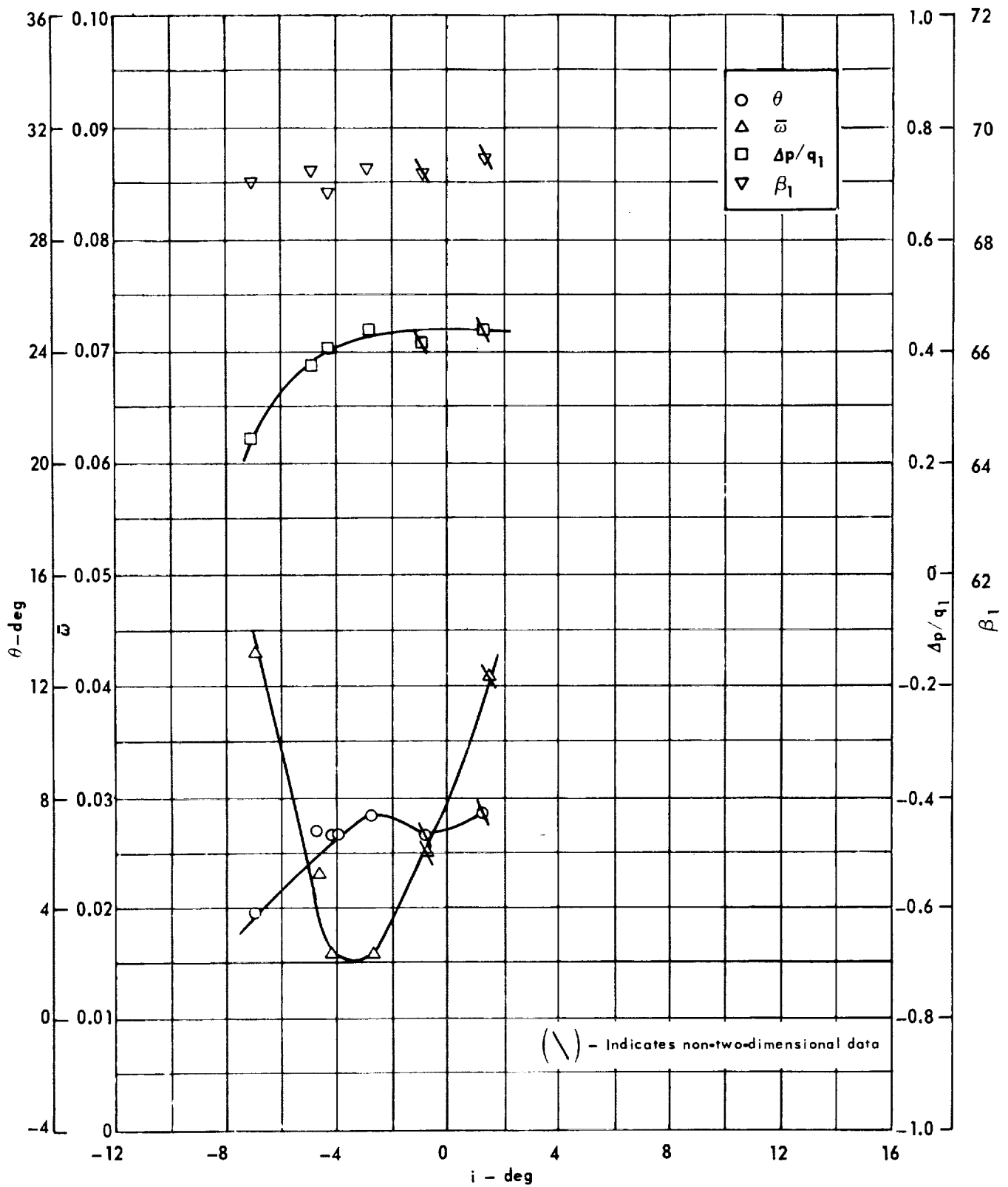
Figure 81 . - Cascade characteristics as functions of incidence.



Cascade configuration: $\beta_{1N} = 70$, $\sigma = 0.75$
 Double circular-arc profile: $\phi = 20$, $t/c = 0.10$

(b) D, θ^*/s , K, δ°

Figure 81. - Concluded.

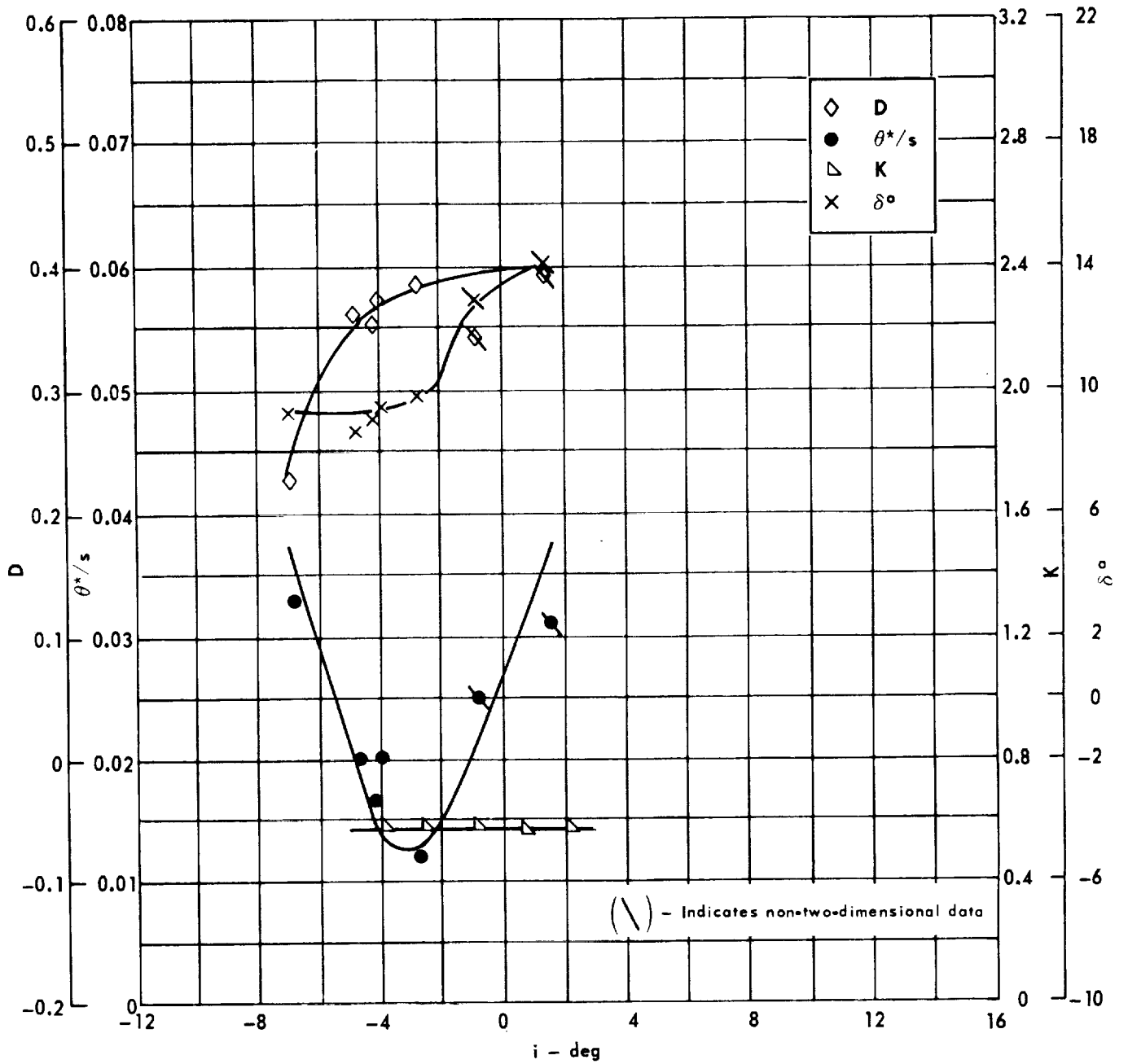


Cascade configuration: $\beta_{1N} = 70$, $\sigma = 1.00$

Double circular-arc profile: $\phi = 20$, $t/c = 0.10$

(a) $\theta, \omega, \Delta p/q_1, \beta_1$

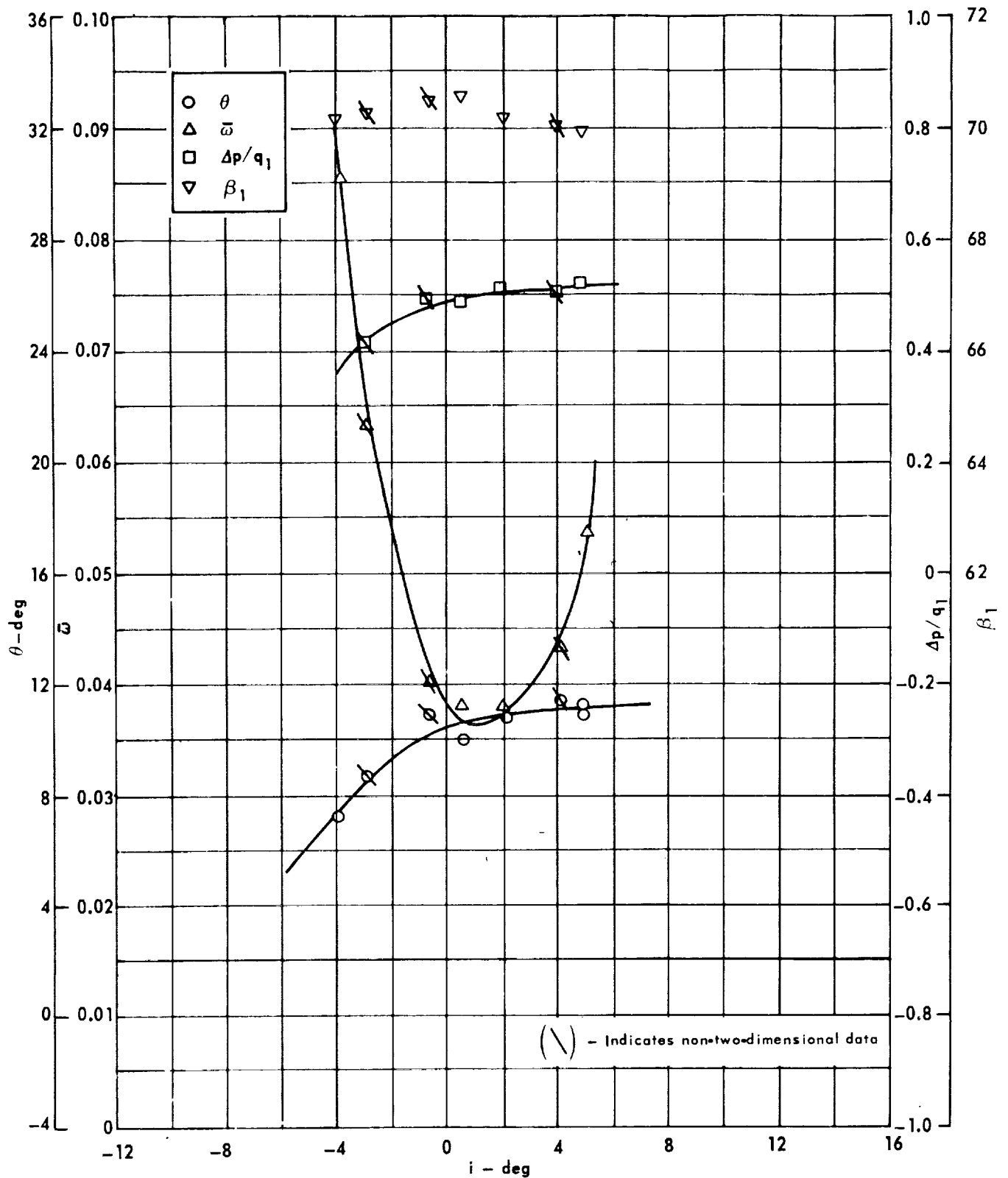
Figure 82. - Cascade characteristics as functions of incidence.



Cascade configuration : $\beta_{1N} = 70, \sigma = 1.00$
 Double circular-arc profile : $\phi = 20, r/c = 0.10$

(b) D, θ^*/s , K, δ°

Figure 82 . - Concluded.

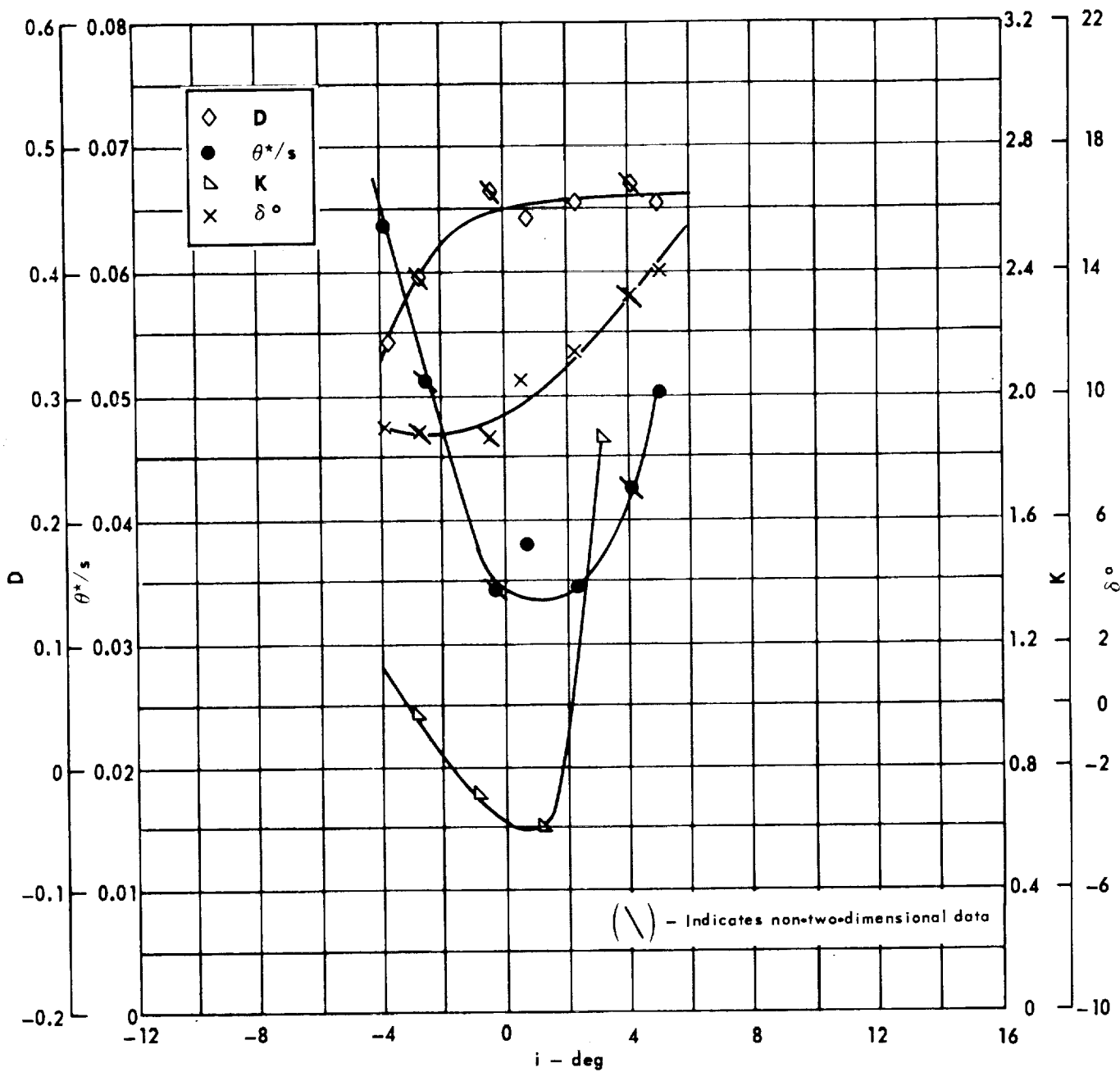


Cascade configuration : $\beta_{1N} = 70, \sigma = 1.50$

Double circular-arc profile : $\phi = 20, t/c = 0.10$

(a) $\theta, \bar{\omega}, \Delta p/q_1, \beta_1$

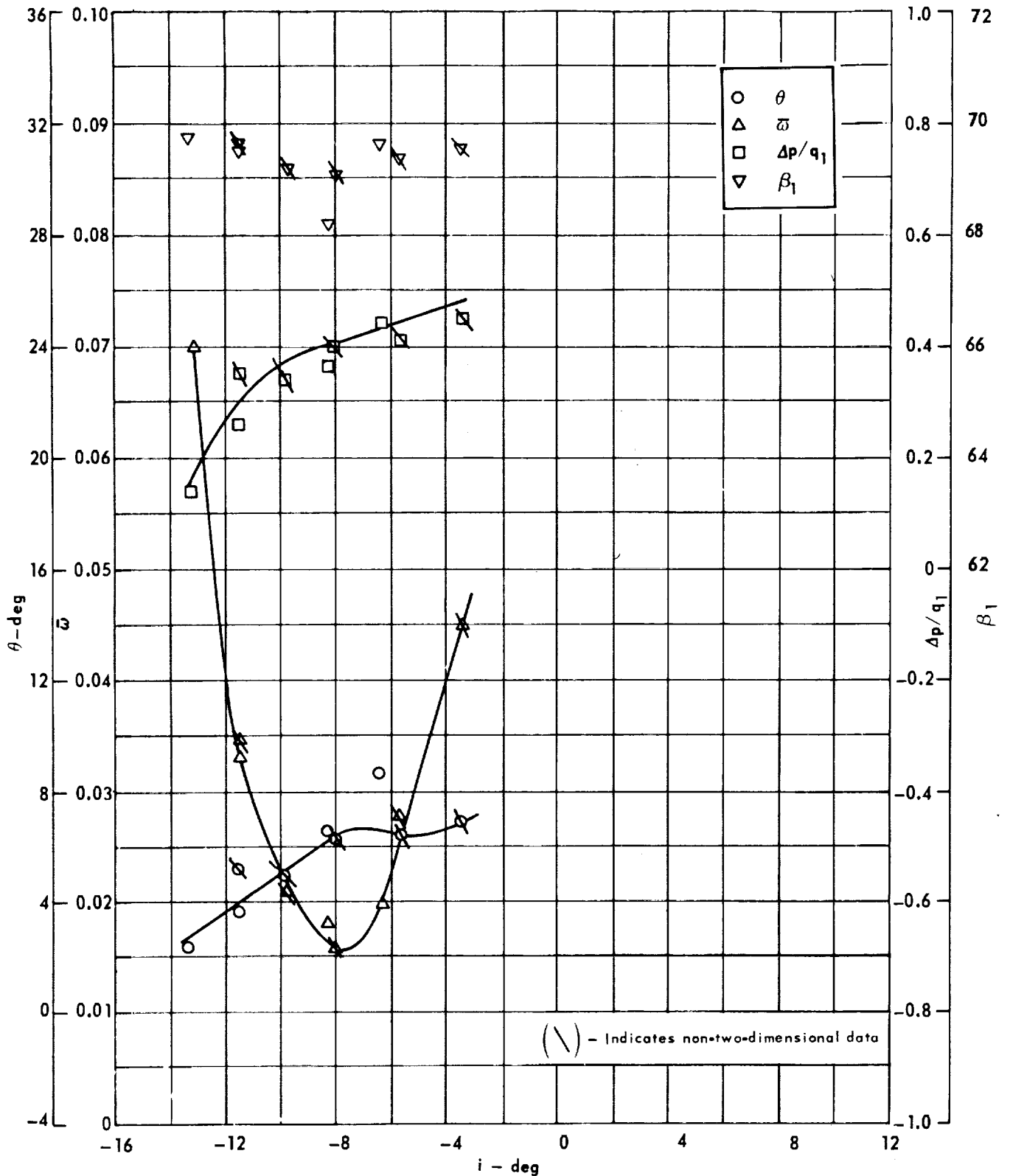
Figure 83 . - Cascade characteristics as functions of incidence.



Cascade configuration: $\beta_{1N} = 70$, $\sigma = 1.50$
 Double circular-arc profile: $\phi = 20$, $t/c = 0.10$

(b) $D, \theta^*/s, K, \delta^\circ$

Figure 83. - Concluded.

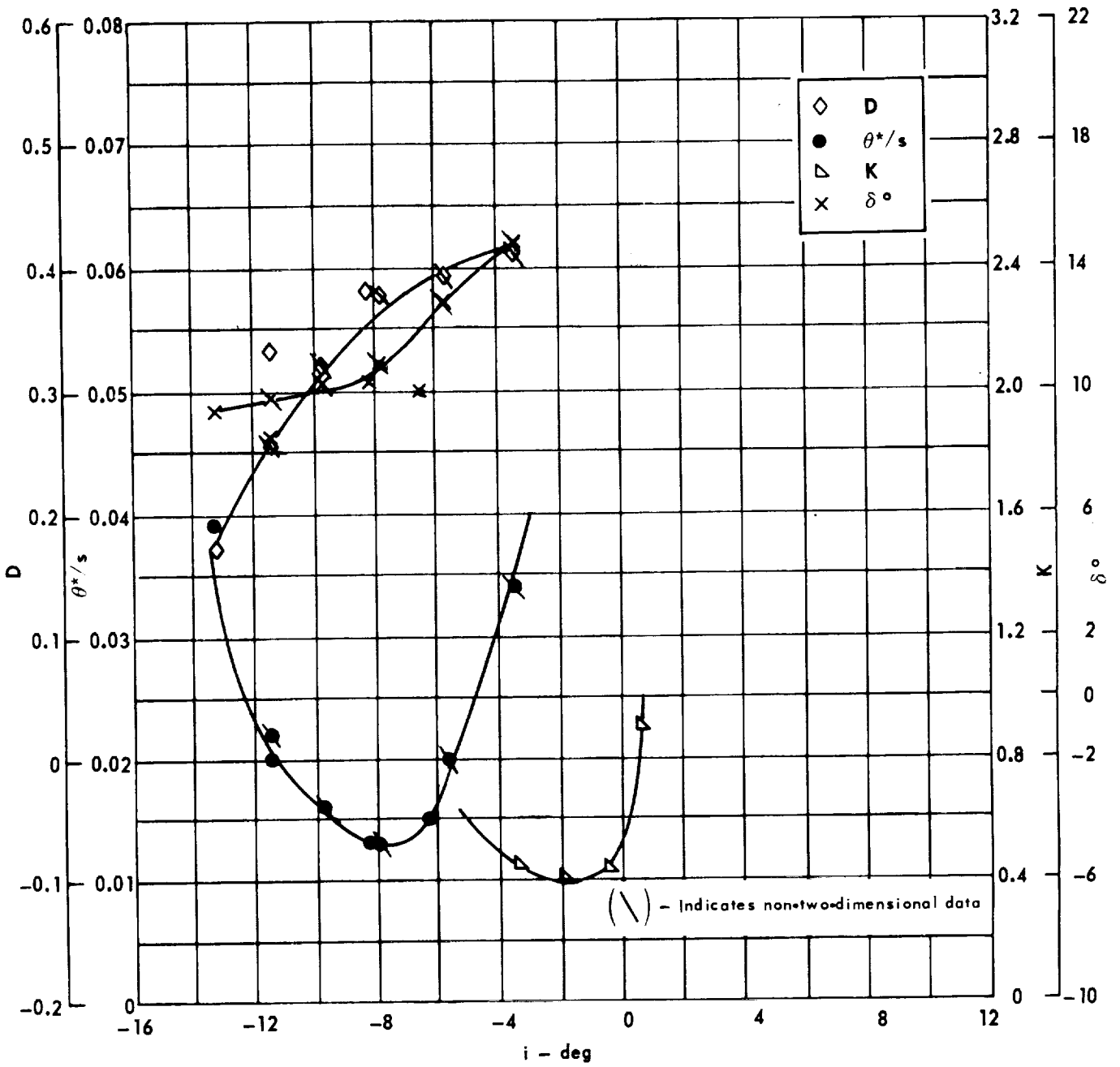


Cascade configuration : $\beta_{1N} = 70$, $\sigma = 0.75$

Double circular-arc profile : $\phi = 25$, $t/c = 0.06$

(a) $\theta, \omega, \Delta p/q_1, \beta_1$

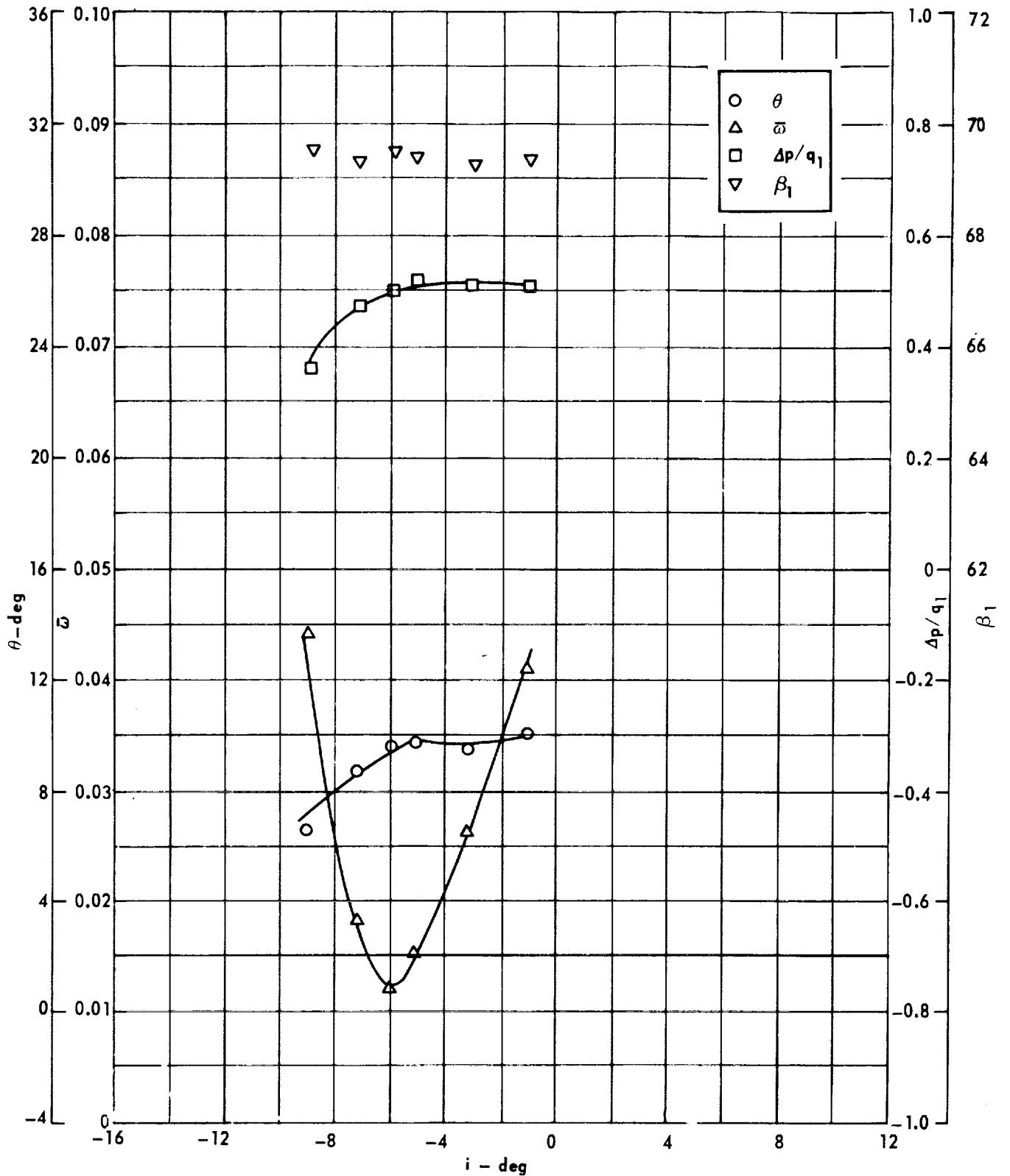
Figure 84 . - Cascade characteristics as functions of incidence.



Cascade configuration: $\beta_{1N} = 70, \sigma = 0.75$
 Double circular-arc profile: $\phi = 25, t/c = 0.06$

(b) D, θ^*/s , K, δ°

Figure 84 . - Concluded.

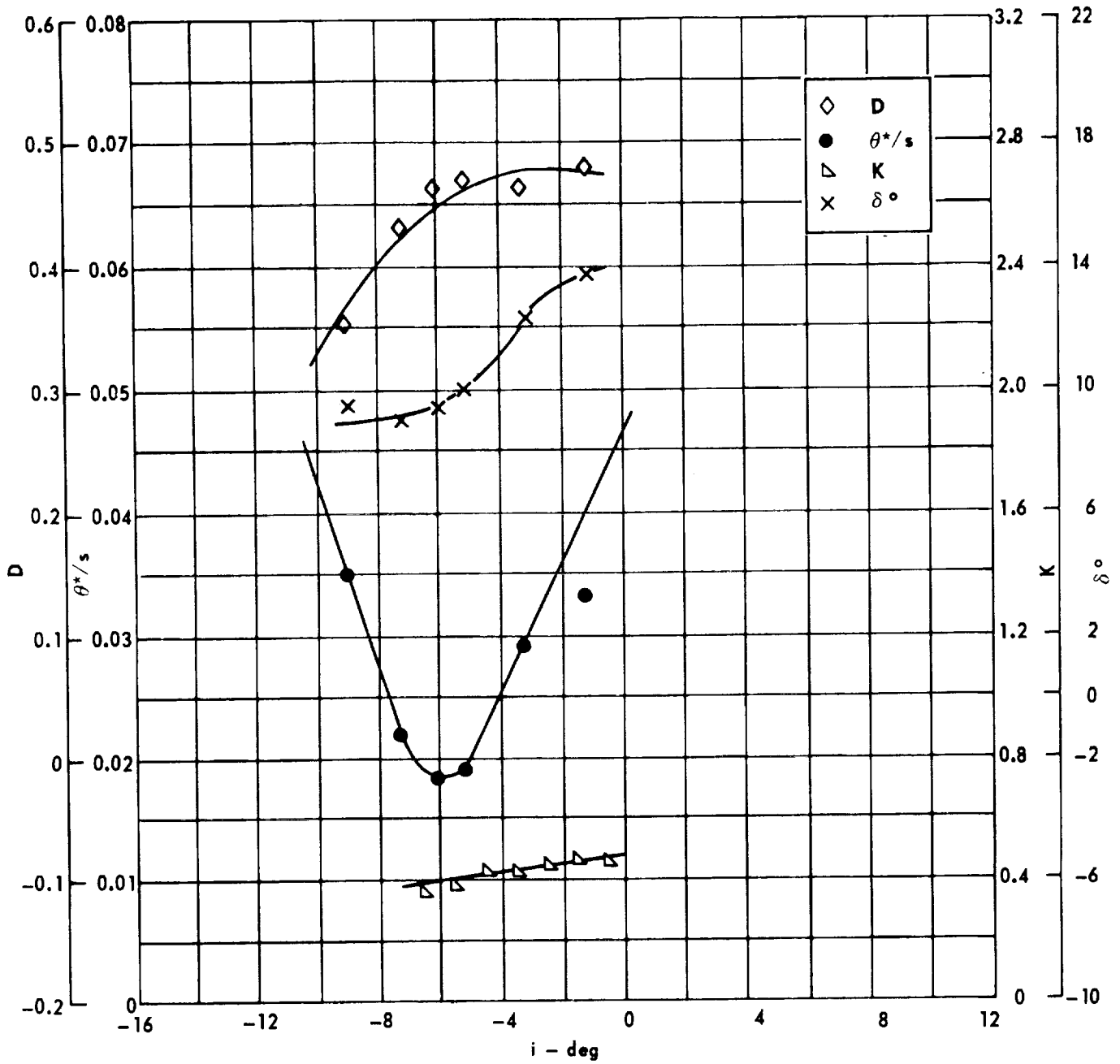


Cascade configuration : $\beta_{1N} = 70$, $\sigma = 1.00$

Double circular-arc profile : $\phi = 25$, $t/c = 0.06$

(a) $\theta, \bar{\omega}, \Delta p/q_1, \beta_1$

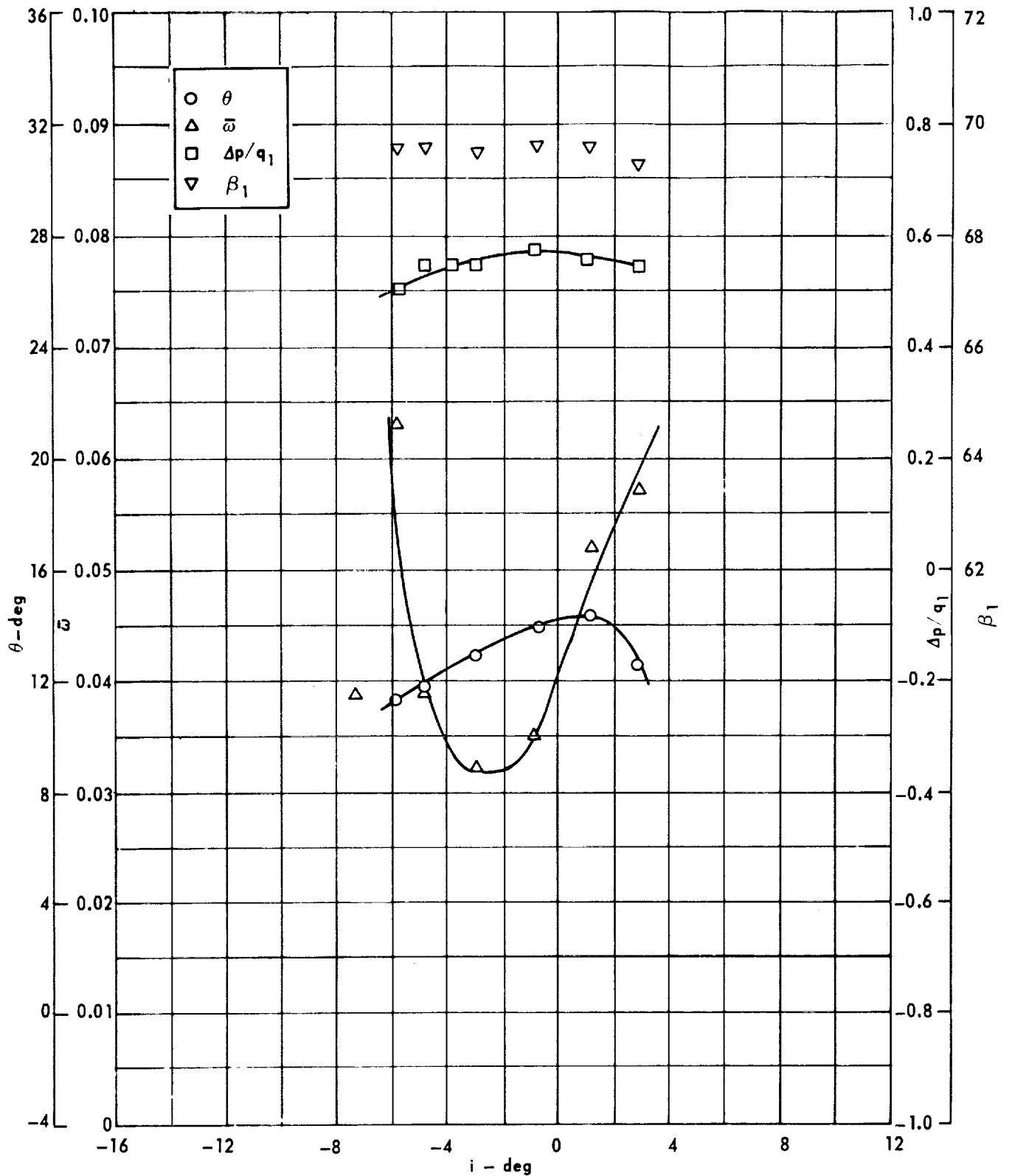
Figure 85. - Cascade characteristics as functions of incidence.



Cascade configuration: $\beta_{1N} = 70$, $\sigma = 1.00$
 Double circular-arc profile: $\phi = 25$, $t/c = 0.06$

(b) $D, \theta^*/s, K, \delta^\circ$

Figure 85. - Concluded.

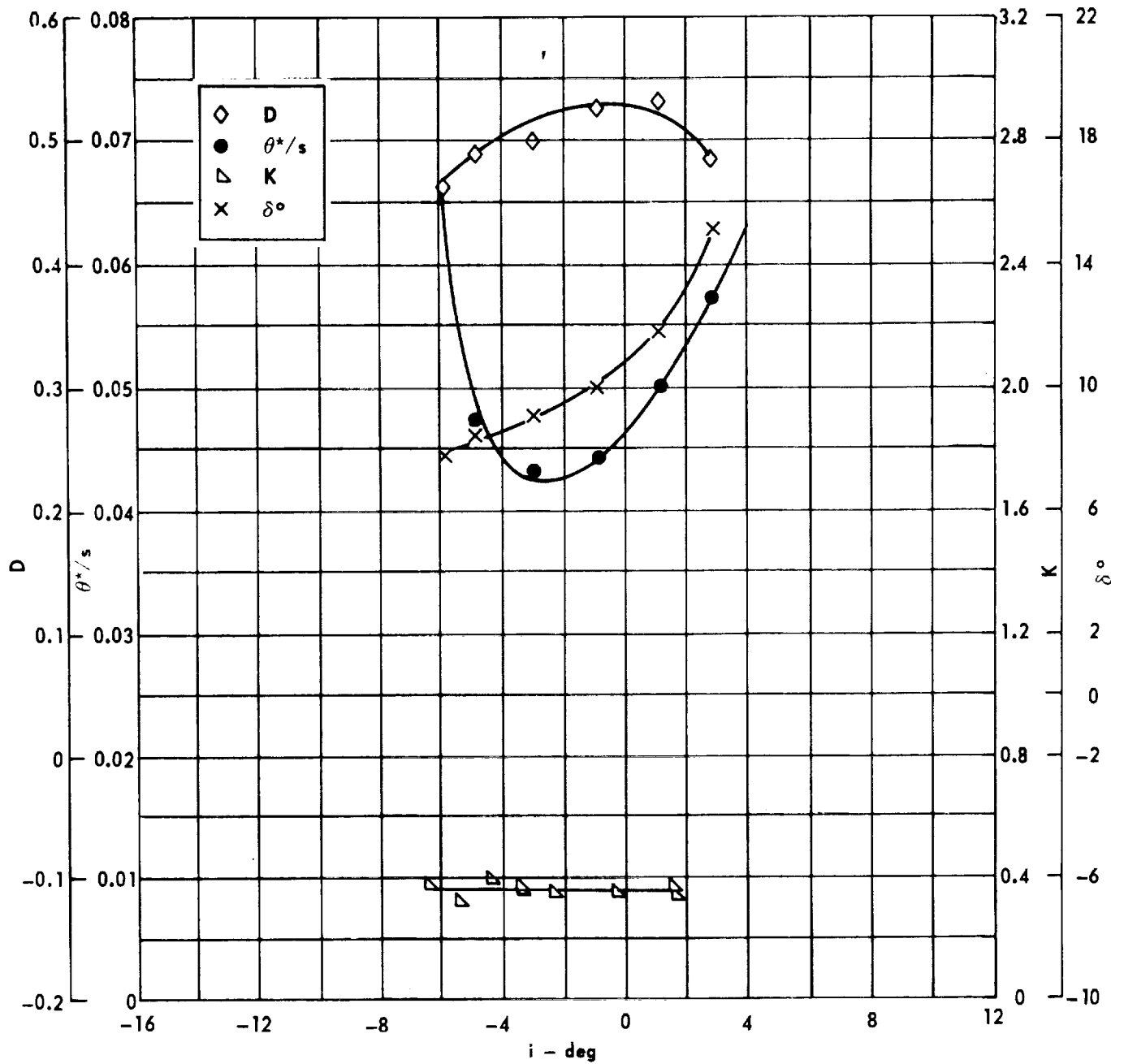


Cascade configuration : $\beta_{1N} = 70$, $\sigma = 1.50$

Double circular-arc profile : $\phi = 25$, $t/c = 0.06$

(a) $\theta, \bar{\omega}, \Delta p/q_1, \beta_1$

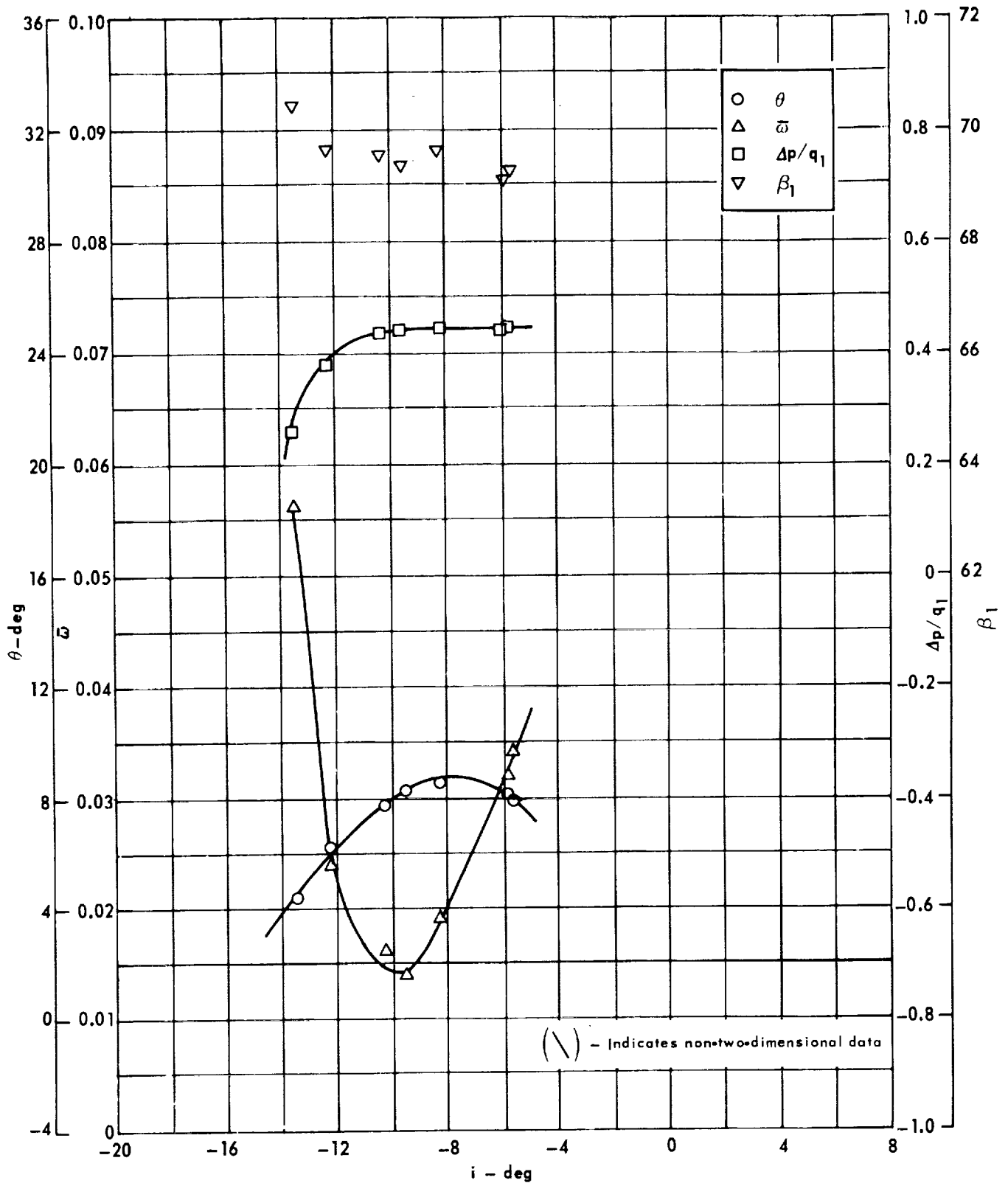
Figure 86 . - Cascade characteristics as functions of incidence.



Cascade configuration : $\beta_{1N} = 70, \sigma = 1.50$
 Double circular-arc profile : $\phi = 25, t/c = 0.06$

(b) D, θ^*/s , K, δ°

Figure 86. - Concluded.

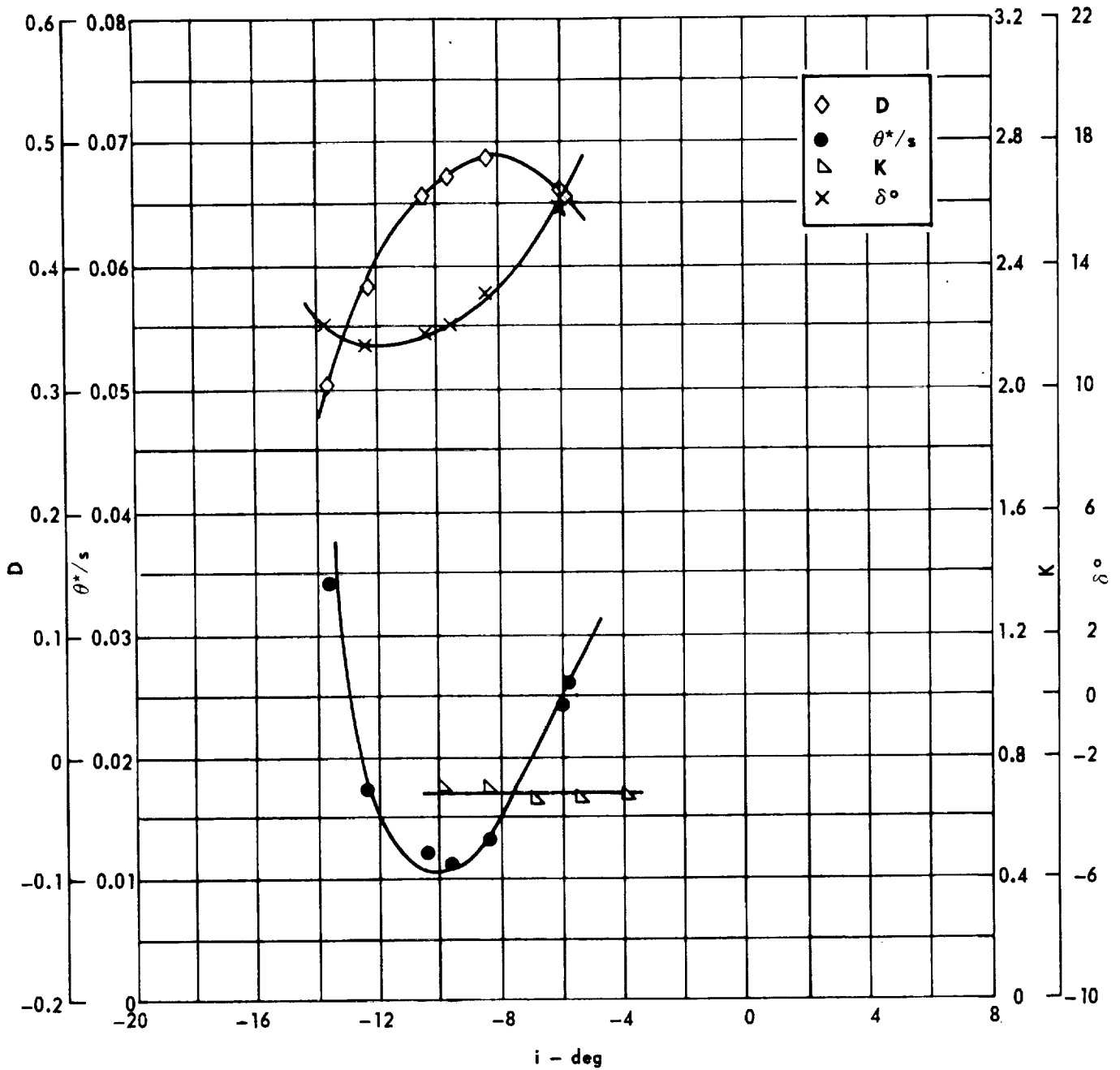


Cascade configuration: $\beta_{1N} = 70, \sigma = 0.75$

Double circular-arc profile: $\phi = 30, t/c = 0.06$

(a) $\theta, \bar{\omega}, \Delta p/q_1, \beta_1$

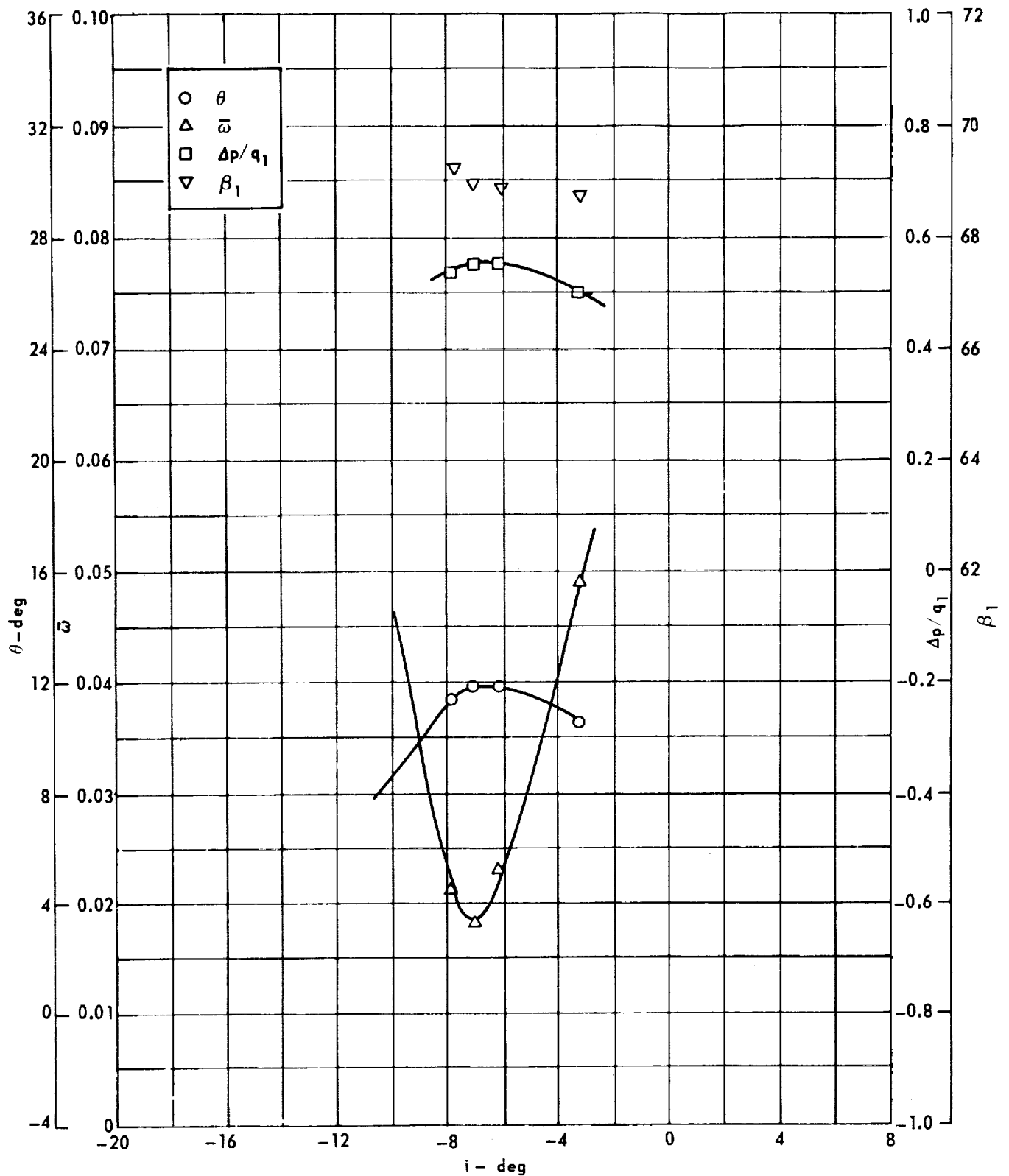
Figure 87. - Cascade characteristics as functions of incidence.



Cascade configuration : $\beta_{1N} = 70, \sigma = 0.75$
 Double circular-arc profile : $\phi = 30, t/c = 0.06$

(b) D, θ^*/s , K, δ°

Figure 87. - Concluded.

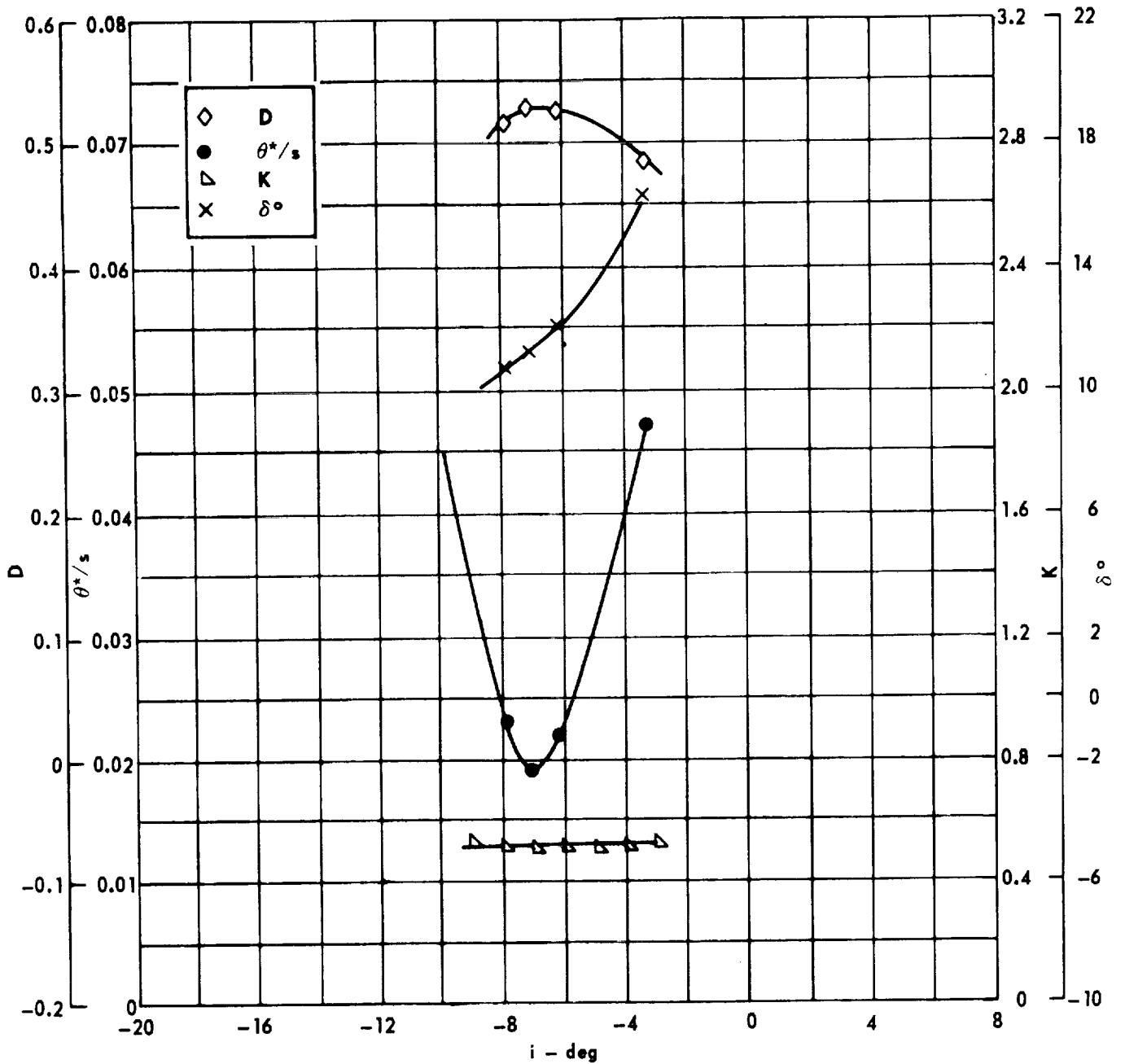


Cascade configuration : $\beta_{1N} = 70, \sigma = 1.00$

Double circular-arc profile : $\phi = 30, t/c = 0.06$

(a) $\theta, \bar{\omega}, \Delta p/q_1, \beta_1$

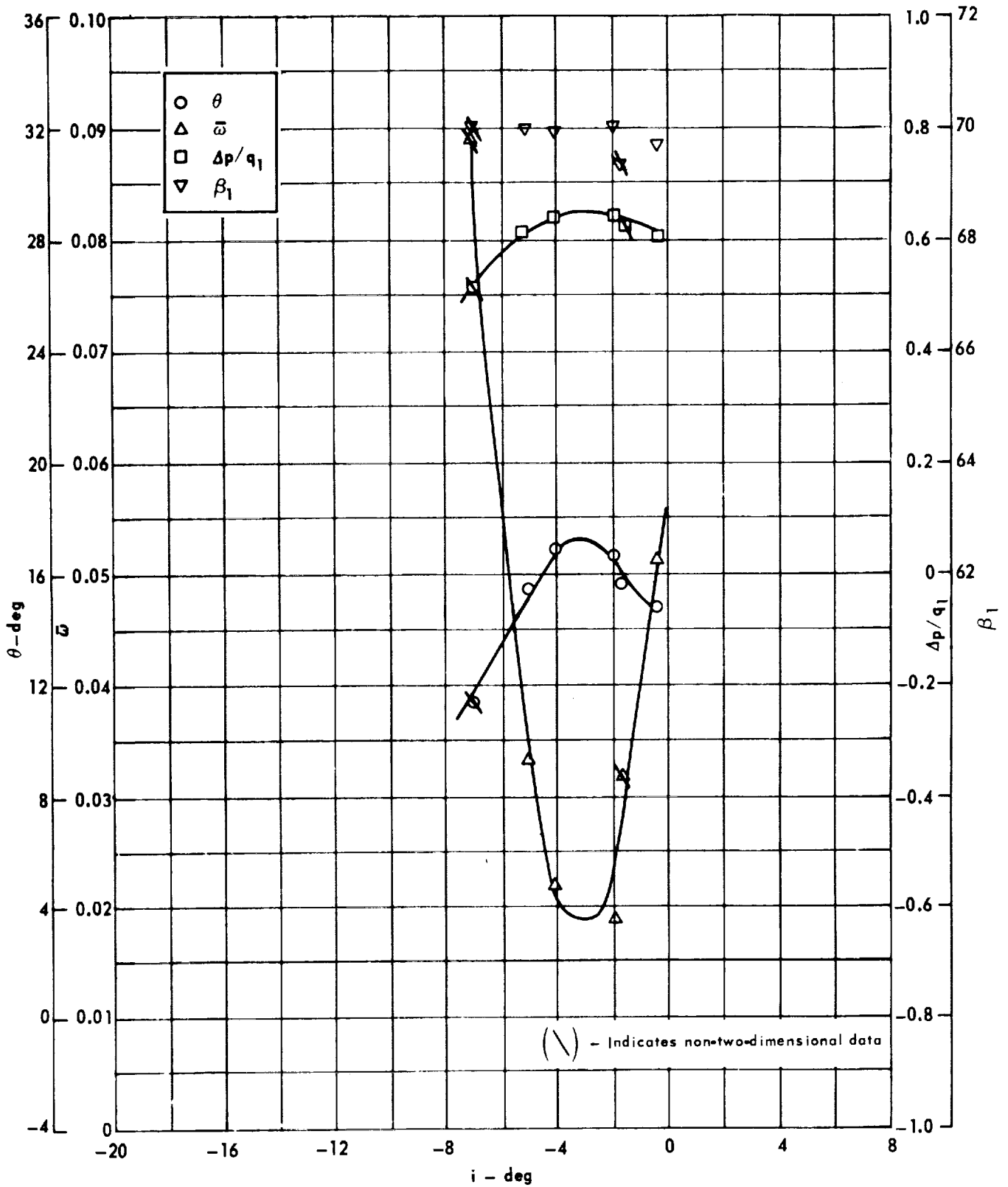
Figure 88. - Cascade characteristics as functions of incidence.



Cascade configuration : $\beta_{1N} = 70$, $\sigma = 1.00$
 Double circular-arc profile : $\phi = 30$, $t/c = 0.06$

(b) D, θ^*/s , K, δ°

Figure 88 . - Concluded.

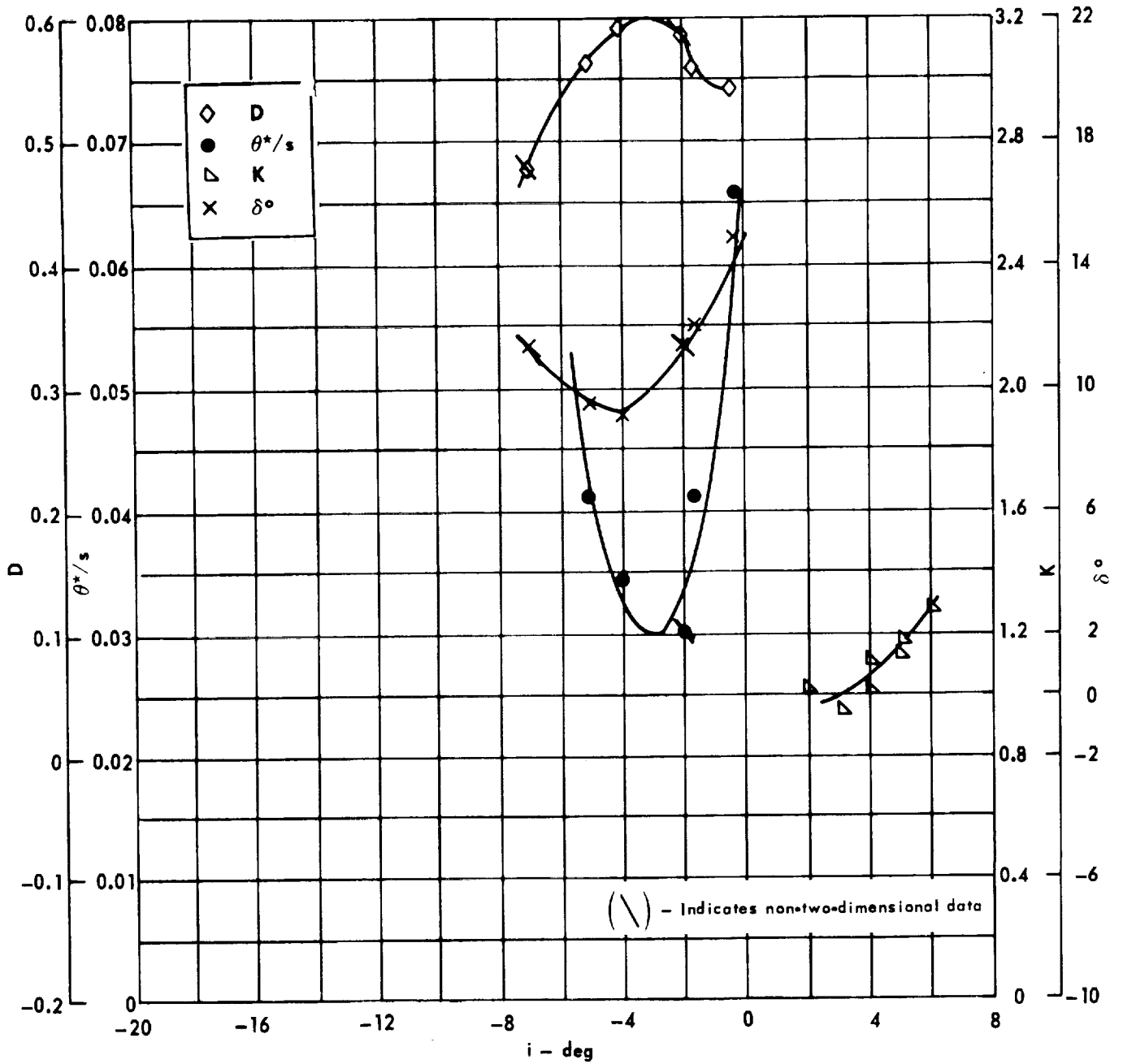


Cascade configuration: $\beta_{1N} = 70$, $\sigma = 1.50$

Double circular-arc profile: $\phi = 30$, $t/c = 0.06$

(a) $\theta, \bar{\omega}, \Delta p/q_1, \beta_1$

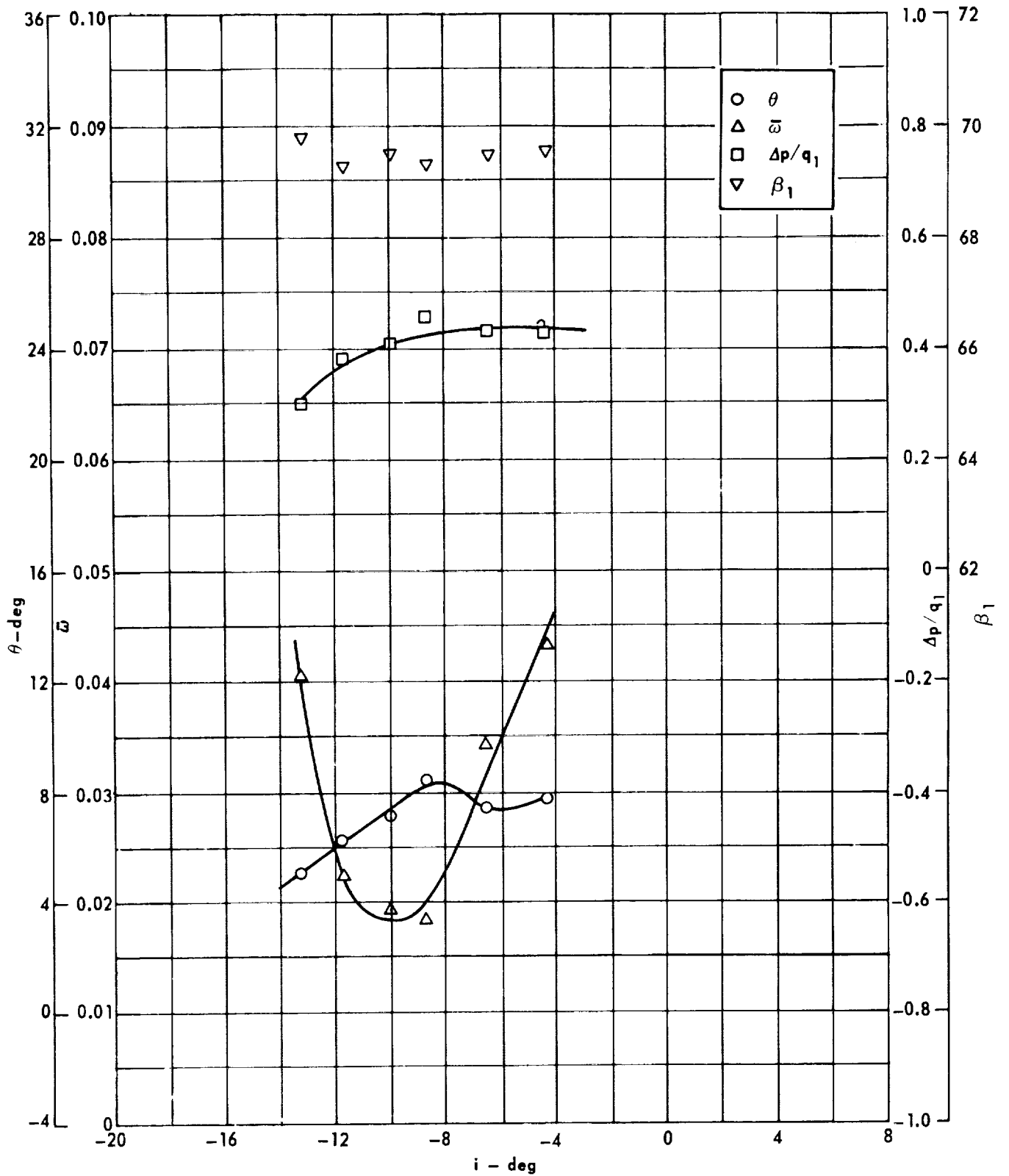
Figure 89. - Cascade characteristics as functions of incidence.



Cascade configuration : $\beta_{1N} = 70$, $\sigma = 1.50$
 Double circular-arc profile : $\phi = 30$, $t/c = 0.06$

(b) D, θ^*/s , K, δ°

Figure 89 . - Concluded.

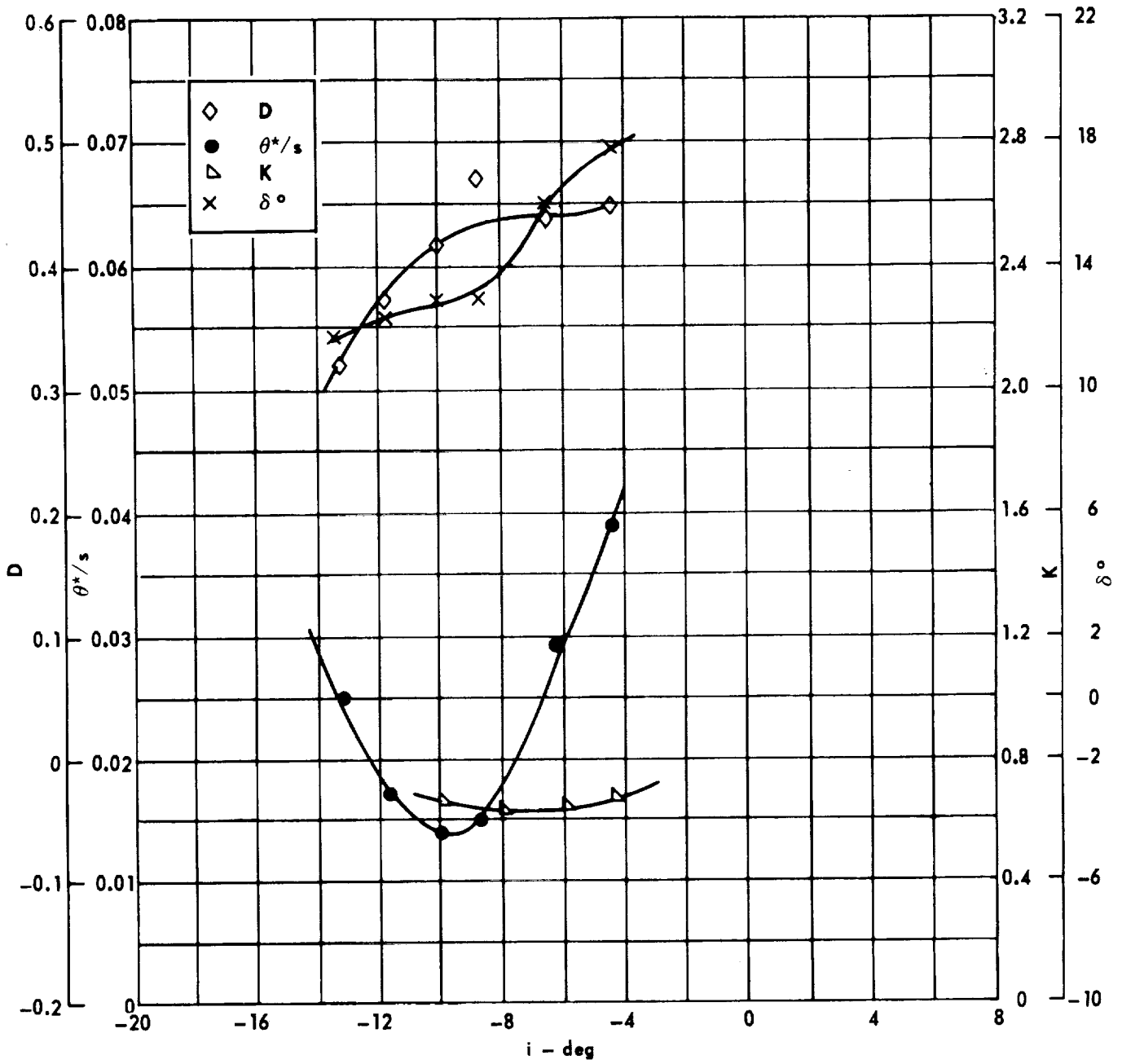


Cascade configuration : $\beta_{1N} = 70$, $\sigma = 0.75$

Double circular-arc profile : $\phi = 30$, $t/c = 0.10$

(a) $\theta, \bar{\omega}, \Delta p/q_1, \beta_1$

Figure 90 . - Cascade characteristics as functions of incidence.

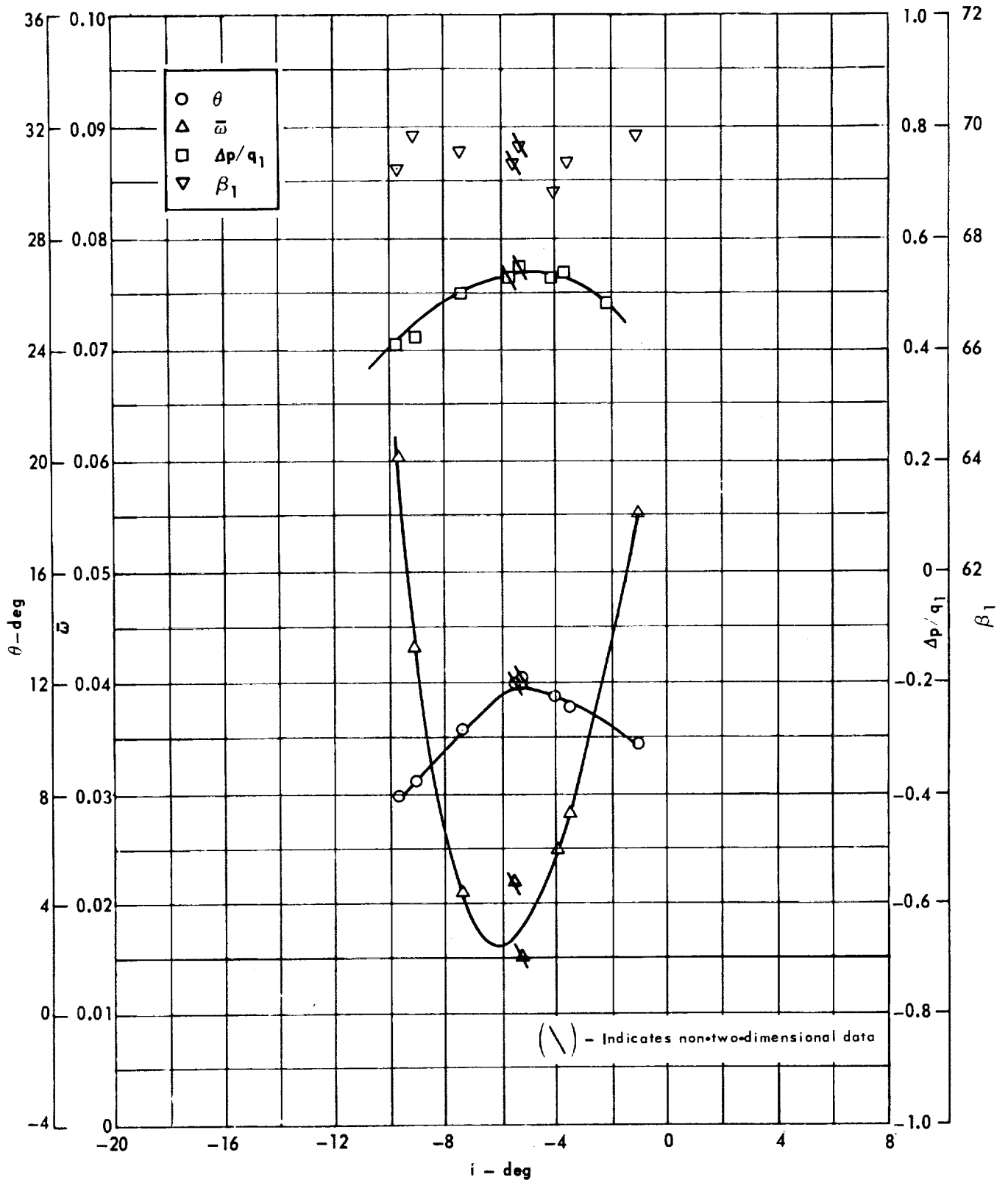


Cascade configuration: $\beta_{1N} = 70, \sigma = 0.75$

Double circular-arc profile: $\phi = 30, t/c = 0.10$

(b) $D, \theta^*/s, K, \delta^\circ$

Figure 90. - Concluded.

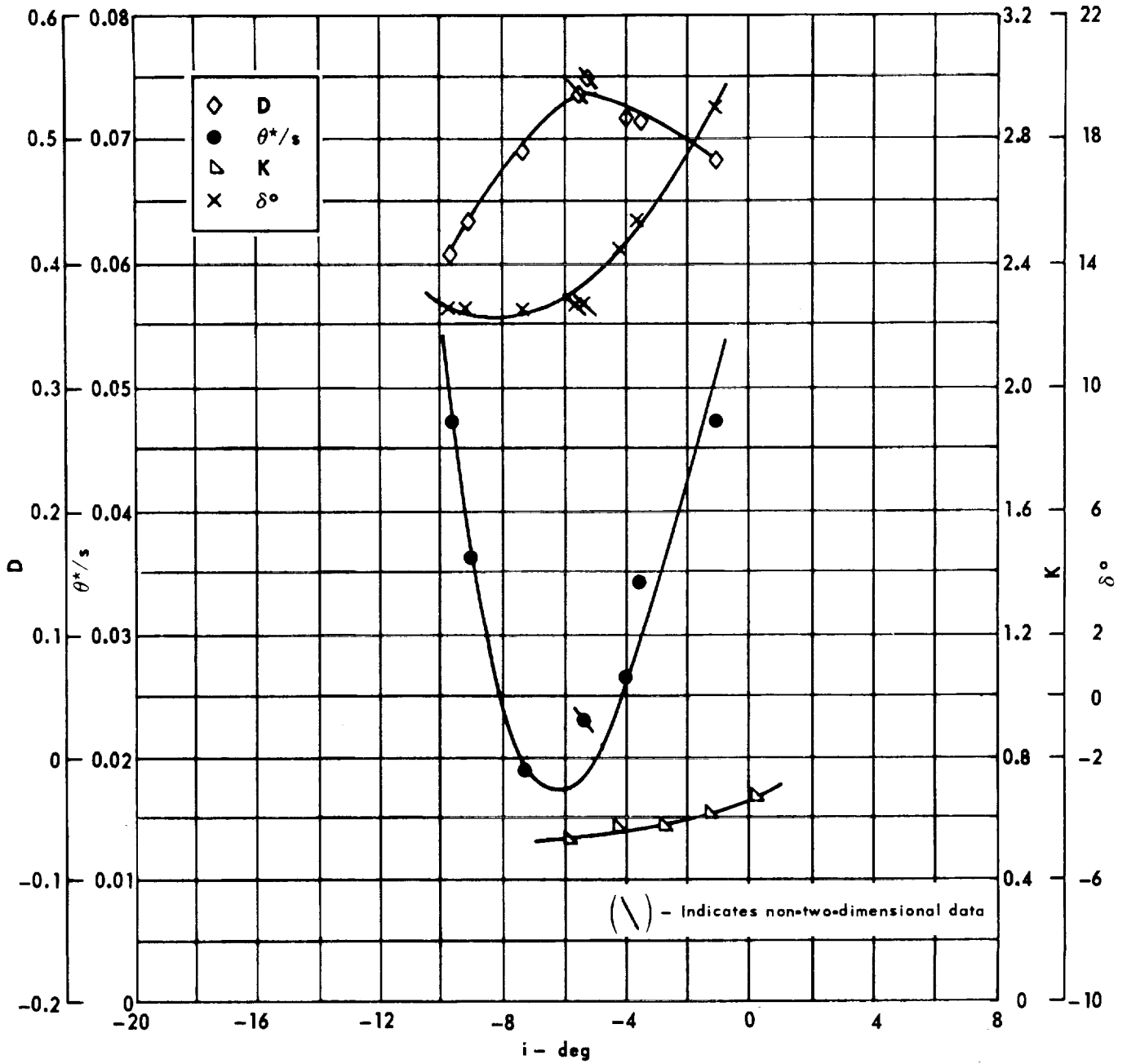


Cascade configuration: $\beta_{1N} = 70, \sigma = 1.00$

Double circular-arc profile: $\phi = 30, t/c = 0.10$

(a) $\theta, \bar{\omega}, \Delta p/q_1, \beta_1$

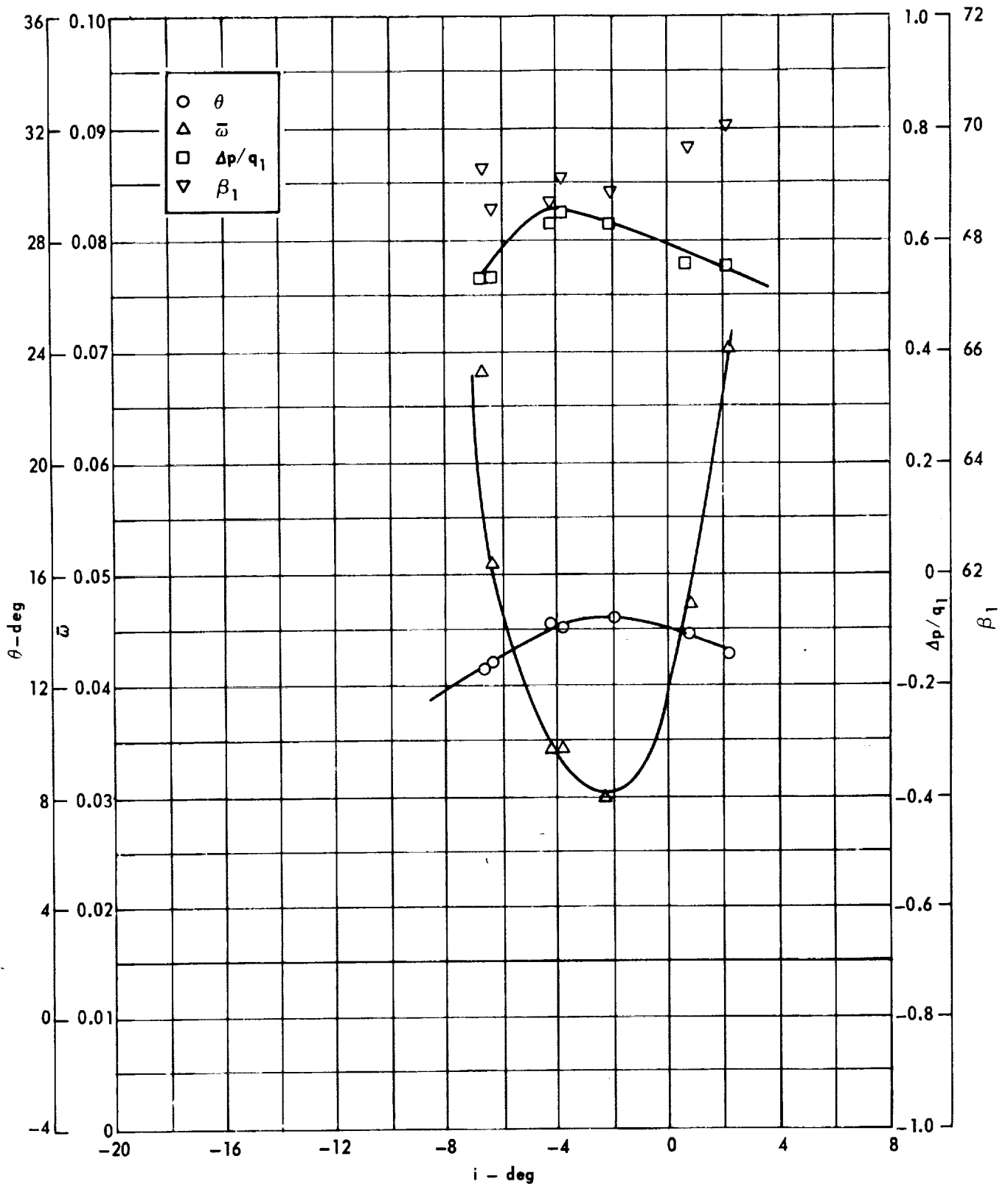
Figure 91. - Cascade characteristics as functions of incidence.



Cascade configuration : $\beta_{1N} = 70, \sigma = 1.00$
 Double circular-arc profile : $\phi = 30, t/c = 0.10$

(b) $D, \theta^*/s, K, \delta^\circ$

Figure 91. - Concluded.

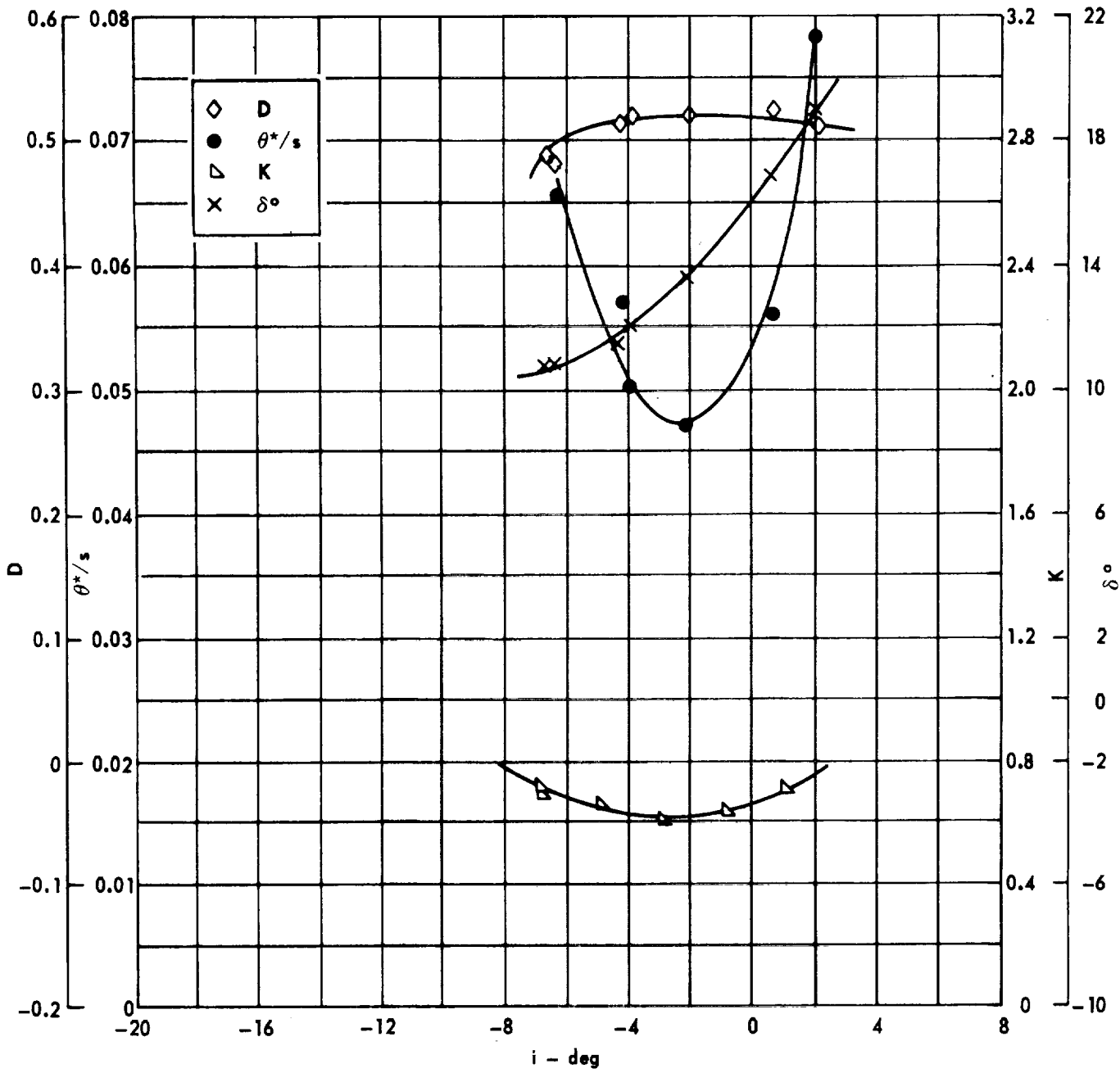


Cascade configuration : $\beta_{1N} = 70, \sigma = 1.50$

Double circular-arc profile : $\phi = 30, t/c = 0.10$

(a) $\theta, \bar{\omega}, \Delta p/q_1, \beta_1$

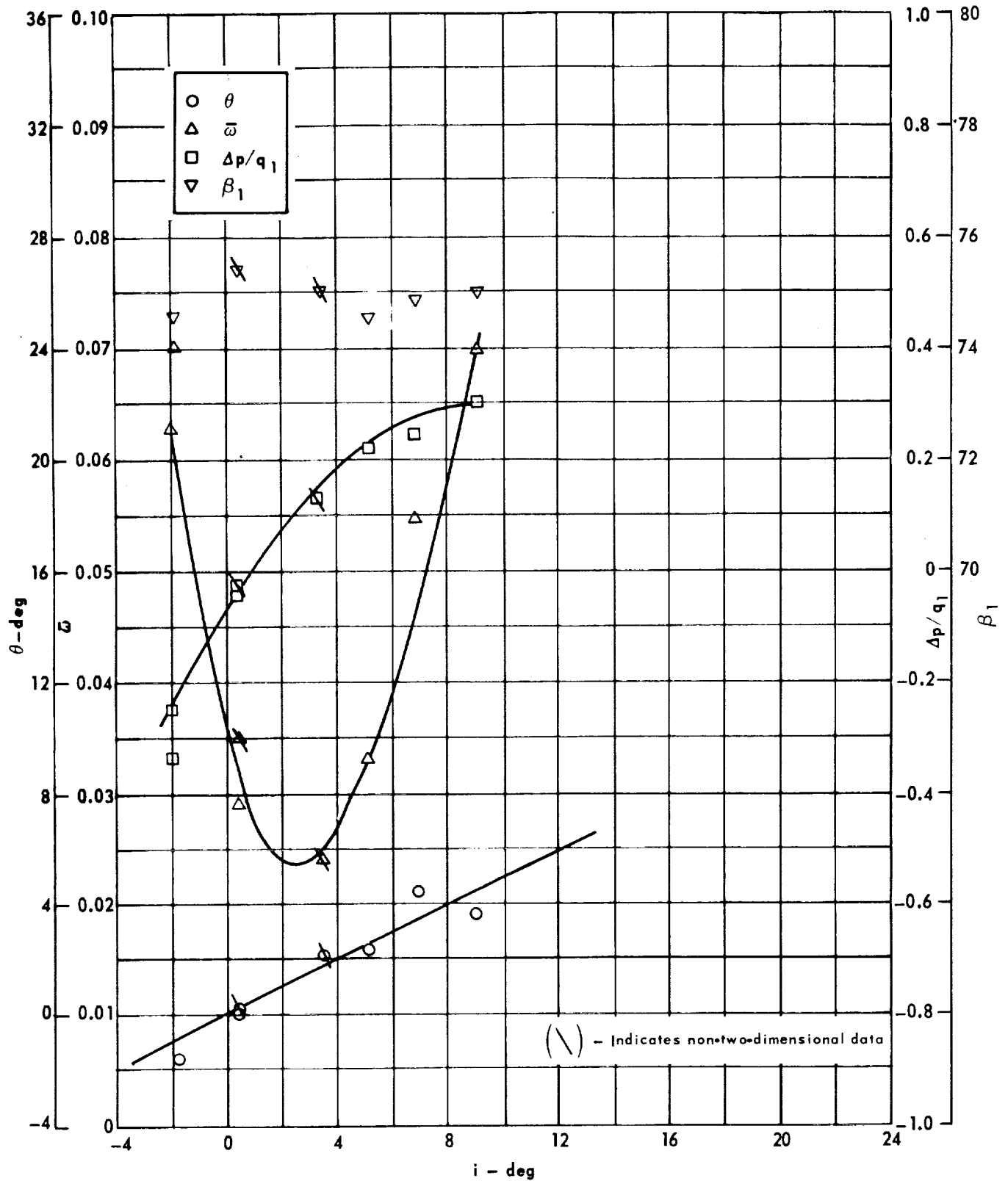
Figure 92. - Cascade characteristics as functions of incidence.



Cascade configuration : $\beta_{1N} = 70, \sigma = 1.50$
 Double circular-arc profile : $\phi = 30, t/c = 0.10$

(b) D, θ^*/s , K, δ°

Figure 92. - Concluded.

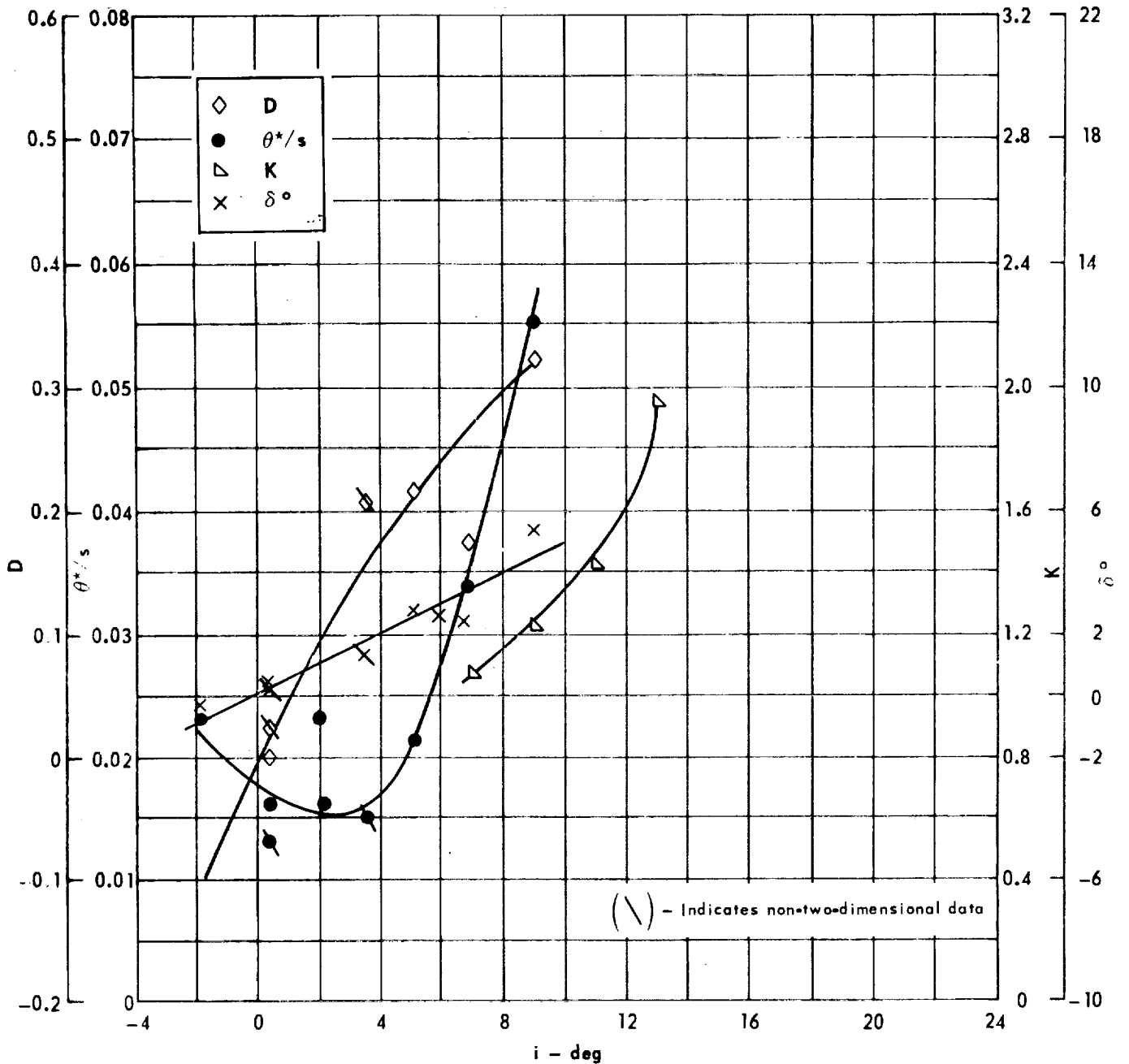


Cascade configuration: $\beta_{1N} = 75$, $\sigma = 0.75$

Double circular-arc profile: $\phi = 0$, $t/c = 0.06$

(a) $\theta, \bar{\omega}, \Delta p/q_1, \beta_1$

Figure 93 . - Cascade characteristics as functions of incidence.

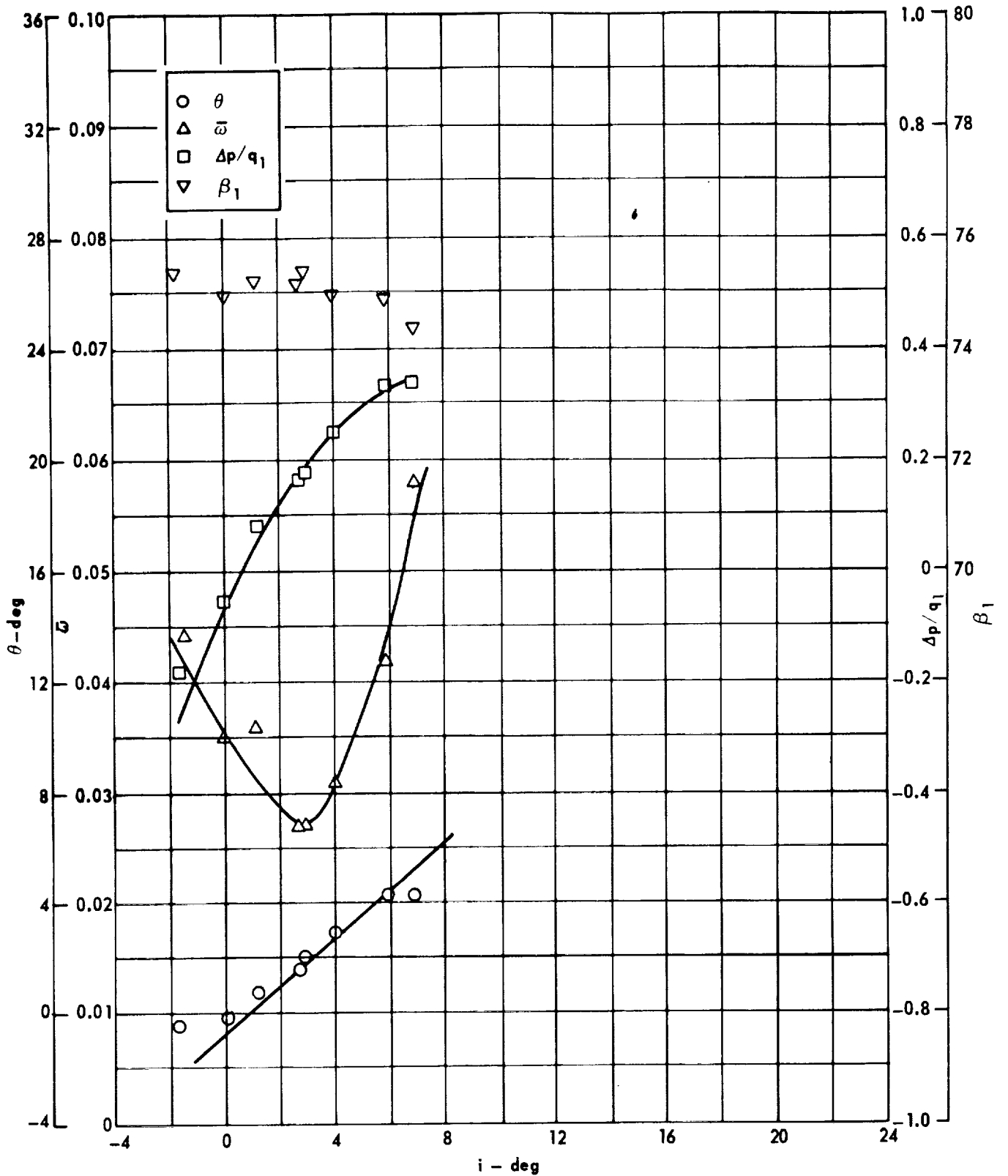


Cascade configuration: $\beta_{1N} = 75, \sigma = 0.75$

Double circular-arc profile: $\phi = 0, t/c = 0.06$

(b) D, θ^*/s , K, δ°

Figure 93 . - Concluded.

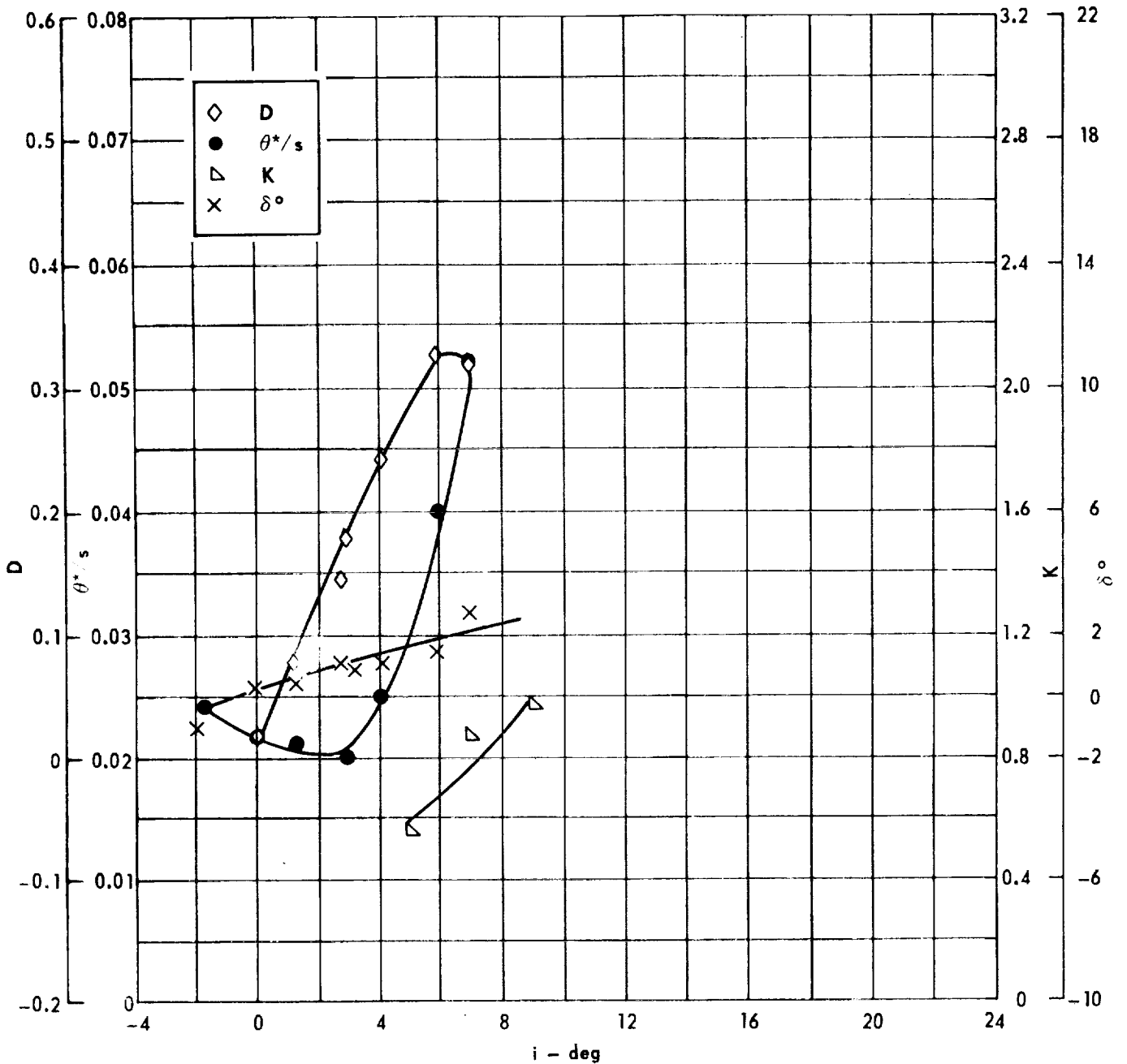


Cascade configuration: $\beta_{1N} = 75$, $\sigma = 1.00$

Double circular-arc profile: $\phi = 0$, $t/c = 0.06$

(a) $\theta, \omega, \Delta p/q_1, \beta_1$

Figure 94 . - Cascade characteristics as functions of incidence.

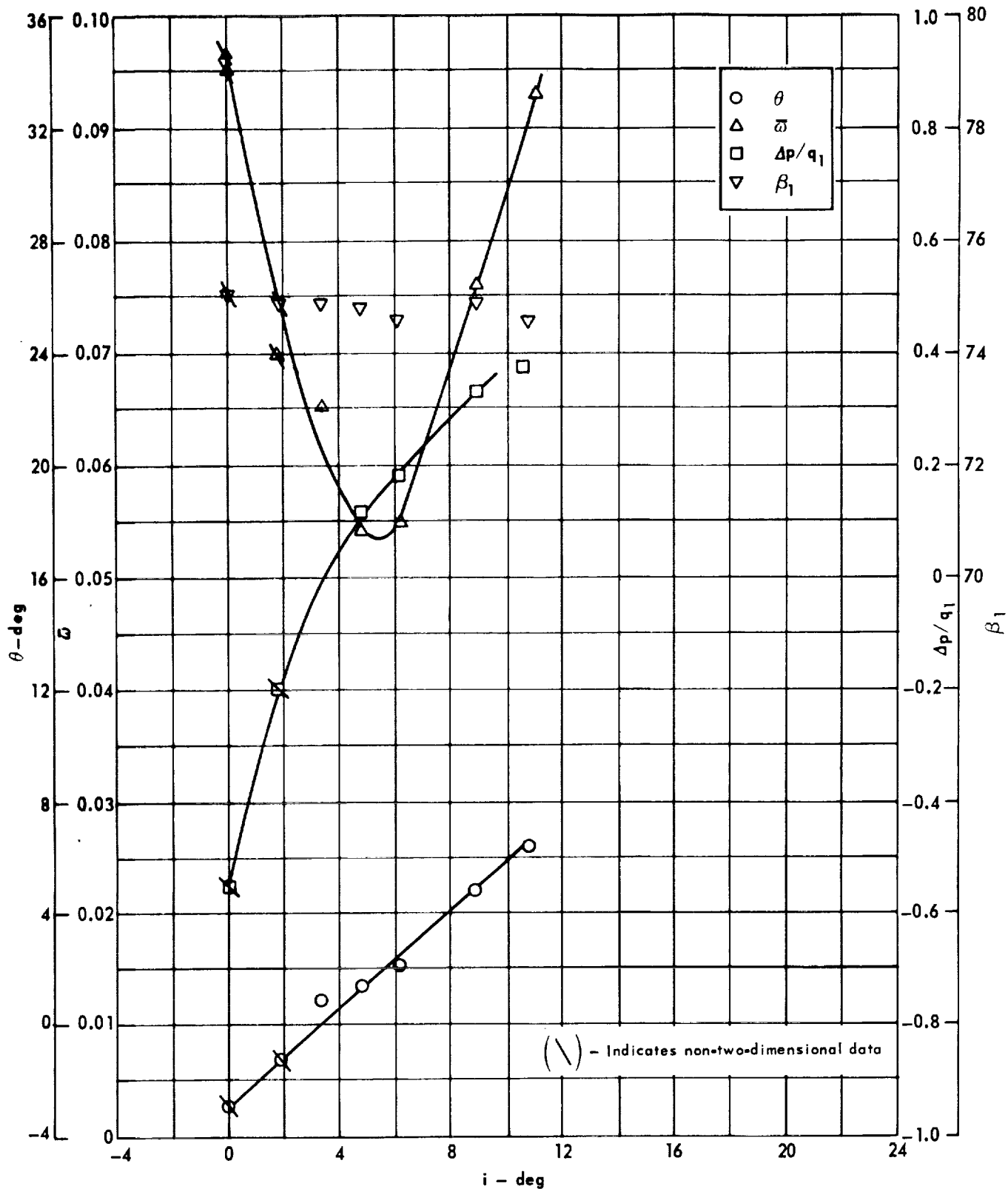


Cascade configuration: $\beta_{1N} = 75, \sigma = 1.00$

Double circular-arc profile: $\phi = 0, t/c = 0.06$

(b) $D, \theta^*/s, K, \delta^\circ$

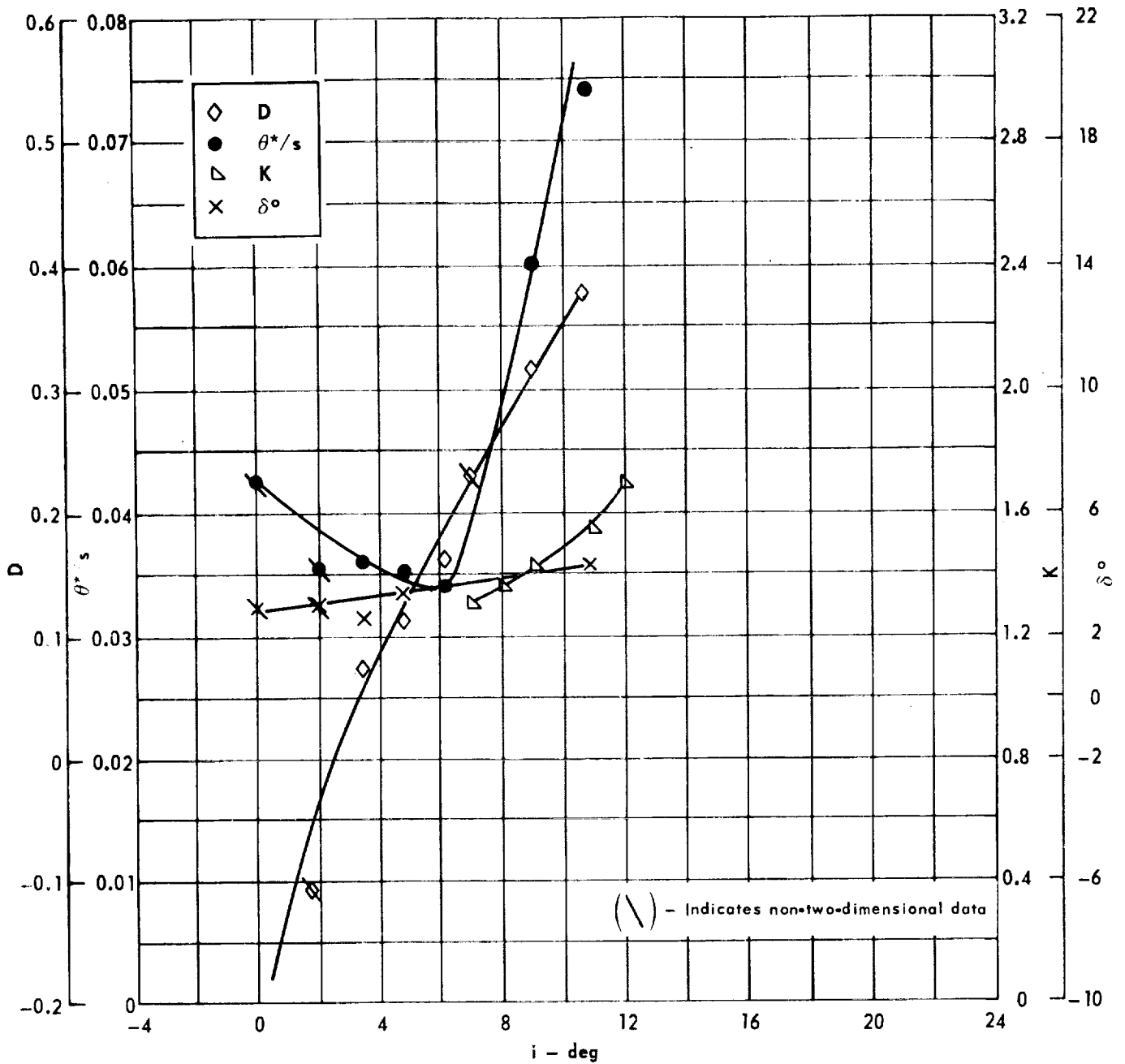
Figure 94 . - Concluded.



Cascade configuration: $\beta_{1N} = 75$, $\sigma = 1.50$
 Double circular-arc profile: $\phi = 0$, $t/c = 0.06$

(a) $\theta, \bar{\omega}, \Delta p/q_1, \beta_1$

Figure 95. - Cascade characteristics as functions of incidence.

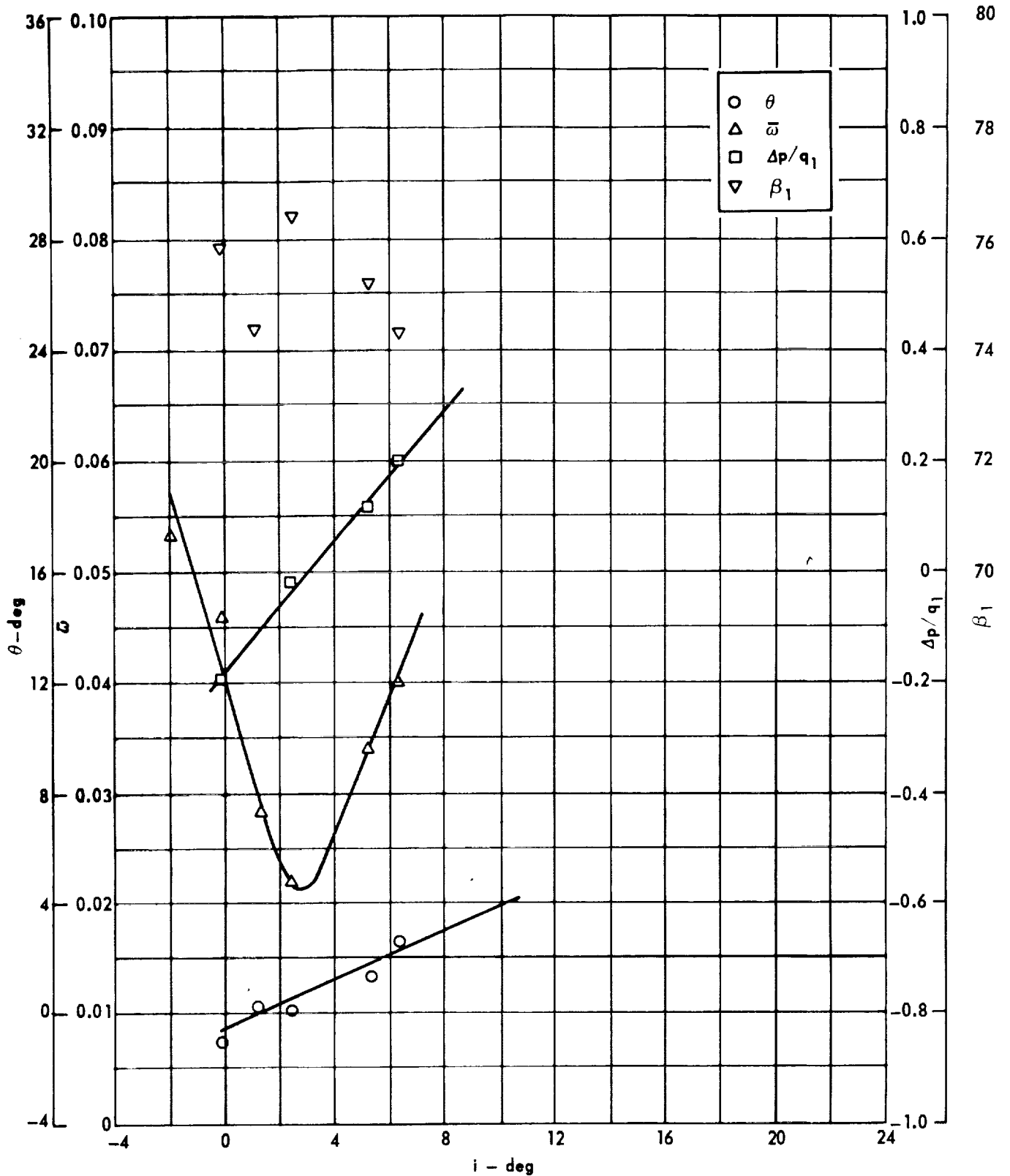


Cascade configuration: $\beta_{1N} = 75^\circ, \sigma = 1.50$

Double circular-arc profile: $\phi = 0, t/c = 0.06$

(b) D, θ^*/s , K, δ°

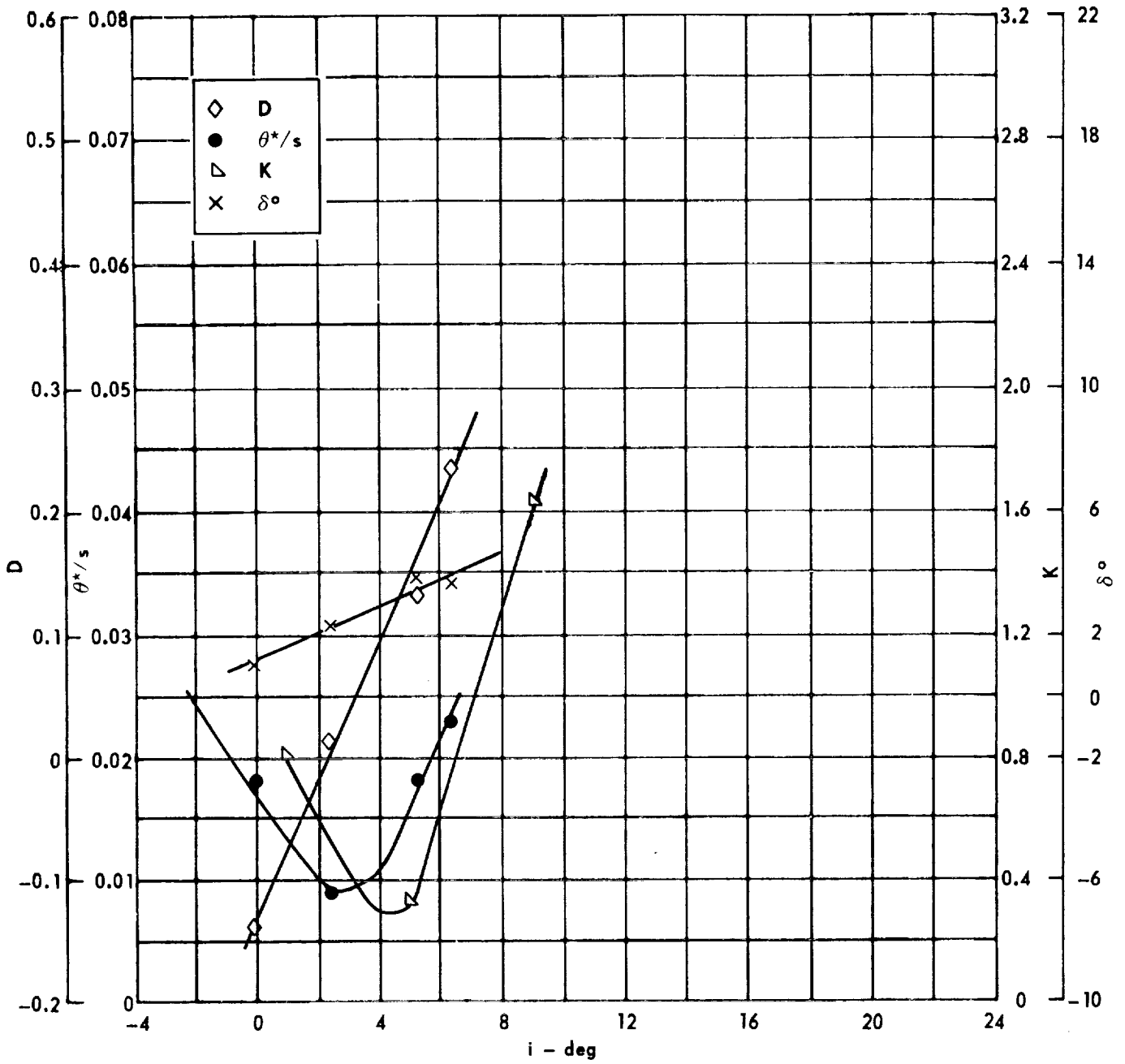
Figure 95 . - Concluded.



Cascade configuration: $\beta_{1N} = 75, \sigma = 0.75$
 Double circular-arc profile: $\phi = 0, t/c = 0.10$

(a) $\theta, \bar{\omega}, \Delta p/q_1, \beta_1$

Figure 96 . - Cascade characteristics as functions of incidence.

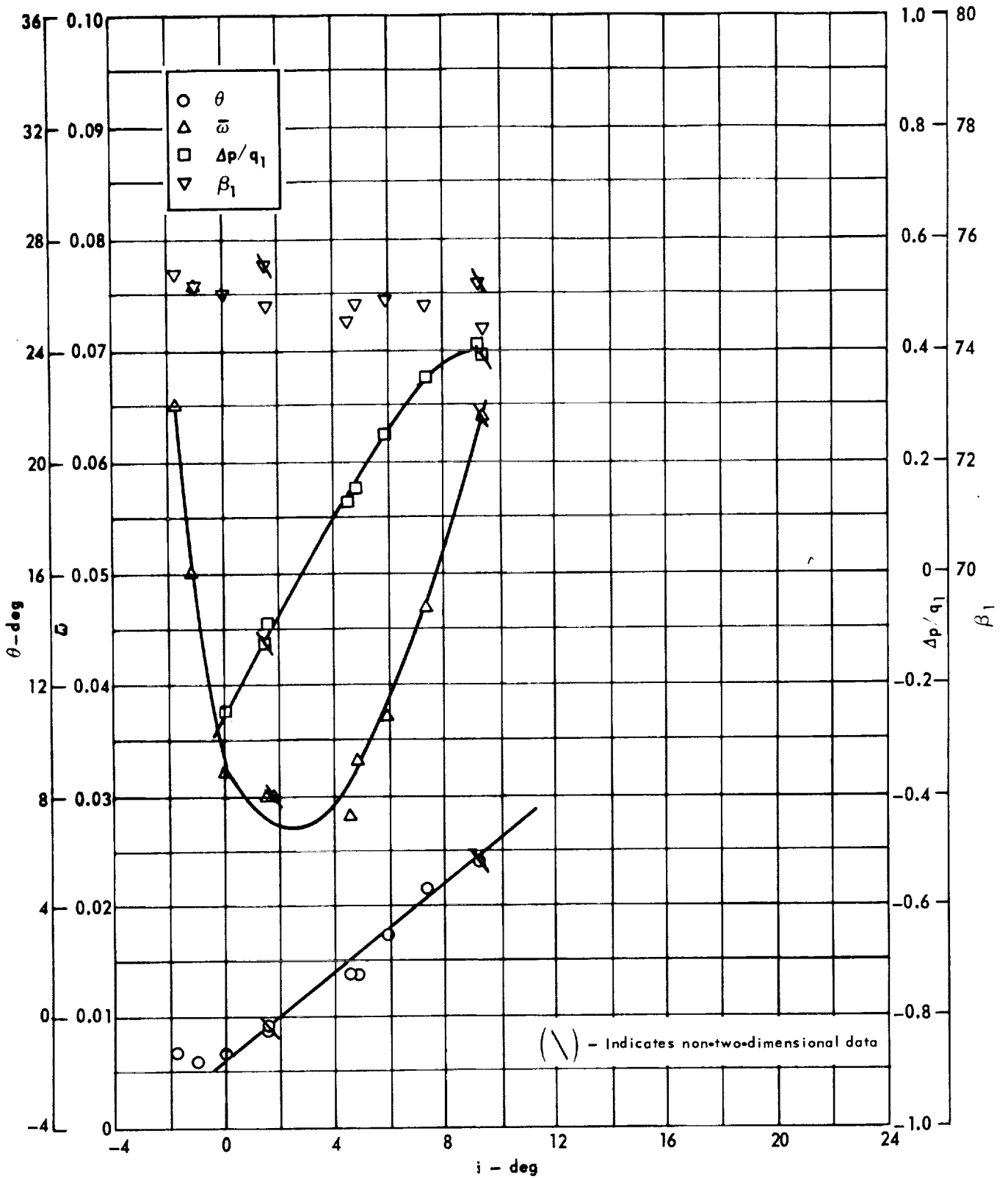


Cascade configuration: $\beta_{1N} = 75$, $\sigma = 0.75$

Double circular-arc profile: $\phi = 0$, $t/c = 0.10$

(b) D, θ^*/s , K, δ°

Figure 96 . - Concluded.

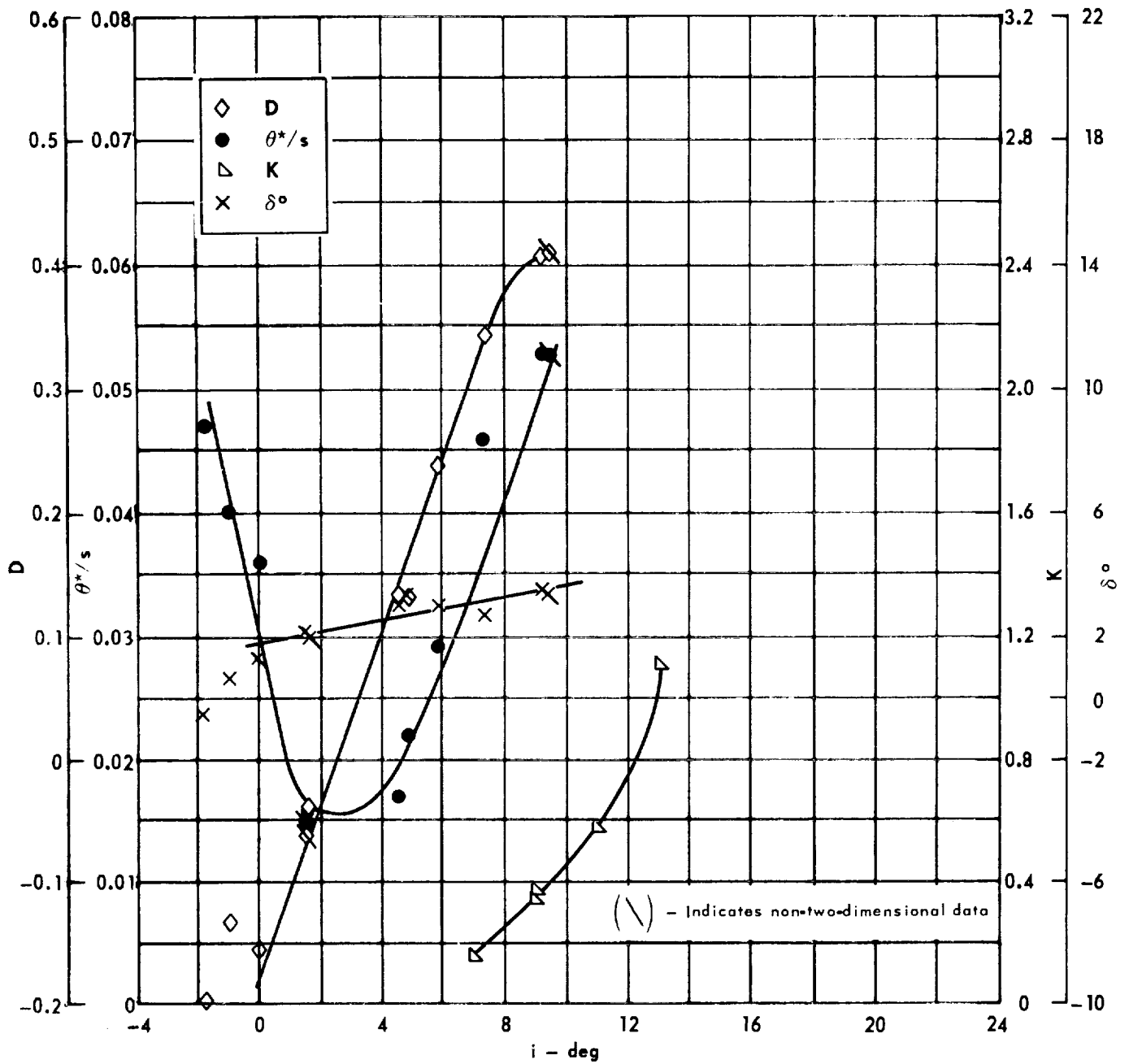


Cascade configuration: $\beta_{1N} = 75, \sigma = 1.00$

Double circular-arc profile: $\phi = 0, t/c = 0.10$

(a) $\theta, \bar{\omega}, \Delta p/q_1, \beta_1$

Figure 97. - Cascade characteristics as functions of incidence.

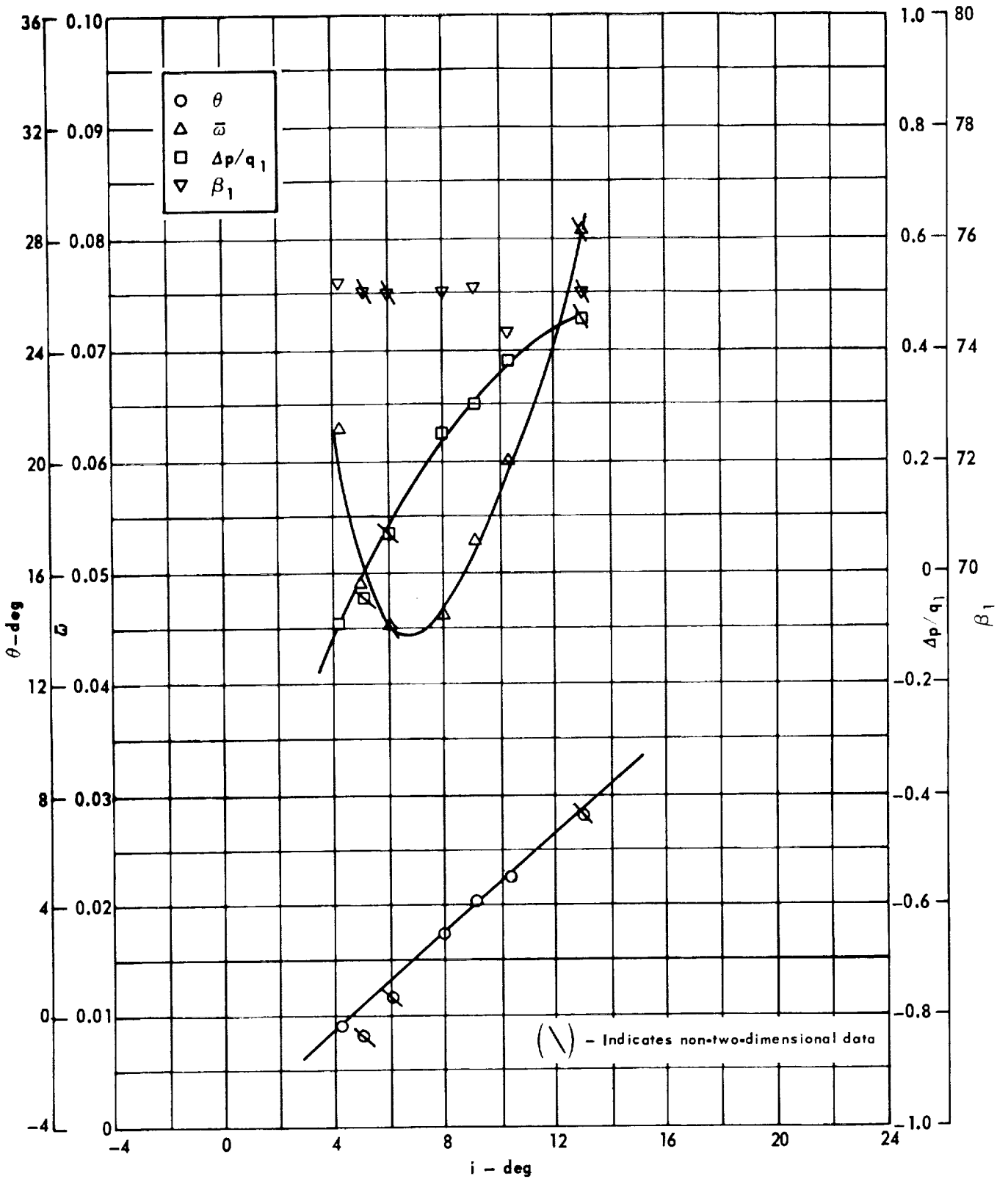


Cascade configuration: $\beta_{1N} = 75$, $\sigma = 1.00$

Double circular-arc profile: $\phi = 0^\circ$, $t/c = 0.10$

(b) D, θ^*/s , K, δ°

Figure 97 . - Concluded.

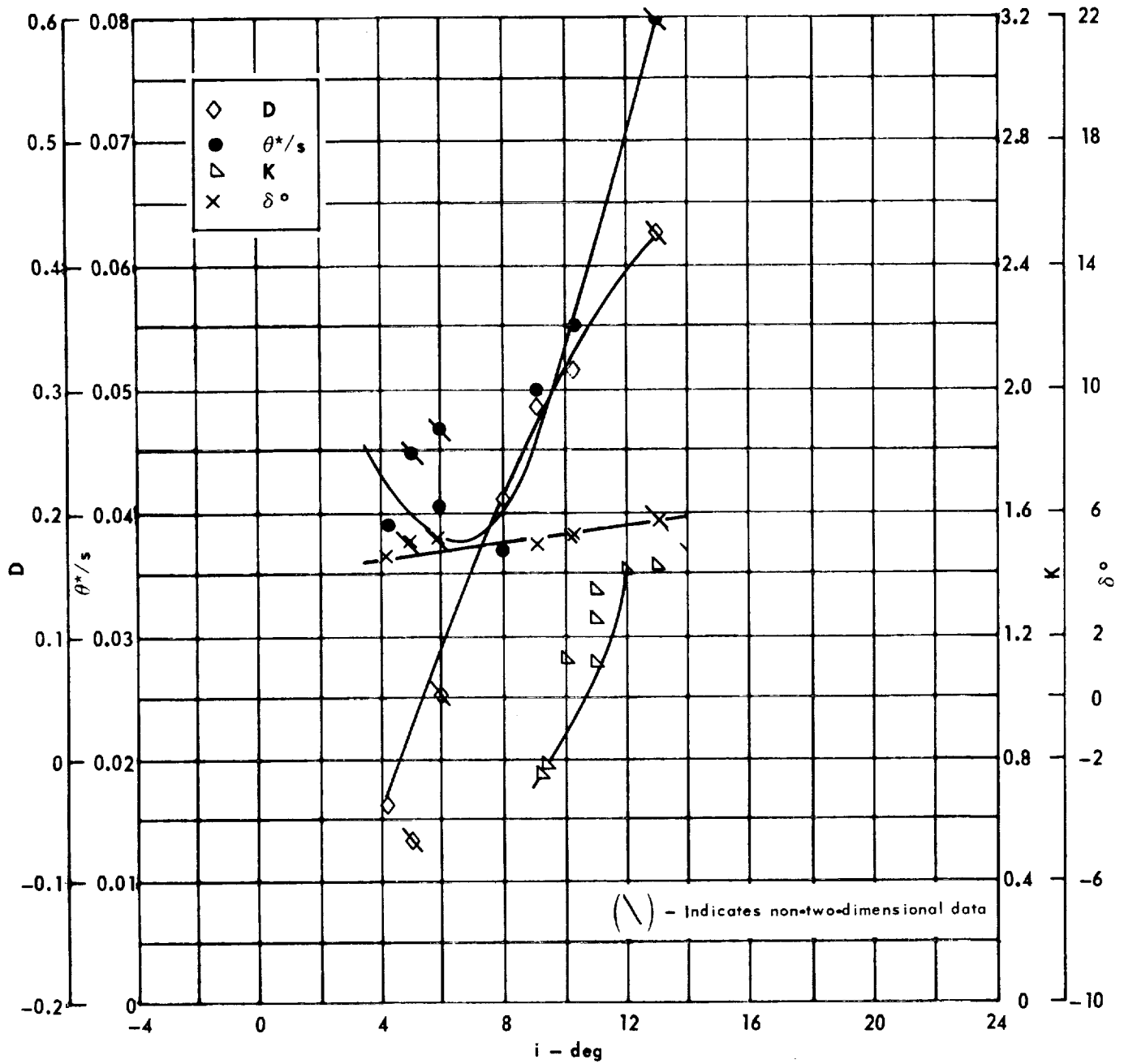


Cascade configuration: $\beta_{1N} = 75$, $\sigma = 1.50$

Double circular-arc profile: $\phi = 0$, $t/c = 0.10$

(a) $\theta, \bar{\omega}, \Delta p/q_1, \beta_1$

Figure 98 . - Cascade characteristics as functions of incidence.

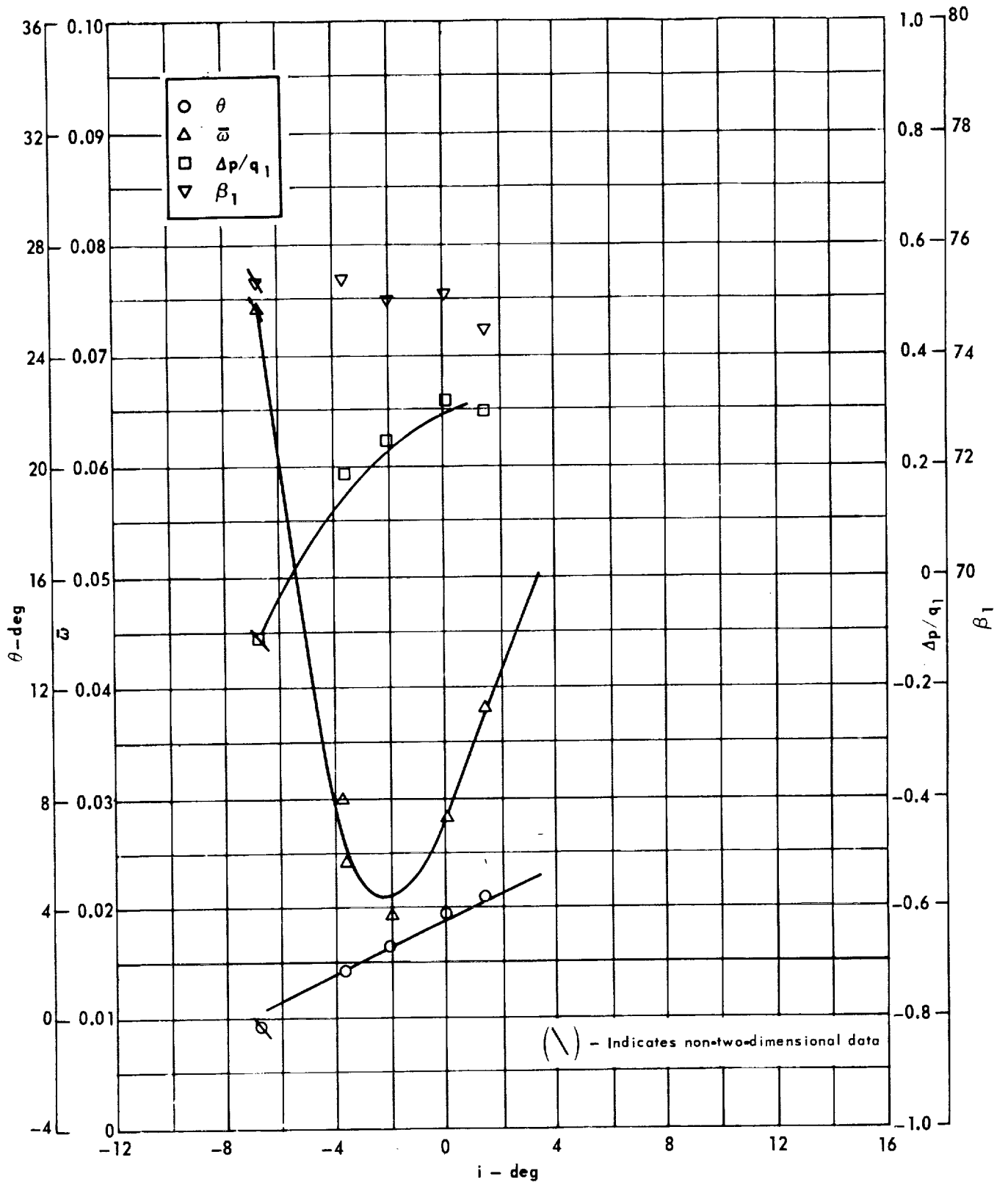


Cascade configuration: $\beta_{1N} = 75, \sigma = 1.50$

Double circular-arc profile: $\phi = 0, t/c = 0.10$

(b) D, θ^*/s , K, δ°

Figure 98 . - Concluded.

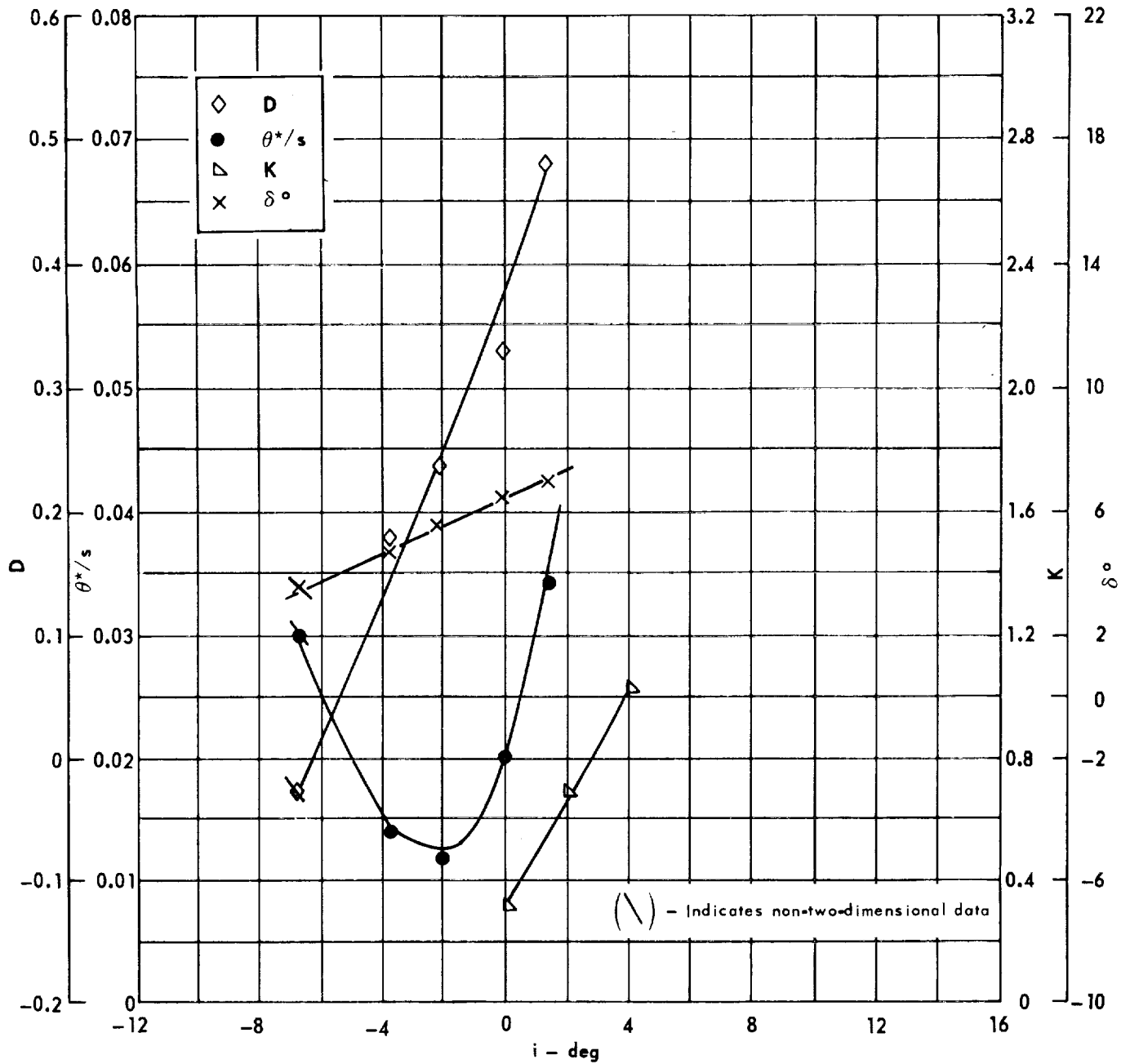


Cascade configuration: $\beta_{1N} = 75$, $\sigma = 0.75$

Double circular-arc profile: $\phi = 10$, $t/c = 0.06$

(a) $\theta, \bar{\omega}, \Delta p/q_1, \beta_1$

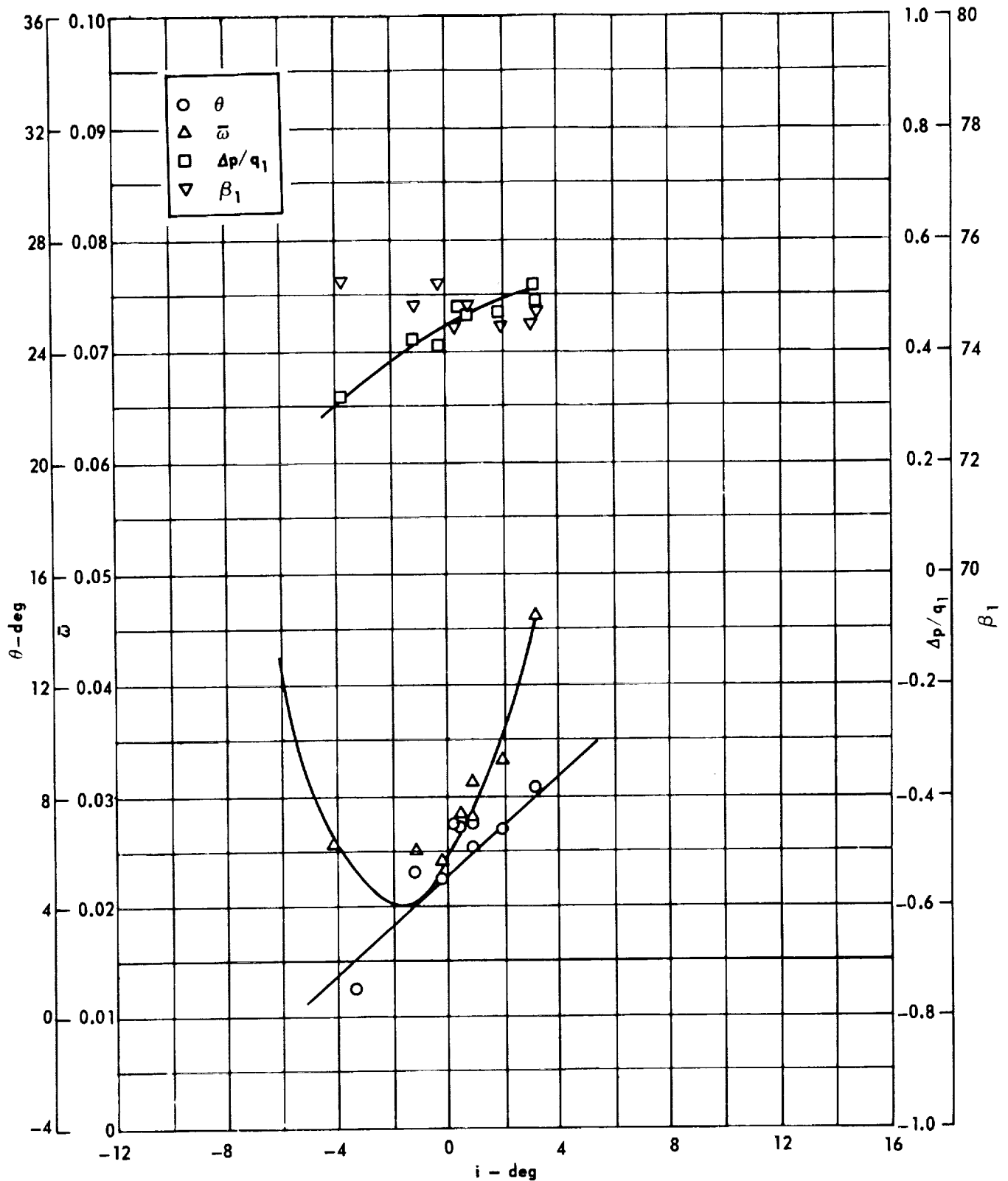
Figure 99. - Cascade characteristics as functions of incidence.



Cascade configuration : $\beta_{1N} = 75$, $\sigma = 0.75$
 Double circular-arc profile : $\phi = 10$, $t/c = 0.06$

(b) D, θ^*/s , K, δ°

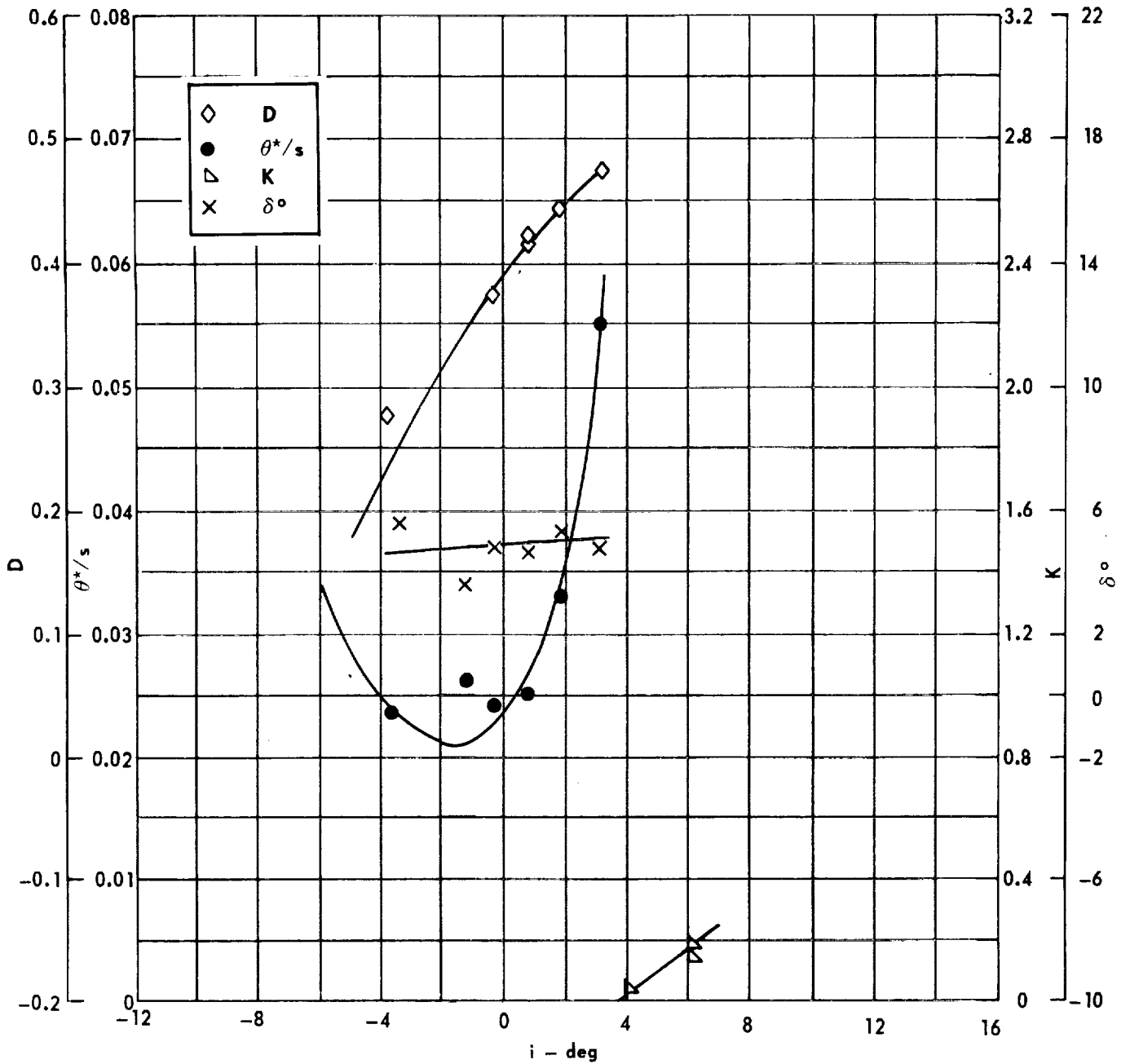
Figure 99 . - Concluded.



Cascade configuration : $\beta_{1N} = 75, \sigma = 1.00$
 Double circular-arc profile : $\phi = 10, t/c = 0.06$

(a) $\theta, \bar{\omega}, \Delta p/q_1, \beta_1$

Figure 100. - Cascade characteristics as functions of incidence.

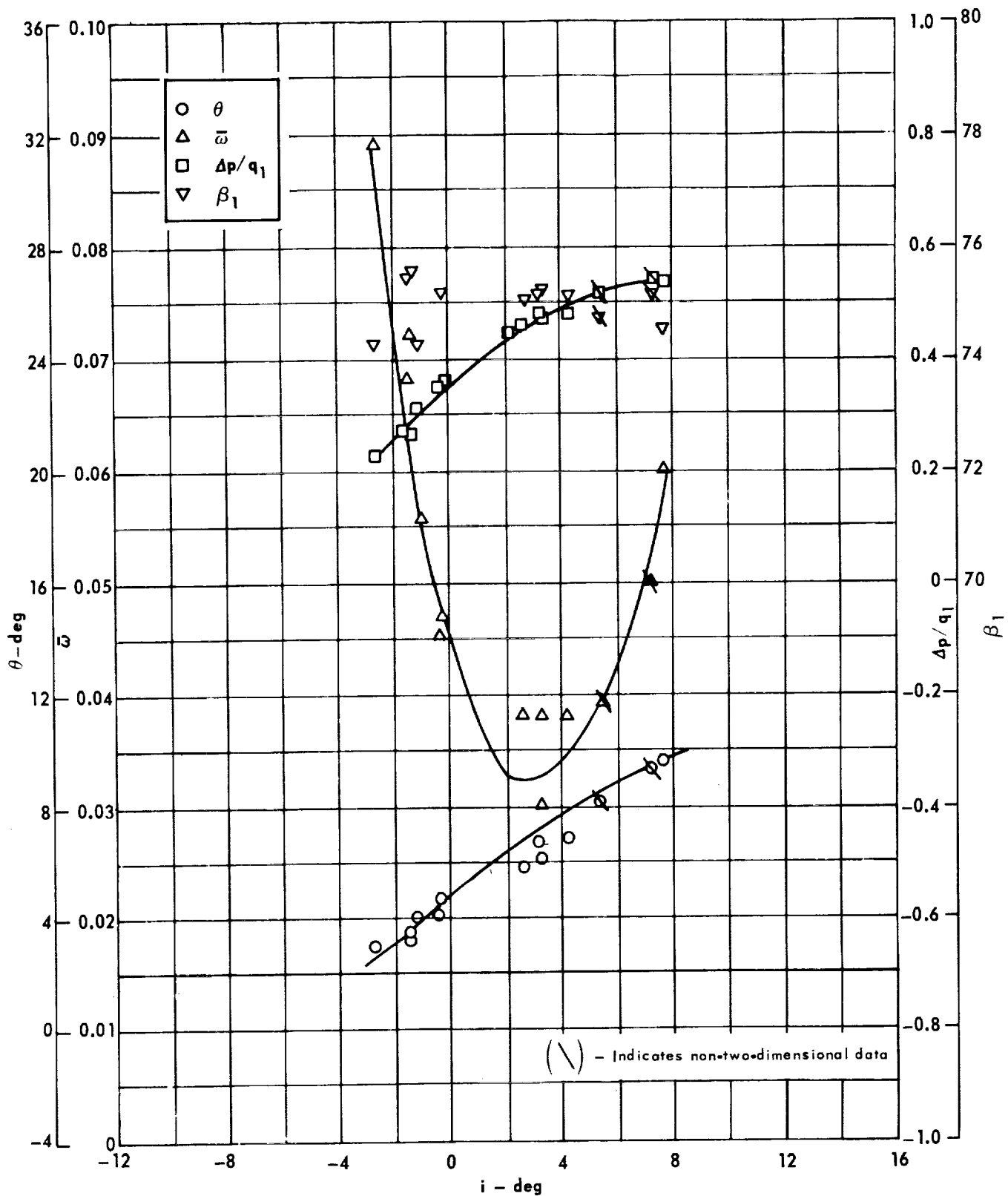


Cascade configuration: $\beta_{1N} = 75$, $\sigma = 1.00$

Double circular-arc profile: $\phi = 10$, $t/c = 0.06$

(b) D, θ^*/s , K, δ°

Figure 100 . - Concluded.

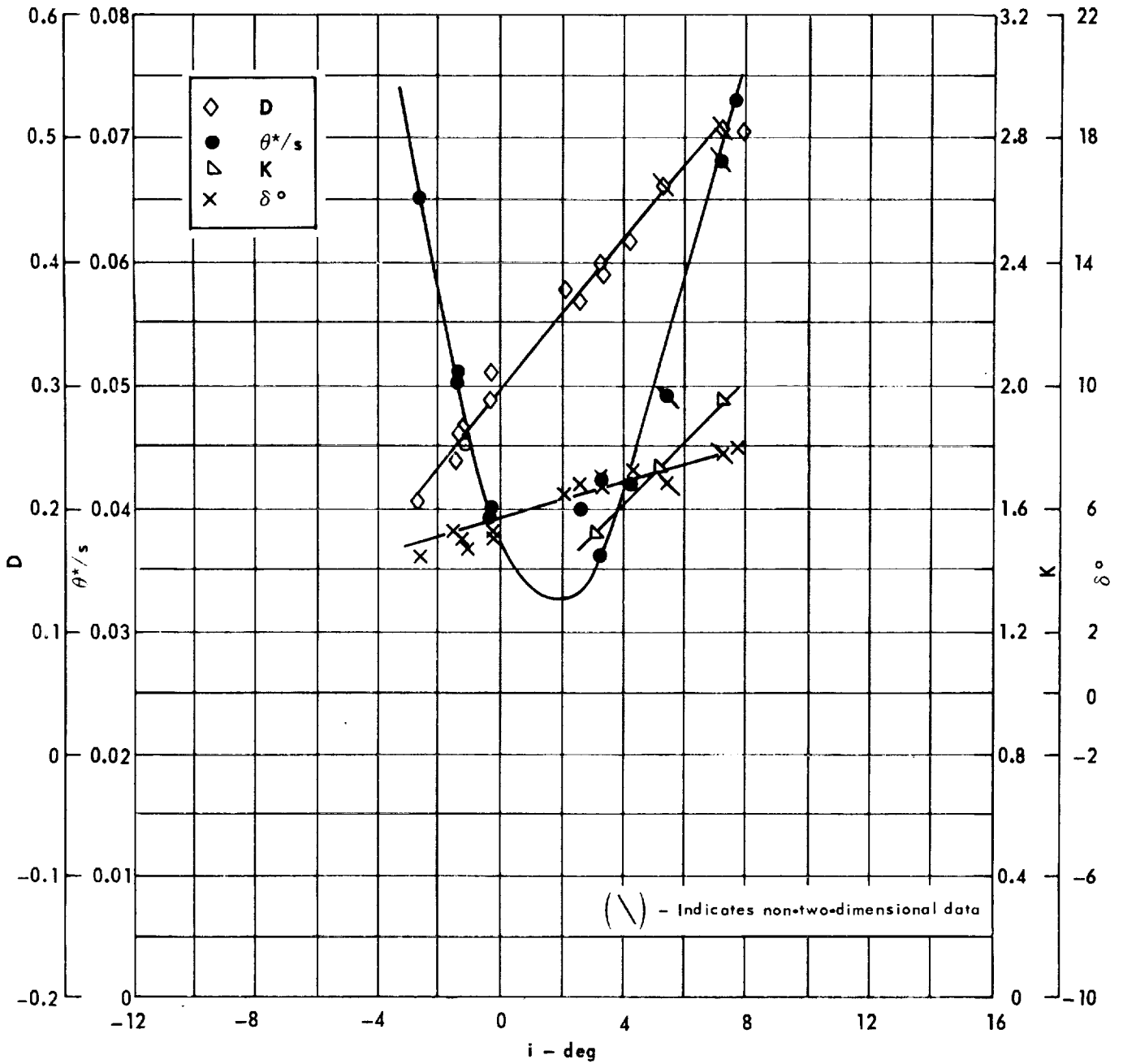


Cascade configuration : $\beta_{1N} = 75$, $\sigma = 1.50$

Double circular-arc profile : $\phi = 10$, $t/c = 0.06$

(a) $\theta, \bar{\omega}, \Delta p/q_1, \beta_1$

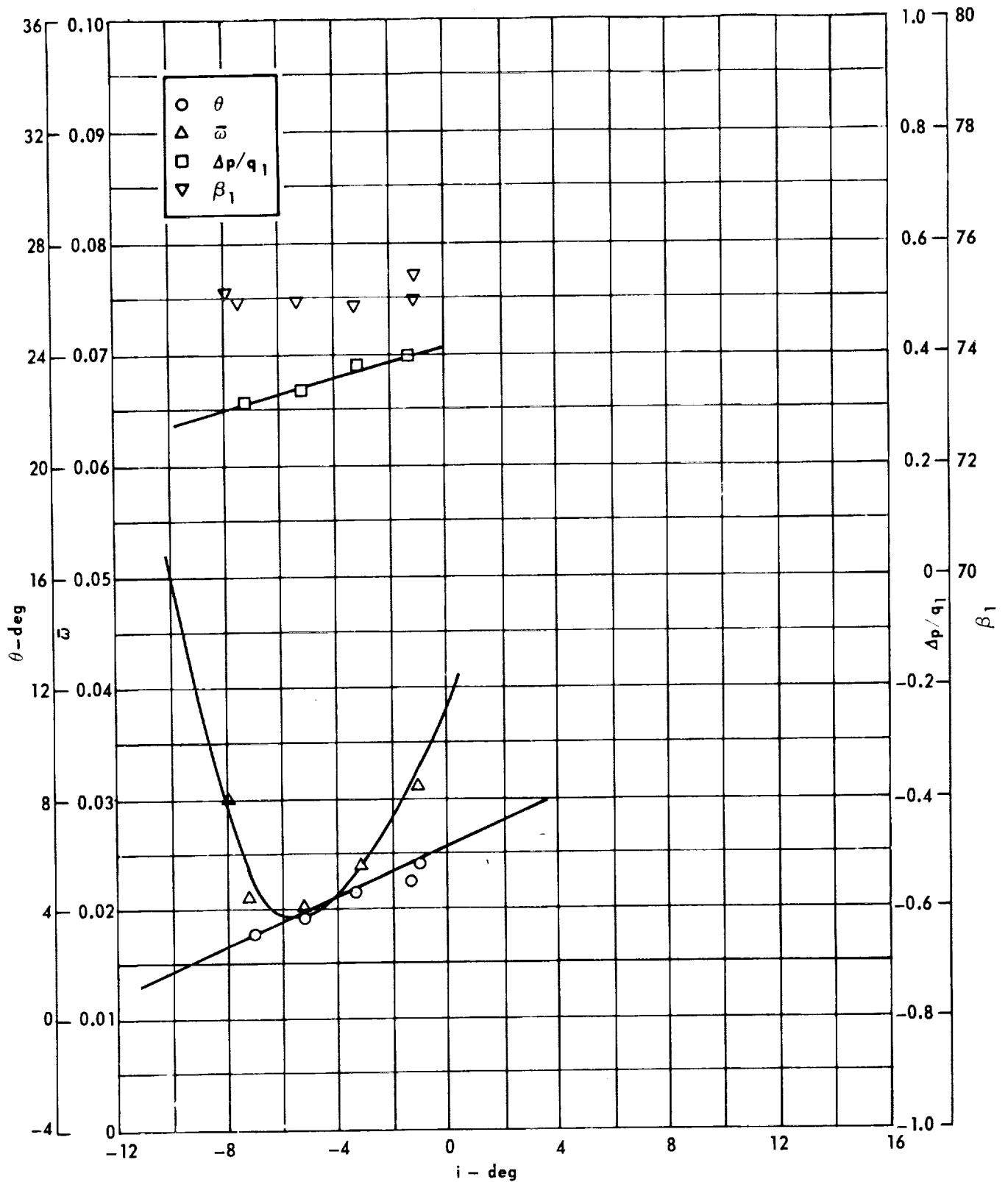
Figure 101. - Cascade characteristics as functions of incidence.



Cascade configuration: $\beta_{1N} = 75$, $\sigma = 1.50$
 Double circular-arc profile: $\phi = 10$, $t/c = 0.06$

(b) D, θ^*/s , K, δ°

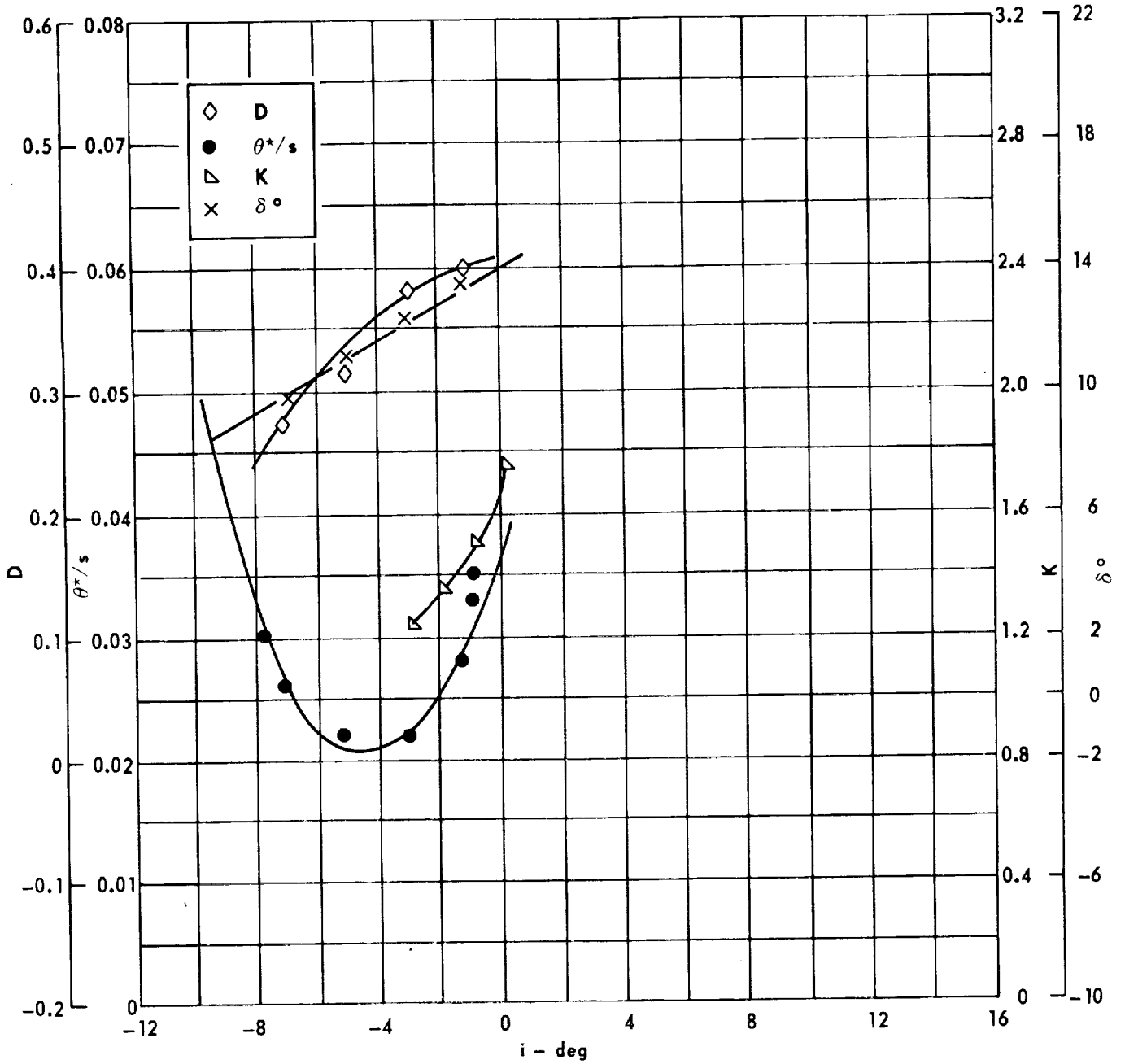
Figure 101 . - Concluded.



Cascade configuration : $\beta_{1N} = 75, \sigma = 0.75$
 Double circular-arc profile : $\phi = 20, r/c = 0.06$

(a) $\theta, \bar{\omega}, \Delta p/q_1, \beta_1$

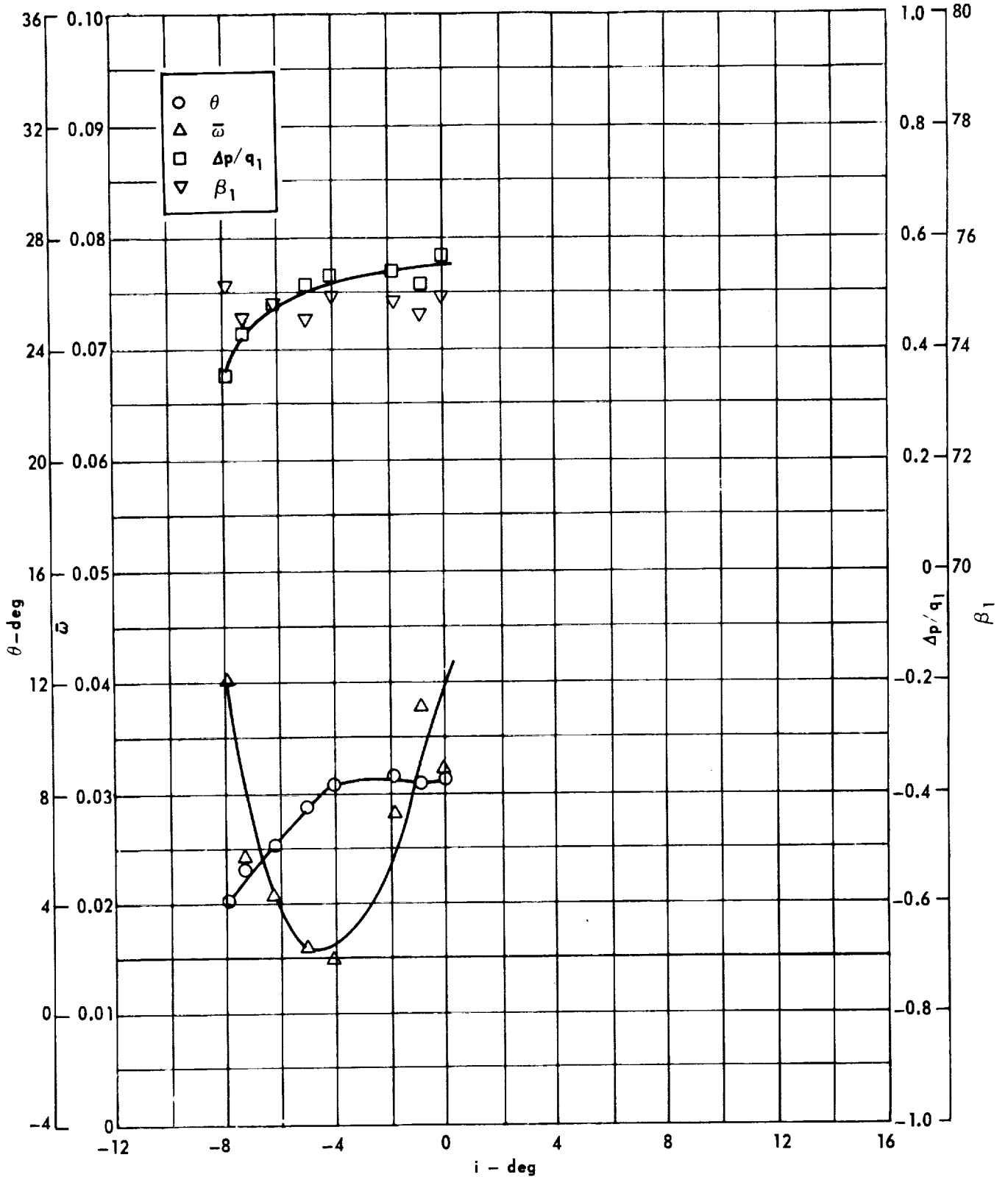
Figure 102. - Cascade characteristics as functions of incidence.



Cascade configuration : $\beta_{1N} = 75, \sigma = 0.75$
 Double circular-arc profile : $\phi = 20, t/c = 0.06$

(b) D, θ^*/s , K, δ°

Figure 102. - Concluded.

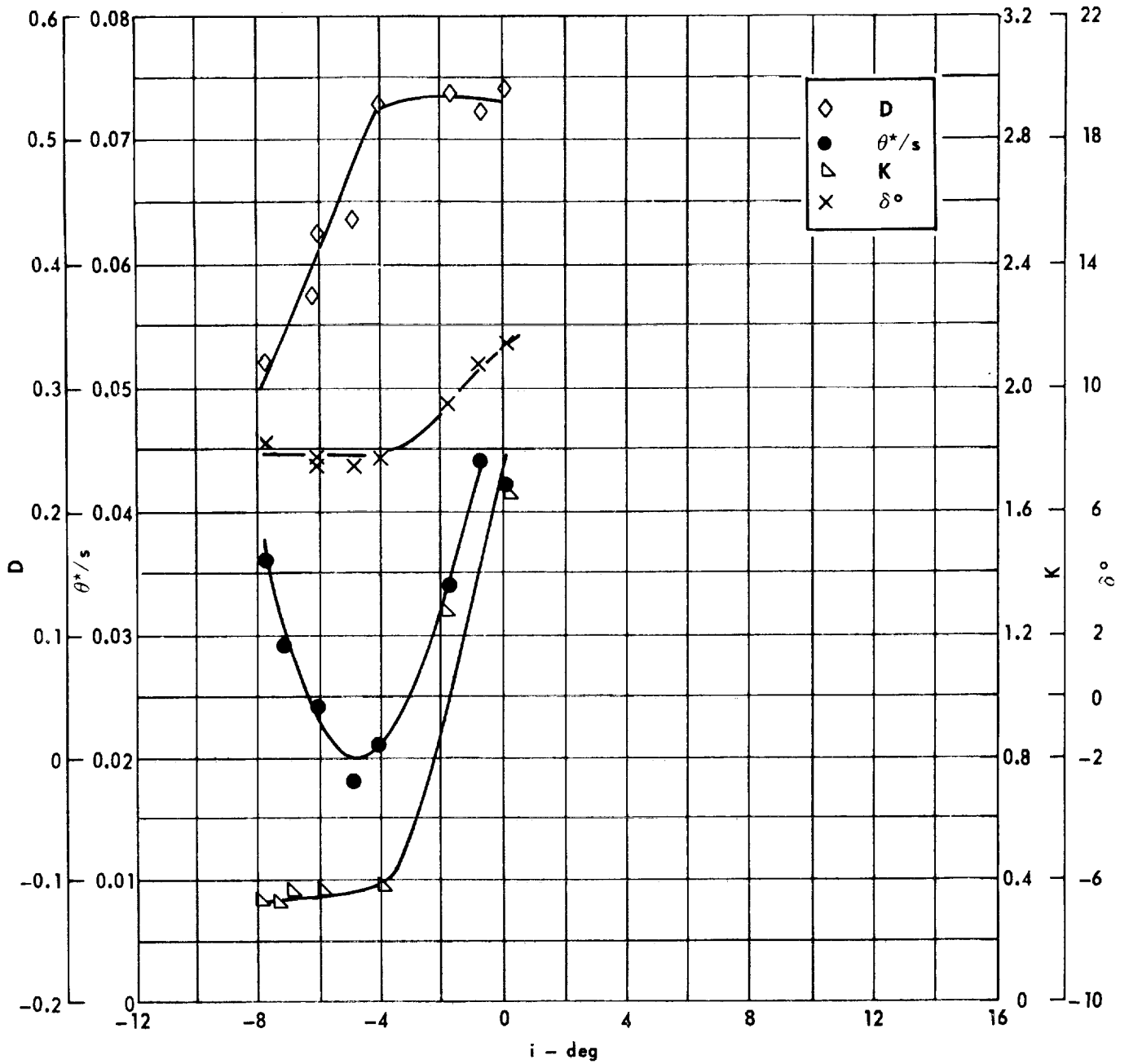


Cascade configuration : $\beta_{1N} = 75$, $\sigma = 1.00$

Double circular-arc profile : $\phi = 20$, $t/c = 0.06$

(a) $\theta, \bar{\omega}, \Delta p/q_1, \beta_1$

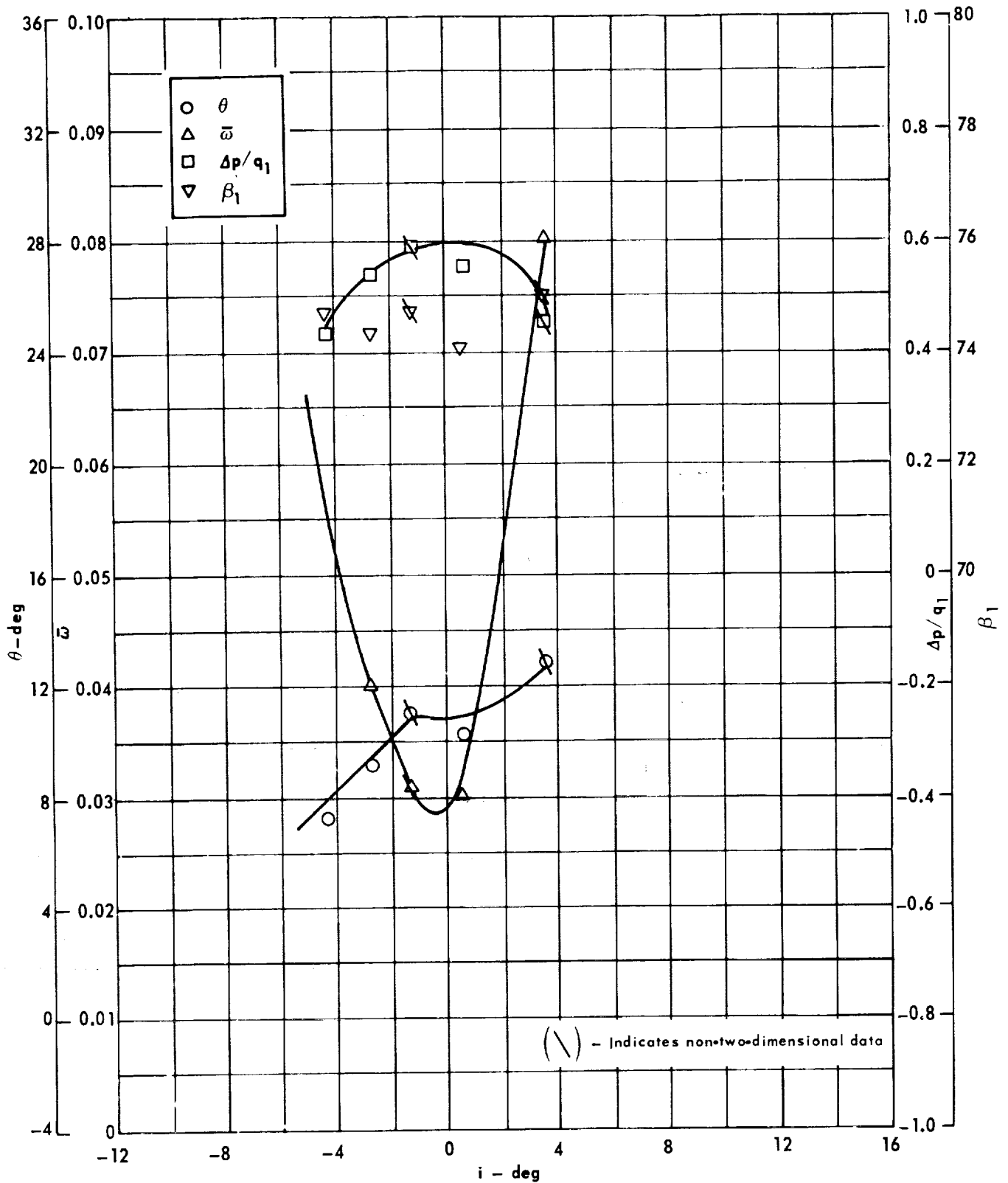
Figure 103. - Cascade characteristics as functions of incidence.



Cascade configuration : $\beta_{1N} = 75$, $\sigma = 1.00$
 Double circular-arc profile : $\phi = 20$, $t'/c = 0.06$

(b) D, θ^*/s , K, δ°

Figure 103. - Concluded.

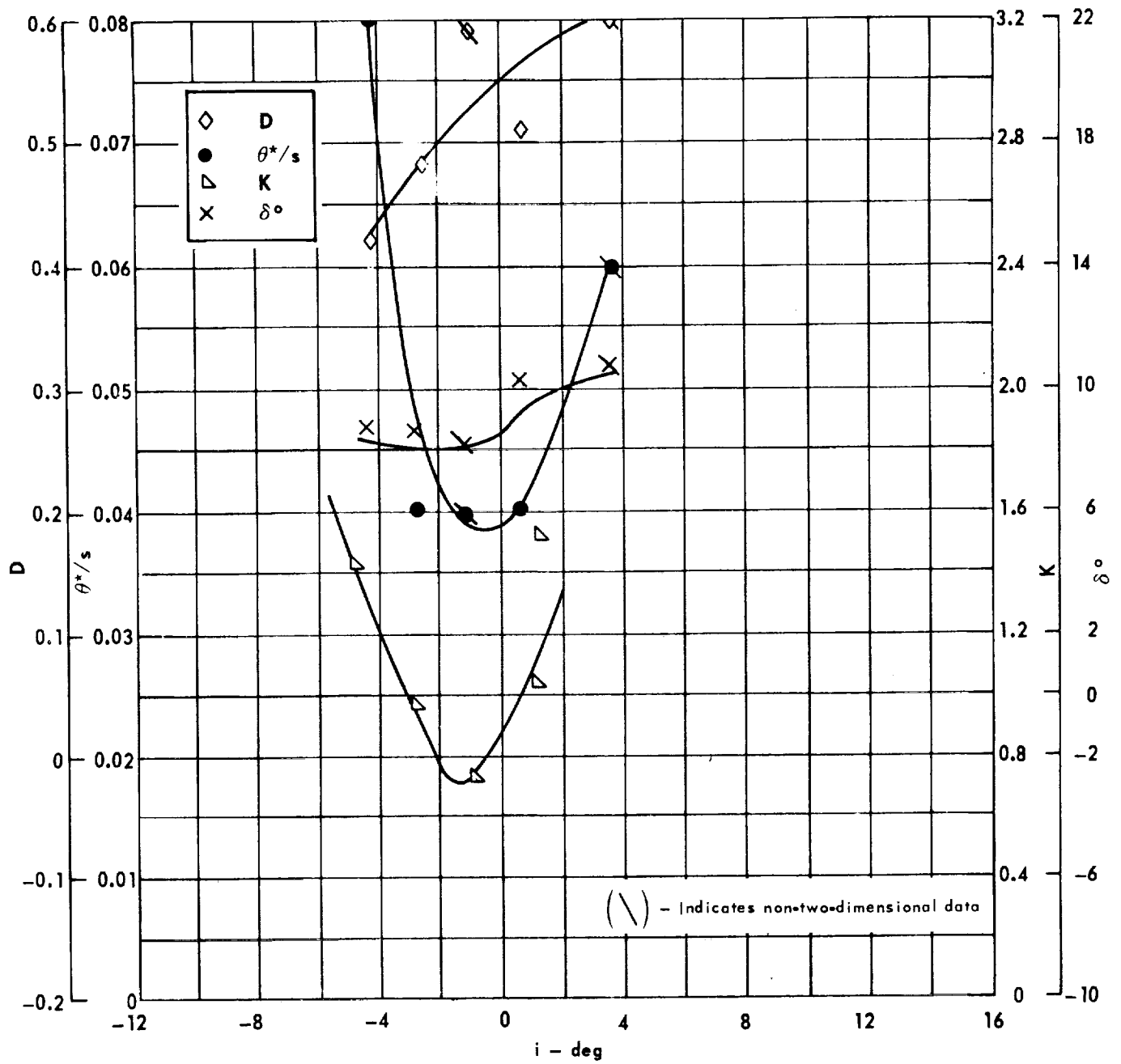


Cascade configuration: $\beta_{1N} = 75$, $\sigma = 1.50$

Double circular-arc profile: $\phi = 20$, $t/c = 0.06$

(a) $\theta, \bar{\omega}, \Delta p/q_1, \beta_1$

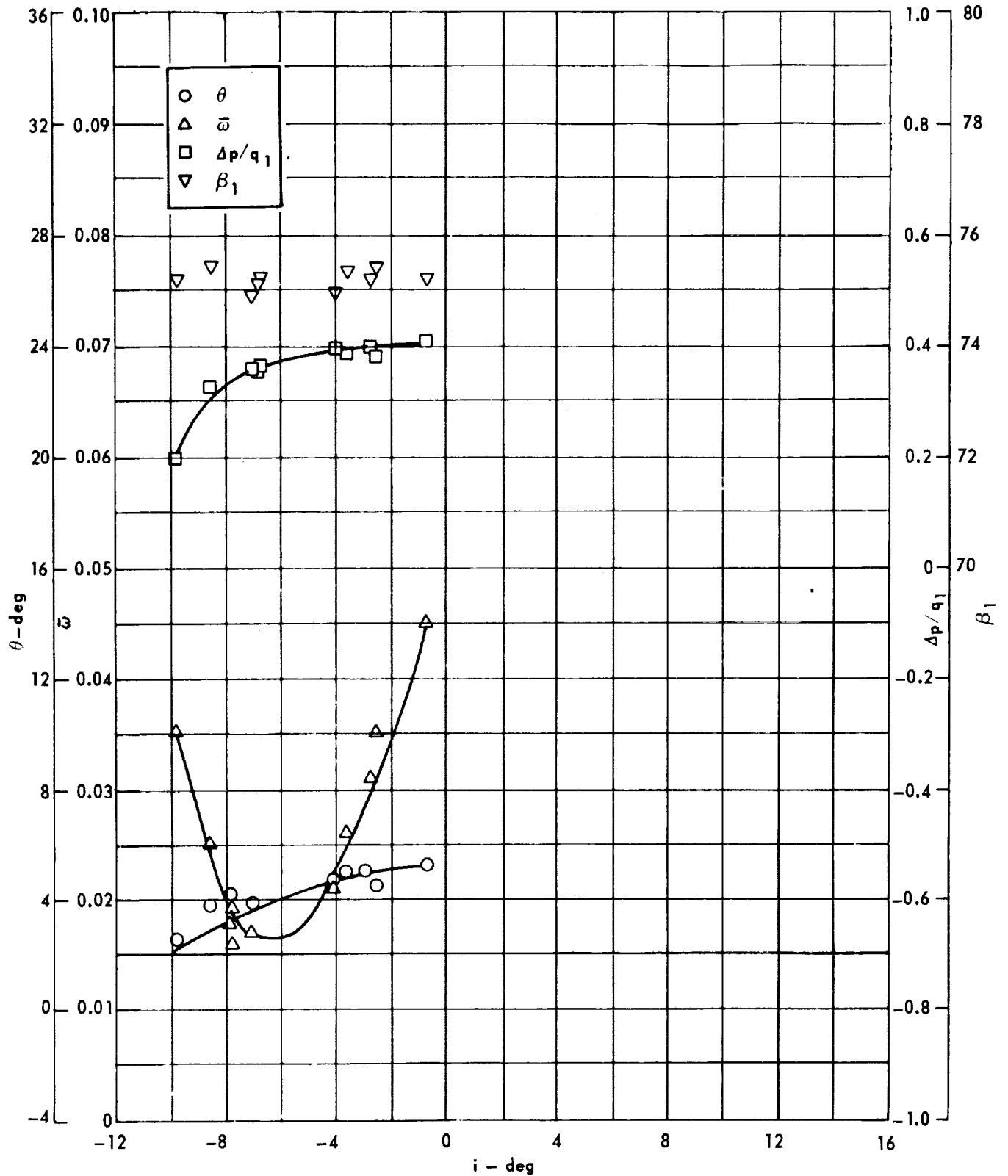
Figure 104 . - Cascade characteristics as functions of incidence.



Cascade configuration: $\beta_{1N} = 75$, $\sigma = 1.50$
 Double circular-arc profile: $\phi = 20$, $t/c = 0.06$

(b) D, θ^*/s , K, δ°

Figure 104. - Concluded.

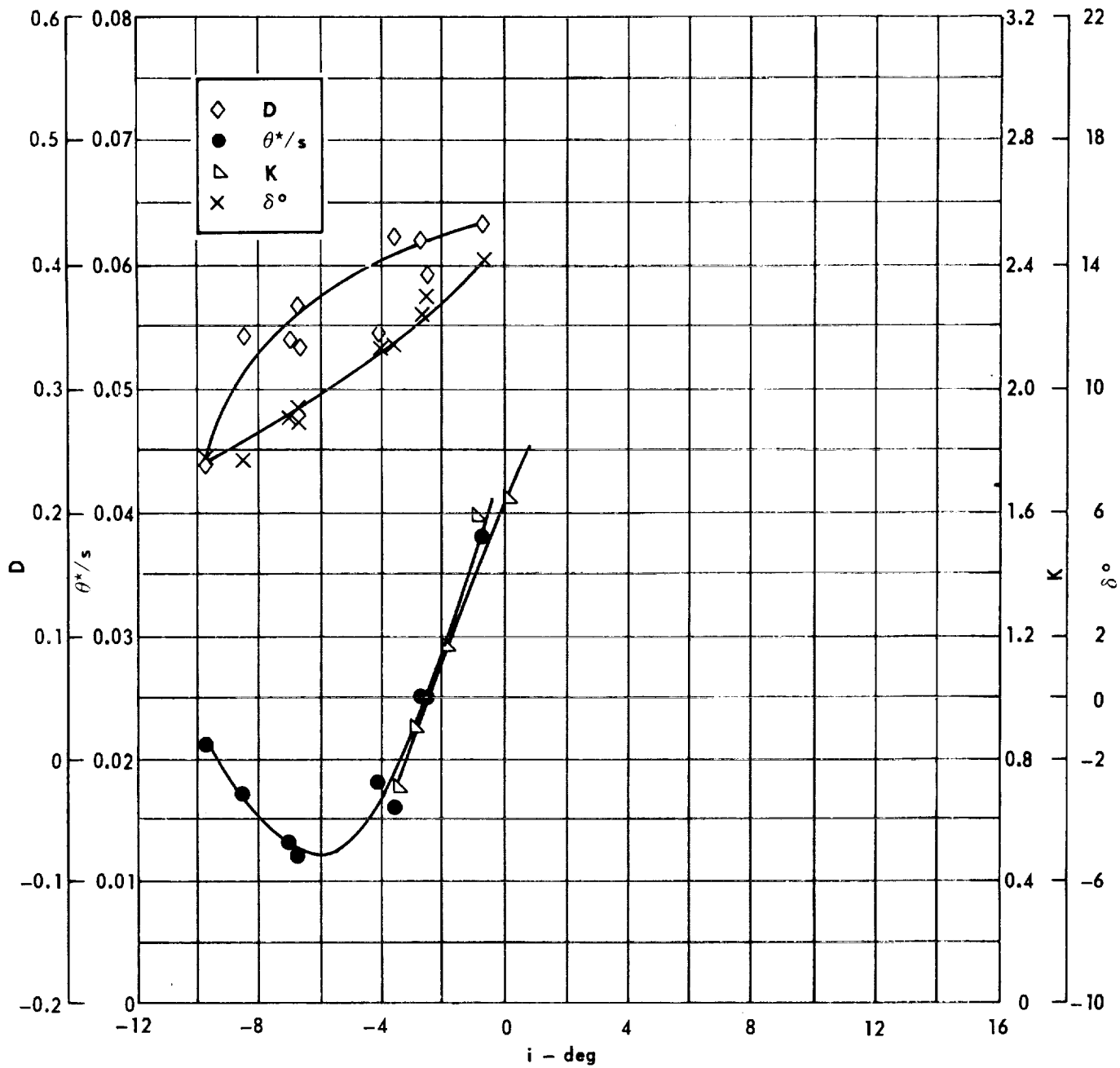


Cascade configuration : $\beta_{1N} = 75$, $\sigma = 0.75$

Double circular-arc profile : $\phi = 20$, $t/c = 0.10$

(a) $\theta, \bar{\omega}, \Delta p/q_1, \beta_1$

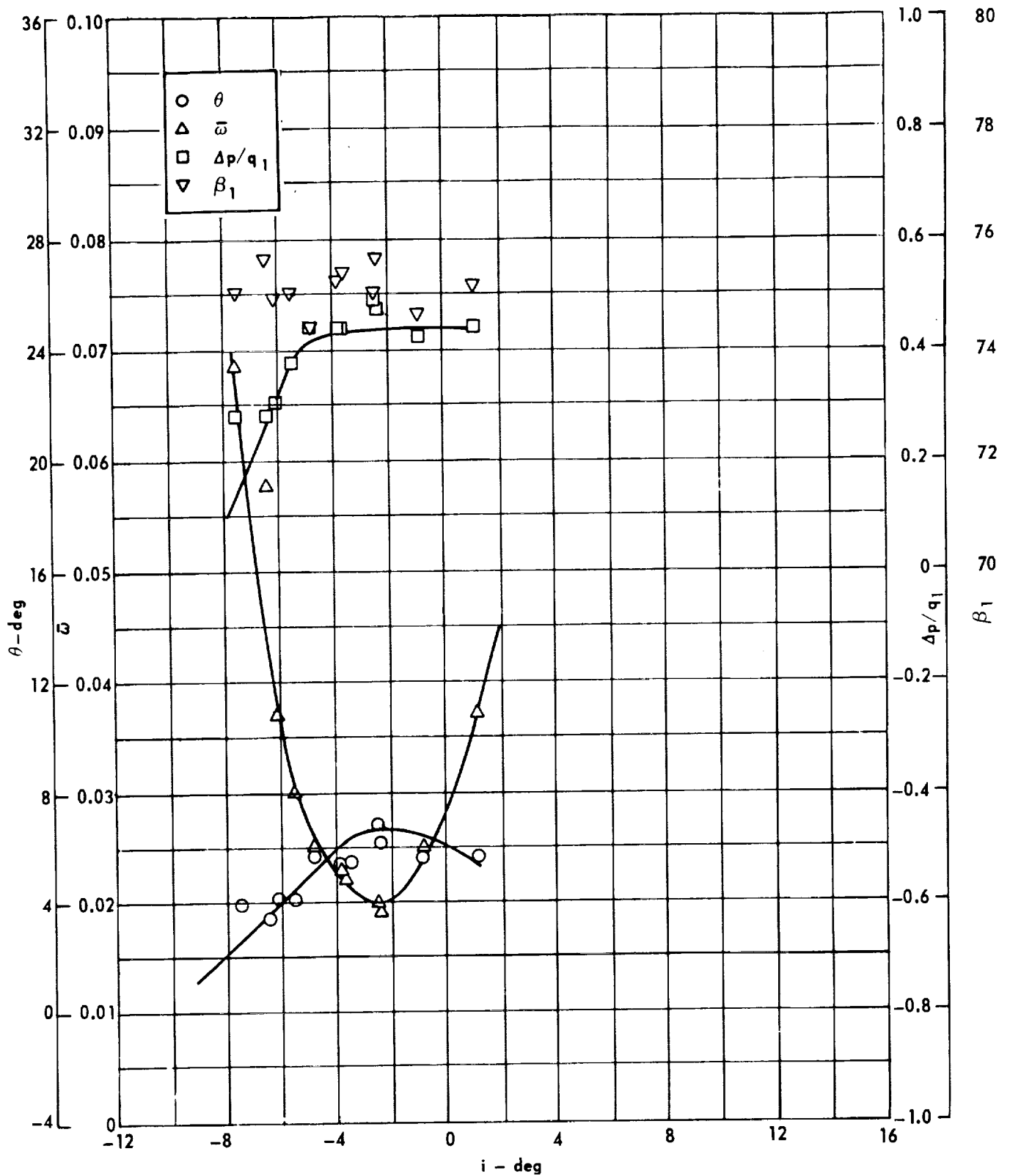
Figure 105. - Cascade characteristics as functions of incidence.



Cascade configuration: $\beta_{1N} = 75, \sigma = 0.75$
 Double circular-arc profile: $\phi = 20, t/c = 0.10$

(b) D, θ^*/s , K, δ°

Figure 105 . - Concluded.

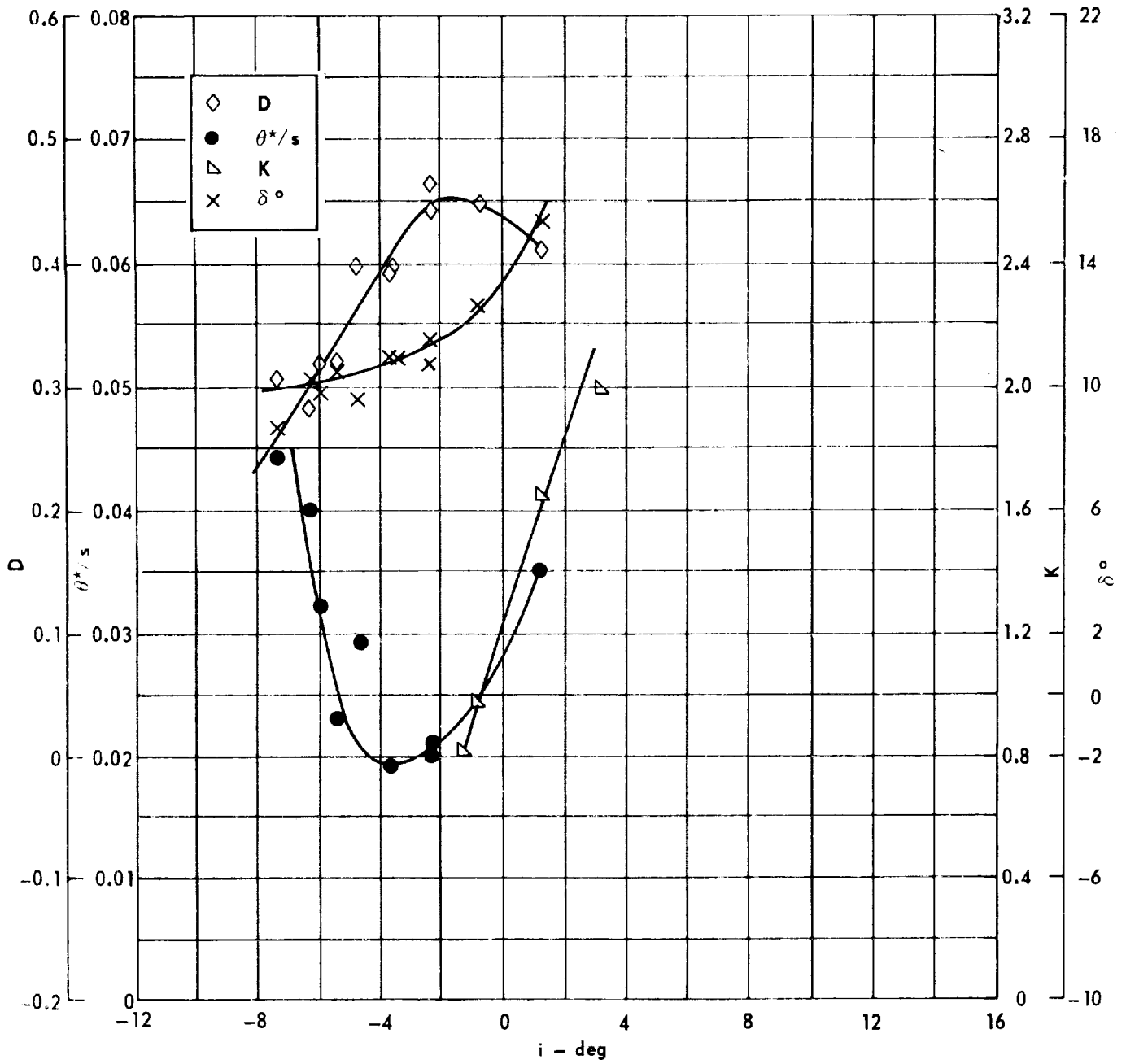


Cascade configuration: $\beta_{1N} = 75$, $\sigma = 1.00$

Double circular-arc profile: $\phi = 20$, $t/c = 0.10$

(a) $\theta, \bar{\omega}, \Delta p/q_1, \beta_1$

Figure 106. - Cascade characteristics as functions of incidence.

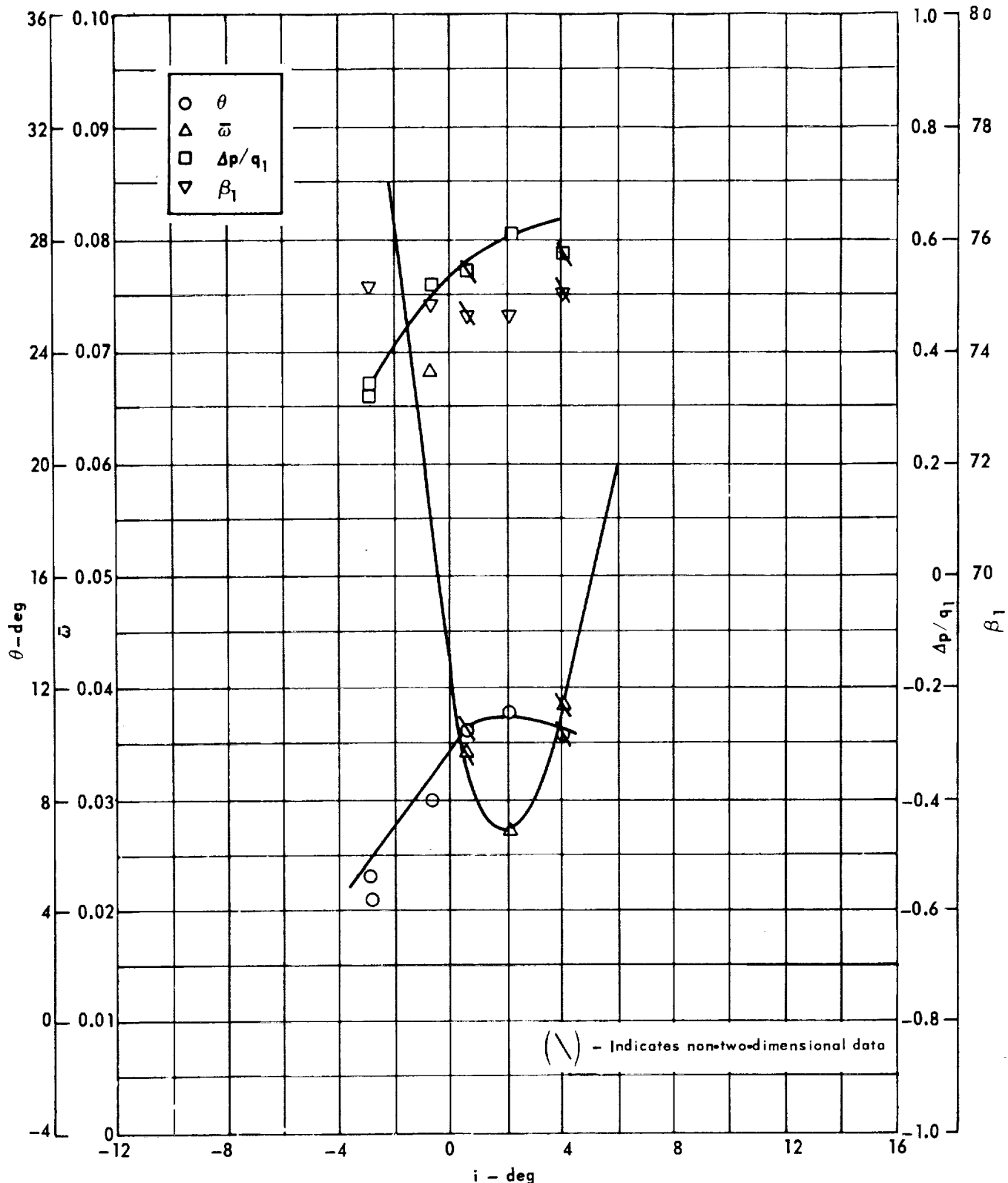


Cascade configuration: $\beta_{1N} = 75, \sigma = 1.00$

Double circular-arc profile: $\phi = 20, r/c = 0.10$

(b) D, θ^*/s , K, δ°

Figure 106. - Concluded.

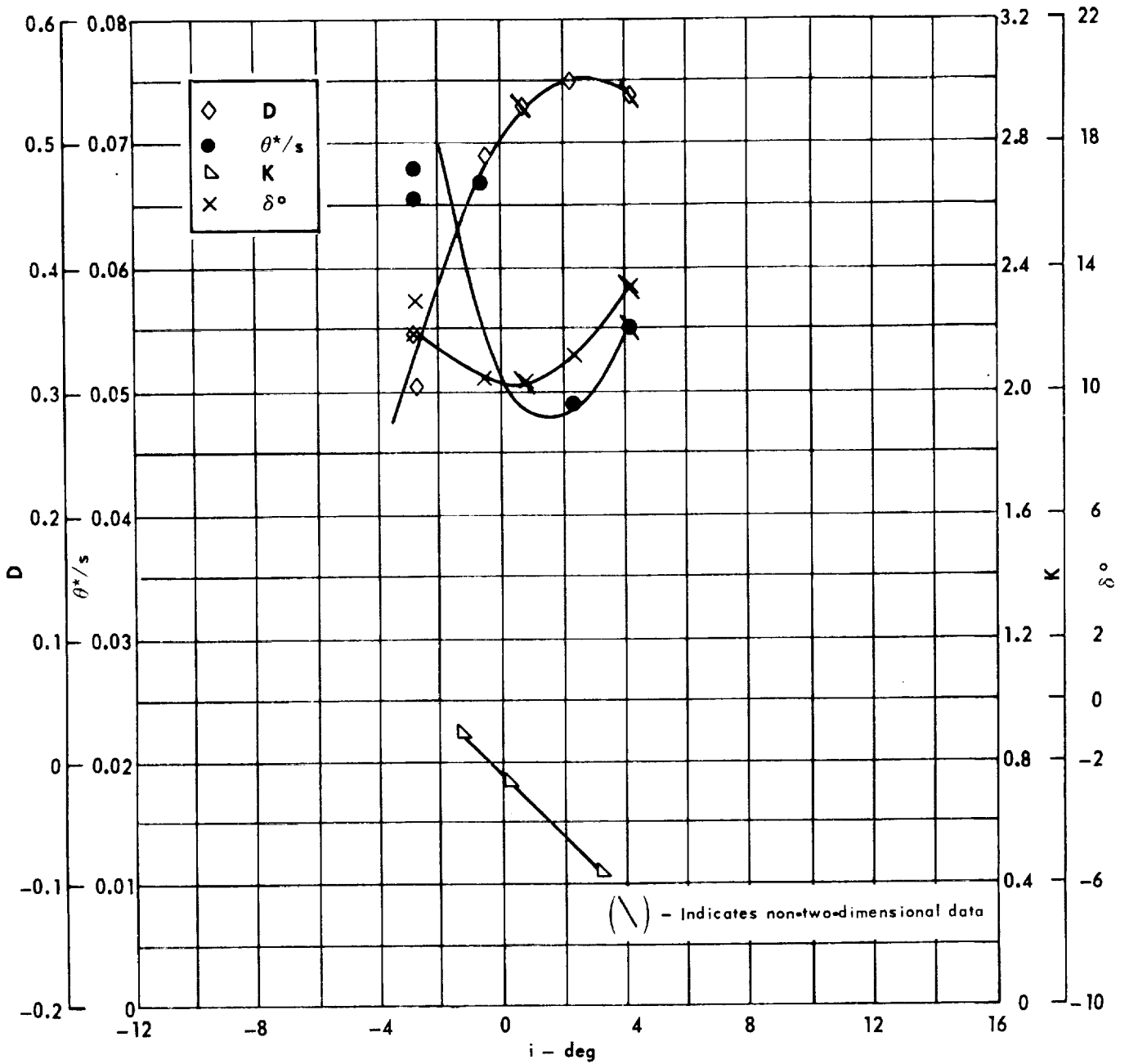


Cascade configuration: $\beta_{1N} = 75, \sigma = 1.50$

Double circular-arc profile: $\phi = 20, t/c = 0.10$

(a) $\theta, \bar{\omega}, \Delta p/q_1, \beta_1$

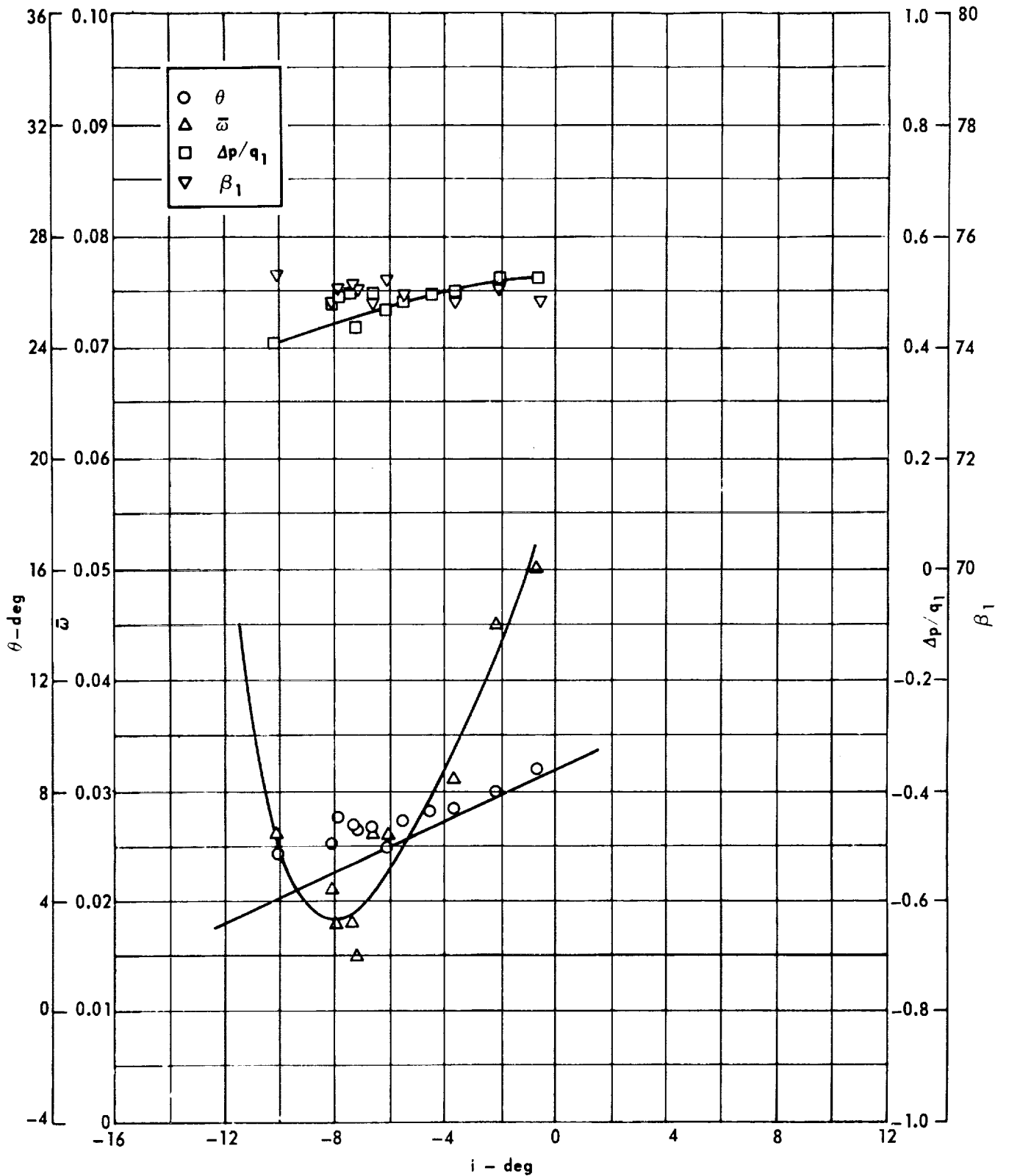
Figure 107. - Cascade characteristics as functions of incidence.



Cascade configuration : $\beta_{1N} = 75, \sigma = 1.50$
 Double circular-arc profile : $\phi = 20, t/c = 0.10$

(b) D, θ^*/s , K, δ°

Figure 107 . - Concluded.

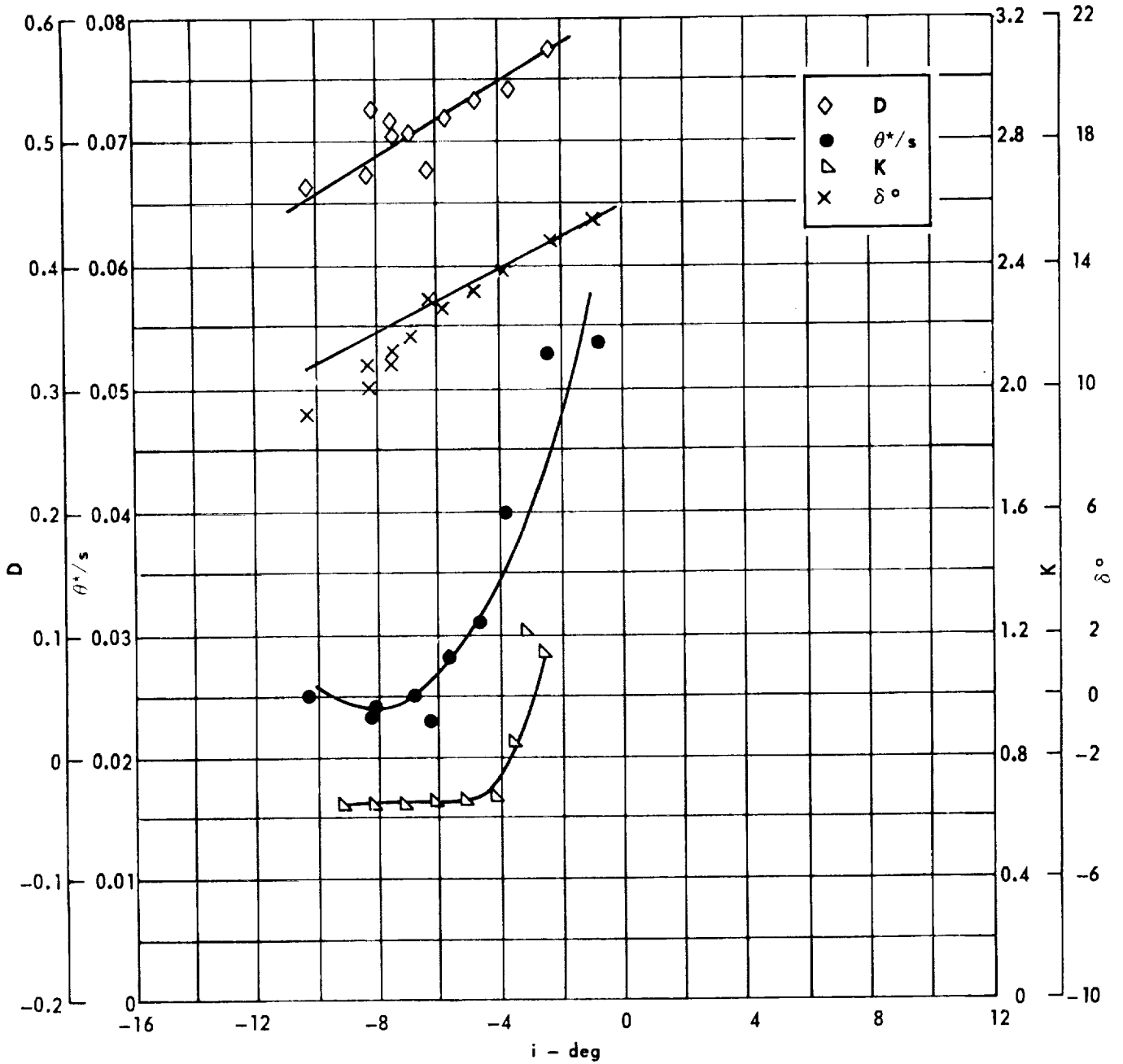


Cascade configuration : $\beta_{1N} = 75, \sigma = 0.75$

Double circular-arc profile : $\phi = 25, t/c = 0.06$

(a) $\theta, \bar{\omega}, \Delta p/q_1, \beta_1$

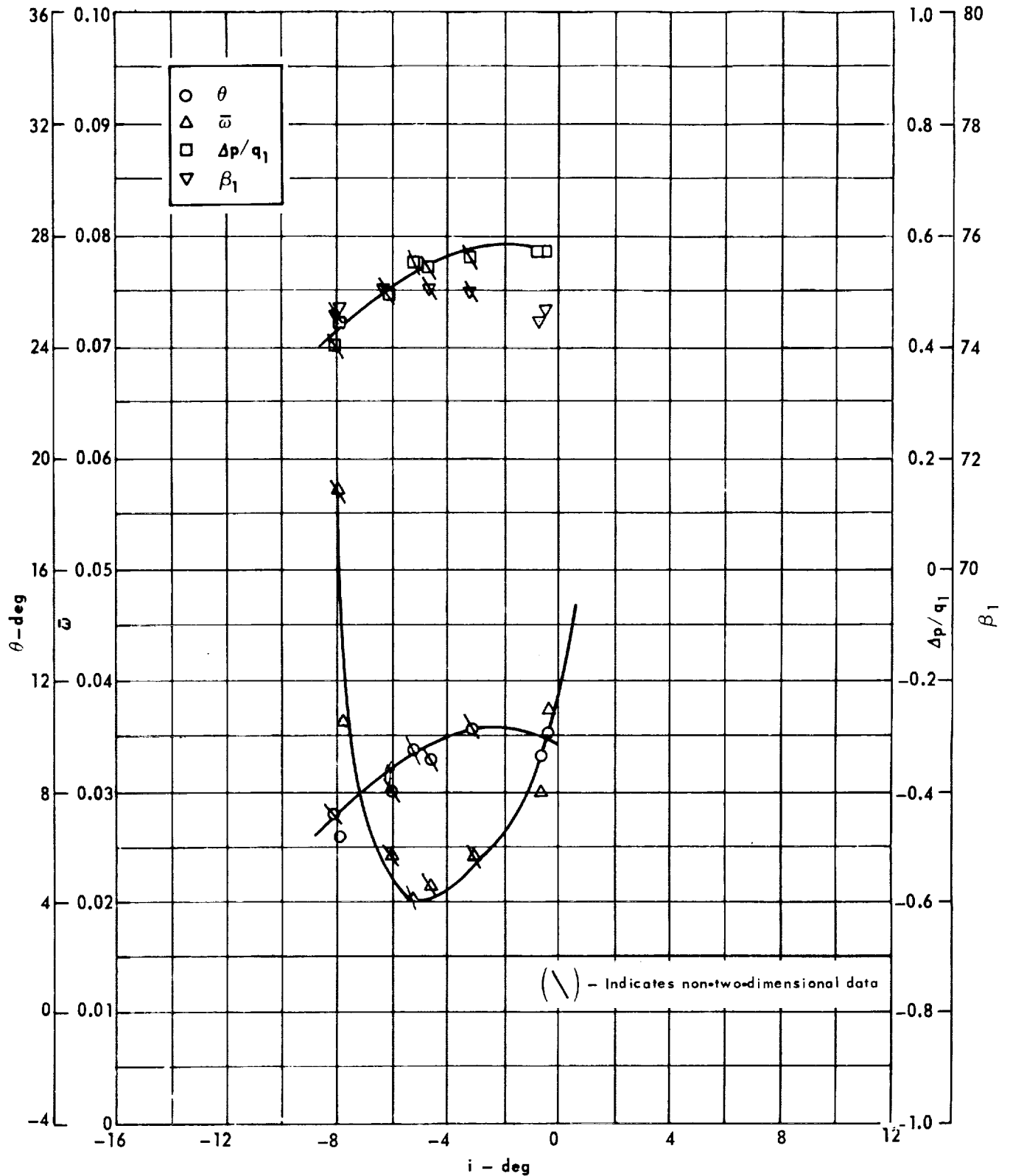
Figure 108. - Cascade characteristics as functions of incidence.



Cascade configuration: $\beta_{1N} = 75, \sigma = 0.75$
 Double circular-arc profile: $\phi = 25, t'/c = 0.06$

(b) D, θ^*/s , K, δ°

Figure 108. - Concluded.

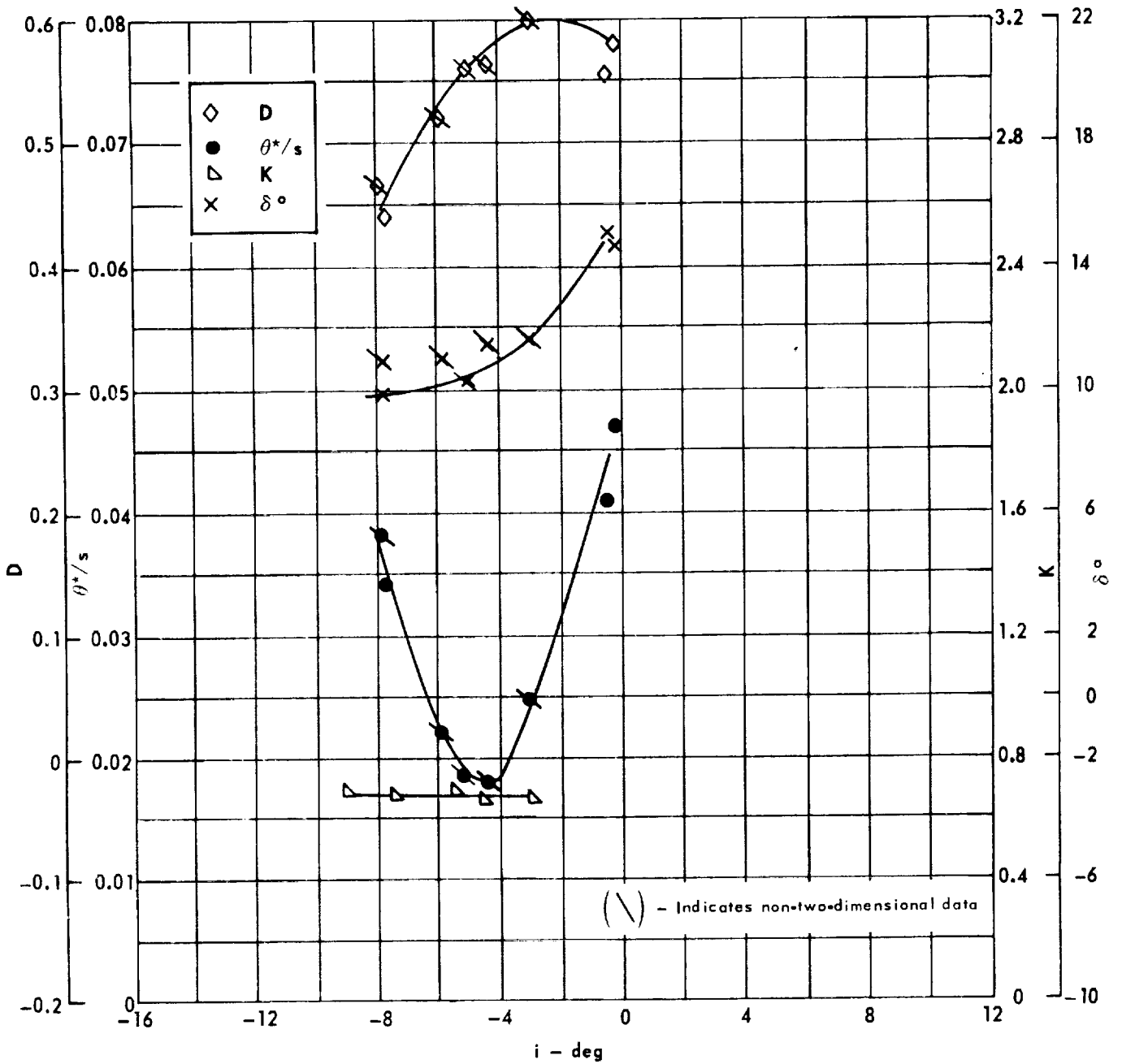


Cascade configuration: $\beta_{1N} = 75, \sigma = 1.00$

Double circular-arc profile: $\phi = 25, r/c = 0.06$

(a) $\theta, \bar{\omega}, \Delta p/q_1, \beta_1$

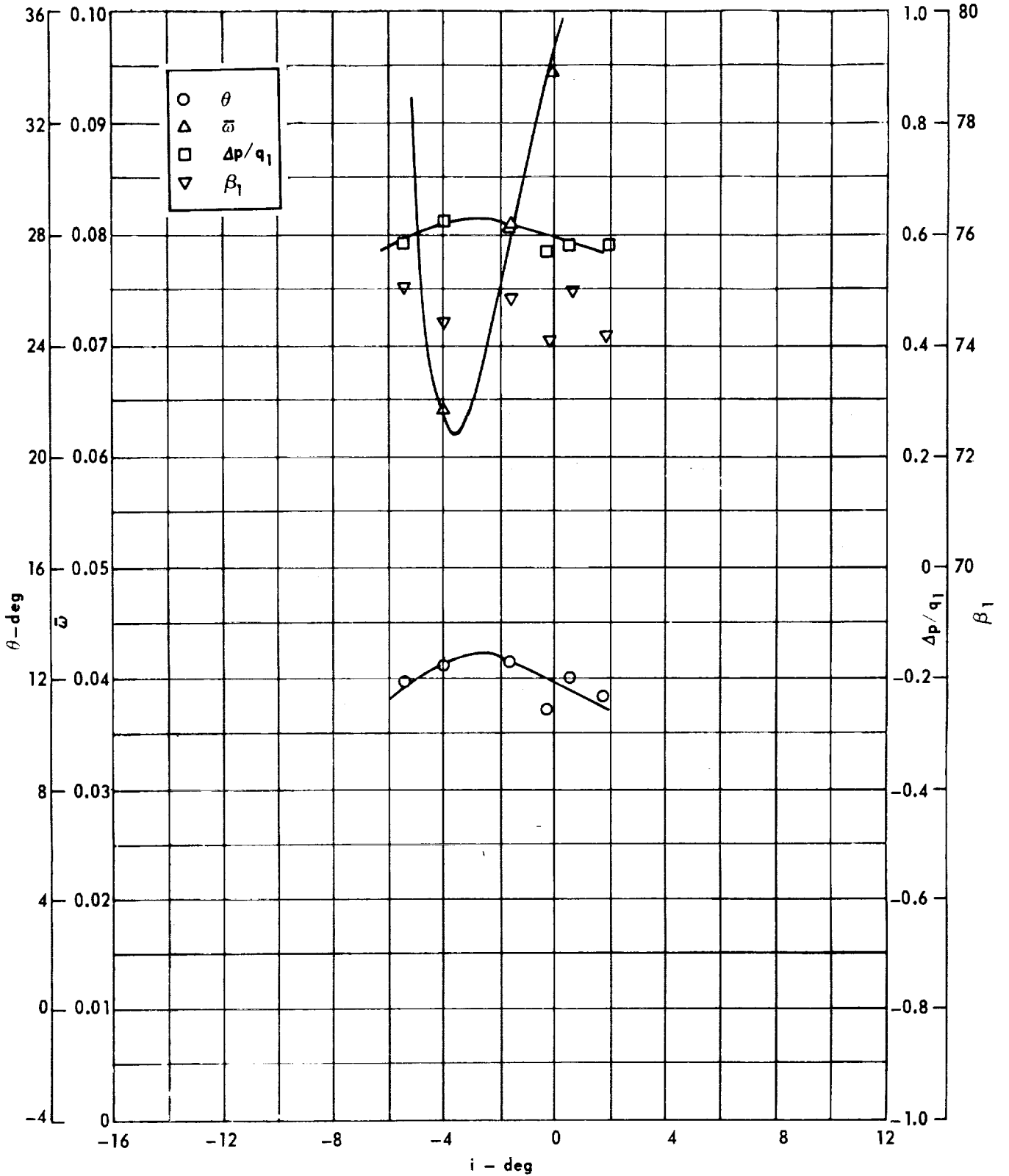
Figure 109. - Cascade characteristics as functions of incidence.



Cascade configuration: $\beta_{1N} = 75$, $\sigma = 1.00$
 Double circular-arc profile: $\phi = 25$, $t/c = 0.06$

(b) D, θ^*/s , K, δ°

Figure 109 . - Concluded.

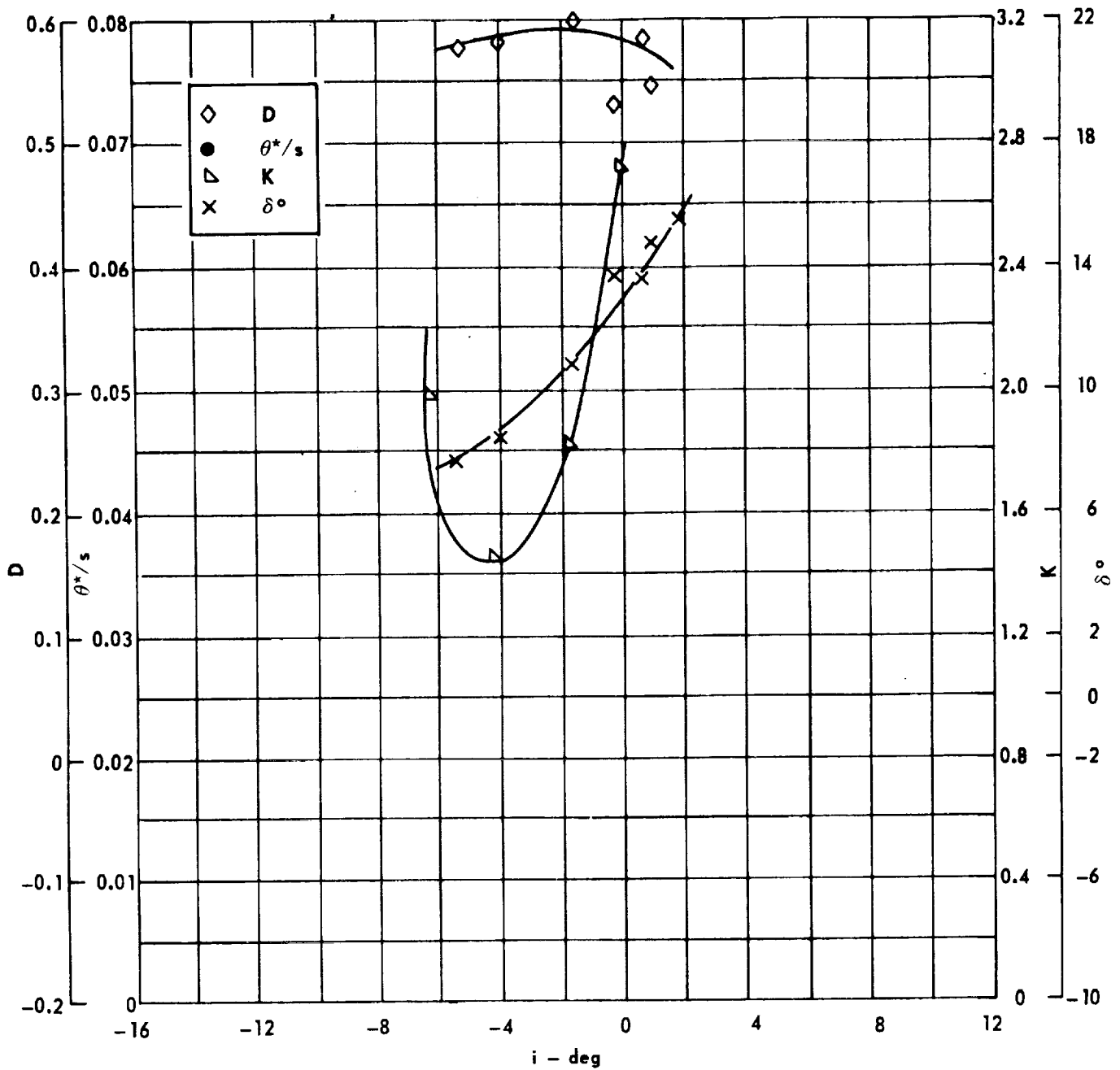


Cascade configuration: $\beta_{1N} = 75, \sigma = 1.50$

Double circular-arc profile: $\phi = 25, t/c = 0.06$

(a) $\theta, \bar{\omega}, \Delta p/q_1, \beta_1$

Figure 110. - Cascade characteristics as functions of incidence.

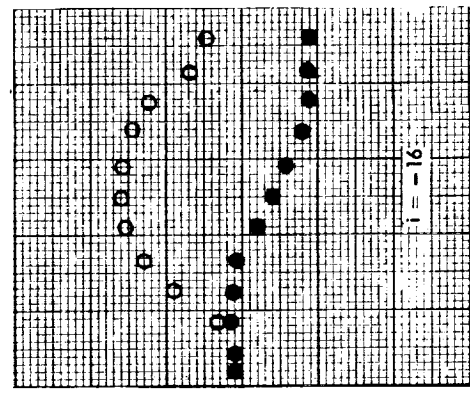
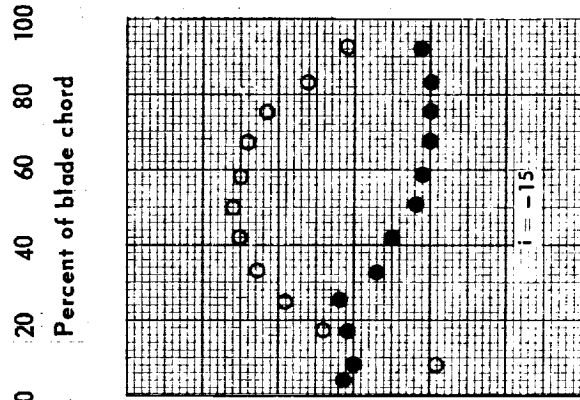
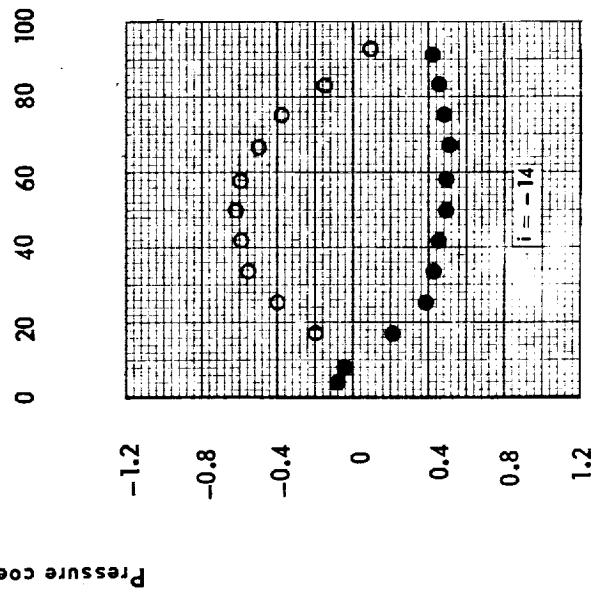
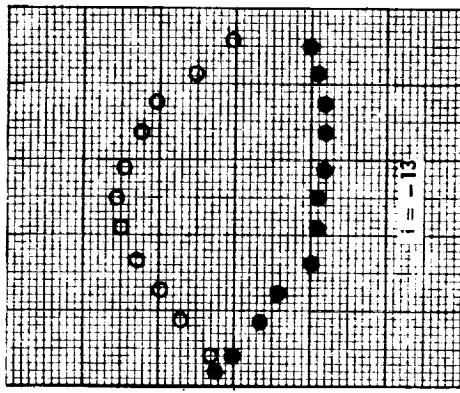
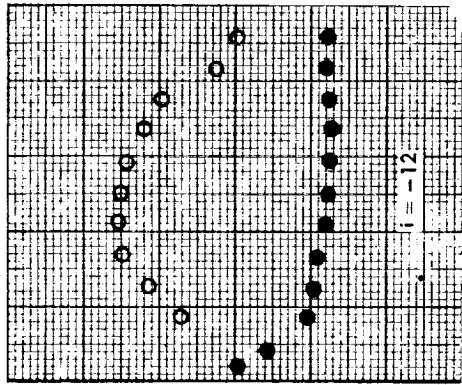
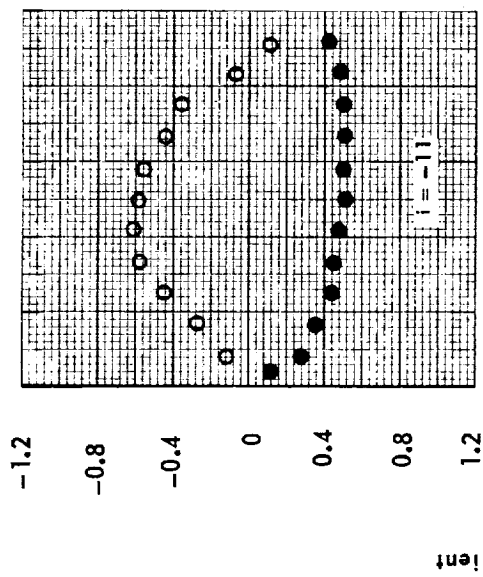


Cascade configuration: $\beta_{1N} = 75$, $\sigma = 1.50$
 Double circular-arc profile: $\phi = 25$, $t/c = 0.06$

(b) D, θ^*/s , K, δ°

Figure 110. - Concluded.

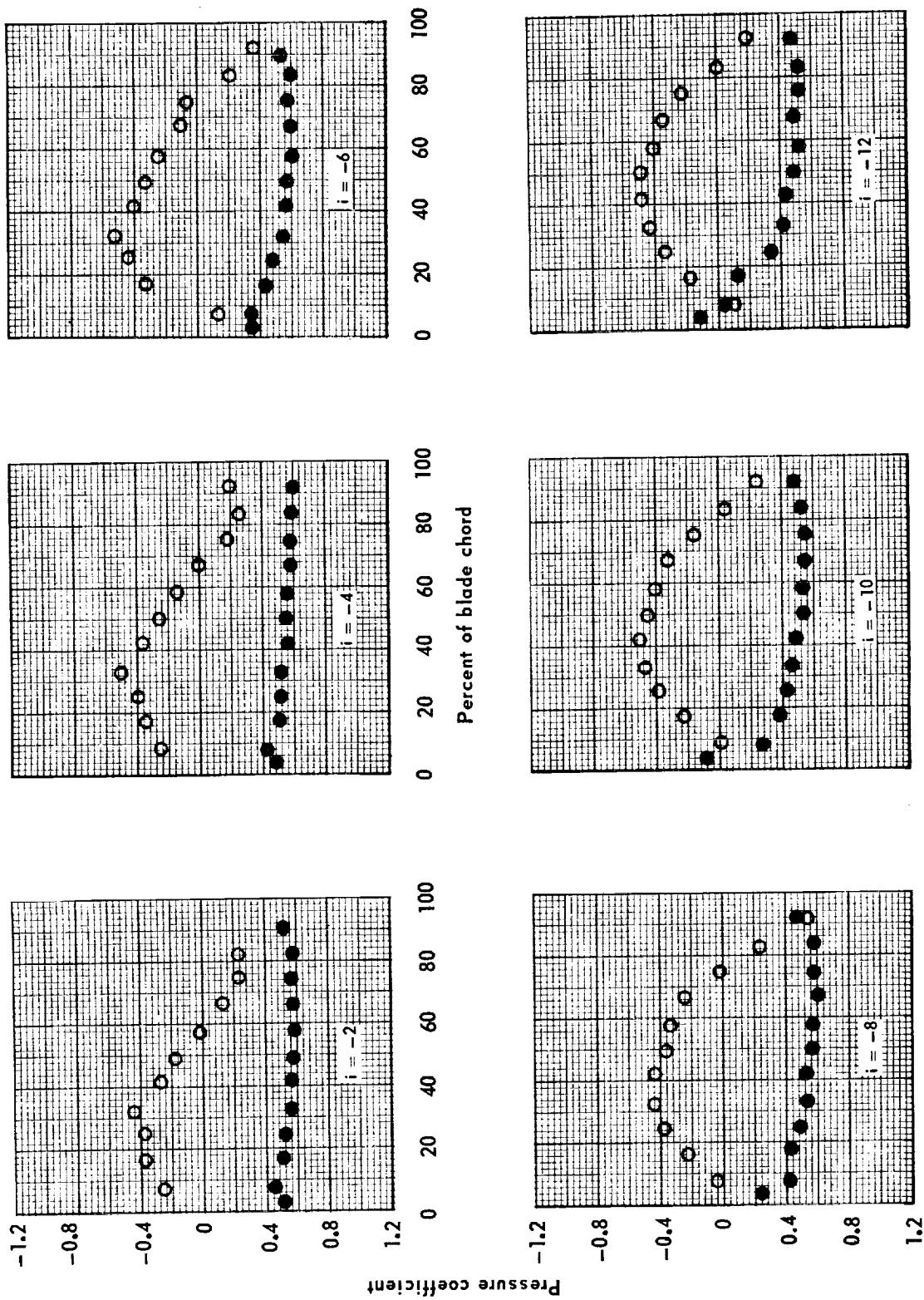
○ Suction surface
● Pressure surface



(a) $\phi^* = 40$, $r/c = 0.06$, $\beta_{IN} = 60$, $\sigma = 0.75$

Figure 111. - Pressure distribution for double circular-arc hydrofoils.

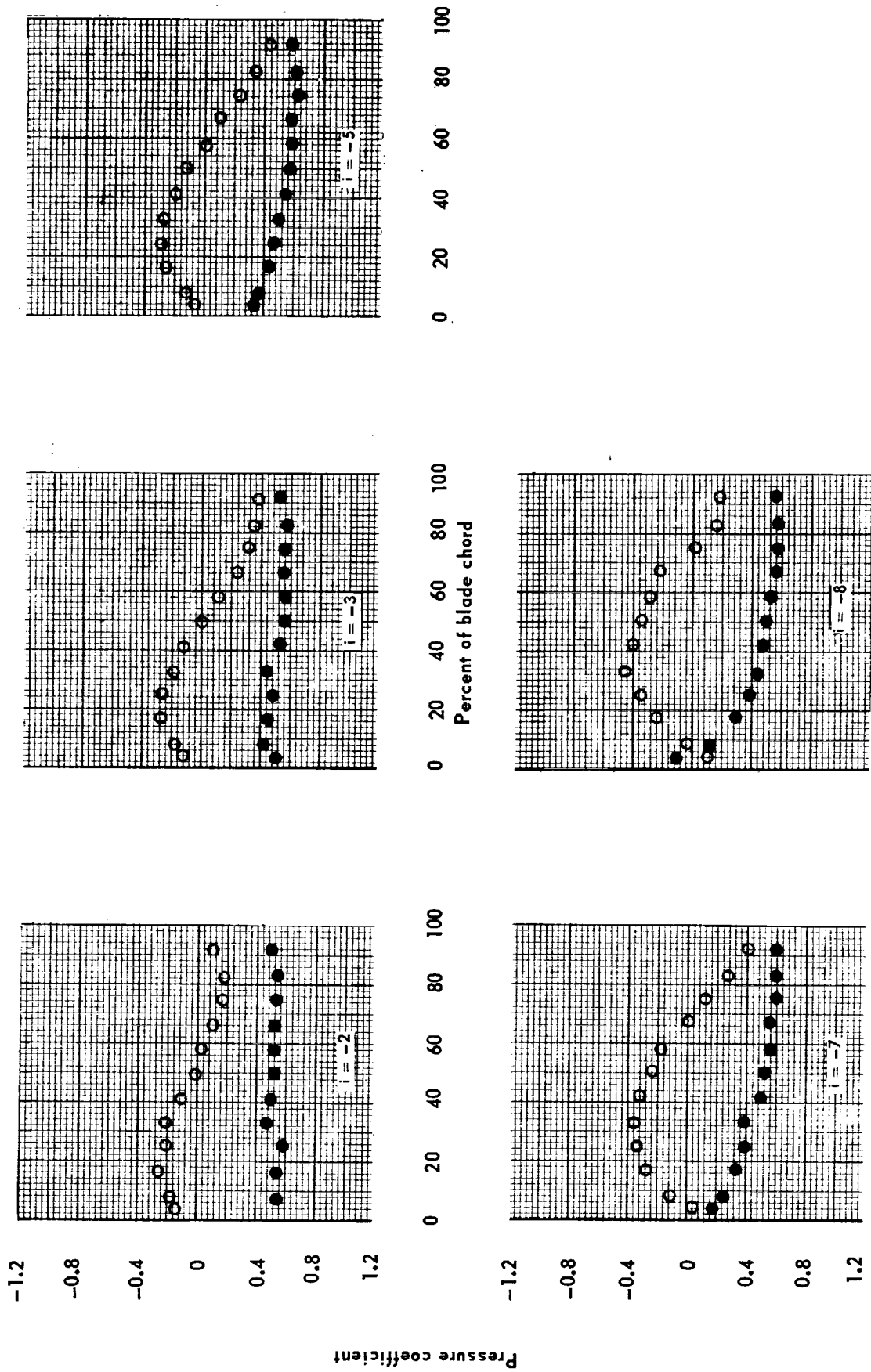
○ Suction surface
● Pressure surface



(b) $\phi = 40$, $t/c = 0.06$, $\beta_{TN} = 60$, $\sigma = 1.0$

Figure 111. - Continued.

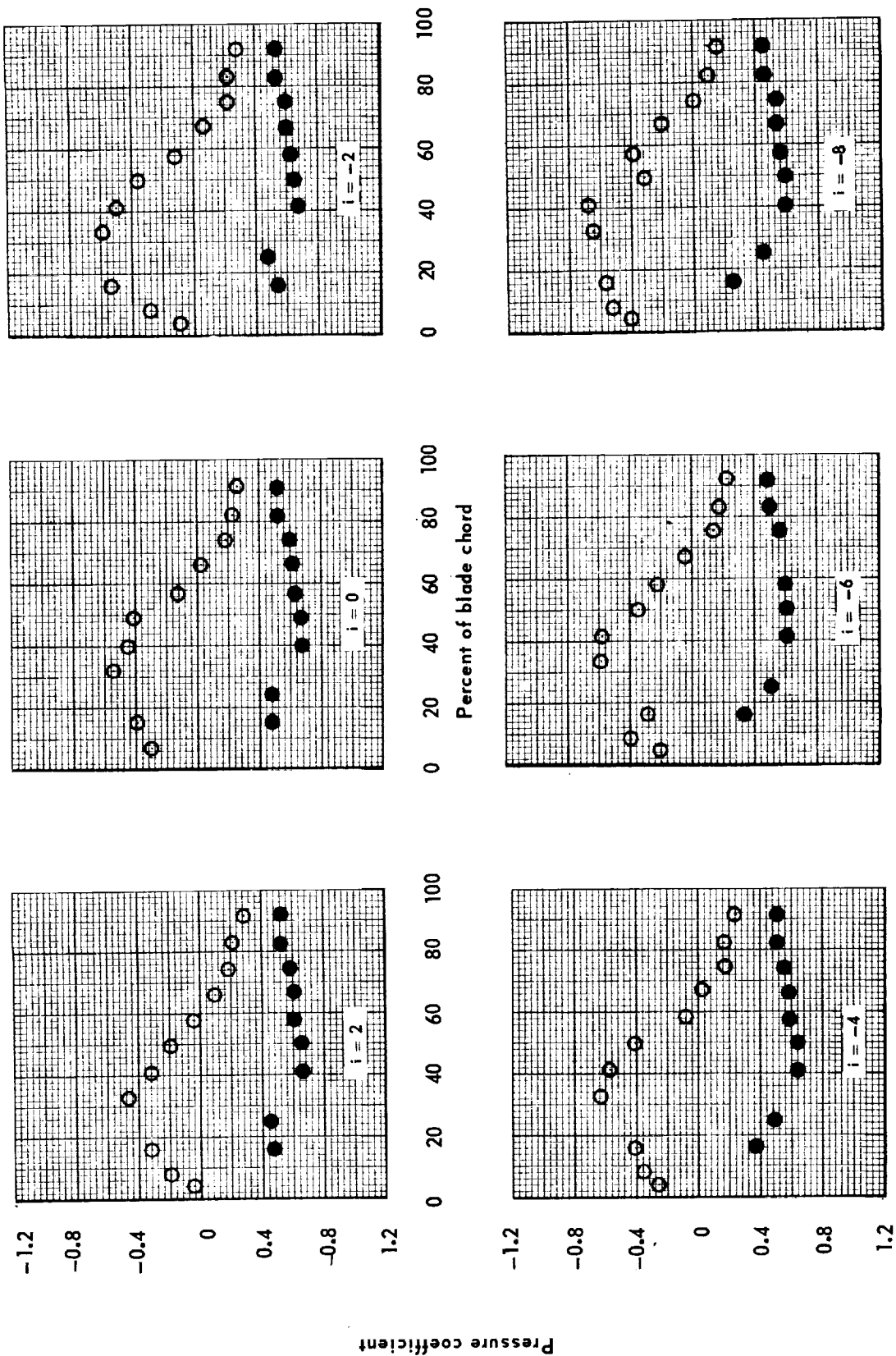
○ Suction surface
● Pressure surface



(c) $\phi = 40$, $t/c = 0.06$, $\beta_{IN} = 60$, $\sigma = 1.50$

Figure 111. - Concluded.

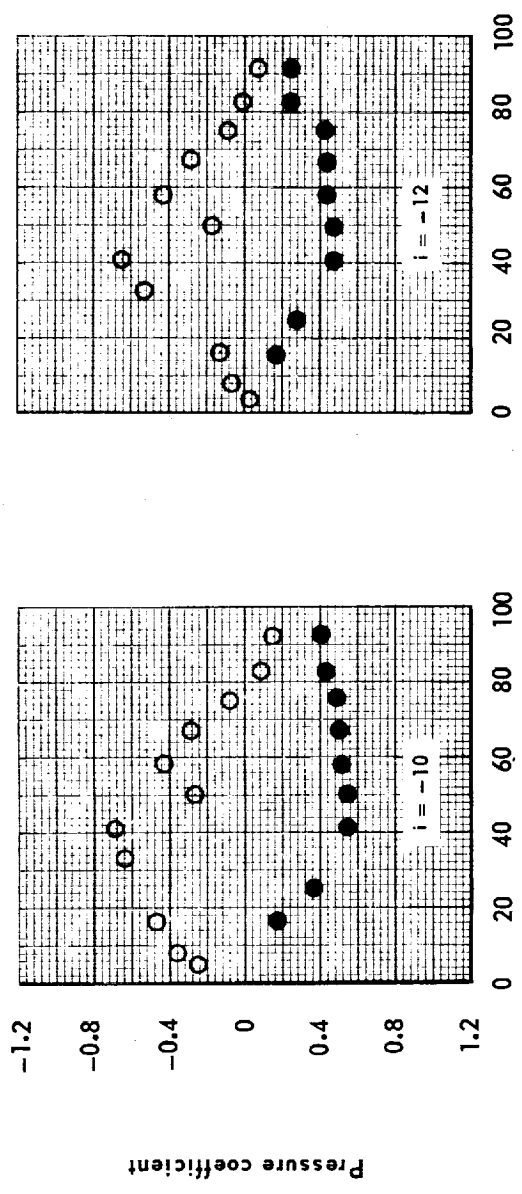
○ Suction surface
● Pressure surface



(a) $\phi = 40$, $t/c = 0.06$, $\beta_N = 60$, $\sigma = 0.75$

Figure 112. - Pressure distribution for slotted double circular - arc hydrofoils.

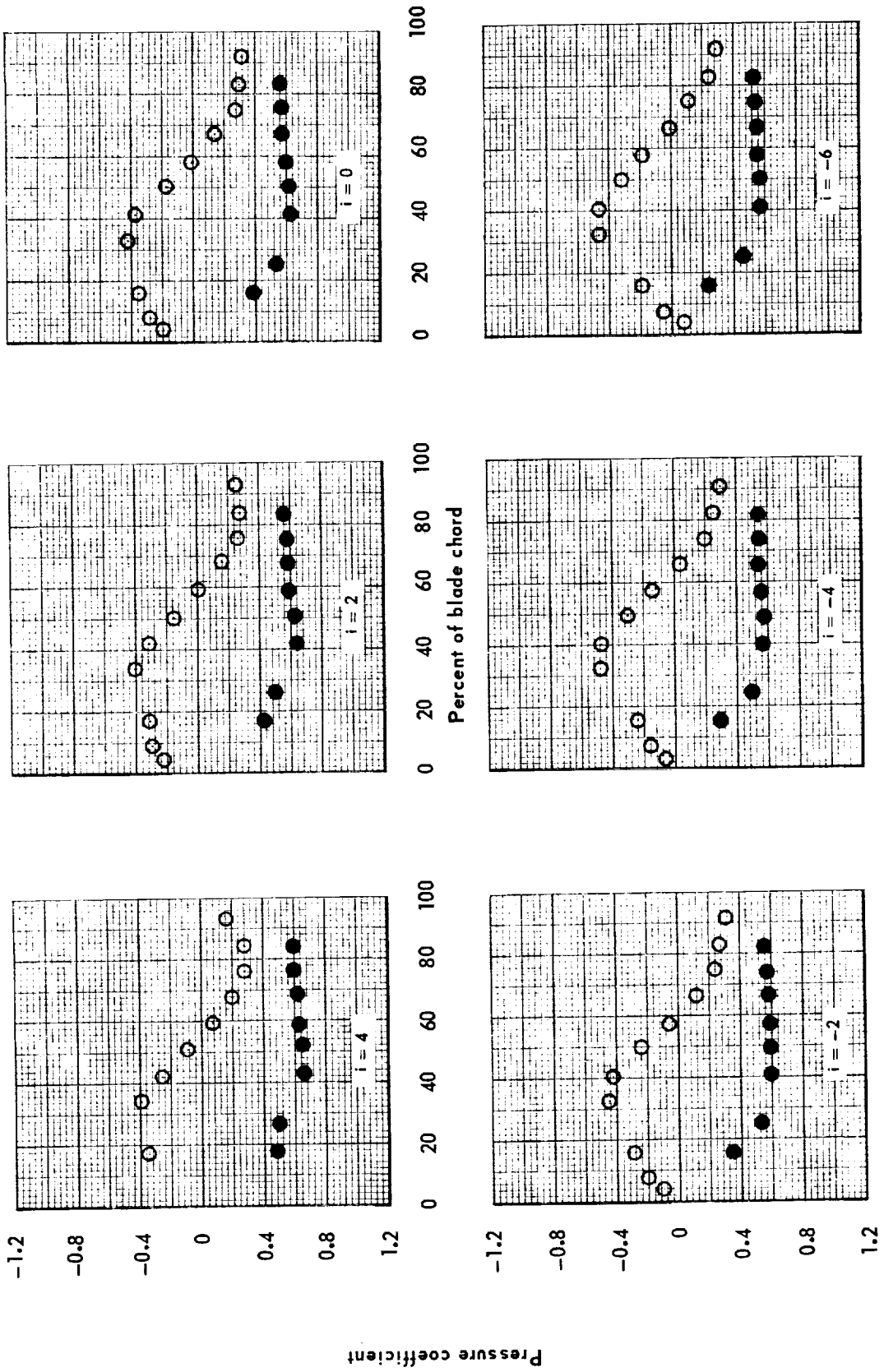
○ Suction surface
● Pressure surface



(b) $\phi = 40$, $t/c = 0.06$, $\beta_{IN} = 60$, $\sigma = 0.75$

Figure 112. -- Continued.

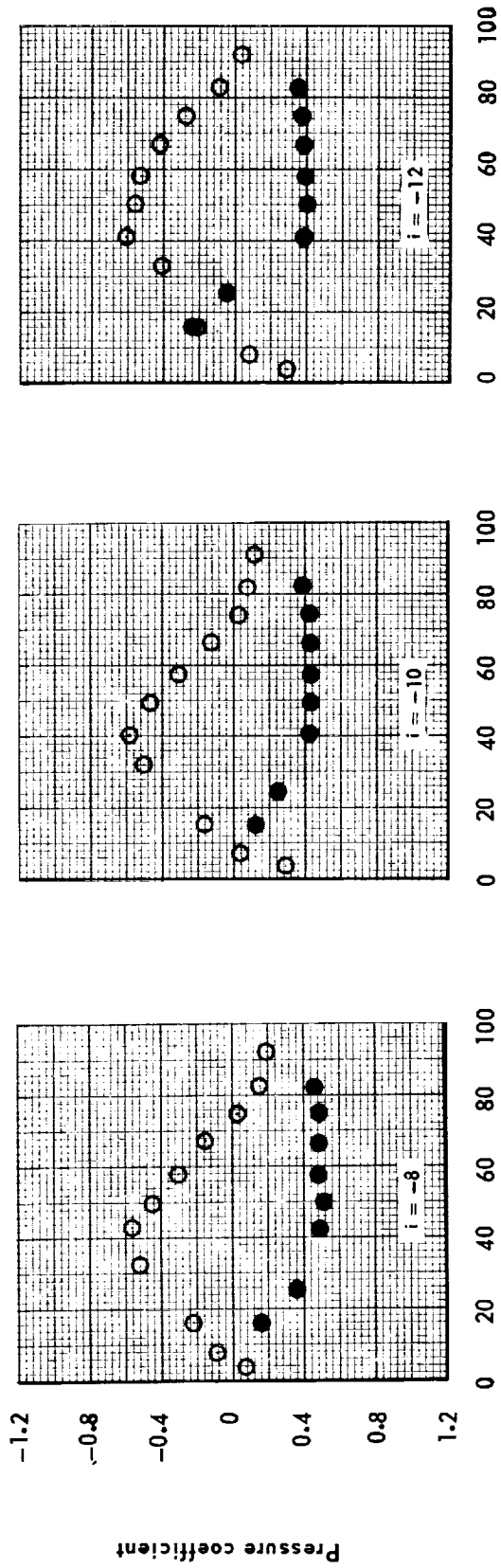
○ Suction surface
● Pressure surface



(c) $\phi = 40$, $r/c = 0.06$, $\beta_N = 60$, $\sigma = 1.00$

Figure 112. - Continued.

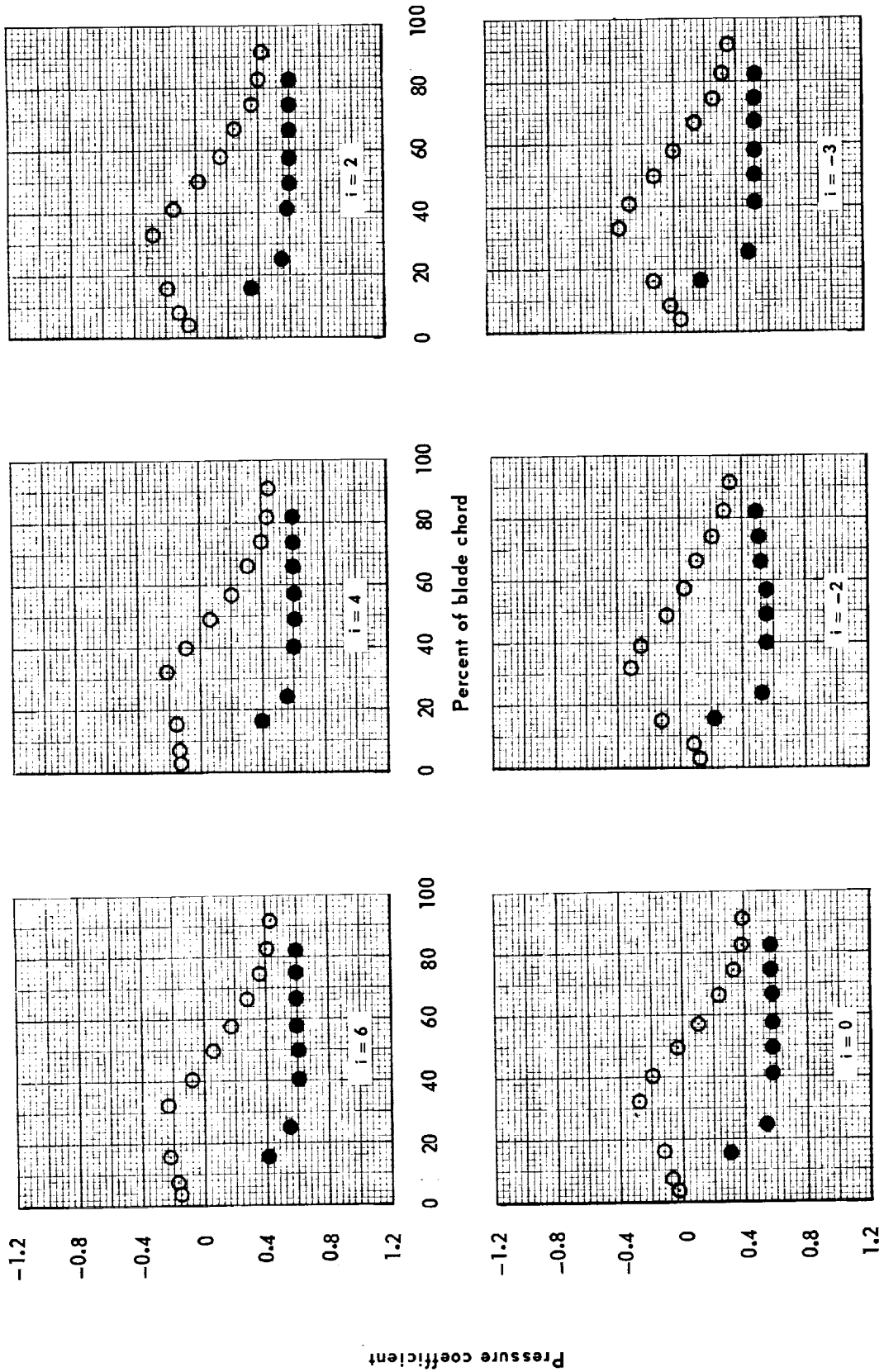
○ Suction surface
● Pressure surface



(d) $\phi = 40$, $r/c = 0.06$, $\beta_{1N} = 60$, $\sigma = 1.00$

Figure 112. - Continued.

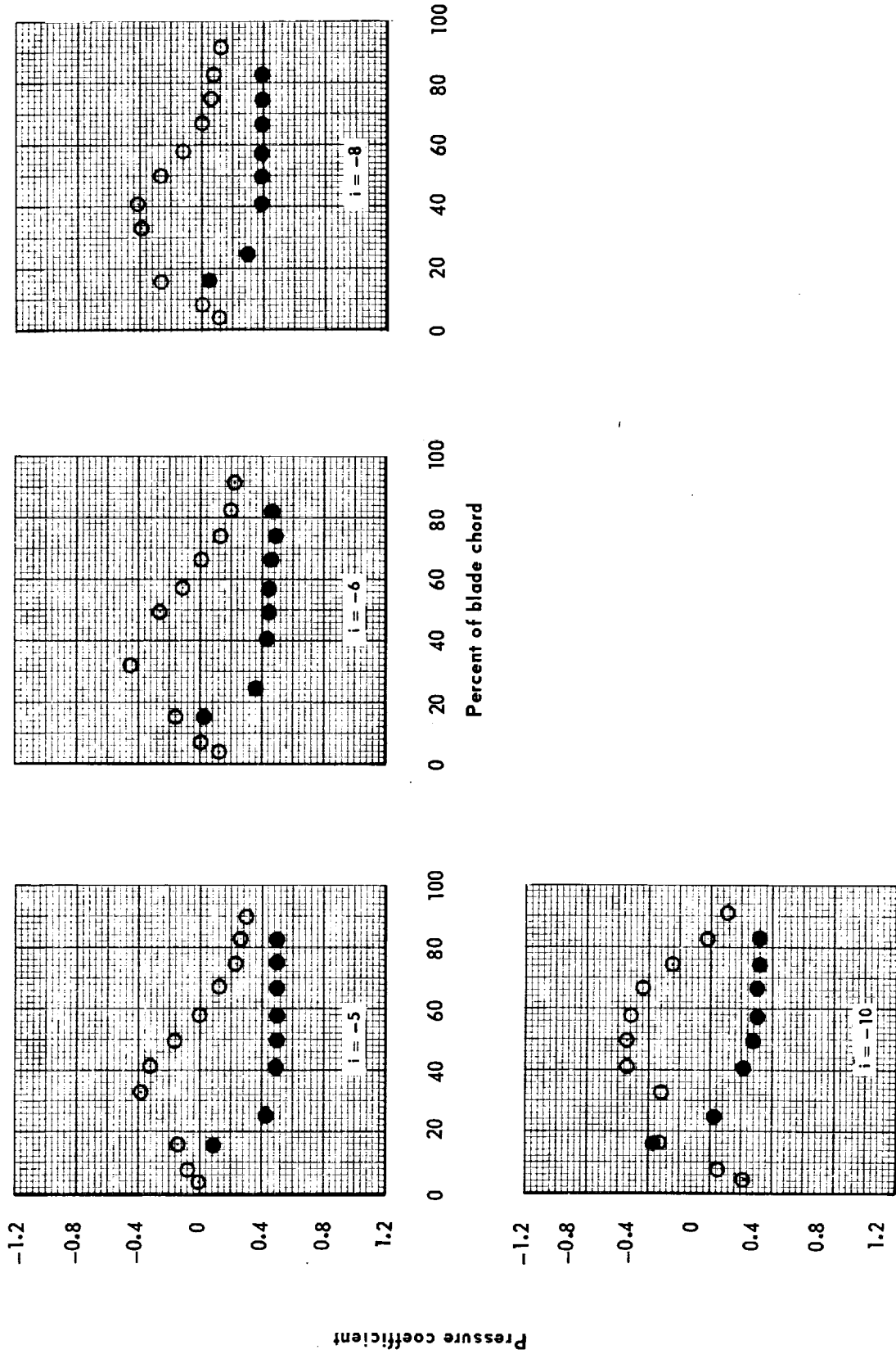
○ Suction surface
● Pressure surface



(e) $\phi = 40$, $t/c = 0.06$, $\beta_{1N} = 60$, $\sigma = 1.50$

Figure 112. - Continued.

○ Suction surface
● Pressure surface



(f) $\phi = 40$, $r/c = 0.06$, $\beta_{IN} = 60$, $\sigma = 1.50$

Figure 112. - Concluded.



(a)



(b)

$$\beta_{1N} = 75, \alpha = 5.1, \sigma = 1.50$$
$$\phi = 20, t/c = 0.10$$

Figure 113. - Cavitation on a cascade of double circular-arc hydrofoils.



(a)

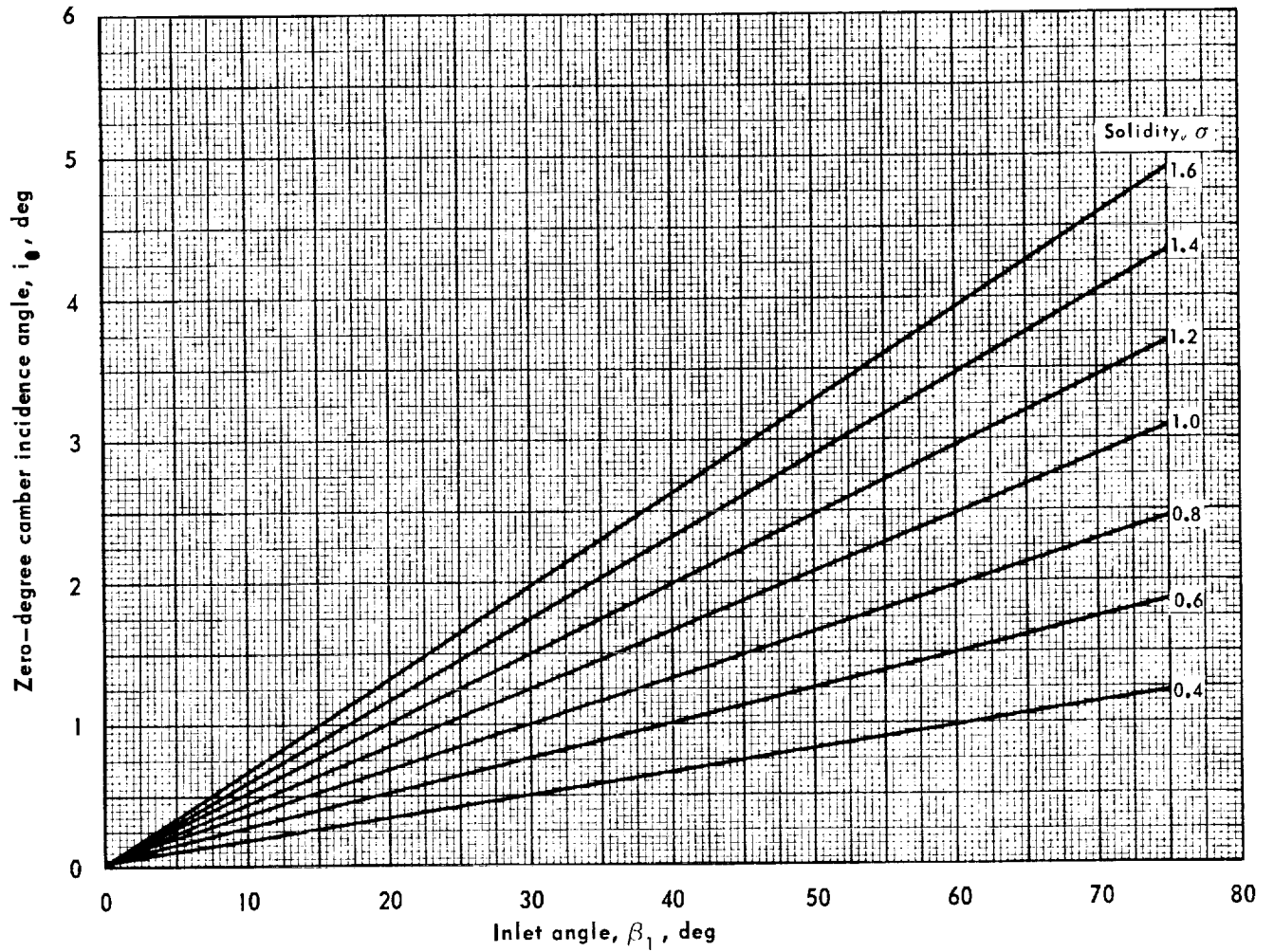


(b)

$$\beta_{1N} = 75, i = 2.0, \sigma = 1.50$$

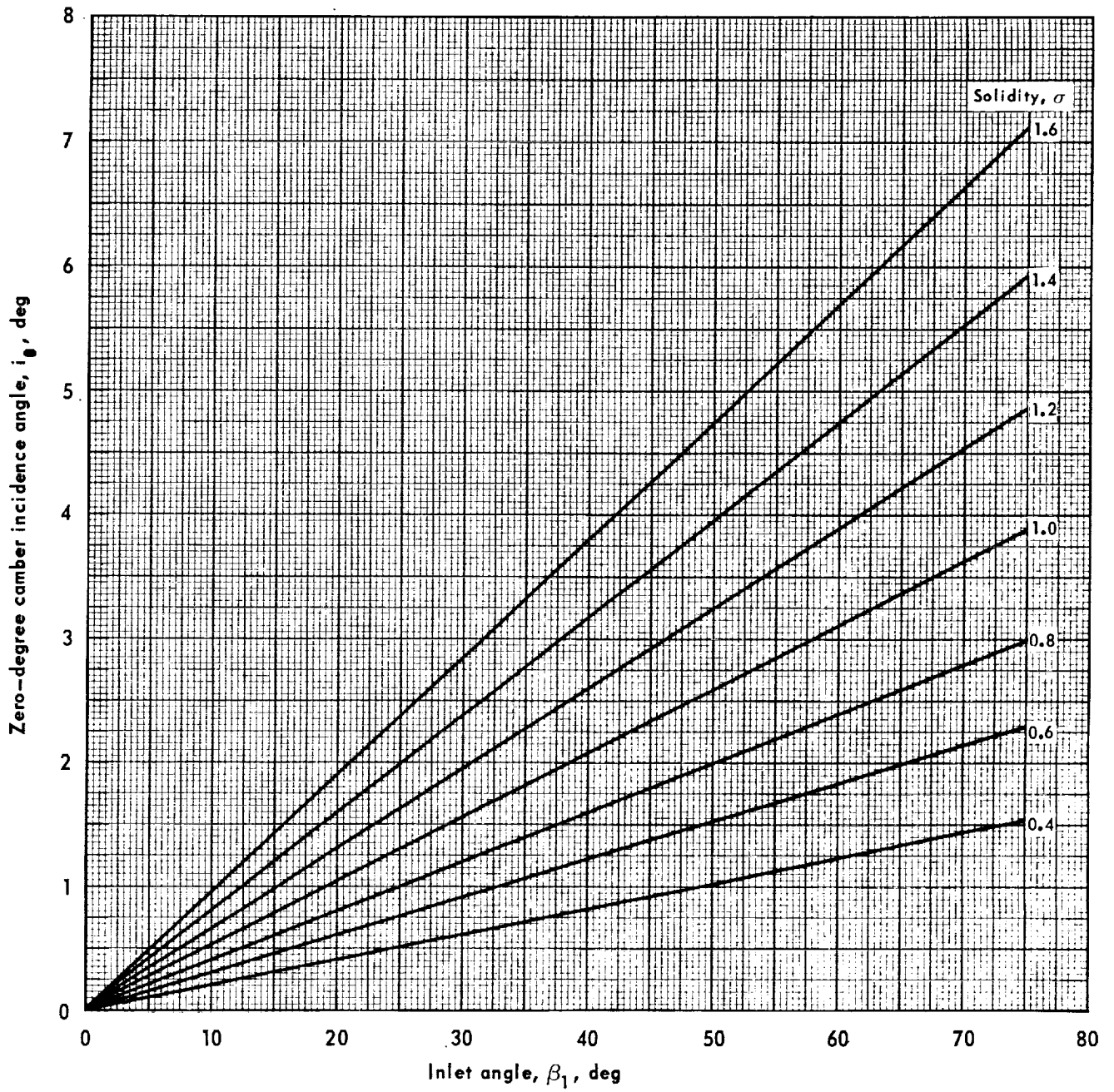
$$\phi = 20, t/c = 0.10$$

Figure 114. - Propagating cavitation on a cascade of double circular-arc hydrofoils.



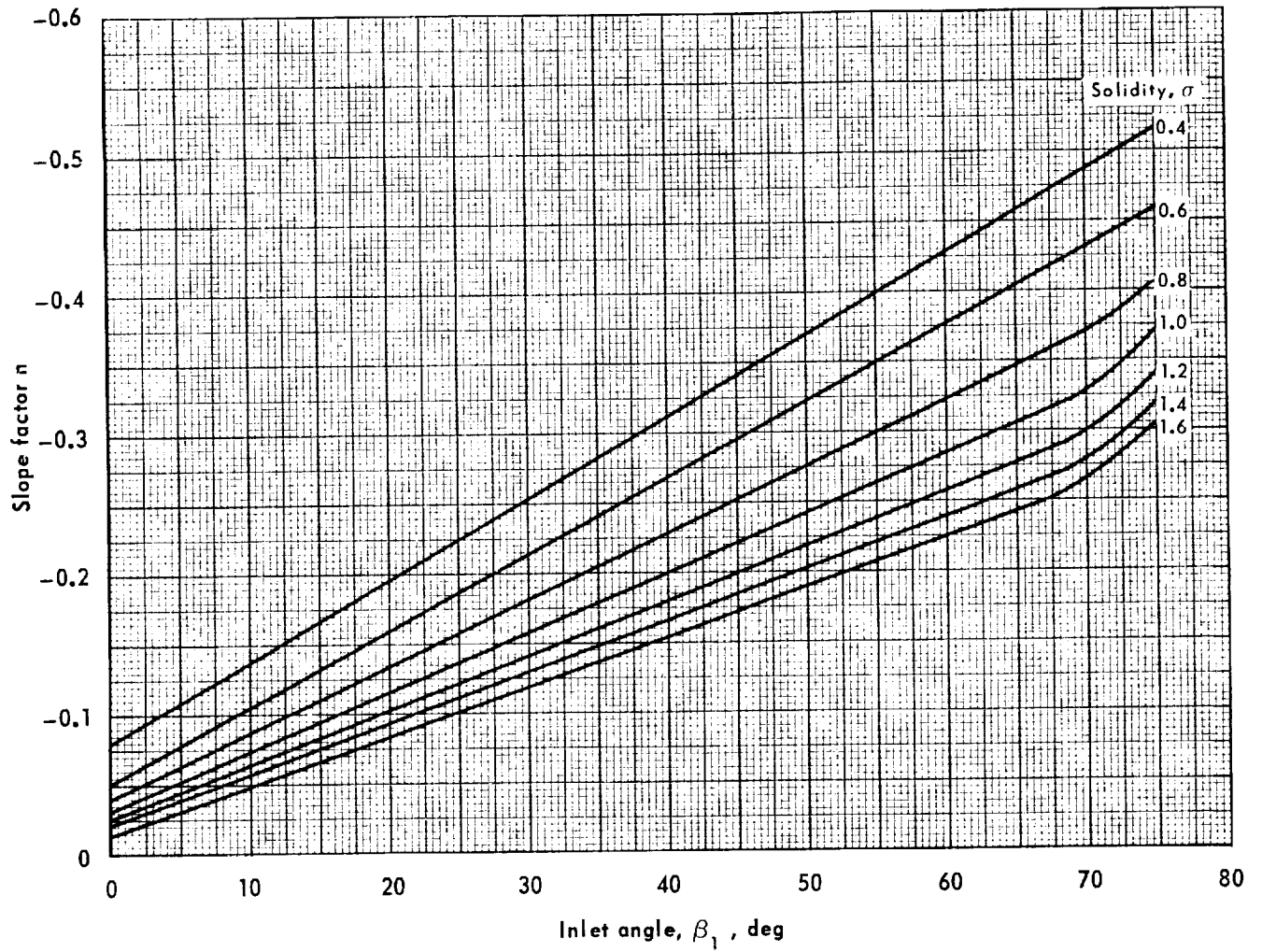
(a) $t/c = 0.06$

Figure 115. — Reference minimum-loss incidence angle for zero-degree camber double circular-arc hydrofoils.



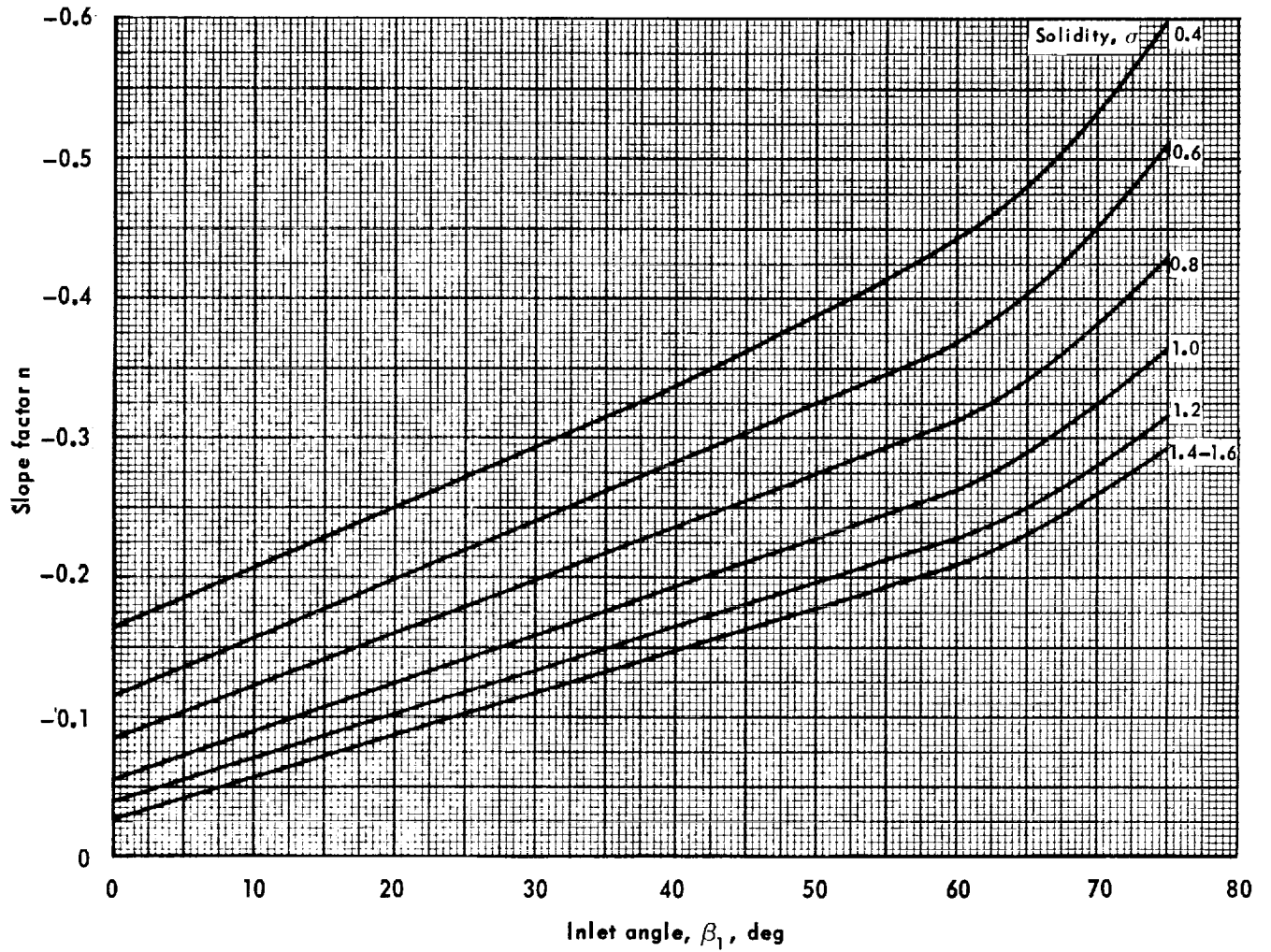
(b) $t/c = 0.10$

Figure 115. - Concluded.



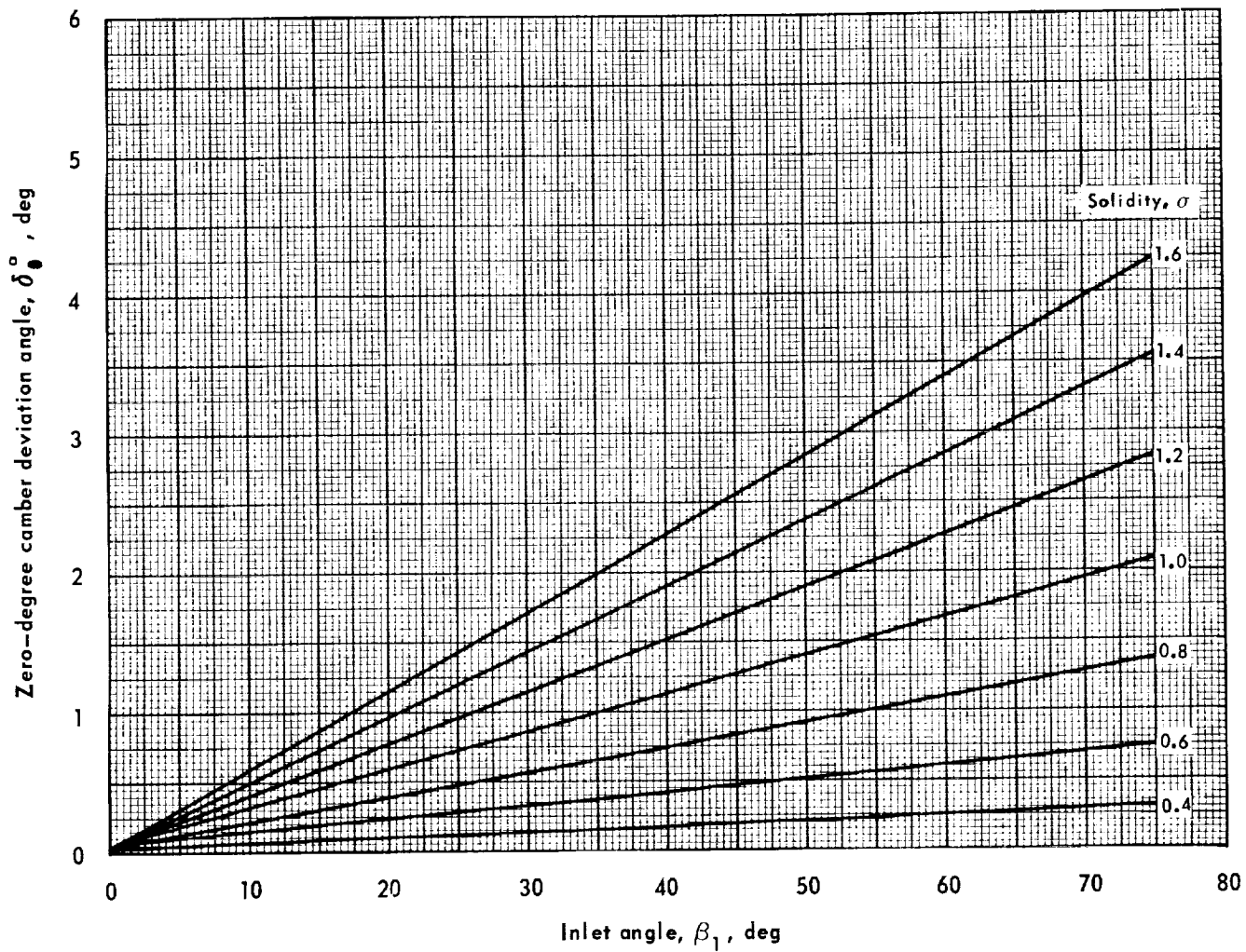
(a) $t/c = 0.06$

Figure 116. — Slope factor for reference minimum-loss incidence angle — double circular-arc hydrofoils.



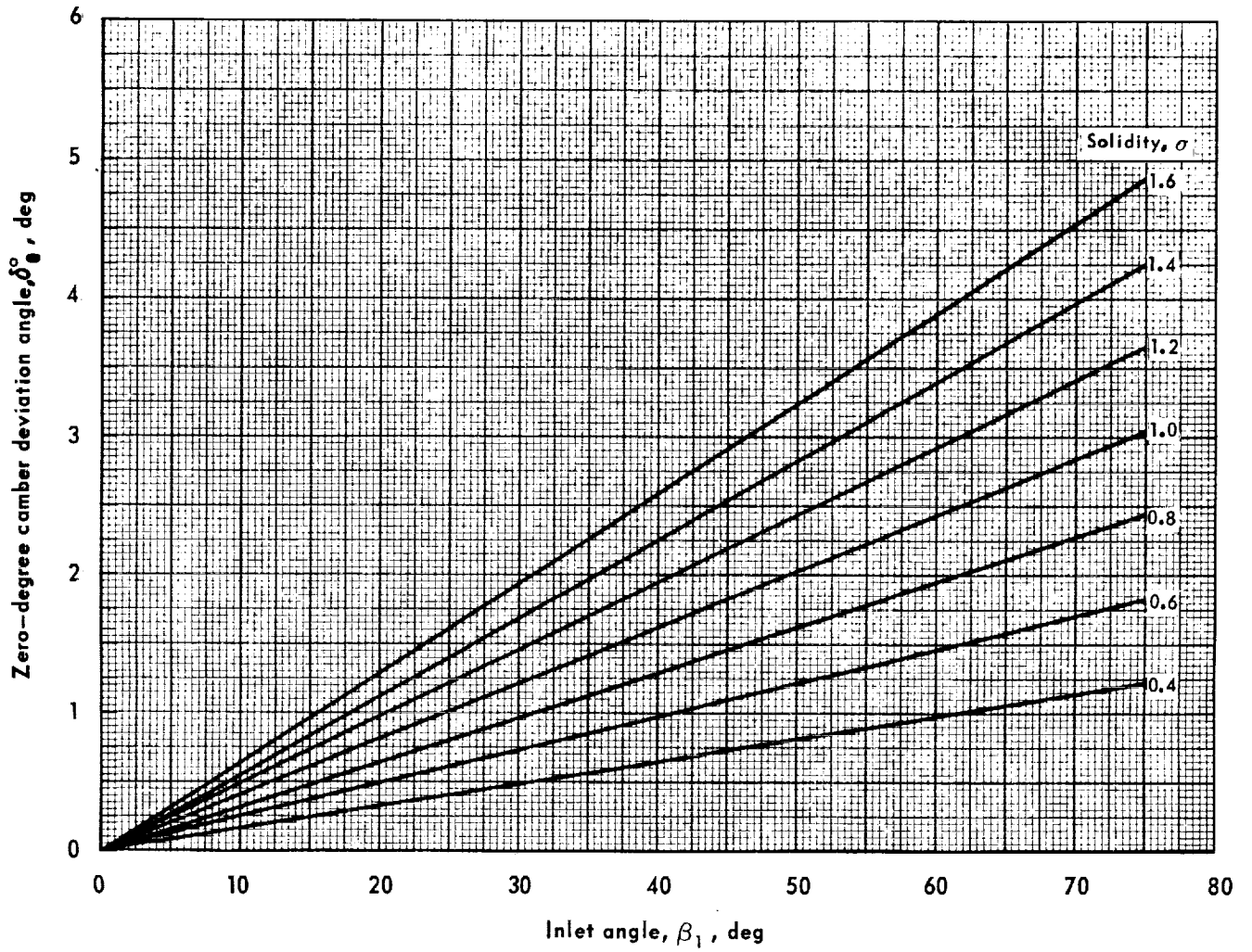
(b) $t/c = 0.10$

Figure 116. - Concluded.



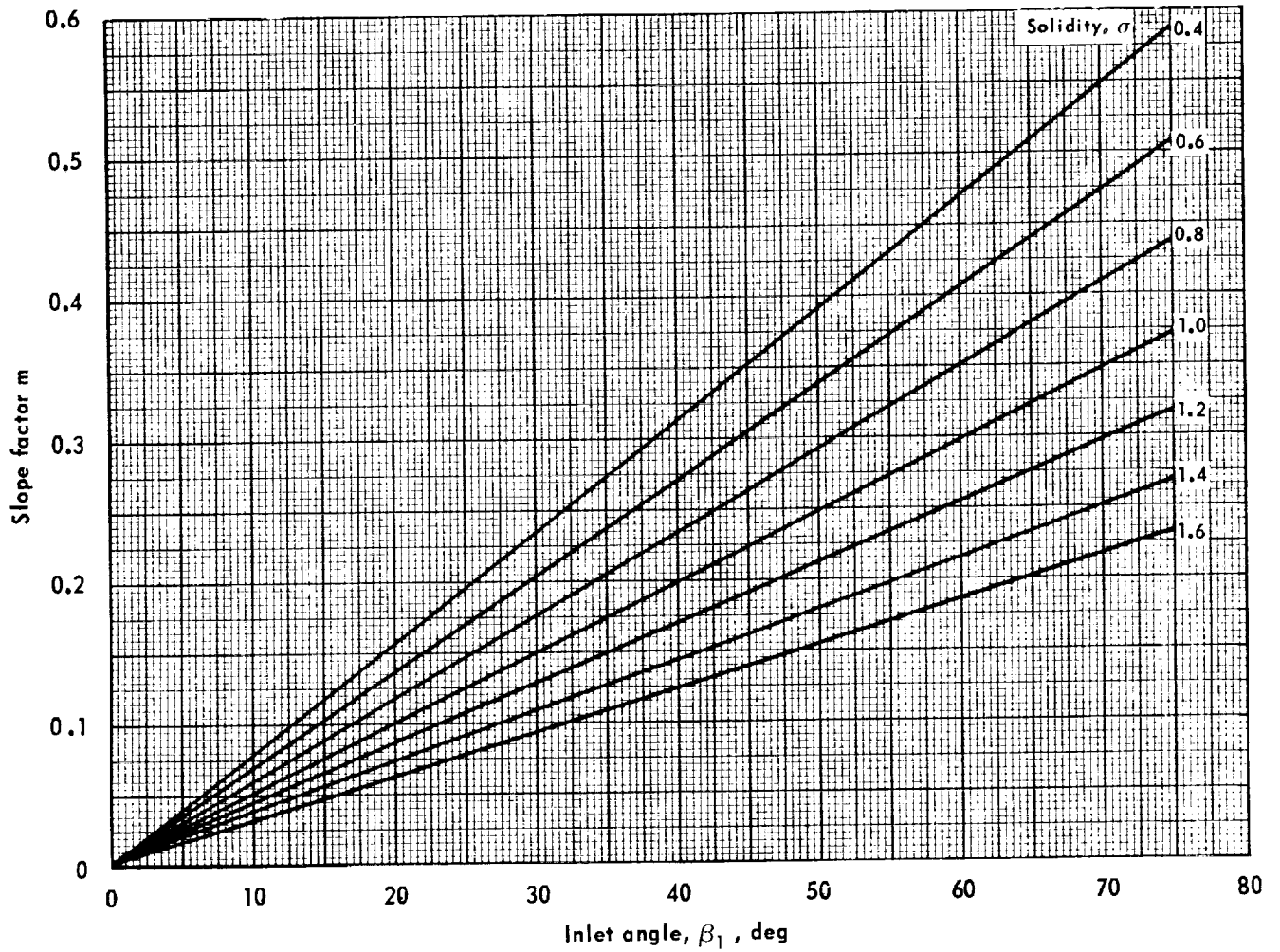
(a) $t/c = 0.06$

Figure 117. — Reference minimum-loss deviation angle for zero-degree camber double circular-arc hydrofoils.



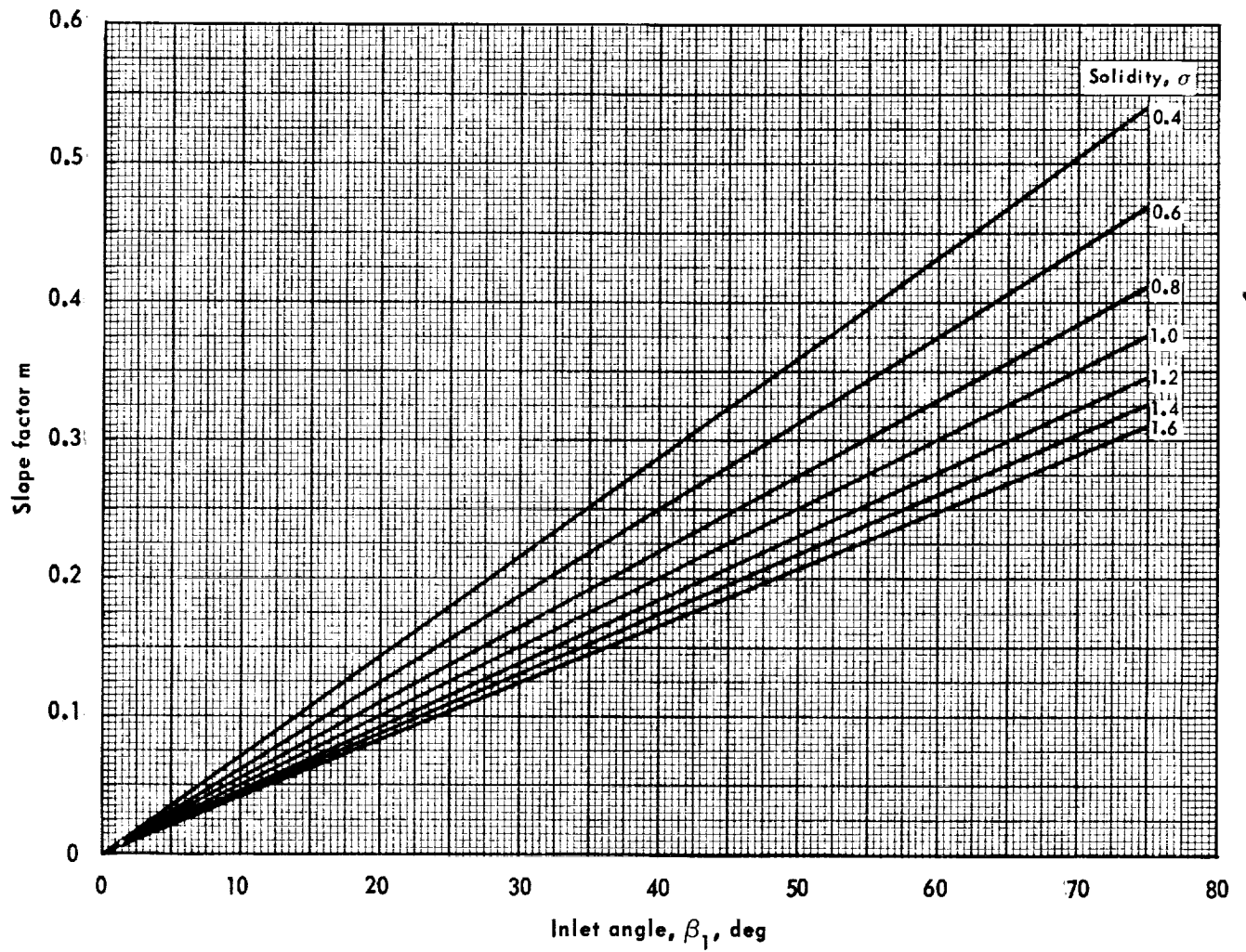
(b) $t/c = 0.10$

Figure 117. - Concluded.



(a) $t/c = 0.06$

Figure 118. — Slope factor for reference minimum-loss deviation angle — double circular-arc hydrofoils.



(b) $t/c = 0.10$

Figure 118. - Concluded.

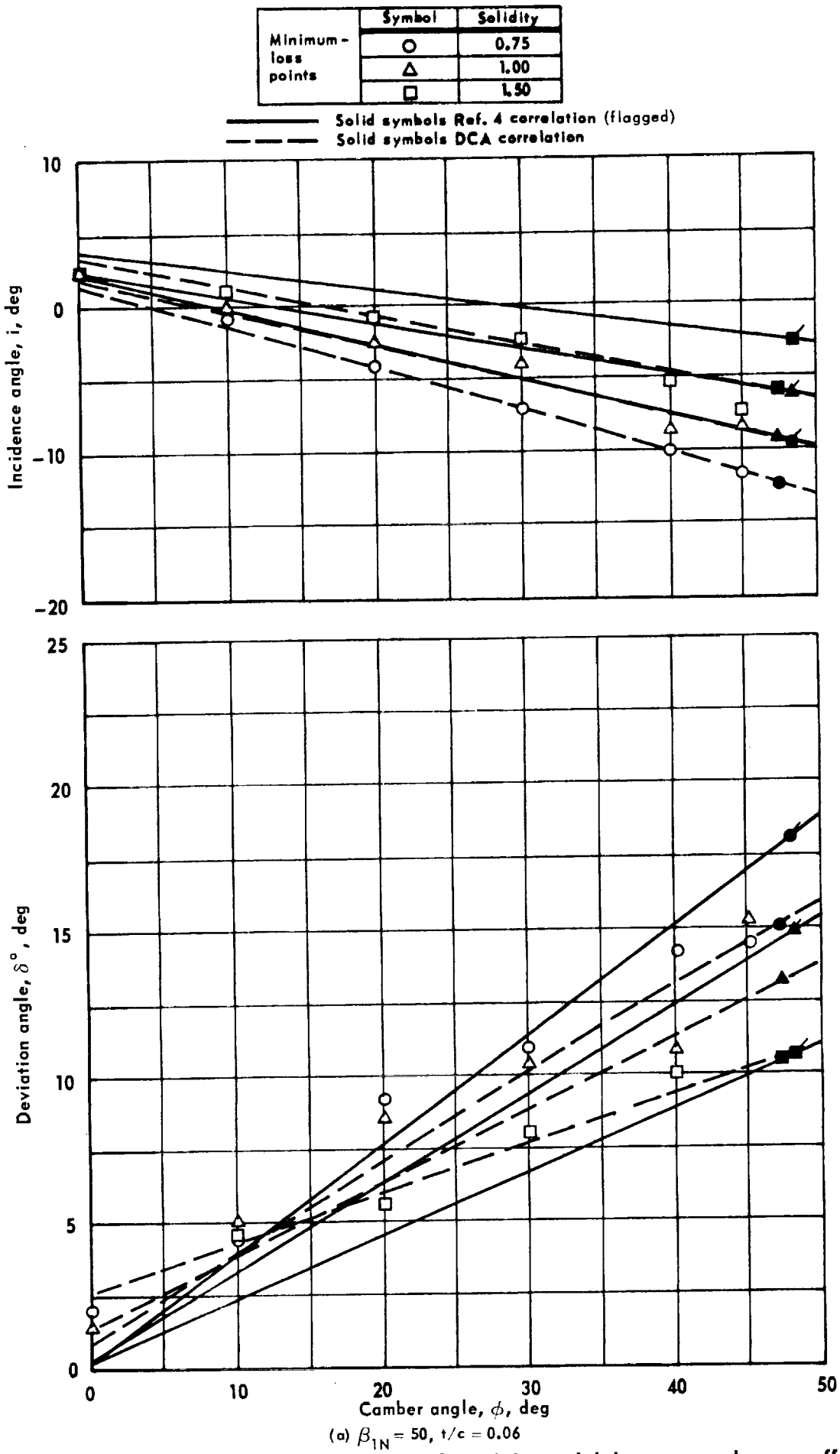
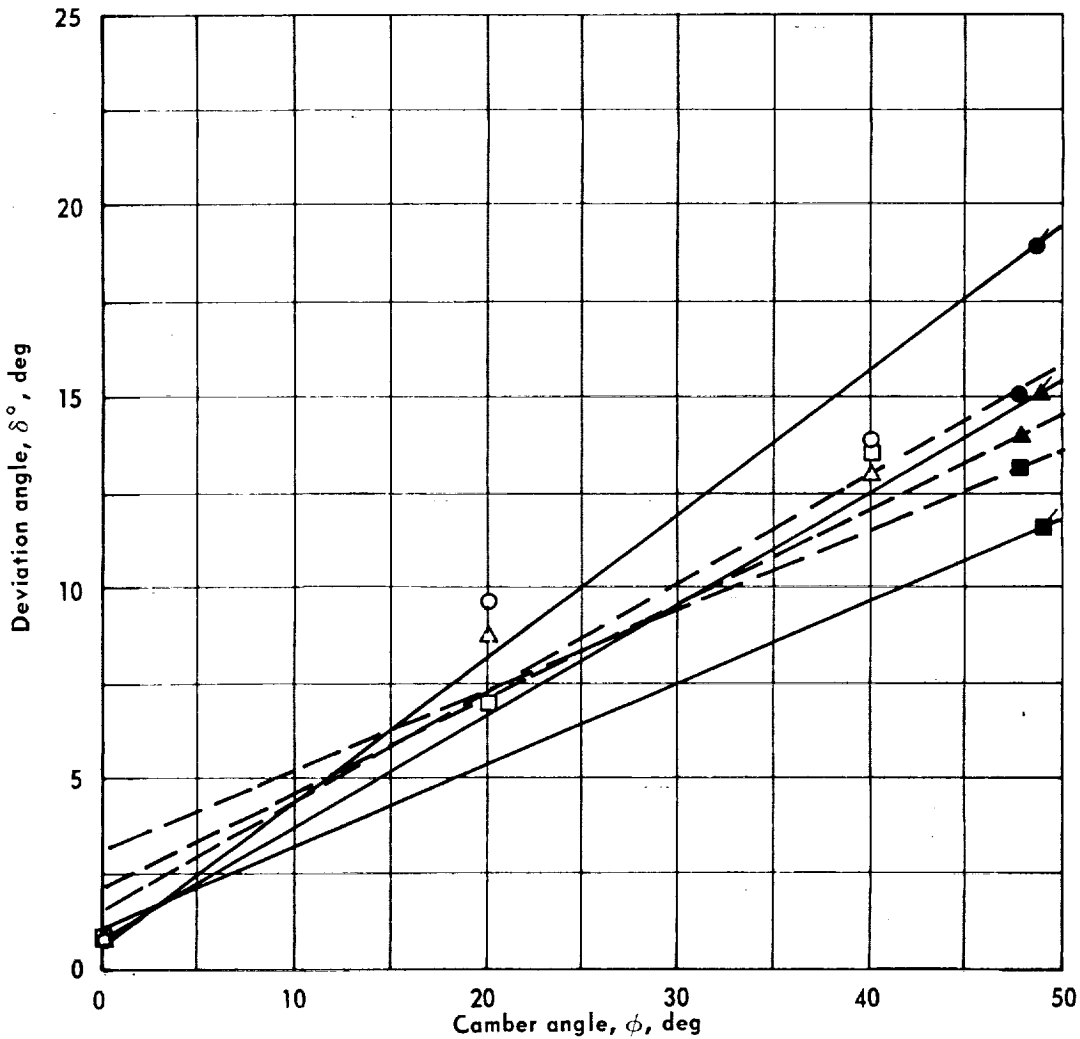
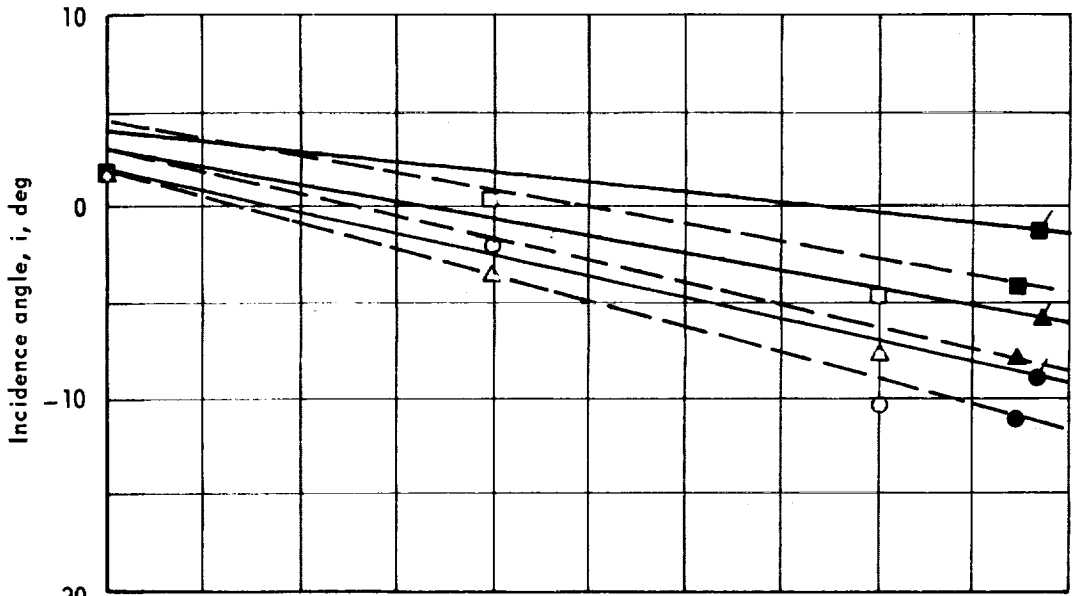


Figure 119. — Incidence and deviation angles for minimum total pressure loss coefficient.

Minimum-loss points	Symbol	Solidity
	○	0.75
	△	1.00
	□	1.50

— Solid symbols Ref. 4 correlation (flagged)
 - - - Solid symbols DCA correlation



(b) $\beta_{1N} = 50$, $t/c = 0.10$

Figure 119. - Continued.

Minimum-loss points	Symbol	Solidity
	○	0.75
	△	1.00
	□	1.50

— Solid symbols Ref. 4 correlation (flagged)
 - - - Solid symbols DCA correlation

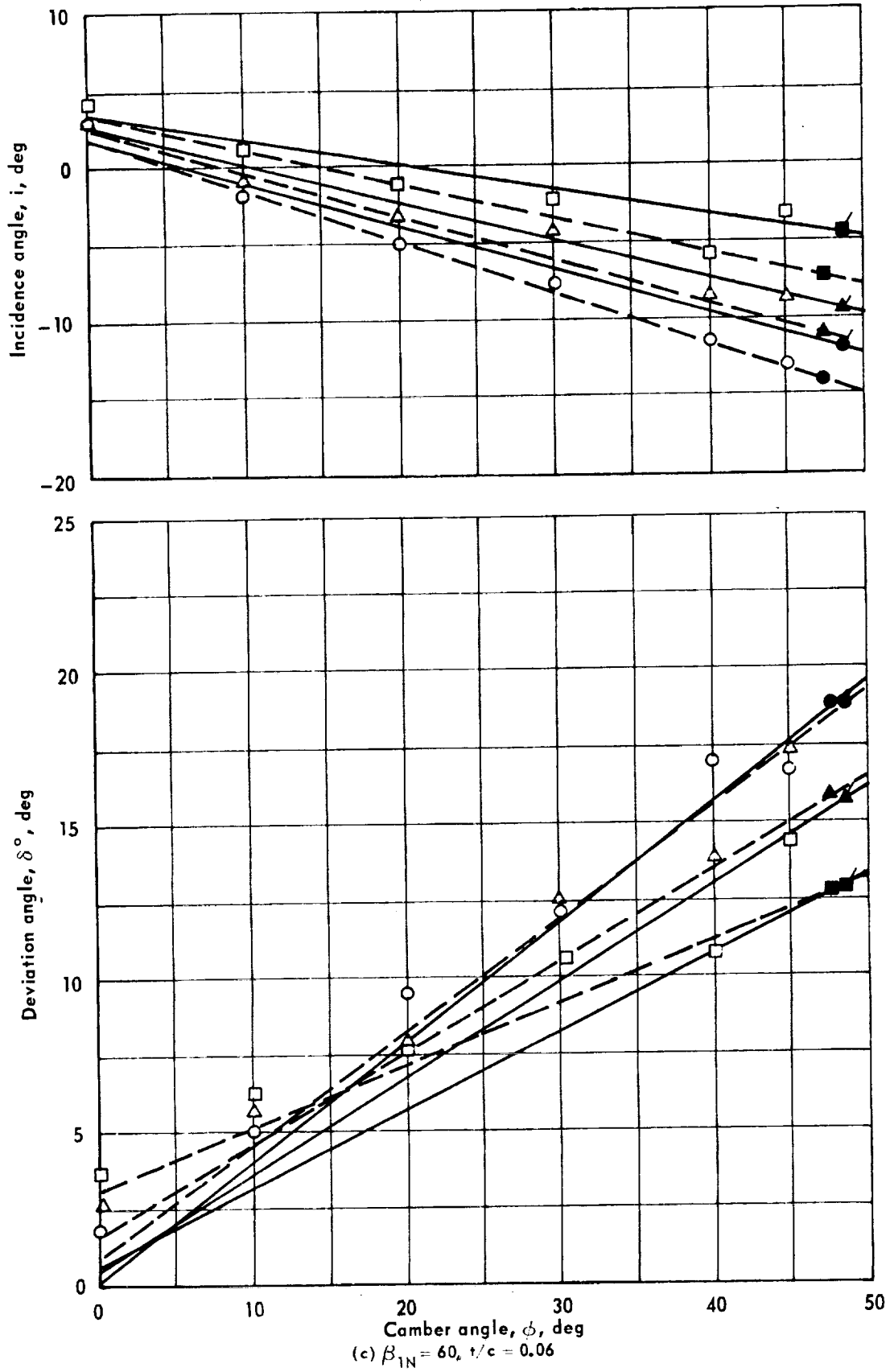
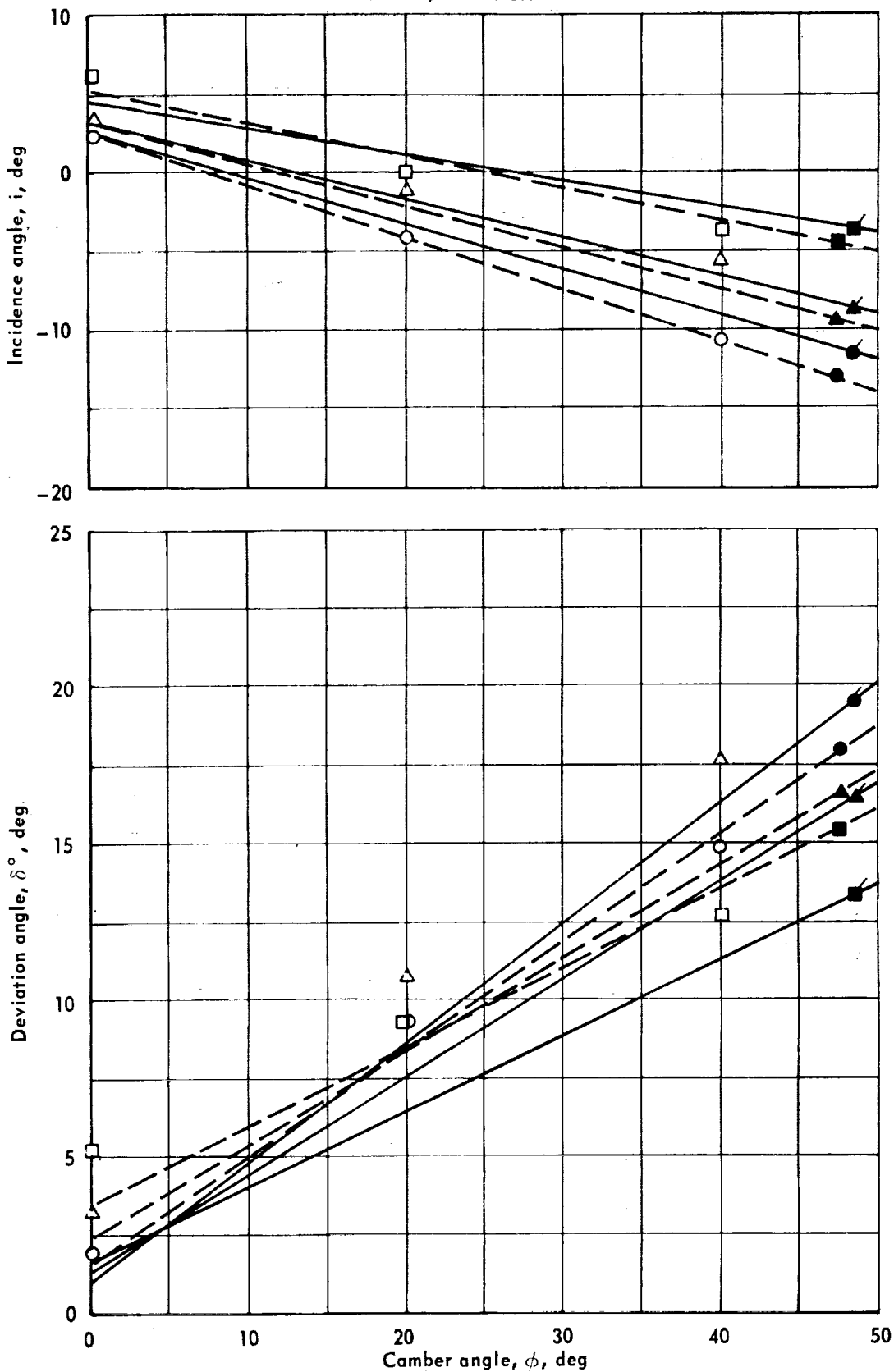


Figure 119. - Continued.

Minimum-loss points	Symbol	Solidity
	○	0.75
	△	1.00
	□	1.50

— Solid symbols Ref. 4 correlation (flagged)
 - - - Solid symbols DCA correlation

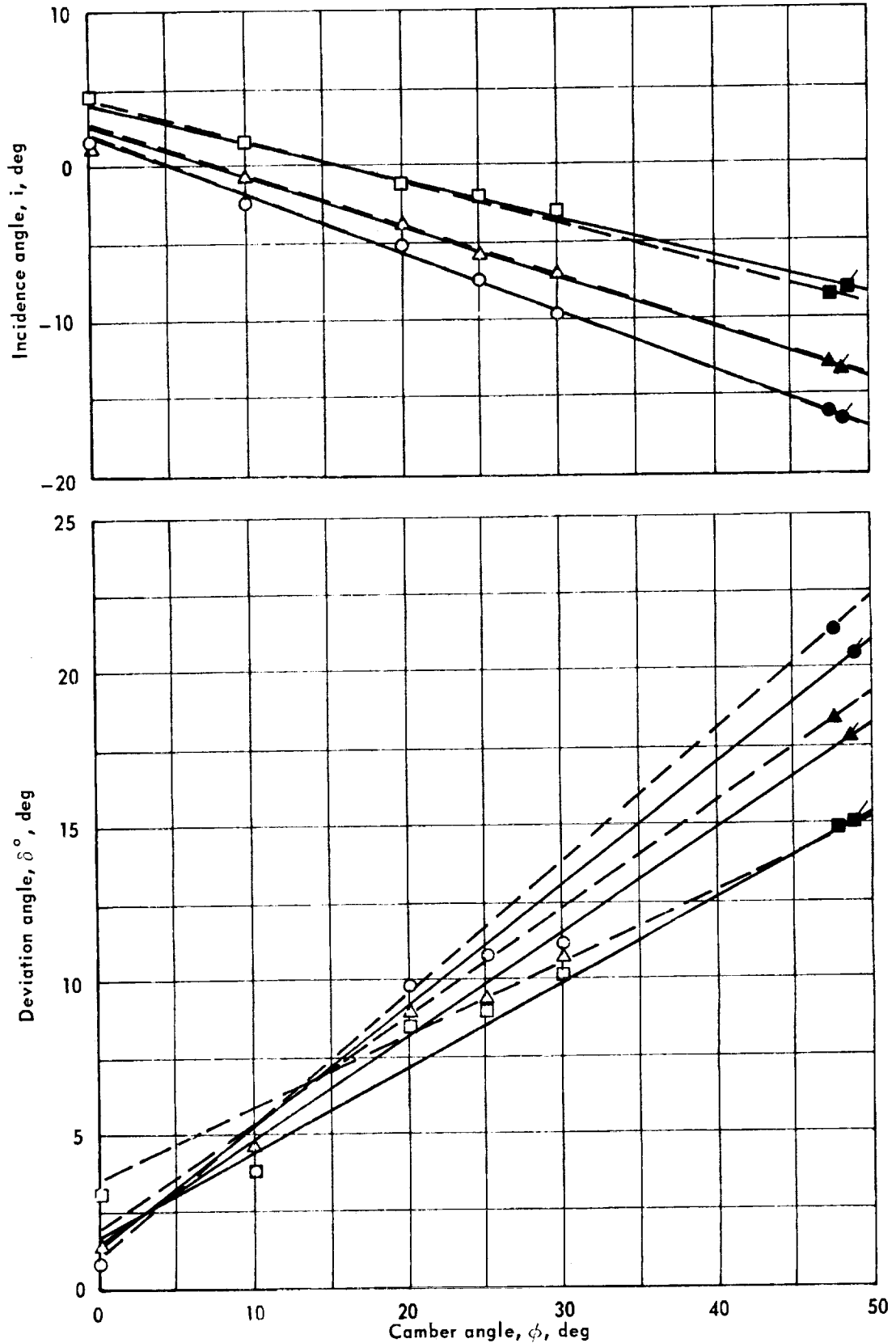


(d) $\beta_{1N} = 60^\circ$, $t/c = 0.10$

Figure 119. - Continued.

Minimum - loss points	Symbol	Solidity
	○	0.75
	△	1.00
	□	1.50

— Solid symbols Ref. 4 correlation (flagged)
 - - - Solid symbols DCA correlation

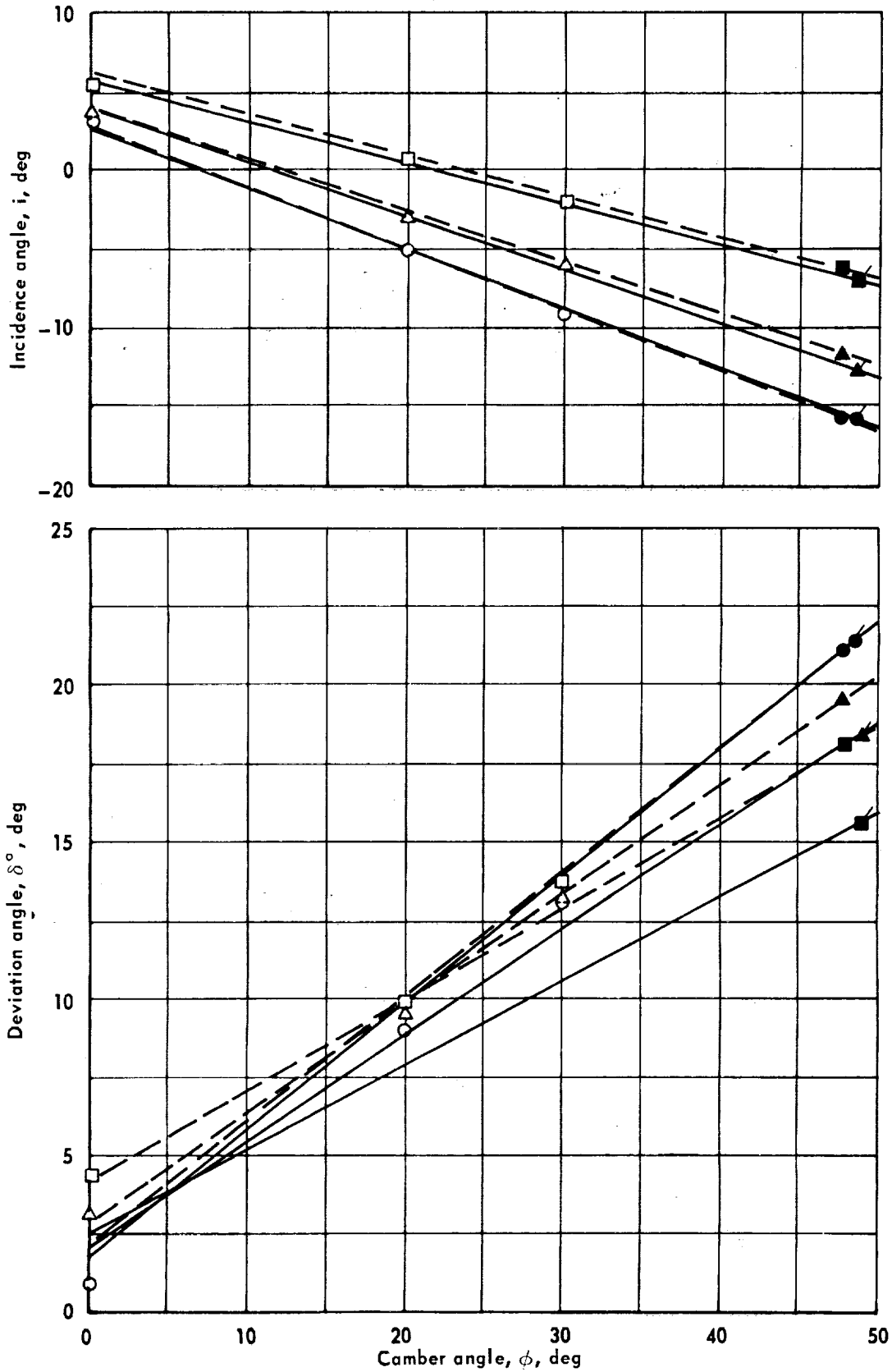


(e) $\beta_{1N} = 70$, $t/c = 0.06$

Figure 119. - Continued.

Minimum-loss points	Symbol	Solidity
	○	0.75
	△	1.00
	□	1.50

— Solid symbols Ref. 4 correlation (flagged)
 - - - Solid symbols DCA correlation

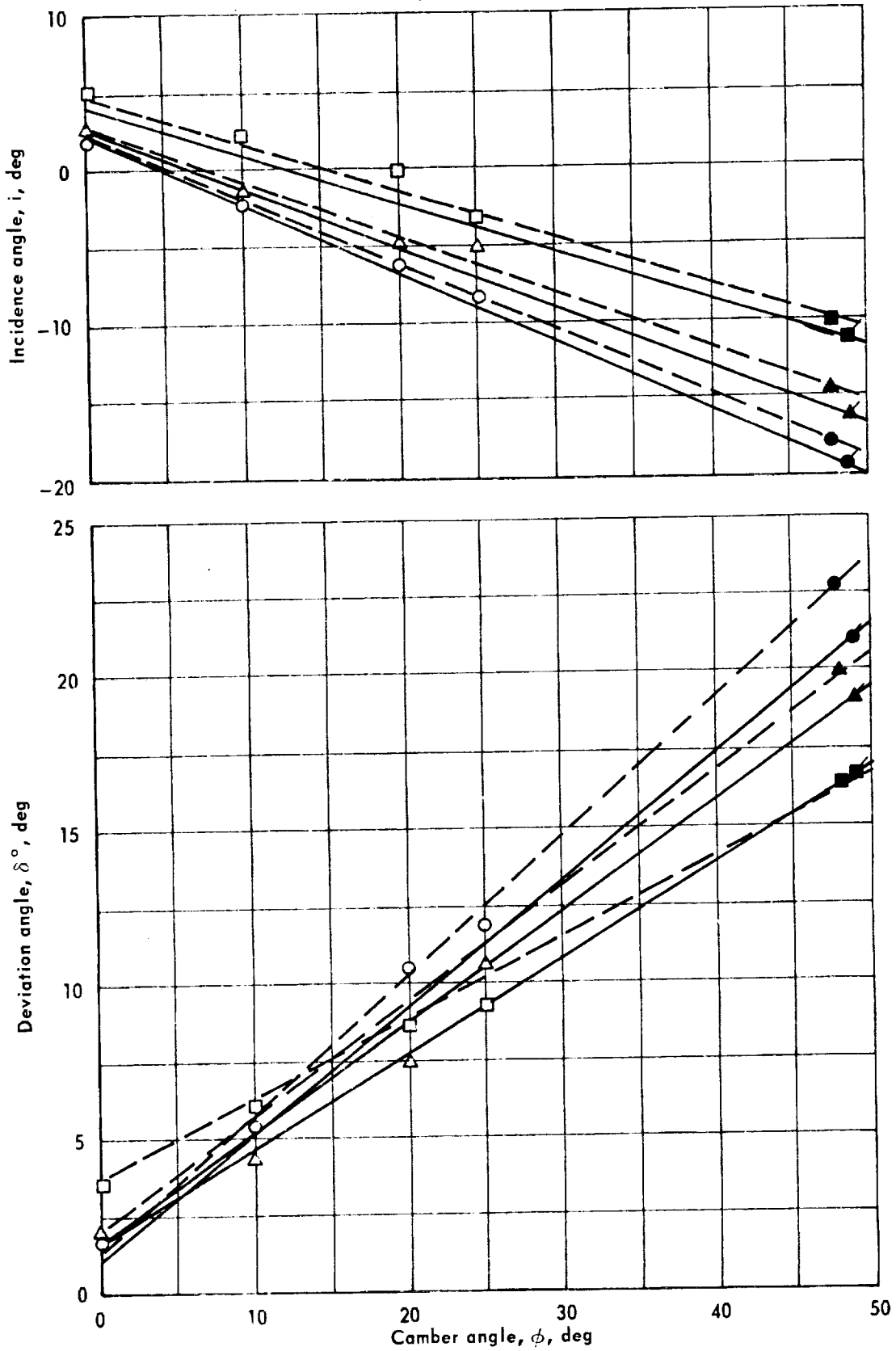


(†) $\beta_{IN} = 70$, $t/c = 0.10$

Figure 119. - Continued.

Minimum-loss points	Symbol	Solidity
	○	0.75
△	1.00	
□	1.50	

— Solid symbols Ref. 4 correlation (flagged)
 - - - Solid symbols DCA correlation

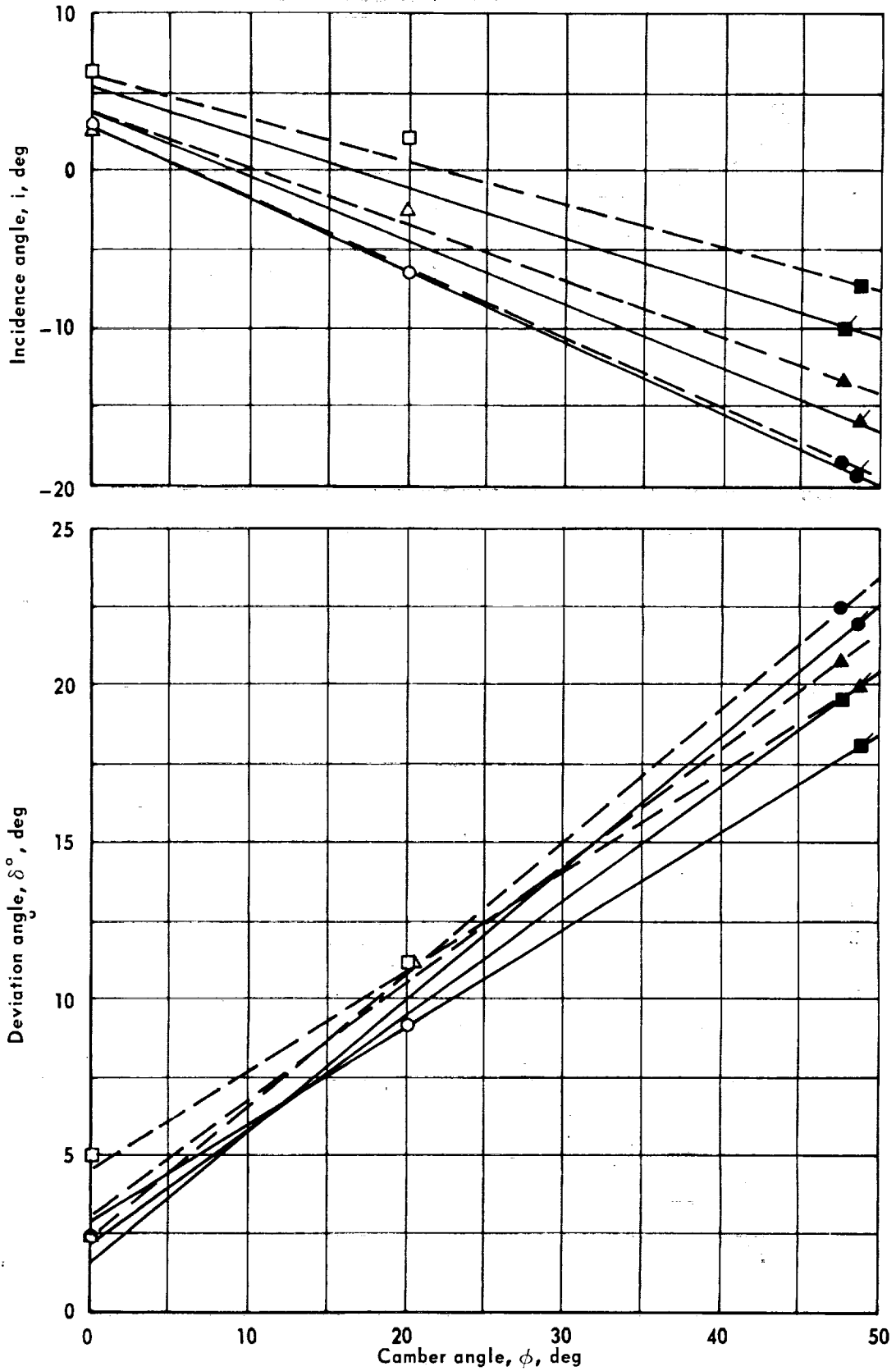


(g) $\beta_{IN} = 75$, $1/c = 0.06$

Figure 119. - Continued.

Minimum-loss points	Symbol	Solidity
	○	0.75
	△	1.00
	□	1.50

— Solid symbols Ref. 4 correlation (flagged)
 - - - Solid symbols DCA correlation



(h) $\beta_{IN} = 75, \nu/c = 0.10$

Figure 119. - Concluded.

DISTRIBUTION LIST FOR VOL. 1 - FINAL REPORT

CONTRACT NAS3-4184

<u>REPORT</u>	<u>COPIES</u>	<u>RECIPIENT</u>	<u>DESIGNEE</u>
<u>R</u>	<u>D</u>		
		National Aeronautics & Space Administration Lewis Research Center 21000 Brookpark Road Cleveland, Ohio 44135	
	1	Attn: Contracting Officer, MS 500-313	
	5	Liquid Rocket Technology Branch, MS 500-209	
	1	Technical Report Control Office, MS 5-5	
	1	Technology Utilization Office, MS 3-16	
	2	AFSC Liaison Office, MS 4-1	
	2	Library	
	1	Office of Reliability & Quality Assurance, MS 500-111	
	1	D. L. Nored, Chief, LRTB, MS 500-209	
	5	<u>W. R. Britsch</u> Project Manager, MS 500-209	
	1	E. W. Conrad, MS 500-204	
	1	R. H. Kemp, MS 49-1	
	4	M. J. Hartman, MS-5-9	
	2	W. A. Benser, MS-5-9	
	1	L. J. Herrig, MS-7-1	
	1	S. Lieblein, MS-100-1	
	1	B. Connelly, MS-501-1	
	2	Chief, Liquid Experimental Engineering, RPX Office of Advanced Research & Technology NASA Headquarters Washington, D. C. 20546	
	2	Chief, Liquid Propulsion Technology, RPL Office of Advanced Research & Technology NASA Headquarters Washington, D. C. 20546	

